

Quakes and wastewater
injection rates pp. 1299 & 1336

Early foundations for neural
crest cells pp. 1316 & 1332

A Middle East free of
nuclear weapons p. 1320

Science

\$10
19 JUNE 2015
sciencemag.org

AAAS

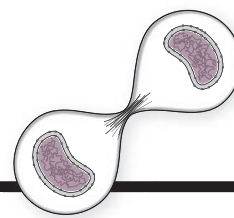
Follow the leader?

Group decisions are
democratic in olive
baboons p. 1358



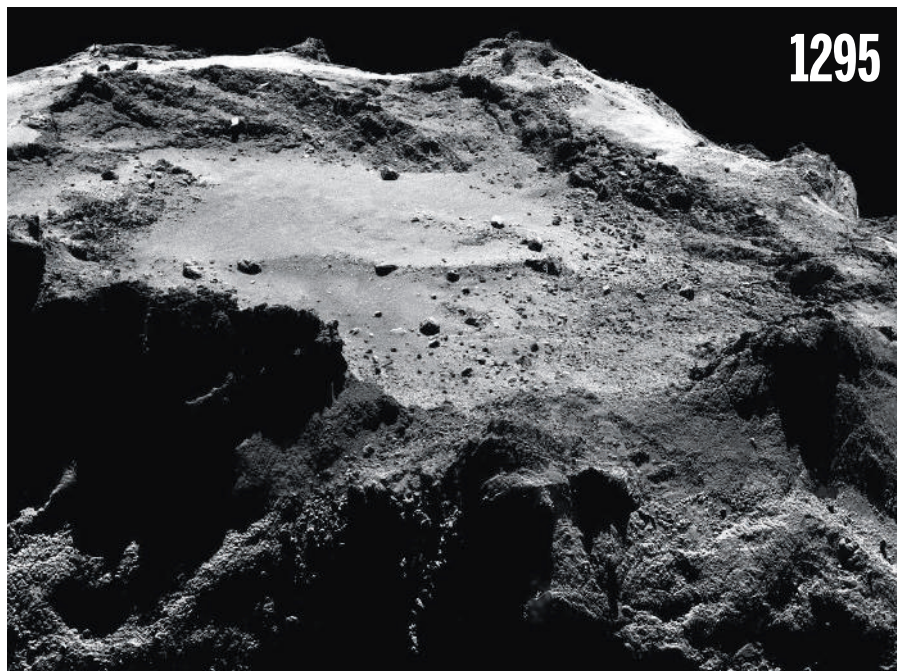
CONTENTS

19 JUNE 2015 • VOLUME 348 • ISSUE 6241



1314

Sealing the
nuclear envelope



1295

NEWS

IN BRIEF

1292 Roundup of the week's news

IN DEPTH

1295 THE RETURN OF PHILAE

Revived after hibernation, comet lander awaits orders *By E. Hand and D. Clery*

1296 RESEARCH CHIMPS WILL SOON BE LISTED AS 'ENDANGERED'

Ruling could disrupt biomedical research *By D. Grimm*

1297 DESIGNER PROTEINS PRODUCE POTENT HIV DEFENSE

AIDS vaccine developers mimic natural route to powerful immune responses *By J. Cohen*

► *SCIENCE EXPRESS* RESEARCH ARTICLES BY
R. W. SANDERS ET AL. 10.1126/science.aac4223
and J. G. JARDINE ET AL. 10.1126/science.aac5894

1298 REPUBLICANS SPLIT ON CLIMATE, SOCIAL SCIENCE SPENDING

House calls for cuts, Senate favors status quo *By J. Mervis*

1299 PUMPED UP TO RUMBLE

Massive studies of wastewater injection wells show fast pumping raises earthquake risk *By J. Rosen*

► REPORT P. 1336; *SCIENCE ADVANCES*
RESEARCH ARTICLE BY F. R. WALSH III ET AL.

FEATURES

1300 LAST DANCE?

An urgent effort to save the West's iconic lesser prairie chicken could point the way to a truce in other endangered-species battles *By M. Lavelle*

1304 Sage grouse war tests limits of partnership in West

By M. Lavelle

► VIDEO



1322 & 1331

INSIGHTS

BOOKS ET AL.

1306 SUMMER READING

Eight book reviews from postdocs and grad students

PERSPECTIVES

1312 WHEN THE HUNTER BECOMES THE HUNTED

Effective predator management relies on social acceptability as well as scientific evidence *By R. Woodroffe and S. M. Redpath*

1314 AN ESCRT TO SEAL THE ENVELOPE

Cellular machinery that remodels different lipid bilayers also closes the nuclear membrane *By W. I. Sundquist and K. S. Ullman*

1316 IT'S ABOUT TIME FOR NEURAL CREST

The unusual pluripotency of neural crest cells is inherited from embryonic stem cells *By S. Hoppler and G. N. Wheeler*

► RESEARCH ARTICLE P. 1332

1317 OUTPERFORMING NATURE'S MEMBRANES

Ultrathin synthetic membranes that reach a record permeability can clean up organic solutions *By V. Freger*

► REPORT P. 1347

1319 ARE YOU WATERING YOUR LAWN?

High-resolution data may help to devise effective water conservation strategies in urban areas around the world

By T. S. Hogue and S. Pincetl

1320 AFTER THE IRAN DEAL: MULTINATIONAL ENRICHMENT

World powers should buy a stake in Iran's enrichment capacity and accept the same rules *By A. Glaser et al.*

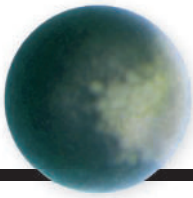
1322 A CHLAMYDIA VACCINE ON THE HORIZON

Results of a new *Chlamydia* vaccine in mice should spur human clinical trials

By R. C. Brunham

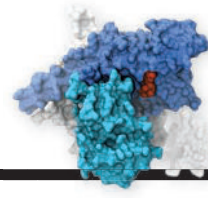
► RESEARCH ARTICLE P. 1331

Science Staff	1290
New Products	1383
Science Careers	1384



1316 & 1332

Neural crest cells retain their origins



1361

Relaying a signal to a G protein

1324 JOHN FORBES NASH JR. (1928–2015)

A distinguished mathematician and Nobel laureate dies tragically
By M. Shubik

LETTERS

1325 GERMLINE GENE THERAPY: WE'RE READY

By H. I. Miller

1325 RESEARCH ETHICS AND HEALTH CARE REFORM

By J. G. Kahn and P. Hofmann

1326 SPITZER'S STELLAR WORK

By M. W. Werner et al.

1326 TECHNICAL COMMENT ABSTRACTS

RESEARCH

IN BRIEF

1327 From *Science* and other journals

REVIEW

1330 OCEAN CIRCULATION

Observing the Atlantic Meridional Overturning Circulation yields a decade of inevitable surprises *M. A. Srokosz and H. L. Bryden*

REVIEW SUMMARY; FOR FULL TEXT:
[dx.doi.org/10.1126/science.1255575](https://doi.org/10.1126/science.1255575)

RESEARCH ARTICLES

1331 VACCINES

A mucosal vaccine against *Chlamydia trachomatis* generates two waves of protective memory T cells *G. Stary et al.*

RESEARCH ARTICLE SUMMARY; FOR FULL TEXT:
[dx.doi.org/10.1126/science.aaa8205](https://doi.org/10.1126/science.aaa8205)
► PERSPECTIVE P. 1322

1332 NEURODEVELOPMENT

Shared regulatory programs suggest retention of blastula-stage potential in neural crest cells *E. Buitrago-Delgado et al.*

► PERSPECTIVE P. 1316

REPORTS

1336 INDUCED SEISMICITY

High-rate injection is associated with the increase in U.S. mid-continent seismicity *M. Weingarten et al.*

► NEWS STORY P. 1299; *SCIENCE ADVANCES*
RESEARCH ARTICLE BY F. R. WALSH III ET AL.

1340 POLARON DYNAMICS

Long-lived photoinduced polaron formation in conjugated polyelectrolyte-fullerene assemblies *R. C. Huber et al.*

1344 BATTERIES

Topological defect dynamics in operando battery nanoparticles *A. Ulvestad et al.*

1347 MEMBRANE FILTRATION

Sub-10 nm polyamide nanofilms with ultrafast solvent transport for molecular separation *S. Karan et al.*

► PERSPECTIVE P. 1317

1352 BRAIN PROCESSING

Cortical information flow during flexible sensorimotor decisions *M. Siegel et al.*

1355 COMETARY NUCLEI

The shape and structure of cometary nuclei as a result of low-velocity accretion *M. Jutzi and E. Asphaug*

1358 GROUP DECISIONS

Shared decision-making drives collective movement in wild baboons *A. Strandburg-Peshkin et al.*

1361 SIGNAL TRANSDUCTION

Structural basis for nucleotide exchange in heterotrimeric G proteins *R. O. Dror et al.*

1365 PROTEIN DESIGN

Design of ordered two-dimensional arrays mediated by noncovalent protein-protein interfaces *S. Gonen et al.*

1369 ENDOCYTOSIS

Endocytic sites mature by continuous bending and remodeling of the clathrin coat *O. Avinoam et al.*

1372 TRANSCRIPTION

Recruitment of RNA polymerase II by the pioneer transcription factor PHA-4 *H.-T. Hsu et al.*

1376 DRUG DEVELOPMENT

Phthalimide conjugation as a strategy for in vivo target protein degradation *G. E. Winter et al.*



DEPARTMENTS

1291 EDITORIAL

Parks for science

By Gary Machlis and Marcia McNutt

1394 WORKING LIFE

Do it for love

By Marek Wagner

ON THE COVER



Olive baboon (*Papio anubis*) troops travel many kilometers each day as a group, remaining together even though group members often disagree about when and where to move.

High-resolution GPS tracking of almost all members of a single baboon troop reveals that movement decisions are shared, and despite differences in rank and social status among group mates, no single individual dominates these choices. See page 1358.

Photo: Manoj Shah/Getty Images

SCIENCE (ISSN 0036-8075) is published weekly on Friday, except the last week in December, by the American Association for the Advancement of Science, 1200 New York Avenue, NW, Washington, DC 20005. Periodicals mail postage (publication No. 484460) paid at Washington, DC, and additional mailing offices. Copyright © 2015 by the American Association for the Advancement of Science. The title SCIENCE is a registered trademark of the AAAS. Domestic individual membership and subscription (51 issues): \$153 (\$74 allocated to subscription). Domestic institutional subscription (51 issues): \$1282. Foreign postage extra: Mexico, Caribbean (surface mail) \$55; other countries (air assist delivery) \$85. First class, airmail, student, and emeritus rates on request. Canadian rates with GST available upon request. GST #R1254 88122. Publications Mail Agreement Number 1069624. Printed in the U.S.A. Change of address: Allow 4 weeks, giving old and new addresses and 8-digit account number. Postmaster: Send change of address to AAAS, P.O. Box 96178, Washington, DC 20090-6178. Single-copy sales: \$10.00 current issue, \$15.00 back issue prepaid includes surface postage; bulk rates on request. Authorization to photocopy material for internal or personal use under circumstances not falling within the fair use provisions of the Copyright Act is granted by AAAS to libraries and other users registered with the Copyright Clearance Center (CCC) Transactional Reporting Service, provided that \$30.00 per article is paid directly to CCC, 222 Rosewood Drive, Danvers, MA 01923. The identification code for Science is 0036-8075. Science is indexed in the Reader's Guide to Periodical Literature and in several specialized indexes.

Editor-in-Chief Marcia McNutt

Executive Editor Monica M. Bradford **News Editor** Tim Appenzeller

Managing Editor, Research Journals Katrina L. Kelner

Deputy Editors Barbara R. Jasny, Andrew M. Sugden(UK), Valda J. Vinson, Jake S. Yeston

Research and Insights

SR. EDITORS Caroline Ash(UK), Gilbert J. Chin, Lisa D. Chong, Julia Fahrenkamp-Uppenbrink(UK), Pamela J. Hines, Stella M. Hurlley(UK), Paula A. Kiberstis, Marc S. Lavine(Canada), Kristen L. Mueller, Ian S. Osborne(UK), Beverly A. Purnell, L. Bryan Ray, Guy Riddihough, H. Jesse Smith, Jelena Stajic, Peter Stern(UK), Phillip D. Szurmi, Brad Wible, Nicholas S. Wigginton, Laura M. Zahn **ASSOCIATE EDITORS** Brent Grocholski, Sacha Vignieri **ASSOCIATE BOOK REVIEW EDITOR** Valerie B. Thompson **ASSOCIATE LETTERS EDITOR** Jennifer Sills **CHIEF CONTENT PRODUCTION EDITOR** Cara Tate **SR. CONTENT PRODUCTION EDITORS** Harry Jach **CONTENT PRODUCTION EDITORS** Jeffrey E. Cook, Chris Filiatreau, Cynthia Howe, Lauren Krmec, Barbara P. Ordway **SR. EDITORIAL COORDINATORS** Carolyn Kyle, Beverly Shields **EDITORIAL COORDINATORS** Ramatoulaye Diop, J. S. Granger, Lisa Johnson, Anita Wynn **PUBLICATIONS ASSISTANTS** Aneera Dobbins, Jeffrey Hearn, Dona Mathieu, Le-Toya Mayne Fod, Shannon McMahon, Scott Miller, Jerry Richardson, Rachel Roberts(UK), Alice Whaley(UK), Brian White **EXECUTIVE ASSISTANT** Anna Bashkirova **ADMINISTRATIVE SUPPORT** Janet Clements(UK), Monika Magon(UK, Intern), Lizanne Newton(UK), Maryrose Madrid, John Wood(UK)

News

NEWS MANAGING EDITOR John Travis **INTERNATIONAL EDITOR** Richard Stone **DEPUTY NEWS EDITORS** Daniel Clery(UK), Robert Coontz, Elizabeth Culotta, David Grimm, David Malakoff, Leslie Roberts **CONTRIBUTING EDITOR** Martin Enserink(Europe) **SR. CORRESPONDENTS** Jeffrey Mervis, Elizabeth Pennisi **NEWS WRITERS** Adrian Cho, Jon Cohen, Jennifer Couzin-Frankel, Carolyn Gramling, Eric Hand, Jocelyn Kaiser, Catherine Maticic, Kelly Servick, Robert F. Service, Erik Stokstad(Cambridge, UK), Emily Underwood **INTERNS** Emily Conover, Emily DeMarco **CONTRIBUTING CORRESPONDENTS** Michael Balter(Paris), John Bohannon, Ann Gibbons, Mara Hvistendahl, Sam Kean, Richard A. Kerr, Eli Kintisch, Kai Kupferschmidt(Berlin), Andrew Lawler, Christina Larson(Beijing), Mitch Leslie, Charles C. Mann, Eliot Marshall, Virginia Morell, Dennis Normile(Tokyo), Heather Pringle, Tania Rabesandratana(London), Gretchen Vogel(Berlin), Lizzie Wade(Mexico City) **CAREERS** Jim Austin(Editor), Donisha Adams, Rachel Bernstein **COPY EDITORS** Kara Estelle (Chief), Julia Cole, Jennifer Levin **ADMINISTRATIVE SUPPORT** Jessica Williams

Executive Publisher Rush D. Holt

Publisher Kent R. Anderson **Chief Digital Media Officer** Rob Covey

BUSINESS OPERATIONS AND ADMINISTRATION DIRECTOR Sarah Whalen **BUSINESS SYSTEMS AND FINANCIAL ANALYSIS DIRECTOR** Randy Yi **MANAGER OF FULFILLMENT SYSTEMS** Neal Hawkins **SYSTEMS ANALYST** Nicole Mehmedovich **ASSISTANT DIRECTOR, BUSINESS OPERATIONS** Eric Knott **MANAGER, BUSINESS OPERATIONS** Jessica Tierney **BUSINESS ANALYSTS** Cory Lipman, Cooper Tilton, Celeste Troxler **FINANCIAL ANALYST** Robert Clark **RIGHTS AND PERMISSIONS ASSISTANT DIRECTOR** Emilie David **PERMISSIONS ASSOCIATE** Elizabeth Sandler **RIGHTS, CONTRACTS, AND LICENSING ASSOCIATE** Lili Kiser

MARKETING DIRECTOR Ian King **MARKETING MANAGER** Julianne Wielga **MARKETING ASSOCIATE** Elizabeth Sattler **SR. MARKETING EXECUTIVE** Jennifer Reeves **SR. ART ASSOCIATE, PROJECT MANAGER** Tzeitel Sorrosor **ART ASSOCIATE** Seil Lee **JR. ART ASSOCIATE** Kim Huynh **ASSISTANT COMMERCIAL EDITOR** Selby Frame **MARKETING PROJECT MANAGER** Angelissa McArthur **PROGRAM DIRECTOR, AAAS MEMBER CENTRAL** Peggy Mihelich **FULFILLMENT SYSTEMS AND OPERATIONS** membership@aaas.org **MANAGER, MEMBER SERVICES** Pat Butler **SPECIALISTS** LaToya Casteel, Terrance Morrison, Latasha Russell **MANAGER, DATA ENTRY** Mickie Napoleoni **DATA ENTRY SPECIALISTS** JJ Regan, Brenden Aquilino, Fiona Giblin

DIRECTOR, SITE LICENSING Tom Ryan **DIRECTOR, CORPORATE RELATIONS** Eileen Bernadette Moran **SR. PUBLISHER RELATIONS SPECIALIST** Kiki Forsythe **PUBLISHER RELATIONS MANAGER** Catherine Holland **PUBLISHER RELATIONS, EASTERN REGION** Keith Layson **PUBLISHER RELATIONS, WESTERN REGION** Ryan Rexroth **SALES RESEARCH COORDINATOR** Aiesha Marshall **MANAGER, SITE LICENSE OPERATIONS** Iquo Edim **SENIOR PRODUCTION SPECIALIST** Robert Koepke **SENIOR OPERATIONS ANALYST** Lana Guz **FULFILLMENT ASSISTANT** Judy Lillibridge **ASSOCIATE DIRECTOR, MARKETING** Christina Schlecht **MARKETING ASSOCIATES** Thomas Landreth, Isa Sesay-Bah

DIRECTOR OF WEB TECHNOLOGIES Ahmed Khadr **SR. DEVELOPER** Chris Coleman **DEVELOPERS** Dan Berger, Jimmy Marks **SR. PROJECT MANAGER** Trista Smith **SYSTEMS ENGINEER** Luke Johnson

CREATIVE DIRECTOR, MULTIMEDIA Martyn Green **DIRECTOR OF ANALYTICS** Enrique Gonzales **SR. WEB PRODUCER** Sarah Crespi **WEB PRODUCER** Alison Crawford **VIDEO PRODUCER** Nguyen Nguyen **SOCIAL MEDIA PRODUCER** Meghna Sachdev

DIRECTOR OF OPERATIONS PRINT AND ONLINE Lizabeth Harman **DIGITAL/PRINT STRATEGY MANAGER** Jason Hillman **QUALITY TECHNICAL MANAGER** Marcus Spiegler **DIGITAL PRODUCTION MANAGER** Lisa Stanford **ASSISTANT MANAGER DIGITAL/PRINT** Rebecca Doshi **DIGITAL MEDIA SPECIALIST** Tara Kelly **SENIOR CONTENT SPECIALISTS** Steve Forrester, Antoinette Hodal, Lori Murphy, Anthony Rosen **CONTENT SPECIALISTS** Jacob Hedrick, Kimberley Oster

DESIGN DIRECTOR Beth Rakouskas **DESIGN EDITOR** Marcy Atarod **SENIOR SCIENTIFIC ILLUSTRATORS** Chris Bickel, Katharine Sutfitt **SCIENTIFIC ILLUSTRATOR** Valerie Altounian **SENIOR ART ASSOCIATES** Holly Bishop, Preston Huey **SENIOR DESIGNER** Garvin Grullón **DESIGNER** Chrystal Smith **SENIOR PHOTO EDITOR** William Douthitt **PHOTO EDITORS** Leslie Blizard, Christy Steele

DIRECTOR, GLOBAL COLLABORATION, CUSTOM PUBLICATIONS, ADVERTISING Bill Moran **EDITOR, CUSTOM PUBLISHING** Sean Sanders: 202-326-6430 **ASSISTANT EDITOR, CUSTOM PUBLISHING** Tianna Hicklin: 202-326-6463 **ADVERTISING MARKETING MANAGER** Justin Sawyers: 202-326-7061 **science_advertising@aaas.org** **ADVERTISING MARKETING ASSOCIATE** Javia Flemmings **ADVERTISING SUPPORT MANAGER** Karen Foote: 202-326-6740 **ADVERTISING PRODUCTION OPERATIONS MANAGER** Deborah Tompkins **SR. PRODUCTION SPECIALIST/GRAPHIC DESIGNER** Amy Hardcastle **PRODUCTION SPECIALIST** Yuse Lajiminmuhup **SR. TRAFFIC ASSOCIATE** Christine Hall **SALES COORDINATOR** Shirley Young **ASSOCIATE DIRECTOR, COLLABORATION, CUSTOM PUBLICATIONS/CHINA/TAIWAN/KOREA/SINGAPORE** Ruolei Wu: +86-386 0822 9345, rwu@aaas.org **COLLABORATION/CUSTOM PUBLICATIONS/JAPAN** Adarsh Sandhu + 81532-81-5142 asandhu@aaas.org **EAST COAST/E. CANADA** Laurie Faraday: 508-747-9395, FAX 617-507-8189 **WEST COAST/W. CANADA** Lynne Stickrod: 415-931-9782, FAX 415-520-6940 **MIDWEST** Jeffrey Dembski: 847-498-4520 x3005, Steven Loerch: 847-498-4520 x3006 **UK EUROPE/ASIA** Roger Goncalves: TEL/FAX +41 43 243 1358 **JAPAN** Katsuyoshi Fukamizu(Tokyo): +81-3-3219-5777 fukamizu@aaas.org **CHINA/TAIWAN** Ruolei Wu: +86-0082-9345

WORLDWIDE ASSOCIATE DIRECTOR OF SCIENCE CAREERS Tracy Holmes: +44 (0) 1223 326525, FAX +44 (0) 1223 326532 tholmes@science-int.co.uk **CLASSIFIED** advertise@sciencecareers.org **U.S. SALES** Tina Burks: 202-326-6577, Nancy Toema: 202-326-6578 **SALES ADMINISTRATOR** Marci Gallun **EUROPE/ROW SALES** Alex Gesatzki, Sarah Lelarge **SALES ASSISTANT** Kelly Grace **JAPAN** Hiroyuki Mashiki(Kyoto): +81-75-823-1109 hmashiki@aaas.org **CHINA/TAIWAN** Ruolei Wu: +86-186 0082 9345 rwu@aaas.org **MARKETING MANAGER** Allison Pritchard **MARKETING ASSOCIATE** Aimee Aponte

AAAS BOARD OF DIRECTORS **RETIRING PRESIDENT, CHAIR** Gerald R. Fink **PRESIDENT** Geraldine (Geri) Richmond **PRESIDENT-ELECT** Barbara A. Schaaf **TREASURER** David Evans **SHAW CHIEF EXECUTIVE OFFICER** Rush D. Holt **BOARD** Bonnie L. Bassler, May R. Berenbaum, Carlos J. Bustamante, Stephen P.A. Fodor, Claire M. Fraser, Michael S. Gazzaniga, Laura H. Greene, Elizabeth Loftus, Mercedes Pascual

SUBSCRIPTION SERVICES For change of address, missing issues, new orders and renewals, and payment questions: 866-434-AAAS (2227) or 202-326-6417, FAX 202-842-1065. Mailing addresses: AAAS, P.O. Box 96178, Washington, DC 20090-6178 or AAAS Member Services, 1200 New York Avenue, NW, Washington, DC 20005

INSTITUTIONAL SITE LICENSES 202-326-6755 **REPRINTS:** Author Inquiries 800-635-7181 **COMMERCIAL INQUIRIES** 803-359-4578 **PERMISSIONS** 202-326-6765, permissions@aaas.org **AAAS Member Services** 202-326-6417 or http://membercentral.aaas.org/discounts

Science serves as a forum for discussion of important issues related to the advancement of science by publishing material on which a consensus has been reached as well as including the presentation of minority of conflicting points of view. Accordingly, all articles published in Science—including editorials, news and comment, and books reviews—are signed and reflect the individual views of the authors and not official points of view adopted by AAAS or the institutions with which the authors are affiliated.

INFORMATION FOR AUTHORS See pages 678 and 679 of the 6 February 2015 issue or access www.sciencemag.org/about/authors

SENIOR EDITORIAL BOARD

Gary King, Harvard University
Susan M. Rosenberg, Baylor College of Medicine, Ali Shilatifard, Northwestern University
Feinberg School of Medicine, Michael S. Turner, U. of Chicago

BOARD OF REVIEWING EDITORS (Statistics board members indicated with \$)

Adriano Aguzzi, U. Hospital Zürich
Takuzo Aida, U. of Tokyo
Leslie Aiello, Wenner-Gren Foundation
Judith Allen, U. of Edinburgh
Sonia Altizer, U. of Georgia
Sebastian Amigorena, Institut Curie
Kathryn Anderson, Memorial Sloan-Kettering Cancer Center
Meinrat O. Andreae, Max-Planck Inst. Mainz
Paola Arolta, Harvard U.
Johan Auwerx, EPFL
David Awschalom, U. of Chicago
Jordi Bascompte, Estación Biológica de Doñana CSIC
Facundo Batista, London Research Inst.
Ray H. Baughman, U. of Texas, Dallas
David Baum, U. of Wisconsin
Carlo Beenakker, Leiden U.
Kamran Behnia, ESPCI-ParisTech
Yasmine Belkaid, NIAID/NIH
Philip Benfey, Duke U.
Stephen J. Benkovic, Penn State U.
May Berenbaum, U. of Illinois
Gabriele Bergers, U. of California, San Francisco
Bradley Bernstein, Massachusetts General Hospital
Peer Bork, EMBL
Bernard Bourdon, Ecole Normale Supérieure de Lyon
Chris Bowler, Ecole Normale Supérieure
Ian Boyd, U. of St. Andrews
Emily Brodsky, U. of California, Santa Cruz
Ron Brookmeyer, U. of California Los Angeles (\$) **Christian Büchel**, U. Hamburg-Eppendorf
Joseph A. Burns, Cornell U.
Gyorgy Buzsaki, New York U. School of Medicine
Blanche Capel, Duke U.
Mats Carlsson, U. of Oslo
David Clapham, Children's Hospital Boston
David Clary, U. of Oxford
Joel Cohen, Rockefeller U., Columbia U.
James Collins, Boston U.
Robert Cook-Deegan, Duke U.
Alan Cowman, Walter & Eliza Hall Inst.
Robert H. Crabtree, Yale U.
Roberta Croce, Vrije Universiteit
Janet Currie, Princeton U.
Jeff L. Dangl, U. of North Carolina
Tom Daniel, U. of Washington
Frans de Waal, Emory U.
Stanislas Dehaene, Collège de France
Robert Desimone, MIT
Claude Desplan, New York U.
Ap Dijksterhuis, Radboud U. of Nijmegen
Dennis Discher, U. of Pennsylvania
Gerald W. Dorn II, Washington U. School of Medicine
Jennifer A. Doudna, U. of California, Berkeley
Bruce Dunn, U. of California, Los Angeles
Christopher Dye, WHO
Todd Ehlers, U. of Tuebingen
David Ehrhardt, Carnegie Inst. of Washington
Tim Elston, U. of North Carolina at Chapel Hill
Gerhard Ertl, Fritz-Haber-Institut, Berlin
Barry Everitt, U. of Cambridge
Ernst Fehr, U. of Zurich
Anne C. Ferguson-Smith, U. of Cambridge
Michael Feuer, The George Washington U.
Toren Finkel, NHLBI, NIH
Kate Fitzgerald, U. of Massachusetts
Peter Fratzl, Max-Planck Inst.
Elaine Fuchs, Rockefeller U.
Daniel Geschwind, UCLA
Andrew Gewirth, U. of Illinois
Karl-Heinz Glassmeier, TU Braunschweig
Ramon Gonzalez, Rice U.
Julia R. Greer, Caltech
Elizabeth Grove, U. of Chicago
Nicolas Gruber, ETH Zurich
Kip Guy, St. Jude's Children's Research Hospital
Taekjip Ha, U. of Illinois at Urbana-Champaign
Christian Haass, Ludwig Maximilians U.
Steven Hahn, Fred Hutchinson Cancer Research Center
Michael Hasselmo, Boston U.
Martin Heimann, Max-Planck Inst. Jena
Yka Helariutta, U. of Cambridge
James A. Hendler, Rensselaer Polytechnic Inst.
Janet G. Hering, Swiss Fed. Inst. of Aquatic Science & Technology
Kai-Uwe Hinrichs, U. of Bremen
Kei Hirose, Tokyo Inst. of Technology
David Hodell, U. of Cambridge
David Holden, Imperial College
Lora Hooper, UT Southwestern Medical Ctr. at Dallas
Raymond Huey, U. of Washington
Steven Jacobson, U. of California, Los Angeles
Kai Johnsson, EPFL Lausanne
Peter Jonas, Inst. of Science & Technology (IST) Austria
Matt Kaeblerlein, U. of Washington
William Kaelin Jr., Dana-Farber Cancer Inst.
Daniel Kahne, Harvard U.
Daniel Kammen, U. of California, Berkeley
Masashi Kawasaki, U. of Tokyo
V. N. Kyri, Seoul National U.
Joel Kingsolver, U. of North Carolina at Chapel Hill
Robert Kingston, Harvard Medical School
Etienne Kochlin, Ecole Normale Supérieure
Alexander Koldkin, Johns Hopkins U.
Alberto R. Kornblitt, U. of Buenos Aires
Leonid Kruglyak, UCLA
Thomas Langer, U. of Cologne
Mitchell A. Lazar, U. of Pennsylvania
David Lazer, Harvard U.
Thomas Lecuit, IBDM
Virginia Lee, U. of Pennsylvania
Stanley Lemon, U. of North Carolina at Chapel Hill
Ottoline Leyser, Cambridge U.
Marcia C. Linn, U. of California, Berkeley
Jianguo Liu, Michigan State U.
Luis Liz-Marzan, CIC bioGUNE
Jonathan Losos, Harvard U.
Ke Lu, Chinese Acad. of Sciences
Christian Lüscher, U. of Geneva
Laura Machesky, CRUK Beatson Inst. for Cancer Research
Anne Magurran, U. of St. Andrews
Oscar Marin, CSIC & U. Miguel Hernández
Charles Marshall, U. of California, Berkeley
C. Robertson McClung, Dartmouth College
Graham Medley, U. of Warwick
Tom Misteli, NCI
Yasushi Miyashita, U. of Tokyo
Mary Ann Moran, U. of Georgia
Richard Morris, U. of Edinburgh
Alison Mottisner-Reif, NC State U. (\$) **Sean Munro**, MRC Lab. of Molecular Biology
Thomas Murray, The Hastings Center
James Nelson, Stanford U. School of Med.
Daniel Neumark, U. of California, Berkeley
Kitty Nijmeijer, U. of Twente
Pär Nordlund, Karolinska Inst.
Helga Nowotny, European Research Advisory Board
Ben Olken, MIT
Joe Orenstein, U. of California
Berkeley & Lawrence Berkeley National Lab
Harry Orr, U. of Minnesota
Andrew Oswald, U. of Warwick
Steve Palumbi, Stanford U.
Jane Parker, Max-Planck Inst. of Plant Breeding Research
Giovanni Parmigiani, Dana-Farber Cancer Inst. (\$) **Donald R. Paul**, U. of Texas, Austin
John H. J. Petrini, Memorial Sloan-Kettering Cancer Center
Joshua Plotkin, U. of Pennsylvania
Albert Polman, FOM Institute AMOLF
Philipp Polm, CNRS
Jonathan Prichard, Stanford U.
David Randall, Colorado State U.
Colin Renfrew, U. of Cambridge
Felix Rey, Institut Pasteur
Trevor Robbins, U. of Cambridge
Jim Roberts, Fred Hutchinson Cancer Research Ctr.
Barbara A. Romanowich, U. of California, Berkeley
Jens Rostrup-Nielsen, Haldor Topsøe
Mike Ryan, U. of Texas, Austin
Mittori Saitou, Kyoto U.
Shimon Sakaguchi, Kyoto U.
Miguel Salmeron, Lawrence Berkeley National Lab
Jürgen Sandkühner, Medical U. of Vienna
Alexander Schlier, Harvard U.
Randy Seeley, U. of Cincinnati
Vladimir Shalayev, Purdue U.
Peter Silliciano, Johns Hopkins School of Medicine
Denis Simon, Arizona State U.
Alison Smith, John Innes Centre
Richard Smith, U. of North Carolina (\$) **John Speakman**, U. of Aberdeen
Allan C. Spradling, Carnegie Institution of Washington
Jonathan Sprent, Garvan Inst. of Medical Research
Eric Steig, U. of Washington
Paula Stephan, Georgia State U. and National Bureau of Economic Research
Molly Stevens, Imperial College London
V. S. Subrahmanian, U. of Maryland
Ira Tabas, Columbia U.
Sarah Teichmann, Cambridge U.
John Thomas, North Carolina State U.
Shubha Tole, Tata Institute of Fundamental Research
Christopher Tyler-Smith, The Wellcome Trust Sanger Institute
Herbert Virgin, Washington U.
Bert Vogelstein, Johns Hopkins U.
Cynthia Volkert, U. of Göttingen
Douglas Wallace, Dalhousie U.
David Wallace, Weizmann Inst. of Science
Ian Walmsey, U. of Oxford
Jane-Ling Wang, U. of California, Davis
David A. Wardle, Swedish U. of Agric. Sciences
David Waxman, Fudan U.
Jonathan Weissman, U. of California, San Francisco
Chris Wikle, U. of Missouri (\$) **Ian A. Wilson**, The Scripps Res. Inst. (\$) **Timothy D. Wilson**, U. of Virginia
Rosemary Wyse, Johns Hopkins U.
Jan Zaenen, Leiden U.
Kenneth Zaret, U. of Pennsylvania School of Medicine
Jonathan Zehr, U. of California, Santa Cruz
Len Zon, Children's Hospital Boston
Maria Zuber, MIT

BOOK REVIEW BOARD

David Bloom, Harvard U. Samuel Bowring, MIT, Angela Creager, Princeton U., Richard Swedder, U. of Chicago, Ed Wasserman, DuPont

Parks for science

In March 1915, a historic conference of scientists, conservationists, and park leaders was held at the University of California, Berkeley. It helped create public support for national parks in the United States and the establishment in 1916 of the National Park Service (NPS). One hundred years later, a similar summit on the same Berkeley campus convened to examine the role of science in the next century of America's national parks. Science remains crucial to the future health of America's parks and protected areas worldwide. But national parks are also vital for science.

The National Park System (which currently includes 407 national parks, historic sites, and other designations) includes invaluable sites for scientific research. The thermophilic bacteria discovered in Yellowstone National Park were used to develop the polymerase chain reaction that is key to DNA research, from forensic science to human genomics. The High Flow Experiments in Grand Canyon National Park have increased our understanding of the response of aquatic ecosystems to transient sand deposits caused by flooding. Parks also serve as unique benchmarks for environmental monitoring: The NPS recently used 1.5 million hours of acoustic data to create a soundscape map of the United States that can help guide the conservation of natural sounds. National parks have contributed to advancing wildlife ecology, developing archaeological techniques and preservation treatments, documenting climate change, and more.

In 2016, the NPS will celebrate its centennial, and science is now even more relevant than 100 years ago. The scientific community should help celebrate this event by increasing its engagement with the National Park System. Parks represent extraordinary national scientific assets—as natural laboratories to study ecological processes; as benchmarks to study climate change; and as control locations for research, in fields from atmospheric chemistry to archaeology. We encourage scientists to use

national parks as reference sites in appropriate scientific research, including long-term studies. Of particular importance is to increase research on understanding coupled human-natural systems, particularly (in an era of climate change) threshold effects and adaptive responses. International collaborations to expand and integrate research from protected areas around the world should be strengthened. Graduate students, postdocs, and early-career scientists should be urged to consider parks as sites for study. Scholarships for students doing research in parks should be established, helping to create the next generation of scientists working in parks.

The NPS can support this scientific engagement with parks. Data sharing and data accessibility for external scientists (including the NPS robust inventory and monitoring data sets) should be increased. The research permit process can be streamlined and made more consistent across the system. Long-term studies should be encouraged, with park staff (including NPS scientists) as collaborative partners. In addition, opportunities for citizen science—including the widely popular BioBlitz programs that bring young

people out to the parks—should be expanded. The use of parks for basic research can also contribute to “usable knowledge.” High-quality science is needed to inform complex decisions about issues such as the future of wolves on Isle Royale, the establishment of marine reserves in the Dry Tortugas, and the prevention of habitat fragmentation and species loss in the Greater Yellowstone Ecosystem. There is a strong and positive feedback loop between “parks for science” and “science for parks.”

The 2016 centennial of the NPS comes at a critical time for science and conservation, in the United States and worldwide. As both the gathering at Berkeley in 1915 and the conference earlier this year remind us, science and parks are indispensable to each other. Let's make the centennial a celebration of science and the national parks.

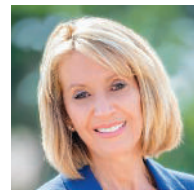
— Gary Machlis and Marcia McNutt



“There is a strong and positive feedback loop between ‘parks for science’ and ‘science for parks.’”



Gary Machlis is the science advisor to the director of the U.S. National Park Service and professor of environmental sustainability at Clemson University, Clemson, SC. E-mail: gary_machlis@nps.gov



Marcia McNutt is the Editor-in-Chief of Science Journals.

“The scientific debate about salt to me is reminiscent of the debate about tobacco in the 1950s.”

Cardiologist Lee Goldman to *The Wall Street Journal*, defending New York City Mayor Bill de Blasio's controversial proposal to require chain restaurants to label salt-heavy foods.

IN BRIEF

The Musée de l'Homme's huge anthropology collection is coming out of mothballs after 6 years in storage.

Paris's historic Museum of Man is reborn

In the years before it closed in 2009, the Musée de l'Homme in Paris had lost its luster as a major research center and museum of anthropology and ethnography. In light of its fading reputation, French officials decided to shut its doors to carry out both interior design and intellectual renovations and scattered its collections and its scientists to other museums and institutes around Paris. But in October, this neoclassical building on the Place du Trocadéro, just across the Seine River from the Eiffel Tower, will reopen to the public. Last week, journalists were treated to a press preview of the newly built laboratories that will house 150 of France's top researchers in the field, including an ancient DNA lab and a state-of-the-art uranium-thorium and paleomagnetism dating facility. Many researchers have already started to move in, although work will continue all summer on the public exhibition spaces, which museum officials promise will be more dynamic than the staid and dusty reconstructions that greeted visitors in the old days.

AROUND THE WORLD

Korea's MERS outbreak contained?

SEJONG, SOUTH KOREA | A joint mission of international and local health experts, brought together by the World Health Organization (WHO) and South Korea's ministry of health, expressed cautious optimism this week that the country may be turning the corner on the recent outbreak of Middle East respiratory syndrome (MERS). Speaking at a press conference 13 June, the experts agreed that the outbreak caught the South Korean health sector by surprise, but noted that the government has recovered its footing. “Those steps needed to control this outbreak are being put in place and strengthened on a very rapid basis,” said panel member Keiji Fukuda, WHO assistant director-general for health security. The team emphasized the need for continued surveillance and strengthening infection control measures in health care facilities, but urged South Korean officials to reopen more than a thousand schools closed because of MERS fears, as the vast majority of MERS cases has occurred inside hospitals, not in homes, public transport, or other public places. <http://scim.ag/MERSpeak>

Promised cuts won't slow warming

PARIS | Nations' pledges to cut greenhouse gases would buy the world only a little time before global temperatures shoot past the 2°C warming goal agreed on during climate talks in 2010, the Paris-based International Energy Agency said 15 June. Promised emissions reductions would keep temperature increases below the 2°C threshold until about 2040—just an extra 8 months compared with projected increases in the absence of those reductions. After that, global temperatures are projected to increase by about 2.6°C by 2100. The agency called for stronger action—including a global peak in energy emissions by 2020—through a series of steps including banning construction of inefficient coal power plants, eliminating fossil fuel subsidies, and a 50% hike in annual renewable energy investment. <http://scim.ag/IEA2015>

PHOTO: © JACQUES VERKEMANS

The universe's earliest stars

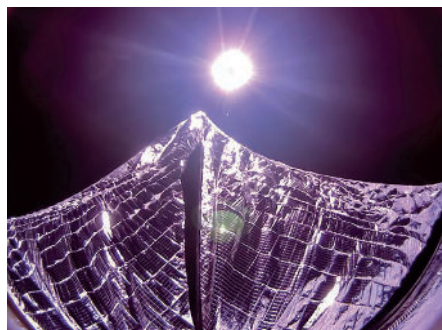
Astronomers using the European Southern Observatory's Very Large Telescope at Cerro Paranal, Chile, have spotted the brightest galaxy seen to date from the early universe. It's three times the brightness of the current record holder—and, they note, some of the galaxy's light contains no trace of any elements other than hydrogen and helium. That, the scientists say, is the strongest evidence yet of a sighting of the universe's very first generation of stars, ones made solely from the light elements created in the big bang. That first generation, known as population III stars, started the process of forging light elements into heavier ones, producing the variety of matter seen today in the universe. "Those stars were the ones that formed the first heavy atoms that ultimately allowed us to be here. It doesn't really get any more exciting than this," team leader David Sobral of the University of Lisbon said in a statement.



An artist's impression of the distant bright galaxy CR7.

LightSail's rise and fall

PASADENA, CALIFORNIA | It was a brief moment in the sun: The nonprofit Planetary Society's LightSail mission successfully deployed a solar sail in low-Earth orbit last week before falling back to Earth days later, landing in the south Atlantic Ocean. LightSail, packed into a tiny, low-cost spacecraft called a CubeSat, hitched a ride on 20 May on a United Launch Alliance Atlas V rocket. It transmitted an image of its unfurled solar sails on 9 June, confirming the mission's primary objective, said Planetary Society CEO Bill Nye at a press conference on 10 June—and paving the way for a larger scale solar sail flight in 2016. Solar sailing works by using sunlight for propulsion; when the photons strike the Mylar sails, they transfer their



LightSail's deployed solar sails on 8 June.

momentum to the spacecraft, accelerating it through space. "We're changing the way humankind explores space," Nye said.

Pope stresses climate science

VATICAN CITY | Pope Francis squarely blames the burning of fossil fuels for climate change, a leaked version of his long-awaited environmental encyclical revealed on 15 June. There is "a very consistent scientific consensus indicating that we are in the presence of a disturbing heating of the climate system," says the leaked draft, which is in Italian. Vatican watchers have speculated whether the pope—who was trained as a chemist—would delve into scientific and policy details or would focus on climate change's impacts. The draft does both, discussing soil and water acidification, methane release feedback loops, and policy ideas for curbing emissions—while decrying a "culture of waste" and noting the damaging health effects of fossil fuel pollution on the poor. As *Science* went to press, the Vatican was expected to release the final document as planned on 18 June. <http://scim.ag/popeencyc>

Research protections overhaul

MINNEAPOLIS, MINNESOTA | The University of Minnesota last week released a 75-page document that announced

sweeping changes to how it protects its research subjects. The report comes after two damning reviews earlier this year related to the suicide in 2004 of Dan Markingson, a 27-year-old who signed on to a psychiatric drug trial while involuntarily committed to a University of Minnesota hospital. One review charged the university with failure to protect the most vulnerable subjects of clinical trials (*Science*, 6 March, p. 1048). The other, an in-depth review of Markingson's case, noted "serious ethical issues," among them that Markingson's treating psychiatrist was also one of the trial's leaders. The university says it plans to tighten conflict-of-interest rules, including a ban on researchers accepting consulting fees from companies for which they're running trials. <http://scim.ag/Minnoverhaul>

FINDINGS

Guinea pigs, rain, and Chagas

Nearly 40% of people in some South American communities are infected with the *Trypanosoma cruzi* parasite that causes Chagas disease, an infection that can lead to heart and bowel failure. Scientists now suggest that—at least in the Andean region of Arequipa, Peru—a combination of fluctuating guinea pig populations and seasonal rains may be behind the high incidence. The guinea pigs, which



A HI-SEAS scientist collects a soil sample during the study.

Back to Earth: Scientists leave Mars simulation dome

After 8 months of living within a solar-powered dome meant to simulate life on Mars, six scientists with the Hawaii Space Exploration Analog and Simulation, or HI-SEAS, “returned” to Earth this week. The dome, on the slopes of the Mauna Loa volcano, is part of a NASA-sponsored study of the effects of a prolonged mission to Mars on an individual’s performance and the cohesion of a crew. The location’s remoteness and rocky scenery helped simulate the martian landscape, and the scientists donned space suits whenever they left the dome to make scientific measurements. Learning how to help astronauts deal with bad food, group conflict, and long, mundane days in cramped quarters could inform potential Mars missions in the future, say the researchers who conducted the study.

are raised as food, can act as reservoirs of *T. cruzi*, infecting kissing bugs that bite them. When alfalfa prices spike in the dry summer months, guinea pig populations plummet as people kill their stock rather than pay more to feed them. The parasite is more likely to become concentrated in the small subset of animals maintained for reproduction—which, in turn, increases the number of human infections, the researchers report this week in the *Proceedings of the Royal Society B*.

Guinea pig populations in Peru are linked to Chagas disease.



NEWSMAKERS

Three Q’s

In 2003, Madagascar’s then-President Marc Ravalomanana promised to triple the island’s preserved land to protect its unusual and highly threatened biodiversity. That goal was more than reached in April with the addition of 94 new parks and preserves totaling 5,783,779 hectares. The effort was aided by local and U.S. scientists affiliated with the Missouri Botanical Garden (MBG), based in St. Louis, which helped prioritize areas and, for a dozen of particularly important ones, developed community-based conservation efforts. MBG’s vice president for science and conservation, **Jim Miller**, describes its role in the conservation feat.

Q: How was MBG involved?

A: We have 100 people working in Madagascar. In 2004 and 2005, we went over Madagascar in 1° of latitude and 1° of longitude squares. We’ve been at some of these sites for more than 10 years and are still surveying them. We’ve identified some 90 [biodiversity-rich] places.

Q: How will these parks affect biodiversity?

A: Madagascar is a massive island, bigger than Arizona and California combined. Adding parks adds a lot of vegetation types. Some of them were chosen because we know they harbor many species that are endangered, or species that are new to science.

Q: What’s next for scientists there?

A: Madagascar is so incredibly diverse that we don’t seem able to find the bottom of it. We can’t name the new species fast enough. In the 1980s, we thought there were 8000 [total species]; now we think there are more than 13,000. Protecting these forests gives us more time to explore them.

In and out at NIH

The National Institutes of Health (NIH) is losing its extramural grants chief and gaining a permanent director for its neurological institute. **Sally Rockey** is stepping down in September after 5 years as NIH’s deputy director for extramural research. Rockey, who served during a time of unprecedented budget pressures on biomedical research, drew praise for sharing grants data and policies on her Rock Talk blog. An entomologist by training, she will direct a new agricultural research foundation created by the 2014 Farm Bill (http://scim.ag/_Rockey). Elsewhere at NIH, neurologist **Walter Koroshetz**, deputy director of the \$1.6 billion National Institute of Neurological Disorders and Stroke (NINDS), has been named NINDS director. Koroshetz had been acting director of NINDS since last fall.

A Nobelist’s fall

Nobel laureate **Tim Hunt**, 72, who made headlines in 2001 when his work on cell division earned a share of the prize in physiology or medicine, dominated the news cycle last week for a more unfortunate reason: remarks he made about women in science at the World Conference of Science Journalists in Seoul. His comments—he said he supports “single-sex labs,” in part because female scientists cry when criticized and “fall in love” with male scientists—were widely decried as sexist. In the ensuing firestorm, Hunt has resigned from his post as an honorary researcher at University College London and from the European Research Council’s Scientific Council, as well as from the Royal Society’s Biological Sciences Awards Committee. While apologizing for his “inexcusable” statements—meant to be funny, he has said—he told *The Guardian* this week that he felt the response has been extreme and unfair.



SPACE SCIENCE

The return of Philae

Revived after hibernation, comet lander awaits orders

By **Eric Hand** and **Daniel Clery**

Nap's over, Philae; it's time to get back to work. Now that the initial euphoria over the comet lander's reawakening has worn off, the operations team at the European Space Agency (ESA) is furiously trying to figure out how to cope with Philae's still awkward situation on comet 67P/Churyumov-Gerasimenko and get it producing science again. Following the lander's surprise first message during the evening of 13 June, it made contact again—very briefly—late on 14 June. As *Science* went to press, mission controllers were planning to alter the orbit of Rosetta—Philae's orbiting mothership—on 17 June to improve the chances of radio contact.

"We can see that systems are improving and the temperature is getting better" for Philae, ESA director general designate Johann-Dietrich Wörner told a press conference on 15 June. "In a few days—less than 1 week—we can start to do science."

Following Philae's historic but bumpy touchdown on comet 67P on 12 November 2014, the lander came to rest somewhere in shadow, depriving its solar panels of power. The craft's activity and communication lasted just 57 hours as its batteries quickly drained. But ESA hoped Philae would reinitiate contact as the comet neared the sun and the lander received more light. Last weekend, ESA mission managers received a precious 85-second-long transmission, containing 300 data packets—bare-bones information about the health of the lander. There followed an ominous silence for about 24 hours,

until a second, even shorter, dispatch arrived. "[This] did provide some additional status information on the lander that is currently [being] analyzed," says Hermann Böhnhardt of the Max Planck Institute for Solar System Research in Göttingen, Germany, one of Philae's lead scientists.

There was good news in this meager haul of data: Even in its relatively dark location, Philae's solar panels are now getting nearly 3 hours of light during each 12-hour comet day and generating 24 watts of peak power—more than the minimum of 19 watts required for communications. The lander's temperature is -5°C , warmer than the -45°C necessary to boot the computer. And most surprising, more than 8000 data packets—records of earlier activity—are still sitting in the lander's computer memory.

"Everything in principle demonstrates that Philae did not suffer from the very low temperatures it faced in the months of hibernation," says Jean-Pierre Bibring, Philae's other lead scientist, of the Institute for Space Astrophysics in Orsay, France. Taken together, the data suggest that Philae had woken from its 7-month-long slumber a day or two earlier, but had been unable to communicate with Rosetta to relay messages to Earth. "Fantastic, right?" says Stephan Ulamec, Philae's project manager at the German Aerospace Center near Cologne. "It's healthy, temperature is good, power is sufficient. The only thing we have to work on is the duration of the radio link."

Böhnhardt says that as yet, no commands have been sent to the lander and no science operations have started. Once regular con-

Analyses of Rosetta's comet images suggested a possible location where Philae settled (oval).

tact has been achieved and engineers better understand the spacecraft's daily thermal and power cycles, they will consider uploading commands—developed over the past month—for measurements that can be performed quickly, in 2- or 3-hour-long bursts, and that do not require waiting for Philae's batteries to recharge.

The new commands would activate the lander's 10 scientific instruments step by step, starting with ones that make no movements and that have low power demands (about 5 watts). These include instruments that measure temperatures, magnetic fields, and electrical conductivity of the comet surface. Instruments with medium power demands (about 15 watts), including the cameras and radio ranging instrument, could then be activated if engineers were willing to use them with no radio contact. Fresh pictures, along with distance readings to Rosetta, could help pinpoint the lander's location. Last week, the Rosetta team, analyzing images of the comet, suggested it might be in a crevice outside a crater on the "head" of the two-lobed comet.

Finally, if Philae's power supply improves, instruments with high power demands (about 25 watts) come into play, including two ovens that analyze the chemistry of comet samples. "It is, I believe, in reach. But we have to understand what the details of the available power are," Böhnhardt says.

There could even be an unplanned bonus to Philae's long sleep and sheltered position, Wörner says: It is still working as the comet approaches the sun and should stay cool enough to survive and gather data during its closest approach, inside the orbit of Mars, on 13 August. Bibring is simply glad to be busy with the lander again. "The dream is not only alive, it's continuing," he says. "It's a great adventure." ■



A retired lab chimpanzee at Chimp Haven, an independent sanctuary in Louisiana.

ANIMAL RESEARCH

Research chimps will soon be listed as 'endangered'

Ruling could disrupt biomedical research

By David Grimm

The presence of Jane Goodall was a giveaway. In a press conference last week featuring the famed primatologist, the U.S. Fish and Wildlife Service (USFWS) announced that it will classify all captive chimpanzees as endangered under the Endangered Species Act (ESA). The move gives captive chimps the same status as their wild counterparts and could deal a significant blow to biomedical research involving the animals.

"This decision will have a chilling impact to the point where little if any chimpanzee research will be conducted in the U.S.," says John VandeBerg, the former director of the Southwest National Primate Research Center in San Antonio, Texas, which provides nonhuman primate resources for biomedical research and currently houses 129 chimpanzees.

USFWS has been considering the status change since a coalition of animal organizations—including the Humane Society of the United States (HSUS) and the Jane Goodall Institute—petitioned it in 2010. The group claimed that research chimps were treated inhumanely and that the animals were too cognitively advanced to be kept in captivity. It also argued that USFWS had erred when, in 1990, it first listed wild chimpanzees as endangered but made the unusual move to keep captive chimps—including those used in research, zoos, and entertainment—listed as threatened. (All chimps had been labeled

as threatened in 1976 due to threats from poaching, disease, and capture for research.)

No other species has this split status, but USFWS was pressured by the biomedical community, which feared that an endangered listing would compromise HIV research and other important studies. The agency also hoped that keeping chimps in captivity would protect wild populations, because the animals could be bred rather than taken from the wild.

"That was a well-intentioned decision, but now we realize it was a mistake," said USFWS Director Dan Ashe at the press conference. "What we actually did was encourage a culture that treats these animals as a commodity."

When USFWS reviewed its policy, it concluded that the ESA does not allow for a split designation. It also found that giving the estimated 1750 chimps in captivity (including more than 700 research chimps) a less protected status could create a way to "launder" wild chimps as captive ones, and that the split status had done little to reduce the threat to wild chimpanzees.

Under the new designation, which goes into effect on 14 September, anyone doing scientific research on captive chimps in the United States must apply for a permit from USFWS. Permits will also be required for the sale and import of these animals. Organizations that want to continue working with chimpanzees will have to document that the work enhances the survival of the species and benefits chimps in the wild—

for example, by boosting habitat restoration or contributing to improved management. "We have been working closely with the NIH [National Institutes of Health] and the biomedical research community to make sure they understand the implications of our final rule," Ashe said. "If anyone is actively engaged in chimpanzee research, they should apply for a permit now."

Ashe said some biomedical research with chimps may be allowed to continue if it is critical for understanding human disease. "But the entity would have to make a [monetary] contribution or support conservation of wild chimpanzees."

The decision "shows an awakening, a new consciousness," Goodall said at the press conference. HSUS also applauded the move. "We were sending the wrong message by using these animals so readily for research, entertainment, and as pets," says Kathleen Conlee, the organization's vice president of animal research issues. Even if the new status doesn't completely end research on chimpanzees, she says the permitting process will make public all the work being done with them in pharmaceutical companies and other private research labs, which have not been subject to NIH scrutiny. "We hope this compels private labs to start thinking about sanctuaries for these animals."

The USFWS decision comes on the heels of a 2013 NIH announcement that it would phase out most government-funded chimpanzee research and retire the majority of its research chimps. In a statement, the agency said that it isn't supporting any biomedical research projects using chimpanzees, and that it will work with USFWS to comply with any implications of its ruling.

To Susan Larson, an anatomist at Stony Brook University in New York who has worked with lab chimps for decades, the USFWS announcement adds yet another hurdle to studying these animals. "We already have to apply for grants, get institutional approval, and be subject to regular inspections," she says. "This is going to make it increasingly difficult to get these projects off the ground."

VandeBerg says no new chimpanzee studies have been initiated since USFWS began considering the new status in 2013. Stopping chimpanzee research, he says, will hurt chimps in the wild, as well as human beings. "Chimpanzees are needed to develop vaccines for Ebola and AIDS," he says. "There will be a lot of people who die who would not have died." VandeBerg also worries that animal rights groups will now move on to monkeys and other primates. "It's a slippery slope." ■

INFECTIOUS DISEASES

Designer proteins produce potent HIV defense

AIDS vaccine developers mimic natural route to powerful immune responses

By Jon Cohen

Glimmers of a way to bypass the biggest obstacle to a successful AIDS vaccine may be emerging. The AIDS virus defeats candidate vaccines—and the body's own defenses—because it varies so rapidly, eluding immune responses. A decade ago, several researchers embarked on a fundamentally different strategy to vaccine development: figuring out how to coax the immune system into making a rare class of powerful, “broadly neutralizing” antibodies that can thwart almost every HIV variant. Now, three different groups have taken early but critical steps toward that goal.

Many HIV-infected people naturally make broadly neutralizing antibodies (bNAbs), but they typically emerge years after the initial infection, which means they do little to help contain the virus. Yet several monkey experiments have proved that injecting bNAbs into uninfected animals can block infection with the AIDS virus. This week, in two papers published online in *Science* (<http://scim.ag/RWSanders> and <http://scim.ag/JGJardine>) and one in *Cell*, researchers describe progress with two different approaches to spurring the immune system to make bNAbs.

Although neither approach will directly lead to an AIDS vaccine, they bolster confidence that giving the right pieces of the virus—the immunogens—in the right order can steer antibody-producing B cells along a path to secreting these versatile immune-system molecules. “We’re really starting to see that rational vaccine design can work,” says Dennis Burton, an immunologist at the Scripps Research Institute in San Diego, California, who is a co-author of the two *Science* studies.

All three studies attempt to reverse-engineer parts of the B cell maturation process that, in rare cases, yields cells capable of producing HIV bNAbs. In one *Science* paper, a team led by David Nemazee and William Schief at Scripps describes kick-starting the maturation

process by using a tailor-made piece of HIV's surface protein, gp120, that they first described in *Science* 2 years ago (10 May 2013, p. 711). The new work shows that this nanoparticle indeed bound to germline B cells and set them on the road to maturing into cells that secreted antibodies with telltale bNAb features.

Antibodies, Y-shaped proteins, have what are called heavy and light chains on each arm of the Y. In HIV bNAbs isolated from infected people, one specific region of the light chain is extremely short. The nanoparticle immunogen led to more than

antibodies. The particle in question is the complex of three gp120 proteins that studs the surface of HIV. Studying this trimer in its “native” form has been a challenge, because it falls apart when it is not attached to the virus particle. But John Moore of the Weill Cornell Medical College in New York City has learned how to stabilize trimers that resemble the native form. Now, Moore, Cornell's Rogier Sanders, and a large team of collaborators have injected one of these native trimers into rabbits and monkeys. As they report in *Science*, the antibodies elicited by the native trimer were potent and, at least

in the test tube, derailed a hardy isolate of HIV—a test that other lab-made trimers failed.

The next step is to see whether administering a different immunogen first, to start the B cell maturation process, and then giving the trimer could result in antibodies that are both broad and potent. The *Cell* paper suggests such a one-two punch might be possible. Michel Nussenzweig's lab at Rockefeller University in New York City created a mouse with B cells genetically engineered to produce antibodies showing some bNAb features—an analog of what an initial immunogen might do. Working with Moore, Sanders, and Schief, Nussenzweig showed that the trimer then stimulated the B cells to make antibodies that had still more bNAb features.

Ultimately, Mascola says, the gp120 nanoparticle may serve as the initial “primer” shot that

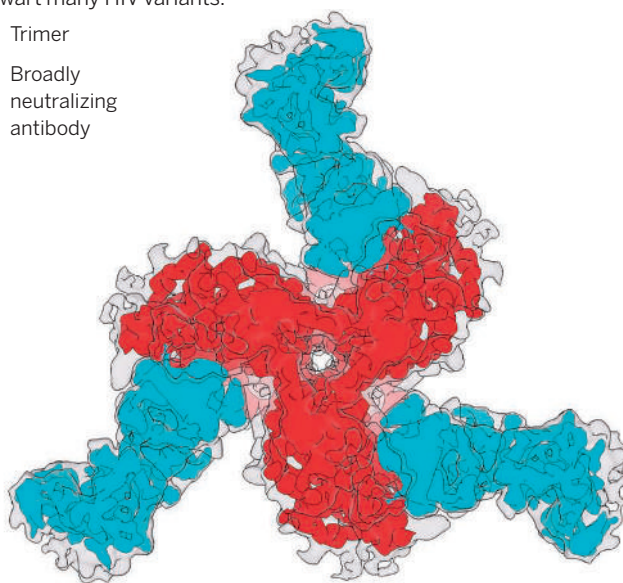
prods the right germline B cells into action. A shot of the native trimer may come in later as something of a finishing school. “A successful vaccine approach will require both the right germline signaling and some sort of trimer immunogen at some point to mature the antibody,” Mascola says. “They form two parts of a platform.”

Then again, no one yet knows which immunogens will guide bNAb B cells through the difficult steps in between. “You have to be realistic: There's no short-term pathway to an AIDS vaccine,” Mascola says. “But we should take any success we get and run with it.” ■

Mimicking nature

Researchers hope this natural-looking but lab-made version of HIV's surface protein trimer will trigger production of antibodies able to thwart many HIV variants.

- Trimer
- Broadly neutralizing antibody



a 100-fold increase in antibodies that had the truncated light chain region. “It’s encouraging news,” says John Mascola, head of the Vaccine Research Center at the U.S. National Institutes of Health in Bethesda, Maryland. “It wasn’t obvious that would happen.” Schief says his group now wants to develop a different immunogen that, given as a booster shot, would elicit bNAb-like features in the heavy chain.

Work reported in the other two papers suggests that another HIV protein complex might be capable of coaxing B cells that are already on their way to making bNAbs into producing more potent versions of the

U.S. RESEARCH FUNDING

Republicans split on climate, social science spending

House calls for cuts, Senate favors status quo

By Jeffrey Mervis

Republicans control both houses of Congress, but they don't speak with one voice on funding research at the National Science Foundation (NSF), NASA, and other agencies. That difference became clear last week after the Senate Appropriations Committee approved a 2016 spending bill that does not call for the steep cuts to climate and social science programs approved a week earlier by the House of Representatives. And although the House would give NSF a bit more money, the Senate version hews closer to the balanced portfolio that most scientists prefer.

In the House, key lawmakers have made headway with the notion that the social sci-

ences and climate research contribute less to the nation than "pure" disciplines, such as physics, biology, engineering, and computing. That worldview is reflected in a \$51 billion spending bill approved by the House on 4 June to fund NSF, NASA, the National Oceanic and Atmospheric Administration (NOAA), and several other federal agencies.

At NOAA, for example, the so-called CJS (Commerce, Justice, and Science) bill would cut climate research programs by \$30 million, or 19% below current levels, and \$60 million below the president's request. At NASA, it would keep overall science spending flat, but cut earth science spending by \$90 million, or 5%, a level \$264 million less than the president's request. At the same time, the House would boost NASA's planetary science programs \$216 million above the president's request, including a big hike for a proposed mission to the jovian moon Europa.

The NSF portion of the House bill takes a swipe at both the geosciences and the social and behavioral sciences. Although NSF's overall budget would inch up by \$50 million, to \$7.4 billion, the bill would significantly reshuffle NSF's research priorities. It directs NSF to put 70% of its \$6 billion research account into four of its six research directorates—biology, computing, engineering, and math and physical sciences. (They now receive about 65%.) That change, combined with language protecting a research infrastructure program and graduate fel-

The Heartland Institute, a libertarian group that vociferously challenges mainstream climate science, in which he praised the House's effort to cut NASA's earth science budget. "NASA spends a lot of money on climate change—they call it earth science—so we cut NASA's earth science budget by close to 40%," Smith said, exaggerating the 6% cut from current levels. "The reason we did it is that there's only one agency dealing with space exploration, while there are a dozen agencies dealing with climate change."

The Senate CJS panel, led by Senator Richard Shelby (R-AL), has taken a very different tack. Its bill, approved by the full appropriations panel on 11 June, gives NASA's earth science program most of the large increase requested by the president and tops the House number for NASA science by \$50 million. At NOAA, it would shave just \$5 million from climate research, a 3% cut from current levels. And Senate appropriators do not single out any of NSF's six directorates for rough treatment. Instead, they list all of them by name in a report accompanying the bill. Those words are "the subcommittee's subtle way to say that it does not agree with the House's approach," says Joel Widder of Federal Science Partners, a small consulting firm in Washington, D.C.

The Senate language could come into play later this year when the two bodies try to reconcile their differences, Widder says. Last year, he notes, the Senate did not oppose a House move to block any increase for geosciences, which made it into the final CJS bill. This year, it is "well aware of our concerns," says Amy Scott of the Association of American Universities in Washington, D.C., which opposes the earth and social science cuts. "And [staffers] have told us that their members have a different perspective than in the House."

The dispute is playing out in the shadow of a broader question: How much money will be available for all federal programs? Two years ago, the Obama administration and congressional Republicans struck a deal on overall spending levels that helped ease passage of spending bills for 2014 and 2015. But there's no such agreement for fiscal year 2016, which starts on 1 October. Republican leaders are sticking to strict annual spending caps set by a 2011 law as they assemble their budget bills. In contrast, most Democrats and some Republicans want the caps lifted so they can spend more on both defense and civilian programs.

Senate Democrats are threatening to block work on several spending measures in hopes of getting Republicans to the negotiating table. Without some kind of compromise, the entire federal government would have to shut down after 30 September. ■

Dueling visions for NSF, NASA, and NOAA

The White House, House of Representatives, and Senate have embraced divergent 2016 budgets for these key science agencies (\$ billions).

AGENCY	2015	WHITE HOUSE	HOUSE	SENATE PANEL
NSF overall	\$7.344	▲ 5%	▲ 1%	◀▶ 0%
Geo and social, behavioral & economic sciences	\$1.576	▲ 5%	▼ 16%	◀▶ 0%
NASA science	\$5.295	▲ 1%	◀▶ 0%	▲ 1%
Earth science	\$1.773	▲ 10%	▼ 5%	▲ 9%
Planetary science	\$1.438	▼ 5%	▲ 8%	▼ 5%
NOAA climate research	\$0.158	▲ 20%	▼ 19%	▼ 3%

lowships, would result in a combined 16%, \$255 million cut to the two directorates under attack—geosciences and the social and behavioral sciences (see chart).

"I'm asking NSF to prioritize," said Representative John Culberson (R-TX), who led the writing of the CJS bill, after his spending panel approved it last month. "I want ... them to make the hard sciences—math and physics and pure science—a priority."

That's a view shared by a fellow Texan, Republican Representative Lamar Smith, head of the House science panel. The pure sciences "typically yield better results," he told *Science* last week. "That's why we moved the money."

Smith's comment came after a speech to

Smith's comment came after a speech to

Pumped up to rumble

Massive studies of wastewater injection wells show fast pumping raises earthquake risk

By Julia Rosen

Before 2008, Oklahoma experienced roughly one noticeable earthquake per year. By 2014, that number had soared to almost one a day, and the state is not alone. Scientists have documented an astronomical rise in seismic activity across the central and eastern United States, linking it to wastewater pumped into the ground from burgeoning oil and gas production. Now, new research suggests that high rates of fluid injection—rather than other factors such as volume or depth—may be the root of the problem.

Since the 1960s, geologists have recognized that fluid injection can induce earthquakes by raising the hydraulic pressure along a fault, pushing the two sides apart to let the crust slide along it. But scientists don't know exactly which aspect of well operation matters most.

Until now, most studies have focused on individual earthquakes and their connection to nearby wells. But that approach can make it hard to spot the difference between wells that are linked to quakes and those that aren't, says Matthew Weingarten, a Ph.D. student at the University of Colorado, Boulder, and lead author of the new study, published on page 1336 of this issue. "You would never know that cancer or other diseases are more likely in smokers if you don't look at the vast majority of other people who don't smoke," he says.

So Weingarten's team compiled the first comprehensive data set of all injection wells operating in the central and eastern United States. They looked both at wells used for enhanced oil recovery—in which fluid is injected to flush lingering oil from a depleted reservoir—and at those used to dispose of wastewater from conventional oil and gas extraction or from hydraulic fracturing (fracking).

The scientists found that disposal wells were 1.5 times more likely to be associated with earthquakes, although the region contains far more enhanced recovery wells. The link was strongest at higher injection rates, above about 300,000 barrels per month. Other potentially important factors—such as the pressure at the well-head, the total volume of fluid injected, and

whether fluid was injected near basement rock—did not appear to make much difference at a regional scale, the researchers say.

They propose that injecting fluid quickly may induce earthquakes by jacking up reservoir pressure more drastically and over a larger area than adding it more slowly would. The elevated pressures increase the chances of triggering slip on a nearby fault that is already under natural stress. "You're looking at a balance between the rate you're putting fluid in and the rate it can diffuse away," says Katie Keranen, a seismologist at Cornell University who was not involved in the study. That would explain why wells used for enhanced oil recovery are less likely to trigger earthquakes: Pumping out oil as water is injected helps keep the pressure in check.

Weingarten says the team's results suggest that limiting injection rates may reduce earthquake hazard. Previous studies that showed a potential link have already spurred some states to take action. In Kansas, regulators issued an order in March to ramp down injection rates in three hard-hit areas. Since then, earthquake activity appears to have quieted down, says Rex Buchanan, the interim director of the Kansas Geological Survey in Lawrence, although it's too early to say for sure.

The Oklahoma Corporation Commission has also adopted a "traffic light" system to force operators to decrease or even halt injection at potentially quake-prone wells. "All options available to us to address

this are on the table," said Tim Baker, director of Oklahoma's Oil and Gas Conservation Division in Oklahoma City, in a statement issued last month.

Another new study, published this week in *Science Advances*, found that Oklahoma's earthquake activity has increased in areas where disposal rates have skyrocketed. However, it raises questions about the benefits of reducing the injection rates at individual wells. "A number of wells injecting right next to each other could have the same effect as one well injecting their combined volume," says Rall Walsh, a Ph.D. student in geophysics at Stanford University

in Palo Alto, California, and the lead author of the study. For neighboring wells, he says, the question is, "how close is close?"

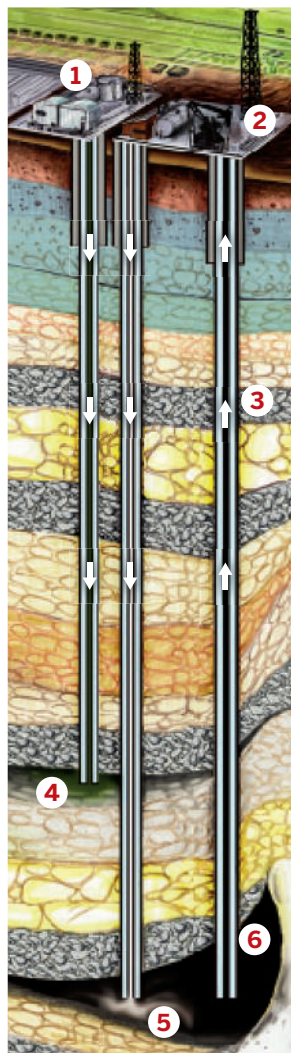
Nor does the new research explain why large areas of the country—including North Dakota, the Gulf Coast, and the Michigan Basin—have experienced few earthquakes despite having disposal wells with high injection rates. Maybe fluids aren't reaching the bedrock there, or background stress levels in the crust are lower, says William Ellsworth, a geophysicist with the U.S. Geological Survey in Menlo Park, California. Understanding the reason could help well operators and regulators "assess the hazard of a project perhaps before it has begun," Ellsworth says.

The new study sets the stage for work that may provide more answers about the relatively new problem of induced earthquakes. "I'm very happy they did it in a time frame that actually makes sense so people can discuss it," says Murray Hitzman, a geologist at the Colorado School of Mines in Golden, who chaired the National Research Council's committee on induced seismicity. "All this is happening really fast." ■

Julia Rosen is a freelance writer based in Portland, Oregon.

What goes down ...

Fluid disposal (left) raises underground pressure and earthquake risk, but using fluid to drive out oil (right) keeps pressure in check.



1. Disposal well 2. Enhanced oil recovery 3. Production well 4. Injected brine 5. Injected fluid 6. Oil

LAST DANCE?

An urgent effort to save the West's iconic lesser prairie chicken could point the way to a truce in other endangered-species battles

By **Marianne Lavelle**, in *Healy, Kansas*

At first, there's no sound or motion on the dance floor, just the far-off howl of a lone coyote and the rhythmic thump of a distant oil well. So the scientists wait, keeping a close watch on a scraggly patch of grassland lit only by a crescent moon. Spatial ecologist Tom Lipp, a graduate student at Bowling Green State University (BGSU) in Ohio, sets a sound recorder in a clearing. Avian ecologist Samantha Robinson, who is doing her graduate work at Kansas State University (KSU), Manhattan, zips herself into a snug tent-style blind with a thermos of coffee and a notebook.

The coffee is cold by the time the first gobbles ripple through the predawn darkness and the dancers strut in. Soon, nearly a dozen male lesser prairie chickens are cackling, stamping, and showing off fluffy yellow eye combs and the bright red air sacs that balloon from their necks. They will spend nearly 2 hours facing off in feather-ripping squabbles, aiming to attract a mate. But for the researchers ringing this lek, or mating ground, on a ranch in northwestern Kansas, the sometimes comical males aren't the main focus. They're after the drabber females who lurk in the nearby grass, sizing up the male dancers. The scientists hope to trap the hens and attach satellite and radio tags, so they can track the birds as they build nests and raise chicks.

The stakeout is a part of an urgent \$5 million effort, stretching across five states and

involving nearly 100 researchers, to learn more about this relatively mysterious bird and save it from extinction. Last year, after a severe drought caused populations of lesser prairie chickens to decline drastically, U.S. officials declared the bird "threatened" under the Endangered Species Act, spurring controversy and intensifying the research initiative. It's "a one-of-a-kind effort never done before at this scale for this bird," says KSU avian ecologist Reid Plumb.



Hostile territory

Lesser prairie chickens face multiple threats.

CENTER-PIVOT IRRIGATION

Fragments habitat (above)

ENERGY

Birds avoid wells, wind turbines, and other vertical structures

ROADS AND POWER LINES

Birds avoid gaps in landscape

FENCES

Collisions cause fatal injuries

INVASIVE TREES

Offer perches to predators

CLIMATE CHANGE

Survival plummets in drought and severe heat

OVERGRAZING

Less grass for hiding

More is at stake than the fate of a single showy bird, whose home range coincides with the heartland of American agriculture and the epicenter of an energy boom. The research effort could help generate tens of millions of dollars to protect prairie habitats—and determine how lucrative industries that employ thousands of people will operate in prairie chicken country. It will test the scientific, political, and economic feasibility of a controversial Obama administration plan to give state governments and private landowners a bigger voice in endangered species management. And it could provide a valuable template for resolving a much bigger looming battle over the fate of another rangeland bird: the greater sage grouse (see sidebar, p. 1304).

"That's the scary and exciting part about doing this work right now," says ecologist Andrew Gregory of BGSU. "We're doing work that matters [and is] going to feed directly into management recommendations."

BIOLOGISTS ESTIMATE that as many as 2 million lesser prairie chickens once lent crimson to the often beige landscape of the midwestern and southwestern United States. But just some 22,000 birds remain today, occupying about 16% of the species' historic range. The birds are found in five states: Texas, New Mexico, Oklahoma, Colorado, and Kansas—which holds an estimated 60% to 70% of the remaining population.

The birds "are facing a tremendous number of threats," says retired biologist Randy

PHOTOS: (LEFT) GRANT HELLMAN PHOTOGRAPHY/ALAMY, (OPPOSITE PAGE) © MIKAEL MALES/DREAMSTIME

Males spar
for dominance on
a lek. Just 20% of
contestants will win
80% of matings.



Rodgers, an expert on “lessers” who spent 37 years with the Kansas wildlife department. Lessers can tolerate some human disturbance, he says; in fact, they often seek out clear patches of ground that have been grazed or trampled for their leks—which are a bit like “a rowdy college bar,” Gregory says. Once, wildfire and grazing bison helped create those prairie dance floors. And even after settlers destroyed the bison herds and quenched the fires, the chickens did well at first. As the bison vanished, the grass grew taller, providing more hiding places. And farmers planted grains that supplied a new food source, helping populations explode from the 1870s through the 1920s. “But as with many things,” Rodgers says, “a little is good. A lot is not.”

Beginning in the 1950s, modern center-pivot irrigation farming became a major threat, carving crop circles into some of the lesser’s favored vegetation: sand sagebrush and shrublike sand shinnery oak. Oil and natural gas wells further fragmented the bird’s range, as have roads, power lines, wind farms, and housing developments.

It took a climate shift, however, to push the lesser prairie chicken to the brink of disaster. In 2012 and 2013, a punishing drought hit the heart of its territory. Biologists estimate the population plummeted by half, to about 18,000 birds, before rebounding by about 20% in 2014.

The crash was a major reason the U.S. Fish and Wildlife Service (USFWS) decided in March 2014 to formally list the bird as threatened. “The lesser prairie chicken is in dire straits,” said USFWS Director Daniel Ashe at the time. Some environmentalists, however, were disappointed. They had pushed the agency to designate the bird as “endangered,” a status that gives federal officials greater regulatory power to crack down on threats. But Ashe and others argued that the “threatened” tag gave the federal government flexibility to try out new, potentially less confrontational conservation approaches. In particular, they called for forging closer collaborations with western state governments, which are often uneasy with federal action, and with the private landowners who control an estimated 95% of the prairie chicken’s habitat.

Under the plan, for example, the agency said it would not prosecute landowners or businesses that unintentionally kill, harm, or disturb the bird, as long as they had signed a range-wide management plan to restore prairie chicken habitat. Negotiated by USFWS

and the states, the plan requires individuals and businesses that damage habitat as part of their operations to pay into a fund to replace every acre destroyed with 2 new acres of suitable habitat. The fund will also be used to compensate landowners who set aside habitat. USFWS also set an interim goal of restoring prairie chicken populations to an annual average of 67,000 birds over the next 10 years. And it gives the Western Association of Fish and Wildlife Agencies (WAFWA), a coalition of state agencies, the job of monitoring progress. Overall, the idea is to let “states remain in the driver’s seat for managing the species,” Ashe said.

Not everyone buys the win-win rhetoric. Some members of Congress are trying to block the plan, and at least a dozen industry groups, four states, and three environmental groups are challenging it in federal court. Not surprisingly, industry groups and states generally argue it goes too far; environmentalists say it doesn’t

go far enough. “The federal government is giving responsibility for managing the bird to the same industries that are pushing it to extinction,” says one critic, biologist Jay Lininger of the Center for Biological Diversity in Ashland, Oregon.

WHEN NEWS of the escalating controversy reached ecologist Gregory—who has been studying prairie chickens for nearly a decade and wears polo shirts decorated with their image—he thought, “This will fund my work for the next couple of years,” he recently recalled, laughing. The three dozen or so studies now underway are likely to figure heavily in decisions about how to keep the species alive, and they will undoubtedly provide ammunition for all sides in the legal battle.

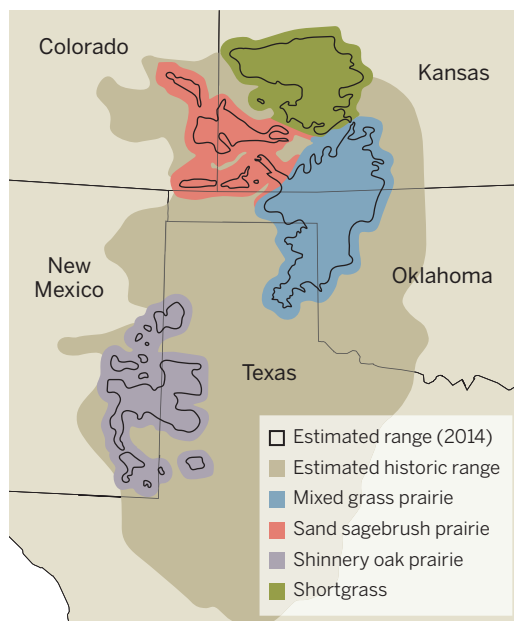
It’s an unusually far-reaching research effort, says KSU biologist David Haukos, leader of the U.S. Geological Survey’s Kansas Cooperative Fish and Wildlife Research Unit, who is coordinating the studies. “These birds use very large areas,” he notes, “and in order to get meaningful information, it takes a large investment of people, equipment, and money.” The questions are big, too. Exactly how much habitat does the lesser prairie chicken need, not only to survive, but to thrive? Why does the bird seem to avoid some perfectly suitable grasslands? How tolerant is it of the churn of new oil pumps, wind turbines, and roads?

To answer these questions, researchers have to follow and observe a species that is skilled at hiding. Robinson and other KSU researchers use stealth. During their predawn stakeouts, they quietly encircle leks with a zigzag trap of chicken wire. Females arriving to scrutinize the males find themselves funneled into welded wire cages. The approach is “passive,” but “really successful, strangely enough,” Robinson says. The researchers then attach leg bands and radio or GPS tags to the hens. When their chicks hatch in early summer, the researchers try to catch and tag them, too. (Once, a hen jumped into Plumb’s lap to peer at his head lamp as he sewed a transmitter onto its chick in the dark. “I don’t think she knew what we were, and she just saw this big light,” he recalls. “I had to push her off because I had a needle in my hand.”)

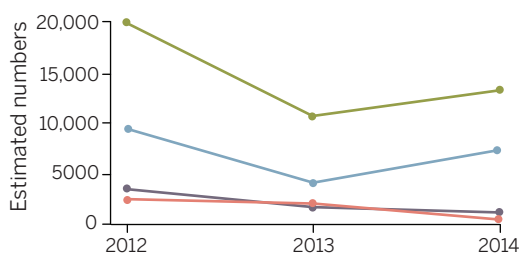
The tracking data from these devices “is going to revolutionize our understanding of the species,” Plumb says. For example, lessers were once thought to be homebodies. “Due to their heavy wing loading, they are relatively poor fliers,” USFWS noted in its

Four ecosystems, four fortunes

The lesser prairie chicken is experiencing different population trends in each of its four main habitats; 60% of the birds live in the grasslands of northwest Kansas.



Population trends





Females are drab compared with colorful males (rear), but researchers focus on hens to locate nests and study survival.

listing notice. But the preliminary GPS data has shown that some females travel as far as 80 kilometers. That suggests the birds may be able to move between widely separated swaths of habitat in fragmented landscapes. Robinson says she's hoping to use such data to create practical models of exactly which landscape patterns might enable prairie chickens to thrive. "None of my landscapes will be 'turn it all back to grasslands,' because that's not realistic," she says. "I'm trying to work with what we have—how the fragmentation they're experiencing affects their survival and how much they are moving."

A related challenge is understanding which habitats the birds consider acceptable. In one sense, it's simple, Rodgers says: "I tell people shin-high to thigh-high [grass or shrubs]. ... You don't have to get complicated and say 'X' centimeters." But the birds haven't done well recently in some seemingly perfect places, such as the protected 43,700-hectare Cimarron National Grassland in southern Kansas. In contrast, they are thriving on a relatively small 3600-hectare working ranch in western Kansas, near Scott City. Past use of weed-killing chemicals and the lingering effects of the drought may be playing a role, the researchers say, but they also suspect that ranching helps create the mosaic of open areas and grassy,

shrubby enclaves that the lessers prefer.

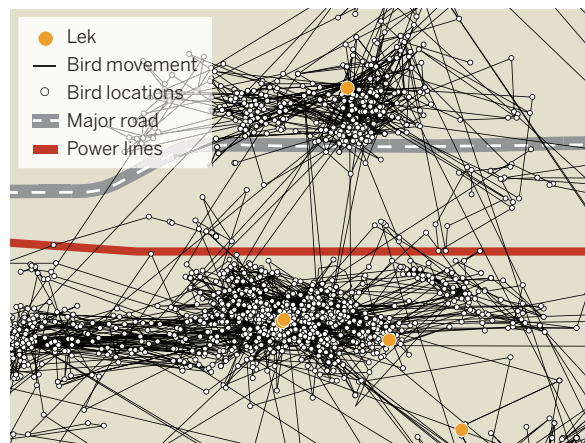
To better understand what the birds like, researchers have been painstakingly surveying vegetation in different habitats, one transect at a time, looking for even subtle differences. They are also experimenting with less labor-intensive data collection methods, including flying drones carrying sensors and cameras that map the vegetation patterns. If the method works, the drones could also play an important role by helping confirm that landowners are following agreements to set aside large chunks of quality habitat.

SCIENTISTS ARE ALSO TRYING to understand how lessers cope with development and environmental change. They already know that the birds have an aversion to tall structures such as wind turbines, transmission lines and poles, and drilling rigs, probably because some of these structures provide potential perches for hawks and other predators. That may also help explain why prairie chicken numbers have declined in south-central Kansas and western Oklahoma, where invasive eastern red cedar trees have spread into the previously flat landscape. But energy installations and other facilities are often not only tall, but also noisy. That could matter to a bird that relies on sound in its mating dance and has a scientific name—*Tympanuchus pallidicinctus*—that derives from the Latin word for drum. "When their feet are going," Plumb says, "the sound is so deep that you can feel it in your chest."

Lipp has been recording and measuring sound at leks, oil pumping stations, and wind farms in Kansas to see if there is a correlation between noise and the bird's landscape use, nest placement, reproductive success, and ultimate survival. Ironically, energy industry efforts to muffle drilling noise by switching from diesel pumps to quieter electric ones may actually have worsened the disturbance. The new

Chickens avoid crossing the road

Radio tagging data collected over 7 years in northwest Oklahoma show how lesser prairie chickens avoid both roads and power transmission lines.



pumps, it turns out, emit low-frequency sound that may be in the same range as that used by the birds.

Lipp and Gregory are also exploring whether energy development creates a heat island effect that may be harmful. The concrete, metal, and roads common at well pads tend to absorb and hold heat, helping boost nearby temperatures, and studies have shown that the birds won't nest when ground temperatures rise above 40°C. So the researchers are using small candy bar-sized sensors to map thermal landscapes and see if the birds are avoiding hot zones.

Such thermal studies are a reminder that climate change—and the hotter, drier weather it is expected to bring to many parts of the bird's range—will also play a role in the lesser prairie chicken's future. The disastrous 2012 to 2013 drought offered a stark example of what can happen, say researchers who lived through it. "All my broods pretty much tanked and fried

to a crisp. ... The chicks just desiccated," Plumb recalls. "If we're going to have more of those bad years, as conservationists we're really going to have to take this into account and try to figure out how to offset it," perhaps by planting vegetation that provides better shade.

There's also some worry that climate change could be one reason lessers have moved north of the Arkansas River in Kansas within the past decade—enabling them to interbreed with a close northern cousin, the greater prairie chicken (*Tympanuchus cupido*). The interbreeding could threaten both species. USFWS estimates that hybrids now account for less than 2% of the population of lessers, or about 350 birds, but warns that hybridization could become a "significant threat." For the moment, researchers are trying to determine whether the hybrids—which can be identified by their unusual calls and air sac colors—can reproduce and, if they can, whether their offspring are less fit.

ONLINE

Video of prairie chickens: <http://scim.ag/prairiechick>

PERHAPS THE BIGGEST QUESTION shadowing the prairie chicken's future is how our own species will respond. The entire federal plan for studying and saving the bird is, in a sense, a giant experiment aimed at understanding how to create incentives for private landowners to help conserve the species.

One of those landowners is Stacy Hoeme, owner of the working ranch near Scott City where the birds have been doing unusually well. In his home office, Hoeme has about 20 trophy deer heads and a digital frame that displays photos of his hunting expeditions. But there are also images of scientists holding handfuls of prairie chicken fledglings born on his ranch, which has at least six leks.

"I love wildlife," Hoeme says, explaining why, a few years ago, he agreed to let the scientists tromp around on his ranch and track the birds. He isn't happy with the USFWS listing, but he was glad that the bird was not declared "endangered." And he hopes the research will ultimately lead to the prairie

Sage grouse war tests limits of partnership in West

By Marianne Lavelle

When Jack Connelly first began studying the greater sage grouse in Idaho in the late 1970s, "it was not unusual to see 500 in a single flock," says the biologist, who is retired from the Idaho Department of Fish and Game. "Today, it would be unusual to see 200."

That dramatic decline has made the sage grouse—a large, pointy-tailed bird with showy mating habits—the subject of one of the biggest endangered-species battles ever in the United States. President Barack Obama's administration is under court order to decide by 30 September how to protect the bird: declare it an endangered species—the nuclear option in conservation—or opt for the less onerous conservation strategies that officials are testing on its fellow rangeland bird, the lesser prairie chicken (see main story, p. 1300).

An endangered listing could have widespread economic and environmental consequences.

The sage grouse's remaining population is spread over 67 million hectares in 11 western states, pitting it against farming, ranching, mining, and energy interests. Some members of Congress are trying to block any listing, because of the potential cost to industry and private land owners. They have even vowed to stop ongoing government efforts to protect

grouse on federal lands, which hold about 65% of its key remaining habitat.

"I don't think it's an overstatement to say that this issue is the mother of all [endangered species] decisions," says forestry scientist Eric Washburn, of the law and lobbying firm Bracewell & Giuliani in Washington, D.C. He is advising the Environmental Defense Fund and other conservation groups.

The greater sage grouse (*Centrocercus urophasianus*) is the largest North American grouse and gives the illusion of being the proudest. On mating grounds, males flaunt ermine-like neck wraps while inflating bright yellow air sacs on their breasts. As many as 16 million grouse once ranged the western steppe, according to some estimates; today, the population is believed to have dropped to fewer than 500,000. The decline "all boils down to habitat loss," says Connelly, considered a leading expert on the bird. Sage grouse are entirely dependent on sagebrush, a low, woody shrub, to survive. But sagebrush ecosystems are among the



The greater sage grouse, with habitat spread over 11 states, has touched off perhaps the biggest U.S. endangered-species battle ever.

PHOTO: © VYN, GERRIT/ANIMALS

chicken's recovery and removal from the threatened list. "I say have it all out there—the truth about it," he says. "I think [the research] will benefit the bird, but I think it will benefit the ranchers, too. It might take 5 years or so, but I'm hoping it will help delist them."

Plumb, the KSU ecologist, has spent hours drinking coffee and chatting with Hoeme and other ranchers since 2013, when he began intensively studying leks on private land. The heart-to-heart talks became a turning point in his own thinking, he says. "The way you are going to preserve the species is collaborative efforts. It has to balance the landowner's interest with the interest of the prairie chicken. You can't just strip all the landowner's interest away."

Ultimately, Plumb developed collaborations with 35 landowners who gave researchers access to some 20,000 hectares of



Researchers track lesser prairie chicken nestlings to better understand factors that aid survival. Some say the striped young look like bumblebees when they first take wing.

habitat in Kansas. But in a sign of the growing sensitivity surrounding the bird, landowners controlling about one-quarter of that land pulled out after USFWS issued its listing last year. "Landowners feel they're being targeted," Plumb says, in part, he believes, because of the sometimes heated

continent's most imperiled, eroded by drought, fire, and invasive species—and by development.

To blunt the threat, U.S. agencies have been trying to craft what U.S. Fish and Wildlife Service (USFWS) Director Daniel Ashe has called an "epic-scale partnership" with state governments, industry groups, and private landowners. A major goal is to avoid a federal listing, which many observers fear will spur expensive, lengthy court battles and strengthen efforts in Congress to gut the 42-year-old Endangered Species Act.

Last month, the federal Bureau of Land Management, which controls most of the grouse's prime habitat, took a major step toward implementing that partnership. It released a plan for avoiding further loss of grouse habitat on 20 million hectares of federal land by minimizing the footprint of energy developments, creating buffers around mating grounds (known as leks), and taking steps to improve and restore habitat.

"This is the single largest public land planning effort in United States history," says Theo Stein, spokesman for USFWS's mountain prairie regional office in Lakewood, Colorado. Similar plans are in the works in states such as Wyoming, home to the largest population of birds as well as expanding oil and gas operations. The goal, as with the lesser prairie

chicken, is to demonstrate that a federal listing isn't needed and that grouse and development can coexist.

Some environmental groups are open to the approach. Washburn's clients, for example, would like to see "good conservation plans that would avoid a listing," he says. But others doubt that a win-win is possible. They note that the birds appear to be extremely sensitive to industrial activities, often abandoning areas with new wells or wind turbines. A recent study commissioned by Pew Charitable Trusts found that grouse living in oil and gas fields near Wyoming's Powder River Basin and North and South Dakota may already be dropping into an "extinction vortex." In some areas, populations dropped 70% between 2007 and 2013.

Listing advocates also point out that restoring sage habitat, or creating new habitat, has proved difficult. So "you can't say we're going to go build 150 wind towers here, but we'll build a sage grouse habitat to replace it over there," Connelly says.

Whatever the Obama administration decides later this year, the issue may end up in court, with any final decision made by a federal judge. Meanwhile, the clock will keep ticking for the sage grouse. Given the rapid habitat loss and population decline, Washburn says, "there's not that much room for error at this point." ■

rhetoric spouted by interest groups on all sides. But, from his perspective, "that's not accurate at all."

Despite such turbulence, the current collaborative efforts have a better chance of success than "bringing a strong regulatory arm down," believes William Van Pelt, an official in WAFWA, the state coalition, who is based in Phoenix. One key, he says, will be effectively using the tens of millions of dollars for research and conservation incentives that WAFWA expects to collect from energy and other firms operating in prairie chicken habitat. Already, the group has collected \$45.9 million in fees and mitigation payments—money that Van Pelt says would not be available if the bird had been declared endangered. "We feel this is a better way of getting conservation," he says. And he's impatient with those who criticize the approach as untested: "Just because something's new doesn't mean it won't work."

WAFWA has a team of scientists that will evaluate the new studies and then recommend any changes in habitat management to the five relevant states. In particular, the team will be watching for "new information [that] tells us to do something different," Van Pelt says. "We want to ensure we just don't keep doing the same thing over and over."

LESSERS HAVE COME BACK from the brink before, most notably after the Dust Bowl of the 1930s, when populations also crashed. They "live in a very hostile environment" and are prone to boom and bust cycles, Haukos says. "It's just the last 15 or 20 years or so, they don't seem to be exhibiting that boom."

This year, though, the drought has eased in many places, and "every indication right now is that the population is going to go up again," Van Pelt says.

When Lipp and Robinson made their trip this past April to the lek in northwest Kansas, however, the males danced in vain. No females appeared. But Lipp and Robinson aren't taking that as a bad sign. Just a few weeks before, hens had crowded the dance floor and filled the traps. Now the researchers are tracking the tagged birds as they navigate a perilous, disputed landscape.

Many who study the lesser prairie chicken hope such research will help define a middle ground where the birds and people can both thrive. "Watch them for a morning," Gregory says. "Then tell me whether or not they should just disappear from the landscape." ■

Marianne Lavelle is a freelance journalist in Arlington, Virginia.

INSIGHTS



BOOKS *et al.*

SUMMER READING

Summer books for the science-minded

Packed with adventure, intrigue, and even a romance or two, this year's picks feature all the fun of a good “summer read” without the fluff. Join a quest to find the elusive, endangered saola in a remote mountain range in Laos, or reflect on a life spent unlocking the secrets of the mind with the incomparable Oliver Sacks. Tag along on a trek to the rainiest place on earth, embark on a sci-fi space odyssey, or explore the rich ecosystem surrounding a derelict farm in the heart of France. Is digital currency poised to change the world? How does our sense of taste divide the world into delight and disgust? Why are we obsessed with invisibility, and how have advances in optics and metamaterials brought us closer to attaining it? These answers and more await you in the books reviewed below.

Tasty

Reviewed by **Pina Fritz**

Sweet, bitter, salty, sour, and umami—sensations we experience every day, dividing the world into delight and disgust. But how do we actually perceive these qualities? How did the tasting sense develop over millions of years? And how does it influence our food habits?

Great intellectuals such as Plato and Kant discarded taste as an unsophisticated sense. Only recently have scientists revealed its complexity and importance, and it has

begun to gain the attention it deserves. In his book *Tasty: The Art and Science of What We Eat*, John McQuaid places taste in the foreground, arguing that flavor is “the most important ingredient at the core of what we are” and that smell is “the biological currency of feeling and action.”

Tracing a path from single-celled creatures that lack a centralized processing center for flavor cues; through the jawless hagfish, an eel-like vertebrate that detects its decomposing dinner via taste bud-like organs coupled to the brain; to the modern human, he examines how the sense of taste developed throughout evolution. By

Tasty The Art and Science of What We Eat

John McQuaid

Scribner, 2015. 301 pp.



combining taste buds on the tongue and olfactory receptors in the nose, we learn, the perception of manifold flavors in the brain as we know it today became possible.

McQuaid uses insights from the fields of neuroscience, psychology, chemistry, and biology to give a good overview of the poten-



tial effect of integrative food science on the future of modern food development. He explains, for example, how flavors develop and evolve during cooking and food processing; describes the complex communication between taste buds and the hypothalamus; and even delves into the philosophical facets of culinary delight and disgust. Anecdotes from kitchens, food corporations, science laboratories, and food markets add to the vivid feel of the book and, for the most part, are woven well into the scientific narrative.

His explanations render complicated scientific approaches accessible and digestible (pun intended) for lay readers. Perhaps as a result of trying to appeal to a wider audience, at times his explanations remain too vague—for example, when he refers to the olfactory bulb as “just a single synapse removed from the neocortex”—and not always accurate, as when he makes the claim that sugars in a coffee bean break down into “water, carbon dioxide, fatty acids, and an assortment of flavor compounds” when roasted.

Overall, however, the book is highly enjoyable and interesting, encouraging us to think more deeply about the question we ask from day to day: “Honey, what’s for dinner?”

10.1126/science.aab2361

The reviewer is at Food Concept and Physical Design, “The Mill,” CH-4112 Flüh, Switzerland. E-mail: pfritz@student.ethz.ch

Invisible

Reviewed by **Sean P. Rodrigues**

In a realm separate from our own, gods, mystics, and prophets hold the power of invisibility. Here in this world, humans have made it a mission to achieve this imponderable phenomenon, resorting to fraud, illusions, and optical physics in an attempt to mimic invisibility. *Invisible: The Dangerous Allure of the Unseen*, by Philip Ball, recounts humanity’s fixation with invisibility and its uncanny prevalence in society throughout time.

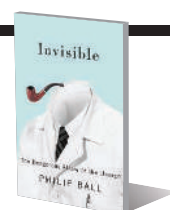
Ball begins with the fictional story of Gyges—a shepherd who stumbles upon a ring of invisibility and uses it to seduce the queen, slay the king, and install himself as the new ruler. The tale, as told by Plato, sets the stage for the book’s text by introducing the motivations that underlie our desire for invisibility, including power, sex, and murder. The book goes on to describe a series of tales of crooks, frauds, and sages claiming to possess powers of invisibility or equivocal sorcery.

Having previously served as an editor at the journal *Nature*, Ball provides an authoritative account of science’s most recent progress in the quest to emulate invisibility—including advances in metamaterials, metal-dielectric nanoengineered structures, and advanced camera-display techniques.

Invisible **The Dangerous Allure** **of the Unseen**

Philip Ball

University of Chicago Press,
2015. 330 pp.



Invisible also brings to light the more unusual pursuits of some of science’s most influential minds. For instance, we learn that the English physicist J. J. Thomson—who contributed to the discovery of the electron at the turn of the 20th century—was also interested in telepathy. Although we may regard telepathy with amusement today, Thomson believed the brain acted as both a transmitter and a receiver of unseen information and dedicated a great deal of research to the topic. He was a long-standing member of the Society for Psychical Research, an organization dedicated to supporting scholarly research into human experiences that challenge contemporary scientific models.

In chapter 8, Ball unearths details regarding James Clerk Maxwell’s efforts to disprove the second law of thermodynamics in the late 19th century. Motivated by his Catholic

The reviewer is at the School of Electrical and Computer Engineering, Georgia Institute of Technology, Atlanta, GA 30332, USA. E-mail: srodrigues7@gatech.edu

faith, Maxwell sought to reconcile the idea of free will with “a universe heading inexorably towards an inert, lifeless state.” In 1867, he sketched a theory in which unseen devices, later called “demons,” would decrease the overall entropy of the universe.

The book also captures how fantastical concepts molded a path for science to take form. For instance, in chapter 2, Ball introduces the occult forces known as vortices and vectors, which would later become known as electricity and magnetism. This blurred line between magic and science continued to exist even into the early 1900s, when Guglielmo Marconi and Thomas Edison “professed to be investigating devices that would make electronic contact with the dead” via radio technology. Ball presents such a captivating fusion of fiction and nonfiction that the reader must analyze the transcendental nature of science, religion, and magic and is left with a sense of uncertainty about the fabric of today’s science.

Invisible exemplifies Ball’s compelling craft of narrative, providing a seamless assembly of historical, cultural, and scientific tales, thus synthesizing a compendium of knowledge about invisibility. Despite Plato’s warnings, it seems nothing will prevent humans from pursuing the feat of the unseen.

10.1126/science.aab2187

The Last Unicorn

Reviewed by **David W. Redding**

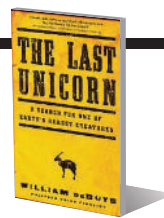
An expedition to find a live unicorn would certainly seem foolhardy. Fortunately, in his latest book, *The Last Unicorn: A Search for One of Earth’s Rarest Creatures*, William deBuys attempts a slightly more achievable aim: accompanying conservation biologist William Robichaud to the Annamite Mountains on the Laos-Vietnam border in search of the elusive saola. This recently discovered species is most straightforwardly described as an ox that looks like an oryx, or an antelope-like cow. It is a ghostlike animal with two curving, sabre-like horns and a natural history that we know practically nothing about.

The book reads like a gripping travelogue, but it also operates at a deeper level, leading us to question how we choose which species to conserve, how growing human populations can fit into a fracturing landscape, and how to value nature in the light of widespread poverty. A desire to conserve the natural world is one shared by many, but the underlying reasons for such

The Last Unicorn A Search for One of Earth’s Rarest Creatures

William deBuys

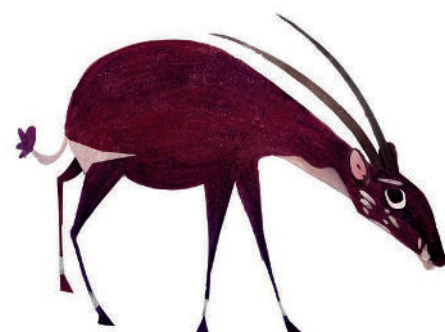
Little, Brown, 2015. 363 pp.



a perspective stubbornly resist attempts to be rationalized: Some see nature as providing irreplaceable services, others see it as housing as-yet-undiscovered biological innovations, and still others believe that the aesthetics of the natural world alone endow it with great value. Although deBuys addresses these arguments directly in his writing, it is telling that we learn so much about how humans interact with nature during the incidental moments of despair, awe, and hope that bubble up throughout the expedition’s narrative.

So why look to protect the saola? It is certainly in need, as it is critically threatened by both hunting and the loss of its natural habitat. Another potential reason is that it has, over time, become isolated from its closest relatives (bison and buffalo) and represents a long, unique evolutionary path—a rare event in nature reserved for the likes of the platypus, the horseshoe crab, and the coelacanth. We know little about evolutionarily isolated species and their specific roles within the ecosystem, and until we know more, their conservation would seem prudent.

But moving from a desire to protect toward effective action is often fraught with problems. Indeed, this book offers valuable insights into the wholly compromised and often chaotic world of field surveying and the reality of conservation in a remote en-



“How do you save a ghost if you are not sure it exists?” asks William deBuys

vironment. The central chapters are replete with lost trails, diminishing rations, and the increasingly conflicting needs and expectations of the crew and local communities.

When describing those living at the coalface of biodiversity loss in the tropics, there is a temptation for condescension: pitting enlightened westerners against the benighted locals. De Buys does not fall into

this trap, remaining both pragmatic about the livelihoods of indigenous populations and horrified by the unbridled extraction of the forest’s rich biological resources. He soberly notes that areas such as the Annamite Mountains “have so much further to fall” in terms of biodiversity that could be lost than, for example, the temperate forests of his childhood in the United States.

Part action adventure, part an exploration of loss, this book is a journey for both the heart and the mind.

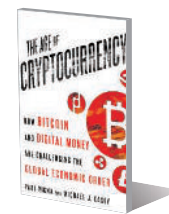
10.1126/science.aab2165

The Age of Cryptocurrency How Bitcoin and Digital Money Are Challenging the Global Economic Order

Paul Vigna and

Michael J. Casey

St. Martin’s, 2015. 367 pp.



The Age of Cryptocurrency

Reviewed by **Marie Vasek**

Given the narrow lens through which the online payment system known as Bitcoin is typically presented, casual observers could be forgiven for mistaking it for a white, libertarian cult revolving around the idol Satoshi Nakamoto. Much of the media coverage of the digital currency phenomenon can be summarized as either an elaborate musing on the real-life identity of Nakamoto or something that reads like a multilevel marketing scheme.

The Age of Cryptocurrency is a welcome break from this tradition. The first part of the book discusses how Bitcoin works technically, as well as some history behind the centralized digital currencies that predated it. It begins with a tale about Afghani women, empowered through Bitcoin to earn and save their own money. (Although traditional banking systems in Afghanistan do not serve women, using Bitcoin only requires one to have computer access.) The book goes on to tell other stories about the Bitcoin user base, taking the reader from a hacker cooperative in San Francisco, California, that is building the next generation of Bitcoin applications to a money changer in Barbados who is using Bitcoin to avoid currency controls. The

The reviewer is at the Centre for Biodiversity and Environment Research, University College London, Gower Street, London, UK. E-mail: dwredding@gmail.com

The reviewer is at the Department of Computer Science and Engineering, Southern Methodist University, Dallas, TX 75275, USA. E-mail: marie.vasek@gmail.com



Oliver Sacks, 1956

general theme stays the same despite the situation: Bitcoin subverts the mainstream banking system, affording the user more control over his or her money.

Technical details are interwoven with stories about the people behind the enabling technology. We are introduced to the “cypherpunks,” a mailing list of cryptography-inclined people who write code to incite social change, of which Nakamoto is a part. Here, the authors cannot resist musing about the identity of the mysterious, pseudonymous Bitcoin creator. Many of the important people involved in this movement are subjected to an analysis of why they may or may not be Nakamoto, and we are left to wonder whether he or she is an influential cryptographer, a designer of a centralized digital currency, or perhaps even a group of individuals from these communities.

Although most of the book is dedicated to the (arguably) good things that Bitcoin enables, the authors also delve into the troubles facing the digital currency movement. We mourn the demise of the first major Bitcoin exchange, Mt. Gox, which was launched in July 2010 in Tokyo and handled 70% of all Bitcoin trading by 2013. After being hacked numerous times, it finally collapsed in early 2014. We also learn about a mysterious entrepreneur known by the pseudonym “Dread Pirate Roberts” and the online marketplace he created, known as the Silk Road. Shut down in late 2013, the Silk Road exclusively accepted Bitcoin (and predominantly sold drugs). The authors cite it as a key player in the introduction of Bitcoin to the masses. In

October 2013, Roberts was identified as Ross Ulbricht, a Texas native living in San Francisco. On 29 May 2015, Ulbricht was sentenced to life in prison for his role in operating the Silk Road.

The book ends on an optimistic note. We are left with a vision of the future as a peer-to-peer world, where the ideologies of Bitcoin are not just confined to payments but spread across other industries. As the authors proclaim, “[w]e may well be on the verge of a profound societal upheaval, perhaps the most significant since the sixteenth century.” We might. Or perhaps Bitcoin will go the way of peer-to-peer music file sharing on Napster, which gave way to the centralized iTunes service. Only time will tell.

10.1126/science.aab2001

On the Move

Reviewed by **Benjamin Combs**

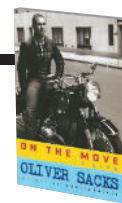
A schoolmaster once wrote that Oliver Sacks, then a 12-year old student, “will go far, if he does not go too far.” These words proved prescient, as that child grew into a preeminent neurologist and widely read author, who often struggled to stay within the professional and personal expectations held by others. Sacks, who recently announced that he has terminal cancer (1), looks back at an exceptional life and career in his captivating new autobiography, *On the Move*.

Readers of Sacks know he is no stranger to writing about himself, having previously written several books detailing his encoun-

On the Move A Life

Oliver Sacks

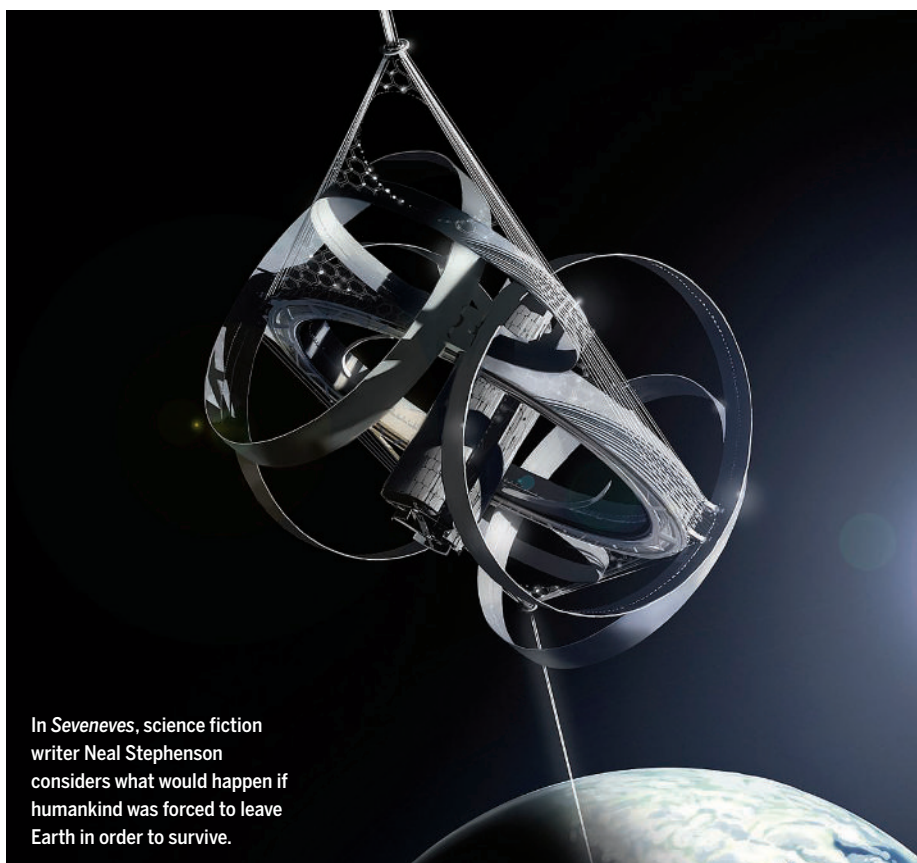
Knopf, 2015. 442 pp.



ters with patients displaying unusual neurological conditions (2, 3). Here, however, he reflects eloquently, and with a more direct focus, on his own past, detailing how his love of writing and discovery has influenced his personal and professional life. Sacks refers to himself as “a storyteller, for better or worse” and one who finds his greatest joy through writing. This passion for storytelling is what compelled him to help revive the lost art of the anecdotal case study in medical literature. The style was not always well received by many in the medical community, but Sacks remained true to it, believing that a greater understanding of the condition was possible through detailed descriptions of a patient’s life as well as their symptoms.

Sacks also applied this method to explain the inner workings of the human mind. At one point, he discusses Gerald Edelman’s theory of consciousness, which posited that consciousness is purely a biological phenomenon, arising from complex cellular processes within the brain. He felt that the theory was revolutionary but was frustrated at Edelman’s dense writing style,

The reviewer is in the Department of Translational Science and Molecular Medicine, Michigan State University, Grand Rapids, MI 49503, USA. E-mail: benjamin.combs@hc.msu.edu



In *Seveneves*, science fiction writer Neal Stephenson considers what would happen if humankind was forced to leave Earth in order to survive.

which was impenetrable to many readers. Feeling that relevant case studies could have helped, much of Sacks's subsequent writing used real examples to bolster Edelman's arguments so as to make them accessible to a wider audience. This is one of several examples in which Sacks served as a bridge between different worlds. He carried on friendships with great scientists, such as Francis Crick, but also with great poets, such as W. H. Auden and Thom Gunn.

In addition to medical and literary interests, Sacks had a taste for wilder pursuits. During his youth, he was a fervent motorcyclist and spent time training as a serious weightlifter (he set a California state powerlifting record in 1961). Sacks also explored the emerging drug culture of the 1960s, eventually overcoming an addiction to amphetamines.

Sacks was not a great student, consistently ranking at the bottom of his undergraduate class at Oxford University, but he was talented enough to win a prestigious essay contest entered on a drunken lark. He brings the same keen eye for detail to a journal entry about a weekend spent at a seedy truck stop while hitching a ride to New York as he does to case descriptions of patients with postencephalitic parkinsonism. Throughout his life, he has remained a prolific writer and describes stacks of

journals and letters he has saved. Many of these letters illuminate a complicated relationship with his family, including imposing parents, a schizophrenic brother, and an encouraging and insightful aunt.

Sacks has written an intimate and moving account of a life full of remarkable experiences. His passion for life and learning infuses the reader with a desire to stay "on the move," just as he has done for more than 80 years.

REFERENCES

1. O. Sacks, My own life: Oliver Sacks on learning he has terminal cancer, *New York Times*, 19 February 2015, A25.
2. O. Sacks, *The Man Who Mistook His Wife for a Hat* (Summit Books, New York, 1985).
3. O. Sacks, *Awakenings* (Summit Books, New York, 1973).
10.1126/science.aab1988

Seveneves

Reviewed by **Daniel Tamayo**

Neal Stephenson's latest novel wastes little time getting started—in the first sentence, the Moon blows up. But this isn't a *Star Wars*-style explosion; it's a softer kind of cataclysm. The breakup of the Moon ignites a self-reinforcing catastrophe as the ejecta collide and fragment into an ever-growing swarm of debris (the same fate we are desperately trying to avoid for our current fleet of artificial satellites). This

Seveneves

Neal Stephenson

Morrow, 2015.

867 pp.



plunges humanity into a desperate race to establish space habitats before the inevitable sterilization of Earth.

The ensuing drama provides a fascinating exploration of how environment shapes human society and remolds its moral norms. What constitutes power aboard a space station with no guns or police? Should individual rights be redefined in an environment where a single person's actions could extinguish the entire species? Stephenson engagingly tackles such issues, ranging from the philosophical to the psychological, all while interspersing a healthy dose of heinous deaths to keep things lively.

As one might expect for a space habitat orbiting in a debris cloud, many crises that the characters must overcome are puzzles in orbital mechanics. Stephenson provides delightful analogies for the relevant physical principles and does a remarkable job building the drama and bringing these moments alive (not a trivial task for phenomena that often unfold on time scales longer than a human lifetime).

As a specialist in orbital mechanics, I found myself furiously scribbling equations as I read—only to find out on the next page that Stephenson had obviously made the same calculation. In fact, I am currently at a scientific conference on orbital dynamics, and over dinner (funnily enough at the same place where one of the book's main characters sees the moon explode) we spent half an hour arguing—not over our research but rather over the orbital mechanics in *Seveneves*. Whatever the standard is for hard science fiction, surely Stephenson has blown it out of the water.

One can always find aspects to quibble over—some important scenes end rather abruptly (or are omitted altogether), only to be explained later to the reader. Also, the idea that some technologies from the first half of the book would be recognizable 5000 years later—the time period in which the second half of the book is set—seems rather improbable.

Despite these minor issues, *Seveneves* is a thrilling page-turner, overflowing with beautifully crafted puzzles and permeated with thorny philosophical questions. The novel is also remarkably refreshing, both

The reviewer is at the Centre for Planetary Sciences, University of Toronto at Scarborough, Toronto, Ontario M1C 1A4, Canada.
E-mail: d.tamayo@utoronto.ca

ILLUSTRATIONS BY WETA WORKSHOP; © NEAL STEPHENSON; LEAD ILLUSTRATOR: CHRISTIAN PEARCE; CREATIVE RESEARCH: BEN HAWKER AND PAUL TOBIN

for its optimism and for Stephenson's decision to make its most capable, decisive, and intelligent characters women. I plan to be first in line to read the sequel.

10.1126/science.aab1992

Rain

A Natural and Cultural History

Cynthia Barnett

Crown, 2015. 366 pp.



Rain

Reviewed by Rachel McCrary

Ask atmospheric scientists and meteorologists why they study the skies and most will tell a story about a childhood obsession with rainfall or a vivid experience with unique or extreme weather. With *Rain: A Natural and Cultural History*, Cynthia Barnett will make a rain fanatic out of anyone, not just self-described weather aficionados.

In many ways, the book is the biography of a vital natural phenomenon. It tells the story of how rain has helped shape Earth's natural landscape as well as human civilization. Through her approachable and engaging writing, Barnett tells this eclectic story by combining science and history with humor, anecdotes, poetry, and personal travel adventures.

Starting with the violent imagery of the first rains on Earth, Barnett moves rapidly forward through time, framing humans as truly remarkable for our "ability to adapt to any conditions the atmosphere blows our way," from long periods of drought to excessive rainfall.

Barnett captivates the reader through her unique way of finding a human face to describe historical climate and weather events. She writes about the human sacrifices of the Aztecs, which were intended to help end devastating drought, as well as the witches who served as scapegoats for the centuries of destructive rainfall that fell over Europe during the Little Ice Age. Through her words, we get a taste of how passionate early weather recorders such as Thomas Jefferson and George James Symons were about keeping track of the rain's comings and goings.

She pauses to share quirky anecdotes, describing, for example, the initial disdain for umbrellas in Europe and recounting the story of the quest to create waterproof clothing, which ultimately resulted in the iconic Macintosh. In a particularly memorable chapter, "Writers on the Storm," Barnett explores

the role that rain has played in the creation of art, including the works of Charles Dickens, Emily Dickinson, Frédéric Chopin, The Smiths, Nirvana, and Woody Allen.

A common theme among a number of Barnett's vignettes is humans' attempts to control and respond to rain—whether through costly early geoengineering programs that bombed "the hell out of the skies" to make it rain or the building of massive levees to control the natural floodplains of the Mississippi River, the construction of which killed many workers. Her examples demonstrate how our attempts to manipulate rain's natural life cycle are often costly, dangerous, and ultimately ineffective.

Although it is not the main focus of the book, Barnett also touches pointedly on the issue of human-caused climate change, suggesting that while the issue "frightens and divides us," the topic of rain—whether too much or not enough—"brings us together." The book culminates with her personal trek to visit the rainiest place on Earth—Cherapunji, India—where monsoon rains have traditionally been celebrated for the life they breathe into the world. Who knows how much longer this will continue, as dry spells become longer and extreme flooding becomes commonplace.

10.1126/science.aab2097

A Buzz in the Meadow

Reviewed by Michelle Duennes

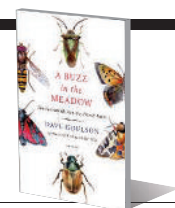
As urban centers grow around the world, more people are living farther from natural and agrarian spaces than ever before. Dave Goulson's *A Buzz in the Meadow* provides a glimpse into these spaces that often go unnoticed, exploring the natural histories of the flora and fauna on a farm in the French countryside. Along the way, the book takes many unexpected turns to much broader (and sometimes very personal) tales of scientific discovery.

Goulson, a biologist by training, begins the book with a tour of Chez Nauche, the abandoned farm he purchased in the Charente region of southwestern France. He gives engaging accounts of the natural histories of the newts, dragonflies, mantises, and other animals he encounters, which are meant to inspire readers to explore their own yards. Goulson hopes that in doing so, they will begin to value not only the "large charismatic, furry or feathery creatures, often living on the other side of the world, glimpsed only in television documentaries" but also smaller, familiar organisms that affect our environment in profound ways. He makes special examples of the insect species living on the farm, using meadow brown butterflies to explain the be-

A Buzz in the Meadow The Natural History of a French Farm

Dave Goulson

Picador, 2015. 281 pp.



ginnings of the field of genetics and flies to highlight the mismanagement of landfills.

In the second part of the book, Goulson weaves tales of complex interactions between plants, animals, and fungi to illustrate the interconnectedness of life. He closes with an examination of the many factors that can lead to the decline and eventual extinction of species, focusing particularly on bumblebees, which he has studied throughout his scientific career. His conclusions are grim: We have, he claims, been culpable in the mass extinction of life on Earth since the beginning of our evolution. But Goulson's goal—"to encourage everyone to cherish what we have, and to illustrate what wonders we stand to lose if we do not change our ways"—is clear and resonates throughout the book.

Many of the life histories, species interac-




Biologist Dave Goulson urges us to cherish and protect life in all its forms.

tions, and ecological concepts outlined in this book can be found elsewhere in published literature, but what stands out are the deeply personal insights Goulson provides into the life of a scientist. When discussing the many species he has studied over his career, he chronicles the trials, small victories, and failures of a young biologist. He also reveals the triumphs and frustrations that can come from attempting to communicate important scientific research to nonplussed policymakers and members of the public. His experiences will resonate with many scientists and will provide the general reader with an interesting and accessible glimpse into the life of a naturalist.

10.1126/science.aab1819

The reviewer is at the Department of Entomology, University of Illinois at Urbana-Champaign, Urbana, IL 61801, USA. E-mail: mduennes@life.illinois.edu



Although gray wolf (*Canis lupus*) populations are recovering in parts of Europe and North America, wolves continue to be killed in attempts to protect livestock and threatened species such as caribou.

CONSERVATION

When the hunter becomes the hunted

Effective predator management relies on social acceptability as well as scientific evidence

By **Rosie Woodroffe**¹
and **Stephen M. Redpath**²

Historically, wild predators were overwhelmingly viewed as threats to livestock, wild “game,” and public health. Over time, public perceptions have broadened to include recognition of predators’ intrinsic value and their role in structuring ecosystems. Nowhere are these changing perceptions better illustrated than in Yellowstone National Park, where the U.S. government deliberately eliminated wolves in the 1920s, only to actively restore them in the 1990s. Large carnivores are now recovering across much of North America and Europe but declining elsewhere (1, 2).

¹Institute of Zoology, Regent’s Park, London NW1 4RY, UK.

²Institute of Biological and Environmental Sciences, University of Aberdeen, Aberdeen AB24 2TZ, UK.

E-mail: rosie.woodroffe@ioz.ac.uk; s.redpath@abdn.ac.uk

Predator control, once widely accepted by the public, has become a source of intense social conflict (3, 4). Robust scientific evidence and broad stakeholder involvement are crucial for effective management of predator populations.

Randomized controlled experiments have repeatedly shown that predator control can bolster populations of prey species, including many of conservation concern (5, 6). However, the complexity of ecological systems means that predator control does not invariably benefit wild prey. In some ecosystems, factors such as habitat loss or weather conditions influence prey numbers more strongly than does predation. Suppressing the populations of one predator species may cause other predators to increase in number, leaving prey to face unchanged or even heightened predation rates. For example, Ellis-Felege *et al.* have shown in an experimen-

tal study that predator control efforts reduce mammalian predation on bobwhite quail nests in the southeastern United States, but these benefits are offset by increased predation from snakes (7). Similarly, pronghorn (which are preyed on by coyotes but seldom by wolves) appear to have declined in response to the extirpation of wolves, which caused a dramatic expansion of coyotes across North America (8).

Predator control is thus not invariably beneficial, and decisions about its use need to be informed by case-specific evidence. The best evidence comes from controlled experimental studies, which have been widely used to understand the effects of predator control on wild prey. However, decisions about controlling predators to protect livestock or manage disease have often been based on much weaker evidence. For example, despite the enormous effort invested in control-

ling populations of red foxes, coyotes, and wolves, we are not aware of any randomized experiments that investigate whether such control reduces livestock predation as intended. This is problematic because it is often difficult to disentangle cause and effect in observational studies.

The ability of experimentation to improve evidence in such cases is illustrated by the management of bovine tuberculosis in Britain. The role of European badgers in transmitting tuberculosis to cattle was recognized in the 1970s, but decades of badger culling failed to prevent the infection from spreading across Britain. A randomized controlled trial revealed that culling consistently increased infection rates in badgers, spreading the disease in space and, under some circumstances, elevating disease risks for cattle (9). This failure of predator control to effect disease control is linked to the social behavior of these territorial animals. When badgers are killed in one area, other badgers migrate into the newly available territory. The resulting social instability is thought to increase opportunities for disease transmission (9). A similar behavioral response was seen among red fox populations culled across Europe in the 1970s to control rabies (10). Such fox control efforts were gradually abandoned as practical experience showed fox vaccination to be far more effective (10).

Predator control conducted for a specific purpose often has broader consequences, which may be as unwelcome as they are unintended. Control or elimination of large carnivores, mainly to reduce livestock depredation, has been linked to increased deer numbers across Europe and North America. These larger deer populations damage forests and crops, reduce road safety, and have cascading effects on ecosystems (11). Extirpating wolves across much of North America stopped wolves from killing sheep, but introduced a new sheep predator as coyotes spread across the continent. Likewise, culling badgers for disease control purposes in the United Kingdom doubled the numbers of another farm pest, the red fox (12). The potential for predator control to cause unwanted side-effects should be considered seriously in environmental impact assessments and other policy decisions.

In deciding how and whether to manage predation, it is also important to bear in mind that the need for predator control is itself often a consequence of human action. For example, in Patagonia, guanacos are kept in low numbers by their natural predator, the puma. Normally predator numbers would fall as their prey decline, but pumas are sustained by sheep, deer, and

hares introduced by people, allowing them to maintain high predation pressure on the few remaining guanacos (13). Similarly, Canadian oil developments have opened up the boreal forest, allowing deer numbers to increase and improving access to the forest for wolves. As a consequence, endangered woodland caribou face unsustainable predation, prompting the Canadian state governments to shoot, trap, and poison wolves in an attempt to protect the caribou (14). More generally, many studies have found predation on birds' nests is higher where human activities have fragmented natural habitat. Predator control efforts aimed at conserving threatened prey may need to be maintained

decision-makers might prioritize economic gains. They might then consider the need for wolf control (or indeed the loss of woodland caribou) a small price to pay for the prosperity achieved through oil exploitation. The caribou inhabiting Canada's boreal forest have come to resemble the partridges struggling to survive in England's wheat fields; both may remain reliant on predator control unless or until society is willing to restore their natural habitat.

Robust scientific evidence alone is not sufficient to manage predators effectively; social acceptability is equally important. Pragmatic conservationists have long recognized that allowing some predator control—whether or not it achieves its stated aims—can help to build tolerance among land managers who might otherwise block conservation efforts (3). Unfortunately, such compromise is not always effective. For example, small-scale culling of badgers on

and around farms experiencing tuberculosis would be more socially acceptable than widespread badger control. However, such localized culling consistently increases cattle tuberculosis (9). Policy-makers are thus faced with a stark choice between near-elimination of a native carnivore (unpopular with the public and potentially unlawful) or no badger control at all (unpopular with farmers). The British government's decision to pursue large-scale badger culling became an issue in the recent national election, and culls have

“...the need for predator control is itself often a consequence of human action.”

in perpetuity unless conservation seeks to restore ecosystem functioning.

Decisions about how to manage predation in such human-altered systems are driven as much by the priorities of decision-makers as by rigorous scientific evidence. For example, decision-makers responding to woodland caribou declines might choose to prioritize biodiversity conservation. They would then prefer habitat restoration over wolf control, because this approach preserves predation as an ecosystem process. Alternatively,



European badgers (*Meles meles*) transmit tuberculosis to cattle, but efforts to control tuberculosis by culling badgers have not been effective because they do not take their social behavior into account.

been repeatedly delayed by legal challenges.

Controversy about predator management can lead to intense social discord, which may undermine management decisions. For example, in Britain conservation efforts for hen harriers have been hampered by persistent illegal killing, while attempts to control cattle tuberculosis by killing badgers have been disrupted by dedicated protestors. Where social conflict is intense, scientific evidence is often used selectively, contested, or dismissed. In such situations, involving stakeholders in the design, implementation, and interpretation of experimental studies may help to build trust and improve social learning. For example, controversy over grizzly bear management in Banff National Park, Canada, was successfully resolved by engaging stakeholders in a problem-solving group, which shared responsibility for interpreting scientific evidence and making management decisions (15).

Similar approaches might benefit the management of ecologically complex and socially divisive issues such as tuberculosis in badgers, wolf predation on caribou, and hen harrier predation on grouse (4). The challenge, especially in more intense social conflicts over predators, is that polarized views may prevent parties from engaging with the process at all. If policy-makers, scientists, and stakeholders from all sides can show leadership in overcoming this challenge, predator management might become more evidence-based, as well as more responsive to changing social perspectives. ■

REFERENCES

1. G. Chapron *et al.*, *Science* **346**, 1517 (2014).
2. W. J. Ripple *et al.*, *Science* **343**, 151 (2014).
3. R. Woodroffe, S. Thirgood, A. R. Rabinowitz, *People and Wildlife: Conflict or Coexistence?* (Cambridge Univ. Press, Cambridge, 2005).
4. S. M. Redpath, R. J. Gutiérrez, K. A. Wood, J. C. Young, *Conflicts in Conservation: Navigating Towards Solutions* (Cambridge Univ. Press, Cambridge, 2015).
5. A. R. Holt, Z. G. Davies, C. Tyler, S. Staddon, *PLOS ONE* **3**, 8 (2008).
6. R. K. Smith, A. S. Pullin, G. B. Stewart, W. J. Sutherland, *Conserv. Biol.* **24**, 820 (2010).
7. S. N. Ellis-Felege, M. J. Conroy, W. E. Palmer, J. P. Carroll, *J. Appl. Ecol.* **49**, 661 (2012).
8. K. M. Berger, E. M. Gese, J. Berger, *Ecology* **89**, 818 (2008).
9. J. Bourne *et al.*, *Bovine TB: The Scientific Evidence* (Defra, http://archive.defra.gov.uk/foodfarm/farmanimal/diseases/atoz/tb/isg/report/final_report.pdf, London, 2007).
10. D. W. Macdonald, *Rabies and Wildlife—a Biologist's Perspective* (Oxford Univ. Press, Oxford, 1980).
11. S. D. Cote, T. P. Rooney, J. P. Tremblay, C. Dussault, D. M. Waller, *Annu. Rev. Ecol. Evol. Syst.* **35**, 113 (2004).
12. I. D. Trewby *et al.*, *Biol. Lett.* **4**, 170 (2008).
13. A. J. Novaro, R. S. Walker, in *Large Carnivores and the Conservation of Biodiversity*, J. C. Ray, K. H. Redford, R. S. Steneck, J. Berger, Eds. (Island Press, Washington, DC, 2005), pp. 268–288.
14. D. Hervieux, M. Hebblewhite, D. Stepiwnski, M. Bacon, S. Boutin, *Can. J. Zool.* **92**, 1029 (2014).
15. M. L. Gibeau, *Wildl. Prof.* **6**, 62 (2012).

10.1126/science.aaa8465

CELL BIOLOGY

An ESCRT to seal the envelope

Cellular machinery that remodels different lipid bilayers also closes the nuclear membrane

By Wesley I. Sundquist¹
and Katharine S. Ullman²

Metazoan cells divide by “open” mitosis, in which disassembly of the nucleus allows microtubules of the mitotic spindle to access kinetochores, proteinaceous structures that associate with specialized regions of chromosomes called centromeres. Duplicated chromosomes align on the spindle, and as they segregate toward opposite ends of the dividing cell, nuclear membrane reassembly initiates (1). This requires recruiting membrane, reconstituting nuclear pores, and severing microtubule connections between chromosomes and the spindle organizing centers (centrosomes). The nuclear envelope must seal to reestablish proper separation of the genome from the cytoplasm, but just how the nuclear membrane closes and overcomes the physical roadblocks presented by spindle microtubules has been unclear. Recent studies (2, 3) now demonstrate that the endosomal sorting complex required for transport (ESCRT) membrane fission machinery orchestrates this mysterious process.

Membrane fission, the process by which a continuous lipid bilayer separates into two discontinuous bilayers, occurs constantly as cells remodel their membranes. It can occur with two distinct topologies: one in which the juxtaposing membranes are drawn together at a cytoplasm-filled neck, and another in which they are drawn together at a cytoplasm-surrounded neck. Many familiar processes, such as endocytic vesicle formation, correspond to the latter topology, where the cytoplasmic protein dynamin encircles the constricting neck and “pushes” the membranes toward the fission point. By contrast, ESCRT protein assemblies work from inside membrane necks to “pull” the constricting membranes toward themselves (4, 5).

Two keys to this activity are the ability of ESCRT-III family members to form spiraling filaments that can draw membranes toward the fission point (6–8), and the ability of vacuolar protein sorting 4 (VPS4) to remodel these filaments and thereby provide the power for membrane fission (4, 5). ESCRT-III subunits also recruit relevant proteins through their exposed terminal

tails. Because of its unique activity, the ESCRT machinery is used in a variety of different membrane remodeling processes, including intraluminal vesicle formation in the late endosome, enveloped virus budding, wound healing, and the final stage of daughter cell physical separation (cytokinetic abscission) during cell division (4, 5, 9, 10).

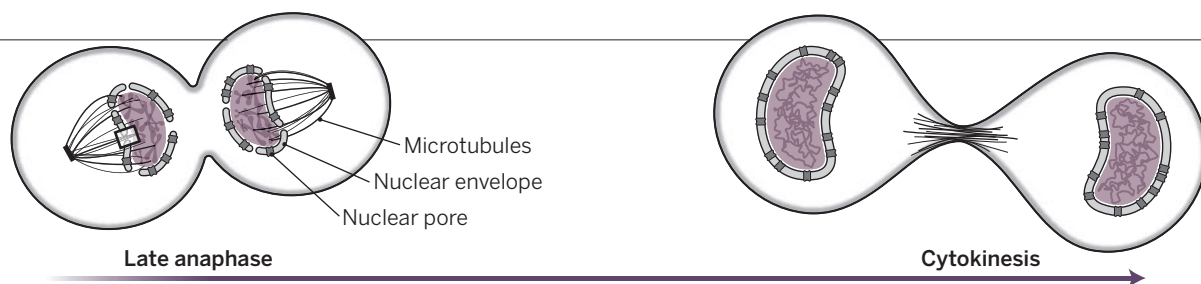
The studies by Vietri *et al.* (2) and Olmos *et al.* (3) reveal that the ESCRT pathway also reseals the nuclear envelope during late anaphase-early telophase stages of the cell division cycle (see the figure). The breakthrough was made possible, in part, because the investigators studied specific sites in the nuclear envelope at relevant times by combining live-cell imaging of transient events and higher-resolution

“Mechanisms that reseal the nuclear envelope have been unclear, but a role for ESCRT machinery should now be considered.”

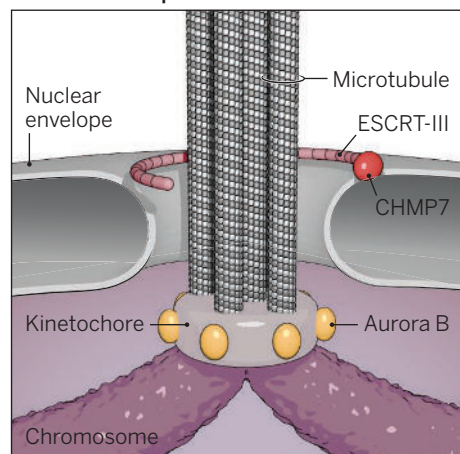
microscopic techniques, including structured illumination microscopy and correlative light and electron microscopy. The studies report that ESCRT-III and VPS4 assemble briefly at fenestrations in the growing nuclear envelope, and that assembly of core ESCRT-III subunits occurs in a canonical fashion, with component charged multivesicular body protein 4 (CHMP4), CHMP3, and CHMP2 proteins recruited sequentially (5). In the absence of successful ESCRT assembly, postmitotic nuclear envelopes have unsealed holes and are functionally “leaky.”

Although the two studies agree on the essential role of ESCRT machinery in closing nuclear fenestrations, each also adds unique insights into this process. ESCRT-III proteins function at many different mem-

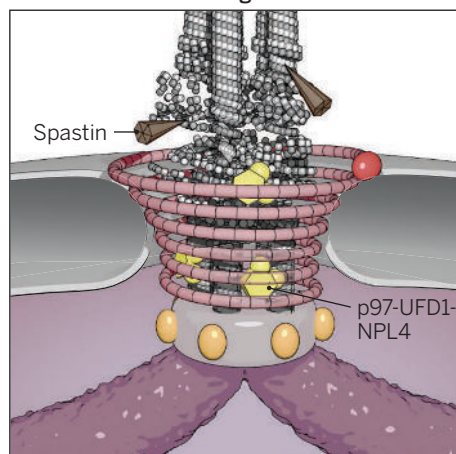
¹Department of Biochemistry, University of Utah School of Medicine, Salt Lake City, UT 84112-5650, USA. ²Department of Oncological Sciences, Huntsman Cancer Institute, University of Utah, Salt Lake City, UT 84112-5650, USA.
E-mail: wes@biochem.utah.edu; katharine.ullman@hci.utah.edu



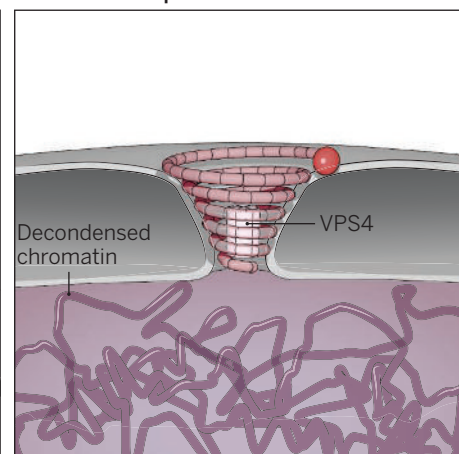
Nuclear envelope fenestration



Microtubule remodeling



Nuclear envelope closure



Seeking closure. Soon after chromosome segregation begins, ESCRT machinery is recruited to fenestrations where the forming nuclear envelope encounters microtubules that are still attached to centromeres. ESCRT factors draw the membrane together to accomplish fission, and co-recruitment of ancillary factors, such as spastin and p97 ATPases, helps coordinate microtubule remodeling with nuclear membrane closure.

branes because they remain soluble until recruited by membrane-specific adapter proteins. These adapters often nucleate ESCRT-III filament assembly in concert with the early-acting ESCRT factors apoptosis-linked gene 2 interacting protein X (ALIX), ESCRT-I, and ESCRT-II (4). Vietri *et al.* show that in the case of nuclear envelope closure, a previously uncharacterized ESCRT-III-like protein, CHMP7, plays a role in recruiting and initiating ESCRT-III assembly. The authors also demonstrate that the spastin family adenosine triphosphatases (ATPases), which sever microtubules, are recruited by an ESCRT-III subunit called increased sodium tolerance 1 (IST1). This coordinates release of spindle-kinetochore connections with closure of fenestrations. In addition, Vietri *et al.* show that failure to seal holes in the nuclear membrane leads to proximal DNA damage.

In complementary studies, Olmos *et al.* connect yet another ATPase, p97, to nuclear fenestrations by discovering a previously unknown interaction between a p97 adapter protein called ubiquitin fusion degradation 1 (UFD1) and the ESCRT-III subunit CHMP2A. This finding further underscores how ESCRT-III filaments accommodate and coordinate the complex series of events required to form a nucleus. The CHMP2A-UFD1 interaction ties into observations that p97-UFD1-nuclear protein

localization 4 homolog (NPL4) complexes are required to close the nuclear envelope (11) and to remove Aurora B (the enzyme that controls progression of mitosis and cytokinesis) from chromatin as the envelope is closed (12). It could be that ESCRT-mediated p97 localization is also important for microtubule remodeling. Even the “canonical” function of p97-UFD1-NPL4 in retrotranslocating proteins from the endoplasmic reticulum could be called upon to remove integral membrane proteins and prime highly curved membranes for fission.

The findings of Vietri *et al.* and Olmos *et al.* provide a fresh basis for thinking about other dynamic events at the nuclear envelope. The ESCRT machinery is also implicated in creating vesicles that bud from the nuclear membrane and carry cargoes such as ribonucleoprotein complexes, herpes viral cores, and defective nuclear pore assemblies out of the nucleus (13). These processes can now be viewed as part of a continuum of ESCRT-mediated nuclear membrane fission events. Indeed, the recent studies provide precedence for the idea that quality control of nuclear pore complexes could involve coupled extraction of assembled but defective pores, with ESCRT machinery closing the resulting membrane holes. The importance of nuclear membrane maintenance is further highlighted by studies that reveal the pro-

pensity of nuclei to rupture, especially in tumors and other disease states such as laminopathies (14). Mechanisms that reseal the nuclear envelope have been unclear, but a role for ESCRT machinery should now be considered. It will also be of great interest to understand how postmitotic nuclear envelope closure is coordinated with other important ESCRT-dependent activities, particularly the Aurora B-dependent abscission checkpoint (15) and the ensuing step of cytokinetic abscission (10), which completes cell division. ■

REFERENCES

1. C. Wandke, U. Kutay, *Cell* **152**, 1222 (2013).
2. M. Vietri *et al.*, *Nature* 10.1038/nature14408 (2015).
3. Y. Olmos, L. Hodgson, J. Mantell, P. Verkade, J. G. Carlton, *Nature* 10.1038/nature14503 (2015).
4. J. McCullough, L. A. Colf, W. I. Sundquist, *Annu. Rev. Biochem.* **82**, 663 (2013).
5. W. M. Henne, H. Stenmark, S. D. Emr, *Cold Spring Harb. Perspect. Biol.* **5**, a016766 (2013).
6. G. Fabrikant *et al.*, *PLOS Comput. Biol.* **5**, e1000575 (2009).
7. A. G. Cashikar *et al.*, *eLife* **3**, e02184 (2014).
8. J. Guizetti *et al.*, *Science* **331**, 1616 (2011).
9. A. J. Jimenez *et al.*, *Science* **343**, 1247136 (2014).
10. J. G. Carlton, J. Martin-Serrano, *Science* **316**, 1908 (2007).
11. M. Hetzer *et al.*, *Nat. Cell Biol.* **3**, 1086 (2001).
12. K. Ramadan *et al.*, *Nature* **450**, 1258 (2007).
13. B. M. Webster, C. P. Lusk, *Nucleus* **10.1080/19491034.2015.1035844** (2015).
14. E. Hatch, M. Hetzer, *J. Cell Biol.* **205**, 133 (2014).
15. J. G. Carlton, A. Caballe, M. Agromayor, M. Kloc, J. Martin-Serrano, *Science* **336**, 220 (2012).

10.1126/science.aac7083

DEVELOPMENTAL BIOLOGY

It's about time for neural crest

The unusual pluripotency of neural crest cells is inherited from embryonic stem cells

By Stefan Hoppler¹ and Grant N. Wheeler²

What has made vertebrates so successful has been the evolution of their superior sensory organs, a more sophisticated organization of the brain, and—eventually—toothed powerful jaws, which gradually supported an ecological shift from passive filter feeding to a more active predatory lifestyle. Building this “new head” in vertebrate embryos relies on an elite group of cells called the neural crest (1). Indeed, the English developmental biologist Peter Throgood famously recounted that as a young scientist he was told by a senior professor (in an authoritative tone), “The only interesting thing about vertebrates is the neural crest” (2). On page 1332 of this issue, Buitrago-Delgado *et al.* (3) provide further support for this bold statement in demonstrating that neural crest cells uniquely retain pluripotent stem cell programming until later in development than the three classic germ layers.

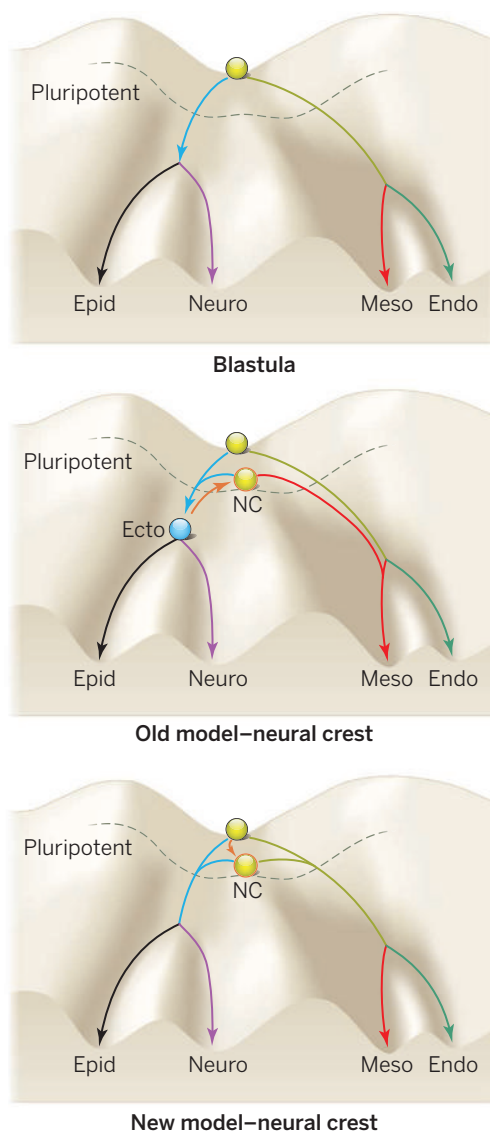
The neural crest is a population of cells in vertebrate embryos with a remarkable ability to generate a variety of structures in the adult. The neural crest arises from within the so-called ectoderm germ layer, at the border between the future neural tissue and the future epidermis. However, unlike their neighbors on either side, neural crest cells undergo an epithelial-to-mesenchymal transition (EMT), during which they delaminate from the ordered tissue layer of the ectoderm and migrate as loose groups along defined paths to different and sometimes distant locations in the embryo, where they differentiate into a variety of cell types. Cell labeling and chimera experiments have been instrumental in uncovering these migration and differentiation patterns (4). Neural crest cells differentiate into cell types that generally arise from other germ layers such as the mesoderm, with the tissues they migrate through and those of their destination determining the cell types they become. Because this is particularly important for the formation of our “new head,” including the face, neck, and

teeth, it is the neural crest that also allows us all to smile, or to frown.

Neural crest development in the vertebrate embryo is controlled by a largely conserved gene regulatory network, which has been described in detail (5). However, it had remained unclear where the remarkable differentiation ability of these cells came from. Prior to the study by Buitrago-Delgado *et al.*, it seemed that neural crest cells were induced to selectively regain increased differentiation ability, unlike their cellular neighbors in the rest of the ectoderm. In this view, the neural crest could be described as an endogenous population of induced pluripotent stem cells. Although many stem cell biologists liked this idea, it sat uncomfortably with traditional developmental biologists brought up on the paradigm of progressively restricted developmental potential, as illustrated by Waddington's developmental landscape (see the figure) (6).

Now, Buitrago-Delgado *et al.* provide insight into how neural crest cells retain far greater developmental potential than other ectoderm cells. They show that neural crest cells, rather than gaining developmental potential, retain pluripotency that they selectively inherit from the embryonic stem cells from which they are derived (see the figure, bottom panel). The authors noticed that neural crest potency factors are also expressed in pluripotent embryonic stem cells at an earlier stage of development. They show that these genes regulate pluripotency in these early embryonic stem cells, and that the experimentally extended expression of these factors can confer a delay in restricting developmental potential even to cells that would normally not give rise to neural crest. The maintenance of expression of these factors is what maintains neural crest differentiation potential.

Waddington can therefore rest in peace: Neural crest cells do not violate his paradigm of progressive restriction of developmental potential, they just manage to delay its onset for a little bit longer than their cellular neighbors. This remarkable differentiation ability—at a stage of development when the three conventional germ layers have already formed—had led to the neural crest being described as the “fourth germ layer” (7). However, the new study shows that such a moniker is not re-



Developmental potential in embryonic development. (Top)

A pluripotent blastula or embryonic stem cell “rolls” like a marble down one of four differentiation pathways: endoderm (Endo), mesoderm (Meso), neural ectoderm (Neuro), and non-neural ectoderm or prospective epidermis (Epid). The dashed line indicates where pluripotency is lost. **(Middle)** Previous models implied that the differentiation ability of neural crest cells (NC, orange) was induced from an ectoderm germ layer (Ecto, blue), by “pushing” the marble representing a neural crest cell uphill toward increased differentiation potential back above the dashed line (orange arrow). **(Bottom)** The new model by Buitrago-Delgado *et al.* shows that neural crest cells, unlike their cellular neighbors, remain pluripotent before they differentiate, even potentially into endodermal derivatives.

¹Institute of Medical Sciences, Foresterhill Health Campus, University of Aberdeen, Aberdeen AB25 2ZD, Scotland, UK.

²School of Biological Sciences, Norwich Research Park, University of East Anglia, Norwich NR4 7TJ, UK.
E-mail: s.p.hoppler@abdn.ac.uk

quired, because neural crest cells have now been shown to be little different from earlier embryonic cells; they are able to differentiate into cell types of all three conventional germ layers, including endoderm, albeit just a little bit later in development.

The work by Buitrago-Delgado *et al.* sheds further light on the evolution of the neural crest and therefore of vertebrates. Retaining pluripotency may not have been the crucial evolutionary step that defines the neural crest. Closely related nonvertebrate animals share with vertebrates the expression of components of the neural crest gene regulatory network in cells at the neural plate boundary, including what we now understand are regulators of pluripotency (8). Instead, vertebrate neural plate border cells may have evolved the ability to undergo EMT, delaminate from the ectoderm, and migrate to different parts of the embryo (9, 10).

The Buitrago-Delgado *et al.* study raises questions about the identity of what we conventionally call the ectoderm. The most pressing issue is, however, how these cells at the neural plate border region selectively retain pluripotency while cells all around them become restricted in their developmental potential.

Buitrago-Delgado *et al.* follow in the footsteps of pioneering studies that have used the amphibian as a model system to uncover fundamental aspects of vertebrate development, from basic processes in embryonic induction (11–13) through uncovering the principle of somatic cell reprogramming (14). Like these earlier discoveries, now seen as pivotal in understanding human development and disease, this latest research has critically changed our perception of vertebrate evolution and development and demonstrates the importance of the neural crest. ■

REFERENCES

1. C. Gans, R. G. Northcutt, *Science* **220**, 268 (1983).
2. P. Thorogood, *Trends Neurosci.* **12**, 38 (1989).
3. E. Buitrago-Delgado, K. Nordin, A. Rao, L. Geary, C. LaBonne, *Science* **348**, 1332 (2015).
4. N. M. Le Douarin, *The Neural Crest* (Cambridge Univ. Press, Cambridge, 1982).
5. M. Simões-Costa, M. E. Bronner, *Development* **142**, 242 (2015).
6. C. H. Waddington, *Nature* **150**, 563 (1942).
7. B. K. Hall, *Evol. Dev.* **2**, 3 (2000).
8. P. B. Abitua, E. Wagner, I. A. Navarrete, M. Levine, *Nature* **492**, 104 (2012).
9. S. M. Shimeld, P. W. Holland, *Proc. Natl. Acad. Sci. U.S.A.* **97**, 4449 (2000).
10. H. Wada, K. Makabe, *Int. J. Biol. Sci.* **2**, 133 (2006).
11. H. Spemann, H. Mangold, *Roux Arch. Entw. Organ. Mikrosk. Anat.* **100**, 599 (1924).
12. P. D. Nieuwkoop, *Wilhelm Roux Arch.* **162**, 341 (1969).
13. J. C. Smith, B. M. Price, K. Van Nimmer, D. Huybreoek, *Nature* **345**, 729 (1990).
14. J. B. Gurdon, "The egg and the nucleus: A battle for supremacy" (Nobel lecture); www.nobelprize.org/nobel_prizes/medicine/laureates/2012/gurdon-lecture.html.

10.1126/science.aab2719

MEMBRANES

Outperforming nature's membranes

Ultrathin synthetic membranes that reach a record permeability can clean up organic solutions

By Viatcheslav Freger

Industrial chemical reactions or biosynthetic processes rarely yield pure products, and the additional separation steps typically required often make up the largest part of the product cost. Membrane separations are considered among the most efficient methods, deriving inspiration from the membranes in living cells. Intriguingly, on page 1347 of this issue, Karan *et al.* (1) show that synthetic membranes may get close to and eventually outperform their soft biological counterparts in many aspects. They targeted the rapidly developing field of organic solvent nanofiltration (OSN) (2). Such membrane filtration of nonaqueous solutions may help make chemical synthesis (3) more efficient and environmentally friendly by separating and recycling solvents, reactants, products, and catalysts.

Synthetic membrane films work by selectively retaining or passing molecules. These processes require an energy input, e.g., pumping energy in the case of filtration. Development of an efficient membrane faces a twofold challenge: finding a highly selective material, and forming a large and defect-free film of a minimal thickness to maximize permeability and minimize pumping energy. Interfacial polymerization (IP) is a remarkably simple process that simultaneously achieves both goals. Two monomers dissolved in immiscible solvents, e.g., water and hexane, react at the interface to form a polymer film that eventually self-terminates its growth. With the right choice of monomers, typically, an aromatic triacid and a diamine, a thin polyamide membrane is obtained.

Usually, preparation is carried out on top of a thick porous supporting membrane, yielding a composite membrane with a polyamide top layer (see the figure, panel A). The advent of such polyamide composites some three decades ago revolutionized

membrane desalination, which today supplies drinking water to millions of people worldwide with unprecedented thermodynamic efficiency approaching 50% (4).

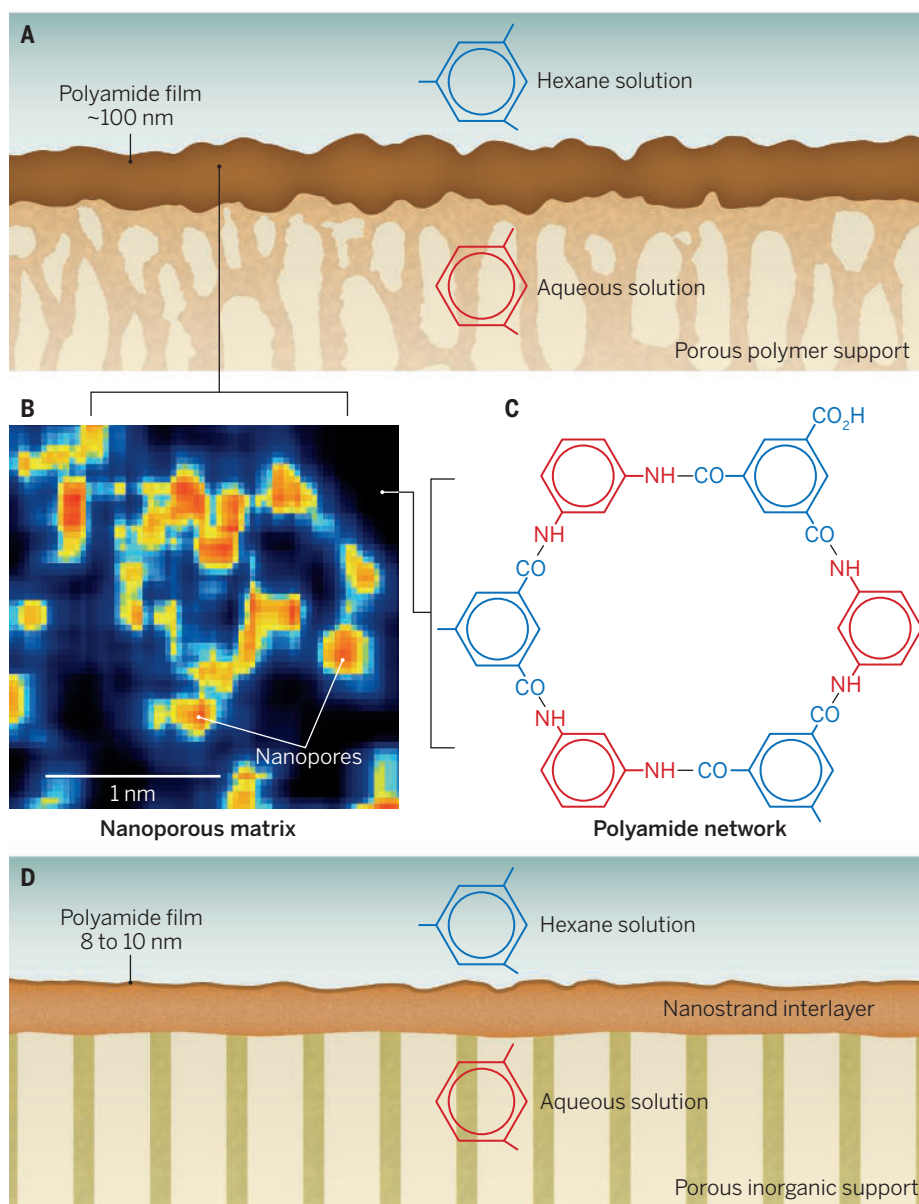
Although OSN membranes have not made a similar breakthrough, Karan *et al.* have taken a large step toward achieving this goal. The seemingly straightforward IP process turns out to be formidably complex as regards understanding the relation between the preparation conditions and the film's thickness, nanostructure, and permeability. Mean-field models (5) and molecular dynamic simulations (6, 7) reveal that IP proceeds as a complex aggregation process, resulting in a film of poorly defined thickness and structural irregularities at all spatial scales involved. The irregularities manifest themselves in intrinsic porosity that results from the high rigidity of the polyamide matrix (7) (see the figure, panels B and C). If not excessive, this porosity is beneficial, as it enhances membrane permeability (8). However, it is not at all straightforward to come up with rational recipes for controlling thickness and porosity and maximizing the permeability.

Karan *et al.* identified several new ways to manipulate the IP process and obtain a dramatic increase in permeability. One ingenious modification was to move film formation somewhat away from the solid

"To expand to new avenues and stay economically attractive, membrane development must constantly strive for higher permeabilities and seek new and better selectivities."

support by adding an intervening sacrificial interlayer made of needle-like cadmium hydroxide nanostrands (see the figure, panel D). Such a layer, easily formed by filtering nanostrand suspension through the supporting membrane and dissolved, once the IP reaction is complete, is far more porous and uniform than the support surface because of the very small size of nanostrands. Apparently, this structure facilitates a uniform access of monomers and enhances their flux into the growing film, which was shown to be inversely related to film thick-

Wolfson Department of Chemical Engineering,
Technion-Israel Institute of Technology, Haifa 32000, Israel.
E-mail: vfreger@tx.technion.ac.il



Making an ultra-permeable membrane. In a standard interfacial polymerization (**A**), an aqueous diamine solution impregnates the polymeric support and reacts with a hexane solution of trifunctional acid monomer to form a thin and highly selective polyamide film. The film is an aggregated structure with random subnanometer pores (**B**) in a rigid molecular network matrix (**C**). A critical difference is made by a sacrificial nanostrand layer that moves the reaction away from the solid support surface (**D**). This layer dramatically decreases polyamide thickness from about 100 nm to between 8 and 10 nm. When combined with film crumpling, “opening up” of polyamide with a swelling solvent, and the stabilizing effect of the rigid inorganic support, membrane permeability is increased by an unprecedented two orders of magnitude.

ness (5). As a result, uniform films could be prepared of a record-breaking 8-nm thickness, just shy of that of biological membranes (5 to 6 nm), yet strong enough to survive straining through a pipette tip.

Another performance-enhancing effect was crumpling of the film when the diamine concentration exceeded a certain threshold. Crumpling or folding increased the effective area and permeation rate for a given area. Suggestions that this effect could explain enhanced permeability of some commercial membranes were made in

the past (9). However, Karan *et al.* managed to explicitly show this by taking advantage of the easy transfer of the polyamide film from nanostrand layer to substrates more suitable for structural examination. They also pointed out that crumpling could be related to instabilities caused by excessive heat generation during IP reaction, in analogy with the Rayleigh-Bénard instability of a fluid layer heated from the bottom.

Although the prepared films already had outstanding characteristics, Karan *et al.* took the process a step further and treated

the film with a swelling solvent (dimethylformamide). This is known to “open up” polyamide, i.e., increase its porosity, but, unfortunately, when dimethylformamide is changed to another solvent, the permeability usually declines. Surprisingly, they found that the performance decline could be entirely prevented by using a rigid inorganic support instead of a regular polymeric one (see the figure, panels A and D). This change resulted in a staggering stable permeability of 112 liter m⁻² hour⁻¹ bar⁻¹ for acetonitrile as the solvent, which surpasses that of biological membranes (10) by an order of magnitude and that of today’s desalination membranes by two orders of magnitude. This result suggests that the support might be as important as the selective layer itself for maximizing and stabilizing performance.

To expand to new avenues and stay economically attractive, membrane development must constantly strive for higher permeabilities and seek new and better selectivities. Karan *et al.* demonstrate great potential for improvements in relatively old approaches via smart manipulation of membrane preparation, use of novel nanomaterials, and attention to all components of the composite membrane. This effort must be assisted by in-depth understanding of the transport, rejection, and membrane formation mechanisms, as well as membrane nanostructure, which at present remains a challenge even for much older desalination membranes. The challenge increases many-fold for OSN, which must operate and remain stable in various media and rely on much weaker molecular interactions, compared to electrostatic forces dominating salt-water separations (11, 12). Nevertheless, the benefits of simpler, faster, and greener processing make it a worthy effort. ■

REFERENCES

1. S. Karan, Z. Jiang, A. G. Livingston, *Science* **348**, 1347 (2015).
2. P. Marchetti, M. F. Jimenez Solomon, G. Szekely, A. G. Livingston, *Chem. Rev.* **114**, 10735 (2014).
3. J. D. Keasling, A. Mendoza, P. S. Baran, *Nature* **492**, 188 (2012).
4. R. Semiat, J. Sapoznik, D. Hasson, *Desalination Water Treat.* **15**, 228 (2010).
5. V. Freger, *Langmuir* **21**, 1884 (2005).
6. E. Harder, D. E. Walters, Y. D. Bodnar, R. S. Faibish, B. Roux, *J. Phys. Chem. B* **113**, 10177 (2009).
7. V. Kolev, V. Freger, *Polymer (Guildf.)* **55**, 1420 (2014).
8. E. Dražević, K. Košutić, V. Freger, *Water Res.* **49**, 444 (2014).
9. T. Fujioka, N. Oshima, R. Suzuki, W. E. Price, L. D. Nghiem, *J. Membr. Sci.* **486**, 106 (2015).
10. Y.-Shen, P. O. Saboe, I. T. Sines, M. Erbakan, M. Kumar, *J. Membr. Sci.* **454**, 359 (2014).
11. A. E. Yaroshchuk, *Separ. Purif. Tech.* **22-23**, 143 (2001).
12. A. Szymczyk, N. Fatin-Rouge, P. Fievet, C. Ramseyer, A. Vidonne, *J. Membr. Sci.* **287**, 102 (2007).

10.1126/science.aab3727

Are you watering your lawn?

High-resolution data may help to devise effective water conservation strategies in urban areas around the world

By Terri S. Hogue¹ and Stephanie Pincetl²

Increases in urban populations, particularly in semi-arid cities, have led to unsustainable water use in many regions of the world. Water is frequently drawn from outside urban boundaries, but these remote water sources are becoming less reliable due to global climate change and regional political conflict. In response, urban water conservation efforts have been expanding and cities are pressured to reduce demand. Yet, as seen currently in California, measures to reduce water use are having limited effect (1). Can better data help to underpin water use policy?

Between 2003 and 2012, Australia experienced the longest and most severe drought on record, prompting extensive conservation efforts to maintain water supplies (2). In Brazil, the states of São Paulo and Rio de Janeiro are at their lowest levels of water supply in 80 years, with reservoirs at ~5% of capacity. Water managers in these states are targeting conservation efforts at those with high consumption levels, offering discounts for reduced use and decreasing allotments to industry and agriculture (3). The ongoing drought in the western United States (see the photos) has also led to accelerated efforts in water conservation and expanded regulation on groundwater consumption.

The governor of California has declared emergency mandatory restrictions to achieve a 25% statewide reduction in potable urban water use. Cities across the state are drafting integrated water management plans that include viewing all water sources (including, for example, recycled wastewater and storm runoff) as suitable for consumption. The cities are also accelerating water conservation efforts, including new tier pricing regimes and mandatory water-

ing restrictions. The City of Los Angeles, which imports over 90% of its water supply, is under mayoral directive to reduce imported water by 50% and increase local water sources.

Policies to conserve water differ widely across urban centers and are formulated based on institutional structure, history, and governing bodies. Common practices include price increases or pricing structure change (altering or expanding a tier structure), volume reductions, policing efforts and fines, watering restrictions, and landscape replacement programs. There is evidence that nonpecuniary strategies such as social comparisons of water use can make some difference in water consumption as well, especially for high users, but the effects are not large (4).



California drought. A field of dead almond trees in Coalinga in the Central Valley, California, on 6 May 2015 (left) illustrates the severity of the ongoing drought. In response, state water regulators have recently adopted mandatory cutbacks in urban water use (right).



However, few studies have evaluated the effect of implemented conservation measures, especially across diverse socioeconomic groups, citywide regions, or water districts. Institutions generally track citywide water consumption trends, but rarely is there detailed spatial and temporal analysis to quantify where and when conservation efforts are successful or where efforts should be reformulated to reach consumers who are insensitive to implemented policies. For example, outdoor water use is often reduced during a period of drought but may rebound or even increase after there has been rain. Moreover, little is known about the relationship between water use reductions and regional urban greenness, although concern about this is often behind resistance to water conservation (5).

Historical research on water use in cities has relied on intelligent intuition, modeled data, or small-sample data. Early work in California was driven by the Pacific Institute (6), which relied mainly on population estimates and empirical coefficients for statewide regions. More recent analyses have used multivariate or statistical regression models to evaluate urban demand (7, 8), although still largely based on modeled data. For example, Balling and Gober evaluated the response of annual water use to climate conditions in Phoenix, Arizona (7). Although overall water use fell over the study period, annual water use rose with higher temperatures, lower precipitation, and drought conditions. Watering habits suggest that many residents were unaware of optimal watering for their landscapes. Mini *et al.* found residential water use in Los Angeles to be driven by household income, landscape greenness, water rates, and allocated volumes (8), with 10% of single-family customers using 30% of all residential water in the city.

Outdoor water use accounts for a large percentage of total water use in many arid cities, ranging from 40 to 70% depending on climate, pricing, and sociodemographic fac-

tors (9). Work in this area is accelerating as managers look for methods to better refine outdoor use and landscape irrigation. For example, Kaplan *et al.* (10) used high-resolution Landsat data and an evapotranspiration model to estimate outdoor water use and drought response in the Phoenix area. Evapotranspiration (the water transmitted back to the atmosphere through plants) and water consumption values stayed elevated over agricultural regions during drought, whereas urban landscape and the surrounding desert regions showed lower evapotranspiration and overall water use during drought. Thus, conservation measures for park areas in Phoenix during drought years appear to have been effective. Mini *et al.* have shown that in Los Angeles, where outdoor use accounts for 54% of residential

¹Department of Civil and Environmental Engineering, Colorado School of Mines, Golden, CO 80401, USA. ²Institute of the Environment and Sustainability, UCLA, Los Angeles, CA 90095, USA. E-mail: thogue@mines.edu

water consumption, mandatory restrictions improved total water savings by up to 23%, whereas voluntary water restrictions resulted in only 6% water savings (11).

Data from water meters can also help to inform water conservation measures. Progress is being made in dual metering (indoor/outdoor billing segregation), smart metering (real-time monitoring that transmits to the utility), and intelligent metering (real-time monitoring that can also include informational feedback and control options) (12, 13). The extensive, detailed data provide valuable information on consumer use to utilities and resource managers. However, smart and intelligent metering systems are expensive and not yet widely used (14). The data are typically not in a user-friendly format, requiring sophisticated data processing for analysis. Further work is also needed to better understand how information from advanced metering technologies can help to influence consumer water use (15).

If detailed observational data are combined with other databases and advanced models, they can inform targeted water conservation efforts. However, many water agencies do not have technical capacity to mine data over time and analyze change. For example, the current drought in California has led to calls to develop and report water use analysis, because agencies lack the ability to differentiate indoor and outdoor water use to evaluate the effectiveness of water conservation measures. Applying water use models that acknowledge sociodemographic characteristics and local characteristics, such as size of residence, outdoor water use, and vegetation, will be crucial for meeting water conservation goals and targets. ■

REFERENCES AND NOTES

1. See, for example, www.theguardian.com/us-news/2015/may/05/california-falls-short-water-saving-target-drought.
2. B. Neal et al., *Water Management* **167**, 435 (2014).
3. NPR, A historic drought grips Brazil's economic capital (10 February 2015; www.npr.org/sections/parallels/2015/02/10/384971276/a-historic-drought-grips-brazils-economic-capital).
4. P. J. Ferraro, M. K. Price, *Rev. Econ. Stat.* **95**, 643 (2013).
5. C. Carandang, thesis, Civil and Environmental Engineering, Colorado School of Mines, Golden, CO (2015).
6. P. H. Gleick et al., *Waste Not Want Not: The Potential for Urban Water Conservation in California* (Pacific Institute, Oakland, CA, 2003), appendix B.
7. R. C. Balling Jr., P. Gober, *J. Appl. Meteorol. Climatol.* **46**, 1130 (2007).
8. C. Mini et al., *Water Policy* **16**, 1054 (2014).
9. R. St. Hilaire et al., *HortScience* **43**, 2081 (2008).
10. S. Kaplan et al., *Environ. Manage.* **53**, 855 (2014).
11. C. Mini et al., *Resour. Conserv. Recycling* **94**, 136 (2015).
12. C. D. Beal, J. Flynn, *The 2014 Review of Smart Metering and Intelligent Water Networks in Australia and New Zealand* (Report prepared for Water Services Association of Australia by the Smart Water Research Centre, Griffith University, Gold Coast, Queensland, Australia, November 2014).
13. T. R. Gurung et al., *J. Clean. Prod.* **87**, 642 (2015).
14. T. Boyle et al., *Water* **5**, 1052 (2013).
15. D. P. Giurco, S. B. White, R. A. Stewart, *Water* **2**, 461 (2010).

10.1126/science.aaa6909



Foreign ministers discuss Iran's nuclear program in Lausanne, April 2015.

NUCLEAR SECURITY

After the Iran deal: Multinational enrichment

World powers should buy a stake in Iran's enrichment capacity and accept the same rules

By Alexander Glaser, Zia Mian,*
Frank von Hippel

In April 2015, Iran and the E3+3 nations (France, Germany, and the United Kingdom, plus China, Russia, and the United States) negotiated a framework for a “comprehensive solution that will ensure the exclusively peaceful nature of the Iranian nuclear program” (1, 2). The final settlement, expected by July 2015 or soon after, would constrain Iran's activities for various extended periods in return for the lifting of sanctions and affirm Iran's right to pursue its nuclear program free of the limits on its uranium enrichment capacity a decade or more from now. What happens when these restrictions begin to phase out? We outline one approach to limit the long-term risk by using the next 10 years to convert Iran's national enrichment plant into a multinational one, possibly including as partners some of Iran's neighbors and one or more of the E3+3 countries.

After Iran's enrichment efforts were made public in 2003, the United States organized a broad alliance to pressure Iran to end this program, fearing that it was seeking nuclear weapons. Despite ever more punishing international sanctions, Iran built up its enrichment capacity, insisting that this program was peaceful and permitted under the 1968 nonproliferation treaty (NPT), which recognizes an “inalienable right of all the Parties to the Treaty to develop research, production

and use of nuclear energy for peaceful purposes without discrimination” (3).

As part of its efforts to address concerns about the proliferation risks from its nuclear program, in November 2013 Iran agreed with the E3+3 on a Joint Plan of Action involving temporary limitations on its nuclear activities in exchange for limited sanctions relief (4). The April 2015 framework for a final settlement builds on the joint plan and includes limiting Iran to one operating enrichment plant (at Natanz); placing limits on its capacity, enrichment level, and stockpile of enriched uranium for “specified durations”; and an agreed-upon plan for Iran's centrifuge research and development. It also includes constraints on the plutonium production capacity of research reactors and an agreement by Iran not to separate plutonium from spent fuel or other irradiated uranium. The final element is increased transparency, including of centrifuge fabrication, and enhanced access for International Atomic Energy Agency (IAEA) inspectors to assure compliance. These transparency measures encompass and go beyond the reporting and access obligations of normal IAEA safeguards on NPT nonweapon states, including an additional protocol to the IAEA safeguards agreement, which Iran has signed and agreed to implement.

Program on Science and Global Security, Princeton University, Princeton, NJ, USA.

*Corresponding author. E-mail: zia@princeton.edu

When restrictions expire, Iran will continue to be bound by the NPT and subject to IAEA inspection of its nuclear program, including the extra transparency measures and access provided by the additional protocol. Despite this transparency, there will remain concerns in the West and among Iran's major competitors for influence in the Middle East about the nuclear-weapon option implicit in Iran's enrichment program. Prince Turki bin Faisal, the former Saudi intelligence chief, recently stated, "Whatever the Iranians have, we will have, too" (5).

ENRICHMENT AND BREAKOUT. The proliferation threat inherent in national uranium enrichment plants was recognized at the beginning of the nuclear era. In 1946, the Acheson-Lilienthal report—drafted in large part by J. Robert Oppenheimer, the scientific director of the U.S. World War II nuclear-weapon-design effort—described uranium enrichment and technology for plutonium separation from irradiated uranium (reprocessing) as "dangerous" and proposed that they be put under international control as part of a global ban on nuclear weapons (6). This idea was revived in the 1970s and again in the early 2000s, but without success (7).

Natural uranium is 0.7% uranium-235 ($U-235$), the chain-reacting isotope used for nuclear power plant fuel. Modern commercial gas-centrifuge enrichment plants typically contain tens of thousands of machines connected in series and in parallel into cascades to enrich uranium hexafluoride (UF_6), the chemical form in which uranium is enriched in centrifuges, to 3 to 5% $U-235$. However, these cascades could quickly be reconnected to produce "weapon-grade" uranium enriched to 90% $U-235$ or more.

Iran demonstrated this flexibility in 2010 when it interconnected pairs of cascades designed to produce 3.5% enriched uranium for eventual use to fuel its Bushehr power reactor and began to produce uranium enriched up to 19.75% for the Tehran Research Reactor (8). Uranium enriched to 20% and above is defined as highly enriched uranium (HEU) and considered weapon-usable by the IAEA.

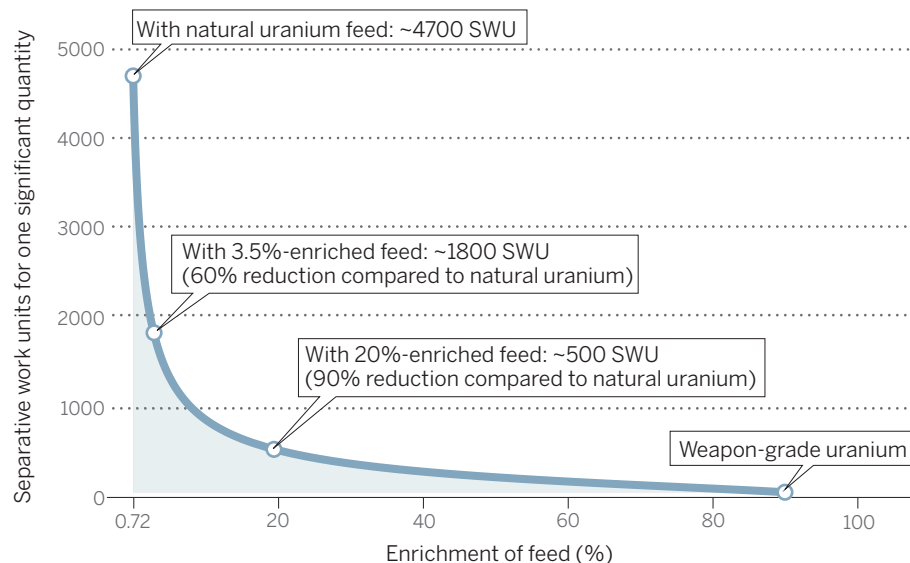
A primary U.S. objective in international negotiations with Iran has been to limit Iran's enrichment capacity to a level from which it would take at least a year to "break out" and produce enough weapon-grade uranium for a first nuclear explosive. On advice from the weapon states, for purposes of establishing safeguards criteria, the IAEA has defined HEU containing 25 kg of $U-235$ as a "significant quantity" (SQ), the approximate amount of nuclear material for which the possibility of manufacturing a nuclear explosive device cannot be excluded (9).

Enrichment capacity is measured in separative work units (SWU), reflecting the effort expended in separating feedstock into enriched and waste products. From IAEA reports on the quantity and enrichment of the product from Iran's first-generation IR-1 centrifuges since 2010, the average IR-1 has been producing 0.7 to 1 SWU per year (10). According to the 2 April 2015 White House fact sheet on the framework agreement (2), Iran has accepted a limit of 5060 operating IR-1 centrifuges for 10 years and has agreed not to deploy more advanced centrifuges during that period.

AFTER 10 YEARS. Looking a decade ahead when limitations begin to loosen, Iran has made clear its intention to produce enough enriched uranium to fuel its Bushehr-1 power

and E3+3 partners could, for example, purchase a share of the Natanz plant based on the investment and operating cost per unit capacity of large commercial enrichment plants. This would mean that Iran would have to continue to subsidize its enrichment program until it became competitive. All the potential E3+3 partners have expertise in centrifuge enrichment. They would not be required to provide technology but could be given full access to the Iranian plant without raising new proliferation concerns. Further transparency would follow, when it becomes politically possible, were Middle Eastern countries to form a regional nuclear inspectorate to supplement IAEA safeguards, as Argentina and Brazil did after they both simultaneously gave up their nuclear weapon programs (13).

Enriching uranium to weapon-grade



The SWU capacity required for a 1-year breakout time would depend on whether the feed into Iran's enrichment cascades was natural or enriched uranium. According to the U.S. fact sheet (2), Iran has agreed to enrich to less than 3.67% and reduce its stock of enriched UF_6 , which could quickly be fed into centrifuges, to much less than the amount required to produce one "significant quantity" (SQ). Feeding enriched uranium into centrifuges dramatically reduces the capacity required to produce an SQ of 90% enriched weapon-grade uranium within a given period of time (11). See the supplementary materials for details on this estimate.

reactor rather than continue to rely on importing Russian fuel. To produce the 27 tons a year of 3.5% enriched uranium for reactor fuel would require more than 100,000 SWU per year (11, 12). If this enrichment capacity were converted to the production of weapon-grade uranium, Iran would be able to produce 20 SQ a year from natural uranium and 50 SQ a year from 3.5% enriched uranium. Converting Iran's enrichment capacity from a national to a multinational enterprise could help limit long-term risk. Regional

A multinational approach to uranium enrichment could be an important step toward a long-hoped-for nuclear weapon-free zone in the Middle East. Iran and Egypt proposed such a zone to the United Nations General Assembly in 1974, and the proposal was broadened by Egypt in 1990 to include all weapons of mass destruction (WMD). The 1995 NPT Review and Extension Conference supported this goal. In 2014, a group of 22 Middle East states (all but Syria and Israel) sent letters to the United Nations

Secretary General confirming support for declaring the Middle East a region free from WMDs (14). Achieving a Middle East nuclear weapon-free zone, as part of a Middle East WMD-free zone, would benefit from all its members accepting the enrichment and reprocessing restrictions and enhanced transparency obligations agreed to by Iran and eventually will require Israel to verifiably give up its nuclear weapons (15).

MULTINATIONAL ENRICHMENT. Multinationalizing Iran's uranium enrichment program could become a step toward phasing out or multinationalizing national enrichment programs worldwide as part of a regime in which nuclear power rules apply equally to all states.

Uranium enrichment is required by the "light" (ordinary) water-cooled reactors that dominate the current global nuclear power reactor fleet. National enrichment programs currently exist in China, France, and Russia. None of these states has enriched uranium for weapon purposes since the end of the Cold War. India, Pakistan, and North Korea enrich uranium on a much smaller scale, including for military purposes. Three non-weapon states also have national enrichment plants: Japan, Brazil, and Iran.

An alternative to national enrichment plants emerged in the 1970s in the form of Urenco, a company jointly controlled by Germany, the Netherlands, and the United Kingdom, which operates one enrichment plant in each of these countries. Urenco currently operates 60% of the enrichment capacity outside Russia and owns the only commercial enrichment facility currently operating in the United States. This plant supplies about 40% of U.S. requirements, with the remainder imported. Most countries with nuclear power plants purchase uranium enrichment services from Urenco and Russia.

Since 1983, the United States has argued with countries interested in launching spent-fuel reprocessing (plutonium-separation) programs, in effect, "We don't reprocess. You don't need to either." This argument, reinforced by the poor economics of plutonium recycling, helped discourage additional countries from launching reprocessing programs. The United States is now in a position to argue similarly with countries like Iran, "We have the largest nuclear power program in the world, but we currently don't have a national enrichment program. You don't need one either."

By committing, as part of the forthcoming deal on Iran's nuclear program, to working on multinational enrichment arrangements for the Middle East, and ultimately around the world, Iran and the E3+3 could chart a path to reduce the proliferation risks from

national control of civilian enrichment plants, regardless of location. In parallel, a Fissile Material Cutoff Treaty would end unsafeguarded uranium enrichment in the weapon states. ■

REFERENCES AND NOTES

1. Joint Statement by EU High Representative Federica Mogherini and Iranian Foreign Minister Javad Zarif Switzerland, 2 April 2015; http://eeas.europa.eu/statements-eeas/2015/150402_03_en.htm.
2. The United States issued a fact sheet on the same day detailing its view of the obligations agreed to in April 2015, "Parameters for a Joint Comprehensive Plan of Action regarding the Islamic Republic of Iran's Nuclear Program"; www.whitehouse.gov/sites/default/files/docs/parametersforajointcomprehensiveplanofaction.pdf.
3. Treaty on the Non-Proliferation of Nuclear Weapons (NPT), United Nations Office of Disarmament Affairs (1968); www.un.org/disarmament/WMD/Nuclear/NPTText.shtml, Article IV.
4. International Atomic Energy Agency (IAEA), "Communication Dated 27 November 2013 Received From the EU High Representative to the Agency Concerning the Text of the Joint Plan of Action," INFCIRC/855, 27 November 2013; www.iaea.org/sites/default/files/publications/documents/infcircs/2013/infcirc855.pdf.
5. D. E. Sanger, "Saudi Arabia Promises to Match Iran in Nuclear Capability," *New York Times*, 13 May 2015.
6. U.S. State Department, *A Report on the International Control of Atomic Energy* (1946); www.fissilematerials.org/library/ach46.pdf.
7. A. Glaser, *Internationalization of the Nuclear Fuel Cycle*, International Commission on Nuclear Non-proliferation and Disarmament, ICNND Research Paper No. 9 (February 2009).
8. The Tehran Research Reactor was provided to Iran by the United States in 1960. It was fueled with weapon-grade uranium fuel. Argentina converted it to 19.75% enriched uranium fuel in 1992. IAEA, Research Reactor Database, nucleus.iaea.org/RRDB/RR/ReactorSearch.aspx.
9. This includes production losses, IAEA, *Safeguards Glossary*, 2001 edition (International Atomic Energy Agency, Vienna, 2002), p. 23.
10. D. Albright, S. Kelleher-Vergantini, A. Stricker, P. Izewicz, D. Schnur, ISIS Analysis of IAEA Iran Safeguards Report (Institute for Science and International Security, Washington, DC, 19 February 2015).
11. It has been assumed that the associated depleted uranium produced contains 0.4% U-235, as has been Iran's practice.
12. Organization of Atomic Energy of Iran, "Bushehr Power Plant Fuel Reserve was replaced," 11 March 2014; www.aeo.org.ir.
13. Brazilian-Argentine Agency for Accounting and Control of Nuclear Materials (ABACC), www.abacc.org.br.
14. The states are Algeria, Bahrain, Comoros, Djibouti, Egypt, Iran, Iraq, Jordan, Kuwait, Lebanon, Libya, Mauritania, Morocco, Oman, Palestine, Qatar, Saudi Arabia, Somalia, Sudan, Tunisia, United Arab Emirates, and Yemen. Note by the Secretary-General regarding letter received from member states confirming support for declaring the Middle East a region free from weapons of mass destruction, including nuclear, chemical, and biological weapons, 6 March 2014; www.un.org/disarmament/WMD/menbletters.
15. F. N. von Hippel, S. Hossein Mousavian, E. Kiyaei, H. A. Feiveson, Z. Mian, "Fissile Material Controls in the Middle East: Steps toward a Middle East Zone Free of Nuclear Weapons and all other Weapons of Mass Destruction," International Panel on Fissile Materials, October 2013; www.fissilematerials.org/library/rr11.pdf.

ACKNOWLEDGMENTS

We thank anonymous reviewers for comments.

SUPPLEMENTARY MATERIALS

www.sciencemag.org/content/348/6241/1320/suppl/DC1

10.1126/science.aac5989

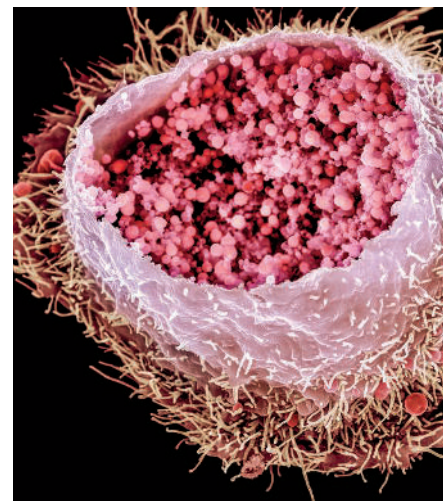
IMMUNOLOGY

A *Chlamydia* vaccine on the horizon

Results of a new *Chlamydia* vaccine in mice should spur human clinical trials

By Robert C. Brunham

Chlamydia trachomatis is the most common reported sexually transmitted bacterial infection in the United States, with more than 1.4 million cases of infection reported to the U.S. Centers for Disease Control and Prevention in 2012 (1). Worldwide, it is likely the most common infectious cause of infertility in women. An estimated 106 million cases of *C. trachomatis* occur globally among both women and men each year, so the worldwide burden of disease is substantial. Current public health efforts to prevent sexually transmitted disease caused by *C. trachomatis* or *Neisseria gonorrhoeae* emphasize prevention, but screening and treatment programs in medium- and low-income countries are rarely implemented because of financial and logistical difficulties. The findings reported by Stary *et al.* on page 1331 of this issue (2) constitute a major step forward in understanding *C. tracho-*



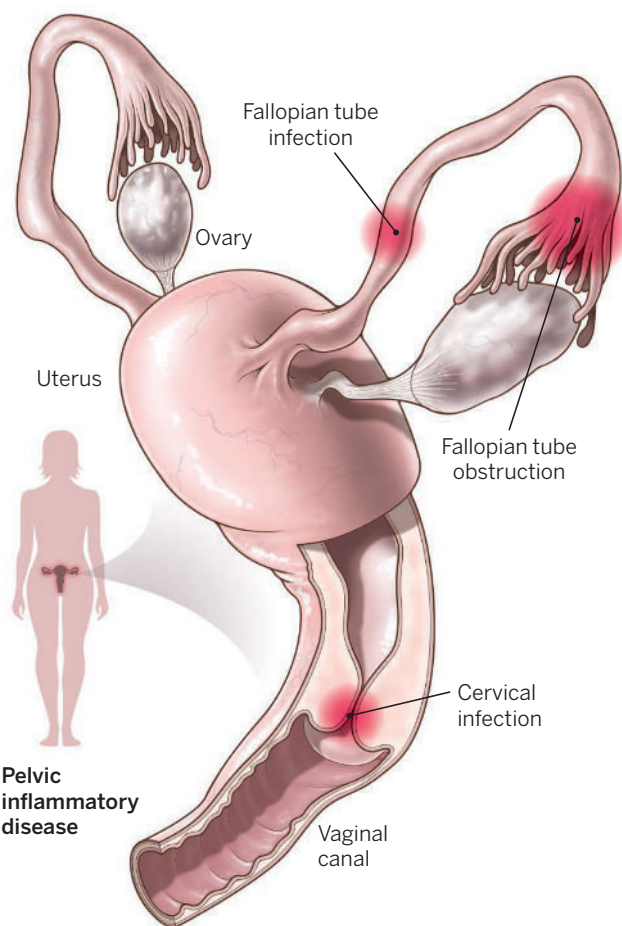
Ready to spread. A colored scanning electron micrograph of a human cervix cancer cell infected with *C. trachomatis* is shown. At the center is an inclusion body (rippled open) containing hundreds of *Chlamydia* particles.

PHOTO: SPL/SCIENCE SOURCE

omatis immunobiology and could translate into a vaccine that galvanizes mucosal T cells against this pathogen.

C. trachomatis is a Gram-negative bacterium that infects both men and women. It is taken up by mucosal epithelial cells, replicates within a vacuole, and within 48 hours, bacteria are released to infect neighboring cells (see the first figure). It can cause serious, permanent damage to a woman's reproductive system, and a pregnant woman can pass an infection to her baby during delivery. It can also cause blindness. Even if treated for a past *C. trachomatis* infection with antibiotics, one can still get infected again through unprotected sex. About 15% of untreated chlamydial infections lead to pelvic inflammatory disease, a condition of public health concern because it can lead to infertility, ectopic pregnancy, and chronic pelvic pain (3) (see the second figure). Many high-income countries have implemented programs to screen and treat women for asymptomatic *C. trachomatis* infection (most infected individuals have no symptoms, or symptoms may not appear until several weeks after sex with an infected partner). These efforts are based on evidence from randomized controlled trials indicating that screening for and treating cervical *C. trachomatis* infection can reduce a woman's risk of pelvic inflammatory disease by approximately 30 to 50% over 1 year. Since the introduction of these public health programs, pelvic inflammatory disease rates have fallen dramatically in developed countries. However, control has been incomplete because of limitations in uptake, cost, and unexpected increases in infection incidence.

The situation is worse in the developing world. Tubal factor infertility is the major sequela of untreated *C. trachomatis* pelvic inflammatory disease and may be present in 65 to 85% of women who seek infertility care in sub-Saharan Africa. The World Health Organization has concluded that the development of a vaccine against *C. trachomatis* is a priority for the prevention of pelvic inflammatory disease and its long-term sequelae.



Reproductive damage. Pelvic inflammatory disease in women caused by *C. trachomatis* (sites of infection shown) can result in tubal factor infertility, ectopic pregnancy, and chronic pelvic pain.

The experiments reported by Stary *et al.* provide a mechanistic explanation for earlier clinical and experimental findings. During the 1960s, human chlamydia vaccine trials in low- and medium-income countries showed that inactivated whole *C. trachomatis* vaccines (given with either an oil/water or alum adjuvant) protected against *C. trachomatis* ocular disease (trachoma) in most subjects, but waned after 1 year (4). Examination of vaccinated nonhuman primates also showed that breakthrough secondary infections could occur with even worse pathology (5). These studies showed that inactivated bacteria could induce a protective response, albeit a subimmunogenic one.

Stary *et al.* demonstrate that mucosal immunization of mice (either intrauterine or intranasal application) with ultraviolet light (UV)-inactivated *C. trachomatis* can elicit either protective CD4 T helper (T_H1) cells or CD4 T regulatory (T_{reg}) cells that tolerate infection, depending on the adjuvant chosen. T_H1 cells function in long-term protective memory after infection. A cationically charged synthetic and biodegradable nano-

carrier adjuvant incorporating the drug resiquimod was used to aggregate inactivated *C. trachomatis* cells as a vaccine (resiquimod is an agonist of Toll-like receptor 7 expressed in immune and nonimmune cells that detect pathogens and elicit immune responses). Within the mucosal environment, UV-inactivated *C. trachomatis*, in the presence or absence of the nanocarrier adjuvant, differentially recruited CD103-negative or -positive dendritic cells, which in turn activated CD4 T_H1 cells or CD4 T_{reg} cells, respectively. Protective CD4 T_H1 cells homed to the mucosa via an adhesion (integrin)-dependent mechanism. CD4 T_{reg} cells correlated with enhanced infection.

Particularly elegant parabiosis experiments (joining the circulatory systems of two mice) allowed Stary *et al.* to assess the movement and function of traceable *C. trachomatis*-specific CD4 T cells. The authors demonstrated that two waves of protective CD4 T_H1 cells develop after mucosal immunization with the UV-inactivated *C. trachomatis*-nanocarrier adjuvant vaccine. The first wave generated mucosal resident T cells that provided early protection, and a second wave generated systemic T cells

that augmented early and late protection. Although mucosal immunization with adjuvant induced both waves of T cells, systemic immunization induced only the second wave and manifested incomplete protection. Thus, early recruitment of mucosal CD4 T_H1 cells is likely key to a successful *C. trachomatis* vaccine. The density of mucosal CD4 T_H1 cells is a known correlate of immunity for this obligate intracellular epithelial cell pathogen (6).

A vaccine to prevent sexually transmitted *C. trachomatis* infection would advance public health efforts to control this prevalent sexually transmitted disease. Translating these findings into human *C. trachomatis* vaccine trials would bring us closer to this goal and spur the development of vaccines for other mucosal pathogens. ■

REFERENCES

1. K. Owusu-Edusei *et al.*, *Emerg. Infect. Dis.* **21**, 960 (2015).
2. G. Stary *et al.*, *Science* **348**, aaa8205 (2015).
3. R. C. Brunham *et al.*, *N. Engl. J. Med.* **372**, 2039 (2015).
4. D. C. Mabey *et al.*, *Vaccine* **32**, 1572 (2014).
5. J. T. Grayston, S. Wang, *J. Infect. Dis.* **132**, 87 (1975).
6. J. U. Igiertseme, R. G. Rank, *Infect. Immun.* **59**, 1346 (1991).

Department of Medicine, University of British Columbia, Vancouver, BC V6X 1N4, Canada.
E-mail: robert.brunham@bccdc.ca

10.1126/science.aac6528

RETROSPECTIVE

John Forbes Nash Jr. (1928–2015)

A distinguished mathematician and Nobel laureate dies tragically

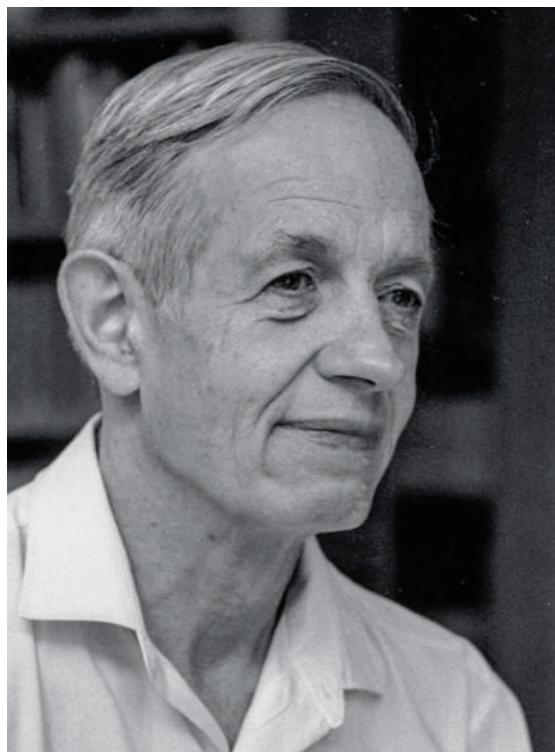
By Martin Shubik

On 23 May, John Nash and his wife Alicia were killed in a car accident in New Jersey. This tragedy came just after he received, at age 86, yet another distinguished award. John's contributions were in pure mathematics and game theory, which continues to influence the behavioral sciences. His achievements were remarkable, especially given his constant battle with mental illness.

In the fall of 1949, many graduate students at Princeton University were assigned rooms in the Graduate College. In one suite, John Nash inhabited a single room, while I shared the double with Lloyd Shapley. John and Lloyd were the mathematicians and I was the economist, and together we pursued our interest in game theory. John was one of the youngest students at the Graduate College. He was from West Virginia, where his father was an engineer and his mother a Latin teacher. He graduated from the Carnegie Institute of Technology with bachelor's and master's degrees in mathematics, and arrived at the math department in Princeton in 1948.

Highly engaged with game theory, all three of us recognized that a key problem in cooperative games involved establishing a "threat point" from which any bargaining procedure could proceed. Mathematician John Von Neumann and economist Oskar Morgenstern had faced this problem. They had developed a sophisticated theory of cooperative games based on an evaluation of what every subset (S), out of all players (N), could obtain by itself if it did not cooperate with the remaining excluded players (N-S). But they did not give a reasonable way to do this evaluation. Shapley and I worked on this problem, but it was Nash who produced a mathematically elegant solution, as is seen in his paper, published in *Econometrica* in 1953.

With the publication of his thesis, John proved the full generalization of the Cournot equilibrium. When I asked John if he had heard of Cournot, he said that he had, in an economics course. Augustin Cournot conceived of the equilibrium in 1836, but it was not until John gener-



alized it that others started to pick it up, augmenting its influence in economics and other fields. The basic idea behind John's solution was self-fulfilling expectations. In other words, if individual 1 guesses what individual 2 will do, and vice versa, there will be a pair of actions such that both will be right and neither will be motivated to change. For this, he shared the Nobel Prize in Economics in 1994.

John, Lloyd, and I were competitive in our research, which John enhanced with practical jokes such as removing the light bulb from a fixture in our joint bathroom and filling it with water, poised to drench his roommates. Many of us at Princeton also enjoyed inventing playable games that illustrated points and difficulties in game theory development. John had invented a board game called Nash (coincidentally also invented in Denmark as "Hex"), but he also helped craft a game we called So Long Sucker, which required that individuals form coalitions but, in order to win, someone in a coalition had to double-cross his partner. Nash, Shapley, John McCarthy (computer scientist), and I were playing So Long Sucker at tea time in Fine Hall. At a

critical point in the game, Nash saw that a coalition with McCarthy was helpful, and to win, he would have to double-cross McCarthy. Nash did just that. McCarthy was furious and used his last remaining resources to prevent Nash from winning. Nash was completely hurt and surprised. He turned to McCarthy and said, in essence, I do not understand why you are mad at me; you could do the backward induction to have seen that it was completely rational for me to double-cross you, and it was not personal.

After receiving his doctorate from Princeton, John joined the mathematics faculty at the Massachusetts Institute of Technology from 1951 to 1959, where he was absorbed with abstract geometry. He married Alicia during that time, but his mental decline escalated and he would face years of hospitalization. John's battle with

schizophrenia became popular knowledge through the 2001 film "A Beautiful Mind." When in the hospital, he'd send me postcards that were either numerology or Little Richie Rich cartoons. When I finally saw John after his hospital stays in Boston, he was standing in front of the Princeton library looking like a wraith. Gradually over the years, and especially with the boost of a 1/3 share in the Nobel prize, he seemed somewhat stronger and far less disturbed, but the piercing light appeared to have gone out. My wife and I were delighted to see him and Alicia on occasion. We regarded Alicia as a truly wonderful woman who was John's support and mainstay for much of his life. The last time I saw John was at Stony Brook University a few years ago at a game theory conference.

I congratulated John after the announcement of the 2015 Norway award in mathematics (Abel Prize), which he shared with mathematician Louis Nirenberg. I heard from another friend that when John was asked about whether he rated it higher or lower than the Nobel Prize, he replied "is 1/2 better than 1/3?"

Covles Foundation, Yale University, New Haven, CT, 06520.
E-mail: martin.shubik@yale.edu

10.1126/science.aac7085

LETTERS

Edited by Jennifer Sills

Germline gene therapy: We're ready

RECENTLY, CHINESE researchers attempted to modify embryos using “germline gene therapy.” If successful, this technique would create a heritable change and affect future generations, were those embryos to be used (1). A firestorm in the scientific community followed, with some researchers calling for an absolute ban on attempts to treat even lethal diseases with germline gene therapy. D. Baltimore, P. Berg, and a group of “interested stakeholders” met to discuss the issue and concluded: “At present, the potential safety and efficacy issues arising from the use of this technology must be thoroughly investigated and understood before any attempts at human engineering are sanctioned, if ever, for clinical testing” (“A prudent path forward for genomic engineering and germline gene modification,” D. Baltimore *et al.*, *Perspectives*, 3 April, p. 36; published online 19 March).

With apparent nostalgia, Baltimore *et al.* noted that the group “included some of the leaders in the original 1970s discussions about recombinant DNA research at Asilomar and elsewhere.” Many in the biomedical community do not regard the Asilomar experience as a success (2, 3). It exaggerated the potential risks of recombinant DNA technology, modern biotechnology’s core technique; gave rise to a years-long research moratorium; and

induced NIH to draft and promulgate “biosafety” guidelines. Those process-based guidelines, which were focused on the use of a single technique instead of on the risks of experiments, have plagued genetic engineering research ever since: Although NIH pared back the stringency of its guidelines, stultifying process-based approaches to regulation have remained at other federal agencies (4).

A moratorium would once again be misguided, as are the arguments of those who advocate it. In his Letter “Eugenics lurk in the shadow of CRISPR” (22 May, p. 871), R. Pollack invokes abstract concerns about “eugenics,” showing remarkable insensitivity to the current suffering of patients with horrific genetic diseases. Rudolf Jaenisch, a biology professor at the Massachusetts Institute of Technology, has argued that gene editing is unethical for diseases such as Huntington’s (5), which is genetically dominant, meaning that only one defective gene copy causes the disease and only half of the parents’ embryos will inherit it. Jaenisch objects because the editing procedure must begin before we know whether the embryo has the Huntington’s gene, posing the unacceptable risk of altering a normal embryo. However, Jaenisch has knocked down a straw man. Nobody is proposing to modify normal embryos in the foreseeable future.

An appropriate—and, indeed, compelling—application would be to correct the debilitating and ultimately lethal sickle cell anemia. In genetics terms, sickle cell anemia is an autosomal recessive disease, which means that every one of a patient’s chromosomes carries a defective gene (unlike Huntington’s disease). The sickle cell gene bears a mutation in one nucleotide of DNA, which in turn gives rise to a single amino

acid substitution in one discrete location of the protein chains of hemoglobin.

Unlike Huntington’s disease, 100% percent of the offspring of two parents with sickle cell disease will be afflicted with the disease. The repair of this sort of molecular lesion has been performed successfully in animals for decades. Shouldn’t 21st-century medicine offer the possibility of repairing embryos that will become patients with sickle cell disease, and eliminate the disease from future generations?

Technologies are seldom successful right out of the gate, but the concept of “perfecting” a technology seems to have eluded Harvard stem-cell researcher George Q. Daley, who recently said about germline gene therapy, “This is an unsafe procedure and should not be practiced at this time, and perhaps never” (5). Never? Maybe it has been a while since Dr. Daley has seen a patient like one I remember well—a 20-year-old with sickle cell anemia who had suffered three strokes, been crippled by hemorrhages into his major joints, and was in unrelenting pain from the arthritis that resulted.

Germline gene therapy should be used sparingly and with scrutiny, to be sure, but we don’t need a moratorium. We do need to push the frontiers of medicine to rid families of monstrous genetic diseases.

Henry I. Miller

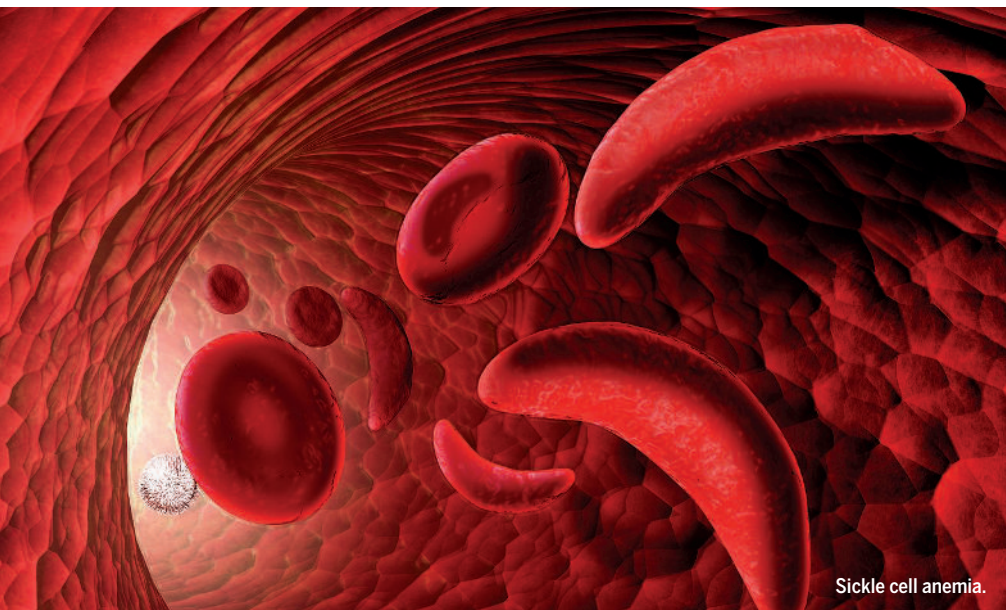
Robert Wesson Fellow in Scientific Philosophy and Public Policy, Hoover Institution, Stanford University, Stanford, CA 94305, USA. E-mail: miller@hoover.stanford.edu

REFERENCES

1. *The Economist*, “To the crack of doom” (2 May 2015); www.economist.com/news/science-and-technology/21649607-scientists-china-have-just-crossed-one-biotechnology-red-line-crack.
2. DNALearning Center, “Initial feelings on Asilomar meeting, James Watson” (www.dnalc.org/view/15423-Initial-feelings-on-Asilomar-meeting-James-Watson.html).
3. “Trying to Bury Asilomar,” James Watson Papers (1978); <http://wellcomelibrary.org/player/b19847051#?asi=0&ai=7&z=0%2C0.1956%2C1.0001%2C0.8925>.
4. D.L. Kershen, H.I. Miller, *Iss. Sci. Technol.* XXXI, 2 (2015); <http://issues.org/31-2/miller-5/>.
5. G. Kolata, “Chinese scientists edit genes of human embryos, raising concerns,” *The New York Times* (23 April 2015); www.nytimes.com/2015/04/24/health/chinese-scientists-edit-genes-of-human-embryos-raising-concerns.html.

Research ethics and health care reform

A. FINKELSTEIN AND S. Taubman report on the underuse of randomized controlled trials for U.S. health care reform (“Randomize evaluations to improve health care delivery” Policy Forum, 13 February, p. 720). This reliance on suboptimal research compromises information needed for policy. However, a second problem about health reform decision-making is more serious,



Sickle cell anemia.

constituting a major ethical breach.

The principles of research with humans require that deviations from the standard of care are allowable only if there is real uncertainty regarding which intervention is better. This is called the “principle of equipoise”; only when we don’t know which strategy yields the best results is it acceptable to compare them (1).

Yet for health care reform writ large—i.e., the basic payment system—there is no equipoise. Research from dozens of developed countries demonstrates convincingly that single-payer financing reduces costs, assures access, and improves outcomes (2, 3).

To ignore this compelling evidence risks lives in the United States as we experiment with partial fixes to the multi-payer system. This experimentation would be rejected by any responsible university institutional review board as violating the principle of equipoise and causing unacceptable patient harm.

James G. Kahn¹* and Paul Hofmann²

¹University of California, San Francisco, San Francisco, CA 94104, USA. ²Moraga, CA 94556, USA.

*Corresponding author. E-mail: jgkahn@gmail.com

REFERENCES

1. B. Freedman, *N. Engl. J. Med.* **317**, 141 (1987).
2. K. Davis, K. Stremikis, D. Squires, C. Schoen, “Mirror, Mirror on the Wall, 2014 Update: How the U.S. Health Care System Compares Internationally” (The Commonwealth Fund, 2014); www.commonwealthfund.org/publications/fund-reports/2014/jun/mirror-mirror.
3. World Health Organization, “The World Health Report 2000: Health Systems: Improving Performance” (WHO, Geneva, 2000).

Spitzer’s stellar work

IN THE NEWS Feature “After Hubble” (24 April, p. 388), D. Clery inappropriately characterizes the Spitzer Space Telescope as “now largely blind.” In fact, Spitzer is alive and well and continuing to make substantial contributions to the advancement of astrophysics and to scientific preparations for the James Webb Space Telescope (JWST). The exhaustion of Spitzer’s cryogen in mid-2009 left the observatory with two functioning imaging arrays at wavelengths of 3.6 and 4.5 μm . The performance of what is now called “Warm” Spitzer at these wavelengths matches that achieved during the cryogenic mission. Despite its small size, Spitzer is by far the most sensitive telescope, space or ground, available at these wavelengths. The science community has used Warm Spitzer for important scientific investigations, including studies of exoplanets, the early universe, variable stars to define better the cosmic distance ladder, clusters of galaxies, near-Earth asteroids, and comets. Spitzer remains very much in demand; for the past

2 years, the oversubscription for requested observing time has been the highest of the mission.

Much of the Spitzer work anticipating JWST is done jointly with the Hubble Space Telescope (HST). To take just one example, the two telescopes together are carrying out a “Frontier Fields” imaging study of half a dozen dense clusters of galaxies, using their gravitational lensing properties to uncover distant galaxies seen as they were when the universe was less than 5% of its current age. The two observatories work together to determine the distance, stellar masses, and stellar ages of these objects; neither HST nor Spitzer could do this alone. Galaxies studied by HST and Spitzer in the distant universe are faint enough to be challenging—but important—targets for spectroscopic study from JWST. These targets will allow JWST to begin spectroscopy at the start of the mission without awaiting results from its own survey programs. Lastly, Spitzer has been an important technical and engineering pathfinder for JWST. In particular, Spitzer successfully pioneered the passive, radiative cooling that allows it to remain very cold and thus highly sensitive even without stored cryogen, and which is essential for the success of JWST.

We indeed celebrate the significance and success of HST. However, we feel that Spitzer has been and will continue to be a vital collaborator with HST in establishing the scientific landscape for JWST.

M. W. Werner,¹* B. T. Soifer,² L. Storrie Lombardi,² G. Helou²

¹Spitzer Space Telescope, Jet Propulsion Laboratory/California Institute of Technology, Pasadena, CA 91109, USA. ²Spitzer Science Center, California Institute of Technology, Pasadena, CA 91125, USA.

*Corresponding author.
E-mail: mww@ipac.caltech.edu

TECHNICAL COMMENT ABSTRACTS

Comment on “Early *Homo* at 2.8 Ma from Ledi-Geraru, Afar, Ethiopia”

John Hawks, Darryl J. de Ruiter, Lee R. Berger Villmoare *et al.* (Reports, 20 March 2015, p. 1352) report on a hominin mandible from the Ledi-Geraru research area, Ethiopia, which they claim to be the earliest known representative of the genus *Homo*. However, certain measurements and observations for *Australopithecus sediba* mandibles presented are incorrect or are not included in critical aspects of the study. When correctly used, these data demonstrate that specimen LD 350-1 cannot be unequivocally assigned to the genus *Homo*.

Full text at <http://dx.doi.org/10.1126/science.aab0591>

Response to Comment on “Early *Homo* at 2.8 Ma from Ledi-Geraru, Afar, Ethiopia”

Brian Villmoare, William H. Kimbel, Chalachew Seyoum, Christopher J. Campisano, Erin DiMaggio, John Rowan, David R. Braun, J. Ramon Arrowsmith, Kaye E. Reed Hawks *et al.* argue that our analysis of *Australopithecus sediba* mandibles is flawed and that specimen LD 350-1 cannot be distinguished from this, or any other, *Australopithecus* species. Our reexamination of the evidence confirms that LD 350-1 falls outside of the pattern that *A. sediba* shares with *Australopithecus* and thus is reasonably assigned to the genus *Homo*.

Full text at <http://dx.doi.org/10.1126/science.aab1122>

Comment on “Missing gas-phase source of HONO inferred from Zeppelin measurements in the troposphere”

Chunxiang Ye, Xianliang Zhou, Dennis Pu, Jochen Stutz, James Festa, Max Spolaor, Christopher Cantrell, Roy L. Mauldin, Andrew Weinheimer, Julie Haggerty Li *et al.* (Reports, 18 April 2014, p. 292) proposed a unity nitrous acid (HONO) yield for reaction between nitrogen dioxide and the hydroperoxyl-water complex and suggested a substantial overestimation in HONO photolysis contribution to hydroxyl radical budget. Based on airborne observations of all parameters in this chemical system, we have determined an upper-limit HONO yield of 0.03 for the reaction.

Full text at <http://dx.doi.org/10.1126/science.aaa1992>

Response to Comment on “Missing gas-phase source of HONO inferred from Zeppelin measurements in the troposphere”

Xin Li, Franz Rohrer, Andreas Hofzumahaus, Theo Brauers, Rolf Häseler, Birger Bohn, Sebastian Broch, Hendrik Fuchs, Sebastian Gomm, Frank Holland, Julia Jäger, Jennifer Kaiser, Frank N. Keutsch, Insa Lohse, Keding Lu, Ralf Tillmann, Robert Wegener, Glenn M. Wolfe, Thomas F. Mentel, Astrid Kiendler-Scharr, Andreas Wahner

Ye *et al.* have determined a maximum nitrous acid (HONO) yield of 3% for the reaction $\text{HO}_2 \cdot \text{H}_2\text{O} + \text{NO}_2$, which is much lower than the yield used in our work. This finding, however, does not affect our main result that HONO in the investigated Po Valley region is mainly from a gas-phase source that consumes nitrogen oxides.

Full text at <http://dx.doi.org/10.1126/science.aaa3777>

TECHNICAL COMMENT

PALEOANTHROPOLOGY

Comment on “Early *Homo* at 2.8 Ma from Ledi-Geraru, Afar, Ethiopia”

John Hawks,^{1,2*} Darryl J. de Ruiter,^{2,3} Lee R. Berger²

Villmoare *et al.* (Reports, 20 March 2015, p. 1352) report on a hominin mandible from the Ledi-Geraru research area, Ethiopia, which they claim to be the earliest known representative of the genus *Homo*. However, certain measurements and observations for *Australopithecus sediba* mandibles presented are incorrect or are not included in critical aspects of the study. When correctly used, these data demonstrate that specimen LD 350-1 cannot be unequivocally assigned to the genus *Homo*.

Specimen LD 350-1 is substantially similar to mandibles of australopiths in dental dimensions, corpus size, and anatomy (Fig. 1). Despite its generally australopith-like morphology, Villmoare *et al.* (1) attribute LD 350-1 to *Homo* because of (i) the parallel alveolar and basal corpus margins, with corpus height at P₃ only slightly more than at M₂; (ii) the posteriorly directed mental foramen; (iii) the poste-

riorly positioned anterior margin of its ascending ramus; (iv) the nearly vertical buccal walls of its M₂ and M₃; (v) the buccolingually narrow and relatively salient cusp apices; (vi) the mesially tapered M₂ and M₃ compared to australopiths; and (vii) its mesiodistally short M₃.

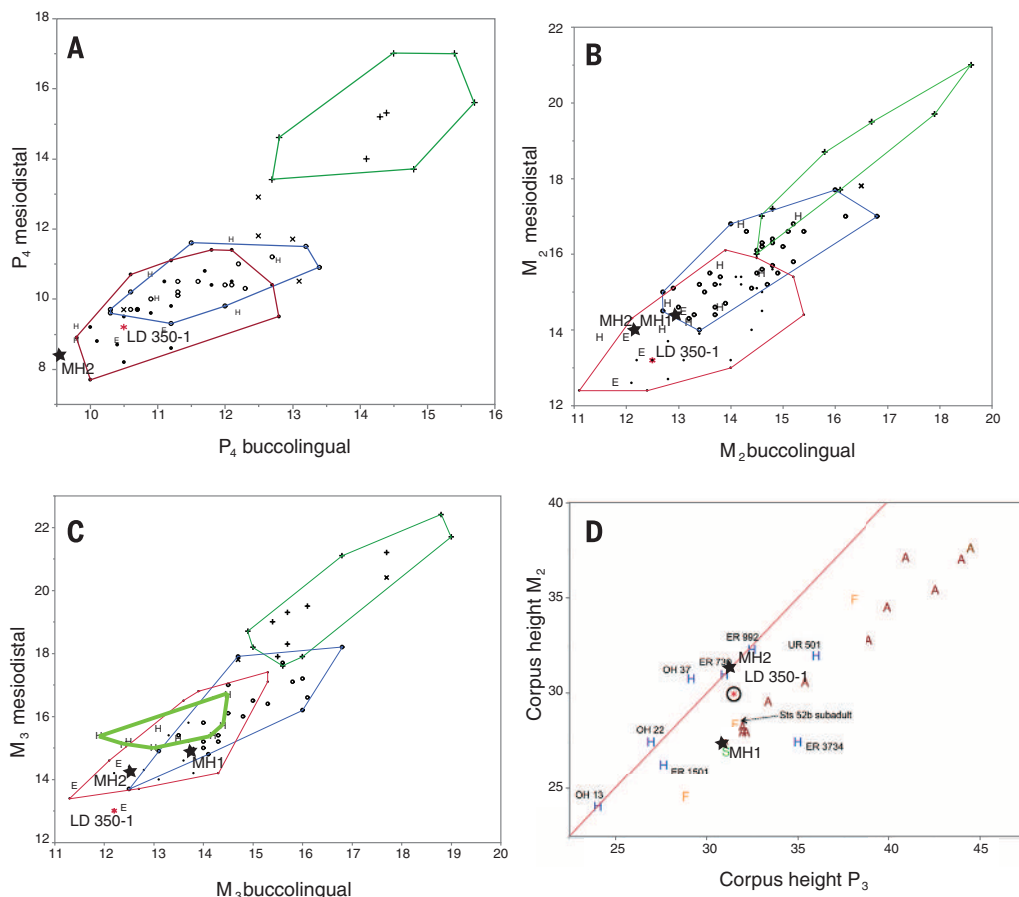
Parallel alveolar and basal corpus margins are found in the *Australopithecus sediba* specimen MH2, contrary to Villmoare *et al.*, who provide

inaccurate P₃ and M₂ corpus height measures of 31.1 and 27.0 mm, respectively [table S5 in (1)]. The actual measures, taken from the re-assembled original fossil, are 31.0 and 30.5 mm, respectively (Fig. 1), and the nearly parallel nature of the alveolar and basal margins of MH2 is visible in published photographs [figure 1 in (2)]. Villmoare *et al.* also suggest that the mandibular corpus in MH1 of *A. sediba* is deep anteriorly [text S3 in the supplementary materials of (1)], but the specimen is a subadult (3), so corpus depth cannot be reliably established at the level of M₂. In addition, several specimens of early *Homo* show anteriorly divergent alveolar and basal corpus margins, so parallel corpus margins cannot be considered an exclusive indicator of *Homo*. The mental foramina in MH1 and MH2 of *A. sediba* are oriented predominantly laterally (not anteriorly in MH2, as inaccurately reported by Villmoare *et al.*), similar to nearly all specimens of early *Homo*, with a slight posterior orientation similar if not identical to that of LD 350-1. The origin of the ascending ramus is distinctly posteriorly

¹Department of Anthropology, University of Wisconsin, Madison, WI 53706, USA. ²Institute for Human Evolution, University of the Witwatersrand, Johannesburg, South Africa. ³Department of Anthropology, Texas A&M University, College Station, TX 77843, USA.

*Corresponding author. E-mail: jhawks@wisc.edu

Fig. 1. Figures S1A, S2 B, S3 C, and S6D from (1) with *A. sediba* specimens MH1 and MH2 added to the plots (stars). The MH1 and MH2 locations are newly added to these plots, except for (D), in which (1) used an incorrect measurement. *H. habilis* and *H. rudolfensis* specimens are indicated in each plot by “H” markers, and African *H. erectus* specimens are indicated by “E” markers, as in (1). The original convex hull plots belong to *A. afarensis* (red), *A. africanus* (blue), and *Paranthropus boisei* (green). (A) The P₄ of MH2 is markedly reduced relative to LD 350-1. (B) M₂ dimensions do not distinguish *A. sediba*, *A. afarensis*, or LD 350-1. (C) In M₃ MD length, *A. sediba* is likewise shorter than nearly all specimens attributed to *H. habilis* or *H. rudolfensis*. The convex hull surrounding these early *Homo* species has been added to show the clear difference between LD 350-1 and these early *Homo* samples. (D) The correct measurement for corpus height at M₂ makes a marked difference to the position of *A. sediba* in this comparison. MH2 is clearly more “*Homo*-like” than LD 350-1, and the juvenile MH1 is comparable to other australopiths. The variability of this relation between anterior and posterior corpus height in early *Homo* also appears to characterize *A. sediba*.



positioned in MH2 of *A. sediba*, contrary to the claim of Villmoare *et al.* that it originates between the M_2/M_3 [table S6 in (1)]. In fact, the ascending ramus of MH2 takes its origin at about mid- M_3 , identical to that of LD 350-1, as can be seen in published photographs of MH2 [figure 1 in (2) and figure 1 in (3)]. Therefore, the mandibular corpus does not support LD 350-1's assignment to *Homo*.

Dental characters and measurement also do not support such an assignment (Fig. 1). The sloping buccal faces of the molars are different from MH1 of *A. sediba* but not from MH2. Only the mesial tapering of M_2 and M_3 and

the short mesiodistal length of M_3 separate LD 350-1 from *A. afarensis*, *A. africanus*, and *A. sediba*. The definition of *Homo* cannot hinge on M_3 mesiodistal length, because every specimen of *H. habilis* and *H. rudolfensis* known in Africa has a longer M_3 than LD 350-1, MH1, or MH2. With reference to mesial tapering, as noted by Villmoare *et al.*, there is substantial overlap in mesial:distal breadth ratios between *Australopithecus* and early *Homo*, and the unique tapering of LD 350-1 cannot exclusively link it with *Homo*.

We do not assert that LD 350-1 should be allocated to *A. afarensis* or to *A. africanus*, nor do

we contend that LD 350-1 belongs in *A. sediba*, although the evidence cannot reasonably reject these hypotheses. Rather, we would urge caution when assessing the taxonomic affinities of such isolated remains, because at present we cannot be certain what the rest of the dentition, skull, or skeleton of LD 350-1 might have looked like.

REFERENCES

1. B. Villmoare *et al.*, *Science* **347**, 1352–1355 (2015).
2. D. J. de Ruiter *et al.*, *Science* **340**, 1232997–1 (2013).
3. L. R. Berger *et al.*, *Science* **328**, 195–204 (2010).

5 March 2015; accepted 28 April 2015
10.1126/science.aab0591

TECHNICAL RESPONSE

PALEOANTHROPOLOGY

Response to Comment on “Early *Homo* at 2.8 Ma from Ledi-Geraru, Afar, Ethiopia”

Brian Villmoare,^{1,4,6*} William H. Kimbel,^{2*} Chalachew Seyoum,^{2,7}
Christopher J. Campisano,² Erin DiMaggio,³ John Rowan,² David R. Braun,⁴
J. Ramon Arrowsmith,⁵ Kaye E. Reed²

Hawks *et al.* argue that our analysis of *Australopithecus sediba* mandibles is flawed and that specimen LD 350-1 cannot be distinguished from this, or any other, *Australopithecus* species. Our reexamination of the evidence confirms that LD 350-1 falls outside of the pattern that *A. sediba* shares with *Australopithecus* and thus is reasonably assigned to the genus *Homo*.

Hawks *et al.* (1) claim that we misinterpreted the mandibular anatomy of the Malapa hominins and, as a result, failed to satisfactorily distinguish the LD 350-1 jaw from *Australopithecus*.

We stand by our assessments of the mandibular and dental anatomy of *A. sediba*. On the right side of the MH2 mandibular corpus, the

inferior border is damaged posterior to mid- M_2 , but any reasonable estimate of “minimum corpus depth” [as defined in (2); Hawks *et al.* do not specify their method] below M_2 is 2.5 to 3.5 mm less than the depth below P_3 . The left side of the MH2 corpus [specimen UW88-55 (3)] is also preserved, however, and is undamaged from the M_1 level to posterior to M_3 . The inferior margin of the damaged right corpus (4) can be inferred by photographically superimposing the left side onto the right (Fig. 1), which reveals the primitive (australopith-like) height relationships of the corpus, deeper anteriorly and considerably less so posteriorly. On a cast of MH2, we measure minimum lingual corpus height at left M_2 as 26.6 mm and at right P_3 as 30.3 mm.

With regard to the juvenile MH1 mandible (M_3 unerupted), our data on chimpanzees and *A. afarensis* show that, although corpus depth does indeed change with emergence of the final molar, the relative anterior to posterior depth

($P_3:M_2$) is essentially stable from the time of M_2 emergence. Therefore, in MH1, the clear discrepancy in corpus depth [see figure 1 in (3)] is unlikely to have changed substantially with the attainment of adulthood, confirming our assessment of a posteriorly shallowing corpus in the Malapa hominins, as commonly seen in *Australopithecus*.

Hawks *et al.* argue that the orientation of the mental foramen in MH2 is lateral, rather than anterior, as we described. Without prejudicing our assessment of MH2, we note that a lateral orientation of the foramen fits the description of *A. africanus* [as noted in (2)], whereas a clear posterior opening of the foramen into a short groove on the corpus, as in LD 350-1, is typically seen only in *Homo* among nonrobust early hominins. With regard to the root of the ascending ramus, our definition [as noted in the legend of figure S7 in (2)] is the point at which the anterior ramus margin becomes independent of the corpus, which on MH2 clearly occurs at M_2/M_3 , as we described (Fig. 1). It is the concave vertical segment of the anterior margin that leaves the M_3 visible in lateral view, not an extreme posterior origin of the margin as in LD 350-1.

The flaring buccal face of the molars in MH1, the standard condition in *Australopithecus*, may or not have been present in MH2. Heavy occlusal wear, to the point of substantially reducing crown height and eliminating virtually all cusp detail, precludes assessing the trait for MH2. Although Hawks *et al.* acknowledge that the LD 350-1 M_3 is shorter than the M_2 , a trait that is not seen in *A. sediba*, they propose that M_3 length cannot be used to discriminate LD 350-1 from this taxon. Our argument was not about overall length of M_3 , however; rather, it is the relative length of the M_3 to the M_2 that discriminates LD 350-1 (and *Homo* more broadly) from the great majority of *Australopithecus* mandibular tooth rows. We made no taxonomic case with regard to mesial/distal tapering of M_2 , so it is unclear why it is part of Hawks *et al.*'s

¹Department of Anthropology, University of Nevada Las Vegas, Las Vegas, NV, 89154, USA. ²School of Human Evolution and Social Change and Institute of Human Origins, Arizona State University, Tempe, AZ 85287, USA. ³Department of Geosciences, Pennsylvania State University, University Park, PA 16802, USA. ⁴Center for the Advanced Study of Hominin Paleobiology, George Washington University, Washington, DC 20052, USA. ⁵School of Earth and Space Exploration, Arizona State University, Tempe, AZ 85281, USA. ⁶Department of Anthropology, University College London, London WC1H 0BW, UK. ⁷Authority for Research and Conservation of Cultural Heritage, Addis Ababa, Ethiopia. *Corresponding author. E-mail: brian.villmoare@unlv.edu (B.V.); wkimbel.iho@asu.edu (W.H.K.)

Fig. 1. (Left) Reversed image of the lingual aspect of the MH2 left mandibular corpus (cast of UW88-55) superimposed on the lingual aspect of the right side, with the damaged right inferior corpus margin indicated by a black dotted line. The left side was overlapped to match the size and position of the M_3 , the inferior margin of the corpus, and the preserved contours of the ramus of the right. Note the visible shallowing of the corpus toward the rear of the toothrow, indicated by the dashed red lines at P_3 and M_2 . **(Right)** MH2 right mandible fragment UW 88-54 (cast) in anatomical position, lateral view. The origin of the anterior ramus margin (arrow) is clearly located at the M_2/M_3 level.



argument. We do note that, in this feature, MH1 falls well within the range of *A. afarensis* and *A. africanus* and does not overlap the *Homo* distribution [see table S7 in (2)].

Hawks *et al.* state that “the evidence cannot reasonably reject” the taxonomic allocation of LD 350-1 to *A. afarensis*, *A. africanus*, or *A. sediba*. We find this confusing, because irrespective of whether or not it would be reasonable to assign LD 350-1 to *A. sediba*, we provided a detailed account of the characters distinguishing LD 350-1 from both *A. afarensis* and *A. africanus*, which these authors do not contest. We acknowledge that there is variation in some of these traits across early hominins, as noted in our analysis, but it is their appearance in combination that

supports assigning the LD 350-1 mandible to an early part of the *Homo* lineage.

There is further confusion in Hawks *et al.*’s argument that LD 350-1 cannot reasonably be attributed to *Homo*. Although they assigned the Malapa hominins to *Australopithecus* based on a methodological choice that emphasizes primitive characters in taxonomy, Berger and colleagues identified derived characters in these fossils that they argued supported a unique phylogenetic link of *A. sediba* to the *Homo* lineage (3, 5). Now, however, they contend that our identification in the LD 350-1 mandible and teeth of derived features seen in later *Homo* cannot support the assignment of the specimen to this genus because of their (supposed) occurrence in *Australopithecus*

sediba. Our emphasis on derived traits marries taxonomic practice to phylogenetic inference; their emphasis on primitive traits divorces the two. This contradiction is a common source of confusion in paleoanthropology and here renders Hawks *et al.*’s objections to our taxonomic conclusions regarding LD 350-1 logically incoherent.

REFERENCES

1. J. Hawks, D. J. de Ruiter, L. R. Berger, *Science* **348**, 1326 (2015).
2. B. Villmoare *et al.*, *Science* **347**, 1352–1355 (2015).
3. L. R. Berger *et al.*, *Science* **328**, 195–204 (2010).
4. D. J. de Ruiter *et al.*, *Science* **340**, 1232997–1 (2013).
5. L. Berger, *J. Anthropol. Sci.* **90**, 117–131 (2012).

5 April 2015; accepted 28 April 2015
10.1126/science.aab1122

TECHNICAL COMMENT

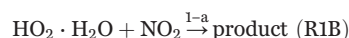
ATMOSPHERIC SCIENCE

Comment on “Missing gas-phase source of HONO inferred from Zeppelin measurements in the troposphere”

Chunxiang Ye,¹ Xianliang Zhou,^{1,2*} Dennis Pu,² Jochen Stutz,³ James Festa,³ Max Spolaor,³ Christopher Cantrell,⁴ Roy L. Mauldin,^{4,5} Andrew Weinheimer,⁶ Julie Haggerty⁶

Li *et al.* (Reports, 18 April 2014, p. 292) proposed a unity nitrous acid (HONO) yield for reaction between nitrogen dioxide and the hydroperoxyl-water complex and suggested a substantial overestimation in HONO photolysis contribution to hydroxyl radical budget. Based on airborne observations of all parameters in this chemical system, we have determined an upper-limit HONO yield of 0.03 for the reaction.

The hydroxyl radical (OH) is the most important oxidant in the atmosphere, affecting the steady-state concentrations and lifetimes of most gaseous pollutants (1). Ground-based field studies have demonstrated that nitrous acid (HONO) is an important or even a major OH precursor via its photolysis (2, 3). However, Li *et al.* (4) proposed a new HONO source through the reaction between nitrogen dioxide (NO₂) and the hydroperoxyl-water complex (HO₂·H₂O) (R1A). Because this source mechanism consumes an HO₂ radical and NO₂ (defined as an internal mechanism), they suggested that HONO photolysis might not be an important net hydrogen oxide radical (HO_x) source, as previously believed.



Li *et al.* (4) presented some high-quality HONO observations in the residual layer (RL) during the morning hours, one of only a few airborne HONO measurements (4–6). Decoupled from the ground surface emission and upper troposphere convection, the RL is an ideal environment to study the nighttime-to-daytime evolution of HONO chemistry within an air mass. High HONO concentration observed after sunrise, ~150 parts per trillion (ppt), indicates a high HONO production rate in the air mass. Their model simulation suggested that an external HONO source, defined as HONO production from a mechanism without consuming HO_x radicals and oxides

of nitrogen (NO_x = NO + NO₂), would lead to an overprediction of NO_x concentration after sunrise, whereas the internal source based on reaction R1A well reproduced both HONO and NO_x concentrations in the RL. The authors thus recommended the internal HONO source R1A over the external ones for sustaining the high

HONO concentrations, with a HONO yield (α) of 1. However, there have been no reports of direct laboratory evidence suggesting HONO formation via reaction R1A, and the assumed α value of 1 seems unreasonably high.

We conducted HONO measurements on board National Science Foundation's National Center for Atmospheric Research (NSF/NCAR) C-130 research aircraft during the 2013 summer NOMADSS (Nitrogen, Oxidants, Mercury and Aerosol Distributions, Sources, and Sinks) field study. HONO was measured by two long-path absorption photometric (LPAP) systems (6, 7); NO and NO₂ were measured by a four-channel chemiluminescence instrument (8); HO₂ was measured by a chemical ionization mass spectrometer (9); and photolysis frequency of HONO, *J*_{HONO}, was derived from light measurement by a scanning actinic flux spectroradiometer (10). Figure 1, A to C, shows measurement data, including HONO, NO, NO₂, HO₂, water vapor (H₂O), and HONO photolysis frequency (*J*_{HONO}), during a 1-hour segment of research flight on 29 June 2013 at 800 m above ground over central Georgia, USA. The mean HONO (±SD) concentration was 18 (±6) ppt. Elevated HONO concentrations were observed in the power plant plumes, at 19:01, 19:09, and 19:24 UTC (A, B, and C in Fig. 1A). The maximum HONO concentration in these plumes was 37 ppt, much lower than the ~150 ppt reported by Li *et al.* (4), even though the NO₂ and HO₂ levels were

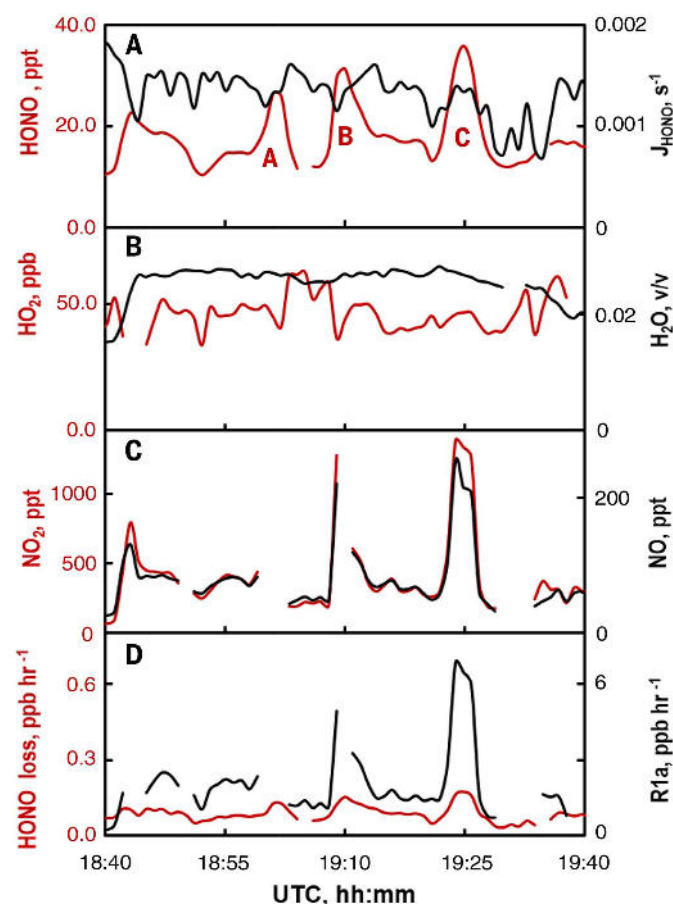


Fig. 1. Time series.

Time series of (A) HONO and *J*_{HONO}, (B) HO₂ and H₂O, (C) NO₂ and NO, and (D) HONO photolysis loss rate and the upper-limit HONO production rate from reaction R1A. The upper-limit HONO production rate from reaction R1A is calculated under the same assumption as that of Li *et al.* (4). Three power plant plumes were encountered, as indicated by A, B, and C in (A). The flight altitude was 800 m above ground level.

¹Wadsworth Center, New York State Department of Health, Albany, NY, USA.

²Department of Environmental Health Sciences, State University of New York, Albany, NY, USA.

³University of California, Los Angeles, CA, USA.

⁴University of Colorado, Boulder, CO, USA.

⁵Department of Physics, University of Helsinki, Helsinki, Finland.

⁶National Center for Atmospheric Research, Earth System Laboratory, Boulder, CO, USA.

*Corresponding author. E-mail: xianliang.zhou@health.ny.gov

higher. Figure 1D compares the HONO photolytic loss rate and the upper limit for a hypothetical HONO formation rate from reaction R1A. The calculated HONO formation rate is at least 10 times greater than the observed HONO photolytic loss rate. This suggests that HONO contribution from reaction R1A as assumed by Li *et al.* (4) has been grossly overestimated since the photolytic loss is the dominant sink for HONO.

Indeed, an upper-limit α of 0.03 is calculated for reaction R1A through Eq. 1, assuming it is the sole source to counterbalance the HONO photolytic loss in the plume C (Fig. 1A)

$$\alpha = \frac{[\text{HONO}] \times J_{\text{HONO}}}{k[\text{HO}_2 \cdot \text{H}_2\text{O}][\text{NO}_2]} \quad (\text{Eq. 1})$$

where $[\text{HONO}]$, $[\text{HO}_2 \cdot \text{H}_2\text{O}]$, and $[\text{NO}_2]$ are concentrations of HONO, $\text{HO}_2 \cdot \text{H}_2\text{O}$, and NO_2 , respectively. J_{HONO} is the HONO photolysis frequency calculated from irradiance measurement; k is the overall rate constant of reaction between $\text{HO}_2 \cdot \text{H}_2\text{O}$ and NO_2 (i.e., R1A + R1B). Other HONO sources (11)—including OH radical and NO reaction, NO_2 heterogeneous reactions on aerosol particles, and the photolysis of absorbed nitrate—are ignored here. Therefore, even the low value of 0.03 may still greatly overestimate the true α value.

With such a small α , this internal mechanism (R1A) is not able to sustain the HONO level ob-

served in Li *et al.* (4), and other internal and external sources need to be considered. The HONO source calculated in Li *et al.* (4) was $4.05 \times 10^5 \times J_{\text{HONO}}$ ($\text{ppt} \cdot \text{s} \cdot \text{h}^{-1}$), indicating a photochemical process with a precursor of substantially long lifetime, such as the photolysis of particulate nitrate (6, 12). Although particulate nitrate loading was not measured in Li *et al.* (4), the aerosol surface area density, up to $1.8 \times 10^{-4} \text{ m}^2 \text{ m}^{-3}$, suggests that a relatively high aerosol loading, and perhaps high particulate nitrate loading in the industrial region of the Po Valley, Northern Italy, could be an explanation for their observation.

Li *et al.* (4) reported that NO_x concentration would be overpredicted in their simulation if an external HONO source was considered. We argue that their model may have underpredicted the NO_x loss rate. Model parameterization should be updated and be constrained by measurements to accurately assess important NO_x sink processes, such as formation of organic nitrates from alkylperoxy radicals and NO reaction (13), peroxyacyl nitrates (PANs) from peroxyacyl radicals and NO_2 reactions (14), and bromine nitrate from bromine oxide and NO_2 reactions (15).

Finally, HONO will remain an important net OH precursor, as demonstrated by many field studies (2, 3), because HONO formation from reaction R1A is negligible, with an α value lower than 0.03.

REFERENCES AND NOTES

1. B. J. Finlayson-Pitts, J. N. Pitts Jr., *Chemistry of the Upper and Lower Atmosphere: Theory, Experiments and Applications* (Academic Press, San Diego, CA, ed. 1, 2000).
2. J. Kleffmann *et al.*, *Geophys. Res. Lett.* **32**, L05818 (2005).
3. K. Acker *et al.*, *Geophys. Res. Lett.* **33**, L02809 (2006).
4. X. Li *et al.*, *Science* **344**, 292–296 (2014).
5. R. Häseler, T. Brauers, F. Holland, A. Wahner, *Atmos. Meas. Tech. Discuss.* **2**, 2027–2054 (2009).
6. N. Zhang *et al.*, *Geophys. Res. Lett.* **36**, L15820 (2009).
7. N. Zhang *et al.*, *Atmos. Chem. Phys.* **12**, 8285–8296 (2012).
8. B. Ridley *et al.*, *J. Geophys. Res.* **109** (D17), D17305 (2004).
9. R. S. Hornbrook *et al.*, *Atmos. Meas. Tech.* **4**, 735–756 (2011).
10. R. E. Shetter, L. Cinquini, B. L. Lefer, S. R. Hall, S. Madronich, *J. Geophys. Res.* **108** (D2), 8234 (2003).
11. J. Kleffmann, *Chem. Phys. Chem.* **8**, 1137–1144 (2007).
12. X. Zhou, H. Gao, Y. He, G. Huang, *Geophys. Res. Lett.* **30**, 2217 (2003).
13. E. C. Browne *et al.*, *Atmos. Chem. Phys.* **13**, 4543–4562 (2013).
14. J. M. Roberts *et al.*, *J. Geophys. Res.* **112** (D20), D20306 (2007).
15. R. Grilli *et al.*, *Geophys. Res. Lett.* **40**, 791–796 (2013).

ACKNOWLEDGMENTS

This research is funded by NSF grants AGS-1216166, AGS-1215712, and AGS-1216743. We appreciate the help and assistance from fellow scientists and NCAR's C130 crews during the NOMADSS field study. The data are available in our project data archive (http://data.eol.ucar.edu/master_list/?project=SAS). Any opinions, findings, and conclusions or recommendations expressed in this paper are those of the authors and do not necessarily reflect the views of NSF.

30 October 2014; accepted 28 April 2015
10.1126/science.aaa1992

TECHNICAL RESPONSE

ATMOSPHERIC SCIENCE

Response to Comment on “Missing gas-phase source of HONO inferred from Zeppelin measurements in the troposphere”

Xin Li,^{1*} Franz Rohrer,^{1*} Andreas Hofzumahaus,¹ Theo Brauers,^{1†} Rolf Häseler,¹ Birger Bohn,¹ Sebastian Broch,¹ Hendrik Fuchs,¹ Sebastian Gomm,¹ Frank Holland,¹ Julia Jäger,¹ Jennifer Kaiser,² Frank N. Keutsch,^{2‡} Insa Lohse,¹ Keding Lu,^{1§} Ralf Tillmann,¹ Robert Wegener,¹ Glenn M. Wolfe,^{2||} Thomas F. Mentel,¹ Astrid Kiendler-Scharr,¹ Andreas Wahner¹

Ye *et al.* have determined a maximum nitrous acid (HONO) yield of 3% for the reaction $\text{HO}_2\text{-H}_2\text{O} + \text{NO}_2$, which is much lower than the yield used in our work. This finding, however, does not affect our main result that HONO in the investigated Po Valley region is mainly from a gas-phase source that consumes nitrogen oxides.

The self-cleansing capacity of the atmosphere is largely dependent on the concentration level of hydroxyl radicals (OH) (1). Nitrous acid (HONO) is an important precursor of OH in the troposphere (2–4). Based on observations of HONO and its budget in the Po Valley region in Italy, we concluded that HONO formation in a sunlit layer separated from the ground surface is from a gas-phase source consuming nitrogen oxides ($\text{NO}_x = \text{NO} + \text{NO}_2$) and potentially hydrogen oxide ($\text{HO}_x = \text{OH} + \text{HO}_2$) radicals (5). In our work, we proposed that the reaction $\text{HO}_2\text{-H}_2\text{O} + \text{NO}_2$ could be the HONO source if its HONO yield was 100%. Based on airborne observations in the United States, Ye *et al.* (6) determined an upper limit of 3% for the HONO yield in the reaction $\text{HO}_2\text{-H}_2\text{O} + \text{NO}_2$, much less than necessary to explain our HONO observations. Ye *et al.* therefore imply that other HONO sources are active. As an example, they suggest photolysis of particulate nitrate and speculate that the corresponding net source of NO_x may be lower than predicted in our work because of missing NO_x sinks in our model calculations.

The major conclusion of our paper (5) is based on the analysis of the observed NO_x and HO_x

budgets, where we considered sources that either release HONO from stable precursors (external source) or generate HONO by consuming NO_x and/or HO_x [see Section 1.2 in the supplementary materials of (5)]. The important aspect is that if HONO is formed by a mechanism that consumes HO_x , the net contribution of HONO photolysis to the HO_x production can become small. Our sensitivity tests analyzing observed NO_x and OH concentrations point to a gas-phase source that requires NO_x and, at a less confident level, also HO_x . At this stage, we did not make any assumption regarding the exact mechanism forming HONO, and thus this main finding is independent of the specific reaction in question.

Given the availability of the measured parameters, we only considered reactions that directly consume NO_x and HO_x to produce HONO. Experiments still ongoing in the atmospheric simulation chamber SAPHIR (Simulation of Atmospheric Photochemistry In a large Reaction Chamber) at our institute imply that none of these reactions (including $\text{HO}_2\text{-H}_2\text{O} + \text{NO}_2$) can substantially contribute to the HONO formation. This is in agreement with the results by Ye *et al.* If the process producing HONO is not related to the consumption of HO_x radicals, we agree with the conclusion by Ye *et al.* that HONO should remain an important net OH precursor.

Furthermore, Ye *et al.* suggest particulate nitrate photolysis as a potential HONO source under our measurement conditions. Particulate nitrate photolysis is an external source of HONO and was therefore not considered in our work. During the Pan-European Gas-Aerosols Climate Interaction Study (PEGASOS) field campaign in the Po Valley [see Section 1.1 in the supplementary materials of (5)], the spatial distribution of aerosol

composition was measured on a number of flights. The average particulate nitrate concentration in the residual layer was ~ 1 to $2 \mu\text{g m}^{-3}$ (7). If we assume that the observed HONO was formed exclusively from photolysis of particulate nitrate, the required photolysis frequency would be $\sim 3 \times 10^{-4} \text{ s}^{-1}$, which is an order of magnitude greater than that reported in the literature for surface adsorbed HNO_3 under full sun conditions (8). Substantial HONO formation by nitrate photolysis is therefore unlikely.

Regarding potentially missing NO_x sinks in our model, we note that the full RACM-MIM-GK mechanism (9) was applied. In addition to the $\text{OH} + \text{NO}_2$ reaction, the formation of organic nitrates (RONO_2) and peroxyacyl nitrates (PANs) is included in the mechanism as NO_x sinks. Moreover, the model calculations for NO_x [i.e., model scenario M2 and M3 in figure 3 of (5)] are constrained by measured OH, trace gases, relative humidity, temperature, pressure, and photolysis frequencies [see section 1.2 in the supplementary materials of (5)]. In general, our model calculations show that the NO_x sinks during our observations are dominated by the $\text{OH} + \text{NO}_2$ reaction. We did not measure alkylperoxy radicals (RO_2), PANs, or bromine monoxide (BrO) during the field campaign. However, based on the model scenario assuming externally formed HONO [i.e., model scenario M2 in figure 3 of (5)], we performed additional sensitivity studies on the NO_x sinks as suggested by Ye *et al.* To explain the discrepancy between the measured and modeled NO_x concentration via formation of RONO_2 , precursor volatile organic compound concentrations would be required to be an order of magnitude higher than the measured values. This results in modeled OH reactivities that are three times greater than measured. Note that for model calculations shown in figure 3 and 4 in (5), given the accuracy of OH reactivity measurement, good agreement is always found between the modeled and measured values. The formation of PANs shows minor influence on the NO_x simulation. When we change the initial PANs concentration from 200 parts per trillion (ppt) to 0 in the model, the calculated NO_x concentration only decreases by less than 10%. When we include the formation and photolysis of BrONO_2 and set the BrO concentration to a constant value of 3 ppt, the modeled NO_x concentration decreases by $\sim 10\%$ and thus still remains significantly higher than the measured values. The match between the modeled and measured NO_x concentration can only be reached if the BrO concentration is higher than 30 ppt. High BrO concentrations are usually found under maritime conditions. According to (10), which is cited by Ye *et al.*, a BrO concentration of 3 ppt is a very high value even for a coastal environment. Because our observation area is 100 km away from the Mediterranean coastline, we do not expect high BrO concentrations.

In summary, we do agree with Ye *et al.* that the specific $\text{HO}_2\text{-H}_2\text{O} + \text{NO}_2$ reaction is not an important HONO source, but our main conclusion that HONO is from a gas-phase source that

¹Institut für Energie und Klimaforschung, Troposphäre (IEK-8), Forschungszentrum Jülich, Jülich, Germany. ²Department of Chemistry, University of Wisconsin-Madison, Madison, WI, USA. *Corresponding author. E-mail: f.rohrer@fz-juelich.de (F. R.), x.li@fz-juelich.de (X. L.) †Deceased. ‡Present address: School of Engineering and Applied Sciences, Department of Chemistry and Chemical Biology, Harvard University, Cambridge, MA, USA. §Present address: College of Environmental Sciences and Engineering, Peking University, Beijing, China. ||Present address: Joint Center for Earth Systems Technology, University of Maryland Baltimore County, Baltimore, MD, USA. Atmospheric Chemistry and Dynamics Laboratory, NASA Goddard Space Flight Center, Greenbelt, MD, USA.

consumes NO_x and is not related to processes at Earth's surface remains valid for the investigated Po Valley region.

REFERENCES

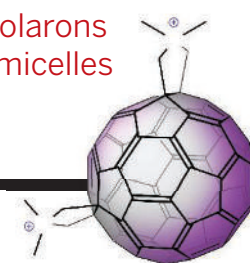
1. B. J. Finlayson-Pitts, J. N. Pitts, *Chemistry of the Upper and Lower Atmosphere: Theory, Experiments and Applications* (Academic Press, San Diego, CA, ed. 1, 2000).
2. B. Alicke *et al.*, *J. Geophys. Res.* **108** (D4), 8247 (2003).
3. J. Kleffmann *et al.*, *Geophys. Res. Lett.* **32**, L05818 (2005).
4. K. Acker *et al.*, *Geophys. Res. Lett.* **33**, L02809 (2006).
5. X. Li *et al.*, *Science* **344**, 292–296 (2014).
6. C. Ye *et al.*, *Science* **348**, 1326 (2015).
7. F. Rubach, Aerosol processes in the planetary boundary layer: High-resolution aerosol mass spectrometry on a Zeppelin NT airship, thesis, Universität Wuppertal, Germany (2013).
8. X. Zhou, H. Gao, Y. He, G. Huang, *Geophys. Res. Lett.* **30**, 2217 (2003).
9. K. D. Lu *et al.*, *Atmos. Chem. Phys.* **12**, 1541–1569 (2012).
10. R. Grilli *et al.*, *Geophys. Res. Lett.* **40**, 791–796 (2013).

6 December 2014; accepted 28 April 2015
10.1126/science.aaa3777

RESEARCH

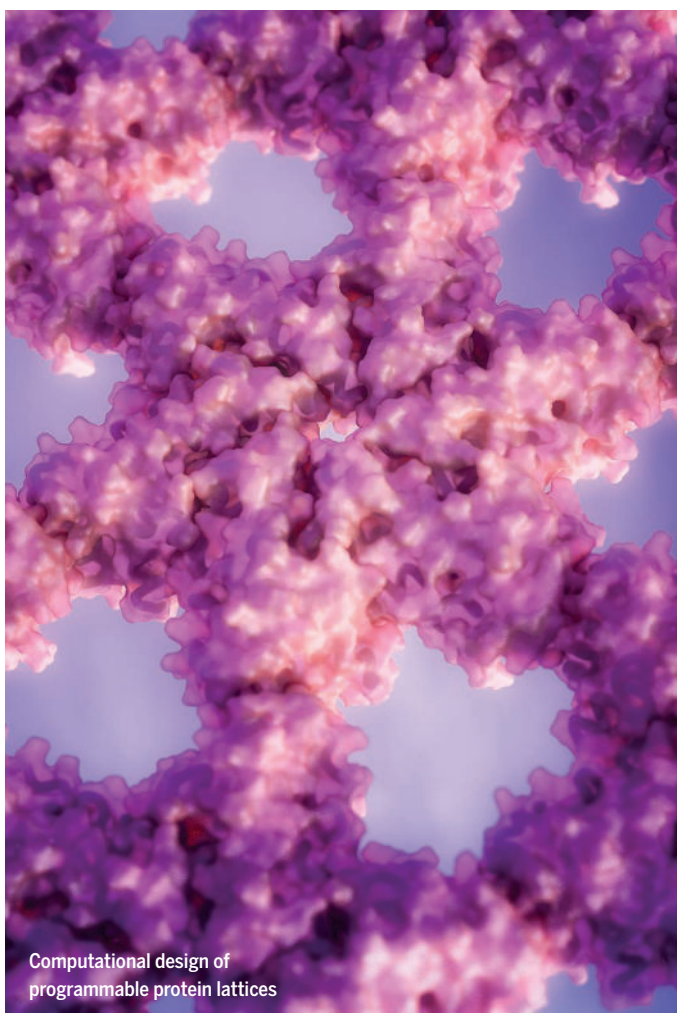
Long-lived synthetic polarons produced in aqueous micelles

Huber et al., p. 1340



IN SCIENCE JOURNALS

Edited by Stella Hurtley



Computational design of programmable protein lattices

PROTEIN DESIGN

Designing proteins to self-assemble

DNA has been used as a nano building material since the 1980s. Protein nanostructures have the potential to give greater geometric control and shape variability. Gonen *et al.* describe the computational design of proteins that self-assemble into two-dimensional arrays. These programmable protein lattices should enable new approaches in biomolecular structure determination and molecular sensing. — VV

Science, this issue p. 1365

INDUCED SEISMICITY

Making quakes depends on injection rates

Wastewater injection wells induce earthquakes that garner much attention, especially in tectonically inactive regions. Weingarten *et al.* combined information from public injection-well databases from the eastern and central United States with the best earthquake catalog available over the past 30 years. The rate of fluid injection into a well appeared to be the most likely decisive triggering factor in regions prone to induced earthquakes. Along these lines, Walsh III and Zoback found a clear correlation between areas in Oklahoma where waste saltwater is being injected on a large scale and areas experiencing increased earthquake activity. — BG

Science, this issue p. 1336; *Sci. Adv.* 10.1126/sciadv.1500195 (2015).

CANCER

Telomerase stabilized by a sphingolipid

In normal adult cells, the structures at the ends of chromosomes, called telomeres, becomes progressively shorter with each replication cycle. When telomeres get too short or damaged, the cell stops dividing and becomes senescent. The enzyme telomerase maintains the integrity of telomeres, and phosphorylation stabilizes the catalytic subunit (called TERT) of this enzyme. In both normal fibroblasts and lung cancer cells, Selvam *et al.* found that binding of the phospholipid S1P to TERT prevented the degradation of

TERT. Disrupting the interaction between S1P and TERT impaired telomere maintenance and promoted senescence in cultured cells and decreased the growth of lung cancer cell xenografts in mice. — LKF

Sci. Signal. **8**, ra58 (2015).

BATTERIES

Watching defects during battery cycling

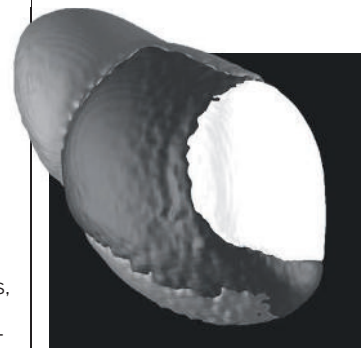
Dislocations affect the mechanical properties of a material. Ulvestad *et al.* studied the influence of dislocations on a nanoparticle undergoing charge and discharge cycles in a lithium ion battery. The defects influenced the way the material expanded and contracted during cycling. In the future, it may be possible to tune the properties of a material through controlled defect engineering. — MSL

Science, this issue p. 1344

COMETARY NUCLEI

Collisions give comets their shape

The shape and structure of comets are relicts of collision processes from long ago.



Simulated comet shape

Despite recent and ongoing spacecraft missions that offer direct measurements of cometary nuclei, it is difficult to test what is important in comet shaping. Jutzi and Asphaug ran ~100 three-dimensional collision simulations across a wide range of target and impactor masses and trajectories. Slow and less violent collisions produced the layering and bi-lobed shapes of actual comets. — NW

Science, this issue p. 1355

GROUP DECISIONS

Baboons follow the pack, not the leader

How do groups of animals, including humans, make decisions that affect the entire group? Evidence collected from schooling animals suggests that the process is somewhat democratic, with nearest neighbors and the majority shaping overall collective behavior. In animals with hierarchical social structures such as primates or wolves, however, such democracy may be complicated by dominance. Strandburg-Peshkin *et al.* monitored all the individuals within a baboon troop continuously over the course of their daily activities. Even within this highly socially structured species, movement decisions emerged via a shared process. Thus, democracy may be an inherent trait of collective behavior. — SNV

Science, this issue p. 1358

ENDOCYTOSIS

Bend me, shape me: Clathrin in action

Endocytic clathrin-coated pits were among the first cellular structures described by electron microscopy over five decades ago. Despite this, the question remains: Does clathrin bind to the membrane as a flat lattice and then bend during coated pit invagination, or does clathrin assemble with a defined curvature as membranes invaginate? Avinoam *et al.* applied two state-of-the-art imaging approaches to resolve this conflict. They suggest that

clathrin assembles into a defined flat lattice early in endocytosis, which predetermines the size of the vesicle. The assembled clathrin coat then rearranges through dynamic exchange of clathrin with the cytosolic pool to wrap around the forming vesicle. — SMH

Science, this issue p. 1369

DRUG DEVELOPMENT

A degrading game plan for cancer therapy

Certain classes of proteins that contribute to cancer development are challenging to target therapeutically. Winter *et al.* devised a chemical strategy that, in principle, permits the selective degradation of any protein of interest. The strategy involves chemically attaching a ligand known to bind the desired protein to another molecule that hijacks an enzyme whose function is to direct proteins to the cell's protein degradation machinery. In a proof-of-concept study, they demonstrated selective degradation of a transcriptional coactivator called bromodomain-containing protein 4 and delayed the progression of leukemia in mice. — PAK

Science, this issue p. 1376

MEMBRANE FILTRATION

Composite membranes for filtering solvents

Much research has focused on finding membranes that can purify water or extract waste carbon dioxide. However, there is also a need for the removal of small molecules from organic liquids. Many existing processes are energy-intensive and can require large quantities of solvents. Karan *et al.* grew confined polymer layers on a patterned sacrificial support to give rippled thin films that were then placed on ceramic membranes (see the Perspective by Freger). The composite membrane showed high flux for organic solvents and good stability and was able to separate out small molecules with high efficiency. — MSL

Science, this issue p. 1347; see also p. 1317

IN OTHER JOURNALS

Edited by **Kristen Mueller**
and **Jesse Smith**



Canopy of a carbon-rich tropical forest in the Amazon

CHROMOSOMES

Y genes find new chromosomal homes

The mammalian Y chromosome has lost many genes throughout evolution. However, they are not lost for good, as Hughes *et al.* report. The authors found that in eight mammals, including humans, apes, rodents, cattle, and marsupials, four genes formerly found on the Y chromosome now reside on other, nonsex chromosomes. A handful of genes on the X chromosome met a similar fate. In some cases, the transposed genes acquired broad tissue

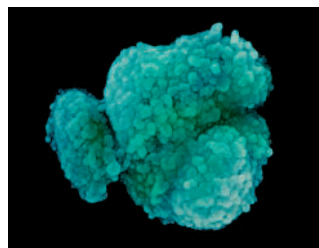
expression, perhaps to maintain a gene dosage required for fitness. In other cases, the relocated genes were expressed specifically in the testes, pointing to newly acquired functions in spermatogenesis. — LC

Genome Biol. **16**, 104 (2015).

BEHAVIOR

Differences in strategy across the globe

Economists measure the extent of a person's preference for risk in a number of ways. Most commonly, they ask people to make choices between gambles—such as a 40% chance of winning \$2.00 and a 60% chance of winning \$1.60 versus a 40% chance of winning \$3.85 and a 60% chance of winning \$0.10. Chassy and Gobet offer a new measure of risk derived from the choice of opening moves in chess. They document global risk preference based on more than half a million games played by people ranked expert and above



A color-enhanced scanning electron micrograph of the human Y chromosome



BIOGEOCHEMISTRY

Measuring carbon uptake by tropical forests

The carbon uptake by tropical forests is a key part of the global carbon budget. Yet accurately measuring this quantity—termed the net primary production or NPP—in tropical forests is challenging, hampering efforts to predict how it may respond to climatic and environmental change. Cleveland *et al.* have compared NPP estimates from small-scale observations, satellite data, and biogeochemical models. Although the large-scale estimates are similar for all three approaches, the spatial and temporal patterns are very different. Each approach is sensitive to different environmental drivers (such as drought), and it remains unclear which results are correct. The authors explain how an integrated monitoring network could capture the diversity of tropical forest landscapes. — JFU

Global Biogeochem. Cycles
10.1002/2014GB005022 (2015).

from 11 different civilizations. Civilizations differed in their risk preferences: Some favored settling for peace, whereas others preferred riskier moves. — GJC

Cognition **141**, 36 (2015).

PLANT SCIENCE

Leaf recycling requires a two-step process

During leaf senescence, plants recycle nutrients and other molecules from unneeded leaves for use by seeds and other new growth. Hormones, including ethylene, regulate this process. Studying the leaves of *Arabidopsis* plants, Ueda and Kusaba found that those carrying mutations affecting the synthesis of the hormone strigolactone did not curl up and die in the dark as did the leaves of normal plants. Dark-induced leaf senescence required another hormone, strigolactone, which the plant synthesized in the leaves in response to ethylene. Separately, ethylene

induced leaf senescence better than strigolactone. But together, they synergized. This multistep process probably preserves leaves when possible, only carrying through to leaf senescence when the stress becomes too much. — PJH

Plant Physiol. 10.1104/
pp.15.00325 (2015).

CHEMISTRY

Boroxine cages

Boronic acids, in which a boron atom bears two hydroxyl (OH) groups and an organic group, can trimerize by dehydration to form six-membered boroxine rings, and molecules bearing more than one boronic acid group can form polymer networks. Ono *et al.* extend the architectures that can be formed to cages. They designed pincer-like organic groups that set B(OH)₂ groups at desired angles. After heating and dehydration, the molecule with an 84° angle between hydroxyl groups formed an octahedron from six units,

with a 1.5-nanometer cavity, and the molecule with a 117° angle formed a cuboctahedron from 12 units with a 2.5-nanometer cavity. — PDS

J. Am. Chem. Soc. 10.1021/
jacs.5b02716 (2015).

VIROLOGY

Virus dynamics in human lungs

People with cystic fibrosis suffer from progressive bacterial lung infections, often by *Pseudomonas aeruginosa*. This occurs despite a diversity of viruses, known as bacteriophage, that attack these bacteria. For more than 2 years, James *et al.* followed the ecological dynamics of active bacteriophage in the sputa of 10 people with cystic fibrosis. Overall, ongoing lysis triggered by bacteriophage reduced bacterial density in the lung. Different patients' sputa contained different combinations of phage strains, indicating that

these different strains compete. Phage may also exclude infection by different strains of *P. aeruginosa*, which might influence disease among patients. These results indicate that phage may show some therapeutic promise in combination with specific antibiotics. — CA

ISME J. **9**, 1391 (2015).

CLIMATE CHANGE

Weather underground

Climate models indicate that as global temperatures increase, global precipitation also will rise, but that it will become more heterogeneous as well. How will that affect soil moisture, a quantity that often is ignored but has large impacts on agriculture, flooding, and weather? Wu *et al.* report results from a suite of climate models that show that soils in middle and high northern latitudes will get wetter in the wettest months and drier in the driest months. This increase in the annual range of soil water content will affect water resource management, plant adaption, and agriculture, particularly in regions where snowmelt supplies a significant portion of the seasonal water supply. — HJS

Geophys. Res. Lett. 10.1002/
2015GL064110 (2015).

Bacteriophages are viruses that can infect and kill bacteria



ALSO IN SCIENCE JOURNALS

Edited by Stella Hurtley

OCEAN CIRCULATION

On the success (or not) of climate models

Atlantic Meridional Overturning Circulation (AMOC) transports huge amounts of heat from low to high latitudes and has a major influence on climate. Climate models have predicted that global warming will cause the AMOC to slow, but concrete evidence of such a slowdown has been scarce. Srokosz and Bryden review a decade of observations of the AMOC that reveal an unexpected amount of variability over time scales from seasonal to decadal, as well as a general weakening over this time. — HJS

Science, this issue p. 1330

POLARON DYNAMICS

Photoinduction of long-lived polarons

Photosynthetic complexes and organic photovoltaics can rapidly create separated charges upon photoexcitation. However, unproductive charge recombination often occurs in the human-made system. This is in part because the charge acceptor and donor structures are much larger. Huber *et al.* created aqueous micelles that pair conjugated polyelectrolyte charge donors with fullerene acceptors at a much smaller interface. They observed the photoinduced formation of polarons—stable pairs of separated charges—with lifetimes of several days. — PDS

Science, this issue p. 1340

VACCINES

The right combination for protection

Despite its prevalence, no vaccine exists to protect against infection with the sexually transmitted bacterium *Chlamydia trachomatis*. Stary *et al.* now report on one potential vaccine candidate (see the Perspective

by Brunham). Vaccinating with an ultraviolet light-inactivated *C. trachomatis* linked to adjuvant-containing charged nanoparticles protected female conventional and humanized mice against *C. trachomatis* infection. The vaccine conferred protection only when delivered through mucosal routes. Protection relied on targeting the bacteria to a particular population of immunogenic dendritic cells and inducing memory T cells that resided in the female genital tract. — KLM

Science, this issue p. 1331; see also p. 1322

WATER CONSERVATION

How to use less water during drought

Urban populations require a lot of water, which is often sourced from the surrounding countryside. Water conservation strategies implemented during droughts—such as the ongoing drought in California—include watering restrictions and tiered pricing. How effective are these water conservation strategies? In a Perspective, Hogue and Pincetl highlight recent studies that have used highly resolved data, such as those from satellites or water meters, to address this question. Together with advanced data analysis tools and models, these data can help to determine the best local strategies for water conservation. — JFU

Science, this issue p. 1319

NEURODEVELOPMENT

From blastula to neural crest, do not pass go

During vertebrate development, neural crest cells give rise to an unusual diversity of cells, including pigment cells, neurons, and cartilage. Traditionally, neural crest cells have been considered a derivative of neural ectoderm. Buitrago-Delgado *et al.* now show that neural crest

cells have components of the molecular programs characteristic of blastula cells from earlier in development (see the Perspective by Hoppler and Wheeler). Blastula cells have the broad range of developmental potentials necessary to build the embryo. Neural crest cells may thus reflect persistence of the developmental programs characteristic of early development rather than re-specification of developmental programs after differentiation into neuroectoderm. — PJH

Science, this issue p. 1332; see also p. 1316

BRAIN PROCESSING

Signal flow during sensorimotor choices

Little is known about the flow of task signals across the brain. Siegel *et al.* simultaneously recorded from multiple units in the sensory, parietal, prefrontal, and motor cortex while monkeys were cued to perform one among two possible simple tasks. The proportion of neurons coding for stimuli, cues, tasks, and choices, and their response latency, varied across regions. Parietal and prefrontal brain regions encoded task information and choices with the same latency. Interestingly, all brain areas encoded all types of information. However, they differed functionally according to the proportions of neurons and their response latency. — PRS

Science, this issue p. 1352

SIGNAL TRANSDUCTION

How a receptor transmits a signal

G protein-coupled receptors (GPCRs) transmit diverse external signals into the cell. When activated by an outside stimulus, they bind to a G protein inside the cell and accelerate exchange of a bound guanosine diphosphate (GDP) nucleotide for guanosine triphosphate, which

initiates intercellular signaling. Dror *et al.* used atomic-level molecular dynamics simulations to show how GPCRs enhance GDP release. The G protein is dynamic and frequently adopts a conformation that exposes GDP even without the receptor bound. GPCR binding to this conformation favors an additional structural rearrangement that favors GDP release. The authors confirmed these predictions experimentally using double electron-electron resonance spectroscopy. — VV

Science, this issue p. 1361

TRANSCRIPTION

Multifunctional pioneers

Proteins surround cellular DNA to silence gene expression. Early in development, proteins such as pioneer transcription factors facilitate the opening of this silenced chromatin structure. Hsu *et al.* describe an additional role for the PHA-4 pioneer transcription factor in nematode worms. PHA-4 recruited RNA polymerase II to target promoters before transcriptional onset, and this activity preceded its chromatin-opening duty. The multifunctional role identified for PHA-4 may be shared by other pioneer factors. — BAP

Science, this issue p. 1372

CONSERVATION

When is predator control acceptable?

Predators such as wolves were long seen as a problem to be controlled or even eliminated. Today, their value is more widely appreciated, but predators are still widely killed to bolster populations of threatened prey species or to protect livestock. In a Perspective, Woodroffe and Redpath argue that such predator control efforts are not always beneficial for prey species and often have unwelcome effects. Predator pressures on prey are often a result of human actions,

such as habitat fragmentation, making prey species dependent on predator control unless their habitats are restored. Passions often run high on both sides of the predator control debate, and management efforts may not be effective unless they are also socially acceptable. — JFU

Science, this issue p. 1312

CELL BIOLOGY

Sealing the envelope

During animal cell division, the nuclear envelope breaks down, allowing a mitotic spindle to organize duplicated chromosomes for separation into future daughter cells. How the envelope reforms around the chromatin has been a mystery. In a Perspective, Sundquist and Ullman describe how a cellular mechanism involved in a variety of membrane fission events also seals the nuclear envelope. The endosomal sorting complex required for transport (ESCRT) machinery assembles at the growing nuclear envelope and recruits other proteins. These proteins release chromatin from the mitotic spindle and close the membrane, readying the two daughter cells for separation. — LDC

Science, this issue p. 1314

AUTOIMMUNITY

AIREing out autoimmunity

Because of mutations in the *AIRE* gene, patients with autoimmune polyendocrine syndrome type 1 (APS1) suffer dysfunction in multiple endocrine glands and are often infertile. Female infertility can be explained by autoimmune ovarian failure, but the causes of male infertility are unclear. Now Landegren *et al.* report that the prostatic secretory molecule transglutaminase 4 (TGM4) is a male-specific autoantigen in APS1 patients that could contribute to subfertility. Autoantibodies to TGM4 appeared in APS1 patients beginning at puberty, and similar antibodies lead to destructive prostatitis in *AIRE*-deficient mice. Together, these data may explain the infertility observed in male APS1 patients. — ACC

Sci. Transl. Med. **7**, 292ra101 (2015).

REVIEW SUMMARY

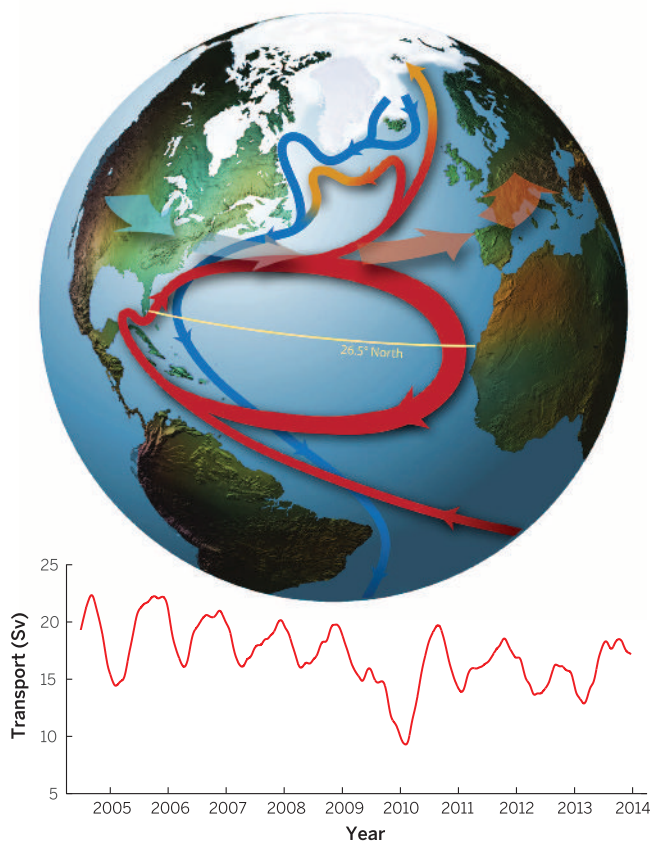
OCEAN CIRCULATION

Observing the Atlantic Meridional Overturning Circulation yields a decade of inevitable surprises

M. A. Srokosz* and H. L. Bryden

BACKGROUND: A 2002 report, *Abrupt Climate Change: Inevitable Surprises*, highlighted the North Atlantic circulation as possibly subject to abrupt change in a warming climate. Likewise, the 2001 Intergovernmental Panel on Climate Change (IPCC) report suggested that the Atlantic Meridional Overturning Circulation (AMOC) could weaken over the 21st

century. As this circulation carries heat northward, giving the United Kingdom and north-west Europe a temperate climate, this generated renewed efforts to make observations of the AMOC. In particular, it led to the deployment of an observing system across the Atlantic at 26.5°N in spring 2004, which last year achieved a decade of measurements.



A simplified schematic (top) of the AMOC. Warm water flows north in the upper ocean (red), gives up heat to the atmosphere (atmospheric flow gaining heat represented by changing color of broad arrows), sinks, and returns as a deep cold flow (blue). Latitude of the 26.5°N AMOC observations is indicated. The actual flow is considerably more complex. **(Bottom)** The 10-year (April 2004 to March 2014) time series of the AMOC strength at 26.5°N in Sverdrups ($1 \text{ Sv} = 10^6 \text{ m}^3 \text{ s}^{-1}$). This is the 180-day filtered version of the time series. Visible are the low AMOC event in 2009–2010 and the overall decline in AMOC strength over the 10-year period.

ADVANCES: In addition to the baseline decade of 26.5°N observations, there have been other ongoing measurements that capture components of the AMOC, some of which are not continuous or of much shorter duration. Together these observations are leading to a more complete picture of the AMOC. The 26.5°N AMOC observations have produced a number of surprises on time scales from sub-annual to multiannual. First, the range of AMOC variability found in the first year, 4 to 35 Sv (Sverdrup, a million cubic meters per second, the standard unit for ocean circulation), was larger than the 15 to 23 Sv found previously from five ship-based observations over 50 years. A similarly large range to that at

26.5°N has subsequently been observed at 34.5°S. Second, the amplitude of the seasonal cycle, with a minimum in the spring and a maximum in the autumn, was much larger ($\sim 6.7 \text{ Sv}$) than anticipated, and the driving mechanism of wind stress in the eastern Atlantic was unexpected as well. Third, the 30% decline in the AMOC during 2009–2010 was totally unexpected and exceeded the range of interannual variability found in climate models used for the IPCC assessments. This event was also captured by *Argo* and altimetry observations of the upper limb of the AMOC at 41°N. This dip was accompanied by significant changes in the heat content of the ocean, with potential impacts on weather that are the subject of active research. Finally, over the period of the 26.5°N observations, the AMOC has been declining at a rate of about 0.5 Sv per year, 10 times as fast as predicted by climate models. Whether this is a trend that is a decline due to global warming or part of the so-called Atlantic Multidecadal Oscillation/Variability, inferred from sea surface temperature measurement, is also a subject of active research. There is no doubt that continuously observing the AMOC over a decade has considerably altered our view of the role of ocean variability in climate.

OUTLOOK: The 26.5°N AMOC observations are stimulating the development of further AMOC observing systems both to the north, in the North Atlantic subpolar gyre, and to the south, in the South Atlantic. The aim is to obtain a holistic picture of the AMOC from south to north. Given the surprises and insights into the Atlantic circulation that observations have produced to date, it is not too much to expect that with the new observations there will be future “inevitable surprises.” ■

The list of affiliations is available in the full article online.

*Corresponding author. E-mail: mas@noc.ac.uk

Cite this article as M. A. Srokosz, H. L. Bryden, *Science* **348**, 1255575 (2015). DOI: 10.1126/science.1255575

REVIEW

OCEAN CIRCULATION

Observing the Atlantic Meridional Overturning Circulation yields a decade of inevitable surprises

M. A. Srokosz^{1*} and H. L. Bryden²

The importance of the Atlantic Meridional Overturning Circulation (AMOC) heat transport for climate is well acknowledged. Climate models predict that the AMOC will slow down under global warming, with substantial impacts, but measurements of ocean circulation have been inadequate to evaluate these predictions. Observations over the past decade have changed that situation, providing a detailed picture of variations in the AMOC. These observations reveal a surprising degree of AMOC variability in terms of the intraannual range, the amplitude and phase of the seasonal cycle, the interannual changes in strength affecting the ocean heat content, and the decline of the AMOC over the decade, both of the latter two exceeding the variations seen in climate models.

In 2002, the U.S. National Research Council Committee on Abrupt Climate Change published its findings in a book entitled *Abrupt Climate Change: Inevitable Surprises* (1). One process highlighted in that book, because it could possibly be subject to abrupt change in a warming climate, was the North Atlantic thermohaline circulation (THC). The work leading up to the publication of this book—together with the conclusions of the Intergovernmental Panel on Climate Change (IPCC) Working Group I Third Assessment Report (2) that most models showed a weakening of the THC over the 21st century—generated renewed efforts to make observations of the Atlantic Meridional Overturning Circulation (AMOC). In particular, it led to the establishment of the Rapid Climate Change program (RAPID) (3). A key element of RAPID was the proposal to monitor the AMOC (4, 5) at 26.5°N in the Atlantic. The observing system (see schematic in Fig. 1) was deployed in March 2004 and results from the first year of observations published in 2007 (6, 7). In 2014, the observing system reached a major milestone by completing a decade of operation. Here, we provide an updated description of what is known about the AMOC from recent observations and highlight some of the surprises that these observations have produced.

Background

The major characteristics of the AMOC are a near-surface, northward flow of warm water and a colder southward return flow at depth. As

the ocean loses heat to the atmosphere at high latitudes in the North Atlantic, the northward-flowing surface waters become denser. These waters then sink and so form the deep return flow of the overturning circulation (Fig. 1). The AMOC transports heat northward across the equator, which makes the Atlantic different from the Indian and Pacific Oceans, where the ocean transports heat away from the equator toward the poles. The maximum northward oceanic heat transport in the Atlantic is 1.3 PW (1 PW = 10^{15} watts) at 24° to 26°N, which is ~25% of the total (atmosphere and ocean) poleward heat transport at these latitudes (8, 9). Further north, at mid-latitudes, the strong transfer of heat from the ocean to the atmosphere contributes to the temperate climate of northwest Europe (10–12). In addition, changes in sea level around the periphery of the North Atlantic are related to changes in the AMOC (13–15). There-

fore, future changes in the AMOC could have substantial impacts (16, 17).

The importance of the AMOC for climate was highlighted by Broecker (18) with his “great ocean conveyor” picture, based on paleoclimatic evidence (19, 20). From the results of calculations using a simple two-box model, Stommel (21) suggested that the circulation could switch between “on” and “off” states under appropriate forcing, such as the addition of freshwater at high latitudes (22, 23). Although this picture of the circulation is now acknowledged to be too simple, the possibility that the AMOC could switch between different states has been shown to occur in more complex climate models (24, 25), so that the AMOC could be bistable.

Given the importance of the AMOC, and its potential to decline and perhaps even switch off, the observing system deployed at 26.5°N in the Atlantic became the first attempt to continuously measure the strength and vertical structure of the AMOC. The measurements began on the last day of March 2004 and have continued since then (26). The key components of the AMOC (Fig. 1) and the methods by which they are quantified are the Gulf Stream transport through the Florida Straits measured by seabed cable; the Ekman transport calculated from wind stress; and the midocean transport measured by an array of moorings at the western and eastern boundaries and the mid-Atlantic Ridge (27–29). The first year of measurements established that the system was able to accurately measure the AMOC (30) and subsequent studies have confirmed this initial assessment (31–33). It is important to note that the measurements provide information not only on the AMOC strength itself but also on the major components of the circulation: Gulf Stream, Ekman, upper mid-ocean recirculation, southward flow of the Upper and Lower North Atlantic Deep Water (UNADW and LNADW), and the northward flow of the Antarctic Intermediate Water (AAIW). In addition to RAPID, there have been other ongoing measurements of the AMOC, but these capture only part of the AMOC, or are not continuous, or are of much shorter duration. They include

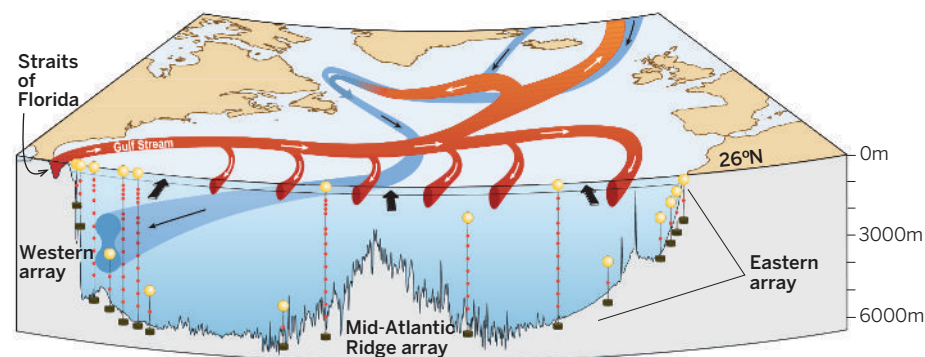


Fig. 1. Schematic showing the components of the RAPID AMOC observing array at 26.5°N in the Atlantic. The flow through the Florida Straits is measured by underwater cable, the midocean flow by the array of moorings at the eastern and western boundaries and the mid-Atlantic Ridge (using geostrophy), and the surface Ekman flow from ocean surface winds (28, 29).

¹National Oceanography Centre, University of Southampton Waterfront Campus, Southampton, UK. ²National Oceanography Centre Southampton, University of Southampton, Southampton, UK.

*Corresponding author. E-mail: mas@noc.ac.uk

the Meridional Overturning Variability Experiment (MOVE) array at 16°N (34), the Deep Western Boundary Current (DWBC) arrays at around 39°N (35) and 53°N (36), the 34.5°S array (37, 38), the use of altimetry and Argo at around 41°N (39, 40), and the Observatoire de la Variabilité Interannuelle et Décennale en Atlantique Nord (OVIDE) hydrographic sections (41). Recently, a new component of the AMOC, the so-called East Greenland spill jet, has been identified from a year of mooring observations (42), but its importance in the long-term for the overall AMOC remains to be confirmed.

The focus of this Review is on observations of the AMOC (43), because models still show considerable differences in their representations of the overturning circulation (44). Figure 2 shows the full 10-year AMOC time series at 26.5°N obtained to date by RAPID. These measurements provide insights into the changes occurring in the AMOC, which include a number of surprises on all time scales: intraannual, seasonal, interannual and multiannual.

Intraannual and seasonal AMOC variability

The first surprise was the range of values found for the strength of the AMOC during the initial year of RAPID observations. Although the annual average strength of 18.7 sverdrups (Sv) (45) was not unexpected, the range from a minimum of 4 Sv (February) to a maximum of 34.9 Sv (September) was a surprise (6). Before the deployment of the 26.5°N observing system, the five ship-based hydrographic measurements of the AMOC made at this latitude since the 1950s had shown a range of ~15 to 23 Sv (46), so the first year's intraannual variability exceeded the historical estimates of the AMOC. Subsequently, a similar range of intraannual variability (3 to 39 Sv) has been found in the 20 months of measurements of the AMOC made at 34.5°S (37).

The next surprise came from the analysis of the AMOC seasonal cycle after 4 years of RAPID observations had been acquired (47). Because the longer-term observations of the Gulf Stream (27, 48) had shown that it exhibited a seasonal cycle of ~4 Sv with a maximum in summer, the seasonal cycle of the AMOC of ~6.7 Sv, with a minimum in the spring and a maximum in the autumn, came as a surprise. In addition, the perceived wisdom was that the seasonality in the AMOC would be dominated by wind-driven northward Ekman transport, but this was found to be small. The result that the seasonal cycle was dominated by the wind stress curl forcing at the eastern boundary came as further surprise (47). Results from the OVIDE analysis (41) of the Portugal to Greenland hydrographic section similarly show, from 1993 to 2010, a seasonal cycle with a peak-to-peak amplitude of 4.3 Sv, mostly due to the geostrophic component, with a much weaker Ekman component. The Argo and altimeter estimates of the AMOC upper limb at around 41°N from 2002 to 2009 show a small and irregular seasonal cycle (39).

Characterization of the seasonal cycle allowed the previous five ship-based hydrographic estimates of the AMOC strength at the RAPID latitude (46) to be corrected for seasonal sampling bias, because they had been acquired at different times of the year. This resulted in a reassessment of the apparent decline of the AMOC between 1957 and 2004 as partially being an artifact of the sampling (49).

The first 4 years of RAPID observations also confirmed the average strength of the AMOC at 26.5°N to be 18.7 ± 2.1 Sv, in agreement with the annual average for the first year. However, the result that the mean strength of the AMOC seemed to be unchanging, despite large seasonal and intraannual fluctuations, seemed at odds with the expectation that the AMOC might

decline, although the time series was acknowledged to be too short at that time to draw any strong conclusions. Nevertheless, the apparent stability of the seasonal cycle paved the way to the next surprise.

Interannual AMOC variability

After having observed 5 years of relatively stable seasonal cycles of the AMOC, when the data for 2009–2010 were recovered from the 26.5°N array, another surprise was in store. From spring 2009 through spring 2010, the AMOC was found to have taken a large ~30% dip in strength before recovering later in 2010 (Fig. 2) (50). For the previous 5 years, the average strength of the AMOC had been 18.5 Sv, whereas in 2009–2010 it was 12.8 Sv (years are taken to run from April to March, due the initial deployment of the observing array in late March 2004). This dip in strength was also seen in the Argo and altimetry observations of the upper limb of the AMOC at 41°N but not in the 16°N observations of the deep western basin return limb of the AMOC (51). This raises the question of the meridional coherence of changes in the AMOC, a point to be discussed below.

The 2009–2010 dip in strength can be partially attributed to an extreme negative North Atlantic Oscillation (NAO) winter that affected the wind field, reducing—and for a period reversing (December 2009 to March 2010)—the northward Ekman transport component of the AMOC. In addition, the upper midocean recirculation component of the AMOC strengthened starting in spring 2009 before the negative NAO winter, leading to a reduction in the AMOC. Finally, the AMOC deep southward return limb flow, the so-called Lower North Atlantic Deep Water (LNADW) at a depth of 3000 to 5000 m, weakened in concert with the upper ocean northward-flowing limb. This change in AMOC strength was found to lie well outside the range of interannual variability predicted by coupled atmosphere-ocean climate models (52).

Because the AMOC carries ~90% of the ocean heat transport at this latitude (with the gyre circulation carrying the remainder) (53), this AMOC reduction had a considerable impact on the heat transport into, and the heat content of, the North Atlantic (54, 55). The heat transported north by the AMOC at 26.5°N in previous years was ~1.3 PW (53), and this transport was reduced by 0.4 PW, resulting in cooler waters to the north and warmer waters to the south. Observations showed that there was an abrupt and sustained cooling of the subtropical North Atlantic in the upper 2000 m between 2010 and 2012, primarily due to the reduction of the AMOC. From late 2009 over a 12-month period, the ocean heat content, between the latitudes of 26.5° and 41°N, reduced by $\sim 1.3 \times 10^{22}$ J (54, 56) and then increased again into 2011. Corresponding to this cooling of the subtropics was a warming of the tropics to the south of 26.5°N in 2010 (Fig. 3). This warming of the region of the Atlantic associated with hurricane genesis coincided with the strongest Atlantic hurricane season since 2005

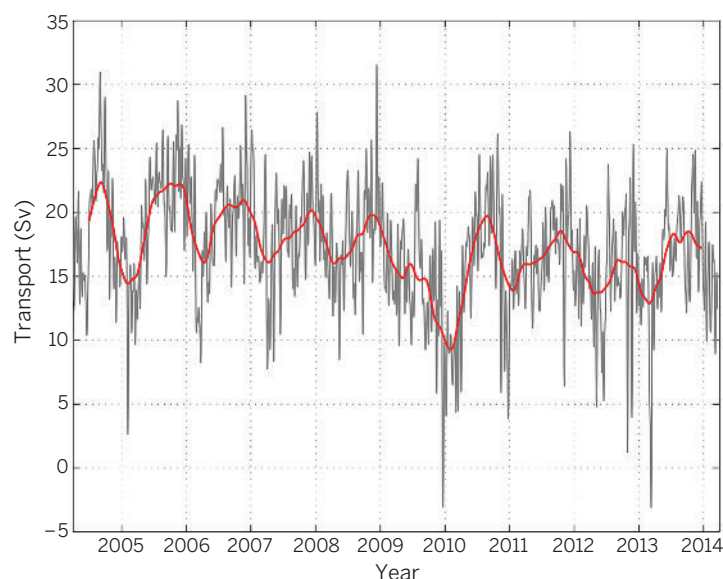


Fig. 2. The 10-year time series of the AMOC measured at 26.5°N. The gray line represents the 10-day filtered measurements, and the red line is the 180-day filtered time series. Clearly visible are the low AMOC event in 2009–2010 and the overall decrease in strength over the 10 years.

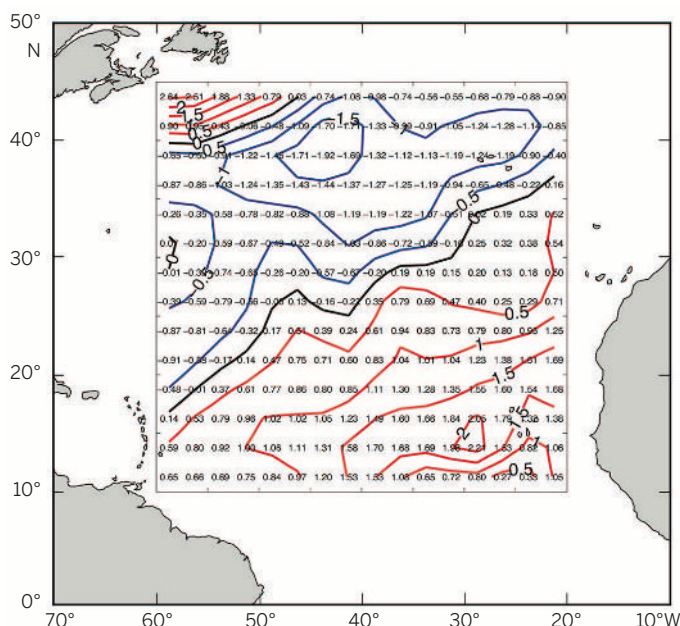


Fig. 3. North Atlantic temperature anomaly ($^{\circ}\text{C}$) at 50-m depth, averaged for May to July 2010 at the end of the 2009–2010 AMOC slowdown event (93). Temperature data are from Argo floats, and the anomaly is calculated relative to the Hydrobase seasonal climatology. Note the cooling (blue contours) of the upper ocean to the north and warming (red contours) to the south of 26.5°N , the latitude of the RAPID observations and of the maximum northward heat transport by the Atlantic.

(as measured by accumulated cyclone energy) (57). The links between changes in the AMOC, upper-ocean heat content, and atmospheric response represent an active area of research. For example, the ocean has been implicated in the re-emergence of sea surface temperature anomalies from the winter of 2009–2010 during the following early winter season of 2010–2011, which contributed to the persistence of the negative winter NAO and wintry conditions in northern Europe (58). Such behavior may lead to improved predictions of the NAO and winter conditions (59, 60).

The origin of and explanation for the 2009–2010 event remain uncertain. Various explanations have been proposed (61, 62) but so far have failed to explain the changes in LNADW (and the lack of change in the UNADW at depths between 1000 and 3000 m) (50). This, together with the fact that the event lies well outside the range of interannual variability predicted by coupled atmosphere-ocean climate models, poses a considerable research challenge.

Multiannual AMOC variability

Although the 26.5°N observing system has only just completed its first decade of observation, and it is premature to comment on decadal change, there is one further surprise that the observations have provided on the multiannual time scale over that decade. Analysis of the first 8-1/2 years of the observations has shown a decline in the AMOC over that period (April 2004 to October 2012; see also Fig. 2) (63). The estimated trend was a decline of ~ 0.5 Sv/year, which exceeds the decline predicted by IPCC-class cli-

mate models over the next 100 years, which is on the order of ~ 0.05 Sv/year (64, 65). This result is robust with respect to the inclusion or exclusion of the 2009–2010 AMOC event described above (63). Although changes in the Gulf Stream and Ekman contribute to the decline, the major components of the AMOC that are changing are increasing southward transport in the upper midocean, that is, a strengthening of the subtropical gyre recirculation and a corresponding decrease in the southward transport of LNADW (63). Earlier observations from the MOVE array at 16°N , which observes the deep western basin limb of the AMOC, found a decline in that flow of ~ 3 Sv over a decade (2000 to 2009) (34). In contrast, observations of the outflow from the Labrador Sea for 1997 to 2009 show no indication of a decline, but again these only measure one component of the AMOC (36). Another recent study, using a model and observations in the North Atlantic (although not direct measurements of AMOC) seems to confirm that the AMOC may be declining at the present time (66). Of course, it is possible that the decline may be part of a longer-term cycle such as the so-called Atlantic Multidecadal Oscillation (AMO) or Variability (AMV) (67), or simply decadal variability, rather than a response to climate change. This underlines the need for continuing observations of the AMOC in order to be able to distinguish between the different mechanisms that might be responsible for the observed changes (100).

Given the lack of direct observations over multiannual and longer time scales, researchers have generally resorted to the use of proxies to try to understand longer-term changes in

the AMOC. Until such proxies can be validated against direct measurement of the AMOC there will always be a question regarding their ability to capture the true behavior of the AMOC. Nevertheless, here we describe two recent attempts to study the AMOC using proxies (68). First, consider the study based on the so-called OVIDE hydrographic section from Portugal to Greenland (41). This makes use of six hydrographic sections from 1997 to 2010 and a proxy based on radar altimeter and Argo measurements from 1993 to 2010 to span the gaps between the sections and extend back in time to 1993. The analysis was carried out in density coordinates and shows an average AMOC strength of 18.1 Sv, with an overall decline of 2.5 Sv over 1993 to 2010. Second, consider another recent study (69) that uses the difference between the surface temperature in the North Atlantic subpolar gyre and the whole Northern Hemisphere as a proxy for the AMOC. Based on temperature reconstructions for the past 1000 years, the study concludes that there has been an exceptional 20th-century slowdown of the AMOC. Of course, how strong a conclusion this is depends crucially on the link between the proxy and the AMOC, over what time scales that link exists, and whether it is robust.

AMOC bistability?

On a more speculative note, one possibility for future AMOC surprises is the issue of the bistability of the AMOC noted earlier. This is related to the transport of freshwater in and out of the South Atlantic (70). Observations (71) suggest that the AMOC transports freshwater southward in the South Atlantic, implying that the AMOC could be bistable with on and off modes (72). Most climate models exhibit northward freshwater transport, seemingly at odds with the observations, implying that the AMOC is stable (73). Some recent climate model results show that their freshwater transports can match the southward freshwater transport in the observations, but in such climate models the AMOC does not shut down under greenhouse gas forcing (64). In point of fact, most climate models do not include a dynamically interactive Greenland ice sheet, so they are unlikely to correctly account for freshwater input into the Atlantic from Greenland melting (74, 75). In addition, the Arctic Ocean supplies freshwater to the North Atlantic, which would affect the stability of the AMOC (76). If the rate of freshwater input were to be greater than currently anticipated, that could lead to unexpected changes in the AMOC. Thus, there is a possibility that the ocean might respond in a way that most climate models cannot. This point has been made previously from a paleoclimate perspective (77, 78), because paleoclimatic evidence suggests that the AMOC can undergo rapid changes that are difficult to reproduce with climate models.

Recent impacts of AMOC variability

The possible impacts of AMOC variability have been discussed in previous reviews (5, 94, 98) so

will not be detailed here. However, much recent work has focused on the effect of changes in the AMOC on sea levels on the eastern seaboard of the United States, so we will briefly discuss that work. As noted earlier, the AMOC affects the sea level around the periphery of the North Atlantic and specifically along the U.S. east coast (13–15, 79), although this is a point of some controversy (15, 80–83). A reduction in the AMOC leads to a rise in sea level along the east coast of North America. Recently, the major reduction in the AMOC in 2009–2010, combined with a negative NAO event, has been shown to lead to an extreme sea level rise on the northeast coast of North America (84). Within a 2-year period the sea level was found to rise by 128 mm, a 1-in-850-year event. The authors state that the event caused persistent and widespread coastal flooding and beach erosion almost on a level with that due to a hurricane. This suggests that a longer-term downturn in the AMOC, which might be in progress, could have important impacts on the U.S. east coast.

Another possible effect identified recently is the role that the AMOC may have in the present so-called “hiatus” in global warming (85). Here, the AMOC is invoked to explain increased heat storage in the North Atlantic, thus reducing the rate of global temperature rise. However, other explanations for the hiatus involving the oceans have been suggested (86), so the role of the AMOC in the hiatus is uncertain.

Unanswered questions and future surprises?

Despite the observational efforts over the past decade, many questions remain unanswered. First, the AMOC is changing, but will these changes persist or will the AMOC “bounce back” to its earlier strength? Second, are the changes being observed at 26.5°N coherent latitudinally in the Atlantic? Third, was the 2009–2010 decrease in the AMOC unusual or not? Fourth, is the AMOC bistable? Could it “flip” from one state to another (87)? Finally, and perhaps most important, what are the effects of changes in the AMOC?

The existence of the 26.5°N AMOC observations is stimulating the development of further AMOC observing systems, both to the north in the North Atlantic Subpolar Gyre and to the south in the South Atlantic. This is an acknowledgment that the 26.5°N observations, although providing many novel insights into the AMOC, cannot by themselves fully characterize the circulation from south to north in the Atlantic. As a result, in 2014 the Overturning in the Subpolar North Atlantic Program (OSNAP) (88) deployed instruments, along a line from Canada to Greenland to Scotland, to observe the AMOC in the subpolar gyre, complementing the 26.5°N observations in the subtropical gyre. At the same time, a South Atlantic MOC observing system is being deployed gradually at 34.5°S. Known as the South Atlantic MOC Basin-wide Array (SAMBA) (89), this will observe the so-called Agulhas ring corridor (which is important for transfer of heat and salt from the Indian to the Atlantic Ocean)

and the eastern and western boundary currents. Another complementary measurement of the AMOC upper limb is that being made by combining data from Argo floats (which measure temperature and salinity down to 2000 m) and radar altimeter sea surface height data (39–41). This approach is limited to regions where the main upper ocean flows are in water depths of 2000 m or greater, thus allowing use of Argo.

Studies are beginning to be made to try to link observations of the AMOC at different latitudes in order to understand its meridional coherence and so obtain a holistic picture of the circulation (90–92). For example, these suggest coherence between measurement of the AMOC between 26.5°N and 41°N on near-annual time scales, with 41°N leading 26.5°N by approximately a quarter of an annual cycle.

Each additional year of observations made by the AMOC observing systems contributes to a better understanding of climate variability and the ocean’s role in that variability. Irrespective of whether the present decline in the AMOC continues, ends, or reverses, the observations will provide a stringent test of different climate models’ abilities and whether their projections will prove valid. Likewise, another event similar to that which occurred in 2009–2010, leading to ocean heat content changes with possible links to NAO winter weather, tropical hurricanes, or sea level rise could stimulate further advances in seasonal forecasting.

The AMOC observations over the past decade have provided both surprises and insights into the Atlantic circulation, but many questions remain unanswered. Perhaps it is not too much to expect that, together with the new observations being made at various latitudes, there are likely to be further “inevitable surprises.”

REFERENCES AND NOTES

1. National Research Council Committee on Abrupt Climate Change, *Abrupt Climate Change: Inevitable Surprises* (National Academy Press, Washington DC, 2002).
2. IPCC, *Climate Change 2001: The Scientific Basis, Contribution of Working Group I to the Third Assessment Report of the Intergovernmental Panel on Climate Change* (Cambridge Univ. Press, Cambridge, 2001).
3. One of the authors (M.A.S.) is the science coordinator of the RAPID program in the U.K., more details of which can be found at www.rapid.ac.uk.
4. The MOC has at times been referred to as the THC—that is, that part of the ocean circulation determined by changes in temperature and salinity; the two are not synonymous. The MOC is what can be determined in practice, as a zonal integral of the meridional velocity, whereas the THC is not directly measurable but is related to one of the mechanisms involved in the overturning (5).
5. T. Kuhlbrodt *et al.*, On the driving processes of the Atlantic meridional overturning circulation. *Rev. Geophys.* **45**, RG2001 (2007). doi: [10.1029/2004RG000166](https://doi.org/10.1029/2004RG000166)
6. S. A. Cunningham *et al.*, Temporal variability of the Atlantic meridional overturning circulation at 26.5°N. *Science* **317**, 935–938 (2007). doi: [10.1126/science.1141304](https://doi.org/10.1126/science.1141304); pmid: [17702940](https://pubmed.ncbi.nlm.nih.gov/17702940/)
7. T. Kanzow *et al.*, Observed flow compensation associated with the MOC at 26.5°N in the Atlantic. *Science* **317**, 938–941 (2007). doi: [10.1126/science.1141293](https://doi.org/10.1126/science.1141293); pmid: [17702941](https://pubmed.ncbi.nlm.nih.gov/17702941/)
8. M. M. Hall, H. L. Bryden, Direct estimates and mechanisms of ocean heat transport. *Deep-Sea Res.* **29**, 339–359 (1982). doi: [10.1016/0198-0149\(82\)90099-1](https://doi.org/10.1016/0198-0149(82)90099-1)
9. K. E. Trenberth, J. M. Caron, Estimates of meridional atmosphere and ocean heat transports. *J. Clim.* **14**, 3433–3443 (2001). doi: [10.1175/1520-0442\(2001\)014](https://doi.org/10.1175/1520-0442(2001)014)

10. R. T. Sutton, D. L. R. Hodson, Atlantic Ocean forcing of North American and European summer climate. *Science* **309**, 115–118 (2005). doi: [10.1126/science.1109496](https://doi.org/10.1126/science.1109496); pmid: [15994552](https://pubmed.ncbi.nlm.nih.gov/15994552/)
11. D. J. Brayshaw, T. Woollings, M. Vellinga, Tropical and extratropical responses of the North Atlantic atmospheric circulation to a sustained weakening of the MOC. *J. Clim.* **22**, 3146–3155 (2009). doi: [10.1175/2008JCLI2594.1](https://doi.org/10.1175/2008JCLI2594.1)
12. T. Woollings, J. M. Gregory, J. G. Pinto, M. Meyers, D. J. Brayshaw, Response of the North Atlantic storm track to climate change shaped by ocean-atmosphere coupling. *Nat. Geosci.* **5**, 313–317 (2012). doi: [10.1038/ngeo1438](https://doi.org/10.1038/ngeo1438)
13. A. Levermann, A. Griesel, M. Hofmann, M. Montoya, S. Rahmstorf, Dynamic sea level changes following changes in the thermohaline circulation. *Clim. Dyn.* **24**, 347–354 (2005). doi: [10.1007/s00382-004-0505-y](https://doi.org/10.1007/s00382-004-0505-y)
14. J. Yin, M. E. Schlesinger, R. J. Stouffer, Model projections of rapid sea level rise on the northeast coast of the United States. *Nat. Geosci.* **2**, 262–266 (2009). doi: [10.1038/ngeo462](https://doi.org/10.1038/ngeo462)
15. T. Ezer, Sea level rise, spatially uneven and temporally unsteady: Why the U.S. east coast, the global tide gauge record, and the global altimeter data show different trends. *Geophys. Res. Lett.* **40**, 5439–5444 (2013). doi: [10.1002/2013GL057952](https://doi.org/10.1002/2013GL057952)
16. For more on impacts, see Srokosz *et al.* (94).
17. For recent results from a high-resolution model, see Jackson *et al.* (95).
18. W. S. Broecker, The great ocean conveyor. *Oceanography* **4**, 79–89 (1991). doi: [10.5670/oceanog.1991.07](https://doi.org/10.5670/oceanog.1991.07)
19. S. Rahmstorf, Ocean circulation and climate during the past 120,000 years. *Nature* **419**, 207–214 (2002). doi: [10.1038/nature01090](https://doi.org/10.1038/nature01090); pmid: [12226675](https://pubmed.ncbi.nlm.nih.gov/12226675/)
20. P. U. Clark, N. G. Pisias, T. F. Stocker, A. J. Weaver, The role of the thermohaline circulation in abrupt climate change. *Nature* **415**, 863–869 (2002). doi: [10.1038/415863a](https://doi.org/10.1038/415863a); pmid: [11859359](https://pubmed.ncbi.nlm.nih.gov/11859359/)
21. H. M. Stommel, Thermohaline convection with two stable regimes of flow. *Tellus* **13**, 224–230 (1961). doi: [10.1111/j.2153-3490.1961.tb00079.x](https://doi.org/10.1111/j.2153-3490.1961.tb00079.x)
22. R. B. Alley, Wally was right: Predictive ability of the North Atlantic “Conveyor Belt” hypothesis for abrupt climate change. *Annu. Rev. Earth Planet. Sci.* **35**, 241–272 (2007). doi: [10.1146/annurev.earth.35.081006.131524](https://doi.org/10.1146/annurev.earth.35.081006.131524)
23. M. Vellinga, R. Wood, Global climatic impacts of a collapse of the Atlantic Thermohaline Circulation. *Clim. Change* **54**, 251–267 (2002). doi: [10.1023/A:1016168827653](https://doi.org/10.1023/A:1016168827653)
24. E. Hawkins *et al.*, Bistability of the Atlantic overturning circulation in a global climate model and links to ocean freshwater transport. *Geophys. Res. Lett.* **38**, L10605 (2011). doi: [10.1029/2011GL047208](https://doi.org/10.1029/2011GL047208)
25. S. Rahmstorf *et al.*, Thermohaline circulation hysteresis: A model intercomparison. *Geophys. Res. Lett.* **32**, L23605 (2005). doi: [10.1029/2005GL023655](https://doi.org/10.1029/2005GL023655)
26. U.K. and U.S. funders confirmed in 2013 that funding for the observations would be extended until 2020. At each stage when continuation of funding has been considered, the RAPID program has been reviewed by an independent international committee of scientists. Reviews have taken place in 2007 and 2012, and the next review will be in 2018.
27. M. O. Baringer, J. C. Larsen, Sixteen years of Florida Current transports at 27°N. *Geophys. Res. Lett.* **28**, 3179–3182 (2001). doi: [10.1029/2001GL013246](https://doi.org/10.1029/2001GL013246)
28. D. Rayner *et al.*, Monitoring the Atlantic Meridional Overturning Circulation. *Deep Sea Res. Part II Top. Stud. Oceanogr.* **58**, 1744–1753 (2011). doi: [10.1016/j.jsr.2010.10.056](https://doi.org/10.1016/j.jsr.2010.10.056)
29. G. D. McCarthy *et al.*, Measuring the Atlantic Meridional Overturning Circulation at 25°N. *Prog. Oceanogr.* **130**, 91–111 (2015). doi: [10.1016/j.pocan.2014.10.006](https://doi.org/10.1016/j.pocan.2014.10.006)
30. One of the most remarkable results in (7) is their figure 2, which shows that the different flow components compensate, to within the measurement accuracy, thus confirming the validity of the observational approach.
31. T. Kanzow *et al.*, Basin-wide integrated volume transports in an eddy-filled ocean. *J. Phys. Oceanogr.* **39**, 3091–3110 (2009). doi: [10.1175/2009JP04185.1](https://doi.org/10.1175/2009JP04185.1)
32. H. L. Bryden, A. Mujahid, S. A. Cunningham, T. Kanzow, Adjustment of the basin-scale circulation at 26°N to variations in Gulf Stream, deep western boundary current and Ekman transports as observed by the RAPID array. *Ocean Sci.* **5**, 421–433 (2009). doi: [10.5194/os-5-421-2009](https://doi.org/10.5194/os-5-421-2009)

33. Kanzow *et al.* (31) and Bryden *et al.* (32) are in part responding to Wunsch (96), who had concluded that detection of AMOC changes by regional measurements "is probably a mirage."
34. U. Send, M. Lankhorst, T. Kanzow, Observation of decadal change in the Atlantic Meridional Overturning Circulation using 10 years of continuous transport data. *Geophys. Res. Lett.* **38**, L24606 (2011). doi: [10.1029/2011GL049801](#)
35. J. M. Toole, R. G. Curry, T. M. Joyce, M. McCartney, B. Peña-Molino, Transport of the North Atlantic Deep Western Boundary Current about 39°N, 70°W: 2004–2008. *Deep Sea Res. Part II Top. Stud. Oceanogr.* **58**, 1768–1780 (2011). doi: [10.1016/j.dsr2.2010.10.058](#)
36. J. Fischer, M. Visbeck, R. Zantopp, N. Nunes, Interannual to decadal variability of the outflow from the Labrador Sea. *Geophys. Res. Lett.* **37**, L24610 (2010). doi: [10.1029/2010GL045321](#)
37. C. S. Meinen *et al.*, Temporal variability of the meridional overturning circulation at 34.5°S: Results from two pilot boundary arrays in the South Atlantic. *J. Geophys. Res.* **118**, 6461–6478 (2013). doi: [10.1002/2013JC009228](#)
38. Garzoli *et al.* (97) use expendable bathythermograph data for 2002–2011, so they do not directly measure the AMOC.
39. J. K. Willis, Can in situ floats and satellite altimeters detect long-term changes in Atlantic Ocean overturning? *Geophys. Res. Lett.* **37**, L06602 (2010). doi: [10.1029/2010GL042372](#)
40. W. R. Hobbs, J. K. Willis, Midlatitude North Atlantic heat transport: A time series based on satellite and drifter data. *J. Geophys. Res.* **117** (C1), C01008 (2012). doi: [10.1029/2011JC007039](#)
41. H. Mercier *et al.*, Variability of the meridional overturning circulation at the Greenland-Portugal OVIDE section from 1993 to 2010. *Prog. Oceanogr.* **132**, 250–261 (2015). doi: [10.1016/j.pcean.2013.11.001](#)
42. W.-J. von Appen *et al.*, The East Greenland Split Jet as an important component of the Atlantic Meridional Overturning Circulation. *Deep Sea Res. Part I Oceanogr. Res. Pap.* **92**, 75–84 (2014). doi: [10.1016/j.dsr.2014.06.002](#)
43. For reviews of other aspects of the AMOC see (5, 94, 98).
44. See, for example, figures 3 and 5 of (99).
45. $S_v = \text{sverdrup} = 10^6 \text{ m}^3 \text{ s}^{-1}$, the standard measurement unit for ocean circulation.
46. H. L. Bryden, H. R. Longworth, S. A. Cunningham, Slowing of the Atlantic Meridional Overturning Circulation at 25°N. *Nature* **438**, 655–657 (2005). doi: [10.1038/nature04385](#); pmid: [16319889](#)
47. T. Kanzow *et al.*, Seasonal variability of the Atlantic Meridional Overturning Circulation at 26.5°N. *J. Clim.* **23**, 5678–5698 (2010). doi: [10.1175/2010JCLI3891](#)
48. C. P. Atkinson, H. L. Bryden, J. J.-M. Hirschi, T. Kanzow, On the seasonal cycles and variability of the Florida Straits, Ekman and Sverdrup transports at 26°N in the Atlantic Ocean. *Ocean Sci.* **6**, 837–859 (2010). doi: [10.5194/os-6-837-2010](#)
49. From (47), revising the estimates in (46).
50. G. McCarthy *et al.*, Observed interannual variability of the Atlantic meridional overturning circulation at 26.5°N. *Geophys. Res. Lett.* **39**, L19609 (2012). doi: [10.1029/2012GL052933](#)
51. See figure 4 in (94).
52. See figure 1(c) in (100).
53. W. E. Johns *et al.*, Continuous, array-based estimates of Atlantic ocean heat transport at 26.5°N. *J. Clim.* **24**, 2429–2449 (2011). doi: [10.1175/2010JCLI3997.1](#)
54. S. A. Cunningham *et al.*, Atlantic Meridional Overturning Circulation slowdown cooled the subtropical ocean. *Geophys. Res. Lett.* **40**, 6202–6207 (2013). doi: [10.1002/2013GL058464](#)
55. H. L. Bryden, B. A. King, G. D. McCarthy, E. L. McDonagh, Impact of a 30% reduction in Atlantic meridional overturning during 2009–2010. *Ocean Sci.* **10**, 683–691 (2014). doi: [10.5194/os-10-683-2014](#)
56. The estimate in (55) is slightly higher at $1.45 \times 10^{22} \text{ J}$ for the somewhat different area of 10° to 45°N, 60° to 20°W.
57. NOAA, 2014 The Atlantic hurricane database reanalysis project, online at [www.aoml.noaa.gov/hrd/hurdat/comparison_table.html](#) (accessed 18-11-14).
58. S. L. Taws, R. Marsh, N. C. Wells, J. Hirschi, Re-emerging ocean temperature anomalies in late-2010 associated with a repeat negative NAO. *Geophys. Res. Lett.* **38**, L20601 (2011). doi: [10.1029/2011GL048978](#)
59. A. Maidens *et al.*, The influence of surface forcings on the prediction of the North Atlantic Oscillation regime of winter 2010/11. *Mon. Weather Rev.* **141**, 3801–3813 (2013). doi: [10.1175/MWR-D-13-00033.1](#)
60. A. A. Scaife *et al.*, Skillful long-range prediction of European and North American winters. *Geophys. Res. Lett.* **41**, 2514–2519 (2014). doi: [10.1002/2014GL059637](#)
61. C. Roberts *et al.*, Atmosphere drives recent interannual variability of the Atlantic meridional overturning circulation at 26.5°N. *Geophys. Res. Lett.* **40**, 5164–5170 (2013). doi: [10.1002/grl.50930](#)
62. A. Duchez *et al.*, A new index for the Atlantic Meridional Overturning Circulation at 26°N. *J. Clim.* **27**, 6439–6455 (2014). doi: [10.1175/JCLI-D-13-00052.1](#)
63. D. Smeed *et al.*, Observed decline of the Atlantic Meridional Overturning Circulation 2004–2012. *Ocean Sci.* **10**, 29–38 (2014). doi: [10.5194/os-10-29-2014](#)
64. A. J. Weaver *et al.*, Stability of the Atlantic Meridional Overturning Circulation: A model intercomparison. *Geophys. Res. Lett.* **39**, L20709 (2012). doi: [10.1029/2012GL053763](#)
65. IPCC, *Climate Change 2013: The Physical Science Basis, Working Group I contribution to the Fifth Assessment Report of the IPCC* (Cambridge Univ. Press, Cambridge, 2013), section 12.4.7.2.
66. J. Robson, D. Hodson, E. Hawkins, R. Sutton, Atlantic overturning in decline? *Nat. Geosci.* **7**, 2–3 (2014). doi: [10.1038/ngeo2050](#)
67. See, for example, Ba *et al.* (101).
68. A further proxy has been developed recently by (62) using models and is presently in the process of being applied to observations.
69. S. Rahmstorf *et al.*, Exceptional twentieth-century slowdown in Atlantic Ocean overturning circulation. *Nat. Clim. Change* **5**, 475–480 (2015). doi: [10.1038/nclimate2554](#)
70. P. de Vries, S. L. Weber, The Atlantic freshwater budget as a diagnostic for the existence of a stable shut down of the meridional overturning circulation. *Geophys. Res. Lett.* **32**, L09606 (2005). doi: [10.1029/2004GL021450](#)
71. H. L. Bryden, B. A. King, G. D. McCarthy, South Atlantic Overturning Circulation at 24°S. *J. Mar. Res.* **69**, 38–55 (2011). doi: [10.1357/00224011798147633](#)
72. On bistability, see (70); from a paleo perspective, see (22).
73. S. S. Drijfhout, S. L. Weber, E. van der Waluw, The stability of the MOC as diagnosed from model projections for pre-industrial, present and future climates. *Clim. Dyn.* **37**, 1575–1586 (2011). doi: [10.1007/s00382-010-0930-z](#)
74. See Bamber *et al.* (102). Weaver *et al.* (64) suggest that Greenland meltwater will have little effect on the AMOC even though it is not accounted for dynamically in the models that they analyze.
75. S. V. Nghiem *et al.*, The extreme melt across the Greenland ice sheet in 2012. *Geophys. Res. Lett.* **39**, L20502 (2012). doi: [10.1029/2012GL053611](#)
76. For example, on the effects of future increases in Arctic precipitation (freshwater addition) on the AMOC, see under Methods in Bintanja *et al.* (103).
77. R. B. Alley, Palaeoclimatic insights into future climate challenges. *Philos. Trans. A Math. Phys. Eng. Sci.* **361**, 1831–1849 (2003). doi: [10.1098/rsta.2003.1236](#); pmid: [14558897](#)
78. P. Valdes, Built for stability. *Nat. Geosci.* **4**, 414–416 (2011). doi: [10.1038/ngeo1200](#)
79. Most recently, on the link between sea level and AMOC, see McCarthy *et al.* (104).
80. R. E. Kopp, Does the mid-Atlantic United States sea level acceleration hot spot reflect ocean dynamic variability? *Geophys. Res. Lett.* **40**, 3981–3985 (2013). doi: [10.1002/grl.50781](#)
81. J. Yin, P. B. Goddard, Oceanic control of sea level rise patterns along the East Coast of the United States. *Geophys. Res. Lett.* **40**, 5514–5520 (2013). doi: [10.1002/2013GL057992](#)
82. T. Rossby, C. N. Flagg, K. Donohue, A. Sanchez-Franks, J. Lillibridge, On the long-term stability of Gulf Stream transport based on 20 years of direct measurements. *Geophys. Res. Lett.* **41**, 114–120 (2014). doi: [10.1002/2013GL058636](#)
83. T. Ezer, Detecting changes in the transport of the Gulf Stream and the Atlantic overturning circulation from coastal sea level data: The extreme decline in 2009–2010 and estimated variations for 1935–2012. *Global Planet. Change* **129**, 23–36 (2015). doi: [10.1016/j.gloplacha.2015.03.002](#)
84. P. B. Goddard, J. Yin, S. M. Griffies, S. Zhang, An extreme event of sea-level rise along the Northeast Coast of North America in 2009–2010. *Nat. Commun.* **6**, 6346 (2015). doi: [10.1038/ncomms7346](#); pmid: [25710720](#)
85. X. Chen, K.-K. Tung, Varying planetary heat sink led to global-warming slowdown and acceleration. *Science* **345**, 897–903 (2014). doi: [10.1126/science.1254937](#); pmid: [25146282](#)
86. K. E. Trenberth, J. T. Fasullo, G. Branstator, A. S. Phillips, Seasonal aspects of the recent pause in surface warming. *Nature Clim. Change* **4**, 911–916 (2014). doi: [10.1038/nclimate2341](#)
87. Note that a "flip" would take a few years, not a few days as in the film *The Day After Tomorrow*.
88. See [www.o-snap.org](#) and [www.ukosnap.org](#), with U.S. and U.K. contributions funded by the National Science Foundation (NSF) and the Natural Environment Research Council (NERC), as for RAPID. OSNAP has initial funding for 4 years of observations.
89. I. J. Ansorge *et al.*, Basin-wide oceanographic array bridges South Atlantic. *Eos* **95**, 53–54 (2014). doi: [10.1002/2014EO060001](#)
90. S. Elipot, C. Hughes, S. C. Olhede, J. M. Toole, Coherence of western boundary pressure at the RAPID WAVE array: Boundary wave adjustments or deep western boundary current advection? *J. Phys. Oceanogr.* **43**, 744–765 (2013). doi: [10.1175/JPO-D-12-067.1](#)
91. S. Elipot, E. Frajka-Williams, C. W. Hughes, J. Willis, The observed North Atlantic Meridional Overturning Circulation: Its meridional coherence and ocean bottom pressure. *J. Phys. Oceanogr.* **44**, 517–537 (2014). doi: [10.1175/JPO-D-13-026.1](#)
92. C. Mielke, E. Frajka-Williams, J. Baehr, Observed and simulated variability of the AMOC at 26°N and 41°N. *Geophys. Res. Lett.* **40**, 1159–1164 (2013). doi: [10.1002/grl.50233](#)
93. Reproduced after (55), where further details may be found.
94. M. Srokosz *et al.*, Past, present and future changes in the Atlantic Meridional Overturning Circulation. *Bull. Am. Meteorol. Soc.* **93**, 1663–1676 (2012). doi: [10.1175/BAMS-D-11-0015.1](#)
95. C. Jackson *et al.*, Global and European climate impacts of a slowdown of the AMOC in a high resolution GCM. *Clim. Dyn.* (2015). doi: [10.1007/s00382-015-2540-2](#)
96. C. Wunsch, Mass and volume transport variability in an eddy-filled ocean. *Nat. Geosci.* **1**, 165–168 (2008). doi: [10.1038/ngeo126](#)
97. S. L. Garzoli, M. O. Baringer, S. Dong, R. C. Perez, Q. Yao, South Atlantic meridional fluxes. *Deep Sea Res. Part I Oceanogr. Res. Pap.* **71**, 21–32 (2013). doi: [10.1016/j.dsr.2012.09.003](#)
98. M. S. Lozier, Overturning in the North Atlantic. *Annu. Rev. Mar. Sci.* **4**, 291–315 (2012). doi: [10.1146/annurev-marine-120710-100740](#); pmid: [22457977](#)
99. G. Danabasoglu *et al.*, North Atlantic simulations in Coordinated Ocean-ice Reference Experiments phase II (CORE-II). Part I: Mean states. *Ocean Model.* **73**, 76–107 (2014). doi: [10.1016/j.ocemod.2013.10.005](#)
100. C. D. Roberts, L. Jackson, D. McNeill, Is the 2004–2012 reduction of the Atlantic meridional overturning circulation significant? *Geophys. Res. Lett.* **41**, 3204–3210 (2014). doi: [10.1002/2014GL059473](#)
101. J. Ba *et al.*, A multi-model comparison of Atlantic multidecadal variability. *Clim. Dyn.* **43**, 2333–2348 (2014). doi: [10.1007/s00382-014-2056-1](#)
102. J. Bamber, M. van den Broeke, J. Ettema, J. Lenaerts, E. Rignot, Recent large increases in freshwater fluxes from Greenland into the North Atlantic. *Geophys. Res. Lett.* **39**, L19501 (2012). doi: [10.1029/2012GL052552](#)
103. R. Bintanja, F. M. Seltin, Future increases in Arctic precipitation linked to local evaporation and sea-ice retreat. *Nature* **509**, 479–482 (2014). doi: [10.1038/nature13259](#); pmid: [24805239](#)
104. G. D. McCarthy, I. D. Haigh, J. J. Hirschi, J. P. Grist, D. A. Smeed, Ocean impact on decadal Atlantic climate variability revealed by sea-level observations. *Nature* **521**, 508–510 (2015). doi: [10.1038/nature14491](#); pmid: [26017453](#)

ACKNOWLEDGMENTS

This review would not have been possible without the outstanding work of those who have been involved in making the AMOC observations at 26.5°N for the past decade, together with continuing funding from NERC, NSF, and the National Oceanic and Atmospheric Administration (NOAA). We thank D. Smeed for the time series in Fig. 2. We pay tribute to all the scientists, technicians, and crew involved in the many U.K. and U.S. cruises that have taken place to deploy and recover the observing array and in the subsequent analysis of the data acquired. We are grateful to two anonymous reviewers whose comments helped to improve this review.

10.1126/science.1255575

RESEARCH ARTICLE SUMMARY

VACCINES

A mucosal vaccine against *Chlamydia trachomatis* generates two waves of protective memory T cells

Georg Stary,^{†*} Andrew Olive,[†] Aleksandar F. Radovic-Moreno,[†] David Gondek, David Alvarez, Pamela A. Basto, Mario Perro, Vladimir D. Vrbanc, Andrew M. Tager, Jinjun Shi, Jeremy A. Yethon, Omid C. Farokhzad, Robert Langer, Michael N. Starnbach, Ulrich H. von Andrian*

INTRODUCTION: Administering vaccines through nonmucosal routes often leads to poor protection against mucosal pathogens, presumably because such vaccines do not generate memory lymphocytes that migrate to mucosal surfaces. Although mucosal vaccination induces mucosa-tropic memory lymphocytes, few mucosal vaccines are used clinically; live vaccine vectors pose safety risks, whereas killed pathogens or molecular antigens are usually weak immunogens when applied to intact mucosa. Adjuvants can boost immunogenicity; however, most conventional mucosal adjuvants have unfavorable safety profiles.

Moreover, the immune mechanisms of protection against many mucosal infections are poorly understood.

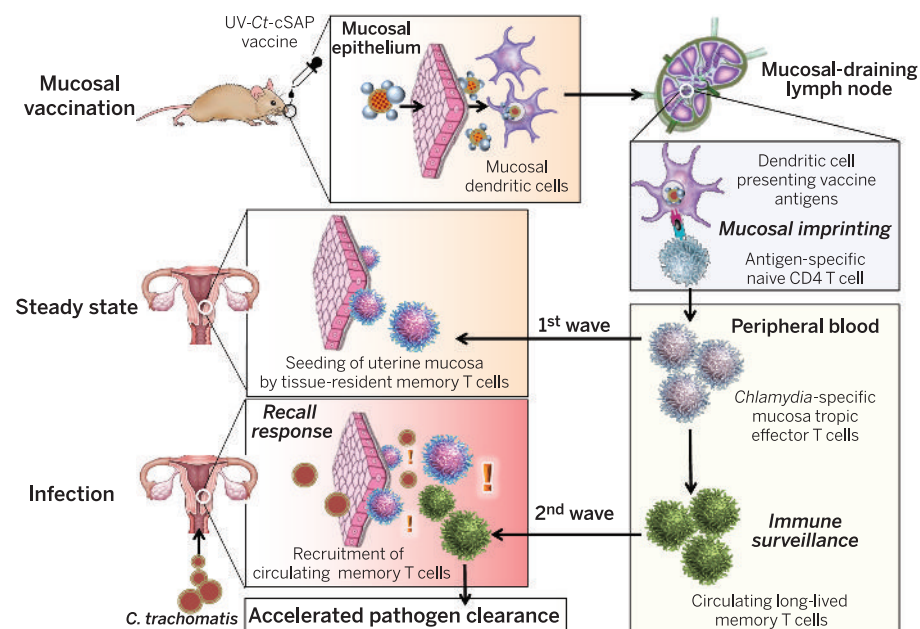
RATIONALE: One case in point is *Chlamydia trachomatis* (Ct), a sexually transmitted intracellular bacterium that infects >100 million people annually. Mucosal Ct infections can cause female infertility and ectopic pregnancies. Ct is also the leading cause of preventable blindness in developing countries and induces pneumonia in infants. No approved vaccines exist to date. Here, we describe a Ct vaccine composed of ultraviolet light-inactivated

Ct (UV-Ct) conjugated to charge-switching synthetic adjuvant nanoparticles (cSAPs). After immunizing mice with live Ct, UV-Ct, or UV-Ct-cSAP conjugates, we characterized mucosal immune responses to uterine Ct rechallenge and dissected the underlying cellular mechanisms.

RESULTS: In previously uninfected mice, Ct infection induced protective immunity that depended on CD4 T cells producing the cytokine interferon- γ , whereas uterine exposure to UV-Ct generated tolerogenic Ct-specific regulatory T cells, resulting in exacerbated bacterial burden upon Ct rechallenge. In contrast,

mucosal immunization with UV-Ct-cSAP elicited long-lived protection. This differential effect of UV-Ct-cSAP versus UV-Ct was because the former was presented by immunogenic CD11b⁺CD103⁻ dendritic cells (DCs), whereas the latter was presented by tolerogenic CD11b⁺CD103⁺ DCs. Intrauterine or intranasal vaccination, but not subcutaneous vaccination, induced genital protection in both conventional and humanized mice. Regardless of vaccination route, UV-Ct-cSAP always evoked a robust systemic memory T cell response. However, only mucosal vaccination induced a wave of effector T cells that seeded the uterine mucosa during the first week after vaccination and established resident memory T cells (T_{RM} cells). Without T_{RM} cells, mice were suboptimally protected, even when circulating memory cells were abundant. Optimal Ct clearance required both early uterine seeding by T_{RM} cells and infection-induced recruitment of a second wave of circulating memory cells.

CONCLUSIONS: Mucosal exposure to both live Ct and inactivated UV-Ct induces antigen-specific CD4 T cell responses. While immunogenic DCs present the former to promote immunity, the latter is instead targeted to tolerogenic DCs that exacerbate host susceptibility to Ct infection. By combining UV-Ct with cSAP nanocarriers, we have redirected noninfectious UV-Ct to immunogenic DCs and achieved long-lived protection. This protective vaccine effect depended on the synergistic action of two memory T cell subsets with distinct differentiation kinetics and migratory properties. The cSAP technology offers a platform for efficient mucosal immunization that may also be applicable to other mucosal pathogens. ■



Protection against *C. trachomatis* infection after mucosal UV-Ct-cSAP vaccination. Upon mucosal vaccination, dendritic cells carry UV-Ct-cSAP to lymph nodes and stimulate CD4 T cells. Effector T cells are imprinted to traffic to uterine mucosa (first wave) and establish tissue-resident memory cells (T_{RM} cells). Vaccination also generates circulating memory T cells. Upon genital Ct infection, local reactivation of uterine T_{RM} cells triggers the recruitment of the circulating memory subset (second wave). Optimal pathogen clearance requires both waves of memory cells.

The list of affiliations is available in the full article online.

*Corresponding author. E-mail: uva@hms.harvard.edu (U.H.v.A.); georg_stary@hms.harvard.edu (G.S.) †These authors contributed equally to this work.

Cite this paper as G. Stary et al., *Science* 348, aaa8205 (2015). DOI: 10.1126/science.aaa8205

RESEARCH ARTICLE

VACCINES

A mucosal vaccine against *Chlamydia trachomatis* generates two waves of protective memory T cells

Georg Stary,^{1†*} Andrew Olive,^{1†} Aleksandar F. Radovic-Moreno,^{2,3†} David Gondek,¹ David Alvarez,¹ Pamela A. Basto,^{2,3} Mario Perro,¹ Vladimir D. Vrbancac,⁴ Andrew M. Tager,⁴ Jinjun Shi,⁶ Jeremy A. Yethon,⁵ Omid C. Farokhzad,^{6,7} Robert Langer,^{2,3} Michael N. Starnbach,¹ Ulrich H. von Andrian^{1,8*}

Genital *Chlamydia trachomatis* (Ct) infection induces protective immunity that depends on interferon- γ -producing CD4 T cells. By contrast, we report that mucosal exposure to ultraviolet light (UV)-inactivated Ct (UV-Ct) generated regulatory T cells that exacerbated subsequent Ct infection. We show that mucosal immunization with UV-Ct complexed with charge-switching synthetic adjuvant particles (cSAPs) elicited long-lived protection in conventional and humanized mice. UV-Ct-cSAP targeted immunogenic uterine CD11b⁺CD103⁻ dendritic cells (DCs), whereas UV-Ct accumulated in tolerogenic CD11b⁻CD103⁺ DCs. Regardless of vaccination route, UV-Ct-cSAP induced systemic memory T cells, but only mucosal vaccination induced effector T cells that rapidly seeded uterine mucosa with resident memory T cells (T_{RM} cells). Optimal Ct clearance required both T_{RM} seeding and subsequent infection-induced recruitment of circulating memory T cells. Thus, UV-Ct-cSAP vaccination generated two synergistic memory T cell subsets with distinct migratory properties.

Although subcutaneous (s.c.) or intramuscular (i.m.) vaccination can generate efficient systemic and cutaneous immunity against many pathogens, vaccination by these nonmucosal routes often induces little or no protection at mucosal surfaces (1). A reason for this shortcoming is thought to be the differential imprinting of activated effector/memory lymphocytes in regional lymphoid tissues. These organs are populated by specialized antigen (Ag)-presenting dendritic cells (DCs) that induce the expression of tissue-specific homing receptors in T and B cells (2–4). Acquisition of tissue tropism enables the preferential migration of Ag-experienced lymphocytes to regions of the body that are associated with the secondary lymphoid organs where Ag was first encountered (2, 3, 5–11). Thus, whereas intracutaneous, s.c., and i.m. vac-

cines act in peripheral lymph nodes (LNs) to induce primarily skin-homing memory cells, mucosal vaccine exposure targets Ags into mucosa-associated lymphoid tissue (MALT) and focuses the ensuing memory response toward mucosal surfaces (6, 12–16). However, only a handful of mucosal vaccines are currently available for use in humans, and most of these vaccines consist of replicating microorganisms, which may themselves cause infections in vulnerable individuals (17). Such safety concerns could be avoided with nonreplicating vaccines, such as killed pathogens or inanimate Ags; however, mucosal exposure to noninfectious Ags is typically insufficient to elicit a protective immune response unless the Ags are combined with potent adjuvants that are often too toxic for use in humans (18, 19).

These immunobiological challenges present formidable obstacles to the development of effective vaccines for many mucosal pathogens. One prominent example among these “intractable” pathogens is *Chlamydia trachomatis* (Ct), a Gram-negative obligatory intracellular bacterium that infects mucosal epithelial cells. Ct is the most common sexually transmitted bacterial pathogen and is the leading cause of female infertility, ectopic pregnancy (20–22), and infectious blindness worldwide (23). Clinical trials in the 1960s with inactivated elementary bodies (EBs), the infectious form of Ct (24), achieved partial early protection, but at later stages some vaccinated individuals experienced more severe symptoms upon ocular Ct exposure than did placebo re-

cipients (24–30). The underlying mechanism for this apparently enhanced risk of Ct-induced pathology after exposure to killed Ct is not understood. To this day, this persistent uncertainty has stymied further clinical development of Ct vaccines.

Effect of uterine mucosal exposure to live and killed Ct

Here, we used mice to explore the immunological consequences of mucosal exposure to live or killed Ct by performing intrauterine (i.u.) inoculations of either infectious Ct (serovar L2 unless stated otherwise) or ultraviolet light-inactivated Ct (UV-Ct). The animals were rechallenged with live Ct 4 weeks later, and uterine bacterial burden was assessed after 6 days (Fig. 1A). Consistent with earlier observations in this model (31), mice that had been previously infected with Ct acquired protective immunity, as evidenced by a factor of ~50 reduction in bacterial burden upon reinfection relative to naïve controls (Fig. 1B). In contrast, the bacterial burden in infected mice that had been previously exposed to UV-Ct was greater than in the nonimmunized group by a factor of 5 to 10. This exacerbated susceptibility to infection in the UV-Ct group was intriguingly reminiscent of the reported outcome of human vaccine trials five decades ago (25–29) and suggested that inactivated Ct was not merely “invisible” to the host immune system but somehow promoted tolerance.

Having thus determined that mucosal exposure to UV-Ct induces a pronounced tolerogenic immune response in mice, we asked whether mixing UV-Ct with an adjuvant could convert UV-Ct into an immunogen that might elicit protective immunity. However, i.u. injection of UV-Ct mixed with alum or with two different TLR agonists, imiquimod (TLR7 ligand) or CpG (TLR9 ligand), not only failed to confer protection but also rendered mice more susceptible to reinfection, similar to UV-Ct alone (Fig. 1C). Interestingly, when mice were instead immunized by s.c. injection, UV-Ct neither provoked a tolerogenic response nor conferred measurable protection, even when combined with adjuvants. Thus, the route of immunization can determine not only the tissue tropism of effector/memory cells but apparently also the tolerogenicity of a given Ag.

Conjugation of UV-inactivated Ct to charge-switching synthetic adjuvant particles

In light of these observations, we speculated that the lack of immunogenicity of i.u. exposure to crude mixtures of adjuvants with UV-Ct may have been due to differential permeability of the intact mucosal barrier to UV-Ct and/or free adjuvants. Thus, we reasoned that physical linkage of an adjuvant to UV-Ct may be necessary to allow both vaccine components to cross the epithelial barrier and be acquired by the same submucosal immunogenic DCs. To test this idea, we engineered modified charge-switching synthetic particles (cSPs), biodegradable nanocarriers that

¹Division of Immunology, Department of Microbiology and Immunobiology, Harvard Medical School, Boston, MA 02115, USA. ²Harvard-MIT Division of Health Sciences and Technology, Cambridge, MA 02139, USA. ³Department of Chemical Engineering, Massachusetts Institute of Technology, Cambridge, MA 02139, USA. ⁴Center for Immunology and Inflammatory Diseases, Massachusetts General Hospital, Harvard Medical School, Boston, MA 02114, USA. ⁵Sanofi Pasteur, Cambridge, MA 02139, USA. ⁶Laboratory of Nanomedicine and Biomaterials, Department of Anesthesiology, Brigham and Women's Hospital, Harvard Medical School, Boston, MA 02115, USA. ⁷King Abdulaziz University, Jeddah, Saudi Arabia. ⁸Ragon Institute of MGH, MIT and Harvard, Cambridge, MA 02139, USA.

*Corresponding author. E-mail: uva@hms.harvard.edu (U.H.v.A.); georg_stary@hms.harvard.edu (G.S.) †These authors contributed equally to this work.

were developed recently to target encapsulated antibiotics to bacterial surfaces (32). Using an emulsion-based manufacturing process, cSPs self-assemble from a triblock copolymer, poly(D,L-lactic-co-glycolic acid)-b-poly(L-histidine)-b-poly(ethylene glycol) (PLGA-PLH-PEG), to form a hydrophobic core (PLGA) and a hydrophilic surface consisting of PLH and PEG (32). At physiologic pH 7.4, cSPs carry a slight negative sur-

face charge, but acidification to below pH 6.5 induces protonation of PLH imidazole groups, rendering cSPs cationic and allowing them to form conjugates with negatively charged bacteria (32). For use in vaccines, we modified cSPs by incorporating a second hydrophobic polymer, poly(D,L-lactic acid), that was covalently coupled to R848 (resiquimod), a potent TLR7/8 agonist (PLA-R848). Recent work has shown that after

s.c. injection into mice, PEGylated PLA-R848-containing nanoparticles are phagocytosed by DCs and release free R848 within endosomes, resulting in efficient activation of endosomal TLR7 and DC maturation while minimizing systemic exposure to this adjuvant (33).

Thus, by incorporating R848 into cSPs, we created charge-switching synthetic adjuvant particles (cSAPs) that were then mixed with UV-Ct EBs in aqueous buffer (Fig. 1D). After acidification, cSAPs formed conjugates with UV-Ct, as confirmed by flow cytometry (Fig. 1, E and F), transmission electron microscopy (Fig. 1G), and dynamic light-scattering analysis (Fig. 1H). By contrast, synthetic adjuvant particles (SAPs) that lacked PLH and could not undergo surface-charge switching failed to bind UV-Ct and were used as a control.

Effect of uterine mucosal vaccination with UV-Ct–cSAP conjugates

Having verified that cSAPs serve as an effective tool to attach a potent small-molecule adjuvant, R848, to UV-Ct, we compared the effect of i.u. exposure to UV-Ct alone or UV-Ct mixed with free SAPs (UV-Ct + SAP) or conjugated with either cSAPs (UV-Ct–cSAP) or adjuvant-free cSPs (UV-Ct–cSP), using the same i.u. prime/challenge protocol as above. Again, preconditioning with UV-Ct rendered mice hypersusceptible to subsequent Ct challenge, and this tolerogenic effect was preserved in animals that had received UV-Ct + SAP or UV-Ct–cSP (Fig. 2A). By contrast, bacterial clearance was accelerated in mice that had been immunized with UV-Ct–cSAP (Fig. 2B). Remarkably, the extent of vaccine-induced protection was equivalent, if not superior, relative to animals with “natural” memory after previous Ct infection. These results were independently confirmed when uteri of challenged mice were analyzed by blinded observers for the presence of infectious Ct by *in vitro* testing of tissue extracts for inclusion-forming units in McCoy cells (Fig. 2C and fig. S1). Robust protection was also achieved when cSAPs were conjugated to formalin-inactivated Ct (fig. S2A) or to another UV-inactivated strain of Ct, serotype E (Ct-E) (fig. S2B), or to *C. muridarum* (Cm), a mouse-adapted strain (Fig. 2D).

Although pathological changes in murine uteri infected with human-adapted strains of Ct are variable, infection of naïve mice with Cm caused reproducible tissue damage resulting in accumulation of serous exudate in fallopian tubes (hydrosalpinx), reminiscent of the pathology induced by chronic Ct infection in humans. By contrast, animals that had received i.u. UV-Cm–cSAP vaccination were profoundly protected against hydrosalpinx formation relative to naïve animals or recipients of UV-Cm alone (Fig. 2E).

The differential effects of i.u. conditioning with UV-Ct–cSAP and UV-Ct persisted unabated for at least 6 months; the former continued to afford profound protection, whereas the latter predisposed to enhanced susceptibility to Ct rechallenge. These findings indicate that mucosal exposure to UV-Ct in both immunogenic and tolerogenic contexts elicits sustained and qualitatively unchanging memory (Fig. 2F).

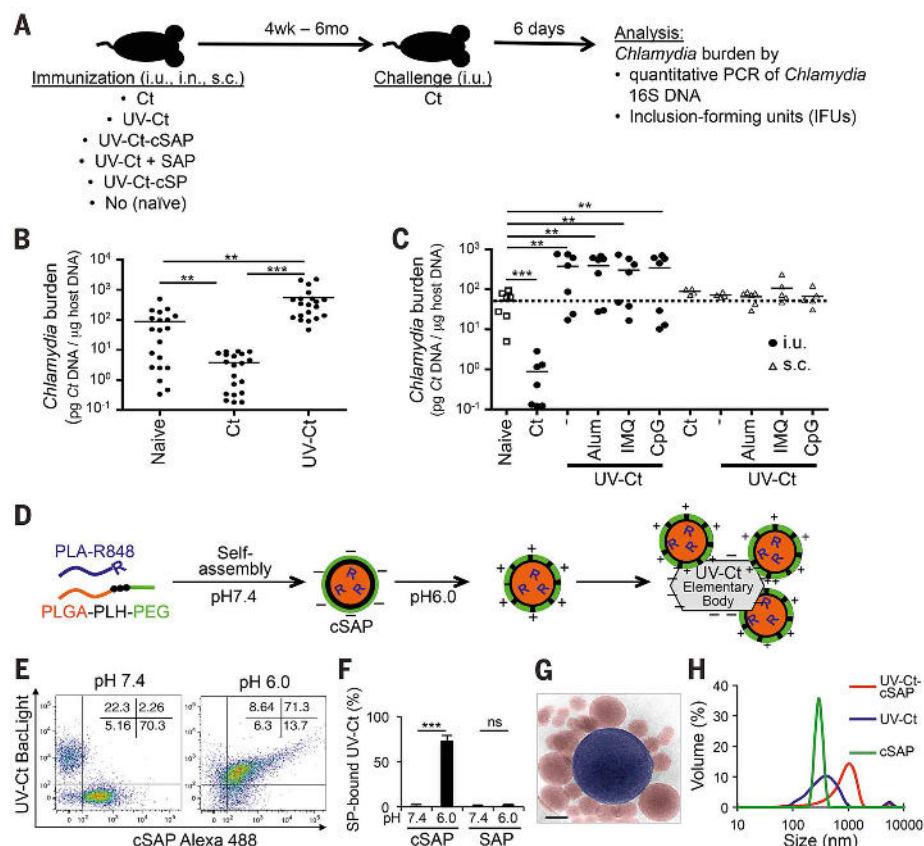
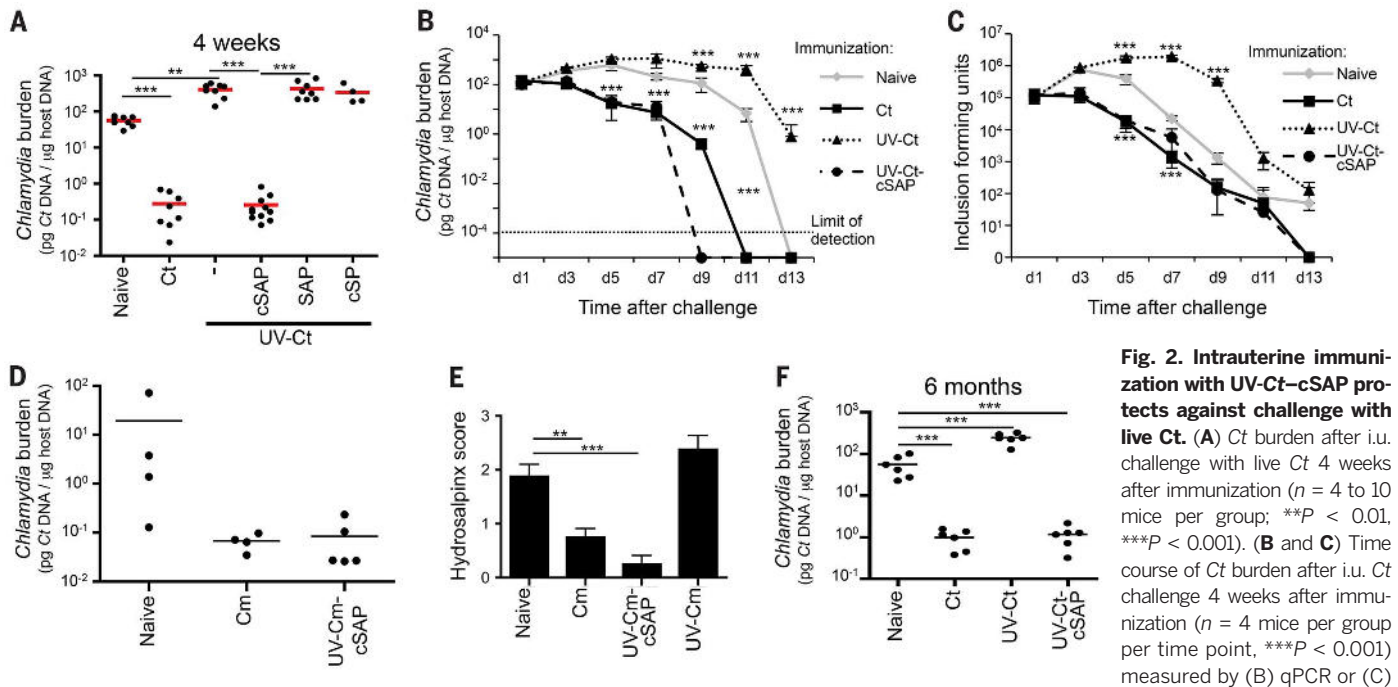


Fig. 1. Differential effects of immunization with Ct/UV-Ct and conjugation of UV-Ct with synthetic nanoparticles. (A) Schematic diagram of the immunization and challenge protocol for Fig. 1, B and C; Fig. 2, A, B, C, and F; Fig. 3, A and B; Fig. 4, E and F; Fig. 6A; and figs. S4 and S7. Mice were immunized with Ct, UV-Ct, UV-Ct–cSAP, or UV-Ct mixed with control nanoparticles (Ct, live *Chlamydia trachomatis*; UV-Ct, inactivated *Chlamydia trachomatis*; UV-Ct–cSAP, inactivated *Chlamydia trachomatis* complexed with charge-switching synthetic adjuvant particles; UV-Ct + SAP, inactivated *Chlamydia trachomatis* mixed with synthetic adjuvant particles (not attached to UV-Ct); UV-Ct–cSP–inactivated *Chlamydia trachomatis* complexed with charge-switching synthetic particles (without adjuvant) via intrauterine (i.u.), intranasal (i.n.), or subcutaneous (s.c.) routes. Challenge with live Ct was always i.u. (B) Uterine Ct burden was measured by qPCR 6 days after i.u. challenge with live Ct in naïve mice and in animals that had been immunized 4 weeks earlier by i.u. injection of infectious Ct or UV-Ct. Data are pooled from 4 independent experiments ($n = 20$ mice per group; ** $P < 0.01$, *** $P < 0.001$; one-way ANOVA followed by Bonferroni posttest). (C) Ct burden after i.u. or s.c. immunization with UV-Ct mixed with adjuvants: alum, aluminum hydroxide; IMQ, imiquimod; CpG, CpG oligodeoxynucleotide type C ($n = 5$ to 7 mice per group; ** $P < 0.002$, *** $P < 0.001$; one-way ANOVA followed by Bonferroni posttest). (D) Schematic representation of surface charge-switching synthetic adjuvant particle (cSAP) production and conjugation to UV-Ct. (E and F) UV-Ct stained with BacLight was incubated with Alexa Fluor 488–labeled cSAP or SAP at pH 7.4 or 6.0. (E) Representative FACS plots and (F) quantification of nanoparticle conjugates with UV-Ct from two independent experiments. *** $P < 0.001$; ns, not significant; two-tailed t tests. (G) A representative cryo–transmission electron micrograph of a UV-Ct–cSAP cluster showing cSAP in red and UV-Ct in blue. Scale bar, 100 nm. (H) Dynamic light scattering profiles of UV-Ct–cSAP, cSAP, and UV-Ct alone. The population distribution is representative of the volume scattering intensity. Data are representative of 10 independent experiments. Error bars represent mean \pm SEM.



in vitro assessment of inclusion-forming units (IFUs). (D) Ct burden after intravaginal challenge with Cm 4 weeks after immunization with Cm and UV-Cm-cSAP. $n = 3$ or 4 mice per group; $^{***}P < 0.001$. (E) Gross uterine pathology determined as hydrosalpinx score 4 weeks after intravaginal challenge of immunized and naive mice with Cm ($n = 8$ mice per group; $^{**}P < 0.01$, $^{***}P < 0.001$). (F) Ct burden after i.u. Ct challenge 6 months after i.u. immunization ($n = 4$ to 10 mice per group; $^{***}P < 0.001$). Statistical differences were assessed using one-way ANOVA followed by Bonferroni posttest.

UV-Ct-cSAP vaccination induces Ct-specific protective T helper 1 memory cells

Because the charge-based conjugation of cSAPs to UV-Ct was apparently sufficient not only to permanently avert the default tolerance response to UV-Ct but also to produce robust long-term protective immunity that prevented infection-induced tissue damage, we set out to dissect the underlying immunological mechanisms. Recent clinical evidence suggests that humans develop at least partially protective immunity upon clearance of genital Ct infection, whereby interferon (IFN)- γ production, presumably by T helper 1 (T_H1) cells, was inversely correlated with the risk for reinfection (34–36). Although mechanistic information in humans is sparse and far from definitive, the available data are consistent with experiments in mice where bacterial clearance after genital Ct or Cm infection is known to require T_H1 cells (31, 37, 38). Mouse experiments have also shown that during Ct or Cm infection, naive T cells (T_N cells) differentiate into effector T cells (T_{Eff} cells) in uterus-draining lymph nodes (LNs), and these T_{Eff} cells are then recruited to the genital mucosa to mediate bacterial clearance (39–41). T_H1 cells are also a key component of long-term protective memory after infection, although a role for B cells and antibodies has also been reported (42–47).

Our analysis of UV-Ct-cSAP immunized mice revealed a robust Ct-specific antibody response that was equivalent to that elicited by Ct infection and about twice as great as in UV-Ct-exposed mice (fig. S3A). Moreover, i.u. immunization with

UV-Ct-cSAP increased uterine mucosa-resident CD8 T cells (fig. S3B) as well as CD4 T cells (see below). To determine which component(s) of this multifaceted response to UV-Ct-cSAP were required for mucosal protection, we measured bacterial burdens after genital Ct infection in vaccinated mutant mice that lacked either B cells (μ Mt mice, which contain a deletion of the IgM heavy chain) or CD8 T cells ($Cd8^{-/-}$ mice) or CD4 T cells [B6.129S2-H2^{dAb1-Ea}/J (referred to as MHC-II^{-/-} mice (48)] or both B and T cells ($Rag2^{-/-}$ mice). Neither the absence of B cells nor that of CD8 T cells had a detectable impact on bacterial levels, whereas $Rag2^{-/-}$ mice (fig. S4) and MHC-II^{-/-} mice were completely unprotected against Ct challenge (Fig. 3A). Of note, unlike wild-type animals, mice that were devoid of CD4 T cells did not suffer increased bacterial burdens after UV-Ct conditioning, indicating that CD4⁺ T cells are needed not only for pathogen clearance but also for UV-Ct-induced tolerance.

Because the above experiments demonstrated that CD4 T cells are required for the sequelae of both UV-Ct and UV-Ct-cSAP exposure, we asked whether CD4 T cells alone were sufficient to confer these effects. Thus, we adoptively transferred purified leukocyte subsets from immunized mice to naive recipients that were subsequently challenged with Ct. Partial protection against genital Ct challenge was achieved after transferring 10^7 splenic CD4⁺ T cells from mice that had received i.u. injections of either Ct or UV-Ct-cSAP, whereas transfer of CD8 T cells or T cell-depleted splenocytes had no effect (Fig. 3B). Transfer of CD4 T cells from UV-Ct-

conditioned donors conferred enhanced susceptibility to infection.

Having determined that CD4 memory T cells are both necessary and sufficient for Ct-specific protective memory, as well as tolerance, after immunization with UV-Ct-cSAP and UV-Ct, respectively, we asked how Ct-specific CD4 T_N cells respond to either stimulus, as compared to Ct infection. To this end, we adoptively transferred T_N cells from CD90.1⁺ transgenic NR1 mice (40), in which most CD4 T cells express a Ct-specific T cell receptor (TCR) (fig. S5), into groups of congenic (CD90.2⁺) hosts that were subsequently immunized i.u. with Ct, UV-Ct, or UV-Ct-cSAP. Four days later, NR1 cells had responded identically to Ct infection and UV-Ct-cSAP immunization; they had vigorously proliferated and expanded in the draining LNs (Fig. 3, C and D), and they also accumulated in the uterine mucosa (Fig. 3E). Moreover, upon in vitro rechallenge with UV-Ct pulsed autologous DCs, the vast majority of uterine and LN-resident NR1 cells in both groups produced one or more effector cytokines, including IFN- γ , interleukin (IL)-2, and tumor necrosis factor (TNF)- α (Fig. 3F). By contrast, in UV-Ct-exposed animals, NR1 cells showed less proliferation and accumulation in LNs and uterus, and they secreted little or no cytokines, similar to T_N cells.

Mucosal exposure to UV-Ct generates Ct-specific regulatory T cells

Although the encounter of UV-Ct evoked a blunted T_{Eff} response by Ct-specific CD4 T cells, this effect alone cannot explain why UV-Ct enhanced host

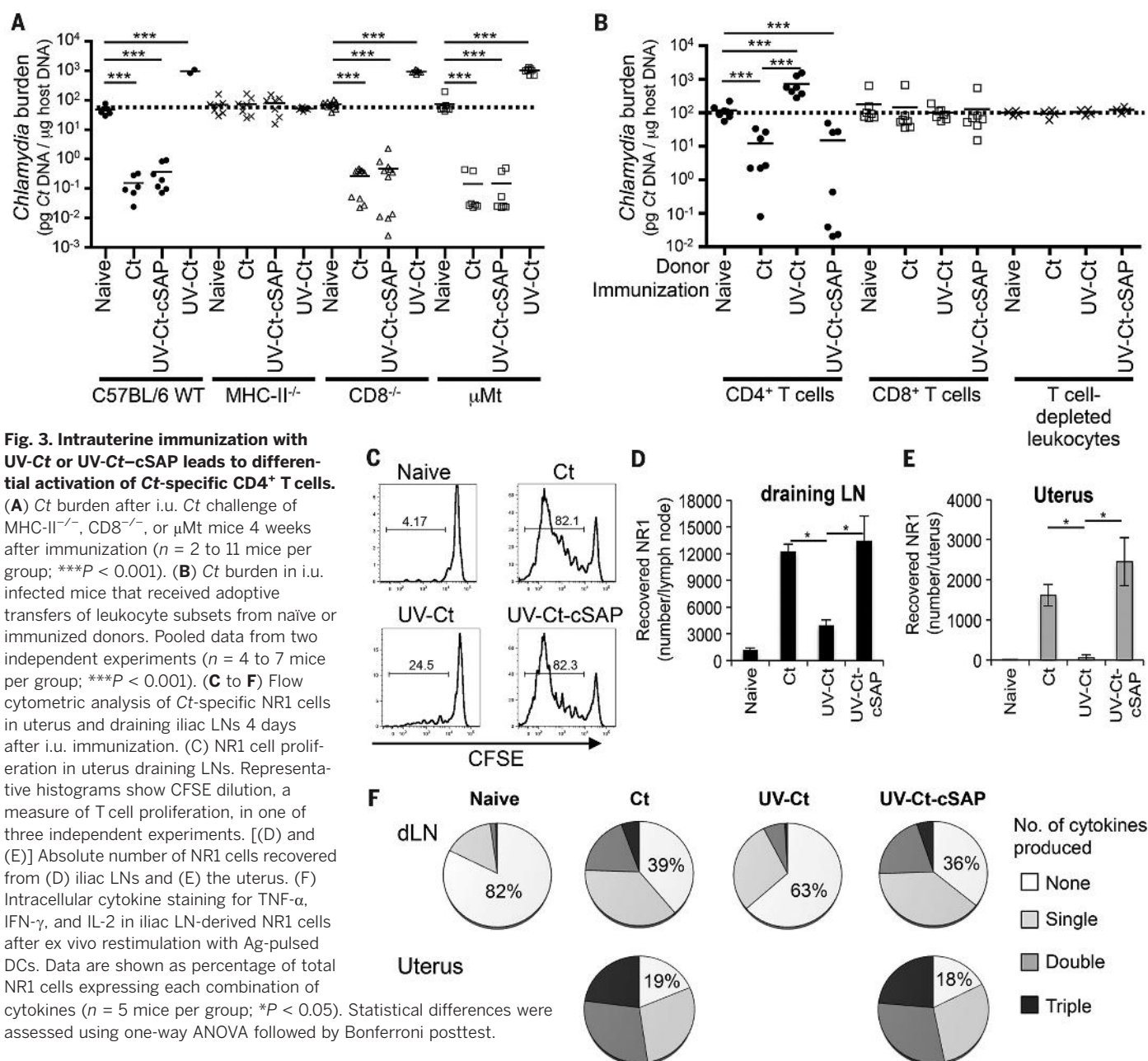


Fig. 3. Intrauterine immunization with UV-Ct or UV-Ct-cSAP leads to differential activation of Ct-specific CD4⁺ T cells.

(A) Ct burden after i.u. Ct challenge of MHC-II^{-/-}, CD8^{-/-}, or μ Mt mice 4 weeks after immunization ($n = 2$ to 11 mice per group; *** $P < 0.001$). (B) Ct burden in i.u. infected mice that received adoptive transfers of leukocyte subsets from naïve or immunized donors. Pooled data from two independent experiments ($n = 4$ to 7 mice per group; *** $P < 0.001$). (C to F) Flow cytometric analysis of Ct-specific NR1 cells in uterus and draining iliac LNs 4 days after i.u. immunization. (C) NR1 cell proliferation in uterus draining LNs. Representative histograms show CFSE dilution, a measure of T cell proliferation, in one of three independent experiments. [(D) and (E)] Absolute number of NR1 cells recovered from (D) iliac LNs and (E) the uterus. (F) Intracellular cytokine staining for TNF- α , IFN- γ , and IL-2 in iliac LN-derived NR1 cells after ex vivo restimulation with Ag-pulsed DCs. Data are shown as percentage of total NR1 cells expressing each combination of cytokines ($n = 5$ mice per group; * $P < 0.05$). Statistical differences were assessed using one-way ANOVA followed by Bonferroni posttest.

susceptibility to subsequent Ct infection. The apparent tolerogenicity of UV-Ct clearly depended on CD4 T cells, because UV-Ct did not tolerize MHC-II^{-/-} mice (Fig. 3A), whereas adoptive transfer of CD4 T cells from UV-Ct-conditioned wild-type mice conferred tolerance to naïve recipients (Fig. 3B). Thus, we hypothesized that mucosal UV-Ct exposure not only may compromise T_{Eff} differentiation of Ct-specific T_N cells but also may instigate an alternative “career decision” driving CD4 T_N cells to differentiate into FoxP3⁺ CD25⁺ regulatory T cells (T_{reg}). To test this idea, we adoptively transferred to naïve hosts T_N cells from NR1xFoxP3-eGFP donors after sorting the enhanced green fluorescent protein (eGFP)-negative fraction (i.e., non-T_{reg}). Recipients were then immunized with live Ct, UV-Ct, or UV-Ct-

cSAP. Indeed, there was a massive increase in FoxP3-eGFP⁺CD25⁺ NR1 cells in the draining LNs (Fig. 4, A and B) and uterus (Fig. 4, C and D) of UV-Ct-exposed mice, whereas very few NR1 cells assumed a T_{reg} phenotype in response to Ct infection or UV-Ct-cSAP vaccination. Because a priori eGFP⁺ T_{reg}s had been removed before T_N transfer, the appearance of eGFP⁺ T_{reg}s after UV-Ct exposure was due to conversion of conventional T_N cells rather than to expansion of existing T_{reg}s. These newly induced T_{reg}s were required for tolerance to Ct infection, because anti-CD25-mediated T_{reg} depletion in UV-Ct-treated mice reduced uterine Ct burden upon subsequent infection to levels comparable to naïve mice (Fig. 4E). Moreover, UV-Ct-conditioned *Il10*^{-/-} mice did not suffer enhanced bacterial

burdens upon i.u. Ct challenge (Fig. 4F), which suggests that the de novo induced Ct-specific T_{reg}s exerted their tolerogenic activity through the IL-10 pathway.

Differential mucosal antigen uptake and presentation by uterine dendritic cell subsets

What mechanisms are responsible for the differential T cell response to Ct or UV-Ct-cSAP versus UV-Ct? To address this question, we examined the phenotype and function of the three predominant uterus-resident MHC-II⁺ leukocyte populations (Fig. S6A): F4/80⁺CD11b⁺ macrophages that were CD11c^{low}, CD103⁻, and expressed variable levels of CX3CR1, as well as two equally sized subsets of CD11c⁺F4/80⁻ DCs. One DC subset was CD103⁺

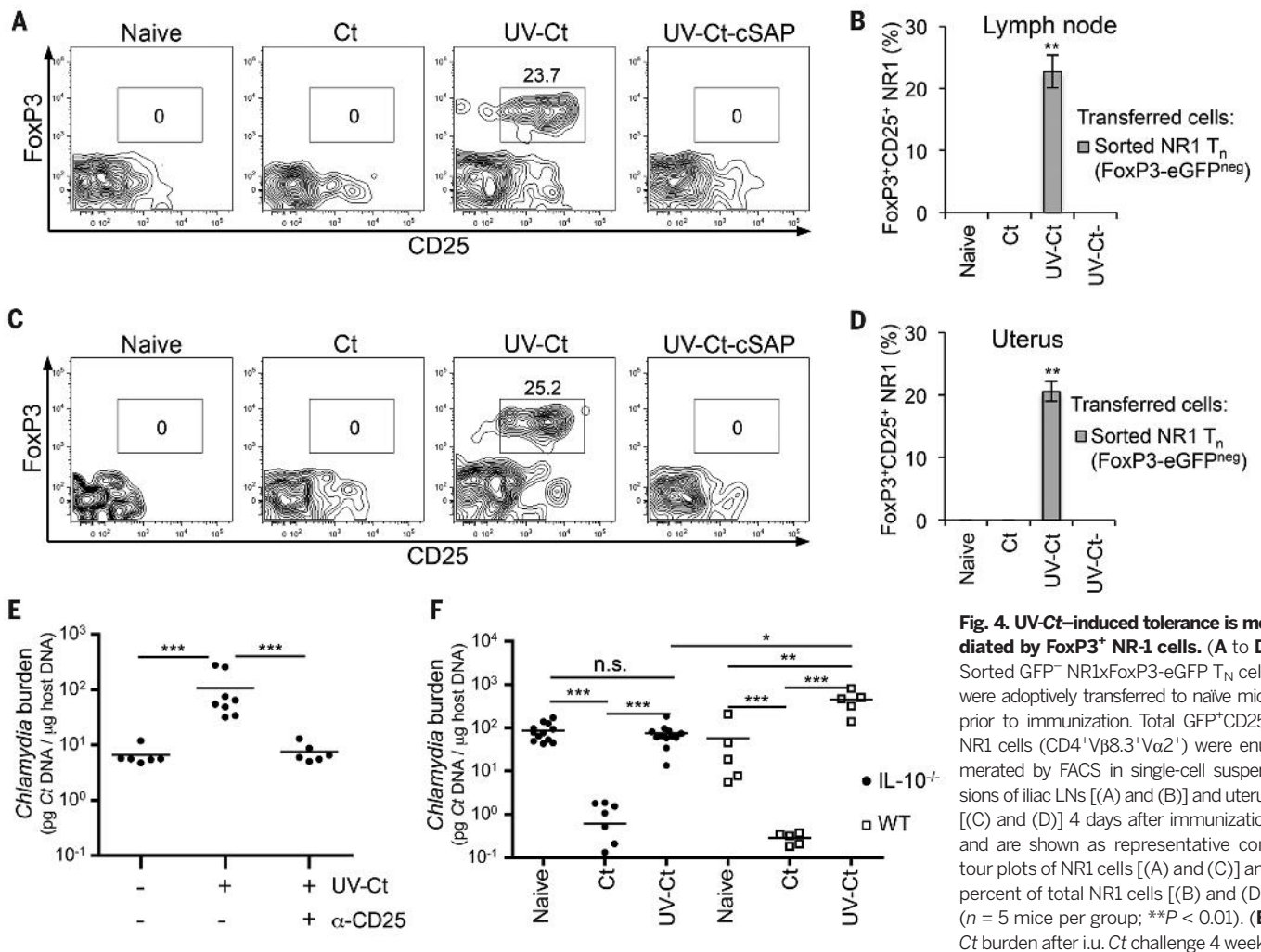


Fig. 4. UV-Ct-induced tolerance is mediated by FoxP3⁺ NR-1 cells. (A to D) Sorted GFP⁺ NR1xFoxP3-eGFP⁺ T_N cells were adoptively transferred to naïve mice prior to immunization. Total GFP⁺CD25⁺ NR1 cells (CD4⁺V β 8.3⁺V α 2⁺) were enumerated by FACS in single-cell suspensions of iliac LNs [(A) and (B)] and uterus [(C) and (D)] 4 days after immunization and are shown as representative contour plots of NR1 cells [(A) and (C)] and percent of total NR1 cells [(B) and (D)] ($n = 5$ mice per group; ** $P < 0.01$). (E) Ct burden after i.u. Ct challenge 4 weeks

after immunization with Ct, UV-Ct, or UV-Ct-cSAP. In some animals T_{regs} were depleted with CD25 mAb (clone PC61) while the other groups received isotype-matched IgG 3 days before and after challenge ($n = 6$ mice per group; *** $P < 0.001$). (F) Ct burden after i.u. challenge with live Ct 4 weeks after immunization of *IL10*^{-/-} mice ($n = 5$ to 11 mice per group; * $P < 0.05$, ** $P < 0.01$, *** $P < 0.001$). Error bars depict mean \pm SEM. Statistical differences were assessed using one-way ANOVA followed by Bonferroni posttest.

and expressed neither CD11b nor CX3CR1; the second DC population was CD103⁺CD11b⁺CX3CR1⁺ (fig. S6B). All three populations were negative for CD207/Langerin and CD301b. Each of these candidate Ag-presenting cells (APCs) was sorted from single-cell suspensions of uteri or draining LNs of naïve and challenged mice and tested for Ct content and ability to stimulate NR1 T_N in vitro and in vivo (Fig. 5A). At 18 hours after i.u. exposure to Ct, UV-Ct, or UV-Ct-cSAP, uterine APCs had not changed significantly in total number or composition (fig. S6, C and D), and the amount of Ct-derived genetic material [determined by quantitative polymerase chain reaction (qPCR)] acquired by both macrophages and CD326⁺ mucosal epithelial cells was similar in each group (Fig. 5B). By contrast, marked differences were apparent among the two DC subsets: live Ct and UV-Ct-cSAP were primarily acquired by CD103⁺ DCs, whereas UV-Ct accumulated preferentially in CD103⁺ DCs. Similarly, at 24 hours after challenge, when sorted APCs were isolated from uterus-draining LNs, bacterial loads were

exclusively detected in CD103⁺ DCs after genital exposure to Ct and UV-Ct-cSAP but not UV-Ct (Fig. 5C).

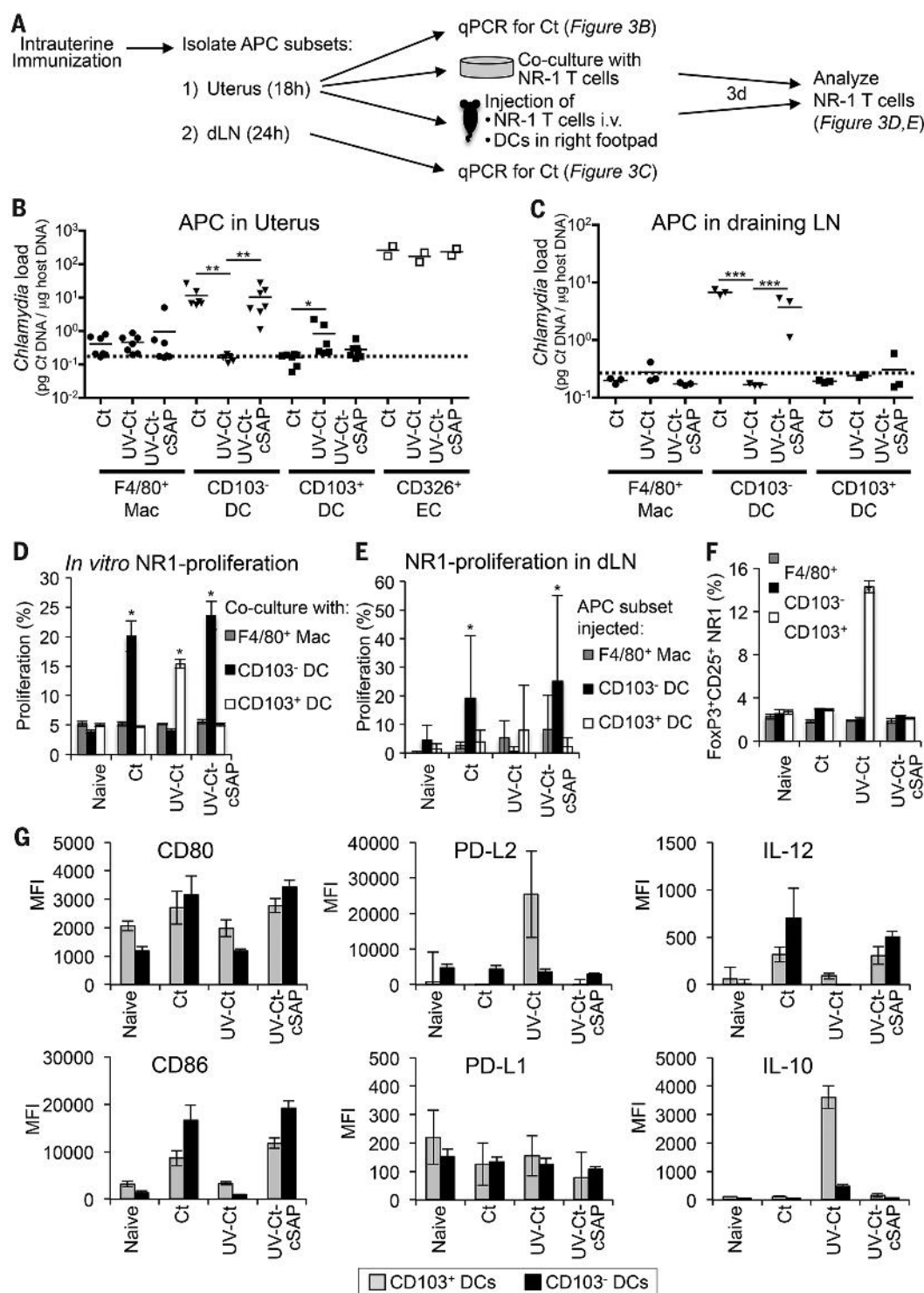
Consistent with the differential acquisition of Ct-derived genetic material, 3-day cocultures of purified uterine APC subsets with NR1 T_N cells revealed that CD103⁺ DCs were singularly efficient at inducing T cell proliferation when they had been isolated from animals exposed to either Ct or UV-Ct-cSAP. By contrast, among UV-Ct-exposed APCs, only the CD103⁺ DCs promoted substantial proliferation of NR1 T cells, whereas macrophages failed to induce T cell proliferation regardless of the immunization regimen (Fig. 5D). This differential APC activity was recapitulated when APC subsets were isolated from vaccinated animals and injected into footpads of naïve mice that had previously received NR1 T_N cells; CD103⁺ DCs, but not CD103⁺ DCs or macrophages, from Ct-infected and UV-Ct-cSAP-immunized mice stimulated NR1 T_N cell proliferation in the recipients' draining LNs (Fig. 5E). Footpad injection of sorted CD103⁺ DCs

did not promote a significant in vivo response by NR1 cells in this experimental setting; however, when CD103⁺ DCs were isolated from UV-Ct-conditioned donors and exposed in vitro to NR1 T_N cells, they uniquely promoted the appearance of FoxP3⁺CD25⁺ T_{regs} (Fig. 5F).

In line with these functional observations, 18 hours after Ct infection or UV-Ct-cSAP immunization, uterine CD103⁺ DCs preferentially up-regulated immunostimulatory molecules, including CD80, CD86, and IL-12 (Fig. 5G and fig. S6E). In contrast, upon immunization with UV-Ct, CD103⁺ DCs selectively up-regulated certain anti-inflammatory pathways, including PD-L2 and IL-10. However, other markers of tolerogenic APCs either remained unchanged or were undetectable on uterine CD103⁺ DCs, such as PD-L1 and RALDH, respectively.

We conclude that after mucosal exposure to live Ct and UV-Ct-cSAP, antigenic material is preferentially acquired and transported to the draining LNs by local immunostimulatory CD103⁺ DCs, whereas exposure to UV-Ct results in Ag

Fig. 5. Distinct uterine DC subsets acquire Ags after i.u. Ct and UV-Ct–cSAP versus UV-Ct immunization and induce differential responses by Ct-specific T cells in vitro and in vivo. (A) Schematic diagram of the experimental protocol for (B) to (F). Mice were immunized i.u. with Ct, UV-Ct, or UV-Ct–cSAP. At indicated time points thereafter, CD45⁺MHC-II⁺ APC subsets were isolated from uteri and LNs and FACS sorted according to CD103 and F4/80 expression. **(B and C)** Uptake of Ct per 1000 sorted APCs in the uterus (B) and draining LN (C) was measured by qPCR. Isolated uterine CD326⁺ epithelial cells (EC) served as positive control for uterine samples. Data are pooled from two independent experiments. Mac, macrophages; DC, dendritic cells. $n = 2$ to 7; broken line, limit of detection; * $P < 0.05$, ** $P < 0.01$, *** $P < 0.001$. **(D)** In vitro proliferation of NR1 T_N was determined by CFSE dilution after incubation with sorted APC subsets for 3 days ($n = 4$ mice per group; * $P < 0.05$). **(E)** In vivo proliferation of CFSE-labeled CD90.1⁺ NR1 cells in a draining popliteal LN 3 days after footpad injection of APC subsets ($n = 4$ mice per group; * $P < 0.05$). **(F)** FoxP3-eGFP–depleted NR1 cells were incubated in vitro with sorted APC subsets. Frequencies of FoxP3-eGFP⁺ T_{regs} were determined by flow cytometry after 3 days ($n = 4$ mice per group; * $P < 0.05$). **(G)** Eighteen hours after immunization, uterine DC subsets were analyzed by FACS for indicated markers ($n = 4$). Error bars represent mean \pm SEM. Statistical differences were assessed using one-way ANOVA followed by Bonferroni posttest.



acquisition by a tolerogenic DC subset that expresses CD103, leading to the induction of T_{regs} that then shift the balance from protection to long-lived tolerance in the genital mucosa. Of note, a similar division of labor between CD103⁺ and CD103⁺ DCs has been described for the induction of intestinal tolerance and immunity, respectively (49). The differential Ag uptake by intestinal DC subsets is regulated by other mucosa-resident cell types (50–52); however, the

mechanism(s) that regulate differential Ag acquisition by uterine DCs remain to be identified.

The route of administration determines UV-Ct–cSAP vaccine efficacy

Having established that targeting of uterine CD103⁺ DCs by transcervical application of UV-Ct–cSAP generates long-term protection against genital Ct infection, we asked whether other routes of immunization could recapitulate this

effect. Thus, mice were immunized with UV-Ct–cSAP either s.c. or intranasally (i.n.) and then challenged by i.u. Ct infection. Consistent with our experiments using mixtures of UV-Ct with conventional adjuvants (Fig. 1C), s.c. immunization with live Ct or UV-Ct–cSAP failed to protect (Fig. 6A). By contrast, exposure of nasopharyngeal mucosa to live Ct or UV-Ct–cSAP rendered mice resistant to genital Ct infection akin to i.u. immunization, and this cross-mucosal protective

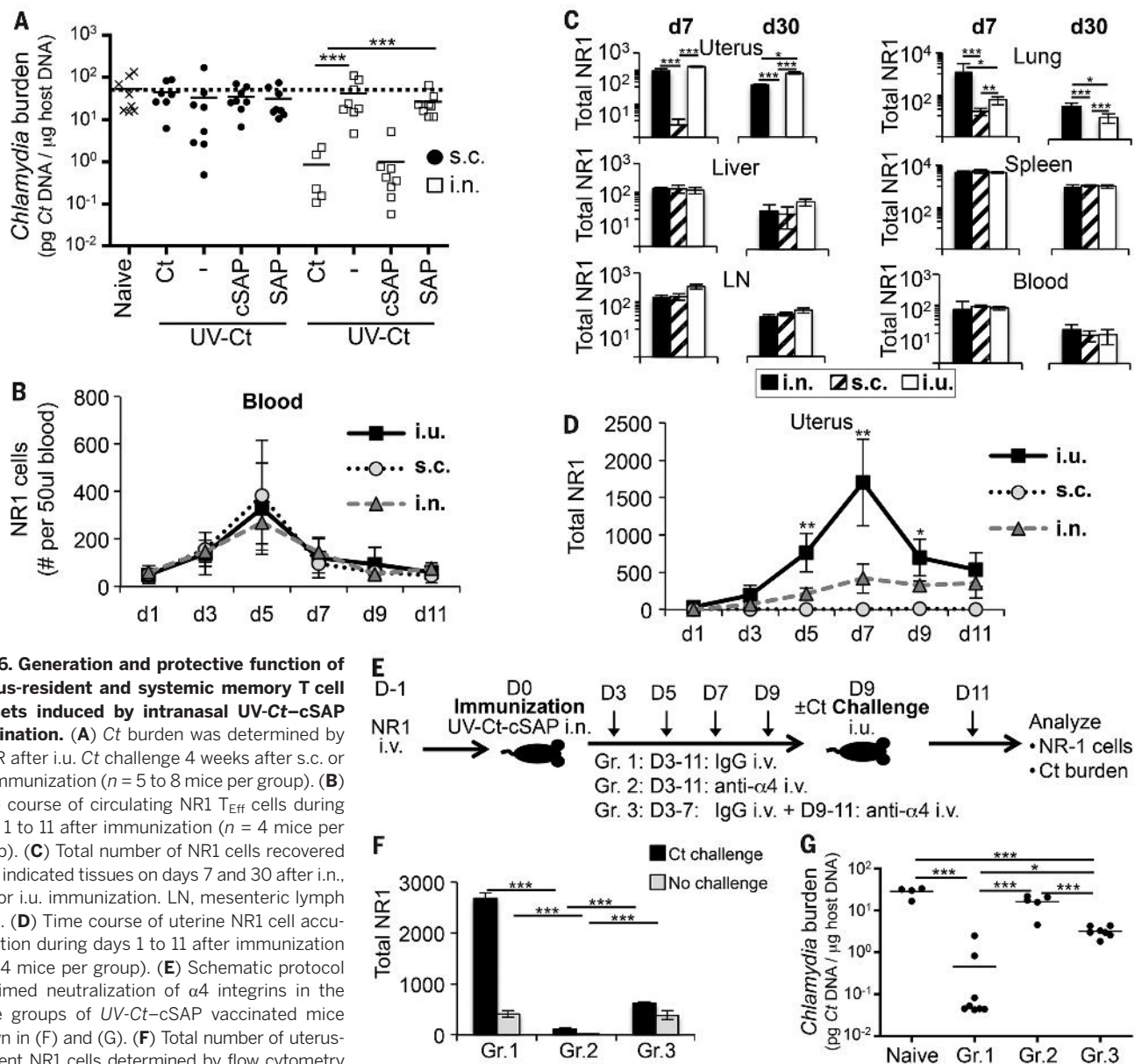


Fig. 6. Generation and protective function of uterus-resident and systemic memory T cell subsets induced by intranasal UV-Ct-cSAP vaccination. (A) *Ct* burden was determined by qPCR after i.u. *Ct* challenge 4 weeks after s.c. or i.n. immunization ($n = 5$ to 8 mice per group). (B) Time course of circulating NR1 T_{Eff} cells during days 1 to 11 after immunization ($n = 4$ mice per group). (C) Total number of NR1 cells recovered from indicated tissues on days 7 and 30 after i.n., s.c., or i.u. immunization. LN, mesenteric lymph node. (D) Time course of uterine NR1 cell accumulation during days 1 to 11 after immunization ($n = 4$ mice per group). (E) Schematic protocol for timed neutralization of $\alpha 4$ integrins in the three groups of UV-Ct-cSAP vaccinated mice shown in (F) and (G). (F) Total number of uterus-resident NR1 cells determined by flow cytometry ($n = 4$ mice per group). (G) Uterine *Ct* burden 3 days after i.u. *Ct* challenge. Data are from two independent experiments; $n = 4$ to 8 mice per group. Statistical differences were assessed using one-way ANOVA followed by Bonferroni posttest.

effect persisted unabated for at least 6 months (fig. S7). Interestingly, unlike i.u. conditioning with UV-Ct, neither i.n. nor s.c. exposure to UV-Ct enhanced the animals' susceptibility to genital *Ct* challenge, which suggests that the rules that govern regional immunity versus tolerance in the uterus may be distinct.

Rapid seeding of uterine mucosa with resident memory T cells (T_{RM} cells) after mucosal but not subcutaneous UV-Ct-cSAP vaccination

The fact that percutaneous immunization was ineffective, while vaccination via two distant mucosal routes generated potent protection against genital *Ct* infection, implied that protective CD4 $^{+}$ T cells required priming in a MALT environ-

ment for efficient mucosal targeting (12). To further investigate this idea, we adoptively transferred 10^4 NR1 T_{N} cells into mice that were then immunized via different routes with UV-Ct-cSAP. Regardless of immunization route, the burst size of NR1 T_{Eff} cells in peripheral blood was equivalent in magnitude and peaked on day 5 (Fig. 6B). Similarly, 7 days and 30 days after i.n., s.c., or i.u. vaccination, NR1 cells were equally represented in blood, spleen, LNs, and liver, indicating that the route of immunization did not affect the differentiation or trafficking of T_{Eff} cells and memory cells to these nonmucosal sites (Fig. 6C). By contrast, i.u. and i.n. immunization generated Ag-experienced NR1 cells in the lung and uterus, while s.c. vaccination failed to generate mucosa-resident T_{Eff} cells (fig. S8, A to C). A closer exam-

ination of the kinetics of uterine T_{Eff} recruitment showed that NR1 T_{Eff} numbers increased gradually after i.n. vaccination, reaching a plateau on day 7. By contrast, i.u. vaccination resulted in a larger peak of uterus-resident NR1 cells on day 7 followed by contraction of the resident T cell pool over the next several days (Fig. 6D). By day 9, both mucosal vaccination strategies had elicited roughly similar uterus-resident T cell numbers, whereas NR1 cells remained essentially undetectable in uteri of s.c. immunized mice.

A critical protective role for uterine T_{RM} cells upon transcervical *Ct* challenge

The above results suggested that two distinct pools of *Ct*-specific memory T cells were induced: One population was modest in size and consisted

of mucosa-resident T_{RM} cells that arose from T_{Eff} cells that accessed the uterus early after mucosal (but not s.c.) priming. The pronounced spike in early NR1 T_{Eff} cell accumulation that was seen after i.u. (but not i.n.) vaccination was presumably a consequence of local tissue irritation that spurred inflammatory recruitment signals in the uterus. It is unlikely that i.n. vaccination altered the steady-state milieu in the uterus, so the fact that uterine T_{Eff} cell numbers increased steadily during the first 7 days after i.n. vaccination suggests the presence of constitutive mucosal recruitment signals for circulating T_{Eff} cells. Although the nature of these steady-state signals remains to be elucidated, our results indicate that T_{Eff} cells were selectively “imprinted” by mucosal (i.e., uterine or nasopharyngeal) APCs to engage this uterine recruitment pathway, whereas T_{Eff} cells generated in skin-draining LNs apparently lacked the pre-requisite traffic molecule(s) for uterine homing. Moreover, the longevity of protection after i.n. vaccination (fig. S7) indicates that T_{Eff} cells that accessed the uterus gave rise to T_{RM} cells that persisted for at least six months without requiring the presence of local Ag.

The second vaccine-induced memory cell population was much larger than the number of uterus-resident T_{RM} cells and resided in blood and lymphoid tissues, where these cells are thought to survey the body for recall Ag (53). Although systemic memory cells were elicited by all immunization routes, their protective capacity may vary because of differential imprinting of mucosal homing pathways during the priming phase (2–4). For example, recent work has shown that protective CD4 T cells require the $\alpha 4\beta 1$ integrin to access uterine mucosa (54). We made use of this fact to assess the relative contribution by each memory pool to the clearance of a recurrent *Ct* infection (Fig. 6E). To this end, we adoptively transferred NR1 T_N cells into three groups of mice that then received i.n. UV-*Ct*-cSAP vaccination. Three days later, when activated NR1 T_{Eff} first appeared in the blood, animals in group 1 were given rat IgG every 48 hours and served as controls in which memory cells had continuous access to the uterus; group 2 received injections of a blocking $\alpha 4$ integrin monoclonal antibody (mAb) every 48 hours, thus preventing uterine T cell homing throughout the experiment; group 3 received control IgG from day 3 to day 7, allowing the first wave of *Ct*-specific T_{Eff} cells to seed the uterine mucosa. On day 9, when i.n. vaccinated control mice had established a stable uterine T_{RM} cell pool (Fig. 6D), all groups were either challenged by i.u. inoculation of *Ct* or left unchallenged, and group 3 was then switched to treatment with $\alpha 4$ integrin mAb to prevent the secondary recruitment of circulating memory cells to the uterus. Animals were sacrificed on day 13 after immunization to assess uterine bacterial burden and/or NR1 cell distribution.

As expected (54), $\alpha 4$ integrin blockade in groups 2 and 3 profoundly affected the accumulation of both NR1 and endogenous CD4 T cells in the infected uterus but had no significant effect on

CD4 T cells in the spleen (Fig. 6F and fig. S9, A to C). However, although continuous mAb treatment in group 2 essentially abrogated NR1 cell trafficking to both steady-state and infected uteri, the number of uterine NR1 cells in group 3 was significantly higher than in group 2 and equivalent to that in uninfected uteri of group 1. *Ct* infection in group 1 induced a factor of ~5 increase in uterine NR1 cells, whereas late inhibition of $\alpha 4$ integrins in group 3 completely prevented this secondary boost in uterine NR1 cell numbers. There was no difference between groups 1 and 3 in challenge-induced BrdU uptake or K_i -67 expression (a marker of ongoing cell division) by NR1 cells, indicating that mucosa-resident and newly recruited memory cells have a similar proliferative capacity (fig. S9D). Thus, the difference in mucosal T cell numbers between *Ct*-challenged animals in group 1 and group 3 likely reflects the $\alpha 4$ integrin-dependent influx of circulating T_{Eff} that occurred in response to infection-induced recruitment signals in the uterus (9). By contrast, the difference between groups 2 and 3 provides a measure for the number of vaccine-induced T_{Eff} that accessed the uterus early after priming and prior to *Ct* infection. Remarkably, although the total number of uterus-resident NR1 cells in group 3 was modest, the bacterial burden was reduced by an order of magnitude relative to naïve mice or animals in group 2, which remained completely unprotected (Fig. 6G). However, bacterial burdens in group 1 were even further reduced than in group 3, indicating that both tissue-resident and circulating T cells are needed to achieve optimal clearance of *Ct*. These findings confirm that the migration of both tissue-resident and circulating CD4⁺ T cells into uterine mucosa depend on $\alpha 4$ integrins, presumably the $\alpha 4\beta 1$ heterodimer (54). It is likely that additional trafficking molecules, such as chemokines, are involved in a tissue-specific multistep adhesion cascade for T cell recruitment to normal uterine mucosa (53), but the molecular identity of these constitutive traffic signals remains to be determined.

Circulating memory T cells induced by mucosal vaccination confer partial protection against *Ct* rechallenge

Having documented the protective capacity of mucosal T_{RM} cells, we next asked whether circulating memory cells can be protective in the absence of preexisting T_{RM} cells. To this end, we performed parabiosis surgery to generate pairs of congenic (CD45.1/CD45.2) mice, which establish a shared circulatory system, allowing genetically traceable hematopoietic cells from each animal to access the blood and tissues of a conjoined partner (55). Control experiments showed that CD4 T cell chimerism (the ratio of partner-derived: endogenous cells) in blood was minimal on day 3 after surgery but approached ~35:65 and 50:50 on days 4 and 5, respectively (fig. S10). Having thus determined that the earliest time point for circulating T cells to gain access to a parabiotic partner's tissues is on day ~4 after surgery, we performed a series of timed parabiosis experiments in congenic pairs of CD90.2⁺ mice,

whereby the CD45.1⁺ animal in each pair was given genetically tagged (CD90.1⁺) NR1 T_N cells, and both mice were immunized with UV-*Ct*-cSAP on the following day (day 0). Congenic pairs were subdivided into six groups: two groups underwent parabiosis surgery on day -14 or -1 before immunization, and four groups were parabiosed on day 1, 4, 14, or 21 after immunization (Fig. 7A). Six weeks after vaccination, the number of uterine NR1 T_{RM} cells was similar in all parabionts that had been conjoined on or before day 1 (Fig. 7B). In contrast, when parabiosis was initiated on day 4 or thereafter, the number of NR1 cells in uteri of nonimmunized CD45.2⁺ partners of immunized CD45.1⁺ animals was equivalent to that in completely naïve parabiotic pairs. These results imply that a transient wave of MALT-derived T_{Eff} cells gave rise to most, if not all, uterine T_{RM} cells within the first 7 days after immunization. Little or no further T cell recruitment to the uterus occurred after this time point. These findings are in perfect agreement with the time course of T_{Eff} cell accumulation in uteri of conventional mice, which increased until day 7 and plateaued thereafter (Fig. 6D).

To assess the protective capacity of the circulating memory subset, we devised a modification of the above protocol (Fig. 7C), whereby two groups of congenic mice were paired and each CD45.2⁺ partner received 10^5 NR1 T_N cells followed by i.n. UV-*Ct*-cSAP vaccination. Animals in group A were vaccinated 2 weeks after parabiosis, while in group B, vaccination preceded parabiosis by 2 weeks. After another 2 weeks, both partners were challenged with *Ct*. Four days later, infected uteri in both vaccinated and naïve parabiotic animals had recruited substantial numbers of *Ct*-specific NR1 cells (Fig. 7, D and E) that exceeded those recovered from uninfected uteri of vaccinated mice (Figs. 6D and 7B). Uterine NR1 cell recruitment was markedly enhanced in all parabionts in group A, where *Ct*-specific memory cells had been generated after a shared circulation was already established so NR1 T_{RM} cells could seed uteri of both partners (Fig. 7D). By contrast, in group B, parabiosis was performed after the early wave of mucosa-seeding T_{Eff} cells had subsided, so uterus-resident NR1 T_{RM} cells were restricted to the immunized CD45.2⁺ partner (Fig. 7E), whereas circulating memory cells could equilibrate between both partners. Consequently, both parabionts in group A were effectively protected against genital *Ct* challenge (Fig. 7F). By contrast, in group B, only the immunized partners were fully protected, while the bacterial burden in nonimmunized animals, which harbored only circulating NR1 memory cells, were indistinguishable from naïve NR1 recipients (Fig. 7G). Of note, UV-*Ct*-cSAP vaccination induced a robust humoral response against *Ct* (fig. S3A), whereby circulating antibodies are expected to fully equilibrate in parabiotic pairs. The preferential protection of only the vaccinated parabionts in group B suggests that antibodies provided little or no protection in this experimental setting.

Although the above experiments permitted simultaneous assessment of the migratory dynamics

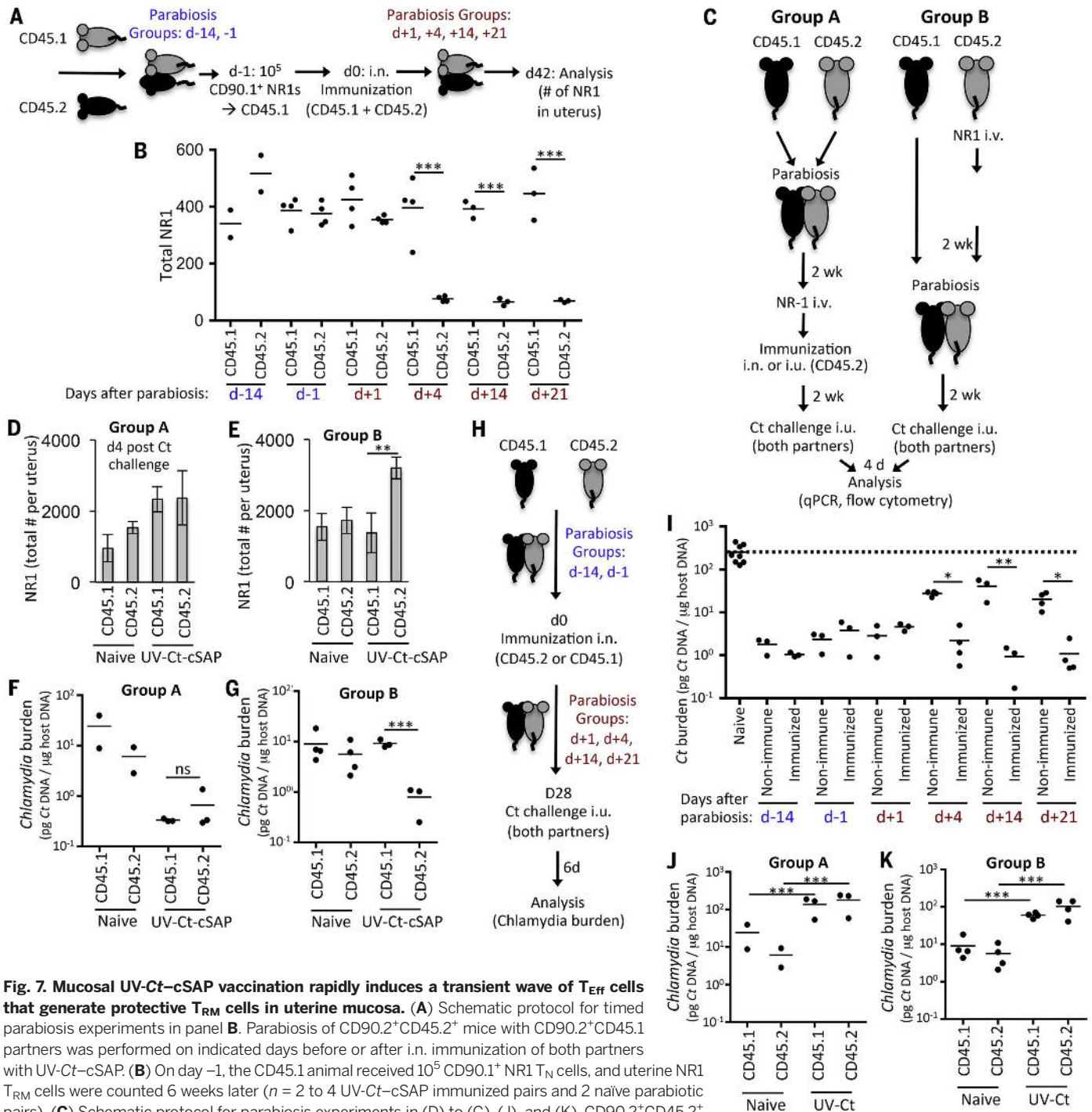
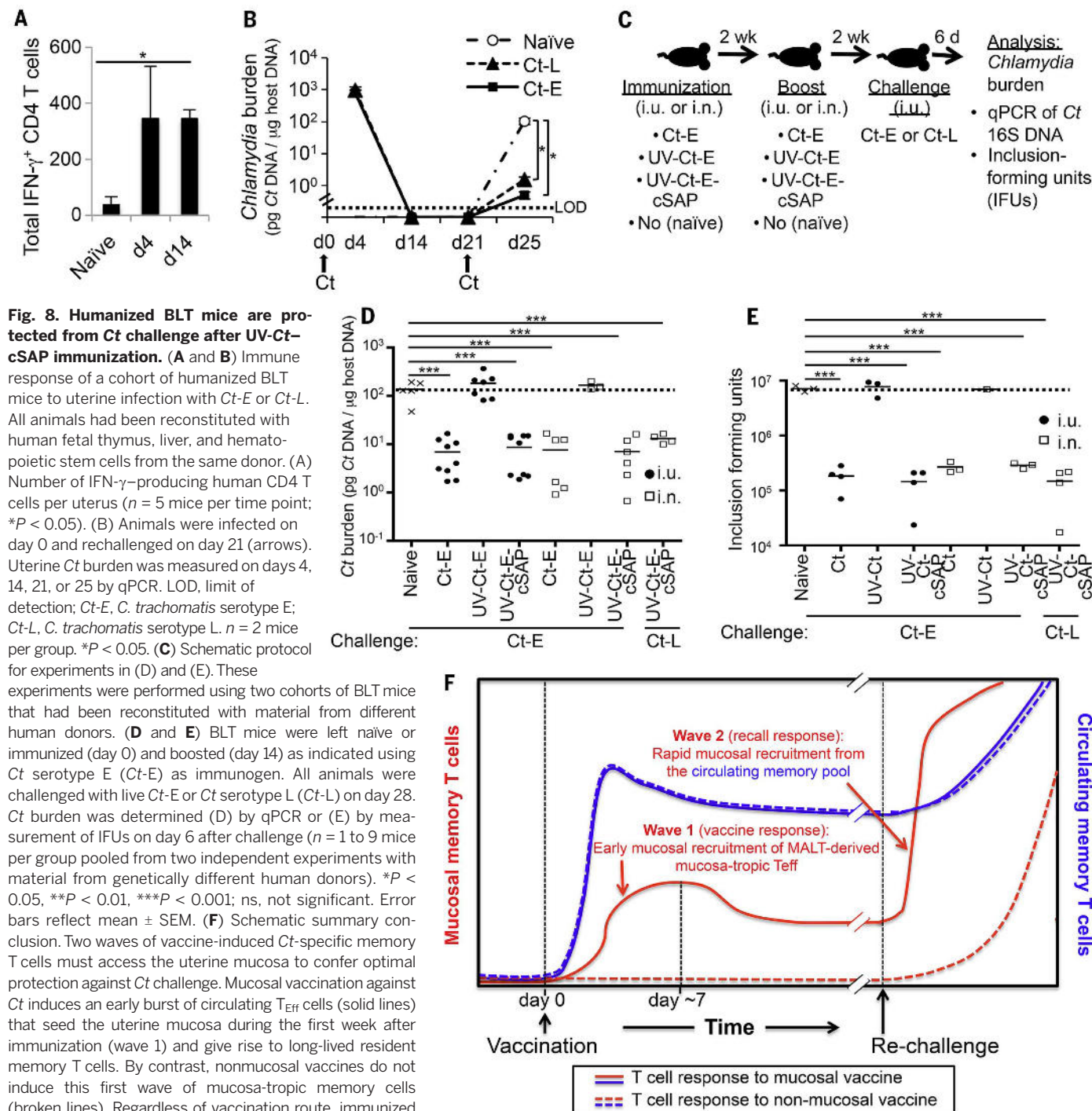


Fig. 7. Mucosal UV-Ct-cSAP vaccination rapidly induces a transient wave of T_{Eff} cells that generate protective T_{RM} cells in uterine mucosa. (A) Schematic protocol for timed parabiosis experiments in panel B. Parabiosis of CD90.2⁺CD45.2⁺ mice with CD90.2⁺CD45.1 partners was performed on indicated days before or after i.n. immunization of both partners with UV-Ct-cSAP. (B) On day -1, the CD45.1 animal received 10^5 CD90.1⁺ NR1 T_N cells, and uterine NR1 T_{RM} cells were counted 6 weeks later ($n = 2$ to 4 UV-Ct-cSAP immunized pairs and 2 naïve parabiotic pairs). (C) Schematic protocol for parabiosis experiments in (D) to (G), (J), and (K). CD90.2⁺CD45.2⁺ mice were immunized with UV-Ct-cSAP i.n. or UV-Ct i.u. 2 weeks before or after parabiosis with a CD90.2⁺CD45.1 partner. 1×10^5 CD90.1⁺ NR1 T_N were adoptively transferred to the CD45.2⁺ animal one day prior to immunization. Animals were either immunized 2 weeks after [group A; (D), (F), (J)] or two weeks before parabiosis surgery [group B; (E), (G), (K)]. $n = 3$ parabiotic pairs immunized with UV-Ct-cSAP or UV-Ct and 2 naïve parabiotic pairs. (D and E) Total number of NR1 cells in the uterus 4 days after Ct challenge ($n = 3$ parabiotic pairs immunized with UV-Ct-cSAP and 2 naïve parabiotic pairs. ** $P < 0.01$). (F and G) Ct burden 4 days after i.u. Ct challenge of both partners in animals that had been conditioned with i.n. UV-Ct-cSAP. (H) Schematic protocol for timed parabiosis experiments in (I). One partner of each CD45.1/CD45.2 congenic pair was randomly chosen to be immunized on day 0 and underwent parabiosis surgery at indicated time points. (I) Both parabionts in each pair ($n = 3$ or 4 per group) were challenged i.u. with Ct on day 28. Nonimmunized parabiotic pairs served as naïve controls ($n = 4$). Ct burden was assessed 6 days after challenge. All groups were significantly different from naïve parabionts ($P < 0.05$; one-way ANOVA followed by Bonferroni posttest.). (J and K) Uterine Ct burden 4 days after both i.u. Ct challenge of parabiotic partners after conditioning with i.n. UV-Ct. *** $P < 0.001$; ns, nonsignificant. Error bars show mean \pm SEM. Unless stated otherwise, statistical differences were assessed using two-tailed t test.

and protective function of *Ct*-specific T cells, the experimental protocol required NR1 T_N cells to be transferred at superphysiologic numbers. To control for potential artifacts of elevated frequencies of *Ct*-specific T cells, we performed timed parabiosis experiments without NR1 cell transfer. To this end, either the CD45.1⁺ or

CD45.2⁺ partner of each congenic pair was immunized before or after parabiosis surgery, and both animals were challenged 4 weeks later with *Ct* i.u. (Fig. 7H). When uterine bacterial burden was assessed 6 days later, both partners were fully protected when parabiosis had been performed on or before day 1 after vaccination

(Fig. 7I). Thus, mucosal UV-*Ct*-cSAP vaccination of animals that could generate both T_{RM} and circulating memory cells elicited similar protection against *Ct* challenge with and without prior adoptive transfer of TCR transgenic NR1 cells and regardless of whether we examined individual mice (compare Fig. 2A and Fig. 6G) or



parabiotic pairs (compare Fig. 7, B and D), indicating that NR-1 cell transfers did not artificially skew the overall vaccine response.

Importantly, when parabiosis was delayed until day 4 or later after vaccination, protection of the nonimmunized parabionts was noticeably compromised. These findings strongly support the notion that mucosal seeding by vaccine-induced T_{RM} cells must occur after day 8 after vaccination (Fig. 7B) and is essential for full-fledged resistance to genital *Ct* challenge. However, even when parabiosis of animals that did not receive NR1 T_N cells was delayed after vaccination until day 4 or later, subsequent *Ct* challenge of nonimmunized partners resulted in significantly lower bacterial burdens than when naïve parabionts were challenged (Fig. 7I). Thus, the circulating memory cells that arose from a polyclonal T cell response provided meaningful, if partial, protection in the absence of T_{RM} cells, while the analogous experiment after adoptive transfer of NR1 T_N failed to reveal protection by circulating memory cells (Fig. 7G). This difference was presumably because conventional naïve mice contain much fewer *Ct*-specific T_N than NR1 cell recipients, allowing the latter to rapidly generate a large burst of T_{Eff} cells after *Ct* challenge that may have masked the activity of circulating memory cells. In aggregate, our results suggest that circulating polyclonal memory T cells that arise after mucosal vaccination can accelerate uterine *Ct* clearance, even in the absence of mucosal T_{RM} cells. However, consistent with the partial protection afforded by adoptive transfer of sensitized splenic CD4 T cells (Fig. 3B), this protective activity is suboptimal.

Mucosal UV-Ct exposure generates suppressive T_{regs} in parabiotic partners

Finally, we examined parabiotic pairs in which the CD45.2⁺ partner had received i.u. conditioning with UV-Ct. Remarkably, both partners displayed similar hypersusceptibility to *Ct* regardless of whether parabiosis was initiated before or after UV-Ct immunization (Figs. 7J, K), indicating that uterus-resident T_{regs} may not be needed for the tolerogenic response to *Ct*. This is in line with observations in a murine colitis model, where tissue-homing of T_{regs} was not required to prevent intestinal inflammation (56).

Mucosal UV-Ct-cSAP vaccination confers protection against *Ct* challenge in humanized mice

The above findings in conventional mice were fully reproducible in two cohorts of BLT mice (57) that had been reconstituted with a human immune system from two unrelated donors (58). Human CD4 T cells in both cohorts mounted a vigorous mucosal T_H1 response to clear uterine infection with two different *Ct* serovars, *Ct-L* and *Ct-E* (Fig. 8, A and B). Moreover, prime-boost vaccination of naïve BLT animals with UV-Ct-cSAP given i.n. or i.u. (Fig. 8C) was highly effective against subsequent i.u. *Ct* challenge, even when BLT mice were challenged with a

different serotype than used for immunization (Fig. 8, D and E).

Conclusion

Using a mucosal immunization strategy, we have dissected the multifaceted adaptive immune mechanisms that control murine host responses against genital *Ct* infection after mucosal vaccination with a vaccine candidate, UV-Ct-cSAP. Our results indicate that optimal protection after *Ct* challenge requires uterine recruitment of two discrete waves of *Ct*-specific CD4 T cells that are inducible in MALT but not in skin-draining LNs (Fig. 8F). After an immunostimulatory mucosal priming event, the first wave is composed of recently activated T_{Eff} cells that give rise to long-lived T_{RM} cells after trafficking to both inflamed and resting mucosal surfaces. This early migratory wave subsides within ~1 week after immunization and depends on a constitutive tissue-specific multistep adhesion cascade (53) involving $\alpha 4$ integrins and presumably other mucosal traffic signals that remain to be identified. Concomitantly, MALT-derived *Ct*-responsive T_{Eff} cells also generate a second population of memory cells that preferentially reside in blood and secondary lymphoid organs. This systemic memory population, which comprises the two classical central and effector memory subsets (59), does not appear to access the resting urogenital mucosa but can be recruited to peripheral tissues (including uterine mucosa) upon the onset of inflammation (60). Although this circulating memory subset contributes to the overall recall response against *Ct*, its protective role is suboptimal in the absence of T_{RM} cells. In an optimally immunized individual, *Ct* infection triggers rapid release of cytokines, particularly IFN- γ , by the mucosal T_{RM} subset, which promotes pathogen clearance (61). This protective effect of uterine T_{RM} may be amplified by their proinflammatory activity that may help recruit circulating memory cells; however, our data show that the tissue-resident memory subset confers substantial protection even when the influx of circulating memory cells is blocked.

Of importance to future *Ct* vaccine trials, our experiments potentially shed light on the decades-old conundrum of how exposure to killed *Ct* in trachoma vaccine trials during the 1960s may have enhanced subsequent *Ct*-induced pathology (25–29). We could provoke a similar hypersusceptibility to *Ct* in our mouse model by exposing mucosal surfaces to UV-Ct, an effect that was due to de novo induction of *Ct*-specific T_{regs} . After conjugating cSAPs to UV-Ct for mucosal immunization, we not only could prevent this tolerogenic effect but also could render mice highly resistant to *Ct* infection—a protective response that was identical in magnitude, longevity, and immunological mechanism to the endogenous memory response against genuine *Ct* infection. Moreover, our findings in BLT mice indicate that human CD4 T cells can also mount a vigorous mucosal T_H1 response to clear uterine *Ct* infection, which suggests that cSAP-based mucosal vaccination

may also elicit protective immune responses in humans. Because cSAPs are fully synthetic and biodegradable nanoparticles that are easily manufactured and well tolerated, they may also offer a powerful and versatile approach for mucosal vaccine development against other challenging pathogens.

Materials and methods

Mice

C57BL/6 and BALB/c mice, 6 to 8 weeks old, were purchased from Charles River or The Jackson Laboratory. B6.129S2-H2^{dAb1-Ea}/J (referred to as MHC class II^{−/−}) (48), *CD8*^{−/−}, μ Mt, *Il10*^{−/−}, *Rag2*^{−/−}, and C57BL/6 B6.SJL Ptprca Pep3b/BoyJ (CD45.1⁺) mice were purchased from The Jackson Laboratory and used at 6 to 12 weeks of age. CD90.1 NR1 mice (TCR tg mice with specificity for the CD4⁺ T cell antigen *Cta1* from *Ct*) were bred in-house. For some experiments, we crossed NR1 and Foxp3eGFP mice (62). For characterization of uterine APC subsets, CXCR3^{GFP/+} mice (63) were used. BLT mice were generated in the MGH Humanized Mouse Program by transplanting irradiated *NOD/SCID*/ γ *c*^{−/−} mice with human fetal liver stem cells and autologous thymic grafts (57). Reconstituted mice developed a fully human lymphoid compartment within ~13 to 18 weeks after reconstitution, at which stage they were used for immunization or vaccination studies. All experiments were performed in accordance with NIH guidelines and approved by the Institutional Animal Committees of Harvard Medical School and MGH.

Chlamydia infection and detection

Ct serovar L2 (434/Bu), referred to as *Ct*, or serovar E (*Ct-E*) or *C. muridarum* (*Cm*) were propagated in McCoy cell monolayers grown in Eagle's MEM (Invitrogen, Grand Island, NY) supplemented with 10% FCS, sodium bicarbonate (1.5 g/liter), 0.1 M nonessential amino acids, and 1 mM sodium pyruvate, as described (41). Aliquots were stored at −80°C in medium containing 250 mM sucrose, 10 mM sodium phosphate, and 5 mM L-glutamic acid and were thawed immediately before use. All mice were treated with 2.5 μ g of medroxyprogesterone s.c. 7 days before immunization to normalize the murine estrous cycle. For UV inactivation, *Ct* or *Cm* suspensions were placed under a UV lamp (15 W) at a distance of 30 cm for 30 min. The efficiency of UV inactivation was always tested by infecting McCoy cell monolayers with an aliquot of UV-inactivated *Ct* and evaluation of inclusion-forming units. Briefly, 30 hours after infection, the medium was removed, and cells were fixed in ice-cold methanol and permeabilized in PBS with 0.05% tween. Cells were then stained with 10 μ l of anti-MOMP antibody and Evans blue counterstain (Pathfinder Diagnostic Kit BioRad) for 1 hour and were then washed three times in PBS-tween. Inclusion-forming units were not observed after UV inactivation of *Ct* or *Cm*.

Intrauterine immunization and challenge were conducted transscervically using an NSET

device (ParaTechs) as described (31). Briefly, 10 μ l of sucrose-phosphate-glutamate medium containing 10^6 Ct or UV-Ct \pm cSAP was placed into the uterus using the NSET pipet tip through the NSET speculum. Subcutaneous immunization was done with a U-100 insulin syringe injecting 10 μ l of sucrose-phosphate-glutamate medium containing 10^5 Ct or UV-Ct \pm cSAP. As 10^6 Ct were lethal for mice when deposited intranasally, i.n. immunization was performed with 10^5 Ct in 10 μ l of sucrose-phosphate-glutamate medium. Cm was administered intravaginally as described previously (6).

To quantify the levels of Ct in tissues, we usually used qPCR with 16S primers specific for Ct, as described previously (64). Briefly, DNA was isolated from uterus homogenates using the QIAamp DNA mini kit (Qiagen). Mouse GAPDH DNA and *Chlamydia* 16S DNA were quantified by qPCR on an ABI Prism 7000 sequence detection system. Using standard curves from known amounts of Ct and mouse DNA, the amount of *Chlamydia* DNA (in pg) per unit weight of mouse DNA (in μ g) was calculated to assess bacterial burden.

Titers of inclusion-forming units were determined in two experiments. Mouse uteri were disrupted using a tissue homogenizer and frozen at -80°C . Aliquots were thawed, and tenfold dilutions of each sample were made in a 96-well plate. Each dilution was then used to infect a confluent monolayer of McCoy cells in a 96-well plate by centrifugation for 1 hour at 37°C . Two hours after centrifugation, medium was supplemented with gentamicin (25 $\mu\text{g}/\text{ml}$) to prevent contamination. Thirty hours after infection, the media was removed, and cells were fixed in ice-cold methanol and permeabilized in PBS with 0.05% tween. Cells were then stained with 10 μ l of anti-MOMP antibody and Evans blue counterstain (Pathfinder Diagnostic Kit BioRad) for 1 hour and then were washed three times in PBS-tween. Total inclusions in each sample were then enumerated by fluorescence microscopy, with at least three fields being counted per sample.

The impact of the cSAP constructs on chlamydia-induced pathology of the upper genital tract was measured 4 weeks after Cm challenge of immunized mice and naïve controls. Gross pathology was scored by hydrosalpinx development as follows: 0: normal; 1: low-level fluid in oviduct; 2: moderate amount of fluid present; 3: high level of fluid.

Vaccine formulation

Synthesis of polymers and formulation of synthetic nanoparticles (SPs) was performed as described previously (32) with minor modifications. Briefly, the triblock copolymer poly(D,L-lactic-co-glycolic acid)-*b*-poly(L-histidine)-*b*-poly(ethylene glycol) (PLGA-PLH-PEG, referred to as charge-switching synthetic particles, cSPs) was synthesized using a polymer end grafting strategy. Control SPs that lacked the PLH block were formulated in a similar manner using PLGA-PEG copolymers. R848-PLA was synthesized by ring-opening polymerization (33). All SPs were formulated using a modified emulsion/solvent evaporation technique.

R848-PLA was added in a 0.4:0.4:0.2 (R848-PLA: PLGA-PLH-PEG:PLGA-PEG) ratio. The polymer-containing ethyl acetate solution was sonicated into 2 ml of pure water using a probe tip sonicator (Misonix Sonicator S-4000, Farmingdale, NY) for 30 s in continuous mode at 40% amplitude and then diluted into 8 ml of pure water under magnetic stirring in a fume hood. The solvent was allowed to evaporate for at least 2 hours, at which point SPs were collected and purified by repeated ultrafiltration using Amicon Ultra-4 100,000 NMWL cutoff filters (Millipore, Billerica, MA). The sizes of Ct-SP constructs were determined by dynamic light scattering on a Zetasizer Nano (Malvern Instruments).

SAPs, cSAPs, and cSPs were prepared, purified, and then resuspended in a dilute pH 6.0 solution, and 2×10^7 UV-Ct were added per mg SPs. This mixture was then incubated at 37°C for at least 30 min in the dark under gentle shaking. To determine SP conjugation to the surface of UV-Ct, Ct was labeled with BacLight (Life Technologies, absorption maximum 581, emission maximum 644) and PLGA-AF488, synthesized using ring-opening polymerization, was blended in to the SPs prior to conjugation with bacteria and analyzed with flow cytometry.

Tissue digestion, flow cytometry, and cell sorting

Spleens, lungs, lymph nodes, and livers were cut into small pieces with a sterile scalpel and passed through 40- μm mesh filters. Uteri were digested with type XI collagenase (Sigma, St Louis, MO) and DNase I (Sigma) for 30 min at 37°C before passing through 40- μm filters. Samples were enriched for lymphocytes by density-gradient centrifugation with NycoPrep 1.077 according to the manufacturer's protocol (Axis-Shield).

For flow cytometry analysis or cell sorting, T cells were stained with anti-CD3e (145-2C11; BioLegend), anti-CD4 (RM4-5; BioLegend), anti-CD90.1 (OX-7; BioLegend), anti-CD25 (PC61; BioLegend), anti- $\text{V}\alpha 2$ (B20.1; BioLegend), anti-V $\beta 8.3$ (1B3.3; BD Biosciences), anti-CD45.1 (104; BioLegend), or anti-CD45.2 (A20; BioLegend). T cell proliferation was measured by anti-K $_k$ -67 (16A8; BioLegend) staining and overnight bromodeoxyuridine (BrdU) labeling according to the manufacturer's protocol (Life Technologies). DCs were characterized and/or sorted with anti-MHC class II (AF6-120.1; BioLegend), anti-F4/80 (BM8; BioLegend), anti-CD103 (2E7; BioLegend), anti-CD11c (N418; BioLegend), anti-CD11b (M1/70; BioLegend), anti-CD207 (eBioL31; eBioscience), anti-CD301b (URA-1; BioLegend), anti-CD80 (16-10A1; BioLegend), anti-CD86 (GL-1; BioLegend), anti-CD274 (PD-L1) (10F.9G2; BioLegend), anti-CD273 (PD-L2) (TY25; BioLegend), anti-IL-10 (JES5-16E3; BioLegend), and anti-IL-12/IL-23 (C15.6; BioLegend). For intracellular T cell cytokine staining, autologous sorted splenic CD11c $^+$ DCs were pulsed with UV-inactivated EBs for 30 min, washed extensively, and added to T cells for 5 hours in the presence of brefeldin A (GolgiStop; BD Biosciences). T cells were stained for anti-IFN- γ (XMG1.2; BioLegend), anti-IL-2 (JES6-5H4; BioLegend), and

anti-TNF- α (MP6-XT22; BioLegend) Abs after permeabilization with the Cytofix/Cytoperm Plus Kit according to the manufacturer's instructions (BD Biosciences). The absolute cell number in each sample was determined using AccuCheck Counting Beads (Invitrogen). Data were collected on a FACSCanto (BD Biosciences) or a LSRII (BD Biosciences) and analyzed using FlowJo 9.3.2. A FACSaria (BD) was used for cell sorting with Diva software, and purity was $>98\%$ for all experiments.

Adoptive transfer of leukocyte subsets

Lymph nodes and spleens were collected from naïve female CD90.1 $^+$ NR1 mice and purified by negative immunomagnetic cell sorting using a mouse CD4 $^+$ T cell isolation kit ($\sim 98\%$ CD4 $^+$, Miltenyi Biotec). Purity was verified with anti-CD4, anti- $\text{V}\alpha 2$, and anti-V $\beta 8.3$ stainings. For some experiments, FoxP3 $^{\text{eGFP}}$ NR1 cells were depleted before adoptive transfer of FoxP3 $^{\text{eGFP}}$ NR1 cells by cell sorting. 10^5 isolated NR1 cells (unless noted otherwise) were intravenously transferred to naïve recipient mice 1 day prior to immunization. In proliferation experiments, NR1 cells were labeled with carboxyfluorescein succinimidyl ester (CFSE) before transfer. For adoptive transfer of polyclonal CD4 $^+$ and CD8 $^+$ T cells and T cell-depleted leukocytes, cell subsets from immunized mice were harvested from donor spleens by immunomagnetic cell sorting (Miltenyi Biotec), and 10^7 cells were transferred to naïve recipients.

NR1 T cell stimulation by APCs

APCs were isolated from single-cell suspensions of uterus and draining LNs 18 and 24 hours after immunization, respectively. CD45 $^+$ MHC class II $^+$ cells were FACS sorted based on their CD103 and F4/80 expression (CD103 $^+$ F4/80 $^+$ macrophages, CD103 $^+$ F4/80 $^-$ DCs, and CD103 $^-$ F4/80 $^-$ DCs). Sorted cells were either subjected to qPCR analysis for Ct 16S content or cocultured with CFSE-labeled NR1 cells for 3 days (500 DCs and 5000 NR1 cells). For in vivo assessment of APC function, naïve mice received 10^5 CFSE-labeled NR1 cells i.v. followed one day later by s.c. injection into the right footpad of 5000 sorted APCs. CFSE dilution of NR1 cells in the right popliteal LN was analyzed 3 days later.

In vivo mAb treatment

Two hundred fifty μg anti-CD25 (PC61) mAb or control IgG were administered intraperitoneally at days -3 and $+3$ of uterine Ct challenge. Anti- $\alpha 4$ mAb (PS/2) or control IgG was administered i.v. at day 3 (100 μg) and every second day (50 μg) until day 11 thereafter. On d9, mice were challenged i.u. with 10^5 IFU of Ct.

Parabiosis

Parabiosis surgery was performed as previously described (55). Briefly, sex- and weight-matched congenic partners were anaesthetized with ketamine (100 mg/kg body weight) and xylazine (10 mg/kg body weight) by i.p. injection. The corresponding lateral aspects of mice were shaved, and the excess hair was wiped off with an alcohol prep pad.

Two matching skin incisions were made from the olecranon to the knee joint of each mouse, and the subcutaneous fascia was bluntly dissected to create about 0.5 cm of free skin. The olecranon and knee joints were attached by a double 4-0 braided silk suture and tied, and the dorsal and ventral skins were approximated by staples or continuous 6-0 braided silk suture. The mice were then kept on heating pads and continuously monitored until recovery. Flunixin ($2.5 \mu\text{g g}^{-1}$) and buprenorphine (0.05 to 0.1 mg/kg body weight) were used for analgesic treatment by subcutaneous injection after the operation. After 3 days to 2 weeks, chimerism of leukocytes from the blood was monitored to ensure equivalent blood exchange between parabiotic partners. Depending on the readout of the experiments, either one of the partners was immunized with UV-Ct-cSAP i.n. or UV-Ct i.u. and both were challenged with Ct i.u., or 10^5 NR1 cells were i.v. injected the day before immunization with UV-Ct-cSAP i.n. without further challenge.

Anti-Ct Ab ELISA

Antibody levels were determined by enzyme-linked immunosorbent assays (ELISA) using a mouse Ct antibody ELISA Kit (MyBioSource). Mice were bled 4 weeks after immunization in order to assess antibody levels.

Confocal and electron microscopy

Uterine tissue was incubated overnight in phosphate-buffered L-lysine with 1% paraformaldehyde/periodate and then cryoprotected by subsequent incubations in 10%, 20%, and 30% sucrose in PBS at room temperature, snap-frozen in TBS tissue-freezing liquid (Triangle Biomedical Sciences), and stored at -80°C . Sections of 30- μm thickness were mounted on Superfrost Plus slides (Fisherbrand) and stained with anti-CD90.1 PE (OX-7, BD Biosciences), anti-CD326 FITC (G8.8; BioLegend), and anti-CD31 (390, BioLegend) in a humidified chamber after Fc receptor blockade with antibody 2.4G2 (BD Pharmingen, $1 \mu\text{g/ml}$). Samples were mounted in FluorSave reagent solution (EMD-Calbiochem) and stored at 4°C until analysis. Images were acquired with an Olympus Fluoview BX50WI inverted microscope and were analyzed by using Velocity software (Improvision).

Transmission electron microscopy (TEM) samples were prepared using the Gatan Cryo-Plunge3 and imaged using a JEOL 2100 FEG electron microscope.

Statistical analysis

Statistical significance was determined between two groups with two-tailed *t*-test. Statistical differences among three or more groups were assessed using one-way or two-way analysis of variance (ANOVA) followed by Bonferroni posttest to account for multiple comparisons. Significance was set at a *P* value of less than 0.05.

REFERENCES AND NOTES

- H. Holmgren, A. M. Svennerholm, Vaccines against mucosal infections. *Curr. Opin. Immunol.* **24**, 343–353 (2012). doi: [10.1016/j.coi.2012.03.014](https://doi.org/10.1016/j.coi.2012.03.014); pmid: [22580196](https://pubmed.ncbi.nlm.nih.gov/22580196/)
- J. R. Mora *et al.*, Selective imprinting of gut-homing T cells by Peyer's patch dendritic cells. *Nature* **424**, 88–93 (2003). doi: [10.1038/nature01726](https://doi.org/10.1038/nature01726); pmid: [12840763](https://pubmed.ncbi.nlm.nih.gov/12840763/)
- J. R. Mora *et al.*, Generation of gut-homing IgA-secreting B cells by intestinal dendritic cells. *Science* **314**, 1157–1160 (2006). doi: [10.1126/science.1132742](https://doi.org/10.1126/science.1132742); pmid: [17110582](https://pubmed.ncbi.nlm.nih.gov/17110582/)
- H. Sigmundsdottir *et al.*, DCs metabolize sunlight-induced vitamin D3 to 'program' T cell attraction to the epidermal chemokine CCL27. *Nat. Immunol.* **8**, 285–293 (2007). doi: [10.1038/ni1433](https://doi.org/10.1038/ni1433); pmid: [17259988](https://pubmed.ncbi.nlm.nih.gov/17259988/)
- D. Guy-Grand, C. Griscelli, P. Vassalli, The mouse gut T lymphocyte, a novel type of T cell. Nature, origin, and traffic in mice in normal and graft-versus-host conditions. *J. Exp. Med.* **148**, 1661–1677 (1978). doi: [10.1084/jem.148.6.1661](https://doi.org/10.1084/jem.148.6.1661); pmid: [31410](https://pubmed.ncbi.nlm.nih.gov/31410/)
- A. Kantele, J. Zivny, M. Hakkinen, C. O. Elson, J. Mestecky, Differential homing commitments of antigen-specific T cells after oral or parenteral immunization in humans. *J. Immunol.* **162**, 5173–5177 (1999). pmid: [10227989](https://pubmed.ncbi.nlm.nih.gov/10227989/)
- D. J. Campbell, E. C. Butcher, Rapid acquisition of tissue-specific homing phenotypes by CD4⁺ T cells activated in cutaneous or mucosal lymphoid tissues. *J. Exp. Med.* **195**, 135–141 (2002). doi: [10.1084/jem.20011502](https://doi.org/10.1084/jem.20011502); pmid: [11781372](https://pubmed.ncbi.nlm.nih.gov/11781372/)
- J. M. Schenkel, K. A. Fraser, V. Vezys, D. Masopust, Sensing and alarm function of resident memory CD8⁺ T cells. *Nat. Immunol.* **14**, 509–513 (2013). doi: [10.1038/ni.2568](https://doi.org/10.1038/ni.2568); pmid: [23542740](https://pubmed.ncbi.nlm.nih.gov/23542740/)
- J. M. Schenkel *et al.*, T cell memory. Resident memory CD8 T cells trigger protective innate and adaptive immune responses. *Science* **346**, 98–101 (2014). doi: [10.1126/science.1254536](https://doi.org/10.1126/science.1254536); pmid: [25170049](https://pubmed.ncbi.nlm.nih.gov/25170049/)
- T. Gebhardt *et al.*, Memory T cells in nonlymphoid tissue that provide enhanced local immunity during infection with herpes simplex virus. *Nat. Immunol.* **10**, 524–530 (2009). doi: [10.1038/ni.1718](https://doi.org/10.1038/ni.1718); pmid: [19305395](https://pubmed.ncbi.nlm.nih.gov/19305395/)
- T. Bergsbaken, M. J. Bevan, Proinflammatory microenvironments within the intestine regulate the differentiation of tissue-resident CD8⁺ T cells responding to infection. *Nat. Immunol.* **16**, 406–414 (2015). doi: [10.1038/ni.3108](https://doi.org/10.1038/ni.3108); pmid: [25706747](https://pubmed.ncbi.nlm.nih.gov/25706747/)
- J. Bienenstock, The mucosal immunologic network. *Ann. Allergy* **53**, 535–540 (1984). pmid: [6391284](https://pubmed.ncbi.nlm.nih.gov/6391284/)
- W. S. Gallichan, K. L. Rosenthal, Long-lived cytotoxic T lymphocyte memory in mucosal tissues after mucosal but not systemic immunization. *J. Exp. Med.* **184**, 1879–1890 (1996). doi: [10.1084/jem.184.5.1879](https://doi.org/10.1084/jem.184.5.1879); pmid: [8920875](https://pubmed.ncbi.nlm.nih.gov/8920875/)
- M. Santosuosso *et al.*, Mechanisms of mucosal and parenteral tuberculosis vaccinations: Adenoviral-based mucosal immunization preferentially elicits sustained accumulation of immune protective CD4 and CD8 T cells within the airway lumen. *J. Immunol.* **174**, 7986–7994 (2005). doi: [10.4049/jimmunol.174.12.7986](https://doi.org/10.4049/jimmunol.174.12.7986); pmid: [15944305](https://pubmed.ncbi.nlm.nih.gov/15944305/)
- H. K. Lee *et al.*, Differential roles of migratory and resident DCs in T cell priming after mucosal or skin HSV-1 infection. *J. Exp. Med.* **206**, 359–370 (2009). doi: [10.1084/jem.20080601](https://doi.org/10.1084/jem.20080601); pmid: [19153243](https://pubmed.ncbi.nlm.nih.gov/19153243/)
- H. Shin, A. Iwasaki, A vaccine strategy that protects against genital herpes by establishing local memory T cells. *Nature* **491**, 463–467 (2012). doi: [10.1038/nature11522](https://doi.org/10.1038/nature11522); pmid: [23075848](https://pubmed.ncbi.nlm.nih.gov/23075848/)
- N. Lycke, Recent progress in mucosal vaccine development: Potential and limitations. *Nat. Rev. Immunol.* **12**, 592–605 (2012). doi: [10.1038/nri3251](https://doi.org/10.1038/nri3251); pmid: [22828912](https://pubmed.ncbi.nlm.nih.gov/22828912/)
- F. W. van Ginkel *et al.*, Enterotoxin-based mucosal adjuvants alter antigen trafficking and induce inflammatory responses in the nasal tract. *Infect. Immun.* **73**, 6892–6902 (2005). doi: [10.1128/IAI.73.10.6892-6902.2005](https://doi.org/10.1128/IAI.73.10.6892-6902.2005); pmid: [16177369](https://pubmed.ncbi.nlm.nih.gov/16177369/)
- L. B. Lawson, E. B. Norton, J. D. Clements, Defending the mucosa: Adjuvant and carrier formulations for mucosal immunity. *Curr. Opin. Immunol.* **23**, 414–420 (2011). doi: [10.1016/j.coi.2011.03.009](https://doi.org/10.1016/j.coi.2011.03.009); pmid: [21511452](https://pubmed.ncbi.nlm.nih.gov/21511452/)
- R. Belland, D. M. Ojcius, G. I. Byrne, Chlamydia. *Nat. Rev. Microbiol.* **2**, 530–531 (2004). doi: [10.1038/nrmicro931](https://doi.org/10.1038/nrmicro931); pmid: [15248311](https://pubmed.ncbi.nlm.nih.gov/15248311/)
- C. L. Satterwhite *et al.*, Sexually transmitted infections among US women and men: Prevalence and incidence estimates, 2008. *Sex. Transm. Dis.* **40**, 187–193 (2013). doi: [10.1097/OLQ.0b013e318286bb53](https://doi.org/10.1097/OLQ.0b013e318286bb53); pmid: [23403598](https://pubmed.ncbi.nlm.nih.gov/23403598/)
- I. J. Bakken, Chlamydia trachomatis and ectopic pregnancy: Recent epidemiological findings. *Curr. Opin. Infect. Dis.* **21**, 77–82 (2008). doi: [10.1097/QCO.0b013e318282f3d7](https://doi.org/10.1097/QCO.0b013e318282f3d7); pmid: [18192790](https://pubmed.ncbi.nlm.nih.gov/18192790/)
- V. H. Hu, M. J. Holland, M. J. Burton, Trachoma: Protective and pathogenic ocular immune responses to Chlamydia trachomatis. *PLOS Negl. Trop. Dis.* **7**, e2020 (2013). doi: [10.1371/journal.pntd.0002020](https://doi.org/10.1371/journal.pntd.0002020); pmid: [23457650](https://pubmed.ncbi.nlm.nih.gov/23457650/)
- D. C. Mabey, V. Hu, R. L. Bailey, M. J. Burton, M. J. Holland, Towards a safe and effective chlamydial vaccine: Lessons from the eye. *Vaccine* **32**, 1572–1578 (2014). doi: [10.1016/j.vaccine.2013.10.016](https://doi.org/10.1016/j.vaccine.2013.10.016); pmid: [24606636](https://pubmed.ncbi.nlm.nih.gov/24606636/)
- J. T. Grayston, R. L. Woolridge, S. Wang, Trachoma vaccine studies on Taiwan. *Ann. N.Y. Acad. Sci.* **98**, 352–367 (1962). doi: [10.1111/j.1749-6632.1962.tb30558.x](https://doi.org/10.1111/j.1749-6632.1962.tb30558.x); pmid: [13901337](https://pubmed.ncbi.nlm.nih.gov/13901337/)
- R. L. Woolridge *et al.*, Field trial of a monovalent and of a bivalent mineral oil adjuvant trachoma vaccine in Taiwan school children. *Am. J. Ophthalmol.* **63** (suppl.), 1645–1650 (1967). doi: [10.1016/0002-9394\(67\)94158-X](https://doi.org/10.1016/0002-9394(67)94158-X); pmid: [6067317](https://pubmed.ncbi.nlm.nih.gov/6067317/)
- R. L. Nichols, S. D. Bell Jr., N. A. Haddad, A. A. Bobb, Studies on trachoma. VI. Microbiological observations in a field trial in Saudi Arabia of bivalent trachoma vaccine at three dosage levels. *Am. J. Trop. Med. Hyg.* **18**, 723–730 (1969). pmid: [4897605](https://pubmed.ncbi.nlm.nih.gov/4897605/)
- R. L. Nichols, S. D. Bell Jr., E. S. Murray, N. A. Haddad, A. A. Bobb, Studies on trachoma. V. Clinical observations in a field trial of bivalent trachoma vaccine at three dosage levels in Saudi Arabia. *Am. J. Trop. Med. Hyg.* **15**, 639–647 (1966). pmid: [5941182](https://pubmed.ncbi.nlm.nih.gov/5941182/)
- S. Sowa, J. Sowa, L. H. Collier, W. A. Blyth, Trachoma vaccine field trials in The Gambia. *J. Hyg.* **67**, 699–717 (1969). doi: [10.1017/S0022172400042157](https://doi.org/10.1017/S0022172400042157); pmid: [5261212](https://pubmed.ncbi.nlm.nih.gov/5261212/)
- J. Schachter, Overview of Chlamydia trachomatis infection and the requirements for a vaccine. *Rev. Infect. Dis.* **7**, 713–716 (1985). pmid: [3840910](https://pubmed.ncbi.nlm.nih.gov/3840910/)
- D. C. Gondek, A. J. Olive, G. Stary, M. N. Starnbach, CD4⁺ T cells are necessary and sufficient to confer protection against Chlamydia trachomatis infection in the murine upper genital tract. *J. Immunol.* **189**, 2441–2449 (2012). doi: [10.4049/jimmunol.1103032](https://doi.org/10.4049/jimmunol.1103032); pmid: [22855710](https://pubmed.ncbi.nlm.nih.gov/22855710/)
- A. F. Radovic-Moreno *et al.*, Surface charge-switching polymeric nanoparticles for bacterial cell wall-targeted delivery of antibiotics. *ACS Nano* **6**, 4279–4287 (2012). doi: [10.1021/nr3008383](https://doi.org/10.1021/nr3008383); pmid: [22471841](https://pubmed.ncbi.nlm.nih.gov/22471841/)
- P. O. Ilyinskii *et al.*, Adjuvant-carrying synthetic vaccine particles augment the immune response to encapsulated antigen and exhibit strong local immune activation without inducing systemic cytokine release. *Vaccine* **32**, 2882–2895 (2014). doi: [10.1016/j.vaccine.2014.02.027](https://doi.org/10.1016/j.vaccine.2014.02.027); pmid: [24593999](https://pubmed.ncbi.nlm.nih.gov/24593999/)
- B. E. Batteiger, F. Xu, R. E. Johnson, M. L. Rekart, Protective immunity to Chlamydia trachomatis genital infection: Evidence from human studies. *J. Infect. Dis.* **201** (suppl. 2), S178–S189 (2010). doi: [10.1086/652400](https://doi.org/10.1086/652400); pmid: [20524235](https://pubmed.ncbi.nlm.nih.gov/20524235/)
- W. M. Geisler, S. Y. Lensing, C. G. Press, E. W. Hook 3rd, Spontaneous resolution of genital Chlamydia trachomatis infection in women and protection from reinfection. *J. Infect. Dis.* **207**, 1850–1856 (2013). doi: [10.1093/infdis/jit094](https://doi.org/10.1093/infdis/jit094); pmid: [23470847](https://pubmed.ncbi.nlm.nih.gov/23470847/)
- R. C. Brunham, Immunity to Chlamydia trachomatis. *J. Infect. Dis.* **207**, 1796–1797 (2013). doi: [10.1093/infdis/jit095](https://doi.org/10.1093/infdis/jit095); pmid: [23470849](https://pubmed.ncbi.nlm.nih.gov/23470849/)
- R. C. Brunham, J. Rey-Ladino, Immunology of Chlamydia infection: Implications for a Chlamydia trachomatis vaccine. *Nat. Rev. Immunol.* **5**, 149–161 (2005). doi: [10.1038/nri1551](https://doi.org/10.1038/nri1551); pmid: [15688042](https://pubmed.ncbi.nlm.nih.gov/15688042/)
- C. M. Farris, R. P. Morrison, Vaccination against Chlamydia genital infection utilizing the murine C. muridarum model. *Infect. Immun.* **79**, 986–996 (2011). doi: [10.1128/IAI.00881-10](https://doi.org/10.1128/IAI.00881-10); pmid: [21078844](https://pubmed.ncbi.nlm.nih.gov/21078844/)
- R. A. Hawkins, R. G. Rank, K. A. Kelly, Expression of mucosal homing receptor $\alpha 4\beta 7$ is associated with enhanced migration to the Chlamydia-infected murine genital mucosa in vivo. *Infect. Immun.* **68**, 5587–5594 (2000). doi: [10.1128/IAI.68.10.5587-5594.2000](https://doi.org/10.1128/IAI.68.10.5587-5594.2000); pmid: [10992458](https://pubmed.ncbi.nlm.nih.gov/10992458/)
- N. R. Roan, T. M. Gierahn, D. E. Higgins, M. N. Starnbach, Monitoring the T cell response to genital tract infection. *Proc. Natl. Acad. Sci. U.S.A.* **103**, 12069–12074 (2006). doi: [10.1073/pnas.0603866103](https://doi.org/10.1073/pnas.0603866103); pmid: [16880389](https://pubmed.ncbi.nlm.nih.gov/16880389/)
- A. J. Olive, D. C. Gondek, M. N. Starnbach, CXCR3 and CCR5 are both required for T cell-mediated protection against C. trachomatis infection in the murine genital mucosa. *Mucosal Immunol.* **4**, 208–216 (2011). doi: [10.1038/mi.2010.58](https://doi.org/10.1038/mi.2010.58); pmid: [20844481](https://pubmed.ncbi.nlm.nih.gov/20844481/)
- S. G. Morrison, R. P. Morrison, A predominant role for antibody in acquired immunity to chlamydial genital tract reinfection. *J. Immunol.* **175**, 7536–7542 (2005). doi: [10.4049/jimmunol.175.11.7536](https://doi.org/10.4049/jimmunol.175.11.7536); pmid: [16301662](https://pubmed.ncbi.nlm.nih.gov/16301662/)
- L. X. Li, S. J. McSorley, B cells enhance antigen-specific CD4 T cell priming and prevent bacteria dissemination following

- Chlamydia muridarum* genital tract infection. *PLOS Pathog.* **9**, e1003707 (2013). doi: [10.1371/journal.ppat.1003707](https://doi.org/10.1371/journal.ppat.1003707); pmid: [24204262](https://pubmed.ncbi.nlm.nih.gov/24204262/)
44. R. C. Brunham, C. C. Kuo, L. Cles, K. K. Holmes, Correlation of host immune response with quantitative recovery of *Chlamydia trachomatis* from the human endocervix. *Infect. Immun.* **39**, 1491–1494 (1983). pmid: [6840846](https://pubmed.ncbi.nlm.nih.gov/6840846/)
 45. T. Moore *et al.*, Fc receptor-mediated antibody regulation of T cell immunity against intracellular pathogens. *J. Infect. Dis.* **188**, 617–624 (2003). pmid: [12898452](https://pubmed.ncbi.nlm.nih.gov/12898452/)
 46. C. M. Farris, S. G. Morrison, R. P. Morrison, CD4⁺ T cells and antibody are required for optimal major outer membrane protein vaccine-induced immunity to *Chlamydia muridarum* genital infection. *Infect. Immun.* **78**, 4374–4383 (2010). doi: [10.1128/IAI.00622-10](https://doi.org/10.1128/IAI.00622-10); pmid: [20660610](https://pubmed.ncbi.nlm.nih.gov/20660610/)
 47. D. F. Tifrea, P. Ralli-Jain, S. Pal, L. M. de la Maza, Vaccination with the recombinant major outer membrane protein elicits antibodies to the constant domains and induces cross-serovar protection against intranasal challenge with *Chlamydia trachomatis*. *Infect. Immun.* **81**, 1741–1750 (2013). doi: [10.1128/IAI.00734-12](https://doi.org/10.1128/IAI.00734-12); pmid: [23478318](https://pubmed.ncbi.nlm.nih.gov/23478318/)
 48. L. Madsen *et al.*, Mice lacking all conventional MHC class II genes. *Proc. Natl. Acad. Sci. U.S.A.* **96**, 10338–10343 (1999). doi: [10.1073/pnas.96.18.10338](https://doi.org/10.1073/pnas.96.18.10338); pmid: [10468609](https://pubmed.ncbi.nlm.nih.gov/10468609/)
 49. C. L. Scott, A. M. Aumeunier, A. M. Mowat, Intestinal CD103⁺ dendritic cells: Master regulators of tolerance? *Trends Immunol.* **32**, 412–419 (2011). doi: [10.1016/j.it.2011.06.003](https://doi.org/10.1016/j.it.2011.06.003); pmid: [21816673](https://pubmed.ncbi.nlm.nih.gov/21816673/)
 50. E. Mazzini, L. Massimiliano, G. Penna, M. Rescigno, Oral tolerance can be established via gap junction transfer of fed antigens from CX3CR1⁺ macrophages to CD103⁺ dendritic cells. *Immunity* **40**, 248–261 (2014). doi: [10.1016/j.immuni.2013.12.012](https://doi.org/10.1016/j.immuni.2013.12.012); pmid: [24462723](https://pubmed.ncbi.nlm.nih.gov/24462723/)
 51. J. R. McDole *et al.*, Goblet cells deliver luminal antigen to CD103⁺ dendritic cells in the small intestine. *Nature* **483**, 345–349 (2012). doi: [10.1038/nature10863](https://doi.org/10.1038/nature10863); pmid: [22422267](https://pubmed.ncbi.nlm.nih.gov/22422267/)
 52. G. Matteoli *et al.*, Gut CD103⁺ dendritic cells express indoleamine 2,3-dioxygenase which influences T regulatory/ T effector cell balance and oral tolerance induction. *Gut* **59**, 595–604 (2010). doi: [10.1136/gut.2009.185108](https://doi.org/10.1136/gut.2009.185108); pmid: [20427394](https://pubmed.ncbi.nlm.nih.gov/20427394/)
 53. U. H. von Andrian, C. R. Mackay, T-cell function and migration. Two sides of the same coin. *N. Engl. J. Med.* **343**, 1020–1034 (2000). doi: [10.1056/NEJM200010053431407](https://doi.org/10.1056/NEJM200010053431407); pmid: [11018170](https://pubmed.ncbi.nlm.nih.gov/11018170/)
 54. S. J. Davila, A. J. Olive, M. N. Starnbach, Integrin $\alpha 4 \beta 1$ is necessary for CD4⁺ T cell-mediated protection against genital *Chlamydia trachomatis* infection. *J. Immunol.* **192**, 4284–4293 (2014). doi: [10.4049/jimmunol.1303238](https://doi.org/10.4049/jimmunol.1303238); pmid: [24659687](https://pubmed.ncbi.nlm.nih.gov/24659687/)
 55. D. E. Wright, A. J. Wagers, A. P. Gulati, F. L. Johnson, I. L. Weissman, Physiological migration of hematopoietic stem and progenitor cells. *Science* **294**, 1933–1936 (2001). doi: [10.1126/science.1064081](https://doi.org/10.1126/science.1064081); pmid: [11729320](https://pubmed.ncbi.nlm.nih.gov/11729320/)
 56. T. L. Denning, G. Kim, M. Kronenberg, Cutting edge: CD4⁺CD25⁺ regulatory T cells impaired for intestinal homing can prevent colitis. *J. Immunol.* **174**, 7487–7491 (2005). doi: [10.4049/jimmunol.174.12.7487](https://doi.org/10.4049/jimmunol.174.12.7487); pmid: [15944246](https://pubmed.ncbi.nlm.nih.gov/15944246/)
 57. D. M. Brainard *et al.*, Induction of robust cellular and humoral virus-specific adaptive immune responses in human immunodeficiency virus-infected humanized BLT mice. *J. Virol.* **83**, 7305–7321 (2009). doi: [10.1128/JVI.02207-08](https://doi.org/10.1128/JVI.02207-08); pmid: [19420076](https://pubmed.ncbi.nlm.nih.gov/19420076/)
 58. A. K. Wege, M. W. Melkus, P. W. Denton, J. D. Estes, J. V. Garcia, Functional and phenotypic characterization of the humanized BLT mouse model. *Curr. Top. Microbiol. Immunol.* **324**, 149–165 (2008). pmid: [18481459](https://pubmed.ncbi.nlm.nih.gov/18481459/)
 59. F. Sallusto, D. Lenig, R. Förster, M. Lipp, A. Lanzavecchia, Two subsets of memory T lymphocytes with distinct homing potentials and effector functions. *Nature* **401**, 708–712 (1999). doi: [10.1038/44385](https://doi.org/10.1038/44385); pmid: [10537110](https://pubmed.ncbi.nlm.nih.gov/10537110/)
 60. W. Weninger, M. A. Crowley, N. Manjunath, U. H. von Andrian, Migratory properties of naive, effector, and memory CD8⁺ T cells. *J. Exp. Med.* **194**, 953–966 (2001). doi: [10.1084/jem.194.7.953](https://doi.org/10.1084/jem.194.7.953); pmid: [11581317](https://pubmed.ncbi.nlm.nih.gov/11581317/)
 61. D. Masopust *et al.*, Dynamic T cell migration program provides resident memory within intestinal epithelium. *J. Exp. Med.* **207**, 553–564 (2010). doi: [10.1084/jem.20090858](https://doi.org/10.1084/jem.20090858); pmid: [20156972](https://pubmed.ncbi.nlm.nih.gov/20156972/)
 62. E. Bettelli *et al.*, Reciprocal developmental pathways for the generation of pathogenic effector TH17 and regulatory T cells. *Nature* **441**, 235–238 (2006). doi: [10.1038/nature04753](https://doi.org/10.1038/nature04753); pmid: [16648838](https://pubmed.ncbi.nlm.nih.gov/16648838/)
 63. S. Jung *et al.*, Analysis of fractalkine receptor CX(3)CR1 function by targeted deletion and green fluorescent protein reporter gene insertion. *Mol. Cell. Biol.* **20**, 4106–4114 (2000). doi: [10.1128/MCB.20.11.4106-4114.2000](https://doi.org/10.1128/MCB.20.11.4106-4114.2000); pmid: [10805752](https://pubmed.ncbi.nlm.nih.gov/10805752/)
 64. I. Bernstein-Hanley *et al.*, Genetic analysis of susceptibility to *Chlamydia trachomatis* in mouse. *Genes Immun.* **7**, 122–129 (2006). doi: [10.1038/sj.gene.6364285](https://doi.org/10.1038/sj.gene.6364285); pmid: [16395389](https://pubmed.ncbi.nlm.nih.gov/16395389/)

ACKNOWLEDGMENTS

We thank E. Nigro for secretarial assistance, L. B. Jones for technical support, and the members of the von Andrian laboratory for discussion. The data presented in this manuscript are tabulated in the main paper and in the supplementary materials. Supported by NIH grants AI078897, AI069259, AI095261, and AI111595, a Harvard Innovation Award from Sanofi Pasteur, and the

Ragon Institute of MGH, MIT and Harvard (U.H.v.A.); NIH grants U54-CA119349, U54-CA151884, and R37-EB000244 and the David Koch Prostate Cancer Foundation (R.L. and O.C.F.); NIH grant 1 R01-EB015419-01 (O.C.F.); NIH grant R00 CA160350 (J.S.); NIH grant T32 HL066987 (D.A.); NIH grant P30-AI060354 and the MGH Humanized Mouse Program by the Harvard University CFAR (A.M.T.); and NIH grant R01 AI062827, NIH grant R01 AI39558, and the Epidemiology and Prevention Interdisciplinary Center for Sexually Transmitted Diseases (NIH grant U19 AI113187) (M.N.S.). G.S. is a Max Kade foundation postdoctoral research exchange grant recipient. A.F.R.-M. acknowledges support from the MIT Portugal Program and the National Science Foundation (NSF-GRFP). G.S., A.R.F.-M., P.A.B., M.N.S., R.L., O.C.F., and U.H.v.A. are inventors on a patent application entitled “Nanoparticle-Based Compositions” (U.S. Application number PCT2014/029000; International Publication No. WO2014/153087) filed by Harvard University together with MIT and Brigham and Women’s Hospital (BWH) that relates to the use of cSAP for mucosal vaccination. A.R.F.-M., R.L., and O.C.F. are inventors on a patent application entitled “pH Sensitive Biodegradable Polymeric Particles for Drug Delivery” (U.S. Application no. PCT2011/0065807) filed by BWH together with MIT that relates to the engineering of charge-switching particles. O.C.F., R.L., and U.H.v.A. disclose financial interests in BIND Therapeutics, Selecta Biosciences, and Blend Therapeutics, three biotechnology companies developing nanocarrier technologies for medical applications. BIND, Selecta, and Blend did not support the research in this study. Selecta and Blend have obtained licenses to a portion of the intellectual property described in this study. O.C.F., R.L., and U.H.v.A. are scientific founders and members of the Scientific Advisory Board and O.C.F. and R.L. are directors of Selecta Biosciences. O.C.F., R.L. and U.H.v.A. are members of the Scientific Advisory Board and O.C.F. and R.L. are scientific founders and directors of Blend Therapeutics. The following reagents used in the paper are subject to MTA: NR-1 transgenic mice, cSAP, cSP, and SAP. All reasonable requests for collaboration involving materials used in the research will be fulfilled, provided that a written agreement is executed in advance between BWH, MIT, or Harvard Medical School and the requester (and his or her affiliated institution). Such inquiries or requests for additional data should be directed to the corresponding author.

SUPPLEMENTARY MATERIALS

www.sciencemag.org/content/348/6241/aaa8205/suppl/DC1

Figs. S1 to S10

31 January 2015; accepted 27 May 2015

10.1126/science.aaa8205

RESEARCH ARTICLE

NEURODEVELOPMENT

Shared regulatory programs suggest retention of blastula-stage potential in neural crest cells

Elsy Buitrago-Delgado,^{1*} Kara Nordin,^{1*} Anjali Rao,¹
Lauren Geary,¹ Carole LaBonne^{1,2†}

Neural crest cells, which are specific to vertebrates, arise in the ectoderm but can generate cell types that are typically categorized as mesodermal. This broad developmental potential persists past the time when most ectoderm-derived cells become lineage-restricted. The ability of neural crest to contribute mesodermal derivatives to the bauplan has raised questions about how this apparent gain in potential is achieved. Here, we describe shared molecular underpinnings of potency in neural crest and blastula cells. We show that in *Xenopus*, key neural crest regulatory factors are also expressed in blastula animal pole cells and promote pluripotency in both cell types. We suggest that neural crest cells may have evolved as a consequence of a subset of blastula cells retaining activity of the regulatory network underlying pluripotency.

Embryogenesis initiates with a totipotent fertilized egg cell, and subsequent development is characterized by progressive restrictions in cellular potential. At blastula stages, when the three primary germ layers are forming, chordate embryos still possess populations of pluripotent cells that are capable of differentiating into all somatic cell types. In mammals, these are inner-cell mass cells, whereas in *Xenopus*, these cells are the deep inner cells of the blastula roof, also termed “animal pole cells” (2). The pluripotency of blastula cells is transient; as embryogenesis proceeds into gastrulation, their potential becomes rapidly restricted into one of three cell types: ectoderm, mesoderm, and endoderm. In all vertebrate species, a population of stem cell–like progenitors, called neural crest cells, represents an exception to this loss of potential. These cells arise from ectoderm positioned at the neural plate border but, in addition to ectodermal cell types, can also differentiate into cartilage, bone, connective tissue, smooth muscle, pericytes, and adipocytes, all of which are also formed by the mesoderm. Neural crest cells represent a major vertebrate innovation, collectively contributing to many of the features that distinguish vertebrates from nonvertebrate chordates, including much of the craniofacial skeleton, the chromaffin cells of the adrenal medulla, and spinal nerve (dorsal root) ganglia. Because neural crest, despite its ectodermal origins, forms numerous cell types considered mesodermal, it has been likened to a fourth germ layer that renders ver-

tebrates quadroblastic and endows them with the potential to form a diversity of new cell types (2).

Much effort has been directed toward determining the developmental mechanisms by which a classic embryonic induction leads to the formation of the neural crest, cells that seemingly possess greater developmental potential than those from which they were derived embryologically or evolutionarily. Under current models, these cells appear to defy the paradigm of progressive restriction in potential, and thus far, no mechanism has been found to explain their apparent gain in potential. An alternative, more parsimonious model for the origins of neural crest cells might be that they selectively retain the regulatory circuitry responsible for the pluripotency of their blastula precursors—a selective retention of earlier features. This model is supported by a shared requirement for *Myc* protein, and its transcriptional target *Id3*, in both neural crest cell genesis and embryonic stem cell pluripotency (3–6). We recently found that another neural crest regulatory transcription factor, *Sox5*, is initially expressed in blastula cells, where it functions as a bone morphogenetic protein (BMP) R-Smad cofactor (7), providing an additional link between neural crest cells and pluripotent blastula cells. On the basis of these observations, we decided to systematically test the alternative model in *Xenopus*.

Neural crest shares regulatory circuitry with pluripotent blastula cells

In mammals, Pou5F1 (Oct4), Sox2, and Nanog constitute a core pluripotency network that is essential for maintaining the uncommitted state of blastula cells (8–13). In *Xenopus*, the Pou5F1 factors expressed in ectoderm are Pou5F3.1 (Oct91), Pou5F3.2 (Oct25), and Pou5F3.3 (Oct60) (14, 15). The functional role of Nanog in *Xenopus*

is assumed by Ventx factors (Vent1/2) (16). These factors, along with *Sox2* and the closely related *Sox3*, are expressed in blastula cells (17) (Fig. 1A). We wondered whether other neural crest regulatory factors besides *Myc*, *Id3*, and *Sox5* were coexpressed with the core pluripotency network in *Xenopus* blastula cells. We found that *Id3*, *TF-AP2*, *Ets1*, *FoxD3*, and *Snail1* were coexpressed with the core pluripotency factors (Fig. 1B). *FoxD3* and *Snail1* are also expressed in mouse embryonic stem cells (18, 19), providing further molecular links between neural crest factors and pluripotency. Although these neural crest and pluripotency factors exhibited broad expression during blastula stages, their expression became progressively restricted as lineage determination progressed, with several genes—including *Oct60*, *Sox3*, *Vent2*, *Ets1*, *Zic1*, *Pax3*, and *Snail1*—showing enhanced expression at the neural plate border by late gastrula stages (fig. S1, A and B). We found that *Vent2* was coexpressed with *Snail2* at late gastrula/neurula stages when neural crest cells retain their full developmental potential, but was down-regulated as these cells begin to migrate and lose multipotency (fig. S1C).

Explanted blastula animal pole cells retain full developmental potential until the onset of gastrulation, when they lose competence to form mesoderm and endoderm (20, 21). We thus examined whether expression of regulatory factors present in pluripotent blastula cells is lost when explants age and their developmental potential becomes restricted. *Oct60*, *Sox3*, *FoxD3*, and *Myc* expression was high in blastula-stage explants but reduced by late gastrula stages, correlating with loss of potential (Fig. 1C). Not all potency factors were down-regulated as these cells lost plasticity; expression of *Vent2* and *Id3* was unchanged as explants aged from blastula to gastrula stages (Fig. 1C). This suggests that a concentration-dependent signature of regulatory factors may be essential to retaining broad developmental potential and preventing lineage restriction, which is consistent with findings in mouse that specific threshold concentrations of Oct4 (50 to 150% of endogenous levels) support pluripotency, whereas levels outside this range lead to differentiation (9, 22).

Neural crest factors are required for pluripotency in blastula cells

Given that neural crest potency factors are coexpressed with core pluripotency factors in blastula cells, we asked whether they were required to maintain expression of these pluripotency factors. Blocking *Snail1* function in the animal pole of blastula embryos cells led to loss of expression of factors linked to the neural crest state, such as *TF-AP2* and *Id3* (Fig. 2A and fig. S3A). Expression of *Oct/Sox/Vent* network components was also lost (Fig. 2A and fig. S3A). We obtained similar results when *Sox5* function was blocked in animal pole cells (Fig. 2B and fig. S3B). Thus, neural crest regulatory factors are not merely expressed in pluripotent blastula cells but also function there to maintain expression of core pluripotency factors.

The developmental plasticity of amphibian animal pole cells was first demonstrated by

¹Department of Molecular Biosciences, Northwestern University, Evanston, IL 60208, USA. ²Robert H. Lurie Comprehensive Cancer Center, Northwestern University, Evanston, IL 60208, USA.

*These authors contributed equally to this work. †Corresponding author. E-mail: clabonne@northwestern.edu

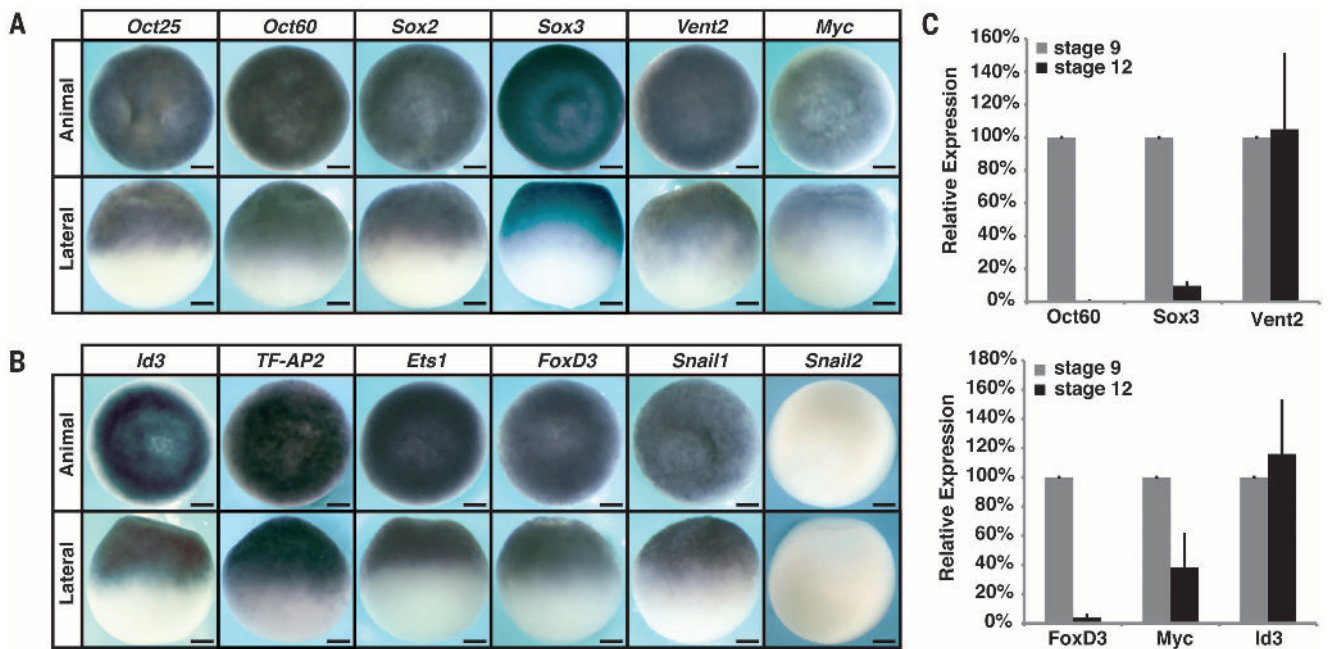


Fig. 1. Neural crest cells and pluripotent blastula cells share a common regulatory circuitry. (A and B) In situ hybridization of wild-type blastula (stage 9) *Xenopus* embryos examining expression of genes associated with (A) pluripotency or (B) neural crest formation. Scale bars, 250 μ M. (C) Quantitative reverse transcription polymerase chain reaction (RT-PCR) of wild-type ectodermal explants examining relative expression of pluripotency genes and neural crest genes over developmental time.

Nieuwkoop, whose recombinant assay drove current understanding of mesendoderm formation (fig. S1D) (23). Because we found that neural crest factors such as *Snail1* are required for maintaining expression of factors linked to pluripotency, we hypothesized that cells lacking *Snail1* function would lack competence to respond to endogenous inducing signals. To test this, animal pole explants from control blastulae, or blastulae in which *Snail1* function had been blocked, were recombined with vegetal tissue from sibling embryos. Control recombinants robustly expressed mesodermal markers *Brachyury* and *MyoD*, whereas animal pole cells blocked for *Snail1* function showed dramatically diminished responsiveness (Fig. 3, A and B, and fig. S3, C and D). Similar results were observed with animal pole cells depleted of *Sox5* (Fig. 3, C and D, and fig. S3, C and D). As with conjugation to vegetal tissue, treatment of pluripotent blastula cells with low or moderate doses of activin instructs them to form mesoderm, and this responsiveness is also lost in cells depleted of *Snail* or *Sox5* function (Fig. 3, E and G, and figs. S1E; S2, A and C; and S3, E and F).

Because *Snail* factors have endogenous roles in mesoderm formation, a more demanding test of their contributions to pluripotency was to ask whether blastula cells lacking *Snail1* function consequently lose their capacity to form endoderm. Blastula explants adopt endodermal fates in response to high activin concentrations, expressing endoderm-specific genes such as *Endoderm* and *Sox17*. However, blastula explants depleted of *Snail* function could no longer form endoderm (Fig. 3F and figs. S2B and S3, G and H). *Snail* proteins are neither expressed in, nor function in, endoderm endogenously; thus, loss of

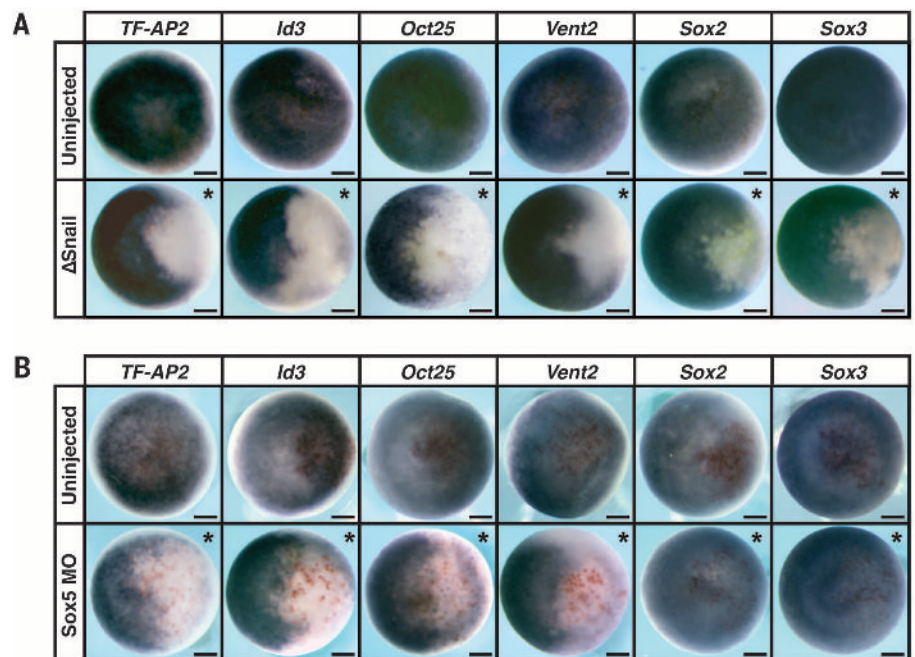


Fig. 2. Neural crest regulatory factors are required for the expression of blastula pluripotency factors. (A and B) In situ hybridization of embryos injected with (A) Δ Snail mRNA or (B) *Sox5* MO. Embryos were collected at blastula stages (stage 9) and examined for expression of genes associated with pluripotency/neural crest formation. Asterisk denotes injected side, with β -gal staining (red) serving as a lineage tracer. Scale bars, 250 μ M.

activin-mediated endoderm induction likely reflects a general lack of competence of *Snail*-depleted animal pole cells to respond to endoderm-inducing signals. Similar results were found when *Sox5* was depleted from blastula cells (Fig. 3H and figs. S2D and S3, G and H).

Reprogrammed neural crest can form endoderm

Given that neural crest potency factors are expressed in pluripotent blastula cells and required for expression of core pluripotency factors, we further explored the link between the neural crest

state and the pluripotent blastula state. Specifically, we asked whether establishing a neural crest state is sufficient to confer pluripotency on, or prevent loss of pluripotency in, descendants of blastula animal pole cells. Animal pole cells explanted at blastula stages are initially competent to give rise to all somatic cell types but lose pluripotency by gastrula stages. Established protocols exist for converting blastula animal pole explants to a neural plate border or neural crest state. Combined expression of Pax3 and Zic1 efficiently converts explants to neural plate border (24–26), whereas Snail2 together with Wnt signaling is sufficient to

establish a neural crest state (27, 28). We therefore asked whether converting these explants to a neural plate border or neural crest state would be sufficient to prevent loss of competence and extend the pluripotency of these cells (fig. S1F).

As predicted, explants treated at blastula stages with mesoderm-inducing concentrations of activin robustly expressed the mesoderm-specific *MyoD* gene, but if explants were aged to gastrula stages before treatment, they were unable to form mesoderm (Fig. 4A). In contrast, explants converted to a neural plate border state retained their potency and formed mesoderm in response to either early

or late activin treatment (Fig. 4A and fig. S4A). We also tested whether this change in plasticity extended to endoderm formation. When blastula-derived cells were treated with endoderm-inducing doses of activin, identical results were achieved (Fig. 4B). Explants treated with high activin at blastula stages expressed the endodermal markers *Endodermis* and *Sox17* but were unable to do so when treated at gastrula stages (Fig. 4B and fig. S2E). In contrast, Pax3/Zic1 programmed explants retain the ability to form endoderm even when treated at gastrula stages (Fig. 4B and figs. S2E and S4, C and E). Similarly, blastula-derived cells programmed to

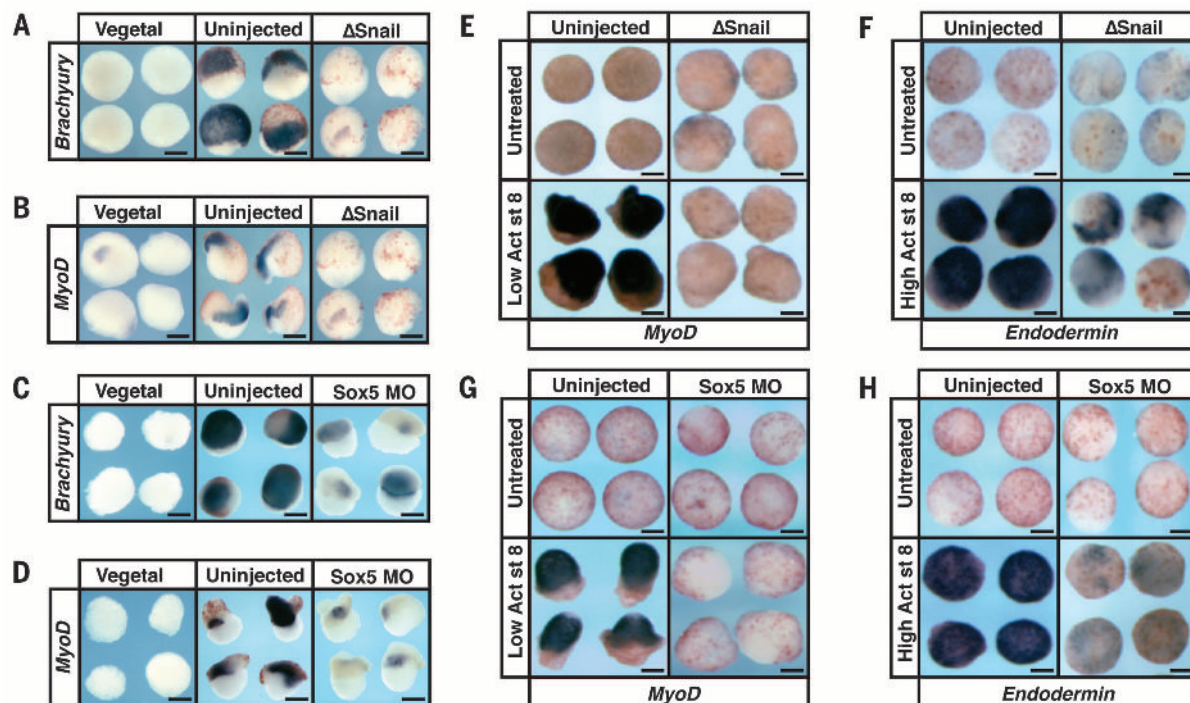


Fig. 3. Neural crest regulatory factors are required for pluripotency of blastula cells. (A to D) Nieuwkoop recombinant assay examining expression of [(A) and (C)] *Brachyury* and [(B) and (D)] *MyoD* after depleting [(A) and (B)] Snail1 or [(C) and (D)] Sox5 function. Recombinants were harvested at gastrulation stages for *Brachyury* expression (stage 11.5) or early neurula stages (stage 13/14) for *MyoD* expression. (E to H) Ectodermal explant assay examining expression of [(E) and (G)] *MyoD* and [(F) and (H)] *Endodermis*. Explants were injected with [(E) and (F)] Δ Snail mRNA or [(G) and (H)] Sox5 MO and cultured with or without activin until early neurula stages for *MyoD* expression (stage 13/14) and midgastrula stages (stage 11.5) for *Endodermis* expression. Scale bars, 250 μ m.

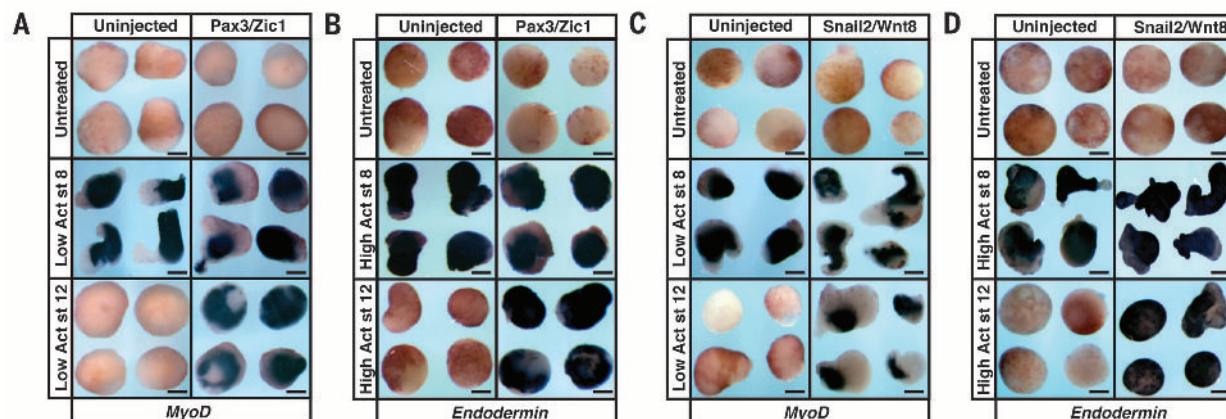


Fig. 4. Establishing a neural crest state prevents loss of potency in blastula-derived cells. (A to D) Ectodermal explant assay examining expression of [(A) and (C)] *MyoD* or [(B) and (D)] *Endodermis* in embryos that were injected with [(A) and (B)] Pax3-GR/Zic1-GR mRNA or [(C) and (D)] Snail2/Wnt8 mRNA. Explants were treated with activin at either stage 8 or 12 and cultured until late neurula stages (stage 18). Scale bars, 250 μ m.

a neural crest state with *Snail2/Wnt8* retain competence to form mesoderm and endoderm through gastrula stages (Fig. 4, C and D, and figs. S2F and S4, B, D and F). The ability of neural plate border or neural crest factors to prevent loss of pluripotency in animal pole-derived cells, combined with the requirement of these factors for the normal plasticity of these cells at blastula stages, suggests a close link between the molecular networks controlling the potency of neural crest and blastula cells.

Endogenous neural crest can form endoderm

If such a link exists, one prediction is that cells isolated from the neural plate border region of an intact neurula-stage embryo should also exhibit broad developmental potential, including the capacity to form both mesoderm and endoderm. This capacity should exist even though there is currently no evidence that neural plate border-derived cells form endoderm during normal development. To test this prediction, we isolated neural plate border cells from neurula-stage embryos and cultured the cells in vitro (fig. S1G). As expected, when these cells were cultured without inducers, they did not express the mesodermal markers *MyoD* or *Brachyury* or the endodermal markers *Endodermin* or *Sox17* (Fig. 5, A to D). However, treatment of neural plate border explants with concentrations of activin sufficient to induce mesoderm or endoderm in pluripotent blastula cells elicited strong expression of all of these genes (Fig. 5, A to D, and figs. S2G and S4, G to J). These findings demonstrate that endogenous neural crest cells possess a much greater degree of potency/plasticity than has previously been appreciated, including an unexpected capacity for endoderm formation.

Discussion

Long-standing models for neural crest formation posit that inductive interactions endow these cells with greater developmental potential than that of the cells they were derived from, developmentally or evolutionarily (fig. S5A) (25–28). This classic

view implies a distinct reversal of trajectory in Waddington's landscape of progressive restriction of developmental potential (29). Based on our findings reported here, we suggest instead a revised model in which neural crest cells are an example of cellular neoteny (30). Select cells with the pluripotent potential characteristic of the blastula state persist to neurula stages, where they can be induced to form the highly diverse lineages that derive from the neural crest (fig. S5B). This retention of pluripotency long after other cells have become fate-restricted has endowed the neural crest with the capacity to contribute the novel attributes characteristic of vertebrates to the simple chordate bauplan. Mechanistically, we propose that neural crest cells arose as a consequence of their retention of all or part of a regulatory network that controls pluripotency in the blastula cells from which they were derived.

Our model is consistent with, and helps explain, an earlier study of avian embryos that detected expression of genes associated with the neural crest state, such as *Pax7*, in the medial epiblast at early gastrula stages (31). Those findings were interpreted at the time as evidence that neural crest induction occurs earlier than previously believed, but we suggest that it reflects the retention of pluripotency in a subset of avian epiblast cells. Our work further suggests that transcription factors such as *Pax7* or *Snail*, which were previously considered and defined as neural plate border or neural crest factors, should instead be viewed as pluripotency maintenance factors. Future studies should address how such factors function to retain potential to contribute to all three germ layers in cells that will become the neural crest. The previously unrecognized capacity of neural crest cells to express endodermal markers in culture raises the question of whether they also contribute endodermal cell types endogenously. Perhaps neural crest contributions to otherwise endodermal organs, such as the parafollicular cells of the thryroid (32), should be considered a contribution of endoderm.

The model for formation of neural crest cells proposed here provides a framework for future

studies in basal chordates to probe the earliest evolutionary origins of these cells. Ascidians, for example, possess a cell lineage that arises from the neural plate border and expresses genes such as *Snail*, *Id*, *FoxD*, and *Ap2*, all of which we find shared between pluripotent blastula cells and neural crest. This a9.49 lineage in ascidians may be homologous to the neural crest lineage in vertebrates (33). Investigating shared and divergent aspects of pluripotency network components in these and other protochordate and basal vertebrate models should therefore shed light on when and how pluripotency was retained in cells that become neural crest and thus provide insight into the evolutionary origins of vertebrates.

REFERENCES AND NOTES

1. M. Furue, M. Asashima, in *Handbook of Stem Cells*, R. Lanza et al., Eds. (Elsevier, Burlington, San Diego, London, 2004), vol. 1, chap. 46.
2. B. K. Hall, *The Neural Crest in Development and Evolution* (Springer, New York, ed. 1, 1999).
3. W. Light, A. E. Vernon, A. Lasorella, A. Iavarone, C. LaBonne, *Development* **132**, 1831–1841 (2005).
4. A. Bellmeyer, J. Krase, J. Lindgren, C. LaBonne, *Dev. Cell* **4**, 827–839 (2003).
5. P. Cartwright et al., *Development* **132**, 885–896 (2005).
6. Q.-L. Ying, J. Nichols, I. Chambers, A. Smith, *Cell* **115**, 281–292 (2003).
7. K. Nordin, C. LaBonne, *Dev. Cell* **31**, 374–382 (2014).
8. J. Nichols et al., *Cell* **95**, 379–391 (1998).
9. H. Niwa, J. Miyazaki, A. G. Smith, *Nat. Genet.* **24**, 372–376 (2000).
10. A. A. Avilion et al., *Genes Dev.* **17**, 126–140 (2003).
11. I. Chambers et al., *Cell* **113**, 643–655 (2003).
12. K. Mitsui et al., *Cell* **113**, 631–642 (2003).
13. R. A. Young, *Cell* **144**, 940–954 (2011).
14. S. R. Frankenberg et al., *Development* **141**, 2921–2923 (2014).
15. G. M. Morrison, J. M. Brickman, *Development* **133**, 2011–2022 (2006).
16. P. Scerbo et al., *PLOS ONE* **7**, e36855 (2012).
17. C. D. Rogers, T. C. Archer, D. D. Cunningham, T. C. Grammer, E. M. S. Casey, *Dev. Biol.* **313**, 307–319 (2008).
18. Y. Liu, P. A. Labosky, *Stem Cells* **26**, 2475–2484 (2008).
19. Y. Lin et al., *Nat. Commun.* **5**, 3070 (2014).
20. E. A. Jones, H. R. Woodland, *Development* **101**, 557–563 (1987).
21. R. M. Grainger, J. B. Gurdon, *Proc. Natl. Acad. Sci. U.S.A.* **86**, 1900–1904 (1989).
22. I. Chambers, S. R. Tomlinson, *Development* **136**, 2311–2322 (2009).
23. P. D. Nieuwkoop, *W. Roux Archiv. Entwicklungsmech.* **163**, 298–315 (1969).
24. T. Sato, N. Sasai, Y. Sasai, *Development* **132**, 2355–2363 (2005).
25. C. S. Hong, J. P. Saint-Jean, *Mol. Biol. Cell* **18**, 2192–2202 (2007).
26. A.-H. Monsoro-Burq, E. Wang, R. Harland, *Dev. Cell* **8**, 167–178 (2005).
27. C. LaBonne, M. Bronner-Fraser, *Development* **125**, 2403–2414 (1998).
28. K. M. Taylor, C. LaBonne, *Curr. Opin. Genet. Dev.* **17**, 326–331 (2007).
29. C. H. Waddington, *Nature* **150**, 563–565 (1942).
30. D. J. Anderson, *Trends Genet.* **5**, 174–184 (1989).
31. M. L. Basch, M. Bronner-Fraser, M. I. García-Castro, *Nature* **441**, 218–222 (2006).
32. N. M. Le Douarin, C. Kalcheim, *The Neural Crest* (Cambridge Univ. Press, Cambridge, ed. 2, 1999).
33. P. B. Abitua, E. Wagner, I. A. Navarrete, M. Levine, *Nature* **492**, 104–107 (2012).

ACKNOWLEDGMENTS

We thank J. Nguyen for technical assistance, S. Sokol for providing activin, and R. Carthew and X. Wang for helpful discussions. K.N. was supported by grants F31DE021922 and T32CA009560-24. L.G. was supported by grant T32GM008061. This work was supported by grant R01GM114058 to C.L. The supplementary materials contain additional data.

SUPPLEMENTARY MATERIALS

www.sciencemag.org/content/348/6241/1332/suppl/DC1
Materials and Methods
Figs. S1 to S5

1 December 2014; accepted 26 March 2015
Published online 30 April 2015;
10.1126/science.aaa3655

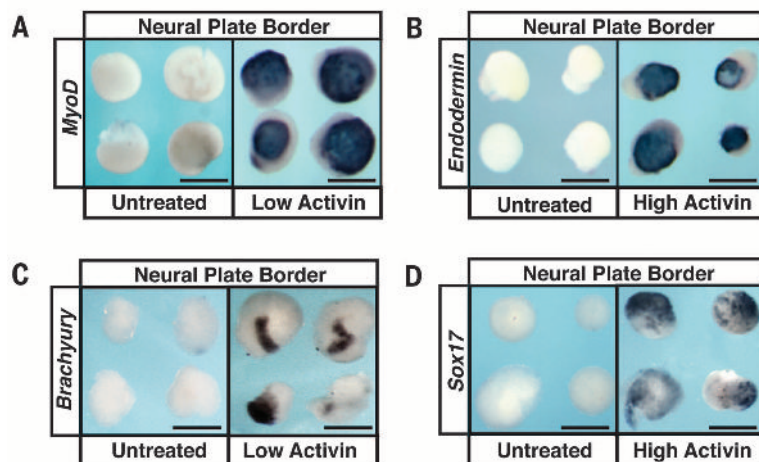


Fig. 5. Neural crest cells possess the capacity for endoderm formation. (A to D) In situ hybridization examining at late neurula stages (stage 18) expression of (A) *MyoD*, (B) *Endodermin*, (C) *Brachyury*, and (D) *Sox17* in neural plate border/neural crest tissue treated with or without activin. Scale bars, 250 μ m.

REPORTS

INDUCED SEISMICITY

High-rate injection is associated with the increase in U.S. mid-continent seismicity

M. Weingarten,^{1*} S. Ge,¹ J. W. Godt,² B. A. Bekins,³ J. L. Rubinstein³

An unprecedented increase in earthquakes in the U.S. mid-continent began in 2009. Many of these earthquakes have been documented as induced by wastewater injection. We examine the relationship between wastewater injection and U.S. mid-continent seismicity using a newly assembled injection well database for the central and eastern United States. We find that the entire increase in earthquake rate is associated with fluid injection wells. High-rate injection wells (>300,000 barrels per month) are much more likely to be associated with earthquakes than lower-rate wells. At the scale of our study, a well's cumulative injected volume, monthly wellhead pressure, depth, and proximity to crystalline basement do not strongly correlate with earthquake association. Managing injection rates may be a useful tool to minimize the likelihood of induced earthquakes.

The injection of fluids into the subsurface has been known to induce earthquakes since the mid-1960s (1–3). However, few additional cases of earthquakes induced by wastewater injection have been documented until 2009 (4). The hazard from these earthquakes was considered small because they were infrequent and not expected to be large (largest observed prior to 2011 was the *M* 4.9 Rocky Mountain Arsenal earthquake in 1967) (4–6). The central and eastern United States (CEUS) has seen an unprecedented increase in earthquake rate since 2009, and many of these earthquakes are believed to be induced (7). Along with the increased rate, several damaging earthquakes have occurred such as the 2011 magnitude (*M*) 5.6 Prague, Oklahoma, earthquake (8, 9), the 2011 *M* 5.3 Trinidad, Colorado, earthquake (10), the 2012 *M* 4.8 Timpson, Texas, earthquake (11), and the 2011 *M* 4.7 Guy, Arkansas, earthquake (12). The increased earthquake rate and occurrence of multiple damaging earthquakes has prompted the scientific community to refocus efforts to understand the hazard posed by injection-induced earthquakes (13).

The sudden appearance of several large, potentially induced earthquakes led to many site-specific case studies (4). These case studies examined the operation of injection wells in close proximity to the earthquakes, showing a link between the timing and location of injection and seismicity (12, 14–18). Though useful to understand the individual systems in which these earthquakes occurred, broader-scale studies are needed to

understand the phenomenon as a whole. One previous study examined earthquakes in Texas's Barnett Shale region and found that earthquakes are commonly located near wells injecting more than 150,000 barrels per month (19). However, to fully understand the possibility of induced seismicity associated with a given injection well, we must analyze a range of geologic, hydrogeologic, and operational differences between injection wells that are potentially associated with earthquakes and those that are not.

We examined the location and timing of earthquakes and their relationship to the location and operation of injection wells across the CEUS (Fig. 1). We compiled a database from publicly available sources that documents the location and operational parameters of underground injection control class II injection wells in the CEUS (Fig. 1 and table S1). Class II injection wells inject fluids associated with oil and gas production and are distinct from hydraulically fractured production wells (20). The database contained 187,570 wells as of December 2014, with 56% actively injecting fluid (Fig. 1) and the remaining 44% being inactive or abandoned. About 75% of the active class II injection wells operated for the purposes of enhanced oil recovery (EOR), whereas nearly all of the remaining wells were designated as salt water disposal (SWD) wells (fig. S1). EOR wells inject fluid into depleted oil reservoirs to increase oil production. SWD wells inject to dispose of waste fluids produced by oil and gas production, which would otherwise be hazardous to surface waters or underground sources of drinking water. Injection wells are geographically clustered in the basins and regions of major oil and gas operations. Texas, Oklahoma, Kansas, and Wyoming contain ~85% of all class II injection wells in the CEUS. The

spatial density of active SWD wells is highest (≥ 5 wells per 5 km²) in the Fort Worth Basin of north-central Texas and the Mississippi Lime Play extending from north-central Oklahoma northward into central Kansas. The spatial density of active EOR wells is highest (≥ 5 wells per 5 km²) in the Permian Basin of West Texas, the Fort Worth Basin, south-central Oklahoma, and southeastern Kansas (fig. S1).

We obtained earthquake location and magnitude data from the Advanced National Seismic System's comprehensive earthquake catalog (ANSS ComCat) (21). During the study period (1973 to 2014), we identified 7175 *M* \geq 0.0 events in the catalog in the CEUS region (Fig. 2). Although the catalog is not complete down to *M* 0.0 during the study period, we treated all earthquakes as potentially induced events to capture the most comprehensive data set of associated earthquakes and injection wells. We used a magnitude of completeness of 3.0 when comparing associated versus nonassociated earthquakes through time (7).

We used spatial and temporal filtering methods to discriminate injection wells that may be associated with earthquakes from those that are probably not. We considered any earthquake within 15 km of an active injection well to be associated with that well. This distance of association is based upon the sum of a 5-km radius within which earthquakes are traditionally considered as potentially induced (22) and a 10-km estimate of the spatial uncertainty in earthquake epicenter location in the CEUS (23). We designed the temporal filter to include only injection wells active at the time of the spatially associated earthquake. Both filters could be considered conservative, because induced seismicity has been found tens of kilometers from injection wells (24) and also after a well is shut-in (25) owing to the injection prior to the well becoming inactive (4, 5). To analyze the sensitivity of our results to these filtering parameters, we also tested our analysis using spatial association distances of 5 and 10 km. This first-order analysis attempts to understand which basic well properties affect the likelihood of earthquake association.

We find 18,757 injection wells (~10% of all wells) associated with earthquakes in the CEUS after filtering, mostly in the states of Oklahoma and Texas (Fig. 1). The number of associated injection wells has tripled since the year 2000 (fig. S2). The spatiotemporal filter identifies every case of induced seismicity from class II injection wells documented in the literature for the CEUS region (table S2). We identify far more injection wells that are potentially related to earthquakes than those indicated by published cases. Of the wells that are associated with earthquakes, 66% are EOR wells. However, active SWD wells are more than 1.5 times as likely as active EOR wells to be associated with an earthquake, which accounts for their respective well totals (Fig. 1). The finding that SWD wells are preferentially associated with earthquakes likely resides with difference in well operation. SWD injection causes a net-positive reservoir pressure change, whereas EOR injection and extraction

¹Department of Geological Sciences, University of Colorado, Boulder, CO, USA. ²United States Geological Survey, Denver, CO, USA. ³United States Geological Survey, Menlo Park, CA, USA.
*Corresponding author. E-mail: matthew.weingarten@colorado.edu

wells are typically operated in tandem with injection rates managed carefully to balance reservoir pressures (7).

Over the past four decades, more than 60% of all CEUS seismicity ($M \geq 3.0$) is associated with injection wells using our filtering criteria (Figs. 2 and 3). Varying the spatial distance of association by several kilometers only changes this percentage by $\pm 5\%$ (fig. S3). Before the year 2000, an average of $\sim 20\%$ of all CEUS seismicity was associated with injection wells. The yearly percentage of associated earthquakes has risen sharply to $\sim 87\%$ from 2011 to 2014 (Fig. 3 and fig. S4). The percentage increase of associated earthquakes, combined with the rising CEUS earthquake rate, implies that recent seismicity in the CEUS is preferentially occurring near injection wells. The number of nonassociated earthquakes during the same period has also remained stable (Fig. 3). This increase in associated earthquake rate does not correspond to an increase in the rate of wells completed; the well completion rate has remained constant over this period (fig. S5) (26). A portion of the increase in associated earthquakes may be due to increasing spatial coverage of wells, but we suggest that this effect is minimal, considering

that the relative increase in spatial coverage was much more rapid between 1960 and 1980 than in recent years (fig. S5). Wells in central and north-central Oklahoma are the main contributors to the dramatic increase in associated seismicity. New production methods in these regions are generating large volumes of produced water, which are injected at high rates (fig. S6, A and B) (27). Regions such as west Texas, southern Colorado, central Arkansas, and southern Illinois also show concentrations of seismicity associated with injection wells (Fig. 2). However, several regions with large numbers of injection wells appear to be aseismic during the study period, including the Williston Basin of North Dakota (28), the Michigan Basin, and extensive areas of the Texas and Louisiana Gulf Coast (Figs. 1 and 2).

Several operational parameters are hypothesized to influence the likelihood of an induced seismic event: injection rate (19, 24), cumulative injected volume (29, 30), wellhead injection pressure (31), and injection in proximity to crystalline basement (18, 32). Four states—Oklahoma, Arkansas, Colorado, and New Mexico—with both natural and induced earthquakes all have more than 15 years of injection data that include readily ac-

cessible information on monthly injection rate and pressure for a large proportion of operational wells. Using these data, we explore injection operational parameter control on the likelihood that SWD and EOR wells will be associated with earthquakes.

The maximum monthly injection rate of wells across these four states varies by several orders of magnitude, ranging from 100 barrels ($\sim 15.9 \text{ m}^3$) per month (bbl/month) up to 2 million bbl/month ($\sim 318,000 \text{ m}^3$) (Fig. 4A) (33). The average SWD well operates at a mean monthly rate of $\sim 13,000$ bbl/month. For each histogram bin in Fig. 4, A and B, we calculate the percentage of wells associated with earthquakes. The likelihood that an SWD well is associated with earthquakes increases as the maximum injection rate increases (Fig. 4C). To discern whether the association is random, we estimated upper (95%) and lower (5%) confidence bounds using a bootstrapped resampling method with 10,000 resamples (Fig. 4C) (34, 35). Wells operating at maximum injection rates greater than 300,000 bbl/month fall outside the bootstrap resampling confidence bounds, suggesting a greater-than-expected likelihood of association with an earthquake at a statistical significance near 99%. This is contrasted with wells operating at maximum injection rates less than 100,000 bbl/month, which mostly fall within the bounds of random association. We confirmed this result using spatial distances of association of 5 and 10 km (fig. S7), as well as restricting our well associations to earthquakes greater than $M \geq 3.0$ (fig. S8). Of the 413 wells operating at injection rates greater than 300,000 bbl/month, 253 (61%) are spatiotemporally associated compared with only 40% of wells operating at injection rates less than 10,000 bbl/month. Additionally, 34 (76%) of the 45 highest-rate SWD wells (injecting more than a million barrels per month) are associated with an earthquake. When SWD operations are examined state by state, the overall percentage associated varies, but the trend of increased earthquake association at higher rates is generally preserved (fig. S9A). Fewer data are available for EOR wells, but we do not observe a clear trend of increasing earthquake association with increasing injection rate for EOR wells (fig. S10A). Without considering geologic or hydrogeologic setting, the highest-rate SWD wells are nearly twice as likely to be near an earthquake as are low-rate SWD wells.

We next examine whether cumulative injected volume affects the likelihood of well association with earthquakes. For the four states examined during the period from 1973 to 2014, cumulative injected volume ranged from 1000 bbl to nearly 100 million bbl (Fig. 4B). Many large cumulative volume wells inject at moderate rates for decades, providing a contrasting data set from maximum injection rate. We do not observe a strong trend of increasing SWD well association as a function of increasing cumulative injected volume (Fig. 4D). The difference between the association rate of wells that have injected more than 1,000,000 bbl cumulatively (45%) and those which

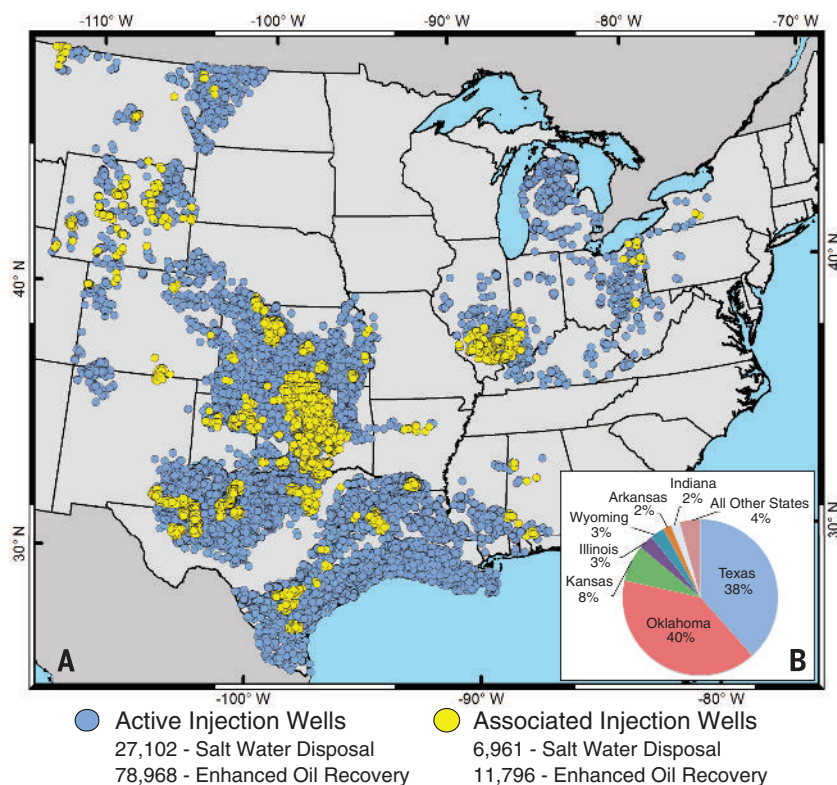


Fig. 1. Active and associated class II injection wells in the CEUS. (A) Map showing the location of active class II injection wells in the CEUS. Active injection wells from the database are shown as blue circles. Spatiotemporally associated injection wells, defined as those within a 15-km radius and active at the time of an earthquake, are shown as yellow circles. The CEUS region comprises all states intersected by 109°W longitude and eastward. The total number of wells, including inactive or abandoned wells in the CEUS, is 188,570. Of the 18,757 associated injection wells, $>77\%$ are currently active. **(B)** The inset pie diagram shows spatiotemporally associated injection wells by state. Only 8% of all injection wells are located in Oklahoma, but 40% of the associated injection wells in the CEUS are located in Oklahoma.

have injected less than 10,000 bbl cumulatively (38%) is not statistically significant, as determined by a bootstrap resampling method (35). The percentage of wells associated with earthquakes at high cumulative injected volumes can be mostly explained by random variation given the total number of associated and nonassociated wells. EOR wells exhibit a trend of earthquake association similar to that of SWD wells as a function of cumulative injected volume (fig. S10B). If we instead calculate cumulative injected volume not for individual wells, but for all wells within 15 km of an associated earthquake, we observe a log-normal distribution of volumes without a clear threshold of increased earthquake association (fig. S11). We do not observe cumulative injected volume as strongly affecting the likelihood of an injection well's association with an earthquake.

The majority of class II injection wells operate at monthly wellhead injection pressures less than 500 pounds per square inch (psi). Reported wellhead pressures for both SWD and EOR wells ranged from 0 to 3000 psi (fig. S12, A and B). In the same four states studied, the proportion of SWD and EOR wells associated with earthquakes show no strong correlation toward increased monthly wellhead pressures (figs. S12 and S13). However, reported monthly wellhead pressure may not always be reliable because many wells report constant wellhead pressures despite changing injection rates. Wellhead injection pressure data may not reflect the pore-pressure conditions in the injection formation due to friction in the wellbore and other factors. In addition, wells reporting zero wellhead pressure still create bottomhole pressure from the hydrostatic fluid column in the well that could be large enough induce an earthquake. There are several hundred wells with zero wellhead pressures that are associated with earthquakes (fig. S12, A and B). This is consistent with field observations of earthquakes induced by wells with zero wellhead pressure (10, 36). We do not consider the reported maximum wellhead pressure to be a controlling factor on injection well and earthquake association. This finding, together with the indication that SWD wells are preferentially associated with earthquakes, underscores the need to collect reservoir pressure data. Ideally, preinjection reservoir pore pressure and bottomhole formation pressure measurements during injection would prove more useful in determining whether a link exists between injection pressure and earthquakes.

Injection depth and proximity to crystalline basement have been hypothesized to affect the likelihood that wells are associated with earthquakes (32). Comparison of injection depths for most states in the CEUS, excluding Mississippi, Indiana, West Virginia, and Alabama, is possible, as these data are more readily available than injection rates and pressures (table S1). Class II injection wells are permitted over a wide range of injection depths from 300 to 4000 m (fig. S14). The majority of both SWD and EOR wells inject between 300 and 1500 m (fig. S14, B and E).

Wells associated with earthquakes also inject over a similarly wide range of injection depths (fig. S14, A and D). We find no clear evidence that increasing injection depth increases the likelihood that a well will be associated with seismicity; the proportion of both SWD and EOR wells associated with earthquakes does not increase with increasing injection depth (fig. S14, C and F).

However, comparison of injection depths neglects the large variations in sediment thickness across the CEUS.

Using a map of sediment thickness across the CEUS (37), we estimate injection proximity to basement for all wells by subtracting injection well depth from the sediment thickness at the closest sediment thickness data point. The

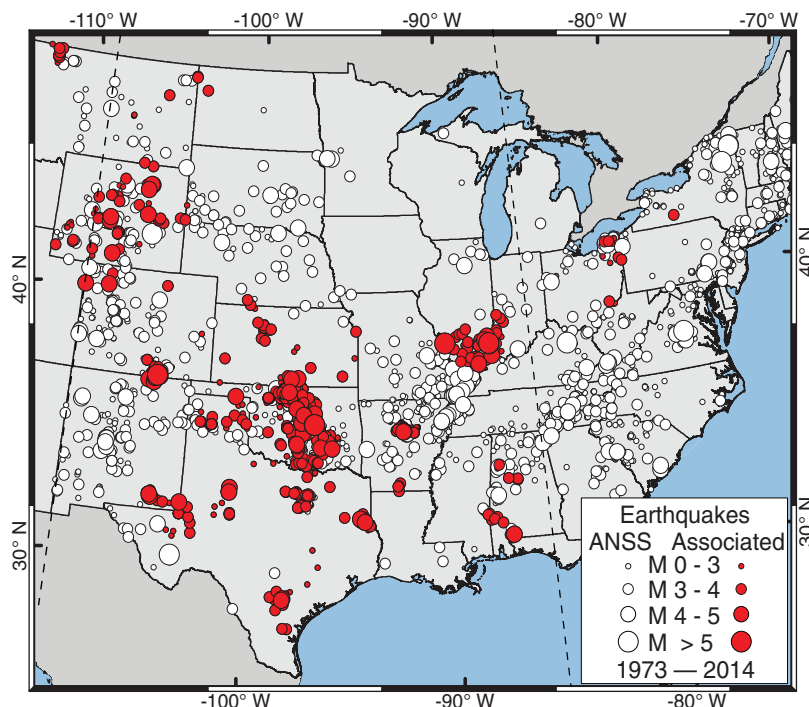
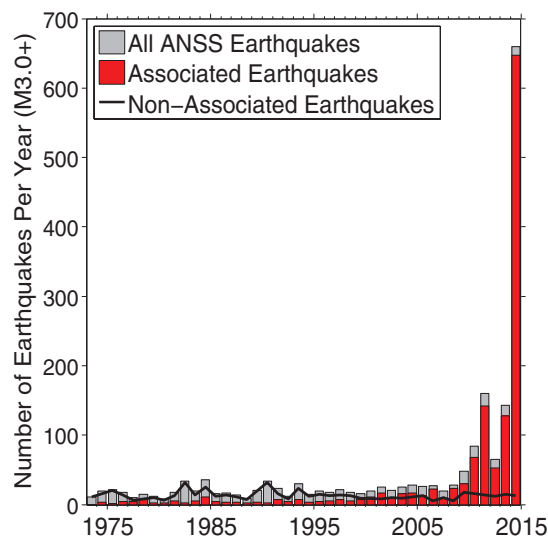


Fig. 2. Associated earthquakes in the CEUS from 1973 to 2014. Map showing the locations of $M \geq 0.0$ earthquakes in the ANSS ComCat earthquake catalog from 1 January 1973 through 31 December 2014. White dots denote earthquakes that are not spatiotemporally associated with injection wells. Red dots denote earthquakes that are spatiotemporally associated with injection wells. Following Ellsworth (7), the U.S. mid-continent is defined by the dashed lines inside of the greater CEUS.

Fig. 3. Associated and nonassociated earthquakes per year in the U.S. mid-continent.

The gray bars represent the number of $M \geq 3.0$ earthquakes per year in the U.S. mid-continent (Fig. 2) located by the networks of the ANSS ComCat earthquake catalog from 1 January 1973 to 31 December 2014. The red bars represent the number of earthquakes that are spatiotemporally associated with injection wells. The black line denotes the number of nonassociated earthquakes per year. Over the time period of the catalog, the number of nonassociated earthquakes per year has stayed roughly constant at 10 to 25 per year. Meanwhile, the number of associated earthquakes per year has risen from ~1 to 7 per year in the 1970s to 75 to 190 per year between 2011 and 2013 and >650 earthquakes in 2014.



sediment thickness map was tested against known reference depths of crystalline basement and found to have errors in thickness up to $\pm 15\%$ (table S3). Thousands of wells in the CEUS inject fluid within 500 m of crystalline basement rock, but only a small proportion are associated with seismicity. When taking into account the error in basement depth over the CEUS region, we did not observe a significant correlation between a well's injecting near basement and earthquakes using a bootstrap resampling method (fig. S15). However, injection wells operating very far from basement, between 7 and 12 km vertically, exhibited an association rate near zero. We found similar results for both depth parameters using only well associations with earthquakes greater than M 3.0 (figs. S16 and S17). This finding supports the notion that detailed stratigraphic knowledge surrounding the injection interval is necessary to quantify the mechanistic linkage between injection and seismicity (32).

The lack of spatiotemporal association between injection and seismicity in several regions highlights the apparent influence of factors other

than injection well operation. The San Juan Basin of New Mexico, the Williston Basin of North Dakota, the Michigan Basin, and extensive areas of the Texas and Louisiana Gulf Coast contain thousands of SWD and EOR wells that are not associated with seismicity (Fig. 1). In some of these regions, wells inject at rates similar to those in areas such as central Oklahoma, where large numbers of wells are associated with earthquakes. In the aseismic Michigan Basin, 30 wells operate at maximum injection rates greater than 200,000 bbl/month (fig. S18). Obviously, other factors in addition to high injection rate must play a role; the regional state of stress, fault size, fault orientation, the presence of fluid pathways between the injection point and faults, as well as other geologic factors must be examined to assess the potential for injection-induced seismicity (4).

Our analysis shows that injection rate is the most important well operational parameter affecting the likelihood of an induced seismic event in regions and basins potentially prone to induced seismicity. High-rate SWD wells are nearly twice as likely as low-rate wells to be near an earthquake. These high-rate wells perturb the

ambient reservoir pressure by a larger magnitude and over a larger area than low-rate wells, thus increasing the likelihood that pressure changes will reach an optimally oriented, critically stressed fault. Previous studies have shown that high-rate wells exert greater influence on the extent and magnitude of reservoir and fault pressure perturbation (24). At the scale of our study, no other operational parameter was found to have a strong influence on the likelihood of association with an earthquake. The important distinction between operational parameters such as injection rate and cumulative injected volume shows the effect of the recent rise of new production methods and high-rate SWD wells. Thus, the oil and gas industry and regulatory bodies can use this operational parameter to lower the likelihood of earthquakes associated with injection wells.

REFERENCES AND NOTES

1. D. M. Evans, *Mt. Geol.* **3**, 23–26 (1966).
2. J. H. Healy, W. W. Rubey, D. T. Griggs, C. B. Raleigh, *Science* **161**, 1301–1310 (1968).
3. C. B. Raleigh, J. H. Healy, J. D. Bredehoeft, *Science* **191**, 1230–1237 (1976).
4. National Research Council, *Induced Seismicity Potential in Energy Technologies* (National Academies Press, Washington, DC, 2013).
5. R. B. Herrmann, S. K. Park, C. Y. Wang, *Bull. Seismol. Soc. Am.* **71**, 731–745 (1981).
6. M. D. Petersen *et al.*, Documentation for the 2008 update of the United States National Seismic Hazard Maps. *U.S. Geol. Surv. Open-File Rep.* **08-1128** (2008).
7. W. L. Ellsworth, *Science* **341**, 1225942 (2013).
8. K. M. Keranen, H. M. Savage, G. A. Abers, E. S. Cochran, *Geology* **41**, 699–702 (2013).
9. A. L. Llenos, A. J. Michael, *Bull. Seismol. Soc. Am.* **103**, 2850–2861 (2013).
10. J. L. Rubinstein, W. L. Ellsworth, A. McGarr, H. Benz, *Bull. Seismol. Soc. Am.* **104**, 2162 (2014).
11. C. Frohlich *et al.*, *J. Geophys. Res.* **119**, 581–593 (2014).
12. S. Horton, *Seismol. Res. Lett.* **83**, 250–260 (2012).
13. M. D. Petersen *et al.*, Incorporating induced seismicity in the 2014 United States National Seismic Hazard Model—Results of 2014 workshop and sensitivity studies. *U.S. Geol. Surv. Open-File Rep.* **2015-1070** (2015).
14. P. A. Hsieh, J. D. Bredehoeft, *J. Geophys. Res.* **86** (B2), 903–920 (1981).
15. C. Nicholson, E. Roelofs, R. L. Wesson, *Bull. Seismol. Soc. Am.* **78**, 188–217 (1988).
16. J. Ake, K. Mahrer, D. O'Connell, L. Block, *Bull. Seismol. Soc. Am.* **95**, 664–683 (2005).
17. C. Frohlich, C. Hayward, B. Stump, E. Potter, *Bull. Seismol. Soc. Am.* **101**, 327–340 (2011).
18. W.-Y. Kim, W.-Y. Kim, *J. Geophys. Res.* **118**, 3506–3518 (2013).
19. C. Frohlich, *Proc. Natl. Acad. Sci. U.S.A.* **109**, 13934–13938 (2012).
20. U.S. Environmental Protection Agency, Evaluation of impacts to underground sources of drinking water by hydraulic fracturing of coalbed methane reservoirs. EPA Publication 816-F-04-017 (2004).
21. ANSS Comprehensive Catalog (ComCat), U.S. Geological Survey, <http://earthquake.usgs.gov/earthquakes/search/>; accessed 15 February 2015.
22. S. D. Davis, C. Frohlich, *Seismol. Res. Lett.* **64**, 207–224 (1993).
23. A. Frankel, *Seismol. Res. Lett.* **66**, 8–21 (1995).
24. K. M. Keranen, M. Weingarten, G. A. Abers, B. A. Bekins, S. Ge, *Science* **345**, 448–451 (2014).
25. Well shut-in occurs when injection operations are either temporarily or permanently ceased, but the tubing and casing of the well remain in place for possible future reactivation of injection operations.

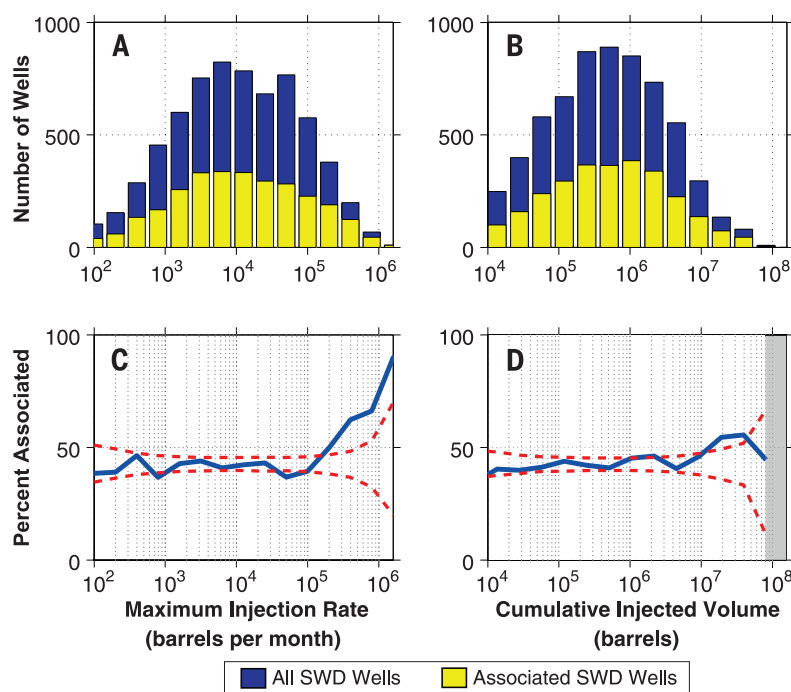


Fig. 4. Well operational parameter analysis. (A) Histogram showing the maximum monthly injection rate of salt water disposal (SWD) wells in Oklahoma, Arkansas, Colorado, and New Mexico. The blue and yellow bars show the number of wells operating at a given maximum monthly injection rate for all SWD wells (blue) and SWD wells spatiotemporally associated with an earthquake (yellow). (B) Histogram showing the cumulative injected volume at all wells in the same states as those in (A). The blue and yellow bars represent the number of wells operating at a given cumulative injected volume for all SWD wells (blue) spatiotemporally associated SWD wells (yellow). Injection data for Oklahoma were available from 1995 to 2013, for Arkansas from 1999 to 2013, for Colorado from 1999 to 2014, and for New Mexico from 1994 to 2014. (C and D) The percentage of all wells that are associated with an earthquake in each histogram bin is plotted as a function of (C) maximum monthly injection rate and (D) cumulative injected volume. The two dashed red lines represent the upper (95%) and lower (5%) confidence bounds in each bin generated by 10,000 bootstrap resamples and following the assumption that the rate of association is random. The shaded gray region of (D) indicates a lack of associated wells at the given volume. These data are also broken down state by state and for EOR wells in figs. S9 and S10.

26. Well completion is the process to ready for injection. This process includes installing tubing used to inject fluid, perforating the portion of the well in the injection zone, and casing the well to ensure no injection fluids leakage.
27. K. E. Murray, A. A. Holland, *Shale Shaker* **65**, 98–106 (2014).
28. C. Frohlich, J. I. Walter, J. F. W. Gale, *Seismol. Res. Lett.* **86** (2A), 492–499 (2015).
29. A. McGarr, *J. Geophys. Res.* **81**, 1487–1494 (1976).
30. A. McGarr, *J. Geophys. Res.* **119**, 1008–1019 (2014).
31. L. V. Block, C. K. Wood, W. L. Yeck, V. M. King, *Seismol. Res. Lett.* **85**, 609–624 (2014).
32. Y. Zhang et al., *Ground Water* **51**, 525–538 (2013).
33. The volume conversion from the oil industry standard of barrels to the metric standard of meters cubed is

~6.29 barrels per meter cubed, assuming a 42-gallon oil barrel.

34. B. Efron, R. J. Tibshirani, *An Introduction to the Bootstrap* (CRC press, Boca Raton, FL, 1994).
35. Information on materials and methods is available on Science Online.
36. J. Rutqvist et al., *Math. Geosci.* **47**, 3–29 (2015).
37. W. D. Mooney, M. K. Kaban, *J. Geophys. Res.* **115**, B12424 (2010).

ACKNOWLEDGMENTS

This work was conducted as a part of the Understanding Fluid Injection Induced Seismicity Project supported by the John Wesley Powell Center for Analysis and Synthesis, funded by the U.S. Geological Survey (grant G13AC00023). We thank J. Hardebeck and W. Ellsworth for their thoughtful comments. This project was aided by injection data

contributed by A. Holland (OK), C. Eisenger (CO), T. Kropatsch (WY), J. Amrhein (IN), T. Tomastik (OH), S. Platt (PA), I. Allred (UT), M. Berry (UT), A. Wickert (TX), and I. Van-Floten (CEUS). This project used earthquake data from the ANSS Comprehensive Catalog. The well data used in this study are available as supplementary materials on Science Online.

SUPPLEMENTARY MATERIALS

www.sciencemag.org/content/348/6241/1336/suppl/DC1
Materials and Methods
Figs. S1 to S18
Tables S1 to S4
References (38–46)

16 March 2015; accepted 28 May 2015
10.1126/science.aab1345

POLARON DYNAMICS

Long-lived photoinduced polaron formation in conjugated polyelectrolyte-fullerene assemblies

Rachel C. Huber,^{1*} Amy S. Ferreira,^{1*} Robert Thompson,¹ Daniel Kilbride,¹ Nicholas S. Knutson,¹ Lekshmi Sudha Devi,¹ Daniel B. Toso,² J. Reddy Challa,¹ Z. Hong Zhou,^{2,3} Yves Rubin,^{1†} Benjamin J. Schwartz,^{1,3†} Sarah H. Tolbert^{1,3,4,†}

The efficiency of biological photosynthesis results from the exquisite organization of photoactive elements that promote rapid movement of charge carriers out of a critical recombination range. If synthetic organic photovoltaic materials could mimic this assembly, charge separation and collection could be markedly enhanced. We show that micelle-forming cationic semiconducting polymers can coassemble in water with cationic fullerene derivatives to create photoinduced electron-transfer cascades that lead to exceptionally long-lived polarons. The stability of the polarons depends on the organization of the polymer-fullerene assembly. Properly designed assemblies can produce separated polaronic charges that are stable for days or weeks in aqueous solution.

In biological photosynthetic systems, energy cascade structures promote the spatial separation of photogenerated charges created at the reaction center, preventing their recombination. These energy cascade structures require close proximity of the electron donors and acceptors, on the scale of ~1 nm, and the corresponding electron transfer (ET) processes take only a few picoseconds (7). Similarly, photoexcitation in artificial organic photovoltaic (OPV) cells generates dissociated charges at a donor-acceptor interface on subpicosecond time scales. However, OPVs suffer a large degree of recom-

bination because they rely on phase separation of the conjugated polymer donor and fullerene acceptor into domains on the length scale of 10 to 20 nm to facilitate efficient exciton diffusion and charge transfer (2, 3). The high charge densities present in OPVs, coupled with the low dielectric constant of organic materials, favor carrier recombination before the charges can be extracted through external electrodes. If OPVs could be designed to use ET cascade structures that are reminiscent of photosynthetic complexes, it should be possible to greatly improve charge separation and reduce recombination losses (4).

Here we describe how molecular self-assembly can enable dissolved OPV materials (conjugated polymers and fullerenes) in aqueous solution to mimic the ET cascade structures of biological complexes and allow us to “spatially” control photogenerated charges. We demonstrate efficient long-time charge separation following photoexcitation: The ET cascade produces separated polarons that are exceptionally stable for weeks, a lifetime that is unprecedented

for OPV materials. Although long polaron lifetimes have been observed in covalently linked donor-acceptor dyads and triads (5) and micellar structures (6), our use of standard organic photovoltaic materials sets this work apart. In addition, our use of self-assembly provides potential future advantages in reproducibility and scalability, both of which are major hurdles for conventional OPVs with kinetically controlled structures (7–9). Finally, the photoinduced charge separation we achieve takes place in water, opening possibilities for the “green” production of artificial photosynthetic devices.

The particular materials used in this study are a combination of a conjugated polyelectrolyte, poly(fluorene-alt-thiophene) (PFT) (10), and several regioisomers of the charged fullerene derivatives C₆₀-N,N-dimethylpyrrolidinium iodide [C₆₀(PI)_n], where *n* is the number of charged pyrrolidinium iodide groups (11) (Fig. 1, A to C). PFT is a water-soluble semiconducting polyelectrolyte whose bis-alkylated sp³-hybridized fluorenyl carbon forms a wedge-shaped monomer that facilitates the assembly of the charged polymer into rod-like micelles (Fig. 1B); details of how this polymer assemblies have been published previously (10). Because of the charged nature of the polymer, the electron acceptor(s) must also carry cationic charges to avoid heterocoagulation. The synthesis of C₆₀(PI)_n, depending on the reaction conditions, produced multiadducts with *n* ranging from 2 to 5, including multiple regioisomers for each *n*. To avoid confusion, we will refer to C₆₀(PI)_n with *n* = 3 to 5 as “higher” adducts and fullerenes with *n* = 2 as “mixed-bis” adducts.

We achieved control over the solution-phase aggregation of these materials by exploiting the different solubility properties of the conjugated polyelectrolyte and charged fullerene derivatives. Mixed-bis adducts show limited solubility (without PFT) in aqueous solution, whereas higher adducts are water soluble at high concentration. This difference suggests that the mixed-bis adducts should coassemble in aqueous solution with PFT, a result we confirmed by cryogenic electron microscopy (cryoEM), small-angle x-ray scattering (SAXS), and luminescence quenching studies. CryoEM images of pure PFT, PFT:mixed-bis adducts, and PFT:high adducts

¹Department of Chemistry and Biochemistry, University of California–Los Angeles (UCLA), Los Angeles, CA 90095-1569, USA. ²Department of Microbiology, Immunology and Molecular Genetics, and the Biomedical Engineering Program, UCLA, Los Angeles, CA 90095, USA. ³The California NanoSystems Institute (CNSI), UCLA, Los Angeles, CA 90095, USA. ⁴Department of Materials Science and Engineering, UCLA, Los Angeles, CA 90095, USA.

*These authors contributed equally to this work. †Corresponding author. E-mail: tolbert@chem.ucla.edu (S.H.T.), schwartz@chem.ucla.edu (B.J.S.), rubin@chem.ucla.edu (Y.R.)

are shown in Fig. 1, D to F. Pure PFT samples self-assemble into branched micelles that are roughly 4 ± 0.5 nm in diameter and 30 to 50 nm in length. CryoEM images of PFT assembled with mixed-bis adducts are visually similar to the pure PFT, indicating association of the $C_{60}(PI)_2$ with the PFT micelles. In contrast, cryoEM images of PFT:high adducts appear blurry because these solutions contain separate PFT and fullerene agglomerates.

This interpretation of coassembly of PFT with mixed-bis adducts is also supported by SAXS measurements (Fig. 2, A and B). We radially averaged the SAXS data and fit it to a power law to extract the exponent α , which is related to the polymer fractal structure (12, 13). Values of $\alpha = 1, 2$, and 4 correlate to rigid rod, lamellar, and spherical structures, respectively, although interactions between molecules cause deviations from these ideal slopes. Analysis of SAXS data for pure PFT yielded $\alpha = 1.5$ at low q (rod-like at large size), increasing to $\alpha = 3.7$ at high q (sphere-like at small size). Deviation from $\alpha = 1$ arose from

the branched network seen by cryoEM (Fig. 1D) (14). SAXS power-law slopes for $C_{60}(PI)_n$ high-adducts correspond to a percolation network at low q and rod-like behavior at high q , indicating aggregation (12, 15). SAXS data from the combined PFT:high adducts solution was well approximated as the mass-scaled sum of the pure PFT and pure fullerene scattering, suggesting a nonassembled mixture, similar to that seen by cryoEM. By contrast, mass-scaled SAXS from solutions of PFT and mixed-bis adducts is nearly identical to the pure PFT. These results provide strong evidence that $C_{60}(PI)_2$ and PFT coassemble into a single micellar aggregate.

Finally, electronic interactions in the polymer-fullerene assemblies were confirmed with luminescence quenching, which provides an indirect measure of the photoinduced charge transfer from the polymer to the fullerenes (16). Solutions of PFT:high adducts showed relatively little photoluminescence (PL) quenching, presumably because the donors and acceptors were

not in close physical proximity, but aqueous solutions of PFT with the mixed-bis adducts had substantial PL quenching, indicating both physical and electronic contact (Fig. 3A). The data indicate that >75% of the PFT excitations were quenched in the presence of the mixed-bis adducts.

We determined the dynamics of charge separation in these donor-acceptor assemblies using ultrafast broadband transient absorption spectroscopy on dilute aqueous solutions of coassembled PFT with mixed-bis adducts (17). Representative transient absorption spectra at different probe delays following excitation at 470 nm are shown in Fig. 3B. We assigned the negative transient absorption peak near 520 nm to stimulated emission, as the spectral features and the lifetime (Fig. 3C) matched the fluorescence emission. Interestingly, the 690-nm absorption of the PFT hole polaron (P^+) appeared on a subpicosecond time scale after photoexcitation (18, 19). This ultrafast appearance of P^+ confirmed that the $C_{60}(PI)_2$ adducts must be coassembled with PFT, because other geometries would require diffusion or other structural rearrangements that could not occur so quickly. Once formed, about 75% of the PFT polarons in these dilute samples decayed back to the ground state in ~ 200 ps (Fig. 3C). The remaining polarons survived past the nanosecond time scale.

To mimic biological charge-separation systems, coassembly and rapid charge separation are required, but if they are followed by rapid recombination, the charges cannot be extracted. A fullerene acceptor that is optimized for charge separation thus needs to contain one class of compounds that can assemble intimately with the PFT for efficient charge transfer, and a second class of compounds that can assemble more loosely, allowing us to pull the electron away from the PFT and prevent recombination. Fortunately, both types of compounds were already available within our mixed-bis sample, and their properties could be examined simply by separating $C_{60}(PI)_2$ regioisomers. Our mixed-bis samples were primarily composed of four isomers (10% *trans*-1, 39% *trans*-2, 44% *trans*-3,

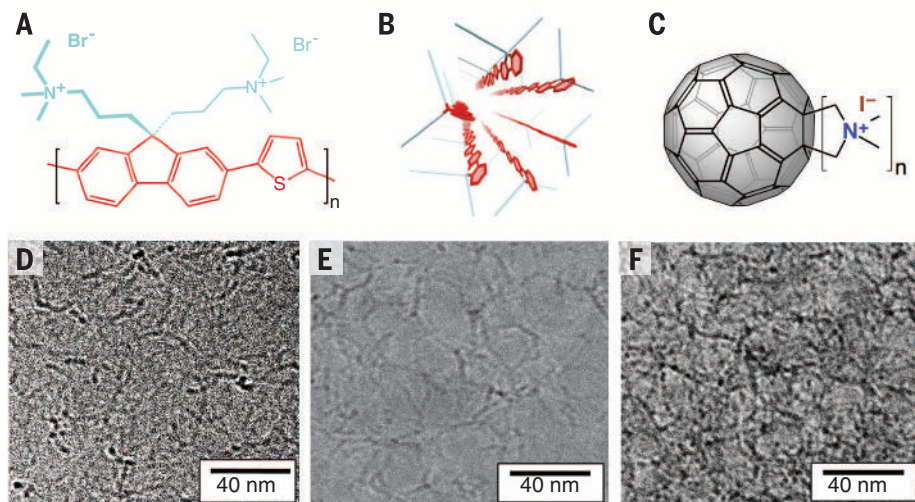


Fig. 1. PFT and charged fullerene structure and assembly. PFT structure (A); cartoon of a PFT micelle (B); charged fullerenes (C). CryoEM images of pure PFT (D), PFT:mixed-bis adducts (E), and PFT:high adducts (F).

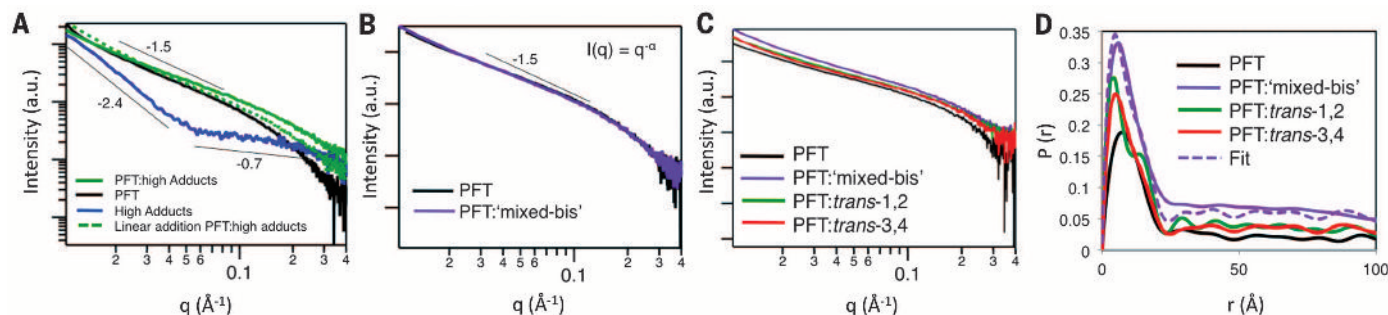


Fig. 2. SAXS data for PFT and PFT/fullerene mixtures. (A) Data for PFT:high-adducts are reasonably approximated by a sum of PFT + high-adducts. (B) The PFT:mixed-bis profile overlap mass-scaled PFT data. (C) Raw scattering data for all PFT and PFT:bis-fullerene samples are similar. (D) Distance distribution functions, $P(r)$, obtained by Fourier transformation of the data in (C) show different fullerene environments for *trans*-1,2 and *trans*-3,4, with PFT:mix-bis corresponding to the sum of the two.

and 7% *trans*-4). Structures of each of the isomers are shown in Fig. 4, A to D. We partially separated these isomers by silica gel column chromatography of the neutral pyrrolidine precursors (prior to quaternization), producing fractions that we refer to as *trans*-1,2 (29% *trans*-1 and 71% *trans*-2) and *trans*-3,4 (14% *trans*-2, 74% *trans*-3, and 12% *trans*-4). The full characterization of all of these materials is found in figs. S1 to S22 of the supplementary materials (17). The *trans*-1,2 fullerenes have charges on nearly opposite sides of the buckyball and can be viewed as isotropically charged molecules that should not easily insert into a PFT micelle. By contrast, the angle between charges in *trans*-3 is $\sim 145^\circ$ and that between charges in *trans*-4 is 103° , suggesting more amphiphilic molecules that could insert into the PFT micelle.

The coassembly of PFT with *trans*-1,2 and *trans*-3,4 was examined via SAXS. Raw scattering data for all of the samples looked similar to the data for pure PFT (Fig. 2C), but Fourier analysis using cylindrical boundary conditions showed subtle variations. In Fig. 2D, PFT and PFT:*trans*-3,4 showed similar probability distributions, supporting the model of insertion of fullerene into the PFT micelle. PFT:*trans*-1,2 shows two peaks, reminiscent of a polymer micelle with a partial “shell” of fullerenes surrounding the outside. The PFT:mixed-bis data were well fit by a simple linear combination of the PFT:*trans*-1,2 and PFT:*trans*-3,4 probability distributions, further supporting the idea that *trans*-3,4 assembles on the inside of the polymer micelle, whereas *trans*-1,2 surrounds the outside. The relative locations of the two different sets of fullerenes were also confirmed via solvatochromic absorption measurements (fig. S25). These measurements show that the ultraviolet absorption of *trans*-1,2 fullerenes assembled with PFT matches that of the fullerenes in pure water, indicating that *trans*-1,2 sits outside of the PFT micelle. In contrast, the absorption of the *trans*-3,4 fullerenes assembled with PFT matches that of the fullerenes in organic solvents, indicating that *trans*-3,4 sits in a lower dielectric environment like the micelle interior.

Figures 4, F and G, show luminescence quenching measurements that further support the idea that different isomers of $C_{60}(PI)_2$ assemble in different places in the PFT micelle. The luminescence decays shown in Fig. 4G were taken with a Kerr-gated time-resolved fluorescence setup using CS_2 as the gate medium, providing a time resolution of ~ 1 ps (20). Clearly, the PFT fluorescence is quenched nearly to the instrument limit in concentrated solutions when assembled with *trans*-3,4 fullerenes, verifying that the photoinduced charge transfer to these fullerenes is ultrafast. In contrast, there is almost no fast quenching of the PFT emission with an equal amount of *trans*-1,2 fullerenes, reflecting their assembled position predominantly on the outside of the micelle, out of range for fast ET. Figure 4F shows steady-state luminescence measurements on these same samples. Con-

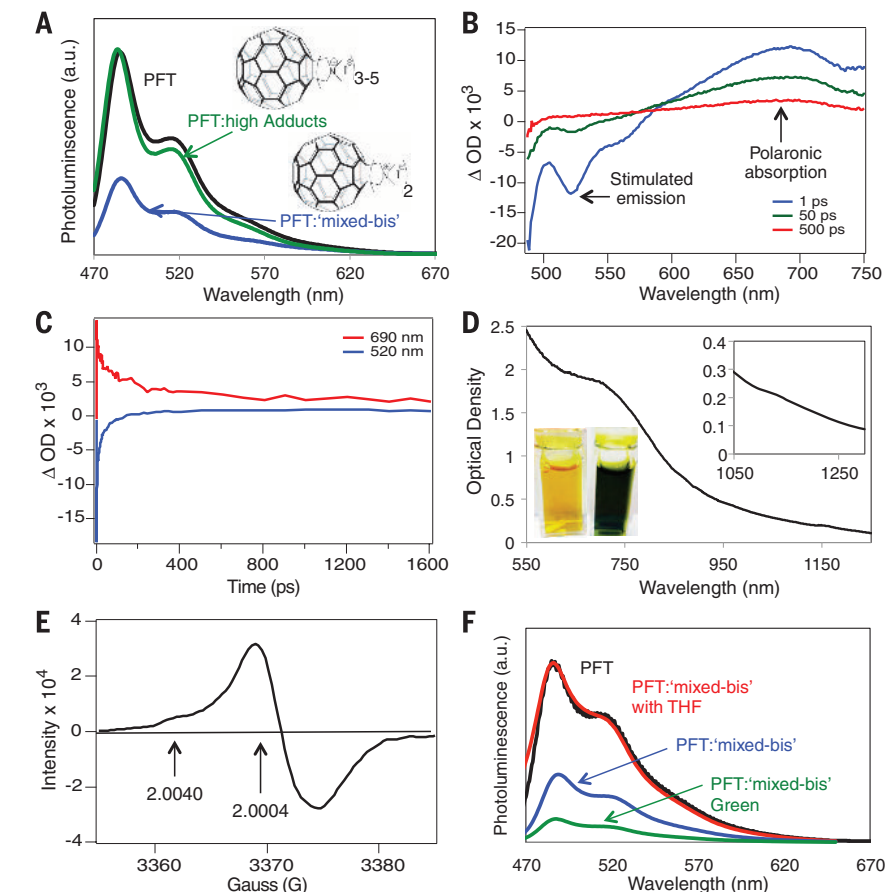


Fig. 3. Formation of P⁺ and N⁻ polarons requires intimate assembly of the polymer and fullerene.

(A) PL of PFT, PFT:high adducts, and PFT:mixed-bis; (B) pump-probe spectroscopy for dilute PFT:mixed-bis solutions excited at 470 nm showing the rapid formation of both excitons and polarons; (C) time decays for the stimulated emission and the polaronic absorption from (B). Absorption from a green concentrated PFT/fullerene solution showing both P⁺ and N⁻ polarons (D). EPR from a similar green solution, again showing both P⁺ and N⁻ polarons (E). PL for various concentrated PFT:mixed-bis solutions showing that polarons quench luminescence, but the addition of THF, which, destroys the PFT/fullerene assembly, restores PL intensity (F).

sistent with the time-resolved data, assemblies of PFT with *trans*-1,2 fullerenes showed little luminescence quenching, whereas PFT assembled with *trans*-3,4 fullerenes had strong quenching. These quenching results suggested that not only can we selectively associate fullerenes with polymer micelles using the number of charges, we can also control the position of the fullerene within the micelle by the placement of the charges (Fig. 4E).

Given this degree of control, the next step was to examine long-lived excitations in assemblies of PFT and mixed-bis adducts containing both intimately assembled *trans*-3,4 and more isotropically charged *trans*-1,2 fullerenes. Ideally, this coassembly should permit rapid photoinduced electron transfer from PFT to the *trans*-3,4 fullerenes, followed by a second ET step to the *trans*-1,2 fullerenes. If this type of directed ET cascade occurs, electrons on the *trans*-1,2 fullerenes would then be stabilized in the high-dielectric environment of the water surrounding the micelle, preventing recombination with

the PFT. Indeed, we found that photoexcitation of aqueous PFT:mixed-bis adduct solutions caused a dramatic color change from yellow to dark green over time (Fig. 3D); once the solution was exposed to light, the color change was essentially permanent, lasting days to weeks. Dilute solutions, like those used to collect the data in Fig. 3, B and C, required extensive light exposure (fig. S24), but when higher concentrations were used, the color change took place in just a few seconds under room lights, indicating that the quantum yield for long-lived charge separation is much higher than the $\sim 25\%$ in dilute solutions (compare Fig. 3B).

PFT is a blue-absorbing polymer with an absorption maximum at 430 nm in water and little to no absorbance above 550 nm (10). The color change from yellow to green was confirmed to arise from the appearance of the PFT hole polaron (P⁺) by comparing steady-state data (Fig. 3D) with transient absorption data (Fig. 3B) and absorption from PFT oxidized with iodine, both of which show absorption in the sub-gap region

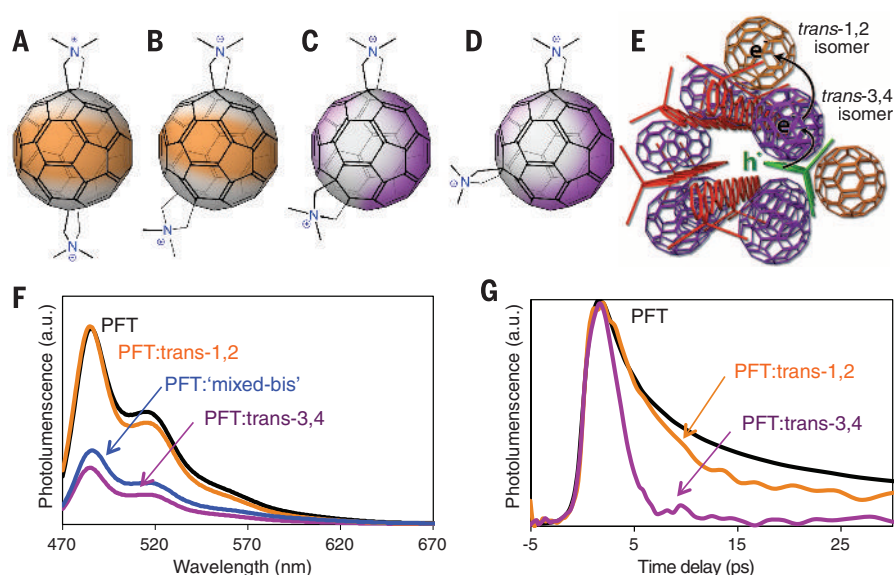


Fig. 4. Spectroscopic evidence for long-lived charged species in solution. Chemical structures of *trans*-1 bis (A), *trans*-2 bis (B), *trans*-3 bis (C), and *trans*-4 bis (D) fullerene derivatives with color emphasizing the hydrophobic regions. Cartoon depicting the assembly of *trans*-1,2 (orange) and *trans*-3,4 (purple) bis fullerenes with PFT (red). Photoexcitation of the PFT backbone leads to charge transfer first to *trans*-3,4 and then to *trans*-1,2, where the electron remains due to stabilization by the reorganization of water. The hole (green, h^+) remains on PFT (E). PL of PFT, PFT:mixed-bis, PFT:*trans*-3,4 bis, and PFT:*trans*-1,2 bis (F). Time-resolved luminescence for assembled concentrated PFT:*trans*-3,4 bis and PFT:*trans*-1,2 bis samples (G).

at ~690 nm (fig. S23) (21). The Fig. 3D inset shows that simultaneously, a substantially weaker negative (N^-) polaron absorption peak caused by the $C_{60}(PI)_2$ molecular anion was observed at 1180 nm. The low intensity of the N^- absorption has several origins: (i) The absorption cross-section of fullerene anions is much smaller than that of the polymer polarons (22); (ii) the weak N^- absorption peak sits on top of a broad scattering background from the coassembled micelles in solution; and (iii) the N^- polaron might react with impurities in the water, despite our best efforts to deoxygenate the solutions by freeze-pump-thaw techniques (23).

To further confirm the formation of stable, separated N^- and P^+ polarons after exposure to light, we performed electron paramagnetic resonance (EPR) experiments. Figure 3E shows the EPR signal from the green PFT:mixed-bis adducts solution; the g -factors for the N^- and P^+ polarons are 2.0004 and 2.0040, respectively, in good agreement with reported values for many other polymer-fullerene systems (24). The N^- polaron line width that we observed is broader than that in other polymer-fullerene systems, both because of the interaction of the water dipoles with the polarons and because of different spin-relaxation times for the electron and hole (25, 26). The critical difference between our coassembled system and previous systems, however, is that the previous EPR work required active photoexcitation (light-induced EPR) in order to observe the polaron signals. In contrast, once exposed to light, the polarons created in our PFT: $C_{60}(PI)_2$ solutions remained stable essentially indefinitely.

Final confirmation that the long-lived separated charges resulted from a self-assembled ET cascade comes by examining the details of absorption and luminescence for a range of samples in different solvents. As discussed above, aqueous solutions of PFT and *trans*-1,2 fullerenes show little PL quenching (Fig. 4, F and G), but they did briefly turn green during the course of the dissolution, indicating polaron formation (possibly from disordered polymer that transiently allowed the fullerene to partly insert into the micelle). By contrast, despite the efficient luminescence quenching in solutions of PFT coassembled with the *trans*-3,4 fullerenes (Fig. 4, F and G), the solutions did not turn green and ultrafast experiments (data not shown) indicate that polarons are formed on subpicosecond time scales (as in Fig. 3B), but recombine with 100% yield over the next few hundred picoseconds. These results indicate that controlling the spatial position of the fullerenes can dramatically affect carrier dynamics. Moreover, photoexcitation of green-colored PFT:mixed-bis fullerene solutions results in increased luminescence quenching because PFT excitons are further quenched by P^+ polarons (Fig. 3F). However, when tetrahydrofuran (THF), which is known to disassemble the polymer micelles (27), was added to the coassembled green system, the luminescence signal regained its intensity, indicating a fully reversible system (Fig. 3F). These results further support the idea that intimate assemblies with well-controlled molecular positions are required to facilitate a charge transfer cascade and avoid recombination. When nanoscale architecture is optimized, the result is stable

polarons that could potentially be applied to improve organic photovoltaic cells via suppression of charge recombination.

REFERENCES AND NOTES

1. A. W. Rutherford, *Trends Biochem. Sci.* **14**, 227 (1989).
2. J. Piris *et al.*, *J. Phys. Chem. C* **113**, 14500 (2009).
3. P. E. Shaw, A. Ruseckas, I. D. W. Samuel, *Adv. Mater.* **20**, 3516 (2008).
4. S. Gellinas *et al.*, *J. Phys. Chem. C* **115**, 7114 (2011).
5. J. Verhoeven, *J. Photochem. Photobiol. Photochem. Rev.* **7**, 40 (2006).
6. T. Miura, K. Maeda, H. Murai, T. Ikoma, *J. Phys. Chem. Lett.* **6**, 267 (2015).
7. C. Lungenschmied *et al.*, *Sol. Energy Mater. Sol. Cells* **91**, 379 (2007).
8. T. Yasuda, Y. Shinohara, T. Ishi-i, L. Han, *Org. Electron.* **13**, 1802 (2012).
9. T. Costa *et al.*, *J. Phys. Chem. B* **118**, 613 (2014).
10. A. P.-Z. Clark *et al.*, *ACS Nano* **7**, 962 (2013).
11. A. Cassell, C. Asplund, J. Tour, *Angew. Chem.* **38**, 2403 (1999).
12. G. Beaucage, *J. Appl. Cryst.* **29**, 134 (1996).
13. S. Choudhary, S. R. Bhatia, *Carbohydr. Polym.* **87**, 524 (2012).
14. Y.-C. Li *et al.*, *Langmuir* **22**, 11009 (2006).
15. U. Jeng *et al.*, *Nucl. Instrum. Methods Phys. Res. A* **600**, 294 (2009).
16. Y. Park *et al.*, *Polymer (Guildf.)* **55**, 855 (2014).
17. See supplementary materials on Science Online for details.
18. R. Österbacka, C. P. An, X. M. Jiang, Z. V. Vardeny, *Science* **287**, 839 (2000).
19. F. Paquin *et al.*, *Phys. Rev. Lett.* **106**, 197401 (2011).
20. S. Arzhantsev, M. Maroncelli, *Appl. Spectrosc.* **59**, 206 (2005).
21. C. Chiang *et al.*, *Phys. Rev. Lett.* **39**, 1098 (1977).
22. T. Kato *et al.*, *Chem. Phys. Lett.* **186**, 35 (1991).
23. D. M. Guldi, M. Prato, *Acc. Chem. Res.* **33**, 695 (2000).
24. V. I. Krinichnyi, *Sol. Energy Mater. Sol. Cells* **92**, 942 (2008).
25. T. J. Savenije *et al.*, *Phys. Chem. Chem. Phys.* **13**, 16579 (2011).
26. J. Ceuster, E. Goovaerts, A. Bouwen, J. C. Hummelen, V. Dyakonov, *Phys. Rev. B* **64**, 195206 (2001).
27. E. G. Kelley, T. P. Smart, A. J. Jackson, M. O. Sullivan, T. H. Epps 3rd, *Soft Matter* **7**, 7094 (2011).

ACKNOWLEDGMENTS

This work was supported by the NSF under grant CHE-1112569 and by the Center for Molecularly Engineered Energy Materials, an Energy Frontier Research Center funded by the U.S. Department of Energy (DOE) under Contract DE-AC06-76RLO-1830. A.S.F. acknowledges support from The Clean Green IGERT (NSF DGE-0903720). This work made use of facilities support by the NSF under equipment grant CHE-1048804. Portions of this work were conducted at the Stanford Synchrotron Radiation Lightsource (SSRL), which is supported under DOE Contract DE-AC02-76SF00515. The SSRL Structural Molecular Biology Program is supported by the DOE Office of Biological and Environmental Research and by the National Institutes of Health, National Institute of General Medical Sciences (including P41GM103393). We acknowledge the use of instruments at the Electron Imaging Center for NanoMachines supported by the NIH (1S10RR23057 to Z.H.Z.) and CNSI at UCLA.

SUPPLEMENTARY MATERIALS

www.sciencemag.org/content/348/6241/1340/suppl/DC1
Materials and Methods
Figs. S1 to S25
References (28–31)

14 January 2015; accepted 21 May 2015
10.1126/science.aaa6850

BATTERIES

Topological defect dynamics in operando battery nanoparticles

A. Ulvestad,¹ A. Singer,¹ J. N. Clark,^{2,3} H. M. Cho,⁴ J. W. Kim,¹ R. Harder,⁵ J. Maser,⁵ Y. S. Meng,^{4*} O. G. Shpyrko^{1*}

Topological defects can markedly alter nanomaterial properties. This presents opportunities for “defect engineering,” where desired functionalities are generated through defect manipulation. However, imaging defects in working devices with nanoscale resolution remains elusive. We report three-dimensional imaging of dislocation dynamics in individual battery cathode nanoparticles under operando conditions using Bragg coherent diffractive imaging. Dislocations are static at room temperature and mobile during charge transport. During the structural phase transformation, the lithium-rich phase nucleates near the dislocation and spreads inhomogeneously. The dislocation field is a local probe of elastic properties, and we find that a region of the material exhibits a negative Poisson’s ratio at high voltage. Operando dislocation imaging thus opens a powerful avenue for facilitating improvement and rational design of nanostructured materials.

Nanoconfinement causes material properties to differ substantially from their bulk counterparts in many ways and can lead to size-tunable thermodynamics, faster intercalation kinetics, and extended life cycles (1). “Defect engineering” can be used to further design and optimize properties owing to the appreciable influence of defects on material properties (2, 3). Motivated by this opportunity, many researchers worked to develop imaging techniques capable of resolving defects, in particular dislocations (4, 5).

The observation of dislocations with techniques such as x-ray topography (6, 7) and reciprocal space mapping dates back to the 1950s (8–10). The coherence of third-generation synchrotron x-ray beams enabled several new defect imaging techniques (11), including phase contrast tomography (12) and Bragg x-ray ptychography (13), which was recently used to visualize the displacement field of a dislocation in silicon. For a recent review of defect imaging using coherent methods, see (14).

Bragg coherent diffractive imaging (BCDI) relies on interference produced by coherent x-rays and phase-retrieval algorithms to reconstruct the three-dimensional (3D) electron density and atomic displacement fields in nanocrystals (15–18). The displacement field information that BCDI provides is complementary to the aforementioned techniques and crucial in identifying the character of single dislocations. BCDI

can also track, with nanoscale resolution, buried single defects under operando conditions.

The role of dislocations in Li-ion battery performance remains largely underexplored, and one of the few areas where materials can be further optimized. The appearance of dislocations correlates with capacity loss (19), as dislocations induce stress and strain (20). Yet, dislocations can relieve strain during phase transformations by allowing the interface between the phases to decohere and thus prevent cracking and the associated active material loss and undesirable surface reactions with the electrolyte (21, 22). To understand these nuances, we must first track single defects in operating devices under working conditions. We use BCDI to study single defects in the nanostructured disordered spinel material $\text{LiNi}_{0.5}\text{Mn}_{1.5}\text{O}_4$ (LNMO). LNMO is a promising high-voltage cathode material in which the lithium diffusion path-

way is three-dimensional (23). In addition, the material exhibits both two-phase coexistence and phase transformations at certain lithium concentrations during charge and discharge, as evidenced by both electrochemical and diffraction data (21, 24–26). The phases are different in their lattice constant but have the same symmetry group ($Fd3m$).

The experimental setup is shown schematically in Fig. 1. Focused coherent x-rays are incident on an in situ coin cell (fig. S1) that contains the nanoparticulate LNMO cathode material. X-ray diffraction data (fig. S2) and electrochemical data (fig. S3) confirm expected behavior of the LNMO cathode. The x-rays scattered by a single LNMO particle satisfying the (111) Bragg condition are recorded on an area detector (27). The experimental geometry, combined with the random orientation of the cathode nanoparticles, ensures that the (111) Bragg reflections corresponding to separate particles are well separated and an individual reflection can be isolated on the detector. The battery was cycled 101 times at a fast rate (30 min for full charge) before the imaging experiment. From the coherent diffraction data, we reconstruct both the 3D distribution of electron density, $\rho(x, y, z)$, and the 3D displacement field along $[111]$, $u_{111}(x, y, z)$, in an individual cathode nanoparticle with 35-nm spatial resolution (fig. S4) (27).

Figure 2A shows the isosurface rendering of the particle shape. Figure 2B shows a cross-section of the 3D displacement field $[u_{111}(x, y, z = z_0)]$ in the cathode nanoparticle. The $[111]$ direction is approximately along the x axis, whereas the x-ray beam is almost parallel to the z axis. To determine the defect type responsible for the displacement field in Fig. 2, B and C, Fig. 2D shows the displacement field magnitudes at a fixed radius, r , as a function of azimuthal angle, θ . Depending on the defect type, this angular distribution will have distinct features. For example, displacement fields generated by screw dislocations must vary linearly with θ (28). Edge dislocations produce

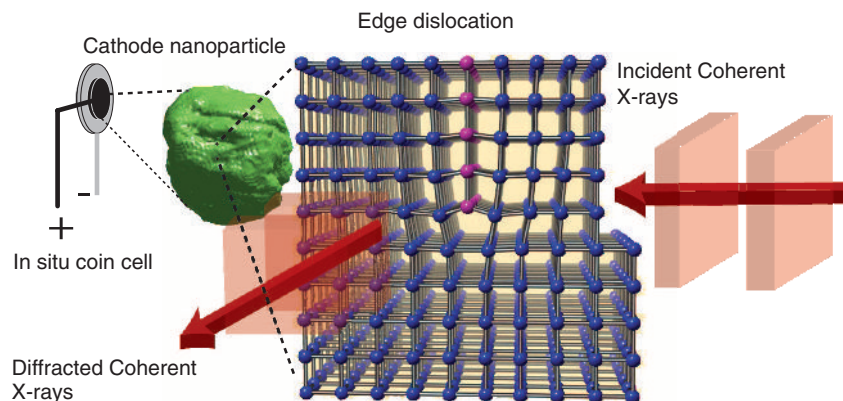


Fig. 1. Bragg coherent diffractive imaging experiment schematic. Coherent x-rays (red) are incident on a cathode nanoparticle (green) containing an edge dislocation. A schematic of an edge dislocation for a cubic unit cell structure is shown with the extra half plane colored purple. The diffracted x-rays carry information about the 3D electron density and atomic displacement fields within the particle that allows the type of dislocation to be identified.

¹Department of Physics, University of California–San Diego, La Jolla, CA 92093-0319, USA. ²Stanford PULSE Institute, SLAC National Accelerator Laboratory Menlo Park, CA 94025, USA. ³Center for Free-Electron Laser Science (CFEL), Deutsches Elektronensynchrotron (DESY), Notkestrasse 85, 22607 Hamburg, Germany. ⁴Department of NanoEngineering, University of California–San Diego, La Jolla, CA 92093-0448, USA. ⁵Advanced Photon Source, Argonne National Laboratory, Argonne, IL 60439, USA.

*Corresponding author. E-mail: shmeng@ucsd.edu (Y.S.M.); oshpyrko@physics.ucsd.edu (O.G.S.)

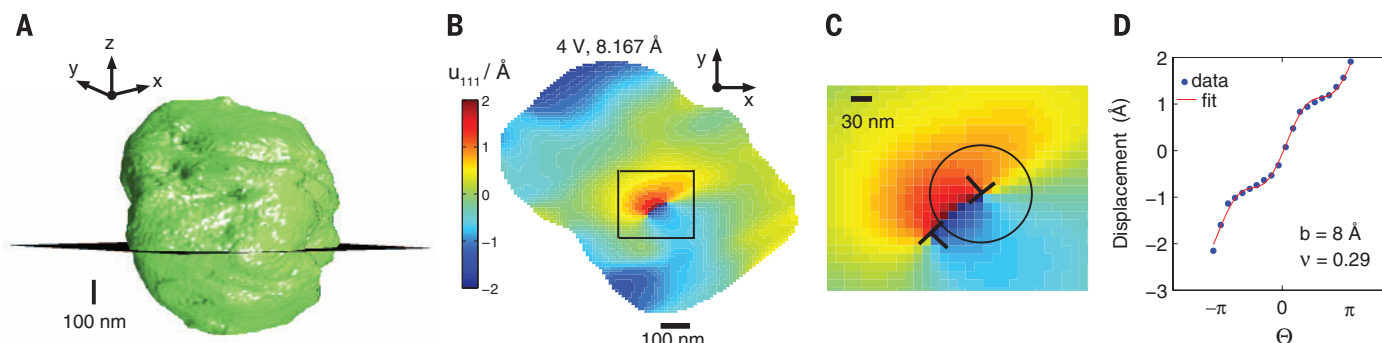


Fig. 2. Edge dislocation displacement field identified in a single LNMO cathode nanoparticle. (A) A green isosurface representing the particle shape. A black plane shows the spatial location of the cross-section of the u_{111} displacement field shown in (B). (C) Magnification of the boxed region in (B). Locations of edge dislocations are indicated by \perp . Data points in (D) correspond to the displacement values as a function of azimuthal coordinate θ at fixed radius r [shown as a black circle in (C)]. The red line is a two-parameter fit to the edge dislocation model described by Eqs. 1a and 1b.

displacements both perpendicular and parallel to the extra half plane given by (28)

$$u_{\perp} = \frac{b}{2\pi} \left(\theta + \frac{\sin 2\theta}{4(1-\nu)} \right) \quad (1a)$$

$$u_{\parallel} = -\frac{b}{2\pi} \left(\frac{1-2\nu}{4(1-\nu)} \log r^2 + \frac{\cos 2\theta}{4(1-\nu)} \right) \quad (1b)$$

where r and θ are the radial and azimuthal coordinate, b is the Burgers vector length, and ν is Poisson's ratio (see fig. S5 for coordinate definition). Thus, an edge dislocation produces a displacement field that varies linearly with θ with an additional periodic modulation. By inspection of Fig. 2D, we identify the displacement field in Fig. 2, B and C, as resulting from edge dislocations.

We quantitatively determined the edge dislocation properties and the elastic properties in the nearby region by using Eqs. 1a and 1b with b and ν as fit parameters (27). Other elastic parameters determined from the displacement field are consistent with expectations (27). The crystallographic geometry of the edge dislocation with respect to $[111]$ is determined from the 3D displacement field to be $50 \pm 8^\circ$, in good agreement with the predicted value of 54° for an edge dislocation along $\langle 100 \rangle$. The fitted Burgers vector magnitude of $8 \pm 1 \text{ Å}$ is in excellent agreement with the lattice constant along $\langle 100 \rangle$, which is 8.16 Å , and the fitted Poisson's ratio of 0.27 ± 0.1 agrees with the bulk value of 0.3 in the discharged state (29). For additional fit information, see figs. S6 and S7.

We mapped the edge dislocations in 3D, and by repeated measurements confirmed that they were static for at least an hour at room temperature (fig. S8). Figure 3 shows the evolution of the dislocation line as a function of charging. The width of the dislocation line reflects the uncertainty in the position as determined by the phase retrieval transfer function (27). The evolution of the single-particle lattice constant during charging and discharging is shown in fig. S9.

We observe dislocation line movement as a function of charge transport, which means that the dislocations are stable at room temperature

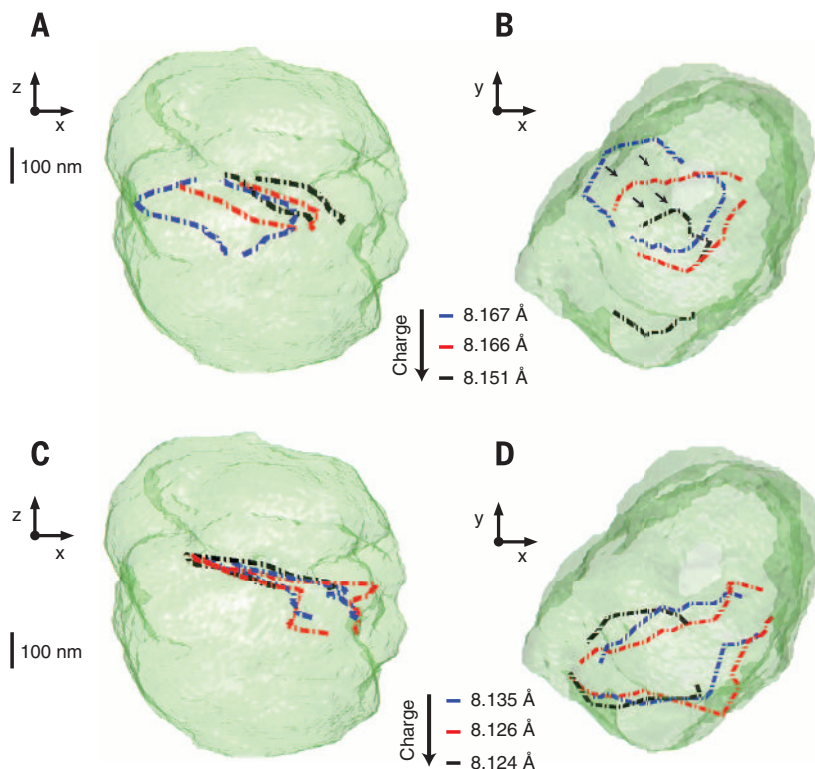


Fig. 3. Three-dimensional edge dislocation line evolution due to charging. The particle shape is represented by a semitransparent green isosurface. (A) Evolution of the dislocation line at three different charge states. (B) The same evolution as in (A) for a different view. (C) Evolution of the dislocation line for the subsequent three charge states. (D) The same evolution as in (C) for a different view.

and dynamic under applied current. There is inhomogeneity in the amount of movement among different line segments, and it does not appear to be random. Instead, there is preferential movement toward the boundary of the particle. Additional time sequences are shown in fig. S10.

We perform fits as shown in Fig. 2 to all dislocations as a function of charge state in order to locally determine the Poisson's ratio in the single particle along the dislocation line (27). Figure 4A shows Poisson's ratio of the particle in the vicinity of the dislocation line as a function of charge state. At full lithiation (discharged), the

local Poisson's ratio is in excellent agreement with the literature value of 0.3 (29). However, the lithium concentration changes as a function of voltage and is known to change material properties, including Young's modulus (30) and the diffusion coefficient (31). Surprisingly, we observe that Poisson's ratio decreases during delithiation, eventually becoming negative at roughly 4.5 V .

The negative Poisson's ratio, or auxetic property, could be due to the peculiar structural changes in LNMO. It is known that materials are auxetic for a variety of reasons, including the presence of microstructures, such as reentrant honeycombs,

and as a result of phase transformations (32). For example, auxetic behavior was attributed to a hinge-like structure in spinel CoFe_2O_4 (33), which has the same structure as LNMO. We hypothesize that a hinge-like mechanism as diagrammed in Fig. 4C is responsible for the reduction in the measured Poisson's ratio. At 4.5 V and higher, all of the Mn^{3+} ions are oxidized to Mn^{4+} , which

makes the Mn-O bond exceptionally strong because of the superior ligand field stabilization energy of Mn^{4+} due to its half-filled t_{2g} level (23). This leads to strong and weak bonds within the crystal, and ultimately to the hinge structure. As the voltage is increased and more lithium is removed, the hinge structure moves more freely and consequently the Poisson's ratio decreases.

If our hypothesis is correct, the delithiated LNMO spinel would be incredibly strain tolerant (34) and might be used to prevent structural collapse in layered oxide materials at high voltages when blended as a nanocomposite (35). The auxetic property may also explain why this material is relatively resistant to losing oxygen from the crystal structure at high voltage.

Near 4.7 V, LNMO exhibits two-phase coexistence and a structural phase transformation during charge and discharge, as evidenced by both electrochemical and diffraction data (24, 25, 36). The two phases differ in their lattice constant, whereas the symmetry group of the crystal remains the same. At the single-particle level, the phase transformation manifests itself as a splitting in the (111) diffraction peak, indicating that two lattice constants are present (see fig. S12 for diffraction data during the onset of the phase transformation and fig. S9 for single-particle lattice constant evolution). Figure S13 shows diffraction data midway through the phase transformation. Figure 5 shows the displacement and strain field evolution within the nanoparticle at two measurement times (left and right) corresponding to 4.7 and 4.69 V during the onset of the phase transformation during discharge. Again, the x axis corresponds to the [111] direction.

In Fig. 5A, we qualitatively identify an edge dislocation by inspection of the displacement field. Approximately 20 nm higher, the Li-rich phase nucleated above the dislocation and created tensile strain due to its larger lattice constant. However, this is below the spatial resolution of the experiment, and thus another cross-section (z_3) that is 40 nm higher is also shown to corroborate the previous statement. Thus, the observed dislocation is near the phase boundary between the Li-rich and Li-poor phase. From their proximity, we

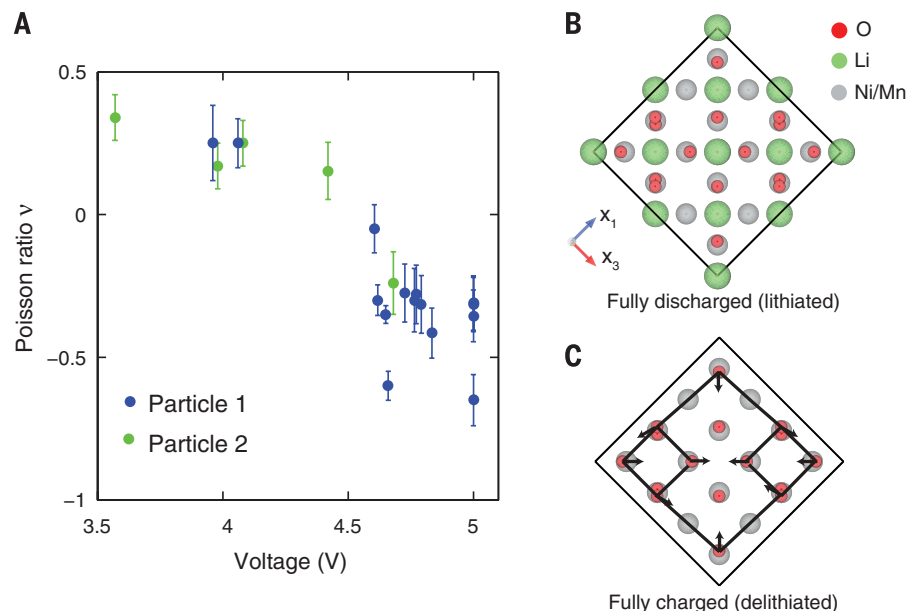


Fig. 4. The evolution of the local Poisson's ratio as a function of voltage and the proposed auxetic mechanism occurring in the LNMO unit cell. (A) Poisson's ratio values measured as a function of voltage for the particle discussed in the main text. Green points correspond to results from an additional measurement on a separate particle in another LNMO cathode battery (see fig. S11). (B and C) The LNMO unit cell when viewed along a primitive cubic lattice vector (x_1 and x_3 are the other primitive cubic lattice vectors) for the fully lithiated (discharged) and fully delithiated (charged) state, respectively. The proposed auxetic reentrant honeycomb structure is shown in black in (C).

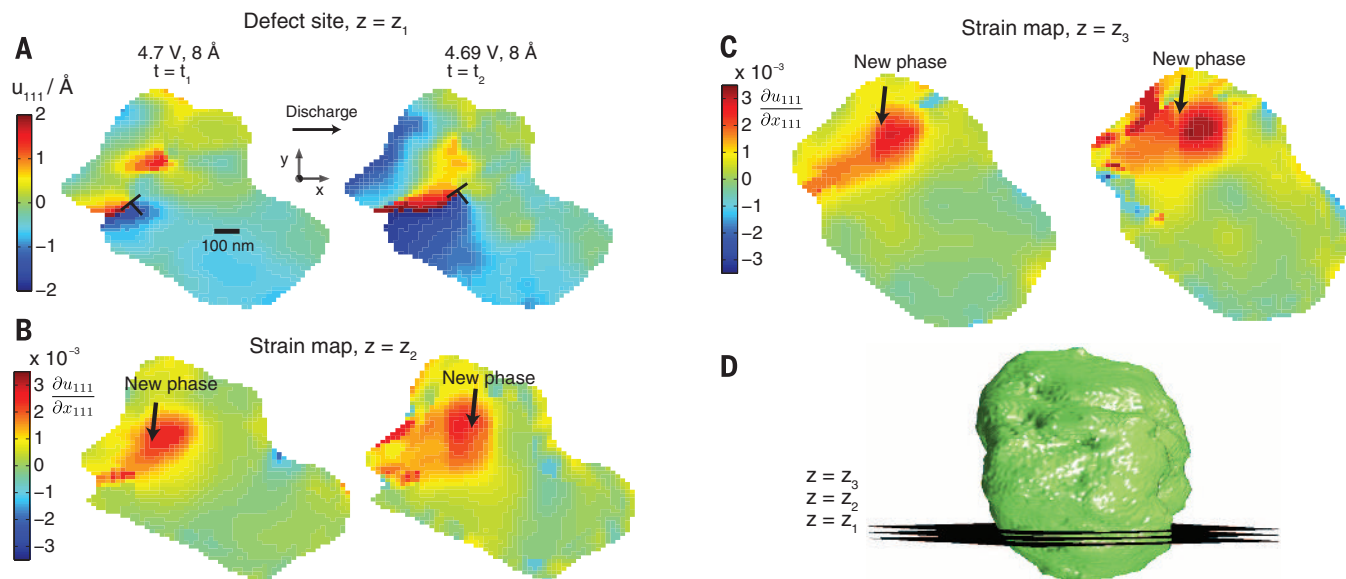


Fig. 5. Displacement and strain dynamics during the onset of the structural phase transformation. The displacement field within the particle is measured during the structural phase transformation during discharge. (A) The time evolution of a displacement field cross section with the edge dislocation indicated. (B) The time evolution of the compressive/tensile strain field in the [111] direction ($\partial u_{111}/\partial x_{111}$) at one cross-section higher than in (A). The new phase manifests itself as tensile (positive) strain and is shown in red. (C) The strain field evolution at another, higher cross-section. (D) A green isosurface representing the particle shape. Black planes show the location of the cross-sections displayed in (A) to (C).

conclude that the dislocation likely acts as a nucleation point for the new phase during the phase transformation, which is expected from theoretical calculations (37). Figure 5, B and C, show that further discharge causes the Li-rich phase to expand further into the particle, as opposed to nucleating a new phase region a considerable spatial distance away. This suggests the near-equilibrium pathway for the phase transformation at the single-particle level. The observation of a phase boundary is quite interesting in light of recent results showing the absence of a phase boundary during fast charging in LiFePO_4 (38). The relatively slow cycling rate (4 hours for full charge) used in this study is most likely responsible for this discrepancy.

We studied topological defect dynamics in crystalline nanoparticles under operando conditions using Bragg coherent diffractive imaging. Edge dislocations that are static at room temperature are dynamic in response to charge transport. The 3D dislocation displacement field serves as a local probe of elastic properties, and we observe that at high voltage, Poisson's ratio in the vicinity of the dislocation is vastly different from that at lower voltages. This calls for further investigation into using lithium ions to tune material properties and could explain why LNMO is resistant to oxygen loss at high voltage. We anticipate that imaging of dislocations can be used as a nanotechnology to locally probe elastic properties in nanomaterials and that LNMO could improve the strain tolerance of other cathodes. We reconstructed the onset of the phase transformation, observed the dislocation act as a nucleation point, and showed how the phase expands into the particle. Our results open up the imaging of weakly strained phase transformations to BCDI and unlock the potential for a synthesis/imaging feedback loop to engineer dislocations at the nanoscale.

REFERENCES AND NOTES

- M. Fichtner, *Phys. Chem. Chem. Phys.* **13**, 21186–21195 (2011).
- N. Shin, M. Chi, J. Y. Howe, M. A. Filler, *Nano Lett.* **13**, 1928–1933 (2013).
- L. D. Carr, M. T. Lusk, *Nat. Nanotechnol.* **5**, 316–317 (2010).
- M. J. Hytch, J. L. Putaux, J. M. Pénisson, *Nature* **423**, 270–273 (2003).
- H. F. Poulsen, *Three-Dimensional X-ray Diffraction Microscopy* (Springer, Berlin, 2004).
- B. K. Tanner, *X-ray Diffraction Topography* (Pergamon, Oxford, 1976).
- G. N. Ramchandran, *Proc. Indiana Acad. Sci.* **19**, 280 (1945).
- J. B. Newkirk, *Phys. Rev.* **110**, 1465–1466 (1958).
- A. R. Lang, *J. Appl. Phys.* **29**, 597 (1958).
- A. R. Lang, A. P. W. Makepeace, *J. Phys. D Appl. Phys.* **32**, A97 (1999).
- D. Le Bolloch et al., *Phys. Rev. Lett.* **95**, 116401 (2005).
- P. Cloetens et al., *Proc. SPIE* **4503**, 82 (2002).
- Y. Takahashi et al., *Phys. Rev. B* **87**, 121201 (2013).
- B. Abbey, *JOM* **65**, 1183–1201 (2013).
- J. N. Clark et al., *Science* **341**, 56–59 (2013).
- G. J. Williams, M. A. Pfeifer, I. A. Vartanyants, I. K. Robinson, *Phys. Rev. Lett.* **90**, 175501 (2003).
- A. Ulvestad et al., *Nano Lett.* **14**, 5123–5127 (2014).
- A. Ulvestad et al., *Appl. Phys. Lett.* **104**, 073108 (2014).
- H. Wang, Y. Jang, B. Huang, *J. Electrochem. Soc.* **146**, 473 (1999).
- H.-Y. Shadow Huang, Y.-X. Wang, *J. Electrochem. Soc.* **159**, A815 (2012).
- A. Van der Ven, C. Marianetti, D. Morgan, G. Ceder, *Solid State Ion.* **135**, 21–32 (2000).
- J.-M. Tarascon, M. Armand, *Nature* **414**, 359–367 (2001).
- B. Xu, S. Meng, *J. Power Sources* **195**, 4971–4976 (2010).
- J.-H. Kim, S.-T. Myung, C. S. Yoon, S. G. Kang, Y.-K. Sun, *Chem. Mater.* **16**, 906–914 (2004).

- A. Singer et al., *Nano Lett.* **14**, 5295–5300 (2014).
- K. Saravanan, A. Jarry, R. Kostecki, G. Chen, *Sci. Rep.* **5**, 8027 (2015).
- Materials and methods are available as supplementary materials on Science Online.
- D. Hull, D. J. Bacon, *Introduction to Dislocations* (Butterworth-Heinemann, Oxford, ed. 5, 2011).
- J. Christensen, J. Newman, *J. Electrochem. Soc.* **153**, A1019 (2006).
- S. Lee, J. Park, A. M. Sastry, W. Lu, *J. Electrochem. Soc.* **160**, A968–A972 (2013).
- M. Yang et al., *Chem. Mater.* **23**, 2832–2841 (2011).
- G. N. Greaves, A. L. Greer, R. S. Lakes, T. Rouxel, *Nat. Mater.* **10**, 823–837 (2011).
- M. Valant, A.-K. Axelsson, F. Aguesse, N. M. Alford, *Adv. Funct. Mater.* **20**, 644–647 (2010).
- K. E. Evans, A. Alderson, *Adv. Mater.* **12**, 617–628 (2000).
- M. S. Whittingham, *Chem. Rev.* **104**, 4271–4302 (2004).
- R. A. Huggins, *Advanced Batteries: Materials Science Aspects* (Springer, New York, 2008).
- C. Collins, *Acta Metall.* **18**, 1209–1215 (1970).
- H. Liu et al., *Science* **344**, 1252817 (2014).

ACKNOWLEDGMENTS

This work was supported by the U.S. Department of Energy (DOE), Office of Science, Office of Basic Energy Sciences, under contract DE-SC0001805. H.M.C. and Y.S.M. acknowledge support on the

in situ CXDI cell design, materials synthesis, electrochemical and materials characterization from the NorthEast Center for Chemical Energy Storage (NECCES), an Energy Frontier Research Center funded by the U.S. Department of Energy, Office of Science, Basic Energy Sciences under Award no. DE-SC0012583. O.G.S. and Y.S.M. are grateful to the University of California–San Diego Chancellor's Interdisciplinary Collaborators Award that made this collaboration possible. J.N.C. gratefully acknowledges financial support from the Volkswagen Foundation. This research used resources of the Advanced Photon Source, a U.S. DOE Office of Science User Facility operated for the DOE Office of Science by Argonne National Laboratory under contract no. DE-AC02-06CH11357. We thank the staff at Argonne National Laboratory and the Advanced Photon Source for their support. The data are deposited at Sector 34-ID-C of the Advanced Photon Source.

SUPPLEMENTARY MATERIALS

www.sciencemag.org/content/348/6241/1344/suppl/DC1
Materials and Methods
Supplementary Text
Figs. S1 to S13
References (39–44)

21 October 2014; accepted 15 May 2015
10.1126/science.aaa1313

MEMBRANE FILTRATION

Sub-10 nm polyamide nanofilms with ultrafast solvent transport for molecular separation

Santanu Karan, Zhiwei Jiang, Andrew G. Livingston*

Membranes with unprecedented solvent permeance and high retention of dissolved solutes are needed to reduce the energy consumed by separations in organic liquids. We used controlled interfacial polymerization to form free-standing polyamide nanofilms less than 10 nanometers in thickness, and incorporated them as separating layers in composite membranes. Manipulation of nanofilm morphology by control of interfacial reaction conditions enabled the creation of smooth or crumpled textures; the nanofilms were sufficiently rigid that the crumpled textures could withstand pressurized filtration, resulting in increased permeable area. Composite membranes comprising crumpled nanofilms on alumina supports provided high retention of solutes, with acetonitrile permeances up to 112 liters per square meter per hour per bar. This is more than two orders of magnitude higher than permeances of commercially available membranes with equivalent solute retention.

Many separation processes used by industry require evaporation and distillation, which have high energy consumption due to the latent heat of vaporization. Membrane technology would require only one-tenth as much energy to process an equivalent amount of liquid (1), but for industrial processes involving large quantities of organic liquids, such membranes should be stable in organic solvents and have high permeance to enable processing within a reasonable time. Thin-film composite (TFC) membranes for water desalination (2, 3), which comprise a polyamide separating layer formed by interfacial polymerization on top of a porous ultrafiltration support

membrane, have been adapted for organic solvent nanofiltration (OSN). However, the permeance of TFC-OSN membranes is still relatively low (~ 2.5 liters m^{-2} hour^{-1} bar^{-1} for membranes that reject $>90\%$ of solutes with molecular weight <300 g mol^{-1}) (4), demanding large membrane areas for industrial applications. Meanwhile, for OSN, Karan et al. (5) used chemical vapor deposition to prepare diamond-like carbon (DLC) nanosheet membranes that showed ultrafast permeance when the thickness of the DLC separation layer was decreased to 30 nm; the DLC layer remained mechanically robust. In contrast, when the same thickness-reduction approach was followed for solution-cast films of a linear polymer (PIM-1), a maximum heptane permeance of ~ 18 liters m^{-2} hour^{-1} bar^{-1} was measured for a film 140 nm thick, after which permeance decreased with decreasing thickness. This was attributed

Department of Chemical Engineering, Imperial College London, South Kensington Campus, London SW7 2AZ, UK.
*Corresponding author. E-mail: a.livingston@imperial.ac.uk

to structural relaxation of the films for thicknesses less than 100 nm (6).

We postulated that thin films comprising network polymers will achieve ultrafast solvent permeance when their thickness is reduced below 100 nm, in contrast to films comprising linear polymers. Hence, we decided to explore the permeation of solvents through highly cross-linked sub-10 nm polyamide nanofilms fabricated via interfacial polymerization of diamine and acid chloride. By controlling the rate of interfacial reaction, *m*-phenylenediamine (MPD)-trimesoyl chloride (TMC) nanofilms were prepared on a sacrificial layer of cadmium hydroxide nanostrands. The fabrication process is shown in Fig. 1, A and B. The nanostrand layer was formed on an ultrafiltration

support membrane [either cross-linked polyimide XP84 (figs. S1 and S2) or porous alumina] via vacuum filtration of nanostrand solution (5, 7, 8) (Fig. 1, C and D, and fig. S3). Polyamide nanofilms with controlled morphology were formed on the nanostrand layer through controlled release of diamine at the water-hexane interface (fig. S4). The nanostrand layer was then removed by acid dissolution, using a dilute aqueous solution of hydrochloric acid, or, for prolonged interfacial polymerization reactions, by virtue of the acid formed in the reaction (Fig. 1B). This resulted in the formation of ultrathin nanofilms comprising a highly cross-linked polyamide network with terminal carboxylic acid groups on the surface facing the hexane (figs. S5 to S7).

The surface morphology of the nanofilms varies with MPD concentration (fig. S8); with increasing MPD concentration, the nanofilm appears crumpled, with feature sizes of 100 to 500 nm (figs. S9 to S13 and table S1). We believe that the crumpling phenomenon occurs when heat generation resulting from high-rate interfacial reactions leads to local temperature rises. These then create interfacial instabilities in the hexane layer through buoyancy driven by Rayleigh-Bénard convection (9). This causes the nanofilm to bend and crumple up, and generates additional interfacial area over the same time scale as the interfacial reaction itself. The resulting nanofilm is thus a “mold” of the interface (10).

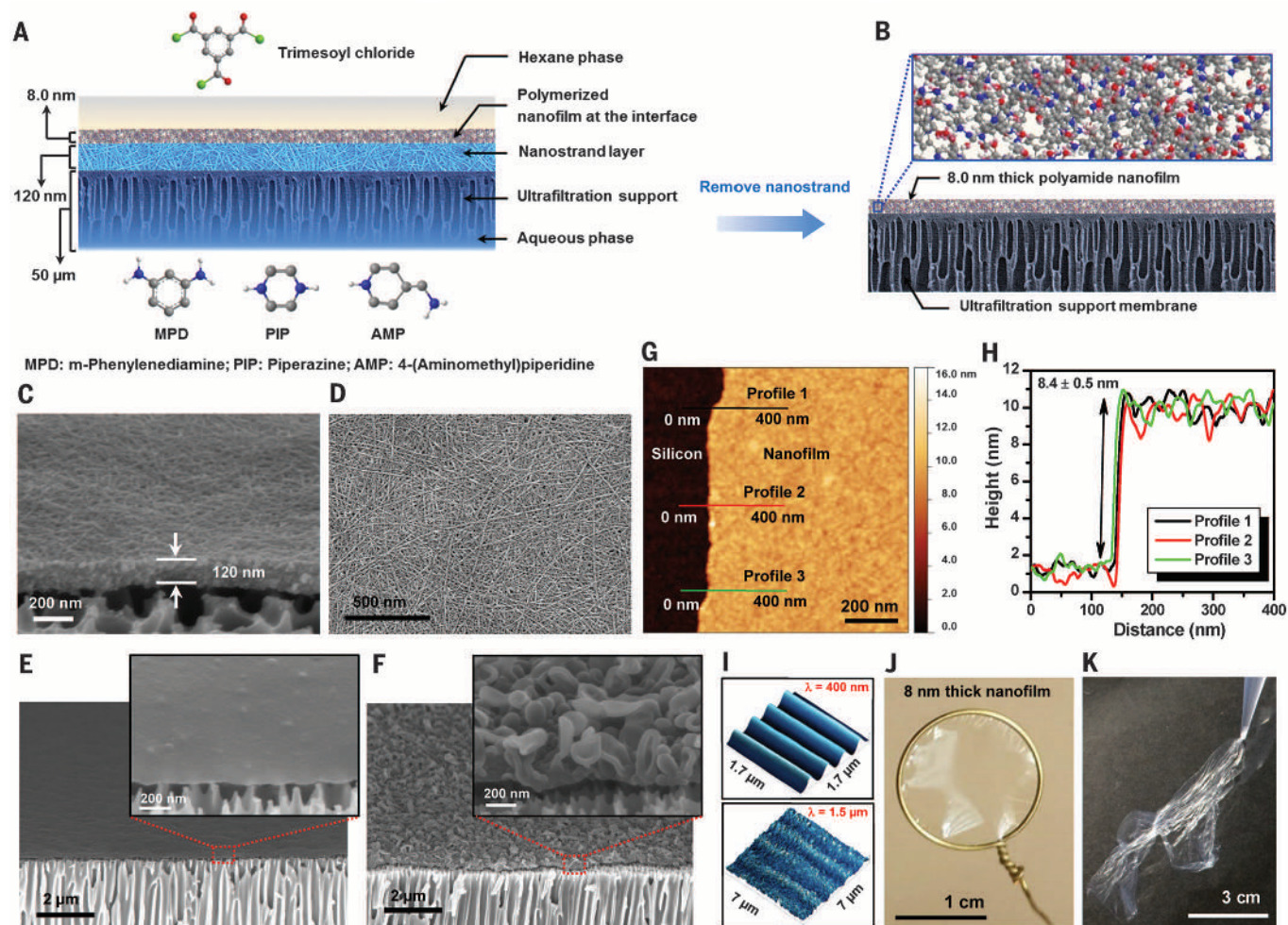


Fig. 1. Description of the controlled interfacial polymerization process and the resulting sub-10 nm nanofilms. (A) A sacrificial $\text{Cd}(\text{OH})_2$ nanostrand layer was prepared on top of an ultrafiltration support membrane [porous alumina or cross-linked polyimide (XP84)]. The nanostrand layer was saturated with an aqueous solution of diamine and contacted with a hexane layer containing TMC, enabling the synthesis of polyamide nanofilms via interfacial polymerization. (B) The nanostrand layer was removed by acid dissolution, resulting in a free-standing nanofilm that was then attached to a support membrane. (C and D) Cross-sectional and surface SEM images of a nanostrand layer, 120 nm thick, formed on an alumina support. The nanofilms with controlled surface morphology were fabricated from MPD-TMC on XP84 and then transferred onto alumina. (E and F) Cross-sectional

SEM images of smooth nanofilm (MPD-0.1%-10min) (E) and crumpled nanofilm (MPD-3%-1min) (F). Insets in (E) and (F) are high-magnification images. (G and H) AFM height image and corresponding height profile of a section of a smooth nanofilm (MPD-0.1%-10min) on top of a silicon wafer. A scratch was made to expose the wafer surface and allow measurement of the height from the silicon wafer surface to the upper nanofilm surface. (I) AFM images of the wrinkles formed when the MPD nanofilms are transferred onto an elastomer substrate and subjected to an applied compressive stress. Top, smooth nanofilm; bottom, crumpled nanofilm. (J) Photograph of a smooth nanofilm ~8 nm thick (MPD-0.1%-10min) transferred to a wire lasso. (K) Aspiration of a crumpled nanofilm through a pipette tip 320 μm in diameter.

Scanning electron microscopy (SEM) images of smooth and crumpled nanofilms (MPD-0.1%-10min and MPD-3%-1min in Table 1, respectively) are shown in Fig. 1, E and F. Atomic force microscopy (AFM) images of a smooth free-standing nanofilm (MPD-0.1%-10min; fig. S14) transferred onto a silicon wafer and scratched to reveal the wafer surface give a thickness of ~8.4 nm (Fig. 1, G and H). Layer-by-layer growth of an MPD-TMC film on a silicon wafer (17) has suggested that the thickness of each cycle is 0.9 nm, and if similar dimensions apply to the MPD-TMC nanofilms formed by interfacial polymerization, these would be 8 to 10 polyamide units thick.

These sub-10 nm nanofilms are robust, flexible, and defect-free over a few square centimeters in area (fig. S15). Wrinkling-based measurements (12, 13) under compressive stress induced by an elastomer substrate (Fig. 1I and fig. S16) confirmed that nanofilms have a Young's modulus in the range 0.11 to 2.71 GPa, depending on the interfacial polymerization conditions (table S2). Figure 1J shows a smooth nanofilm (MPD-0.1%-10min) transferred to a wire lasso; although the film is only ~8 nm thick, it forms an integral surface across the whole 1.5-cm diameter of the lasso. As demonstrated in Fig. 1K, a nanofilm can be aspirated through a narrow pipette tip without visibly tearing or fragmenting.

The strength and flexibility of the nanofilm make it feasible to produce composite membranes in a two-stage process in which the separating nanofilm layer is formed by interfacial polymerization as a free-standing entity and is then placed on top of a support to form a composite membrane. Further, if the crumpled texture is

robust under pressurized filtration, then (relative to a smooth film) it will provide a higher permeable nanofilm area per unit area of composite membrane support. This will enhance composite membrane permeance, which is calculated according to flow normal to the area of the support membrane.

Properties of nanofilms fabricated under different interfacial reaction conditions and with both aromatic and semi-aromatic diamines are listed in Table 1. The thickness of the smooth MPD nanofilms was approximately constant after 1 min, whereas their mass measured with a quartz crystal microbalance increased by a factor of 3 with prolonged reaction time (1 to 10 min) (table S3). The increasing density explains the increase in elastic modulus of the nanofilm (table S2). The top (hexane-facing) surfaces of the nanofilms were characterized by AFM (figs. S17 to S22 and table S4). For crumpled MPD nanofilms, the reported thickness reflects the apparent thickness of the crumpled layer (up to 94 nm, MPD-3%-1min in Table 1) rather than the actual nanofilm thickness. In fig. S23, we show that the conditions that result in a crumpled nanofilm formed on the nanostrand layer give a smooth nanofilm when applied at an aqueous-organic interface between free liquids, which suggests that the crumpling occurs when the film formation is constrained by the nanostrand layer. Under AFM, the reverse (aqueous-facing) surfaces of the nanofilms revealed imprints of the nanostrand layer as well as the porous backside of the crumpled sheet (fig. S24 and table S5).

We estimated the carbon, oxygen, and nitrogen content in the nanofilms by x-ray photo-

electron spectroscopy (XPS) (Table 1 and fig. S25). Deconvolution of the C1s spectrum revealed the signature of amide and carboxyl groups; the percentages of carboxylic acid groups (resulting from the hydrolysis of unreacted acyl chloride groups) and unreacted amine groups were estimated from the N1s and O1s spectra (figs. S26 and S27 and table S6). The extent of chemical cross-linking was calculated from the relative values of N and O measured from XPS (table S7). The thicknesses for smooth MPD nanofilms were also estimated by Ar sputtering in XPS and spectroscopic ellipsometry, confirming a sub-10 nm thickness (fig. S28). Estimated values of C, N, and O from energy-dispersive x-ray (EDX) measurements under transmission electron microscopy (TEM) (table S8) concur with XPS measurements. The contact angles for all MPD nanofilms were in the range 50° to 60°, which suggests similar polarity (surface energy) of the surfaces of all the nanofilms formed. Furthermore, TEM observations confirmed that the nanofilms were amorphous polymers (figs. S29 to S35). Piperazine (PIP) nanofilms required longer reaction times (10 min) to become defect-free (figs. S36 to S38).

Measurement of the MPD nanofilm thickness has been a challenge in understanding the polyamide separating layer in TFC desalination membranes; current estimates are in the range of several hundred nanometers (3, 14, 15). Our nanofilms can be made free-standing without deforming their morphology, thereby enabling close examination. We assert that the rough morphology [length scales ~100 to 500 nm with hollow features (fig. S33)], which results from moderate MPD-TMC concentrations, comprises

Table 1. Composition and surface properties of free-standing nanofilms fabricated by interfacial polymerization (IP). Root mean square (RMS) roughness and thickness of free-standing nanofilms were measured on silicon wafers. The atomic composition was assessed by XPS measurements from free-standing nanofilms transferred onto gold-coated silicon wafers. The density of carboxylic acid groups (–COOH) was calculated from the core-level C1s

XPS spectra (table S6). The degree of network cross-linking was calculated from the ratio of network to linear cross-linked portion of the polymer (table S7). The contact angle of the nanofilms was measured on XP84. Nanofilms with the suffix ACT were activated with DMF by immersion for 4 hours followed by washing in methanol (immersion for 15 min). Nanofilm with the suffix Flip refers to the reverse side. ND, not determined.

Free-standing polyamide nanofilm (aqueous amine phase–wt%–IP time)	TMC in hexane phase (wt%)	Overall thickness from SEM/AFM (nm)	RMS roughness R_{rms} (nm)	Atomic composition from XPS (%)				Degree of network cross-linking (%)	Contact angle (°)
				C	O	N	COOH		
MPD-0.05%-10min	0.0025	8.4 ± 0.4	0.63 ± 0.03	ND	ND	ND	ND	ND	58.2 ± 1.6
MPD-0.1%-1min	0.005	7.5 ± 0.4	0.52 ± 0.04	73.3	14.3	12.4	3.0	78.6	56.8 ± 3.2
MPD-0.1%-1min-ACT	0.005	7.8 ± 0.2	0.69 ± 0.05	73.5	14.5	12.0	2.9	71.7	56.6 ± 2.4
MPD-0.1%-10min	0.005	8.4 ± 0.5	0.60 ± 0.05	73.7	14.3	12.0	3.7	73.8	58.7 ± 1.5
MPD-0.1%-10min-ACT	0.005	8.0 ± 0.3	0.51 ± 0.05	74.0	14.6	11.4	3.3	63.1	59.1 ± 1.9
MPD-3%-1min	0.15	94 ± 7	78.0 ± 1.9	73.6	13.8	12.6	3.2	86.4	51.2 ± 1.9
MPD-3%-1min-ACT	0.15	95 ± 10	64.8 ± 1.7	73.0	14.7	12.3	3.2	73.3	49.3 ± 2.4
MPD-3%-1min-Flip	0.15	ND	11.2 ± 0.7	72.5	14.7	12.8	3.2	79.3	ND
MPD-4%-1min	0.2	63 ± 5	56.2 ± 2.8	73.3	14.7	12.0	3.4	69.7	53.6 ± 2.9
MPD-4%-1min-ACT	0.2	52 ± 8	42.6 ± 3.7	73.2	14.5	12.3	3.4	75.4	53.1 ± 1.8
MPD-10%-1min	0.5	64 ± 3	23.9 ± 3.0	74.5	12.8	12.7	1.8	98.8	60.6 ± 4.0
MPD-10%-1min-ACT	0.5	47 ± 6	24.5 ± 2.7	74.7	12.9	12.4	2.2	94.1	57.6 ± 2.4
PIP-0.1%-10min	0.02	33.2 ± 1.1	4.66 ± 0.25	73.2	14.2	12.6	2.0	82.1	44.1 ± 1.1
PIP-0.1%-10min-ACT	0.02	ND	ND	72.7	14.6	12.7	2.1	79.1	41.9 ± 1.5
AMP-0.1%-10min	0.02	14.5 ± 0.5	2.31 ± 0.88	75.5	13.1	11.4	1.7	79.2	55.7 ± 1.4
AMP-0.1%-10min-ACT	0.02	ND	ND	75.0	13.2	11.5	1.6	79.3	56.2 ± 1.7

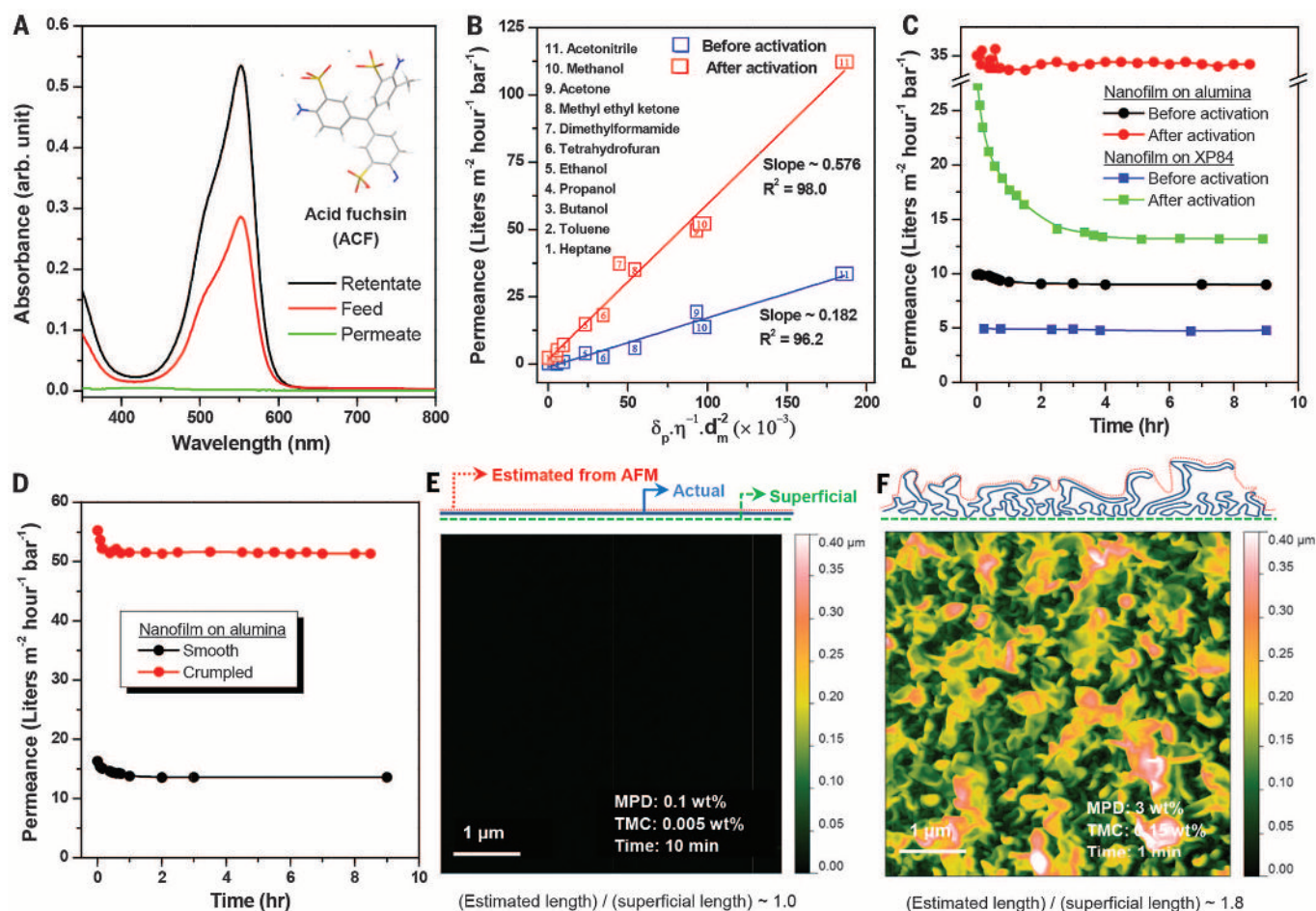


Fig. 2. Nanofiltration performance of smooth and crumpled nanofilm composite membranes. (A) Ultraviolet-visible absorption spectra of acid fuchsin (ACF) dye in methanol to estimate the separation performance of the MPD nanofilm composite membrane. Inset shows the ACF molecular structure. (B) Plot of solvent permeances against the combined solvent property (viscosity, molar diameter, and solubility parameter) for crumpled nanofilm (MPD-3%-1min) on alumina. (C) Variation of methanol permeance through crumpled nanofilm (MPD-

4%-1min) composite membranes with time. Membranes were activated via DMF filtration followed by washing in methanol. (D) Plot of methanol permeance with time for the MPD nanofilm (after DMF activation) on alumina (smooth, MPD-0.1%-10min; crumpled, MPD-3%-1min). Nanofiltration was conducted in a dead-end stirred cell (500 rpm) at 30°C under 10 bar. (E and F) AFM height image and schematic representation of the estimated length from AFM, showing actual and superficial length of smooth nanofilm (E) and crumpled nanofilm (F).

crumpled nanofilms ~8 nm thick (fig. S39) and that it is the thickness of the whole crumpled zone that has been reported previously as the film thickness of TFC membranes.

Figure 2A shows the rejection performance of a typical nanofilm composite membrane. Organic solvent permeance of polyamide TFC membranes is known to be enhanced by dimethylformamide (DMF) activation (4), and the same trend is observed for our nanofilm composite membranes (Table 2, Fig. 2B, and figs. S40 and S41). Seeking to explain this phenomenon, we examined surface morphology, chemical structure, film thickness, and mass per unit area before and after activation with DMF. None revealed any significant differences, and so we attribute the permeance increase to molecular-level modification of the membrane material (see supplementary materials and table S9). Before and after activation, a similar rejection was observed for charged dyes and polystyrene oligomers, whereas neutral dyes exhibited slightly lower rejection (Table 2 and figs. S42 to

S45). MPD nanofilm membranes were tight, with molecular weight cutoff (MWCO) below 246 $g mol^{-1}$ based on the rejection of 6-hydroxy-2-naphthalenesulfonic acid sodium salt (HNSA; molecular weight 246.2 $g mol^{-1}$, size 0.59 nm^3 ; table S10), whereas 4-(aminomethyl)piperidine (AMP) and PIP nanofilms were progressively looser with higher MWCO. These membranes are at least equivalent in selectivity to TFC-OSN membranes reported to date (4). Acetonitrile, with viscosity of 0.32×10^{-3} Pa·s and solubility parameter due to dipole force (δ_p) of 18.0 $MPa^{1/2}$ (table S9), gave the highest permeance of 112 $liters m^{-2} hour^{-1} bar^{-1}$. Methanol (0.49×10^{-3} Pa·s, 12.3 $MPa^{1/2}$) gave the second highest permeance of 52.2 $liters m^{-2} hour^{-1} bar^{-1}$. Methyl ethyl ketone (MEK; 0.38×10^{-3} Pa·s, 9.0 $MPa^{1/2}$), with a molar diameter 20% greater than that of acetonitrile; the relatively nonpolar heptane and toluene gave the lowest permeances. Methanol flux was linear with transmembrane pressure (fig. S15).

From these observations, we propose a phenomenological transport model (16) describing the permeance ($P_{s,i}$) of solvent s through each nanofilm i :

$$P_{s,i} = K_i \left(\frac{\delta_{p,s}}{\eta_s d_{m,s}^2} \right) \quad (1)$$

where K_i is a proportionality constant for nanofilm i ($m^3 Pa^{-0.5}$), $\delta_{p,s}$ is the solubility parameter ($Pa^{0.5}$), η_s is the solvent viscosity (Pa·s), and $d_{m,s}$ is the molar diameter of the solvent s (m). Equation 1 describes solvent permeance well for both activated and nonactivated nanofilms (Fig. 2B and fig. S41).

Methanol permeance for various nanofilm membranes is plotted as a function of time in Fig. 2C. The activated polyamide nanofilm maintained a constant permeance when supported on the aging-resistant alumina. With XP84, permeance decreased by 60% over the first 4 hours; both composite membranes exhibited similar rejection (Table 2). This permeance decline is

Table 2. Organic solvent nanofiltration performance of nanofilm composite membranes. Negatively charged dyes with varying molecular weight dissolved in methanol were used to study solute retention. Nanofilm membranes were prepared on the prefabricated nanostrand layer deposited on cross-linked polyimide (XP84) or alumina. Composite membranes with the suffix ACT were activated with DMF filtration for 15 to 30 min followed

by filtration with methanol under 10 bar in a dead-end cell. Feed solution concentration was 20 mg liter⁻¹ in methanol. Feed volume was 50 ml or 100 ml, half of which was collected as permeate to determine the rejection value. Nanofiltration experiments were conducted in a dead-end stirred cell (500 rpm) at 30°C under 10 bar. Permeance values are expressed as liters m⁻² hour⁻¹ bar⁻¹.

Nanofilm composite membrane type (aqueous amine phase-wt%- IP time)	Pure methanol permeance	HNSA (246.2 g mol ⁻¹ , 0.59 nm ³)		Methyl orange (327.3 g mol ⁻¹ , 0.86 nm ³)		Naphthalene brown (400.3 g mol ⁻¹ , 0.95 nm ³)		Acid fuchsin (585.5 g mol ⁻¹ , 1.18 nm ³)	
		Permeance	Rejection (%)	Permeance	Rejection (%)	Permeance	Rejection (%)	Permeance	Rejection (%)
Alumina support									
MPD-10%-1min	2.45	2.44	91.8	2.39	94.8	2.34	95.5	2.05	96.2
MPD-10%-1min-ACT	6.60	6.58	90.2	6.58	94.1	6.40	95.5	6.32	96.5
MPD-4%-1min	8.99	8.98	98.5	8.98	98.9	8.78	99.9	8.78	99.9
MPD-4%-1min-ACT	34.12	34.12	94.5	31.84	98.8	31.03	99.9	30.17	99.9
MPD-3%-1min	13.73	13.73	98.7	12.97	98.9	12.70	99.9	12.53	99.9
MPD-3%-1min-ACT	52.22	52.22	98.5	52.05	98.9	52.00	99.9	51.84	99.9
MPD-0.1%-10min	3.14	3.10	98.5	2.97	99.7	2.90	99.9	2.82	99.9
MPD-0.1%-10min-ACT	12.21	12.23	98.3	12.11	99.7	11.93	99.9	11.24	99.9
XP84 support									
MPD-4%-1min	4.78	4.78	97.4	4.78	99.1	4.78	99.7	4.35	99.9
MPD-4%-1min-ACT	13.25	13.33	93.5	12.99	97.7	12.74	99.9	12.74	99.9
MPD-3%-1min	7.71	7.71	95.5	7.71	98.9	7.67	99.9	7.52	99.9
MPD-3%-1min-ACT	19.11	19.11	91.0	19.11	95.5	18.62	99.9	18.49	99.9
MPD-0.1%-3min	5.19	5.31	98.7	5.16	99.9	5.31	99.8	4.84	99.9
MPD-0.1%-3min-ACT	8.59	8.32	98.5	7.97	99.9	ND	99.9	8.31	99.9
MPD-0.1%-10min	3.89	3.89	84.6	3.74	96.4	3.87	98.1	3.82	99.6
MPD-0.1%-10min-ACT	9.55	9.09	94.1	9.09	96.8	9.24	98.5	8.31	99.9
PIP-0.1%-10min	1.42	1.34	71.1	ND	ND	1.27	98.2	1.17	99.1
PIP-0.1%-10min-ACT	1.82	1.77	76.2	1.49	96.9	1.70	99.1	1.59	99.5
AMP-0.1%-10min	4.42	4.54	88.4	4.66	97.5	4.35	99.8	4.35	99.9
AMP-0.1%-10min-ACT	4.23	4.25	90.4	4.35	98.6	4.16	99.9	4.16	99.9

presumably a result of physical aging and compaction of the XP84 support membrane with DMF filtration. If so, then these highly cross-linked nanofilms must be adhered to an aging-resistant support material to enable sustained performance. This result is especially interesting because these observations could only have been made through the formation of free-standing nanofilms that can be attached to either support.

Figure 2D shows that an alumina supported crumpled MPD nanofilm provided higher permeance than an alumina-supported smooth MPD nanofilm by a factor of >4 (Table 2). This is consistent with the assertion that the crumpled nanofilm provides an effective permeable area greater than the area of support it covers. Crucially, it appears that this crumpled texture does not collapse and fail under pressure. Linear flux over the pressure range 0.3 to 50 bar (fig. S15D) suggests that the permeable area of the crumpled nanofilm is constant, with no folding or flattening to form overlapping layers as pressure is increased. For a smooth film, the distance traveled by an AFM tip is the same as the distance across the scanned area, whereas the distance traveled by the tip as it moves up and down the ridges of the crumpled film is greater by a factor of 1.8 (Fig. 2, E and F). The permeance data suggest that the permeable area of a crumpled film is at least 4 times that of the smooth film; the AFM data sup-

port this, and the schematic in Fig. 2F illustrates why the AFM value of 1.8 is an underestimate.

The methanol flux through the crumpled MPD nanofilm on a porous alumina support (52.2 liters m⁻² hour⁻¹ bar⁻¹) is more than 20 times the value reported for TFC membranes (4) and is two orders of magnitude higher than commercially available OSN membranes (fig. S46). This ultrafast permeation through a polymeric thin film, without compromising selectivity, improves the potential for energy efficiency in OSN applications (2, 17). A range of chemical processes have a strong demand for solvent-resistant nanofiltration membranes with superior permeance. We provide here a potential candidate in the form of sub-10 nm crumpled nanofilm composite membranes with ultrafast solvent permeance, excellent selectivity, and sufficient mechanical strength for nanofiltration applications.

REFERENCES AND NOTES

- P. Marchetti, M. F. Jimenez Solomon, G. Szekely, A. G. Livingston, *Chem. Rev.* **114**, 10735–10806 (2014).
- J. E. Cadotte, R. J. Petersen, R. E. Larson, E. E. Erickson, *Desalination* **32**, 25–31 (1980).
- M. Elimelech, W. A. Phillip, *Science* **333**, 712–717 (2011).
- M. F. Jimenez Solomon, Y. Bhole, A. G. Livingston, *J. Membr. Sci.* **423–424**, 371–382 (2012).
- S. Karan, S. Samitsu, X. Peng, K. Kurashima, I. Ichinose, *Science* **335**, 444–447 (2012).
- P. Gorgojo et al., *Adv. Funct. Mater.* **24**, 4729–4737 (2014).

- I. Ichinose, K. Kurashima, T. Kunitake, *J. Am. Chem. Soc.* **126**, 7162–7163 (2004).
- S. Karan, Q. Wang, S. Samitsu, Y. Fujii, I. Ichinose, *J. Membr. Sci.* **448**, 270–291 (2013).
- S. J. Vanhook, M. F. Schatz, J. B. Swift, W. D. McCormick, H. L. Swinney, *J. Fluid Mech.* **345**, 45–78 (1997).
- A thin nanostrand containing water is not a good heat transfer medium, and so heat generated at the interface will be dissipated by heating of the hexane, which has low heat capacity (see supplementary materials and fig. S39).
- P. M. Johnson, J. Yoon, J. Y. Kelly, J. Howarter, C. M. Stafford, *J. Polym. Sci. B* **50**, 168–173 (2012).
- C. M. Stafford et al., *Nat. Mater.* **3**, 545–550 (2004).
- J. Y. Chung, J.-H. Lee, K. L. Beers, C. M. Stafford, *Nano Lett.* **11**, 3361–3365 (2011).
- G.-Y. Chai, W. B. Krantz, *J. Membr. Sci.* **93**, 175–192 (1994).
- V. Freger, *Langmuir* **19**, 4791–4797 (2003).
- A. Buekenhoudt et al., *J. Membr. Sci.* **439**, 36–47 (2013).
- G. Szekely, M. F. Jimenez Solomon, P. Marchetti, J. F. Kim, A. G. Livingston, *Green Chem.* **16**, 4440–4473 (2014).

ACKNOWLEDGMENTS

Supported by UK Engineering and Physical Sciences Research Council platform grant EP/J014974/1 and the BP International Centre for Advanced Materials. We thank J. T. Cabral for his suggestions on determining the modulus values of the nanofilms.

SUPPLEMENTARY MATERIALS

www.sciencemag.org/content/348/6241/1347/suppl/DC1
Materials and Methods
Supplementary Text
Figs. S1 to S46
Tables S1 to S10
References (18–59)

16 December 2014; accepted 24 April 2015
10.1126/science.aaa5058

BRAIN PROCESSING

Cortical information flow during flexible sensorimotor decisions

Markus Siegel,^{1,2*} Timothy J. Buschman,^{2,3} Earl K. Miller²

During flexible behavior, multiple brain regions encode sensory inputs, the current task, and choices. It remains unclear how these signals evolve. We simultaneously recorded neuronal activity from six cortical regions [middle temporal area (MT), visual area four (V4), inferior temporal cortex (IT), lateral intraparietal area (LIP), prefrontal cortex (PFC), and frontal eye fields (FEF)] of monkeys reporting the color or motion of stimuli. After a transient bottom-up sweep, there was a top-down flow of sustained task information from frontoparietal to visual cortex. Sensory information flowed from visual to parietal and prefrontal cortex. Choice signals developed simultaneously in frontoparietal regions and travelled to FEF and sensory cortex. This suggests that flexible sensorimotor choices emerge in a frontoparietal network from the integration of opposite flows of sensory and task information.

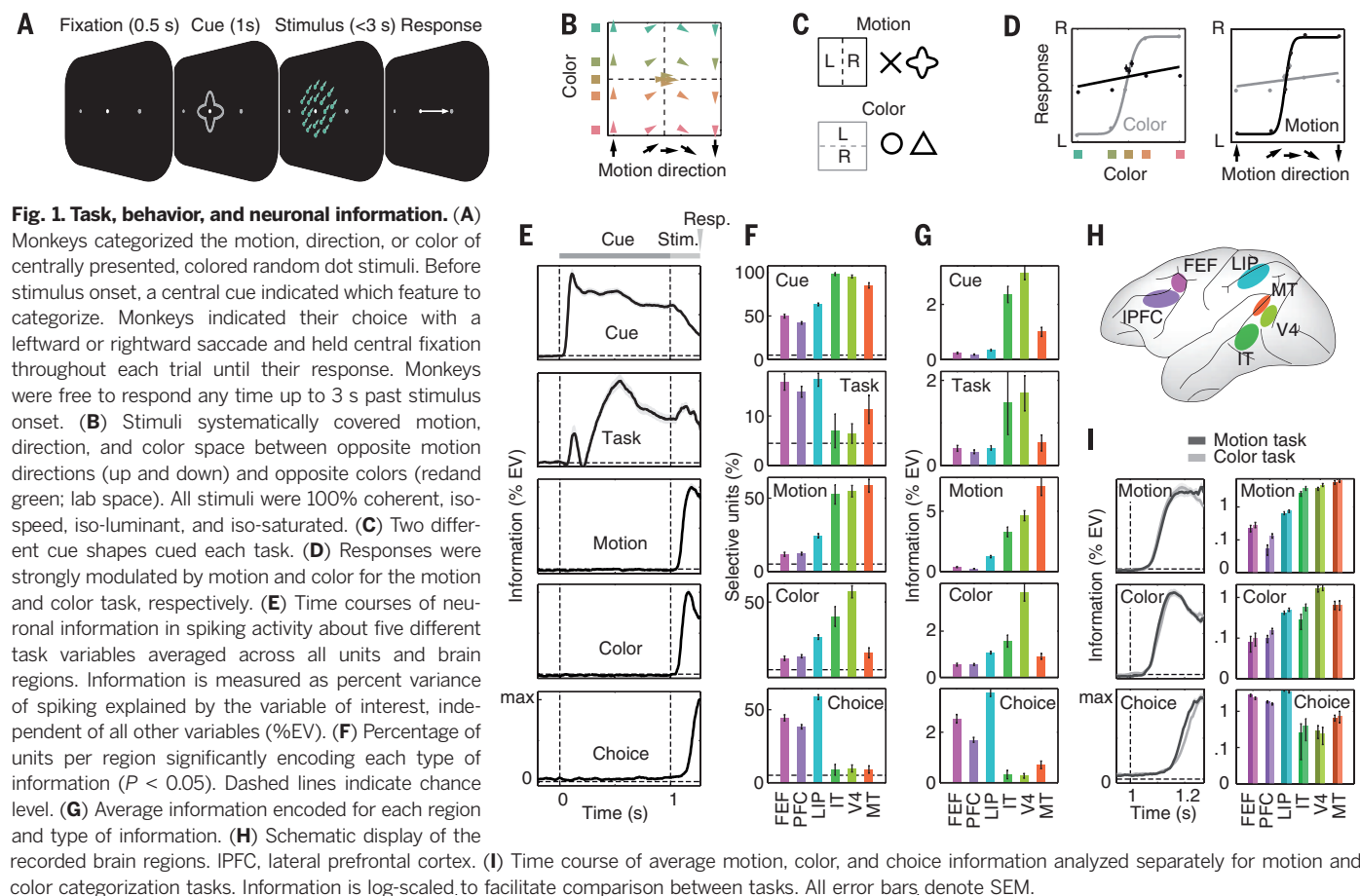
Our reactions are not always the same to the same sensory input. Depending on context, we can map the same input onto different actions. This involves a distributed network of brain regions. During visuomotor decisions, choice predictive activity has been found in frontoparietal regions, including the lateral intraparietal area (LIP)

(1–4), prefrontal cortex (PFC) (1, 5–9), frontal eye fields (FEF) (7), and motor and sensory cortex (10–13). However, it remains unclear how choice signals evolve. Do they flow bottom-up, flow top-down, or evolve concurrently across brain regions? Do choice signals in sensory regions reflect their causal effect on the decisions or feedback from decision stages (12)? Similarly,

little is known about the flow of task signals. Neuronal activity encodes task rules in prefrontal (6, 8, 14, 15), parietal (2), and visual (16) cortices. Task-dependent attention modulates neuronal activity throughout sensory cortices (17–19). It remains unknown how task signals evolve across these regions.

We trained two monkeys on a flexible visuomotor task (Fig. 1 and materials and methods). They categorized either the color (red versus green) or the direction (up versus down) of a colored visual motion stimulus, reporting it with a left or right saccade (Fig. 1A). A visual cue instructed animals about the task (motion or color, Fig. 1C). Each task was indicated by two different visual cues to dissociate cue and task-related activity. Color and motion spanned a broad range around the category boundaries (yellow and horizontal) (Fig. 1B and fig. S1). Both monkeys were proficient at categorizing the cued feature (Fig. 1D) (94% and 89% correct for motion and color tasks, respectively, excluding ambiguous trials with stimuli on the category boundary).

¹Centre for Integrative Neuroscience and MEG Center, University of Tübingen, Tübingen, Germany. ²Picower Institute for Learning and Memory and Department of Brain and Cognitive Sciences, Massachusetts Institute of Technology, Cambridge, MA 02139, USA. ³Princeton Neuroscience Institute and Department of Psychology, Princeton University, Princeton, NJ 08544, USA. *Corresponding author. E-mail: markus.siegel@uni-tuebingen.de



We recorded multi-unit activity (MUA) from up to 108 electrodes simultaneously implanted in six cortical regions acutely each day (Fig. 1H and materials and methods): FEF (532), dorso-lateral PFC (1020), LIP (807), IT (57), V4 (155), and MT (123) (total of 2694 multi-units). For each multi-unit, we quantified how neural activity encoded cue identity, task (motion versus color), stimulus motion direction, stimulus color, and motor choice. Information was quantified as spiking variance across trials explained by each factor. All five types of information were quantified independently; for example, choice measured only information about the choice that was not explained by cue, task, color, or motion (see materials and methods). To rule out activity due to the saccade itself, we included neuronal activity up to 5 ms before saccade onset.

Averaging across all units revealed temporal dynamics of information (Fig. 1E). Cue information peaked directly after cue onset and stayed tonically elevated during cue presentation (latency to reach half maximum: 74 ± 1 ms SE). Task information showed a bimodal dynamic. A transient peak shortly after cue onset had a similar latency as cue information (100 ± 25 ms). This transient peak was followed by a dip and later rise of sustained task information (333 ± 15 ms). In contrast to cue

information, task information increased during stimulus presentation. Motion and color information rose after stimulus onset with a significantly shorter latency for color (98 ± 2 ms) as compared with motion (108 ± 2 ms) information ($P < 0.001$). Last, choice information rose (193 ± 1 ms) before the motor responses ($270 \text{ ms} \pm 3 \text{ ms}$) and significantly later than motion and color information (both $P < 0.0001$).

We quantified for each type of information the percentage of units with significant effects (Fig. 1F) and the average amount of information (Fig. 1G). We used the second half of the cue interval (0.5 to 1 s) for cue and task information, the interval from stimulus onset to the average response latency (1 to 1.270 s) for motion and color information, and the 200-ms interval preceding the saccade for choice information. We found significant encoding of each type of information in each region ($P < 0.05$ for all regions and information), but the regional profiles differed. In accordance with shape selectivity of V4 and IT, we found the most frequent and strongest cue information there. Task selectivity was frequent in all regions and strongest in V4 and IT. Motion and color information were strongest in MT and V4, respectively. Choice information was most frequent and strongest in LIP, FEF, and PFC.

Task (motion versus color) had little effect on strength and dynamics of motion, color, and choice information (Fig. 1I) (20, 2I). There was no evidence that only task-relevant sensory information was routed to frontoparietal stages and no evidence that choice information was present only in the task-relevant sensory region. In sum, all types of information were encoded across the entire visuomotor pathway, albeit with different incidences and strength.

Next, we investigated the temporal dynamics of information across regions. Cue information flowed bottom-up, rising first in MT, followed by LIP, V4, IT, FEF, and PFC (Fig. 2A). Most of the pairwise comparisons revealed significant latency differences between regions (Fig. 2B, $P < 0.001$). Task information showed very different dynamics (Fig. 2C). There was a significant early transient peak of task information (<150 ms) in IT and V4 only, without a latency difference between V4 and IT ($P > 0.05$). The latency of this peak in IT (72 ms) was not different ($P > 0.05$) from the latency of cue information in IT (also 72 ms). In V4, the transient peak of task information was slightly later (96 ms) than cue information (73 ms) ($P < 0.05$). Directly after this transient peak, task information was low in the PFC, but then appeared there first and flowed

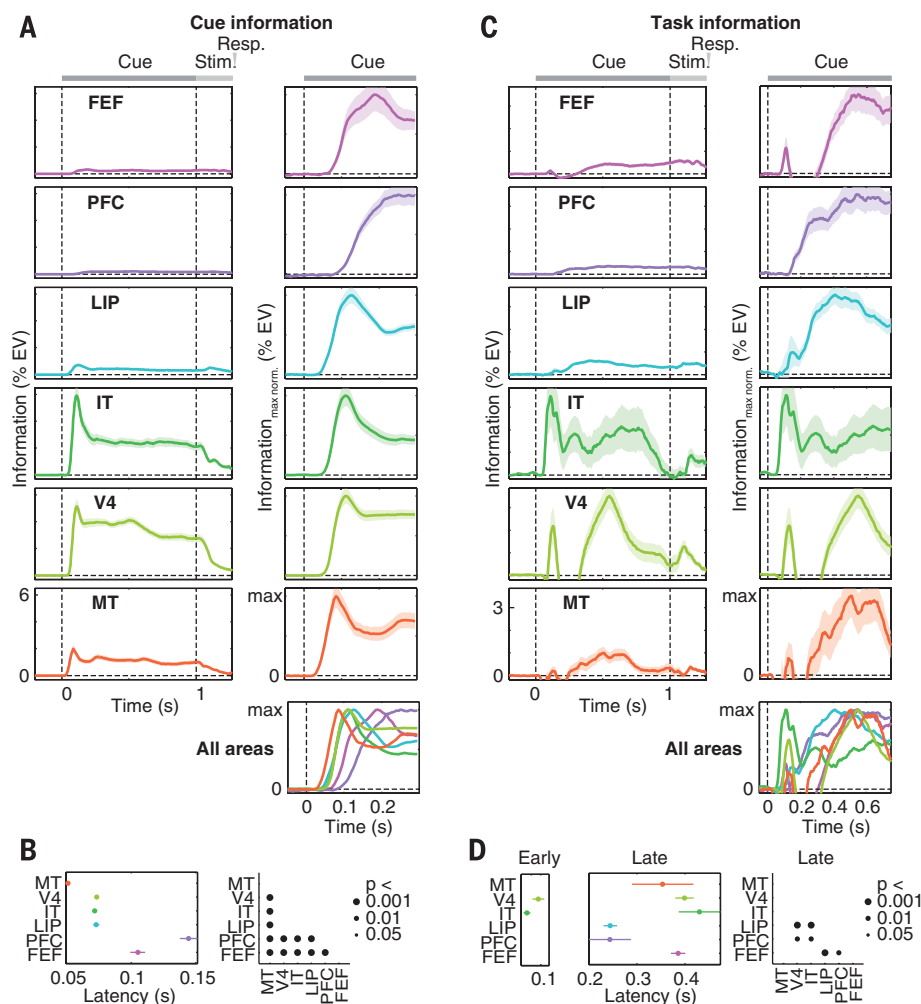


Fig. 2. Dynamics of cue and task information.

(A) Each row displays for one brain region the average time course of neuronal information about cue identity. Left graphs display raw information (% EV, same scale for all regions). To support comparison across regions, right graphs display time courses normalized by maximum information for the interval of interest. The bottom right graph shows an overlay of all regions' information time courses. Cue and stimulus onsets are at time = 0 s and time = 1 s, respectively. (B) Comparison of cue information latencies between regions. Latencies are quantified as the time to reach half maximum information. Black dots in the right graph indicate significant latency differences between regions. (C) Time courses of task information across regions. Same conventions as in (A). (D) Comparison of task information latencies between regions. Latencies were separately analyzed for the early transient peak around 100 ms and for the later sustained increase of task information after 200 ms. Early peak latencies were only estimated for regions that showed a significant effect (V4 and IT, $P < 0.05$). Same conventions as in (B). All error bars denote SEM.

from PFC to LIP, MT, FEF, V4, and IT. Many pairwise latency comparisons were significant according to this pattern (Fig. 2D, $P < 0.01$). In particular, task information rose earlier in PFC and LIP than in FEF, V4, and IT (all $P < 0.01$). In summary, IT and V4 first extracted task information from the cues along with the encoding of cue identity. After this transient burst, there was a flow of sustained task information from PFC and LIP across the entire sensorimotor hierarchy.

Motion information rose first in MT, followed by LIP, V4, IT, FEF, and PFC (Fig. 3A). Color information rose first in MT, followed by V4, LIP, FEF, IT, and PFC (Fig. 3C). Most pairwise comparisons revealed latency differences between regions according to these sequences (Fig. 3, B and D, $P < 0.05$). Furthermore, color information appeared significantly earlier than motion information in V4, MT, PFC, and FEF (all $P < 0.001$). Analyzing motion and color tasks individually confirmed these results and showed that neuronal latencies for motion and color information were almost identical for both tasks (fig. S2).

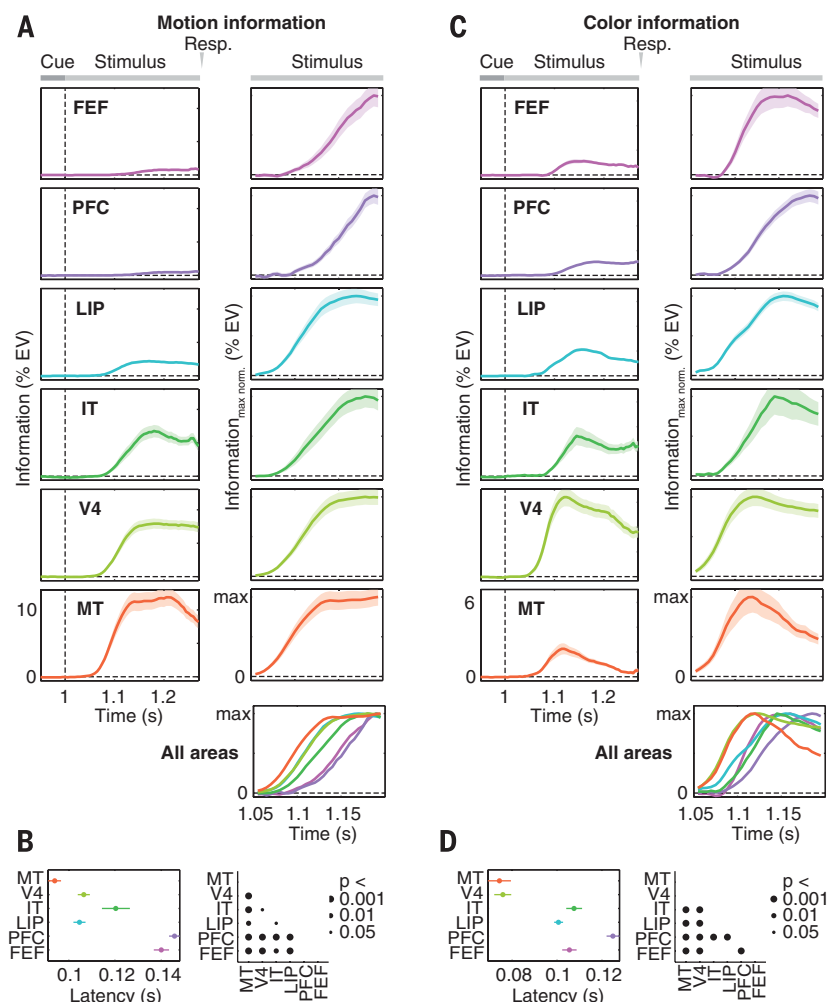


Fig. 3. Dynamics of motion and color information. Time courses and latencies of neuronal information about (A and B) motion direction and (C and D) color of the categorized stimulus. Stimulus onset is at time = 1 s. All other conventions as in Fig. 2.

Choice signals had a different dynamic. If spontaneous fluctuations of activity influenced animals' choices, activity would predict the choice even before presentation of the motion-color stimulus. Indeed, for all regions except IT, significant choice information preceded stimulus onset (-0.5 to 1 s, $P < 0.01$). We ruled out that this prestimulus choice information merely reflected an effect of the previous trial (see materials and methods). We next investigated the build-up of choice information during decisions (Fig. 4). Because this reflects the forthcoming behavioral response, we time-locked analysis to the saccade. Choice information increased in LIP and PFC before FEF (Fig. 4B, $P < 0.05$), but there was no latency difference between LIP and PFC. Choice information increased later in V4 and MT than in LIP and PFC (Fig. 4B, all $P < 0.05$), suggesting feedback of choices from frontoparietal stages. Analyzing choice information for motion and color tasks individually confirmed the above results (fig. S3).

Our results provide insights into the neuronal mechanisms underlying sensorimotor choices (summarized in fig. S4). First, sensory (cue, mo-

tion, or color), cognitive (task), and behavioral (choice) information was not confined to specific cortical regions but instead broadly distributed. This is incompatible with models of compartmentalized cortical function. Our results instead suggest a graded functional specialization of cortical regions with information shared between regions (22). Second, sensory information flowed feed-forward from sensory cortex. Third, task information was first extracted in an early, transient burst in higher sensory cortex (V4 and IT). This early transient may reflect the learned cue associations, that is, the grouping of the two cues for each task into one representation that is then fed forward to PFC and LIP. After the early transient, sustained task information appeared first in PFC and LIP and then spread to other regions. Thus, task information may need to reach PFC and LIP before being broadcast across the

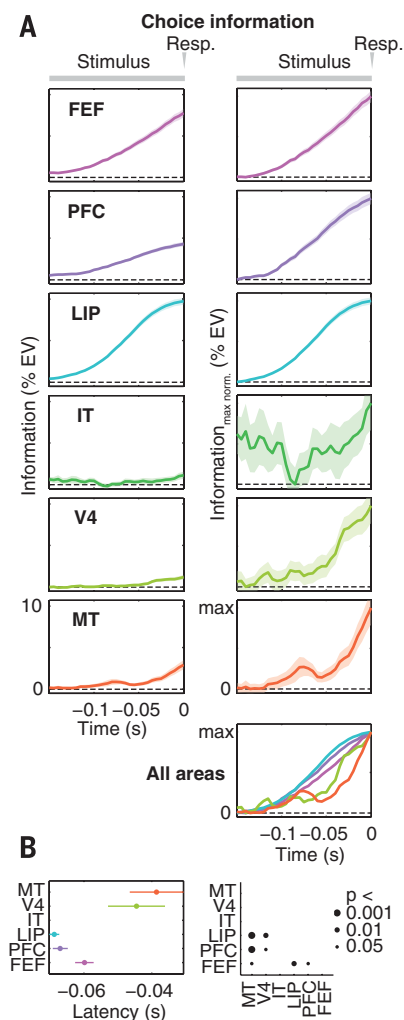


Fig. 4. Dynamics of choice information. Response-locked (A) time courses and (B) latencies of neuronal information about the animals' choice. Responses are at time = 0 s. Latency was not estimated for IT because there was no significant increase of choice information in IT in the analyzed interval (linear regression, $P > 0.05$). All other conventions as in Figs. 2 and 3.

sensorimotor pathway (23). Fourth, choice predictive activity was present in sensory (V4 and MT), frontoparietal (LIP and PFC), and premotor (FEF) cortex before onset of the decision process. This suggests a link between spontaneous fluctuations of neuronal activity along the entire sensorimotor pathway and subsequent decisions. Fifth, choice signals first and simultaneously built up in PFC and LIP and then followed in FEF. Our findings accord with previous reports of ramping choice predictive activity in LIP (3), PFC (7), and FEF (7) but shed light on how choices are made in this network. Our results suggest that, although sensory information reaches LIP and FEF before PFC, the accumulation of sensory evidence occurs first and jointly in LIP and PFC before decision signals are relayed to FEF. Similar dynamics in PFC and LIP could indicate that accumulation of sensory evidence depends on their recurrent interactions (24, 25). The delayed choice signals in FEF may reflect the transformation of accumulated evidence into a discrete choice (26). Sixth, we found an increase of choice signals in LIP and PFC before MT and V4. This is consistent with feedback of choice signals from frontoparietal to sensory cortex (12, 13, 27). This may support co-operative computations between different hierarchical stages (28) and perceptual stability (27). In sum, flexible sensorimotor decisions are not a simple feed-forward process but result from complex temporal dynamics, including feed-forward and feedback interactions between frontal and posterior cortex.

REFERENCES AND NOTES

1. D. A. Crowe et al., *Nat. Neurosci.* **16**, 1484–1491 (2013).
2. S. J. Goodwin, R. K. Blackman, S. Sakellari, M. V. Chafee, *J. Neurosci.* **32**, 3499–3515 (2012).
3. M. N. Shadlen, W. T. Newsome, *Proc. Natl. Acad. Sci. U.S.A.* **93**, 628–633 (1996).
4. D. J. Freedman, J. A. Assad, *Nature* **443**, 85–88 (2006).
5. C. H. Donahue, D. Lee, *Nat. Neurosci.* **18**, 295–301 (2015).
6. M. G. Stokes et al., *Neuron* **78**, 364–375 (2013).
7. J. N. Kim, M. N. Shadlen, *Nat. Neurosci.* **2**, 176–185 (1999).
8. K. Merten, A. Nieder, *Proc. Natl. Acad. Sci. U.S.A.* **109**, 6289–6294 (2012).
9. D. J. Freedman, M. Riesenhuber, T. Poggio, E. K. Miller, *Science* **291**, 312–316 (2001).
10. T. H. Donner, M. Siegel, P. Fries, A. K. Engel, *Curr. Biol.* **19**, 1581–1585 (2009).
11. K. H. Britten, W. T. Newsome, M. N. Shadlen, S. Celebrini, J. A. Movshon, *Vis. Neurosci.* **13**, 87–100 (1996).
12. H. Nienborg, B. G. Cumming, *Nature* **459**, 89–92 (2009).
13. N. K. Logothetis, J. D. Schall, *Science* **245**, 761–763 (1989).
14. J. D. Wallis, K. C. Anderson, E. K. Miller, *Nature* **411**, 953–956 (2001).
15. K. Johnston, H. M. Levin, M. J. Koval, S. Everling, *Neuron* **53**, 453–462 (2007).
16. R. Muhammad, J. D. Wallis, E. K. Miller, *J. Cogn. Neurosci.* **18**, 974–989 (2006).
17. R. Desimone, J. Duncan, *Annu. Rev. Neurosci.* **18**, 193–222 (1995).
18. S. Kastner, L. G. Ungerleider, *Annu. Rev. Neurosci.* **23**, 315–341 (2000).
19. J. H. Reynolds, L. Chelazzi, *Annu. Rev. Neurosci.* **27**, 611–647 (2004).
20. V. Mante, D. Sussillo, K. V. Shenoy, W. T. Newsome, *Nature* **503**, 78–84 (2013).
21. J. Duncan, *J. Exp. Psychol. Gen.* **113**, 501–517 (1984).
22. W. Singer, *Trends Cogn. Sci.* **17**, 616–626 (2013).
23. E. K. Miller, J. D. Cohen, *Annu. Rev. Neurosci.* **24**, 167–202 (2001).
24. M. Siegel, T. H. Donner, A. K. Engel, *Nat. Rev. Neurosci.* **13**, 121–134 (2012).
25. X. J. Wang, *Neuron* **60**, 215–234 (2008).
26. T. D. Hanks et al., *Nature* **520**, 220–223 (2015).
27. K. Wimmer et al., *Nat. Commun.* **6**, 6177 (2015).
28. M. Siegel, K. P. Körding, P. König, *J. Comput. Neurosci.* **8**, 161–173 (2000).

ACKNOWLEDGMENTS

We thank J. Roy, C. von Nicolai, and J. Hipp for helpful discussions. This work was supported by National Institute for Mental Health (NIMH) grant 5R37MH087027 (E.K.M.), MIT Picower Innovation Fund (E.K.M.), National Institutes of Health (NIH) grant R01MH092715 (T.J.B.), and the Centre for Integrative Neuroscience

(Deutsche Forschungsgemeinschaft, EXC 307) (M.S.). All behavioral and electrophysiological data are archived at the Centre for Integrative Neuroscience, University of Tübingen, Germany.

SUPPLEMENTARY MATERIALS

www.sciencemag.org/content/348/6241/1352/suppl/DC1
Materials and Methods
Figs. S1 to S4
References (29–35)

4 March 2015; accepted 8 May 2015
10.1126/science.aab0551

COMETARY NUCLEI

The shape and structure of cometary nuclei as a result of low-velocity accretion

M. Jutzi^{1*} and E. Asphaug²

Cometary nuclei imaged from flyby and rendezvous spacecraft show common evidence of layered structures and bilobed shapes. But how and when these features formed is much debated, with distinct implications for solar system formation, dynamics, and geology. We show that these features could be a direct result of accretionary collisions, based on three-dimensional impact simulations using realistic constitutive properties. We identify two regimes of interest: layer-forming splats and mergers resulting in bilobed shapes. For bodies with low tensile strength, our results can explain key morphologies of cometary nuclei, as well as their low bulk densities. This advances the hypothesis that nuclei formed by collisional coagulation—either out of cometesimals accreting in the early solar system or, alternatively, out of comparable-sized debris clumps paired in the aftermath of major collisions.

Comets or their precursors formed in the outer planets region, possibly millions of years before planet formation. Cometary nuclei may be fluffy condensates (1) or rubble piles (2) assembled by hierarchical accretion (3). Alternatively, they may be relics of catastrophically disrupted progenitors (4). Whether their interior structures preserve a record of their original accumulation is much debated (5, 6), as is their geophysical connection to the Kuiper belt objects (KBOs) that are the likely source (7) of 1P/Halley and Jupiter family comets (JFCs)—all of the comets visited by spacecraft to date. Models of present-day dynamical evolution (4) suggest that KBOs smaller than ~5 km in diameter have catastrophic disruption lifetimes shorter than the age of the solar system, in which case JFCs, even if delivered as intact KBOs, are unlikely to be primordial. Others (8) argue that KBOs larger than ~60 km grew by efficient hierarchical accretion, whereas KBOs smaller than ~4 km probably survived as primordial relics. Models based on gravitational instability along with particle clumping in tur-

bulent flows predict that asteroids and comets were born big (9, 10) and bypassed the primary accretion phase of kilometer-sized bodies entirely. If so, then JFCs are secondary collisional relics from KBO-scale collisions (11, 12). Dynamics is part of the story, chemistry another: In a thermodynamic sense, JFCs are highly primitive. The supervolatiles driving cometary activity and disruption (6) require there to have been minimal processing by internal heating and differentiation inside of a parent body and minimal shock heating by energetic impacts.

Whatever their origin, cometary nuclei come apart easily due to tides (13) and other gentle stresses (14). They are weakly consolidated at scales ~100 m or less (13). Estimated and measured bulk densities are half that of water ice, requiring considerable porosity. These data and other crucial information are obtained from astronomical observations and theoretical interpretations (5, 13), flyby missions (15, 16), and the European Space Agency's Rosetta rendezvous mission to 67P/Churyumov-Gerasimenko (17). Here we focus on the topographic and structural expressions of cometary nuclei identified by spacecraft.

There are two structural clues to cometary origin. First, there is a clear record of layers (18, 19) in 9P/Tempel 1 and 67P/C-G and possibly also in 19P/Borrelly and 81P/Wild 2. The layers of 67P

¹Physics Institute, Space Research and Planetary Sciences, Center for Space and Habitability, University of Bern, Sidlerstrasse 5, 3012 Bern, Switzerland. ²School of Earth and Space Exploration, Arizona State University, PO Box 876004, Tempe, AZ 85287, USA.

*Corresponding author. E-mail: martin.jutzi@space.unibe.ch

range from structural (~10- to 100-m scale) to textural (meter scale), and 9P/Tempel 1 has identifiable layers from >100 m to the limits of resolution (~10 m). Second, about half of comet nuclei have bilobed shapes (1P/Halley, 19P/Borrelly, 67P,

103P/Hartley 2). We apply three-dimensional (3D) collisional models, constrained by these shape and topographic data, to understand the basic accretion mechanism and its implications for internal structure.

According to primary accretion models (3), cometary nuclei coagulated out of ~0.1- to 1-km cometesimals during a formative epoch of low-speed collisions, at speeds comparable to their mutual escape speed v_{esc} . This speed is a few

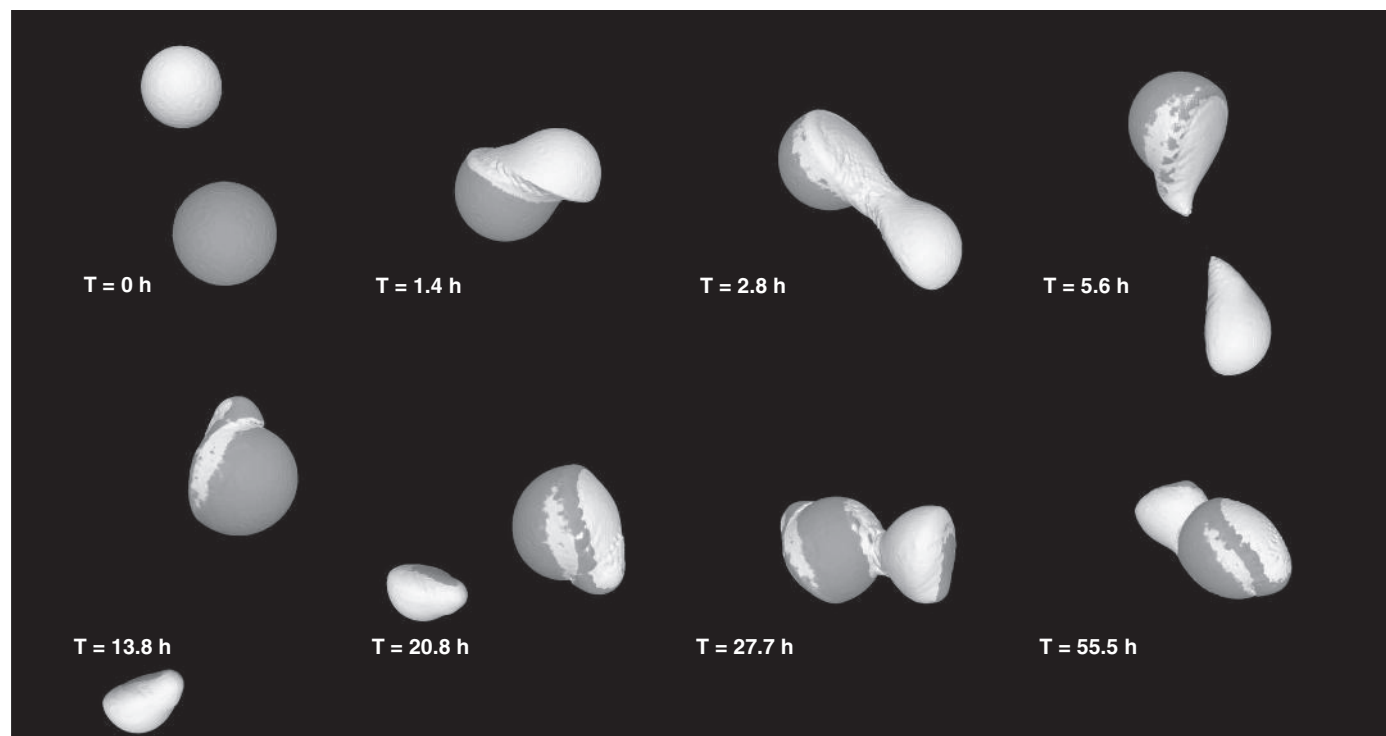


Fig. 1. Time sequence of bilobed formation. Shown are ~1-km cohesionless icy spheres (top left) colliding at $v_{\text{imp}} = 1.5v_{\text{esc}}$, $M_t/M_p = 2$, and $\theta = 52^\circ$ with crushing, friction, and self-gravity. The initial bodies have 50% porosity and a crushing strength of ~0.5 kPa. Their mutual escape speed is ~25 cm/s. The smaller body leaves a trace of material on the larger one during the first impact, where it is slowed down to reimpact the target ~1 day later. T , time.

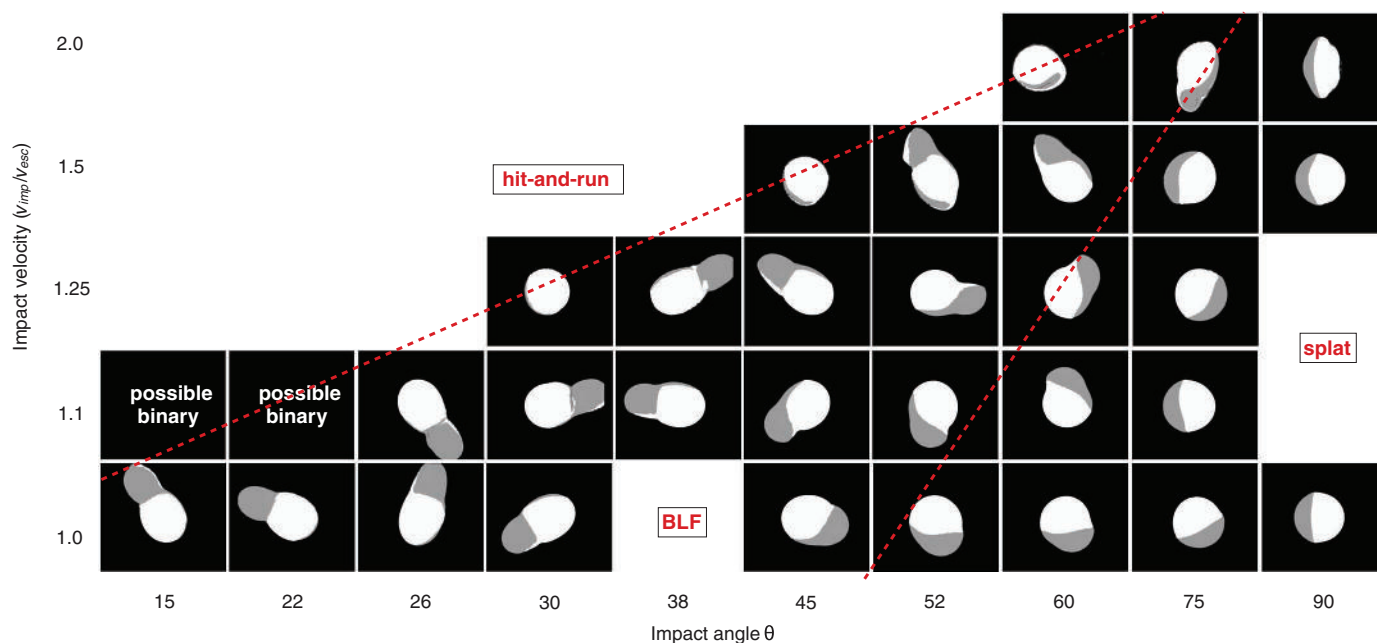


Fig. 2. Different regimes of collisions. The results of SPH simulations for $M_t/M_p = 2$ and cohesionless bodies. A slice through the symmetry plane is shown; white is the target and gray is the impactor. The normalized angular momentum L/L_{ref} can be used to distinguish between splat collisions ($0 \leq L/L_{\text{ref}} \leq 0.9$), BLF collisions ($0.9 \leq L/L_{\text{ref}} \leq 1.4$), and hit-and-run collisions ($L/L_{\text{ref}} \geq 1.4$), as indicated approximately by the dashed lines. The formation of a binary pair is possible in oblique (small θ) impacts.

meters per second, the velocity of a bicycle collision. To study this regime, we used a smooth particle hydrodynamics (SPH) impact code (20–22) that is well suited to modeling planetesimal collisions (23). As weak cometsimals collide and accrete, they crush each other into deformed, rotating assemblages and escaping pieces. Considering the expansive parameter space and great computational expense, we constrain our study to bodies with zero initial rotation, impact velocity $v_{\text{imp}} = 1$ to $2 v_{\text{esc}}$, impact angle $\theta = 15^\circ$ to 90° , and target-to-projectile mass ratio $M_t/M_p = 2$ to 8 .

Material properties are defined by the equation of state (water ice), porosity (50%), tensile strength, compressive strength, and friction (23). The largest tensile strength considered is 100 Pa; this exceeds the tidal stress that broke D/Shoemaker-Levy 9 (S-L9) into a “string of pearls” (13) and is consistent with laboratory materials analysis (24). Tensile strength is damaged at a prescribed failure stress, forming rubble that is treated using a friction law. Tensile strength is defined at the scale of the simulation resolution, ~ 10 m. Subscale cohesive structures (massive clods or sheets) would not influence our tensile stress calculations.

Compressive strength is much greater than tensile strength in a loosely bonded, coarsely textured aggregate. We model compression using a P - α crush curve (P , pressure; α , distention parameter) (23), considering compressive strengths ~ 0.5 to 5 kPa. These represent the low range of dynamic strengths determined by scaling the diameters of craters forming in icy satellite regoliths (25). Larger values of compressive strength would not affect our results, as the colliding bodies experience only minor compaction in

modeled collisions (see below). Energetically, it is easier to deform these bodies than to compactify them, so they flow without much change in density. Substantially lower compressive strength is not possible, as this would lead to collapse under hydrostatic pressure before the collision (fig. S1). The central pressure inside a 10-km diameter, 0.5-g/cm^3 comet nucleus equals 0.8 kPa, the weight of a 15-cm layer of the same material on Earth.

Although cohesion (tensile strength) is low, friction (pressure-dependent shear strength) has recently been identified as singularly important for collisions involving weak aggregate bodies (22, 26). Friction prevents collapse into a spheroid and allows for complex shapes and states of non-equilibrium rotation (27). Previous models of slow rubble-pile collisions have used zero friction materials or hard immutable spheres with ad hoc sticking (28). Our models take into account the combined effects of rheology (friction, porosity, tensile strength) that are especially important in modeling the self-gravitating gentle icy structures considered here.

The time evolution of such a collision is shown in Fig. 1. A summary of comparable collisions for a range of θ and v_{imp} can be seen in Fig. 2, which shows well-defined transitions between three categories of outcomes, denoted by dashed lines of approximately constant angular momentum: (i) “hit-and-runs” (29), in which the colliding bodies fail to accrete; (ii) bilobe-forming (BLF) collisions such as in Fig. 1; and (iii) “splats,” in which the projectile strikes head-on at higher velocity, flattening into an accretionary pile (30). We have not studied binary system outcomes dynamically, but we identify separated binaries near the transition between BLF collisions and hit-and-runs, consistent with studies of the formation of Pluto-Charon and Haumea (11, 12).

For higher-mass ratio collisions [$M_t/M_p = 4$ (fig. S2)], the picture is similar, although bilobed shapes are less pronounced. For $M_t/M_p = 8$ (fig. S3), no bilobed regime is identified, and collisions result in splats [impactor accreted as a layer (30)] or hit-and-runs (impactor continues downrange). In a splat, although the impactor is severely deformed, there is little compaction of pore space for the impact velocities $v_{\text{imp}} \sim v_{\text{esc}}$

considered here. According to our simulations, even multiple layer-forming events do not substantially increase the bulk density, so the final body is compatible with the measured low densities of comets. The degree of compaction is dependent on the crush curve within the limits explained above; detailed analysis of splat-like layers in comets (18) could constrain this aspect of cometary materials.

For two reasons, splats are prevalent and BLF collisions less common for higher-mass ratio collisions: First, a small projectile is usually stopped effectively by a considerably larger target. Even for small θ (near-grazing), all of the body’s mass encounters target material directly. In a similar-sized collision (29), half of the projectile typically has no direct contact with target material, leading to BLF, graze-and-merge, and hit-and-run collisions. Second, for large M_t/M_p , the pancake deformation of a projectile requires less energy than the mobilization of target material against target gravity; splats fill their own craters (30).

The boundaries between splats, BLF collisions, and hit-and-runs can be specified in terms of a reference initial angular momentum $L_{\text{ref}} = M_p v_{\text{esc}} r_{\text{imp}} b_{\text{ref}}$, which is the angular momentum of an impact with $v_{\text{imp}} = v_{\text{esc}}$, reference impact parameter $b_{\text{ref}} = \cos(45^\circ)$, and impact radius $r_{\text{imp}} = r_t + r_p$. Normalized angular momentum is $L/L_{\text{ref}} = (v_{\text{imp}} b)(v_{\text{esc}} b_{\text{ref}})$, where $L = M_p v_{\text{imp}} r_{\text{imp}} b$ (b , impact parameter) and r_t and r_p are the radii of the target and projectile, respectively. Visual inspection of Fig. 2 shows that for mass ratio $M_t/M_p = 2$, splats occur for $0 \leq L/L_{\text{ref}} \leq 0.9$, BLF collisions for $0.9 \leq L/L_{\text{ref}} \leq 1.4$, and hit-and-runs for $L/L_{\text{ref}} \geq 1.4$. Because L increases with v_{imp} , the probability of forming splats and BLF collisions decreases with increasing impact velocity. We find that these boundaries also apply for different mass ratios (fig. S1), although as noted, splats dominate at very small mass ratios (fig. S2).

In principle, the structural morphology of cometary nuclei can be used to quantify their accretionary dynamics. Comet 67P, with estimated mass ratio $M_t/M_p \sim 2$ to 4 between its lobes, is the result of a possible BLF collision. The mutual escape speed from its lobes is

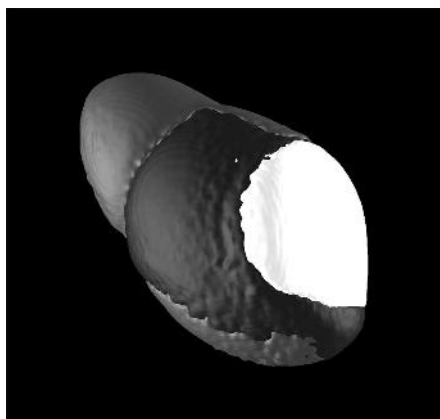


Fig. 3. Result of combined BLF and subsequent splat-forming collisions. An additional impactor (mass M_{p2}) with $M_t/M_{p2} = 8$ and an impact velocity of $v_{\text{imp}} \sim v_{\text{esc}}$ is used to investigate a splat-type event on a bilobed body. The latter was formed in a collision such as shown in Fig. 1 and has a final rotation rate of ~ 12 hours. Simulated bodies are cohesionless. The subsequent impact leads to a splat feature (white) without destroying the bilobed structure of the target. The dark gray and light gray materials correspond to the original target and impactor, respectively.

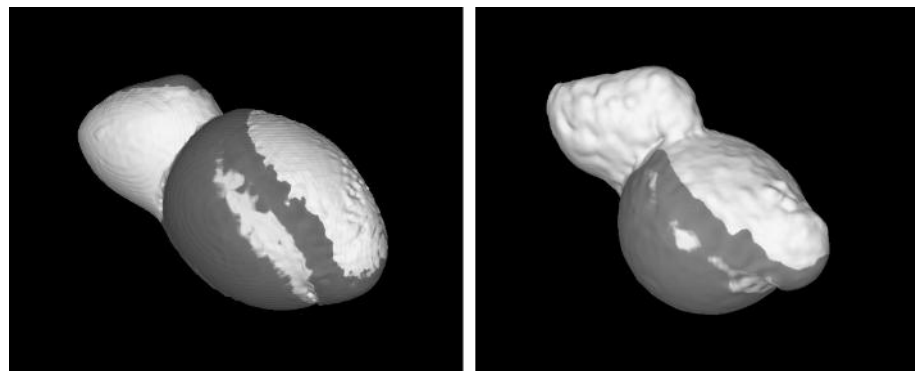


Fig. 4. Effect of tensile strength on the final shape. Comparison between two runs with the same initial conditions (same as in the run shown in Fig. 1) but different material properties. Colors indicate the original colliding bodies. (Left) Zero tensile strength; (right) 100-Pa tensile strength.

$v_{\text{esc}} \sim 0.7$ m/s, assuming a bulk density of 470 kg/m^3 (17), placing 67P well within the modeled BLF regime for impact velocities up to 1.5 m/s (as represented by Fig. 1). The accreted body is spun up to a final rotation period $P_{\text{rot}} \sim 10$ to 12 hours for $M_t/M_p = 2$ and $P_{\text{rot}} \sim 10$ to 14 hours for $M_t/M_p = 4$, depending on initial angular momentum and final shape and elongation of the resulting structure. Although consistent with $P_{\text{rot}} = 12.7$ hours for 67P, this is perhaps not meaningful because P_{rot} increased by 0.4 hours before and after the comet's 2009 perihelion (31).

A relatively narrow range of comet nuclei have been observed by spacecraft: ~ 10 -km radius at largest (1P/Halley and 19P/Borrelly) and ~ 1 km at smallest (103P/Hartley). For these sizes the outcomes of collisions would be comparable to those presented here, for a normalized impact velocity $v_{\text{imp}}/v_{\text{esc}}$ and normalized angular momentum L/L_{ref} to define the boundaries. For bodies much larger than ~ 10 to 100 km, compaction of a weak interior is expected (32) (fig. S1); this would strongly influence the outcomes of collisions by increasing the deep interior binding energy.

In simulations of BLF collisions, traces of the projectile are smeared onto the target and piled along the equator, suggesting the possibility of distinguishing features in remote sensing. We also consider the effect of successive collisions, as these could potentially bury, cover, or otherwise modify a preexisting structure. For this, we first produced a cohesionless BLF collision target (shape held by friction) with initial rotation $P_{\text{rot}} = 12$ hours, followed by a large splat-forming collision (Fig. 3). Splat formation is clearly possible without destroying the preexisting bilobed structure.

We also consider tensile strength at the resolution scale (23) for cometsimals of mass ratio 1/2, 1/4, and 1/8 (figs. S4 to S6). Initially cohesive bodies are partly or fully damaged by the collisions (fig. S7), meaning that final shapes are maintained only by friction, as in Fig. 1. For tensile strength ~ 100 Pa, the results are comparable to identical collisions with zero tensile strength, and the distinct neck of 67P might be better reproduced with some tensile strength (Fig. 4). Greater tensile strength allows smaller "heads" to form, as opposed to cohesionless bodies and lumpy splats. There appears to be a tendency to form more binaries and small satellites with small tensile strength, although we have not evaluated the dynamical stability of pairs.

The major structural features observed on cometary nuclei—evidence for layers and bilobed shapes—can be explained by the pairwise accretion of icy bodies with little tensile strength on ~ 10 - to 100-m scales. Our analysis is compatible with the low bulk densities of comets: Low tensile strength implies high original porosity, while the collisions result in only minor compaction. These slow mergers might represent the quiet, early phase of planet formation (3), before large bodies excited the system to disruptive velocities, supporting the idea that cometary nuclei are primordial remnants of early agglomeration (33). Alternatively, the same processes of coagulation might have occurred among debris clumps ejected

from much larger parent bodies. Apart from requiring the latter scenario to be consistent with the cosmochemistry of nuclei, these clumps would have to be similar in size to produce BLF collisions, and nearly cohesionless, aspects for which there is evidence in simulations of larger collisions (12, 34). In either case, these structures would have to avoid catastrophic disruption until the present.

REFERENCES AND NOTES

- B. Donn, D. Hughes, "A fractal model of a cometary nucleus formed by random accretion," in *Proceedings of the 20th ESLAB Symposium on the Exploration of Halley's Comet* (European Space Agency, Paris, 1986), vol. 3, pp. 523–524.
- P. R. Weissman, *Nature* **320**, 242–244 (1986).
- S. J. Weidenschilling, *Icarus* **127**, 290–306 (1997).
- D. Durda, S. A. Stern, *Icarus* **145**, 220–229 (2000).
- P. R. Weissman, E. Asphaug, S. C. Lowry, "Structure and density of cometary nuclei," in *Comets II*, M. C. Festou, H. U. Keller, H. A. Weaver, Eds. (Univ. of Arizona Press, Tucson, AZ, 2004), pp. 337–357.
- M. J. Mumma, P. R. Weissman, S. A. Stern, "Comets and the origin of the solar system - Reading the Rosetta Stone," in *Protostars and Planets III* (Univ. of Arizona Press, Tucson, AZ, 1993), pp. 1177–1252.
- H. F. Levison, M. J. Duncan, L. Dones, B. J. Gladman, *Icarus* **184**, 619–633 (2006).
- H. E. Schlichting, C. I. Fuentes, D. E. Trilling, *Astron. J.* **146**, 36 (2013).
- A. Morbidelli, W. F. Bottke, D. Nesvorný, H. F. Levison, *Icarus* **204**, 558–573 (2009).
- J. N. Cuzzi, R. C. Hogan, W. F. Bottke, *Icarus* **208**, 518–538 (2010).
- R. M. Canup, *Astron. J.* **141**, 35 (2010).
- Z. M. Leinhardt, R. A. Marcus, S. T. Stewart, *Astrophys. J.* **714**, 1789–1799 (2010).
- E. Asphaug, W. Benz, *Nature* **370**, 120–124 (1994).
- H. Boehnhardt, "Split comets," in *Comets II* (Univ. of Arizona Press, Tucson, AZ, 2004), pp. 301–316.
- M. J. S. Belton, *Icarus* **210**, 881–897 (2010).
- M. F. A'Hearn, *Annu. Rev. Astron. Astrophys.* **49**, 281–299 (2011).
- H. Sierks et al., *Science* **347**, aaa1044 (2015).
- M. J. S. Belton et al., *Icarus* **187**, 332–344 (2007).
- N. Thomas et al., *Science* **347**, aaa0440 (2015).

- W. Benz, E. Asphaug, *Comput. Phys. Commun.* **87**, 253–265 (1995).
- M. Jutzi, W. Benz, P. Michel, *Icarus* **198**, 242–255 (2008).
- M. Jutzi, *Planet. Space Sci.* **107**, 3–9 (2015).
- Materials and methods are available as supplementary materials on Science Online.
- Y. Skorov, J. Blum, *Icarus* **221**, 1–52 (2012).
- M. Arakawa, M. Yasui, *Icarus* **216**, 1–9 (2011).
- M. Jutzi, K. Holsapple, K. Wünnemann, P. Michel, "Modeling asteroid collisions and impact processes," in *Asteroids IV*, in press; preprint available at <http://arxiv.org/abs/1502.01844> (2015).
- P. Tanga et al., *Astrophys. J.* **706**, L197–L202 (2009).
- Z. Leinhardt, D. C. Richardson, T. Quinn, *Icarus* **146**, 133–151 (2000).
- E. Asphaug, C. B. Agnor, Q. Williams, *Nature* **439**, 155–160 (2006).
- M. Jutzi, E. Asphaug, *Nature* **476**, 69–72 (2011).
- S. Mottola et al., *Astron. Astrophys.* **569**, L2 (2014).
- W. B. Durham, W. B. McKinnon, L. A. Stern, *Geophys. Res. Lett.* **32**, L18202 (2005).
- M. J. S. Belton, *Icarus* **231**, 168–182 (2014).
- E. Asphaug, A. Reufer, *Icarus* **223**, 544–565 (2013).

ACKNOWLEDGMENTS

M.J. acknowledges support from the Swiss National Science Foundation through the Ambizione program. The work was carried out partly within the frame of the National Centre for Competence in Research "PlanetS." E.A. was supported by NASA's Planetary Geology and Geophysics Program. We thank the anonymous reviewers for valuable comments. The 3D images were produced using Vapor (www.vapor.ucar.edu). SPH data are available as supplementary materials.

SUPPLEMENTARY MATERIALS

www.sciencemag.org/content/348/6421/1355/suppl/DC1

Materials and Methods

Figs. S1 to S7

Table S1

References (35–38)

Data S1 to S7

11 December 2014; accepted 13 May 2015

Published online 28 May 2015;

10.1126/science.aaa4747

GROUP DECISIONS

Shared decision-making drives collective movement in wild baboons

Ariana Strandburg-Peshkin,^{1*†} Damien R. Farine,^{2,3,4,*†}
Iain D. Couzin,^{1,5,6} Margaret C. Crofoot^{2,3,*}

Conflicts of interest about where to go and what to do are a primary challenge of group living. However, it remains unclear how consensus is achieved in stable groups with stratified social relationships. Tracking wild baboons with a high-resolution global positioning system and analyzing their movements relative to one another reveals that a process of shared decision-making governs baboon movement. Rather than preferentially following dominant individuals, baboons are more likely to follow when multiple initiators agree. When conflicts arise over the direction of movement, baboons choose one direction over the other when the angle between them is large, but they compromise if it is not. These results are consistent with models of collective motion, suggesting that democratic collective action emerging from simple rules is widespread, even in complex, socially stratified societies.

Individuals living in stable social groups may often disagree about where to go but must reconcile their differences to maintain cohesion and thus the benefits of group living. Consensus decisions could be dominated by a single despotic leader (1), determined by a hi-

erarchy of influence (2), or emerge from a shared democratic process (3). Because decisions are typically more accurate when information is pooled (4, 5), theory predicts that shared decision-making should be widespread in nature (6). However, in species that form long-term social bonds,

range from structural (~10- to 100-m scale) to textural (meter scale), and 9P/Tempel 1 has identifiable layers from >100 m to the limits of resolution (~10 m). Second, about half of comet nuclei have bilobed shapes (1P/Halley, 19P/Borrelly, 67P,

103P/Hartley 2). We apply three-dimensional (3D) collisional models, constrained by these shape and topographic data, to understand the basic accretion mechanism and its implications for internal structure.

According to primary accretion models (3), cometary nuclei coagulated out of ~0.1- to 1-km cometesimals during a formative epoch of low-speed collisions, at speeds comparable to their mutual escape speed v_{esc} . This speed is a few

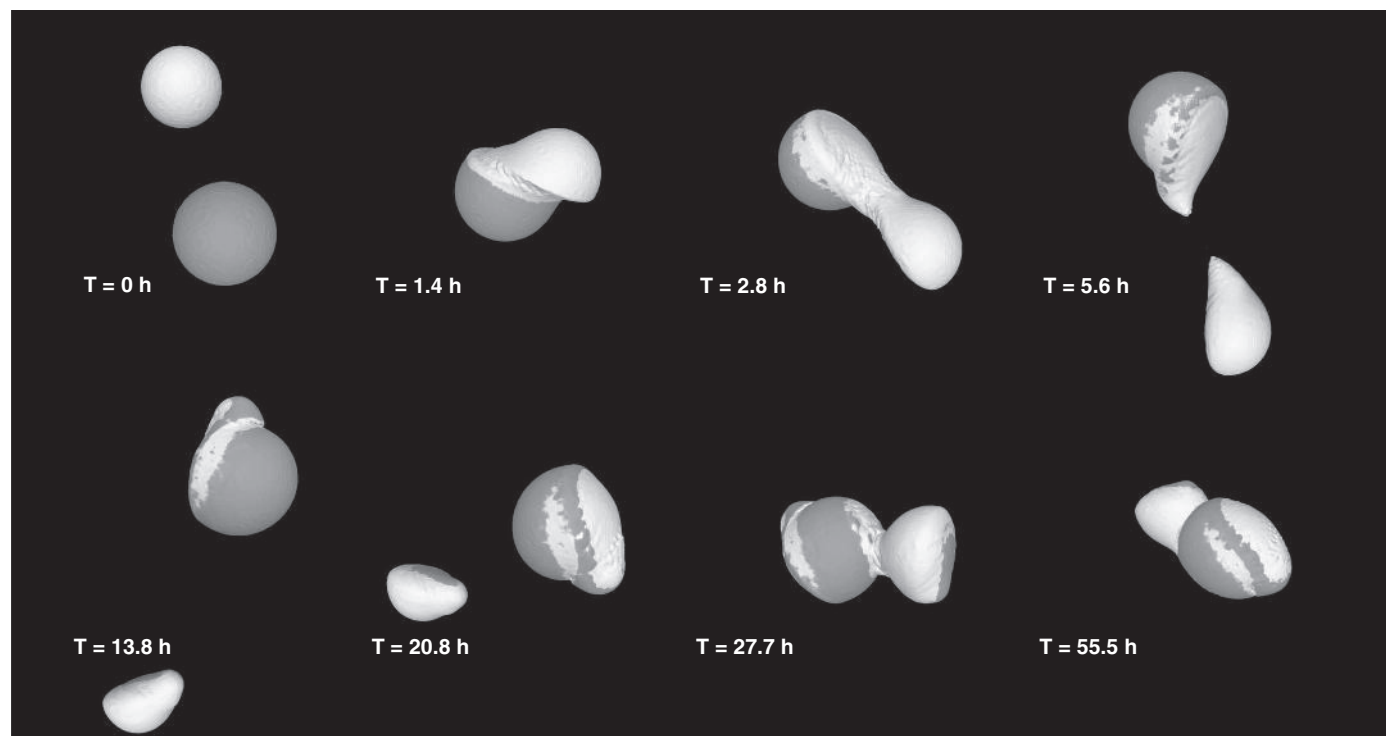


Fig. 1. Time sequence of bilobed formation. Shown are ~1-km cohesionless icy spheres (top left) colliding at $v_{\text{imp}} = 1.5v_{\text{esc}}$, $M_t/M_p = 2$, and $\theta = 52^\circ$ with crushing, friction, and self-gravity. The initial bodies have 50% porosity and a crushing strength of ~0.5 kPa. Their mutual escape speed is ~25 cm/s. The smaller body leaves a trace of material on the larger one during the first impact, where it is slowed down to reimpact the target ~1 day later. T , time.

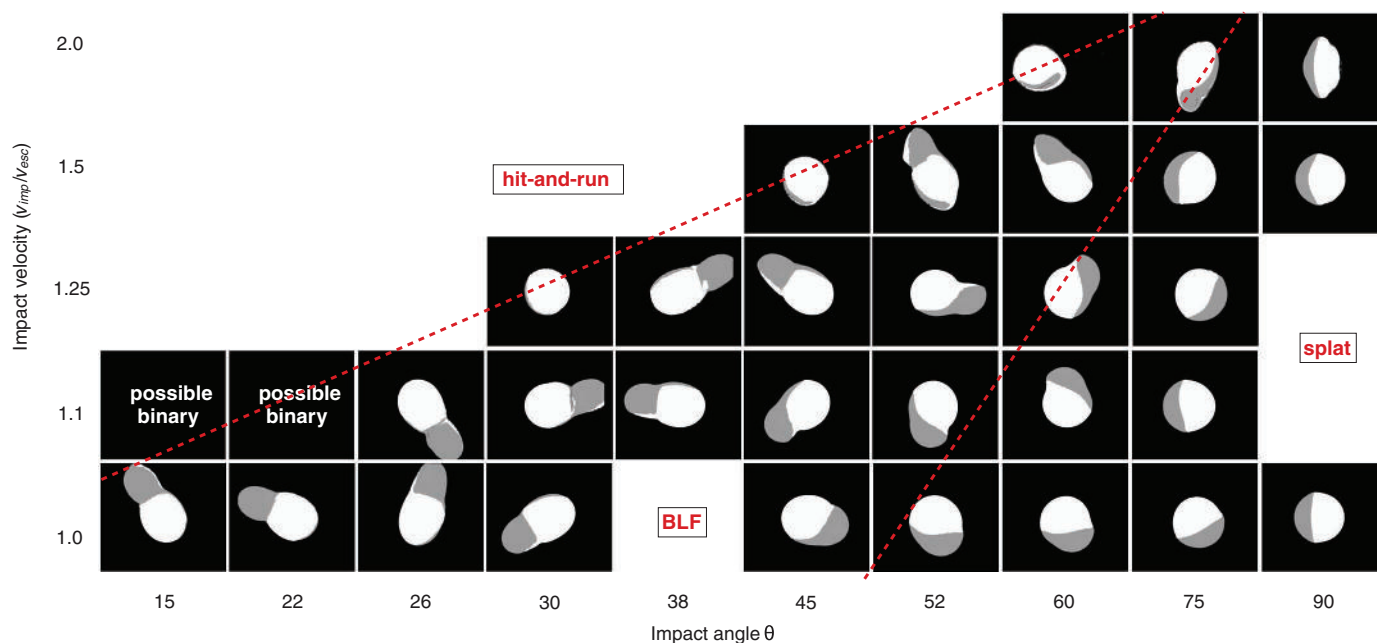


Fig. 2. Different regimes of collisions. The results of SPH simulations for $M_t/M_p = 2$ and cohesionless bodies. A slice through the symmetry plane is shown; white is the target and gray is the impactor. The normalized angular momentum L/L_{ref} can be used to distinguish between splat collisions ($0 \leq L/L_{\text{ref}} \leq 0.9$), BLF collisions ($0.9 \leq L/L_{\text{ref}} \leq 1.4$), and hit-and-run collisions ($L/L_{\text{ref}} \geq 1.4$), as indicated approximately by the dashed lines. The formation of a binary pair is possible in oblique (small θ) impacts.

meters per second, the velocity of a bicycle collision. To study this regime, we used a smooth particle hydrodynamics (SPH) impact code (20–22) that is well suited to modeling planetesimal collisions (23). As weak cometsimals collide and accrete, they crush each other into deformed, rotating assemblages and escaping pieces. Considering the expansive parameter space and great computational expense, we constrain our study to bodies with zero initial rotation, impact velocity $v_{\text{imp}} = 1$ to $2 v_{\text{esc}}$, impact angle $\theta = 15^\circ$ to 90° , and target-to-projectile mass ratio $M_t/M_p = 2$ to 8.

Material properties are defined by the equation of state (water ice), porosity (50%), tensile strength, compressive strength, and friction (23). The largest tensile strength considered is 100 Pa; this exceeds the tidal stress that broke D/Shoemaker-Levy 9 (S-L9) into a “string of pearls” (13) and is consistent with laboratory materials analysis (24). Tensile strength is damaged at a prescribed failure stress, forming rubble that is treated using a friction law. Tensile strength is defined at the scale of the simulation resolution, ~ 10 m. Subscale cohesive structures (massive clods or sheets) would not influence our tensile stress calculations.

Compressive strength is much greater than tensile strength in a loosely bonded, coarsely textured aggregate. We model compression using a P - α crush curve (P , pressure; α , distention parameter) (23), considering compressive strengths ~ 0.5 to 5 kPa. These represent the low range of dynamic strengths determined by scaling the diameters of craters forming in icy satellite regoliths (25). Larger values of compressive strength would not affect our results, as the colliding bodies experience only minor compaction in

modeled collisions (see below). Energetically, it is easier to deform these bodies than to compactify them, so they flow without much change in density. Substantially lower compressive strength is not possible, as this would lead to collapse under hydrostatic pressure before the collision (fig. S1). The central pressure inside a 10-km diameter, 0.5-g/cm^3 comet nucleus equals 0.8 kPa, the weight of a 15-cm layer of the same material on Earth.

Although cohesion (tensile strength) is low, friction (pressure-dependent shear strength) has recently been identified as singularly important for collisions involving weak aggregate bodies (22, 26). Friction prevents collapse into a spheroid and allows for complex shapes and states of non-equilibrium rotation (27). Previous models of slow rubble-pile collisions have used zero friction materials or hard immutable spheres with ad hoc sticking (28). Our models take into account the combined effects of rheology (friction, porosity, tensile strength) that are especially important in modeling the self-gravitating gentle icy structures considered here.

The time evolution of such a collision is shown in Fig. 1. A summary of comparable collisions for a range of θ and v_{imp} can be seen in Fig. 2, which shows well-defined transitions between three categories of outcomes, denoted by dashed lines of approximately constant angular momentum: (i) “hit-and-runs” (29), in which the colliding bodies fail to accrete; (ii) bilobe-forming (BLF) collisions such as in Fig. 1; and (iii) “splats,” in which the projectile strikes head-on at higher velocity, flattening into an accretionary pile (30). We have not studied binary system outcomes dynamically, but we identify separated binaries near the transition between BLF collisions and hit-and-runs, consistent with studies of the formation of Pluto-Charon and Haumea (11, 12).

For higher-mass ratio collisions [$M_t/M_p = 4$ (fig. S2)], the picture is similar, although bilobed shapes are less pronounced. For $M_t/M_p = 8$ (fig. S3), no bilobed regime is identified, and collisions result in splats [impactor accreted as a layer (30)] or hit-and-runs (impactor continues downrange). In a splat, although the impactor is severely deformed, there is little compaction of pore space for the impact velocities $v_{\text{imp}} \sim v_{\text{esc}}$

considered here. According to our simulations, even multiple layer-forming events do not substantially increase the bulk density, so the final body is compatible with the measured low densities of comets. The degree of compaction is dependent on the crush curve within the limits explained above; detailed analysis of splat-like layers in comets (18) could constrain this aspect of cometary materials.

For two reasons, splats are prevalent and BLF collisions less common for higher-mass ratio collisions: First, a small projectile is usually stopped effectively by a considerably larger target. Even for small θ (near-grazing), all of the body’s mass encounters target material directly. In a similar-sized collision (29), half of the projectile typically has no direct contact with target material, leading to BLF, graze-and-merge, and hit-and-run collisions. Second, for large M_t/M_p , the pancake deformation of a projectile requires less energy than the mobilization of target material against target gravity; splats fill their own craters (30).

The boundaries between splats, BLF collisions, and hit-and-runs can be specified in terms of a reference initial angular momentum $L_{\text{ref}} = M_p v_{\text{esc}} r_{\text{imp}} b_{\text{ref}}$, which is the angular momentum of an impact with $v_{\text{imp}} = v_{\text{esc}}$, reference impact parameter $b_{\text{ref}} = \cos(45^\circ)$, and impact radius $r_{\text{imp}} = r_t + r_p$. Normalized angular momentum is $L/L_{\text{ref}} = (v_{\text{imp}} b)(v_{\text{esc}} b_{\text{ref}})$, where $L = M_p v_{\text{imp}} r_{\text{imp}} b$ (b , impact parameter) and r_t and r_p are the radii of the target and projectile, respectively. Visual inspection of Fig. 2 shows that for mass ratio $M_t/M_p = 2$, splats occur for $0 \leq L/L_{\text{ref}} \leq 0.9$, BLF collisions for $0.9 \leq L/L_{\text{ref}} \leq 1.4$, and hit-and-runs for $L/L_{\text{ref}} \geq 1.4$. Because L increases with v_{imp} , the probability of forming splats and BLF collisions decreases with increasing impact velocity. We find that these boundaries also apply for different mass ratios (fig. S1), although as noted, splats dominate at very small mass ratios (fig. S2).

In principle, the structural morphology of cometary nuclei can be used to quantify their accretionary dynamics. Comet 67P, with estimated mass ratio $M_t/M_p \sim 2$ to 4 between its lobes, is the result of a possible BLF collision. The mutual escape speed from its lobes is

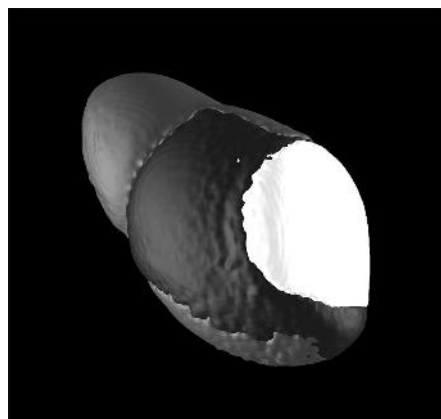


Fig. 3. Result of combined BLF and subsequent splat-forming collisions. An additional impactor (mass M_{p2}) with $M_t/M_{p2} = 8$ and an impact velocity of $v_{\text{imp}} \sim v_{\text{esc}}$ is used to investigate a splat-type event on a bilobed body. The latter was formed in a collision such as shown in Fig. 1 and has a final rotation rate of ~ 12 hours. Simulated bodies are cohesionless. The subsequent impact leads to a splat feature (white) without destroying the bilobed structure of the target. The dark gray and light gray materials correspond to the original target and impactor, respectively.

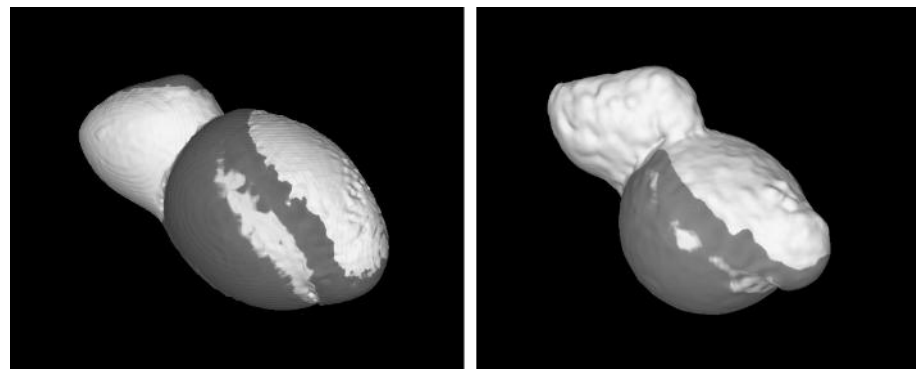


Fig. 4. Effect of tensile strength on the final shape. Comparison between two runs with the same initial conditions (same as in the run shown in Fig. 1) but different material properties. Colors indicate the original colliding bodies. (Left) Zero tensile strength; (right) 100-Pa tensile strength.

$v_{\text{esc}} \sim 0.7$ m/s, assuming a bulk density of 470 kg/m^3 (17), placing 67P well within the modeled BLF regime for impact velocities up to 1.5 m/s (as represented by Fig. 1). The accreted body is spun up to a final rotation period $P_{\text{rot}} \sim 10$ to 12 hours for $M_t/M_p = 2$ and $P_{\text{rot}} \sim 10$ to 14 hours for $M_t/M_p = 4$, depending on initial angular momentum and final shape and elongation of the resulting structure. Although consistent with $P_{\text{rot}} = 12.7$ hours for 67P, this is perhaps not meaningful because P_{rot} increased by 0.4 hours before and after the comet's 2009 perihelion (31).

A relatively narrow range of comet nuclei have been observed by spacecraft: ~ 10 -km radius at largest (1P/Halley and 19P/Borrelly) and ~ 1 km at smallest (103P/Hartley). For these sizes the outcomes of collisions would be comparable to those presented here, for a normalized impact velocity $v_{\text{imp}}/v_{\text{esc}}$ and normalized angular momentum L/L_{ref} to define the boundaries. For bodies much larger than ~ 10 to 100 km, compaction of a weak interior is expected (32) (fig. S1); this would strongly influence the outcomes of collisions by increasing the deep interior binding energy.

In simulations of BLF collisions, traces of the projectile are smeared onto the target and piled along the equator, suggesting the possibility of distinguishing features in remote sensing. We also consider the effect of successive collisions, as these could potentially bury, cover, or otherwise modify a preexisting structure. For this, we first produced a cohesionless BLF collision target (shape held by friction) with initial rotation $P_{\text{rot}} = 12$ hours, followed by a large splat-forming collision (Fig. 3). Splat formation is clearly possible without destroying the preexisting bilobed structure.

We also consider tensile strength at the resolution scale (23) for cometsimals of mass ratio 1/2, 1/4, and 1/8 (figs. S4 to S6). Initially cohesive bodies are partly or fully damaged by the collisions (fig. S7), meaning that final shapes are maintained only by friction, as in Fig. 1. For tensile strength ~ 100 Pa, the results are comparable to identical collisions with zero tensile strength, and the distinct neck of 67P might be better reproduced with some tensile strength (Fig. 4). Greater tensile strength allows smaller "heads" to form, as opposed to cohesionless bodies and lumpy splats. There appears to be a tendency to form more binaries and small satellites with small tensile strength, although we have not evaluated the dynamical stability of pairs.

The major structural features observed on cometary nuclei—evidence for layers and bilobed shapes—can be explained by the pairwise accretion of icy bodies with little tensile strength on ~ 10 - to 100-m scales. Our analysis is compatible with the low bulk densities of comets: Low tensile strength implies high original porosity, while the collisions result in only minor compaction. These slow mergers might represent the quiet, early phase of planet formation (3), before large bodies excited the system to disruptive velocities, supporting the idea that cometary nuclei are primordial remnants of early agglomeration (33). Alternatively, the same processes of coagulation might have occurred among debris clumps ejected

from much larger parent bodies. Apart from requiring the latter scenario to be consistent with the cosmochemistry of nuclei, these clumps would have to be similar in size to produce BLF collisions, and nearly cohesionless, aspects for which there is evidence in simulations of larger collisions (12, 34). In either case, these structures would have to avoid catastrophic disruption until the present.

REFERENCES AND NOTES

- B. Donn, D. Hughes, "A fractal model of a cometary nucleus formed by random accretion," in *Proceedings of the 20th ESLAB Symposium on the Exploration of Halley's Comet* (European Space Agency, Paris, 1986), vol. 3, pp. 523–524.
- P. R. Weissman, *Nature* **320**, 242–244 (1986).
- S. J. Weidenschilling, *Icarus* **127**, 290–306 (1997).
- D. Durda, S. A. Stern, *Icarus* **145**, 220–229 (2000).
- P. R. Weissman, E. Asphaug, S. C. Lowry, "Structure and density of cometary nuclei," in *Comets II*, M. C. Festou, H. U. Keller, H. A. Weaver, Eds. (Univ. of Arizona Press, Tucson, AZ, 2004), pp. 337–357.
- M. J. Mumma, P. R. Weissman, S. A. Stern, "Comets and the origin of the solar system - Reading the Rosetta Stone," in *Protostars and Planets III* (Univ. of Arizona Press, Tucson, AZ, 1993), pp. 1177–1252.
- H. F. Levison, M. J. Duncan, L. Dones, B. J. Gladman, *Icarus* **184**, 619–633 (2006).
- H. E. Schlichting, C. I. Fuentes, D. E. Trilling, *Astron. J.* **146**, 36 (2013).
- A. Morbidelli, W. F. Bottke, D. Nesvorný, H. F. Levison, *Icarus* **204**, 558–573 (2009).
- J. N. Cuzzi, R. C. Hogan, W. F. Bottke, *Icarus* **208**, 518–538 (2010).
- R. M. Canup, *Astron. J.* **141**, 35 (2010).
- Z. M. Leinhardt, R. A. Marcus, S. T. Stewart, *Astrophys. J.* **714**, 1789–1799 (2010).
- E. Asphaug, W. Benz, *Nature* **370**, 120–124 (1994).
- H. Boehnhardt, "Split comets," in *Comets II* (Univ. of Arizona Press, Tucson, AZ, 2004), pp. 301–316.
- M. J. S. Belton, *Icarus* **210**, 881–897 (2010).
- M. F. A'Hearn, *Annu. Rev. Astron. Astrophys.* **49**, 281–299 (2011).
- H. Sierks et al., *Science* **347**, aaa1044 (2015).
- M. J. S. Belton et al., *Icarus* **187**, 332–344 (2007).
- N. Thomas et al., *Science* **347**, aaa0440 (2015).
- W. Benz, E. Asphaug, *Comput. Phys. Commun.* **87**, 253–265 (1995).
- M. Jutzi, W. Benz, P. Michel, *Icarus* **198**, 242–255 (2008).
- M. Jutzi, *Planet. Space Sci.* **107**, 3–9 (2015).
- Materials and methods are available as supplementary materials on Science Online.
- Y. Skorov, J. Blum, *Icarus* **221**, 1–52 (2012).
- M. Arakawa, M. Yasui, *Icarus* **216**, 1–9 (2011).
- M. Jutzi, K. Holsapple, K. Wünnemann, P. Michel, "Modeling asteroid collisions and impact processes," in *Asteroids IV*, in press; preprint available at <http://arxiv.org/abs/1502.01844> (2015).
- P. Tanga et al., *Astrophys. J.* **706**, L197–L202 (2009).
- Z. Leinhardt, D. C. Richardson, T. Quinn, *Icarus* **146**, 133–151 (2000).
- E. Asphaug, C. B. Agnor, Q. Williams, *Nature* **439**, 155–160 (2006).
- M. Jutzi, E. Asphaug, *Nature* **476**, 69–72 (2011).
- S. Mottola et al., *Astron. Astrophys.* **569**, L2 (2014).
- W. B. Durham, W. B. McKinnon, L. A. Stern, *Geophys. Res. Lett.* **32**, L18202 (2005).
- M. J. S. Belton, *Icarus* **231**, 168–182 (2014).
- E. Asphaug, A. Reufer, *Icarus* **223**, 544–565 (2013).

ACKNOWLEDGMENTS

M.J. acknowledges support from the Swiss National Science Foundation through the Ambizione program. The work was carried out partly within the frame of the National Centre for Competence in Research "PlanetS." E.A. was supported by NASA's Planetary Geology and Geophysics Program. We thank the anonymous reviewers for valuable comments. The 3D images were produced using Vapor (www.vapor.ucar.edu). SPH data are available as supplementary materials.

SUPPLEMENTARY MATERIALS

www.sciencemag.org/content/348/6421/1355/suppl/DC1

Materials and Methods

Figs. S1 to S7

Table S1

References (35–38)

Data S1 to S7

11 December 2014; accepted 13 May 2015

Published online 28 May 2015;

10.1126/science.aaa4747

GROUP DECISIONS

Shared decision-making drives collective movement in wild baboons

Ariana Strandburg-Peshkin,^{1*†} Damien R. Farine,^{2,3,4,*†}
Iain D. Couzin,^{1,5,6} Margaret C. Crofoot^{2,3,*}

Conflicts of interest about where to go and what to do are a primary challenge of group living. However, it remains unclear how consensus is achieved in stable groups with stratified social relationships. Tracking wild baboons with a high-resolution global positioning system and analyzing their movements relative to one another reveals that a process of shared decision-making governs baboon movement. Rather than preferentially following dominant individuals, baboons are more likely to follow when multiple initiators agree. When conflicts arise over the direction of movement, baboons choose one direction over the other when the angle between them is large, but they compromise if it is not. These results are consistent with models of collective motion, suggesting that democratic collective action emerging from simple rules is widespread, even in complex, socially stratified societies.

Individuals living in stable social groups may often disagree about where to go but must reconcile their differences to maintain cohesion and thus the benefits of group living. Consensus decisions could be dominated by a single despotic leader (1), determined by a hi-

erarchy of influence (2), or emerge from a shared democratic process (3). Because decisions are typically more accurate when information is pooled (4, 5), theory predicts that shared decision-making should be widespread in nature (6). However, in species that form long-term social bonds,

considerable asymmetries in dominance and social power often exist, and some have proposed that these differences give high-ranking individuals increased influence over group decisions (1, 7, 8). Determining how consensus is achieved in these types of societies remains a core challenge for understanding the evolution of social complexity (6, 9, 10).

We studied the collective movement of a troop of wild olive baboons (*Papio anubis*) at Mpala Research Centre in Kenya to examine how group members reach consensus about whether and where to move. Baboons, long a model system for studying the evolutionary consequences of social bonds (11–13), live in stable multi-male, multi-female troops of up to 100 individuals (11). Despite differing needs, capabilities, and preferred foraging strategies (14–16), troop members remain highly cohesive, traveling long distances each day as a unit, while foraging for diverse and widely dispersed foods. How troops make collective movement decisions, and whether specific individuals determine decision outcomes, remain unclear. Attempts to identify influential individuals by observing which animals initiate departures from sleeping sites (17, 18) or are found at the front of group progressions (19) have yielded conflicting results (9). Studying collective decision-making events requires many potential decision-makers in a group to be monitored simultaneously—a significant logistical challenge.

To tackle this “observational task of daunting dimensions” (8), we analyzed data from 25 wild baboons (~80% of our study troop’s adult and subadult members, table S1), each fitted with a custom-designed global positioning system (GPS) collar that recorded its location every second [Fig. 1 and movies S1 and S2 (20)]. We developed an automated procedure for extracting “movement initiations” based on the relative movements of pairs of individuals (20). These were defined as sequences in which one individual (the initiator) moved away from another (the potential follower) and was either followed (a “pull,” Fig. 1 inset, left) or was not and subsequently returned (an “anchor,” Fig. 1). This definition is agnostic to individual intention and motivation. Although any particular movement sequence may or may not reflect a causal relationship between initiator and follower (supplementary text), analyzing aggregate patterns across many sequences nonetheless yields insight into the processes driving collective movement.

Our method is based on finding all minima and maxima in the distance between pairs

of individuals, allowing it to capture pulls and anchors occurring over a range of time scales, from seconds to minutes [fig. S8 (27)]. It also detects simultaneous movement initiations. We

aggregated concurrent pulls and anchors on the same potential follower into “events” (20). We then examined the behavior of potential followers during these events, including whether

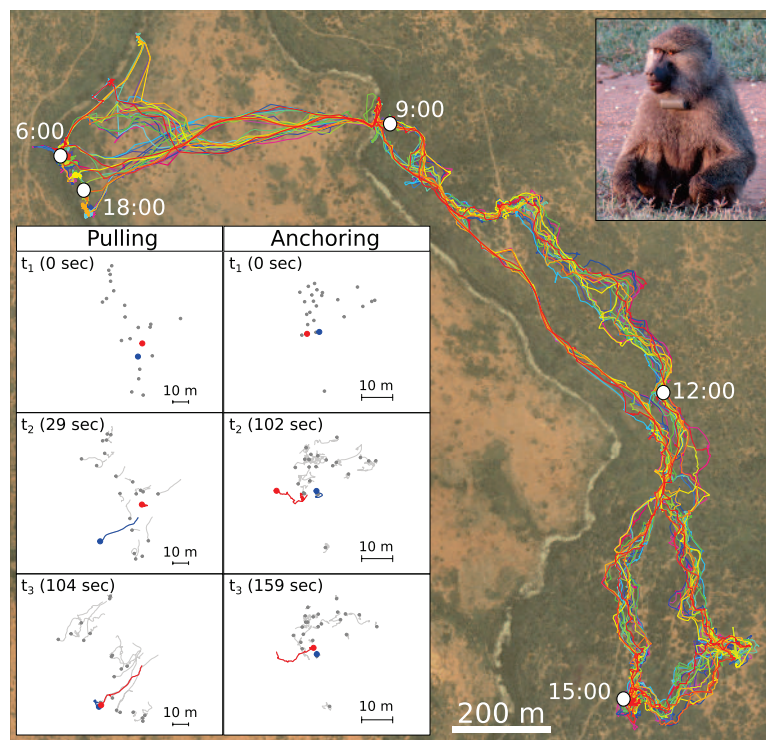


Fig. 1. Extracting pulls and anchors from movement data. Baboon trajectories (25 individuals) during the first day of tracking. (Inset, left) Successful initiation (pull), where the initiator (red) recruits the follower (blue). (Inset, right) Failed initiation (anchor), where the initiator (red) fails to recruit the potential follower (blue). Other individuals’ trajectories are in gray.

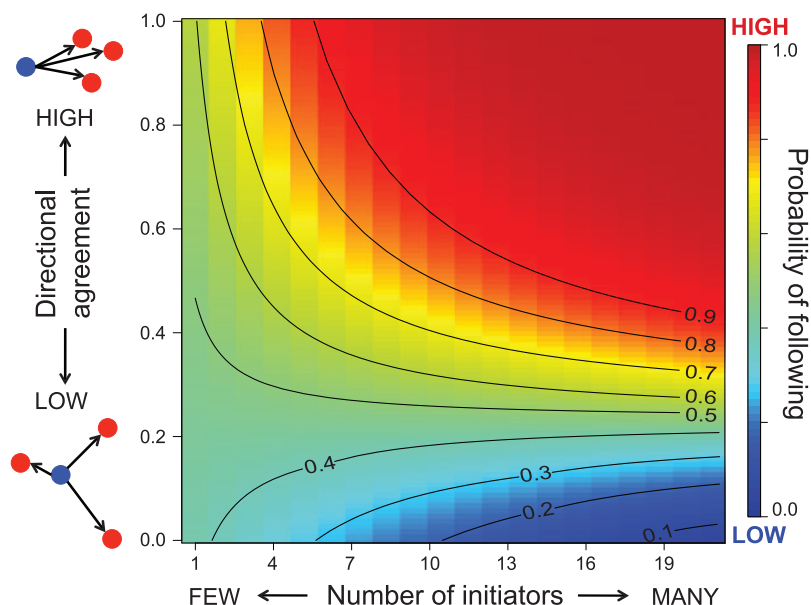


Fig. 2. The probability of following depends on the number of initiators and their directional agreement. Baboons are most likely to follow when there is high agreement among many initiators. When agreement is low, additional initiators do not improve the chances of following and may decrease them. The surface plot shows a GEE fit to the data (table S2).

¹Department of Ecology and Evolutionary Biology, Princeton University, Princeton, NJ, USA. ²Department of Anthropology, University of California, Davis, CA, USA. ³Smithsonian Tropical Research Institute, Panama. ⁴Edward Grey Institute of Field Ornithology, Department of Zoology, University of Oxford, Oxford, UK. ⁵Department of Collective Behaviour, Max Planck Institute for Ornithology, Konstanz, Germany. ⁶Chair of Biodiversity and Collective Behaviour, Department of Biology, University of Konstanz, Konstanz, Germany. *Corresponding author. E-mail: astrand@princeton.edu (A.S.P.); damien.farinne@zoo.ox.ac.uk (D.R.F.); mcrofoot@ucdavis.edu (M.C.C.) †These authors contributed equally to this work.

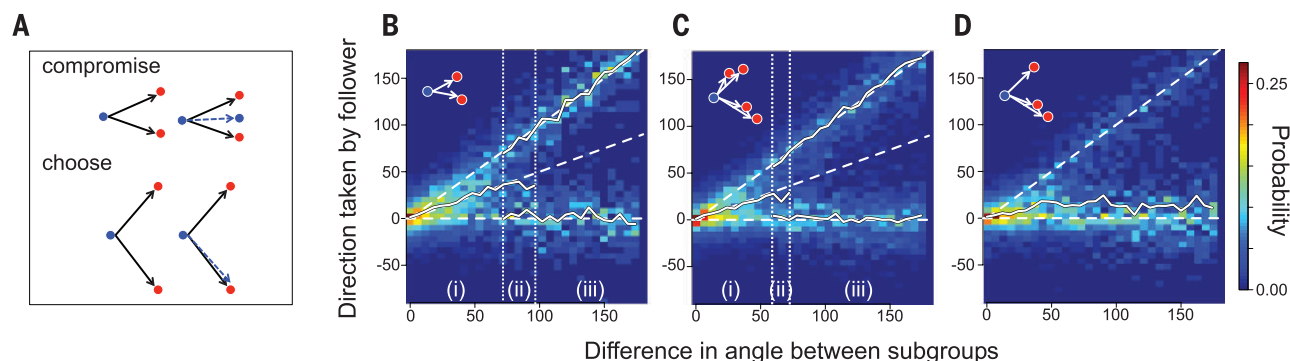


Fig. 3. As predicted by collective movement models (A), as the angle between initiation directions increases, baboon followers exhibit a transition from compromising (moving in the average of the two directions) to choosing one direction over the other. (B to D) Plots show the empirical distribution of follower movement directions as a function of the angle of disagreement between two initiators (B) or two subgroups of initiators (C).

Regions divided by dotted lines are statistically assigned to (i) compromise, (ii) transitional, and (iii) choose (fig. S9). Solid white lines show the median of the directions taken for each mode. Dashed white lines represent the expected direction when compromising (middle line) or choosing (top/bottom lines). When the number of individuals in the clusters differs by 1, followers are more likely to move toward the majority (i.e., along the horizontal line) (D).

they followed any initiators, and if so, in which direction they moved.

Our data show that the probability of following depends on both the number of initiators and their level of directional agreement. To quantify directional agreement among concurrent initiators in an event, we calculated the circular variance (cv) of the unit vectors pointing from the potential follower to each initiator and defined agreement as $1 - cv$. This measure approaches 0 when individuals initiate in opposing directions (low agreement) and 1 when all individuals initiate in the same direction (high agreement). Fitting a binomial generalized estimating equation (GEE) model revealed that a baboon's probability of following depends on an interaction between the number of initiators and their directional agreement (Fig. 2 and table S2). Overall, baboons are most likely to follow when there are many initiators with high agreement. However, when agreement is low, having more concurrent initiators decreases the likelihood that a baboon will follow anyone. This pattern suggests that decisions are delayed when opinions are split.

If social dominance plays a role in determining the outcomes of movement decisions (1), the disproportionate influence of high-ranking animals should be easiest to observe when single individuals make movement initiations (single-initiator events). We found no evidence of this. The dominant male did not have the highest probability of being followed, dominance rank (20) did not correlate with initiation success, and no sex differences existed in initiation success (fig. S1, binomial GLMM: coefficient (male) \pm SE = -0.222 ± 0.159 , $z = -1.402$, $P = 0.161$, initiator and follower fit as random effects), despite males being dominant over females (11). Instead, we found that baboons are more likely to follow initiators who move in a highly directed manner (fig. S2), which is consistent with the findings of a previous study (17).

When multiple members of the troop initiate movement simultaneously, followers must de-

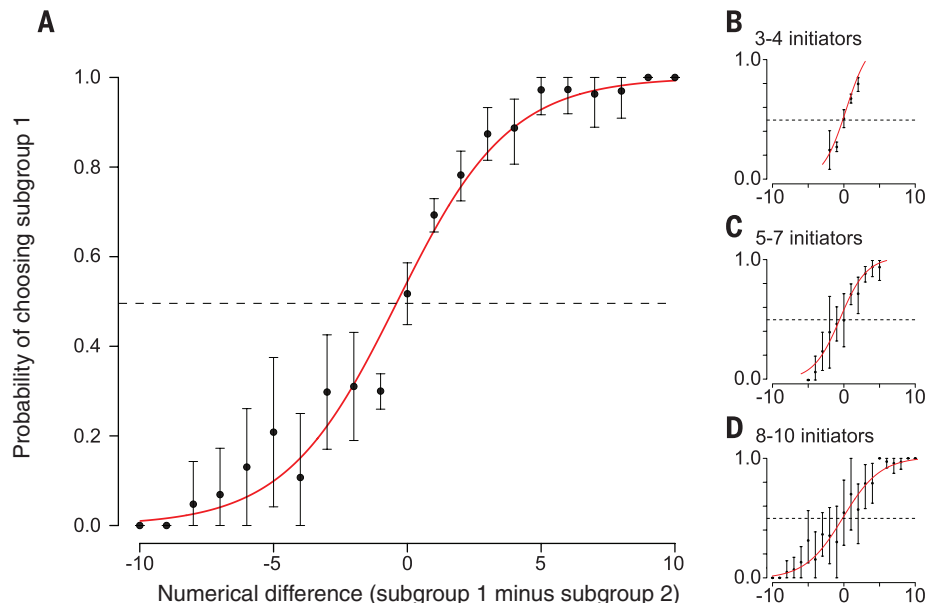


Fig. 4. When initiation directions conflict, followers choose the direction of the largest subgroup of initiators. (A) Empirical data are in black; error bars are 95% confidence intervals estimated by 1000 bootstrapped replications of the data. The red line shows a sigmoidal fit to the data. The tendency to follow the majority is maintained regardless of the total number of initiators (B to D) or whether the troop is moving or stationary (fig. S6).

cide in which direction to move. Theory (22) predicts that, when preferred directions conflict, the type of consensus achieved will depend on the angle between these directions (angle of disagreement, Fig. 3A). When this angle is large, the group travels in one direction or the other ("choose"). Below a critical angle, the same individual rules result in the group moving in the average of preferred directions ("compromise"). Our data reveal that baboon followers exhibit these two predicted regimes. In events with two initiators, followers consistently choose one direction or the other when the angle between the initiators' directions is greater than approximately 90°, but they compromise when the angle falls

below this threshold (Fig. 3B, (20)). The same pattern emerges in events with multiple initiators clustered into two subgroups (Fig. 3C).

When initiators have strongly conflicting directions, how do followers choose which direction to take? When facing a choice between two subgroups of initiators, followers are more likely to move toward the direction of the majority. This tendency grows stronger as the numeric difference between the two subgroups increases (Fig. 4), which is consistent with theoretical (3, 6, 22) and empirical studies (3, 5, 23). Individuals' choices also scale up to group movement. After such conflicts, the troop's travel direction is positively correlated with the direction

associated with successful (but not failed) subgroups of initiators (fig. S4). Thus, failed initiators ultimately move in the direction of the majority (away from their original initiation directions), maintaining cohesion with others.

The failure of high-ranking individuals to dominate movement decisions highlights an important distinction between social status and leadership in wild baboons. Although field-based experiments suggest that dominant individuals, when highly motivated, can shape group movement patterns to their advantage (1), our results provide evidence that the decision-making process driving day-to-day movement patterns in baboons is fundamentally shared. Our study emphasizes the power of using high-resolution GPS tracking data to uncover the interdependencies of animal movements. In conjunction with the rich individual-level data that long-term observational studies provide, these methods open up a new window into the social dynamics of wild animal groups.

REFERENCES AND NOTES

1. A. J. King, C. M. S. Douglas, E. Huchard, N. J. B. Isaac, G. Cowlishaw, *Curr. Biol.* **18**, 1833–1838 (2008).
2. M. Nagy, Z. Akos, D. Biro, T. Vicsek, *Nature* **464**, 890–893 (2010).
3. I. D. Couzin *et al.*, *Science* **334**, 1578–1580 (2011).
4. L. Conradt, C. List, *Philos. Trans. R. Soc. London Ser. B* **364**, 719–742 (2009).
5. D. J. T. Sumpter, J. Krause, R. James, I. D. Couzin, A. J. W. Ward, *Curr. Biol.* **18**, 1773–1777 (2008).
6. L. Conradt, T. J. Roper, *Trends Ecol. Evol.* **20**, 449–456 (2005).
7. A. J. King, G. Cowlishaw, *Commun. Integr. Biol.* **2**, 147–150 (2009).
8. R. W. Byrne, in *On the Move*, S. Boinski, P. A. Garber, Eds. (Univ. of Chicago Press, Chicago, 2000), p. 501.
9. A. J. King, C. Sueur, *Int. J. Primatol.* **32**, 1245–1267 (2011).
10. A. J. King, D. P. Johnson, M. Van Vugt, *Curr. Biol.* **19**, R911–R916 (2009).
11. D. L. Cheney, R. M. Seyfarth, *Baboon Metaphysics* (Univ. of Chicago Press, Chicago, 2008).
12. J. B. Silk, *Science* **317**, 1347–1351 (2007).
13. R. M. Sapolsky, *Science* **308**, 648–652 (2005).
14. S. E. Johnson, J. Bock, *Hum. Nat.* **15**, 45–62 (2004).
15. J. Altmann, *Baboon Mothers and Infants* (Univ. of Chicago Press, Chicago, 1980).
16. A. J. King, G. Cowlishaw, *Anim. Behav.* **78**, 1381–1387 (2009).
17. A. J. King, C. Sueur, E. Huchard, G. Cowlishaw, *Anim. Behav.* **82**, 1337–1345 (2011).
18. S. Stueckle, D. Zinner, *Anim. Behav.* **75**, 1995–2004 (2008).
19. S. A. Altmann, *Foraging for Survival: Yearling Baboons in Africa* (Univ. of Chicago Press, Chicago, 1998).
20. Materials and methods are available as supplementary materials on Science Online.
21. O. Petit, J. Gautrais, J.-B. Leca, G. Theraulaz, J.-L. Deneubourg, *Proc. Biol. Sci.* **276**, 3495–3503 (2009).
22. I. D. Couzin, J. Krause, N. R. Franks, S. A. Levin, *Nature* **433**, 513–516 (2005).
23. C. Sueur, J.-L. Deneubourg, O. Petit, *Behav. Ecol. Sociobiol.* **64**, 1875–1885 (2010).

ACKNOWLEDGMENTS

We thank the Kenya National Science and Technology Council, Kenyan Wildlife Service, and Mpala Research Centre for permission to conduct research. All procedures received Institutional Animal Care and Use Committee approval (2012.0601.2015). We thank M. Wikelski, E. Bermingham, D. Rubenstein, and M. Kinnaird for logistical support; R. Kays, S. Murray, M. Mutinda, R. Lessnau, S. Alavi, J. Nairobi, F. Kuemmeth, W. Heidrich, and I. Brugere for assistance; and T. Berger-Wolf, J. Silk, J. Fischer, B. Sheldon, L. Apelin, D. Pappano, M. Grobis, B. Rosenthal, A. Hein, B. Ziebart, L. Polansky, and J. Li for feedback. We acknowledge funding from NSF (grant EAGER-IOS-1250895), the Max Planck Institute for Ornithology, the Smithsonian Tropical Research Institute, and

Princeton University. A.S.-P. and D.R.F. received additional support from NIH (grant T32HG003284), NSF (a Graduate Research Fellowship to A.S.-P.), and the Biotechnology and Biological Sciences Research Council (grant BB/L006081/1 to B. C. Sheldon). I.D.C. acknowledges support from NSF (grants PHY-0848755, IOS-1355061, and EAGER-IOS-1251585), the Office of Naval Research (grants N00014-09-1-1074 and N00014-14-1-0635), the Army Research Office (grants W911NG-11-1-0385 and W911NF-14-1-0431), and the Human Frontier Science Program (grant RGP0065/2012). Data are deposited at www.datarepository.movebank.org/ (doi.org/10.5441/001/1.kn0816jn).

SUPPLEMENTARY MATERIALS

www.sciencemag.org/content/348/6241/1358/suppl/DC1
Materials and Methods
Supplementary Text
Figs. S1 to S9
Table S1
References (24–30)
Movies S1 and S2

16 December 2014; accepted 20 April 2015
10.1126/science.aaa5099

SIGNAL TRANSDUCTION

Structural basis for nucleotide exchange in heterotrimeric G proteins

Ron O. Dror,^{1,*,†} Thomas J. Mildorf,^{1,*} Daniel Hilger,^{2,*} Aashish Manglik,² David W. Borhani,¹ Daniel H. Arlow,^{1,§} Ansgar Philippssen,¹ Nicolas Villanueva,³ Zhongyu Yang,⁴ Michael T. Lerch,⁴ Wayne L. Hubbell,⁴ Brian K. Kobilka,² Roger K. Sunahara,^{3||} David E. Shaw^{1,5,†}

G protein-coupled receptors (GPCRs) relay diverse extracellular signals into cells by catalyzing nucleotide release from heterotrimeric G proteins, but the mechanism underlying this quintessential molecular signaling event has remained unclear. Here we use atomic-level simulations to elucidate the nucleotide-release mechanism. We find that the G protein α subunit Ras and helical domains—previously observed to separate widely upon receptor binding to expose the nucleotide-binding site—separate spontaneously and frequently even in the absence of a receptor. Domain separation is necessary but not sufficient for rapid nucleotide release. Rather, receptors catalyze nucleotide release by favoring an internal structural rearrangement of the Ras domain that weakens its nucleotide affinity. We use double electron-electron resonance spectroscopy and protein engineering to confirm predictions of our computationally determined mechanism.

G protein-coupled receptors (GPCRs), which represent the largest class of drug targets, trigger cellular responses to external stimuli primarily by activating heterotrimeric G proteins: An activated GPCR, upon binding an inactive, guanosine diphosphate (GDP)-bound G protein, dramatically accelerates GDP release, thus allowing guanosine triphosphate (GTP) to bind spontaneously to the vacated nucleotide-binding site (1, 2). This nucleotide exchange initiates G protein-mediated intracellular signaling. Despite breakthroughs in GPCR structure determination (3–5), key aspects of the

molecular mechanism by which GPCRs accelerate GDP release remain unresolved.

Heterotrimeric G proteins undergo a dramatic conformational change upon binding activated GPCRs (Fig. 1, A and B). Double electron-electron resonance (DEER) spectroscopy has demonstrated that the Ras and helical domains of the G protein α subunit ($G\alpha$), which tightly sandwich the nucleotide in all nucleotide-bound G protein crystal structures, separate by tens of angstroms upon GPCR binding and GDP release (6). A crystal structure of a GPCR-G protein complex (4), and accompanying density-exchange and electron microscopy data (7, 8), confirmed this dramatic domain separation.

These observations have raised several unresolved questions (4, 9). What is the role of domain separation in GDP release? Does a GPCR catalyze GDP release by forcing the domains to separate, or does the GPCR force out GDP, with the absence of GDP leading to subsequent domain separation? More generally, what is the structural mechanism by which a GPCR brings about GDP release?

To address these questions, we performed atomic-level molecular dynamics (MD) simulations of heterotrimeric G proteins with and without bound GPCRs. We initiated simulations from crystal structures of nucleotide-bound G protein heterotrimers [in particular, G_i (10) and a

¹D. E. Shaw Research, New York, NY 10036, USA.

²Department of Molecular and Cellular Physiology, Stanford University School of Medicine, Stanford, CA 94305, USA.

³Department of Pharmacology, University of Michigan Medical School, Ann Arbor, MI 48109, USA. ⁴Jules Stein Eye Institute and Department of Chemistry and Biochemistry, University of California, Los Angeles, CA 90095, USA.

⁵Department of Biochemistry and Molecular Biophysics, Columbia University, New York, NY 10032, USA.

*These authors contributed equally to this work. †Corresponding author. E-mail: ron.dror@deshawresearch.com (R.O.D.); david.shaw@deshawresearch.com (D.E.S.)

‡Present address: Department of Computer Science, Department of Molecular and Cellular Physiology, and Institute for Computational and Mathematical Engineering, Stanford University, Stanford, CA 94305, USA.

§Present address: Biophysics Graduate Group, University of California, Berkeley, CA 94720, USA. ||Present address: Department of Pharmacology, University of California, San Diego, La Jolla, CA 92093, USA.

chimeric G_t (11)], including some in which we omitted the cocrystallized nucleotide, GDP (12). We also initiated simulations from the only crystal structure of a GPCR–G protein complex [β_2 -adrenergic receptor (β_2 AR)– G_s] (4), which is also the only structure of a nucleotide-free heterotrimeric G protein. The 66 simulations we performed, of lengths up to 50 μ s each, are listed in table S1.

In simulations of GDP-bound G protein heterotrimers, the $G\alpha$ Ras and helical domains—which are tightly apposed in all nucleotide-bound crystal structures—unexpectedly and dramatically separated from one another (Fig. 1C and figs. S1 and S2). These domain-separated conformations recall the extreme open conformation of the nucleotide-free β_2 AR– G_s crystal structure (4):

In both cases, the helical domain rotated as a rigid body (fig. S3) from its nucleotide-bound crystallographic conformation about a loose hinge located on the distal (away from GDP) side of helix αF (fig. S4). In GDP-bound simulations, the helical domain fluctuated between tightly apposed and separated positions. The maximal rotation observed, $\sim 90^\circ$, was less extreme

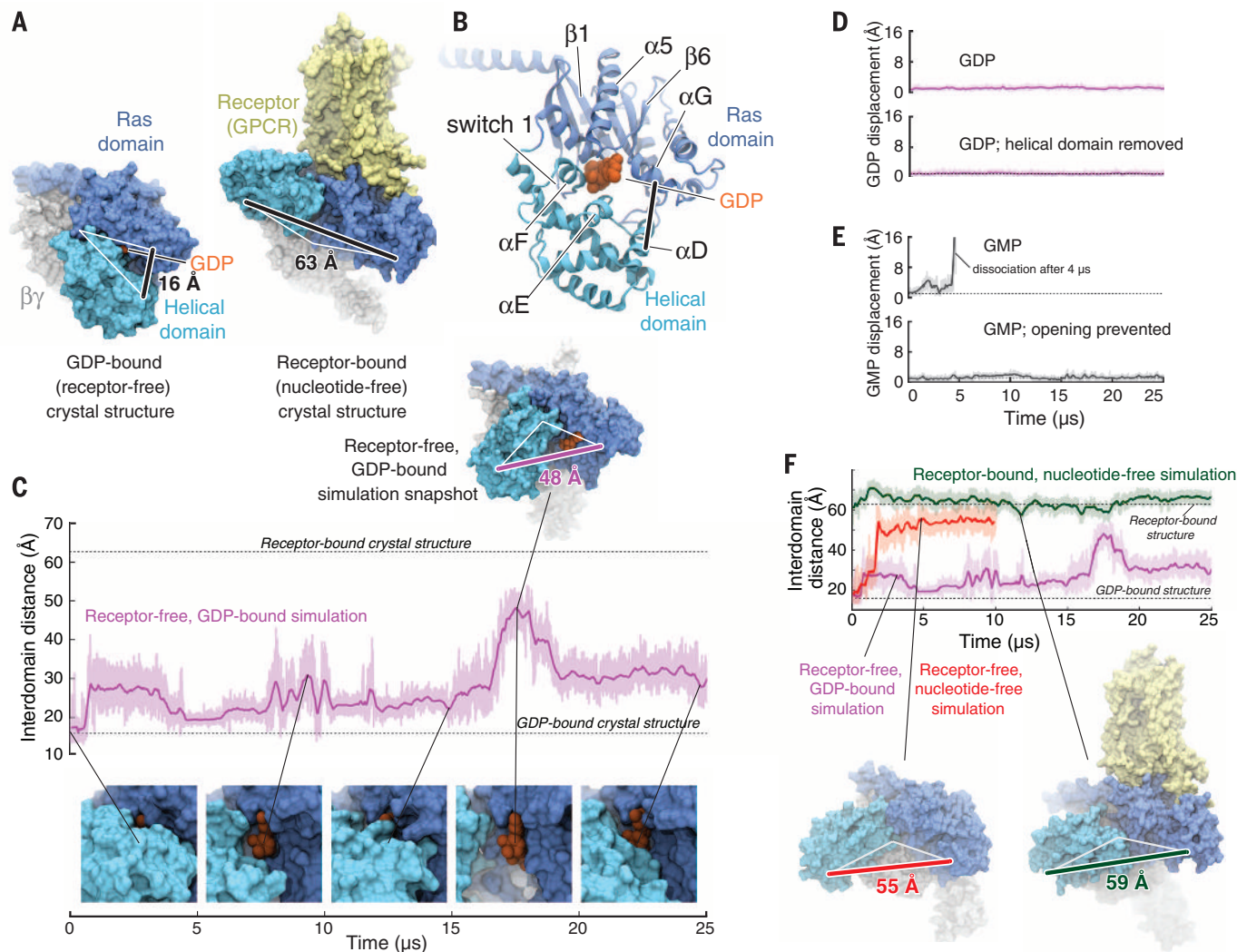


Fig. 1. The Ras and helical domains of the G protein α subunit separate spontaneously and frequently when GDP is bound, even in the absence of a receptor. (A) The Ras and helical domains are tightly apposed in all nucleotide-bound G protein crystal structures, enveloping the nucleotide [left: GDP-bound G_t heterotrimer; Protein Data Bank (PDB) entry 1GOT]. Yet they are dramatically separated in the receptor-bound, nucleotide-free structure [right: β_2 -adrenergic receptor– G_s heterotrimer (β_2 AR– G_s) complex; PDB entry 3SN6]. Orange, GDP; blue, Ras domain; light blue, helical domain; gray, $G\beta\gamma$; yellow, receptor. The degree of domain separation is represented by a thick black line connecting Ala¹³⁴ and Glu²⁷² in $G\alpha_t$ or the corresponding Ala¹⁶¹ and Glu²⁹⁹ in $G\alpha_s$, with both ends connected by white lines to a pivot point near Thr¹⁶⁶ ($G\alpha_t$) or Ser¹⁹³ ($G\alpha_s$). (B) Key structural motifs of the α subunit, illustrated using the GDP-bound G_t structure. (C) Spontaneous domain separation provides an exit pathway for GDP. In simulations of receptor-free, GDP-bound G_t , the Ala¹³⁴-to-Glu²⁷² distance varies substantially as the domains fluctuate between apposed and separated conformations. Raw (light purple) and smoothed (250-ns moving average; dark purple) data are shown. Representative molecular simulation snapshots (top: overview; bottom: nucleotide-binding site) display

varying degrees of GDP exposure. Data are from simulation 2 (table S1). (D) Domain separation is not sufficient for rapid nucleotide release. GDP remains tightly bound to receptor-free G_t (top), even with the helical domain removed (bottom; traces show displacement of the centroid of the nucleotide non-hydrogen atoms relative to the crystal structure). Data are from simulations 2 and 33. (E) Domain separation is necessary for rapid nucleotide release. GMP dissociates spontaneously from receptor-free G_t (top) but remains bound when the interdomain distance is artificially restrained to prevent domain separation (bottom). Data are from simulations 16 and 31. (F) Domain separation is greater in the absence of a nucleotide. In simulations initiated from the receptor-free, GDP-bound G_t crystal structure, but with the GDP removed, the Ras and helical domains exhibited extensive and prolonged separation (red trace; left-hand snapshot). In simulations of the β_2 AR– G_s complex, also nucleotide-free, the helical domain remained widely separated from the Ras domain, although it typically moved away from the membrane toward the β -propeller of $G\beta\gamma$ (green trace; right-hand snapshot). GDP-bound G_t simulation data from (C) are replicated for reference (purple trace). See the supplementary materials for details on structural renderings. Data are from simulations 2, 14, and 22.

than the nearly 150° rotation of the β_2 AR- G_s structure. Nonetheless, the rotation observed in simulation, and the accompanying domain separation of up to ~30 Å (Fig. 1C), dramatically disrupted the interdomain nucleotide-binding site. Such domain separation is particularly notable because it occurred with GDP bound and in the absence of a receptor. Smaller interdomain motions have previously been observed in shorter MD simulations, including some with GDP bound (13–17).

Despite this substantial domain separation, GDP remained bound throughout our multimicrosecond simulations (Fig. 1D and fig. S5), held in place by persistent, tight contacts with the Ras domain

(fig. S4); the few contacts with the helical domain appeared to be weaker, occasionally breaking and reforming. GDP also remained bound to the Ras domain in a simulation with the entire helical domain deleted (Fig. 1D and fig. S5), in accord with the experimental finding that the Ras domain alone is sufficient to bind nucleotides (18).

The $G\alpha$ domain separation observed in simulations cleared an exit pathway for the bound nucleotide, eliminating steric barriers to its escape (fig. S6). Guanosine monophosphate (GMP), which forms fewer contacts with the Ras domain and has a G protein-binding affinity five to six orders of magnitude weaker than that of GDP (7), consistently

dissociated within microseconds in simulations (Fig. 1E and fig. S5). GMP dissociated only when the domains had separated (fig. S7), however, and when we prevented such separation by restraining the interdomain distance, GMP remained bound (Fig. 1E and fig. S5). Loosening the restraint to permit partial domain separation of ~25 Å was sufficient to allow GMP dissociation (fig. S5).

Lack of a bound nucleotide further promoted domain separation. In nucleotide-free simulations—still initiated from the tightly closed, GDP-bound conformation in the absence of a receptor—domain separation was more dramatic and persistent (Fig. 1F and fig. S1), approaching the level observed in the β_2 AR- G_s structure. This increased separation appeared to be due to the loss of nucleotide contacts with residues in and near the helical domain α F helix. α F generally remained in contact with the Ras domain α 1 helix when GDP was bound but readily separated from α 1 in nucleotide-free simulations, adopting much the same position as in the β_2 AR- G_s structure (fig. S8).

In simulations initiated from the β_2 AR- G_s structure, which also lacks a bound nucleotide, the domains consistently remained well separated (Fig. 1F and fig. S1). The helical domain adopted conformations similar to those observed in receptor-free, nucleotide-free simulations.

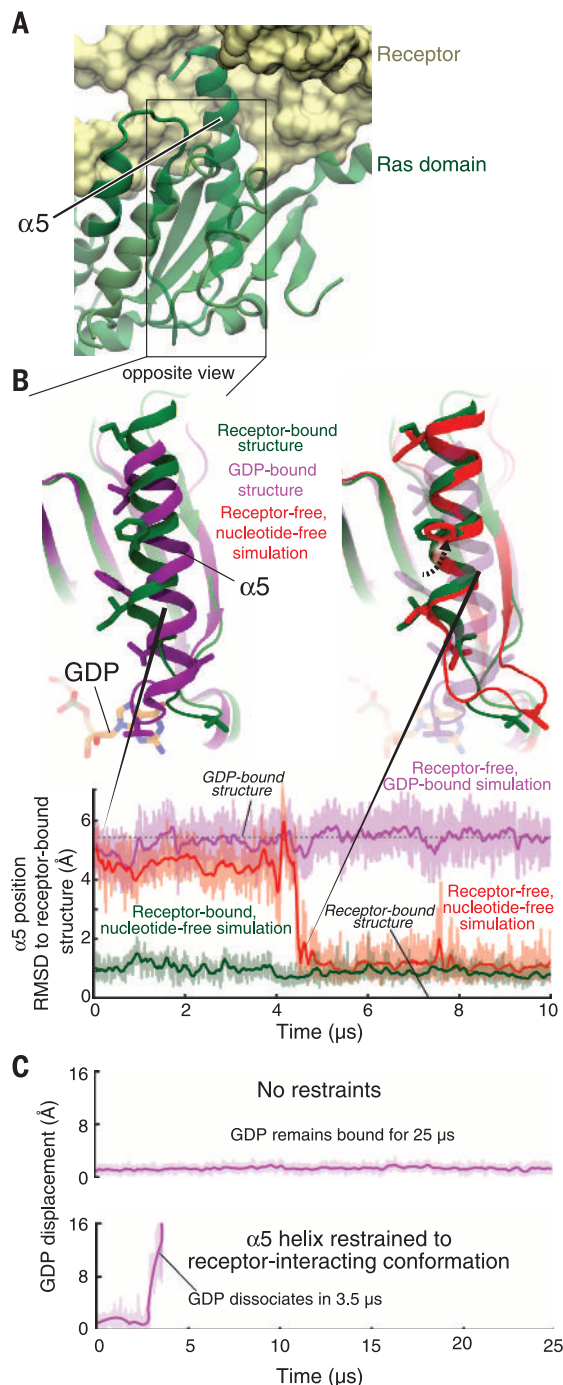
Our nucleotide-bound G protein simulations indicate that a certain degree of $G\alpha$ domain separation is necessary to clear an exit pathway for nucleotide release. Adequate separation occurs frequently and spontaneously even in the receptor-free, GDP-bound state, but separation alone is not sufficient for rapid GDP release. Rather, a weakening of nucleotide-Ras domain contacts also appears necessary. These observations suggest that an activated receptor could accelerate nucleotide release simply by favoring conformational changes in the Ras domain that weaken its interactions with GDP; the receptor need not promote further domain separation. Prior studies have indicated that binding of an activated receptor promotes Ras domain conformational changes, particularly in the C-terminal α 5 helix but possibly also near the $G\alpha$ N terminus (4, 7, 19–22).

To investigate the nature of such conformational changes and how they might affect nucleotide affinity, we compared our simulations of receptor-free G proteins with and without bound GDP, focusing on those structural elements known to interact with receptors. Our guiding thesis was that a conformation that favors GDP release should itself be favored by the absence of GDP; that is, if affinity for GDP is weaker when the G protein adopts a particular conformation than when it does not, then removal of GDP will increase the equilibrium population of that conformation (fig. S9).

Of the G protein structural elements that contact the receptor in the β_2 AR- G_s crystal structure, only the Ras domain α 5 helix displayed clear conformational differences between simulations with and without bound GDP (fig. S10). In the absence of GDP, α 5 often moved away from the

Fig. 2. Receptor-induced displacement of the $G\alpha$ C-terminal α 5 helix disrupts key GDP contacts, thereby promoting nucleotide release.

(A) In the receptor-bound, nucleotide-free crystal structure (PDB entry 3SN6), α 5 docks into the receptor. (B) (Top, left) Superimposition of receptor-free, GDP-bound (PDB entry 1GOT; purple) and receptor-bound, nucleotide-free (PDB entry 3SN6; green) crystal structures shows the displacement of α 5, relative to the rest of the Ras domain, that occurs when a G protein binds to an activated receptor. (Top, right) In a simulation initialized from a receptor-free, GDP-bound G_i structure but with GDP removed (red), α 5 spontaneously rotated 60° and translated 5 Å, adopting a position distal from the nucleotide-binding site that closely matched that of the β_2 AR- G_s complex (green). Several side chains in the α 5 helix and α 5- β 6 loop are shown to facilitate comparison between structures. (Bottom) The position of α 5 in this simulation (red) changed abruptly at ~4.5 μ s to match that of the β_2 AR- G_s complex (green). Data are from simulations 5, 12, and 22 (table S1). RMSD, root mean square deviation. (C) Forcing α 5 into the distal conformation accelerates nucleotide release in simulation. TAMM simulations allow observation of GDP release on computationally accessible time scales, but only when α 5 is restrained to the distal conformation (i.e., the conformation observed in the β_2 AR- G_s complex). Receptor-free, GDP-bound G_i was simulated without (top) or with (bottom) restraints on α 5 (see supplementary materials). GDP displacement is measured as in Fig. 1. Data are from simulations 55 and 56.



nucleotide-binding site (~ 5 Å translation along and $\sim 60^\circ$ rotation around the helical axis), adopting a conformation closely matching that observed in the β_2 AR- G_s structure (4), as well as in a rhodopsin- G_i model (19) (Fig. 2, A and B, and figs. S10 and S11). The shift to this distal $\alpha 5$ conformation was facilitated by the increased mobility of the adjacent $\beta 6$ - $\alpha 5$ loop in the absence of a nucleotide; this loop directly contacts bound GDP and shifts position in its absence (fig. S12). In receptor-free simulations, the distal $\alpha 5$ conformation was ~ 1000 times more prevalent in the absence of GDP than in its presence (fig. S10).

Our simulations thus indicate that a repositioning of $\alpha 5$ reduces the affinity of bound GDP. This $\alpha 5$ motion shifts the $\beta 6$ - $\alpha 5$ loop away from the guanine ring of GDP, thereby weakening its contacts with the Ras domain. Previous computational and experimental work has shown that the distal $\alpha 5$ conformation is favored by the activated receptor (19); the β_2 AR- G_s crystal structure shows that only when $\alpha 5$ is distally positioned can it dock fully into the receptor (4) (fig. S13). The distal $\alpha 5$ conformation, adopted only rarely in our simulations of a receptor-free, GDP-bound G protein (fig. S10), apparently becomes the dominant conformation once the G protein binds an activated receptor (19), thus facilitating GDP dissociation.

Mimicking the effect of the receptor by restraining the $\alpha 5$ helix to the distal conformation substantially accelerated GDP release in temperature-accelerated MD (TAMD) simulations (Fig. 2C and fig. S14). Release of GDP led to increased domain separation, but the receptor-mimicking restraints were not observed to increase domain separation before GDP release, suggesting that a receptor accelerates nucleotide release primarily by weakening the Ras domain's nucleotide affinity rather than by favoring domain separation.

Our simulations thus suggest the following nucleotide-exchange mechanism. The Ras and helical domains of GDP-bound $G\alpha$ separate spontaneously, even in the absence of a receptor (Fig. 3). Such separation is necessary but not sufficient for rapid GDP release. Binding of an activated receptor favors conformational changes within the Ras domain (rotation and translation of the $\alpha 5$ helix away from the nucleotide-binding site, leading to rearrangement of the adjacent $\beta 6$ - $\alpha 5$ loop) that weaken its interactions with GDP, thereby enabling GDP to unbind when the helical and Ras domains spontaneously separate. Because GDP helps stabilize closed domain conformations, nucleotide dissociation shifts the equilibrium toward conformations with the two domains widely separated.

Our computationally determined mechanism predicts that the Ras and helical domains separate spontaneously and frequently, even with GDP bound and in the absence of a receptor. Although no crystal structure of a nucleotide-bound G protein has captured a domain-separated conformation—perhaps because such conformations are less populated and less amenable to crystallization than one with the domains in

tight contact—the DEER spectroscopy study that originally demonstrated domain separation upon receptor binding also noted a small peak at large distances in GDP-bound G_i interdomain distance distributions [figure 1 of (6)].

To better characterize this peak, we performed improved DEER experiments by using a G_i construct with no inserted purification tags (to avoid altering protein dynamics), substantially longer

dipolar evolution times (to increase confidence in the measured distance distribution at large distances), and an experimental protocol that delivers an improved signal-to-noise ratio (12). We also performed similar experiments on G_s . In both GDP-bound G_i and GDP-bound G_s , we found clear evidence for a minority population exhibiting substantial domain separation (Fig. 4A and fig. S15). The results of a recently

Fig. 3. Proposed mechanism of receptor-catalyzed nucleotide release. (Left) The Ras and helical domains (Ras and HD) separate frequently, even in the absence of a receptor, but such separation does not usually lead to GDP release. This rapid (relative to overall GDP release) equilibrium favors the closed conformation (top). (Middle) Binding of an activated receptor (R^*) favors a Ras domain conformational change—displacement of $\alpha 5$ away from GDP—that weakens interactions between GDP and the Ras domain, allowing GDP to escape when the $G\alpha$ domains happen to spontaneously separate (bottom). (Right) Loss of GDP shifts the equilibrium toward $G\alpha$ conformations with widely separated domains (bottom).

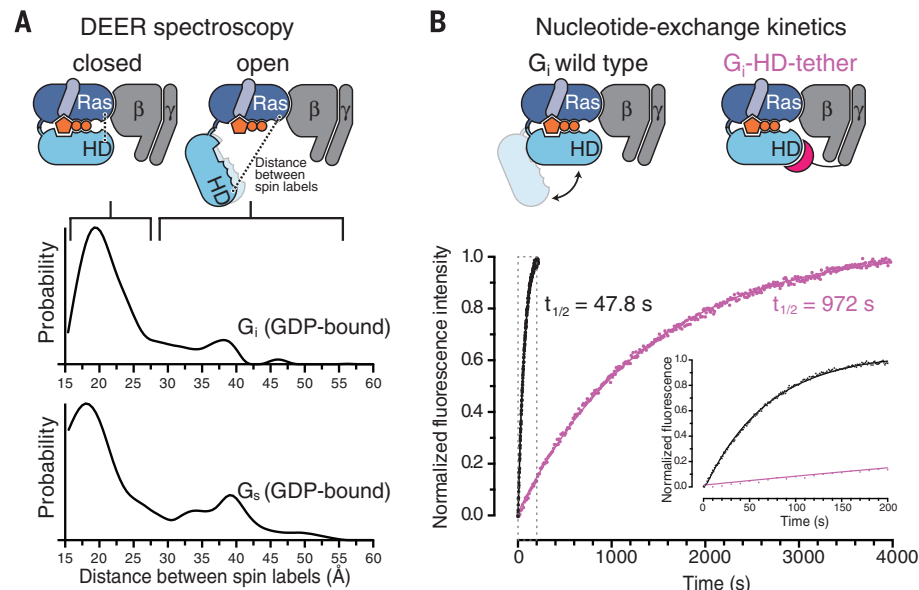
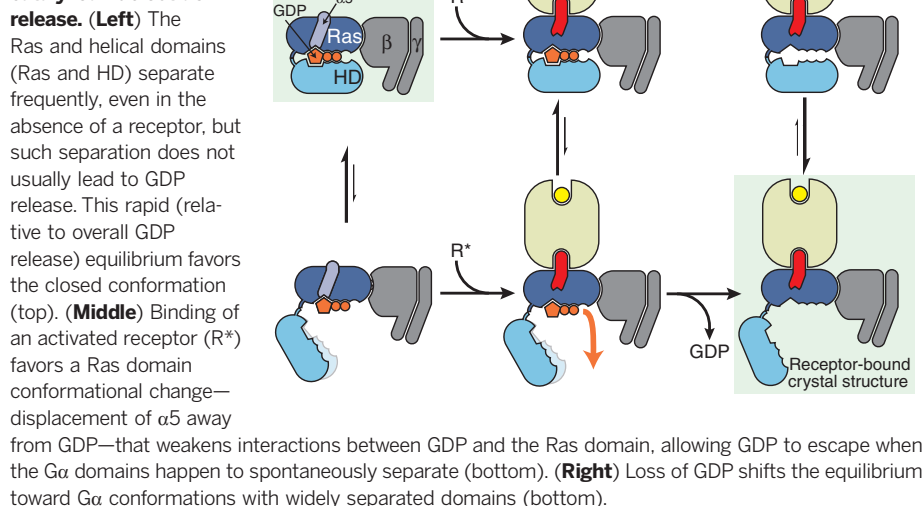


Fig. 4. Experimental validation of spontaneous $G\alpha$ domain separation in GDP-bound heterotrimeric G proteins and its role in nucleotide exchange. (A) DEER distance distributions measured between spin labels attached to the Ras and helical domains of G_i (Glu²³⁸ and Arg⁹⁰) and G_s (Asn²⁶¹ and Asn¹¹²) show multiple distance peaks, consistent with an equilibrium between closed and open conformations of the α subunit in the presence of GDP, despite the absence of an activated receptor. These distance distributions extend to much larger values than would be expected if the G proteins maintained their crystallographic nucleotide-bound conformations (fig. S15). (B) Domain separation affects the basal GDP release rate. The G_i -HD-tether construct (fig. S16), designed to restrict domain separation, exchanges nucleotides 20 times more slowly than the G_i wild type, under conditions where GDP release is rate-limiting. GDP release was monitored by BODIPY-GTP γ S binding kinetics, shown for the G_i wild type (black) and G_i -HD-tether (purple). The inset corresponds to the gray dashed box.

published DEER study on GDP-bound $G\alpha_1$ in the absence of the $\beta\gamma$ subunit also suggest a minority population with separated domains (23).

Our simulations suggest that the minority domain-separated population in GDP-bound G proteins arises due to rapid fluctuations between closed and open conformations and that this spontaneous opening plays an essential role in nucleotide exchange. This implies that constraining domain opening would substantially slow basal nucleotide exchange and, in particular, GDP release. To test this prediction, we engineered a G_i variant to restrict domain opening. In this construct, the N terminus of the γ subunit was fused to a peptide fragment designed to bind the helical domain without impinging on either the nucleotide-binding site or the Ras domain (fig. S16). Binding kinetics measured by fluorescence quenching showed that this helical domain tether slowed basal nucleotide exchange by a factor of 20, under conditions in which GDP release is rate-limiting (Fig. 4B).

Our nucleotide-release mechanism is consistent with earlier mutagenesis studies. Point mutations to the Ras domain $\beta 6$ - $\alpha 5$ loop (24) accelerate nucleotide exchange in the absence of a receptor substantially more than mutations that weaken contacts between the Ras and helical domains (25), suggesting that weakening interactions between $\beta 6$ - $\alpha 5$ and the GDP guanine ring facilitates nucleotide release to a greater extent than does increasing domain separation. Mutations to $\alpha 5$ that energetically favor the distal conformation increase both receptor-catalyzed and basal nucleotide-exchange rates, whereas those disfavoring that conformation decrease nucleotide-exchange rates (21) (fig. S10D).

Several caveats are in order. First, because we did not simulate the complete process of receptor-G protein association, we have not determined the sequence of steps by which a receptor couples to a G protein, nor have we addressed the question of whether a G protein might associate with a receptor before receptor activation (26–28). Second, although our simulations are orders of magnitude longer than previous atomistic G protein simulations, they still lack sufficient length, and perhaps sufficient accuracy, to reliably determine equilibrium populations of the various conformations. However, our simulations strongly imply the existence of certain conformations and dynamical interchange among them. We cannot rule out the possibility that additional conformational changes to the G protein would manifest themselves on longer time scales. Thus, the GPCR might also induce GDP release, in part through other mechanisms, such as displacement of the $\beta 1$ strand of $G\alpha$ (7). Third, because crystal structures of nucleotide-bound and receptor-bound heterotrimers are not available for the same G protein, our analysis combines data from different G proteins, under the common assumption that their high level of structural homology implies similar functional mechanisms (1, 2).

Why might heterotrimeric G proteins have evolved to fluctuate spontaneously between open

and closed conformations? Tight apposition of the Ras and helical domains appears to be essential for efficient hydrolysis of GTP to GDP (29). In the closed conformation, the helical domain plays a role similar to that of the GTPase activating proteins (GAPs) required by small G proteins—which contain only a Ras domain—for efficient catalysis (18). Conversely, our results suggest that rapid GDP release requires an open conformation. Spontaneous fluctuation of the helical domain position thus provides an elegant solution to the conflicting needs of catalysis and nucleotide release.

REFERENCES AND NOTES

- W. M. Oldham, H. E. Hamm, *Nat. Rev. Mol. Cell Biol.* **9**, 60–71 (2008).
- S. R. Sprang, *Annu. Rev. Biochem.* **66**, 639–678 (1997).
- D. M. Rosenbaum, S. G. F. Rasmussen, B. K. Kobilka, *Nature* **459**, 356–363 (2009).
- S. G. F. Rasmussen et al., *Nature* **477**, 549–555 (2011).
- A. J. Venkatakrishnan et al., *Nature* **494**, 185–194 (2013).
- N. Van Eps et al., *Proc. Natl. Acad. Sci. U.S.A.* **108**, 9420–9424 (2011).
- K. Y. Chung et al., *Nature* **477**, 611–615 (2011).
- G. H. Westfield et al., *Proc. Natl. Acad. Sci. U.S.A.* **108**, 16086–16091 (2011).
- H. G. Dohlman, J. C. Jones, *Sci. Signal.* **5**, re2 (2012).
- M. A. Wall et al., *Cell* **83**, 1047–1058 (1995).
- D. G. Lambright et al., *Nature* **379**, 311–319 (1996).
- Materials and methods are available as supplementary materials on Science Online.
- L. V. Mello, D. M. van Aalten, J. B. Findlay, *Biochemistry* **37**, 3137–3142 (1998).
- M. A. Ceruso, X. Periole, H. Weinstein, *J. Mol. Biol.* **338**, 469–481 (2004).
- K. Khafizov, G. Lattanzi, P. Carloni, *Proteins* **75**, 919–930 (2009).
- M. Louet, D. Perahia, J. Martinez, N. Floquet, *J. Mol. Biol.* **411**, 298–312 (2011).
- J. C. Jones, A. M. Jones, B. R. Temple, H. G. Dohlman, *Proc. Natl. Acad. Sci. U.S.A.* **109**, 7275–7279 (2012).
- D. W. Markby, R. Onrust, H. R. Bourne, *Science* **262**, 1895–1901 (1993).
- N. S. Alexander et al., *Nat. Struct. Mol. Biol.* **21**, 56–63 (2014).
- R. Onrust et al., *Science* **275**, 381–384 (1997).
- E. P. Marin, A. G. Krishna, T. P. Sakmar, *J. Biol. Chem.* **276**, 27400–27405 (2001).

- W. M. Oldham, N. Van Eps, A. M. Preininger, W. L. Hubbell, H. E. Hamm, *Nat. Struct. Mol. Biol.* **13**, 772–777 (2006).
- N. Van Eps, C. J. Thomas, W. L. Hubbell, S. R. Sprang, *Proc. Natl. Acad. Sci. U.S.A.* **112**, 1404–1409 (2015).
- T. Iiri, P. Herzmark, J. M. Nakamoto, C. van Dop, H. R. Bourne, *Nature* **371**, 164–168 (1994).
- E. P. Marin et al., *J. Biol. Chem.* **276**, 23873–23880 (2001).
- R. Herrmann, M. Heck, P. Henklein, K. P. Hofmann, O. P. Ernst, *J. Biol. Chem.* **281**, 30234–30241 (2006).
- P. Scheerer et al., *Proc. Natl. Acad. Sci. U.S.A.* **106**, 10660–10665 (2009).
- M. Elgeti et al., *J. Am. Chem. Soc.* **135**, 12305–12312 (2013).
- T. Shnerb, N. Lin, A. Shurki, *Biochemistry* **46**, 10875–10885 (2007).

ACKNOWLEDGMENTS

We thank A. Pan for assistance with TAM, K. Palmo for help with force field parameterization, J. Valcourt and H. Green for advice on figures, and M. Kirk for editorial assistance. Portions of this work were funded by NIH grants R01GM083118 (B.K.K. and R.K.S.) and R01EY05216 (W.L.H.), the Jules Stein Professor Endowment (W.L.H.), National Eye Institute Core Grant P30EY00331 (W.L.H.), and a Research to Prevent Blindness unrestricted grant (to the Jules Stein Eye Institute). D.H. was supported by the German Academic Exchange Service (DAAD). Author contributions: R.O.D. conceived this study and, with D.E.S., oversaw MD simulations and analysis. R.O.D., T.J.M., and D.H.A. designed MD simulations. T.J.M. performed MD simulations and, with D.W.B., modeled proteins based on crystal structures. T.J.M. analyzed MD simulations, with guidance from R.O.D. T.J.M. and A.P. performed molecular visualization. D.H. developed a minimal cysteine construct for G_s , prepared spin-labeled protein, and assisted Z.Y. and M.T.L. in obtaining and analyzing DEER data. A.M. and D.H. designed the HD-tether construct, and A.M. performed the kinetics experiments. W.L.H. and B.K.K. supervised experimental work. R.O.D., T.J.M., N.V., and R.K.S. interpreted and synthesized data. R.O.D., T.J.M., D.W.B., and D.E.S. wrote the manuscript, with input from D.H., A.M., B.K.K., and R.K.S. R.O.D. and D.E.S. supervised the overall research.

SUPPLEMENTARY MATERIALS

www.sciencemag.org/content/348/6241/1361/suppl/DC1
Materials and Methods
Figs. S1 to S17
Table S1
References (30–58)

18 December 2014; accepted 15 May 2015
10.1126/science.aaa5264

PROTEIN DESIGN

Design of ordered two-dimensional arrays mediated by noncovalent protein-protein interfaces

Shane Gonen,^{1,2,3,4} Frank DiMaio,^{2,3} Tamir Gonen,^{1*} David Baker^{2,3,4*}

We describe a general approach to designing two-dimensional (2D) protein arrays mediated by noncovalent protein-protein interfaces. Protein homo-oligomers are placed into one of the seventeen 2D layer groups, the degrees of freedom of the lattice are sampled to identify configurations with shape-complementary interacting surfaces, and the interaction energy is minimized using sequence design calculations. We used the method to design proteins that self-assemble into layer groups P 3 2 1, P 4 2₁ 2, and P 6. Projection maps of micrometer-scale arrays, assembled both in vitro and in vivo, are consistent with the design models and display the target layer group symmetry. Such programmable 2D protein lattices should enable new approaches to structure determination, sensing, and nanomaterial engineering.

Programmed self-assembly provides a route to patterning matter at the atomic scale. DNA origami methods (1, 2) have been used to generate a wide variety of ordered structures, but progress in designing pro-

tein assemblies has been slower owing to the greater complexity of protein-protein interactions. Biology provides a number of examples of ordered two-dimensional (2D) protein arrays: Bacterial S-layer proteins assemble into

oblique, square, or hexagonal planar symmetry (3); gap-junction plaques, abundant in muscle and heart tissue, display hexagonal planar symmetry (4); and water channels display square planar symmetry (5). Although proteins that form ordered 3D crystals have been designed (6) and

2D lattices have been generated by genetically fusing or chemically cross-linking oligomers with appropriate point symmetric groups (7–10), there has been little success in designing self-assembling 2D lattices with order sufficient to diffract electrons or x-rays below 15 Å resolution (7). Naturally occurring 2D arrays and assemblies are stabilized by extensive noncovalent interactions between protein subunits (10, 11), and this principle has been used to design self-assembling tetrahedral and octahedral cages (12, 13).

We sought to design ordered 2D arrays mediated by designed protein-protein interfaces sta-

bilized by extensive noncovalent interactions. We focused on symmetric arrays, as symmetry reduces the number of distinct protein interfaces required to stabilize the lattice (14, 15). There are 17 distinct ways (layer groups) in which 3D objects can come together to form periodic 2D layers (16). In some layer groups, there are only two unique interfaces between identical subunits, in others, three or four (17). To simplify the design challenge, we focused on the layer groups that involve only two unique interfaces and building blocks with internal point symmetry (which already contain one of the two required interfaces), which leaves only one unique interface to be

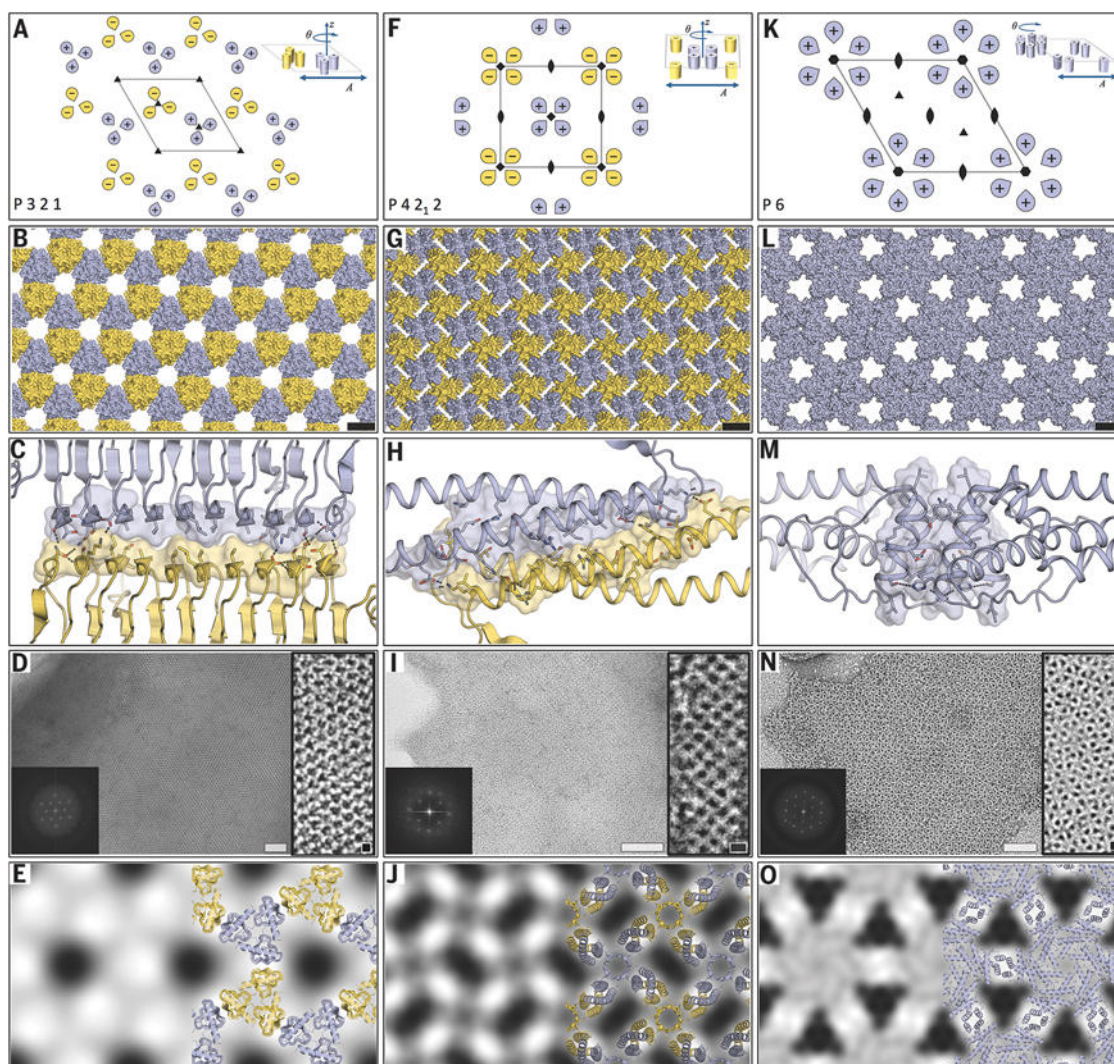


Fig. 1. Computational design strategy and experimental analysis of designed arrays. (A) The P 3 2 1 unit cell with threefold axes represented by triangles. Yellow (–) and purple (+) C3 objects have opposite orientations along the z axis. (Inset) The three degrees of freedom of the lattice. (B) p3Z_42 2D array. (C) p3Z_42 designed interface with “zipper-like” hydrophobic packing and peripheral hydrogen bonds. (D) Large (>1 μm) *E. coli*-grown array (middle), higher magnification view with lattice spacing as in (B) (right), and Fourier transform (amplitudes) of the large array (left). (E) (left) Projection map at 15 Å calculated from a large array. (Right) overlay of the p3Z_42 design model on the projection map. (F) The P 4 2 2 lattice. Ovals represent twofold axes

and squares, fourfold axes. (G) p4Z_9 array. (H) p4Z_9 designed interface. (I) Negatively stained *E. coli*-grown array (main panel), an in vitro refolded lattice at higher magnification (inset), and Fourier transform of the main panel (left). (J) Projection map at 14 Å calculated from an *E. coli* array as in (I) without (left) and with (right) p4Z_9 design model. (K) The P 6 lattice has two degrees of freedom (A, θ) (inset) available for sampling. Sixfolds are represented by hexagons. (L) p6_9H array. (M) p6_9H designed interface. (N) p6_9H lattice grown in vivo with Fourier transform at left and higher magnification view at right. (O) Projection map at 14 Å of p6_9H from *E. coli*-grown arrays as in (N) and cartoon overlay (right). All scale bars: black, 5 nm; white, 50 nm.

designed to form the 2D array. Of the 17 layer groups, 11 have two unique interfaces; we focused here on 6 of these 11 groups involving cyclic rather than dihedral point groups because there are considerably more cyclic oligomers than dihedral oligomers in the Protein Data Bank that can serve as building blocks. The six layer groups with two unique interfaces that can be built from cyclic oligomers are P 2 2₁ 2₁ (from C2 building blocks), P 3 and P 3 2 1 (from C3 building blocks), P 4 and P 4 2₁ 2 (from C4 building blocks), and P 6 (from C6 building blocks). The different groups have different numbers of degrees of freedom describing the placement of an object with cyclic symmetry in the lattice, for example, for P 3 2 1 (Fig. 1A) and P 4 2₁ 2 (Fig. 1F), there are three degrees of freedom, whereas for P 6 (Fig. 1K) there are only two.

We used symmetric docking in Rosetta (14, 18, 19) to search for placements of cyclic oligomers into each of the six layer groups with shape-complementary (20) interfaces between different oligomer copies. The docking scoring function consisted of a soft sphere model of steric interactions and a simple measure of the designable interface area: the number of interface C β s within 7 Å. For each cyclic oligomer in each layer group, ~20 independent Monte Carlo docking trajectories were carried out that started from placements of six to nine copies of the oligomer with its symmetry axis aligned with the corresponding symmetry axes of the layer group (for example, trimers were placed on the threefold symmetry axes indicated by the triangles in Fig. 1A, tetramers on the fourfold symmetry axes indicated by squares in Fig. 1F, and hexamers on the sixfold symmetry axes indicated by hexagons in Fig. 1K). In the Monte Carlo docking simulations, the degrees of freedom sampled were those compatible with the layer group

[Fig. 1, A, F, and K (right)], and hence, the layer group symmetry was preserved throughout the calculations.

We then selected the most shape-complementary (largest number of contacting residues with fewest clashes) solutions from the trajectories and carried out Rosetta sequence design calculations to generate well-packed low-energy interfaces between oligomers. Monte Carlo searches were carried out over all amino acid identities and side-chain rotamer states for residues near the newly formed interface between oligomers, while optimizing the Rosetta all-atom energy of the entire complex (12, 13, 21). After this sequence design step, the energy was further minimized with respect to the side-chain torsion angles of residues near the interface and the symmetric degrees of freedom of the layer group. Finally, the resulting lattice models were filtered on the basis of the shape-complementarity of the designed interface (>0.5), surface area of the designed interface (>400 Å² per monomer), buried unsatisfied hydrogen bonds introduced at the new interface (<4 using a 1.4 Å solvent accessibility probe) (22), and predicted relative free energy (23) of complex formation (≤ 10 Rosetta energy units per subunit) (sample Rosetta script files accompany the supplementary material). After further sequence optimization (13, 24), models passing the filters were manually inspected, and 62 designs were selected for experimental characterization; 16 for P 2 2₁ 2₁, 2 for P 3, 10 for P 3 2 1, 16 for P 4, 3 for P 4 2₁ 2, and 15 for P 6.

Synthetic genes were obtained for the 62 designs, and the proteins were expressed in the *Escherichia coli* cytoplasm by using a standard T7-based expression vector. Of the 62 designs, 43 expressed; of these, 18 had protein in the supernatant after clearing the lysate at

12,000g for 30 min, whereas all 43 had protein in the pellet. To investigate the degree of order in the pelleted material, we examined negatively stained samples by electron microscopy (EM). Regular lattices were observed for four of the designs: One formed only stacked 2D layers (fig. S1), whereas three formed planar arrays. The latter are described in the following sections.

Design p3Z₄₂ is in layer group P 3 2 1. The rigid body arrangement of the constituent β -helix trimers in the lattice was identified by Monte Carlo search over the three degrees of freedom of the lattice: the rotation of the trimer around its axis θ , the lattice spacing A , and the z offset of the trimer from the lattice plane (Fig. 1A). In the lattice identified in the Monte Carlo docking calculations, the oligomeric building blocks pack into a dense array (Fig. 1B; the yellow and purple copies are inverted with respect to each other) stabilized by a large contact surface between adjacent copies with close complementary side-chain packing (Fig. 1C) generated in the sequence design calculations.

p3Z₄₂ formed large and very well ordered 2D crystals (Fig. 1D). Most of the protein expressed in *E. coli* appeared to assemble in these 2D crystals, as there was very little present in the soluble fraction (fig. S3). At low (16°C) expression temperatures, 2D sheets were obtained (Fig. 1D), whereas at 37°C, where larger amounts of proteins are produced, large 2D sheets stacked mainly into thick 3D crystals. Higher magnification (Fig. 1D, inset) showed a trigonal lattice similar to that of the design model [compare Fig. 1D (right) with Fig. 1B]. Fourier transformation of the lattice [Fig. 1D (left)] yielded peaks out to 15 Å resolution; the order in the unstained lattice is probably markedly higher, as the negative stain likely limits the observed resolution. A 15 Å

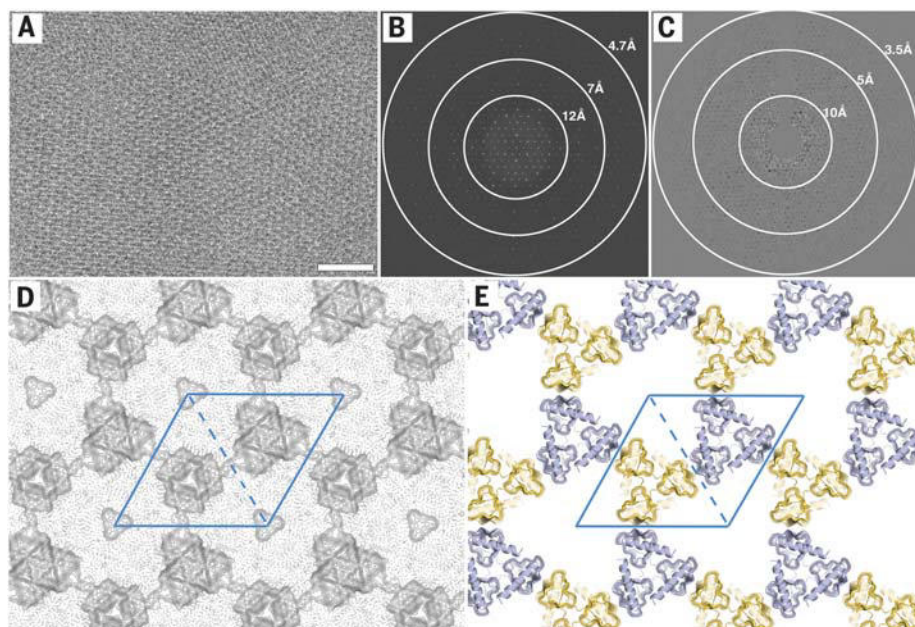


Fig. 2. Cryo-EM analysis of design p3Z₄₂. (A) Cryo-EM micrograph of *E. coli*-grown p3Z₄₂ recorded from nonpurified, resuspended insoluble material. (B) Fourier transform calculated from motion-corrected movies taken from samples like those in (A). (C) Electron diffraction of a crystal as in (A). (D) Projection map at 4 Å calculated from motion-corrected movies from material as in (A) showing a linked repeat-protein arrangement similar to the p3Z₄₂ design model. The unit cell is shown in blue and contains two alternating trimeric units. Triangular density at the corners of the unit cell is likely an averaging artifact. (E) p3Z₄₂ design model in a similar view as in (D). Scale bar, 50 nm.

projection map (Fig. 1E) back-computed from the Fourier components followed the contour of the designed lattice [Fig. 1E (right)] (unit cell dimensions $a = b = 85 \text{ \AA}$, $\gamma = 120^\circ$). It is notable that planar crystals of such large size can grow without support within the confines (and with the many cellular obstacles) of an *E. coli* cell. Cell-free expression of this design yielded large, ordered 2D crystals similar to those formed in *E. coli* (fig. S4A).

Design p4Z_9 is in layer group P 4 2₁ 2. Search over the three degrees of freedom of the layer group [the rotation around the internal C4 axis, the lattice spacing, and the z offset between adjacent inverted tetramers (Fig. 1F)] yielded the close-packed arrangement shown in Fig. 1G (side view in fig. S2B). The designed interface is composed of hydrophobic residues nestled between two α helices surrounded by polar residues (Fig. 1H).

p4Z_9 formed crystals up to $1 \mu\text{m}$ in width (Fig. 1I) with little of the protein present in the soluble fraction (fig. S3). Incubation of the pellet material with 6 M guanidine and subsequent purification and refolding (by dialysis or fast dilution) yielded crystalline 2D arrays and fibers with the same square packing (fig. S4, B and C). Fourier transformation of the negatively stained large 2D lattices generated in vivo yielded peaks out to 14 \AA resolution [Fig. 1I (left)]. The 14 \AA projection map produced by back-transformation had distinctive rectangular voids in alternating directions, which closely matched the design model [Fig. 1J and 1J (right)] (unit cell dimensions $a = b = 56 \text{ \AA}$, $\gamma = 90^\circ$).

Design p6_9 is built from α -helical hexamers in layer group P 6. In this case, all oligomers are in the same orientation along the z axis (perpendicular to the plane in Fig. 1K), and hence, there are only two degrees of freedom—the rotation around the sixfold axis and the lattice spacing [Fig. 1K (right)]. The shape-complementary docking solution (Fig. 1L and side view fig. S2C) is composed of four closely associating α helices along the twofold axis of the lattice (Fig. 1M) with two interacting phenylalanines. We also tested a variant, p6_9H, which introduces a hydrogen bond network across the interface (Fig. 1M).

Design p6_9 expressed in *E. coli* was found in both the supernatant and pellet (fig. S3). EM investigation revealed that the pellet contained highly ordered single-layer 2D hexagonal arrays, whereas the supernatant did not. p6_9H formed even larger arrays (Fig. 1N, fig. S5, and table S1). The 2D layers in the pellet were highly ordered with clearly evident hexagonal packing [Fig. 1N and 1N (inset)]. Fourier transformation of the negatively stained arrays [Fig. 1N (left)] yielded peaks out to 14 \AA resolution; and the back-computed 14 \AA map was again closely consistent with the design model of the array [Fig. 1O and 1O (right)] (unit cell dimensions: $a = b = 120 \text{ \AA}$, $\gamma = 120^\circ$). Large arrays were also formed in vitro after concentration of soluble p6_9H purified from the supernatant after lysis of *E. coli* (fig. S4, D and E).

To achieve higher resolution than possible with negatively stained samples, we analyzed designs without stain by electron cryomicroscopy (cryo-EM). Analysis of p3Z_42 crystals by cryo-EM (Fig. 2, A and B) and electron diffraction yielded data to 3.5 \AA resolution (Fig. 2C). The vast majority of crystals diffracted to this resolution in the cryo preparations, indicating high long-range order. Movie micrographs of the resulting crystals were also collected, motion corrected, and processed in $2dx$ (25) to yield a projection map at 4 \AA resolution in agreement with the design model (Fig. 2, compare D and E). To our knowledge, this is the highest order observed to date for a designed macromolecular 2D lattice.

Our designed planar protein arrays form large planar 2D crystals both in vivo and in vitro that are closely consistent with the design models. Two of the three successes were with layer groups with adjacent building blocks in opposite orientations along the z axis; these have the advantages that (i) there is an additional degree of freedom (the z offset) providing more possible packing arrangements for a given oligomeric building block; (ii) the interfaces are antiparallel rather than parallel so that, in the design calculations, opposing residues can have different identities; and (iii) inaccuracies in the design calculations that result in deviation from planarity effectively cancel out. On the other hand, designed “polar” arrays with all subunits oriented in the same direction—such as p6_9—have advantages for functionalization, as the two sides are distinct and can be addressed separately.

It is notable that, for all three designs, extensive crystalline arrays form unsupported in *E. coli* and from purified protein in vitro. The coherent arrays can extend up to $1 \mu\text{m}$ in length but are only 3 to 8 nm thick by design (fig. S2). We anticipate that even larger and perhaps more highly ordered crystals would form on a solid support, which will be useful for future nanotechnology applications. The ability to precisely design 2D arrays at the near atomic level should enable new approaches in structural biology [fusing proteins of unknown structure to array components for electron crystallography or using these to nucleate 3D crystal growth for x-ray and MicroED (26) applications], new sensing modalities with the coupling of analyte binding domains to the arrays, and the organization of enzyme networks and light-harvesting chromophores in two dimensions.

REFERENCES AND NOTES

- N. C. Seeman, *Annu. Rev. Biochem.* **79**, 65–87 (2010).
- P. W. Rothmund, *Nature* **440**, 297–302 (2006).
- D. Pum, J. L. Toca-Herrera, U. B. Sleytr, *Int. J. Mol. Sci.* **14**, 2484–2501 (2013).
- D. L. Caspar, D. A. Goodenough, L. Makowski, W. C. Phillips, *J. Cell Biol.* **74**, 605–628 (1977).
- J. E. Rash, K. G. Davidson, T. Yasumura, C. S. Furman, *Neuroscience* **129**, 915–934 (2004).
- C. J. Lanci et al., *Proc. Natl. Acad. Sci. U.S.A.* **109**, 7304–7309 (2012).

- J. C. Sinclair, K. M. Davies, C. Vénien-Bryan, M. E. Noble, *Nat. Nanotechnol.* **6**, 558–562 (2011).
- J. Zhang, F. Zheng, G. Grigoryan, *Curr. Opin. Struct. Biol.* **27**, 79–86 (2014).
- J. D. Brodin et al., *Nat. Chem.* **4**, 375–382 (2012).
- F. Baneyx, J. F. Matthaei, *Curr. Opin. Biotechnol.* **28**, 39–45 (2014).
- E. D. Levy, E. B. Erba, C. V. Robinson, S. A. Teichmann, *Nature* **453**, 1262–1265 (2008).
- N. P. King et al., *Science* **336**, 1171–1174 (2012).
- N. P. King et al., *Nature* **510**, 103–108 (2014).
- I. André, P. Bradley, C. Wang, D. Baker, *Proc. Natl. Acad. Sci. U.S.A.* **104**, 17656–17661 (2007).
- I. André, C. E. Strauss, D. B. Kaplan, P. Bradley, D. Baker, *Proc. Natl. Acad. Sci. U.S.A.* **105**, 16148–16152 (2008).
- B. L. Nannenga, M. G. Iadanza, B. S. Vollmar, T. Gonen, in *Current Protocols in Protein Science*, chap. 17, unit 17.15 (Wiley, New York, 2013).
- S. W. Wukovitz, T. O. Yeates, *Nat. Struct. Biol.* **2**, 1062–1067 (1995).
- F. DiMaio, A. Leaver-Fay, P. Bradley, D. Baker, I. André, *PLOS ONE* **6**, e20450 (2011).
- S. J. Fleishman et al., *PLOS ONE* **6**, e20161 (2011).
- M. C. Lawrence, P. M. Colman, *J. Mol. Biol.* **234**, 946–950 (1993).
- B. Kuhlman et al., *Science* **302**, 1364–1368 (2003).
- Z. S. Hendsch, T. Jonsson, R. T. Sauer, B. Tidor, *Biochemistry* **35**, 7621–7625 (1996).
- E. H. Kellogg, O. F. Lange, D. Baker, *J. Phys. Chem. B* **116**, 11405–11413 (2012).
- L. G. Nivón, R. Moretti, D. Baker, *PLOS ONE* **8**, e59004 (2013).
- B. Gipson, X. Zeng, Z. Y. Zhang, H. Stahlberg, *J. Struct. Biol.* **157**, 64–72 (2007).
- D. Shi, B. L. Nannenga, M. G. Iadanza, T. Gonen, *eLife* **2**, e01345 [abstr.] (2013).

ACKNOWLEDGMENTS

We thank D. Shi and J. de la Cruz for help with EM, S. Sanchez-Martinez for help with protein expression, J. Bale and N. King for support and helpful discussions, and W. Sheffler for Rosetta code. We would also like to thank members of both the Baker and Gonen labs for scripts and useful discussions. We thank HHMI's Janelia Research Campus visitor program, the University of Washington's Biochemistry Department and Biological Physics, Structure, and Design program, U.S. Defense Threat Reduction Agency, U.S. Air Force Office of Scientific Research, and the Howard Hughes Medical Institute for funding and support. S.G., F.D., T.G., and D.B. are inventors on a provisional patent application that covers the method for the design of self-assembling 2D protein material. Supporting materials, methods and the design models and sample design files are available in the supplementary materials. Author contributions: S.G. and F.D. worked on the docking and design. S.G. worked on design optimization. F.D. wrote Rosetta code. S.G., F.D., and D.B. computationally analyzed the designs. S.G. worked on the biochemistry, electron microscopy, and data analysis. S.G. and T.G. analyzed the EM data. All authors designed the research and wrote, edited, and contributed to the manuscript.

SUPPLEMENTARY MATERIALS

www.sciencemag.org/content/348/6241/1365/suppl/DC1
Materials and Methods
Supplementary Text
Figs. S1 to S5
Tables S1 and S2
References (27–39)

25 February 2015; accepted 11 May 2015
10.1126/science.aaa9897

ENDOCYTOSIS

Endocytic sites mature by continuous bending and remodeling of the clathrin coat

Ori Avinoam,^{1,2} Martin Schorb,^{2,3} Carsten J. Beese,¹
John A. G. Briggs,^{2,1*} Marko Kaksonen^{1,2*†}

During clathrin-mediated endocytosis (CME), plasma membrane regions are internalized to retrieve extracellular molecules and cell surface components. Whether endocytosis occurs by direct clathrin assembly into curved lattices on the budding vesicle or by initial recruitment to flat membranes and subsequent reshaping has been controversial. To distinguish between these models, we combined fluorescence microscopy and electron tomography to locate endocytic sites and to determine their coat and membrane shapes during invagination. The curvature of the clathrin coat increased, whereas the coated surface area remained nearly constant. Furthermore, clathrin rapidly exchanged at all stages of CME. Thus, coated vesicle budding appears to involve bending of a dynamic preassembled clathrin coat.

Clathrin-mediated endocytosis (CME) is essential for a broad range of cellular processes, including nutrient uptake, signal transduction, synaptic vesicle recycling, and immune responses (1, 2). It initiates with cargo binding by adaptor proteins that recruit clathrin on the plasma membrane, followed by membrane invagination, which leads to dynamin-dependent scission of a coated vesicle (3, 4). Clathrin trimers have a triskelion shape and can assemble into heterogeneous polyhedral coats (5). The relation between coat assembly and membrane invagination is poorly understood. Two alternative models describe the transition from planar membrane to clathrin-coated vesicle (CCV). The first—derived from electron microscopy images showing both relatively flat and invaginated clathrin lattices in cells—suggests that clathrin assembles as a planar lattice that subsequently bends as the membrane invaginates (6) (Fig. 1A). For this to happen, complex rearrangements within the clathrin network must occur during budding. The second model avoids this difficulty by proposing that large, flat clathrin lattices are not precursors of CME and that, at sites of CME, clathrin directly assembles to produce the curved coat as the membrane invaginates (7) (Fig. 1A).

To study clathrin-coated pit (CCP) maturation, we used well-characterized genome-edited human cell lines expressing fluorescently tagged clathrin light chain A at endogenous concentrations (8, 9) (hCLTA^{EN}) (Fig. 1, B and C). To distinguish late stages of CME, we used cells that coexpressed endogenously tagged dynamin-2 (9)

(hCLTA^{EN}/hDNM2^{EN}) (Fig. 1B). To label CCPs that recruit cargo, we incubated cells with fluorescently labeled transferrin (TF), a constitutive cargo of CME (hCLTA^{EN}/TF) (Fig. 1C). CME events imaged by total internal reflection fluorescence (TIRF) microscopy showed a buildup of clathrin fluorescence that reached a plateau before a burst of dynamin preceded the site's disappearance, as previously described (8, 10) (Fig. 1, B and C, and movies S1 and S2).

To distinguish between the models of coat assembly, we applied a correlative fluorescence microscopy (FM) and electron tomography (ET) method to locate CCPs precisely and to obtain three-dimensional information about their shape (11–13) (Fig. 1D and movies S3 to S5). We obtained, in total, 233 tomographic reconstructions of sites where a clathrin signal was detected at the cell periphery (117 from hCLTA^{EN}/hDNM2^{EN} and 116 from hCLTA^{EN}/TF). In all cases, the fluorescent signal correlated with an endocytic site with a clear membrane coat (13). When the coat lay parallel to the imaging plane, the characteristic polygonal architecture of polymerized clathrin was visible (Fig. 1E and fig. S1). We analyzed 199 CCPs and 27 CCVs corresponding to different stages of CME (Fig. 1F) (13).

To characterize changes in membrane shape, we extracted the membrane and coat profiles and analyzed them computationally (12, 13) (Fig. 2). We determined the invagination depth, tip curvature, and coated membrane area. When a constricted neck was detected at the base of the invagination, we measured neck width and height (13) (Fig. 2B and tables S1 and S2). We further determined the maximal angle (θ) between the adjacent plasma membrane (PM) and the invaginating segment of the membrane (Fig. 2B). Independently of invagination size and which model is correct, θ will increase during invagination from 0° to 90° in a U-shaped invagination before tending to 180° at neck constriction and scission (13) (Figs. 1A and 2B and movie S6). θ is therefore a

surrogate for CCP stage and was used to order CCPs from early to late.

We detected no apparent morphological differences between the cargo-labeled CCPs from hCLTA^{EN}/TF and the CCPs observed in hCLTA^{EN}/hDNM2^{EN} cells (fig. S2) and, unless stated otherwise, we pooled the data from these data sets. Dynamin-positive sites consisted exclusively of deep invaginations with a neck and clustered at late stages of CME ($\sim\theta > 90^\circ$; depth, 68 to 155 nm) (Fig. 3, A and B, and fig. S3). The high precision of correlation allowed us to localize dynamin to the base of the invagination close to the PM (13) (Fig. 2C). Dynamin-associated necks had widths of up to 121 nm, which greatly exceeded the diameter of assembled dynamin rings in vitro (<30 nm) (14); these findings suggested that dynamin recruitment and neck constriction begin before ring formation.

If clathrin directly assembles into the curved coat by addition of triskelia during membrane invagination, then the coated membrane area should grow as sites mature. In contrast, we found that the coated membrane area in CCPs did not appreciably change during budding and did not differ significantly between CCPs and CCVs (Fig. 3C and figs. S1C and S2, C and D). This suggests that enough clathrin is recruited before invagination to coat a complete vesicle. Furthermore, if clathrin directly assembles into the curved coat, then the tip curvature of CCPs would remain constant during budding and would be the same as that in the resultant CCVs. In contrast, our analysis showed that tip curvature continuously increased during invagination (Fig. 3, D and E, and fig. S2E). These results show that the curvature of CCPs increases, whereas the surface area remains largely constant. These properties are only consistent with the model where clathrin is initially deposited on a nearly planar membrane followed by subsequent membrane bending.

In order to bend, flat lattices composed primarily of hexagons must acquire pentagons requiring extensive molecular rearrangements and removal of triskelia (7, 15). It has been reported previously that clathrin exchanges at CCPs (16, 17). However, it is unclear if, and at what stages, this occurs during canonical CME. To test this, we performed fluorescence recovery after photobleaching (FRAP) analysis of individual CCPs (13) while simultaneously imaging clathrin and dynamin (Fig. 4A and movie S7). Clathrin fluorescence recovered rapidly, reaching 60% recovery with a half time of ~ 2 s, both before and after dynamin recruitment (Fig. 4, B and C, and fig. S4). This indicates that clathrin is exchanging at early and late stages of CME and explains why blocking clathrin turnover arrests CCPs at all stages (18).

Although fluorescence intensity profiles of individual CCPs display considerable heterogeneity in assembly kinetics and overall persistence at the plasma membrane, recent analysis has shown that clathrin displays an initiation and growth phase, followed by a plateau in which fluorescence intensity is at its maximum (10, 19). Our correlated FM and ET data showed that clathrin recruitment occurs before membrane invagination,

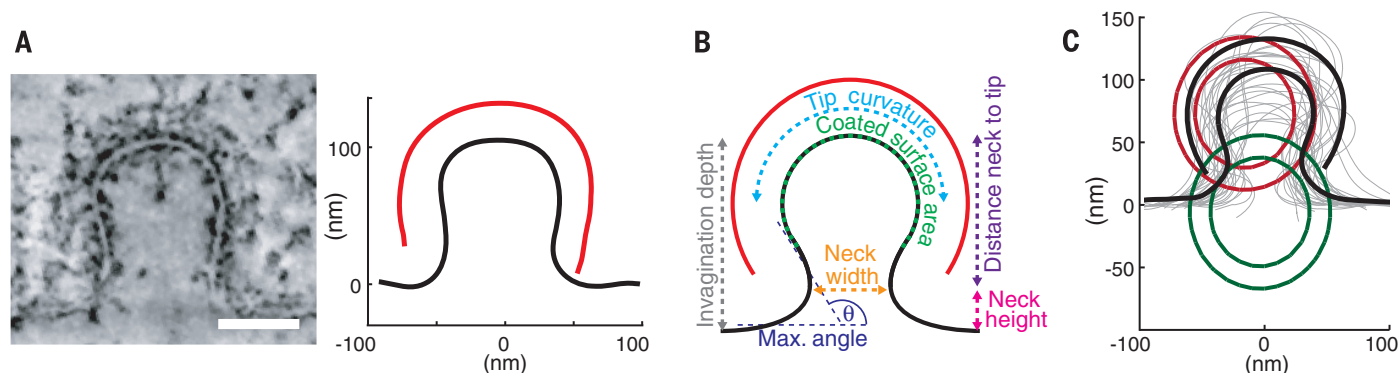
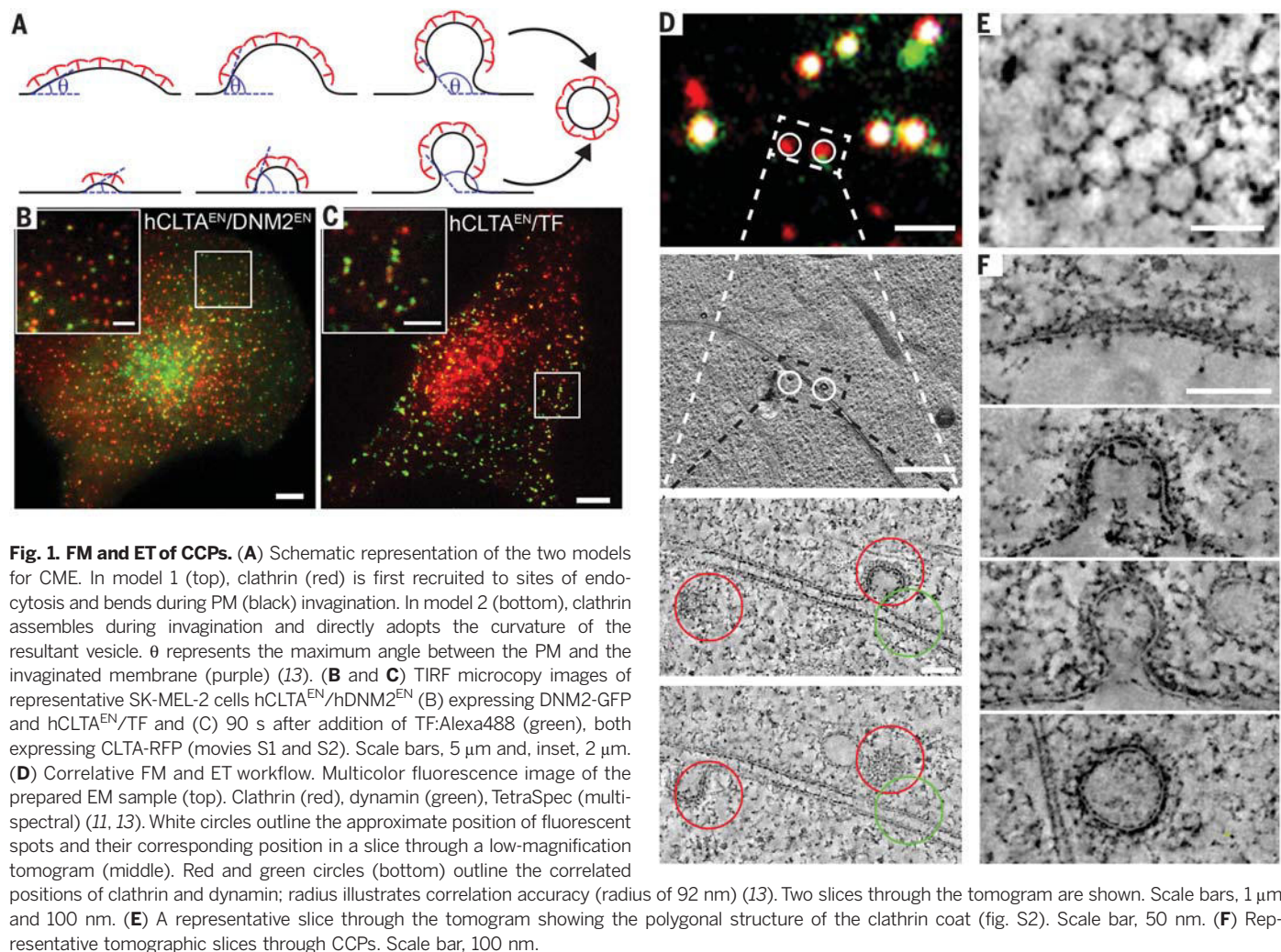
¹Cell Biology and Biophysics Unit, The European Molecular Biology Laboratory, Heidelberg 69117, Germany. ²Structural and Computational Biology Unit, The European Molecular Biology Laboratory, Heidelberg 69117, Germany. ³Electron Microscopy Core Facility, The European Molecular Biology Laboratory, Heidelberg 69117, Germany.

*Corresponding author. E-mail: marko.kaksonen@unige.ch (M.K.); john.briggs@embl.de (J.A.G.B.) †Present address: Department of Biochemistry, University of Geneva, 1211 Geneva, Switzerland.

which suggests that invagination occurs during the fluorescence intensity plateau (Fig. 3C and fig. S5). In yeast, the coat is also recruited before membrane bending, which suggests that this is a

conserved feature (12). Numerous EM studies have documented a population of flat clathrin lattices that could potentially evolve into single vesicles (6, 20). It is likely that these lattices

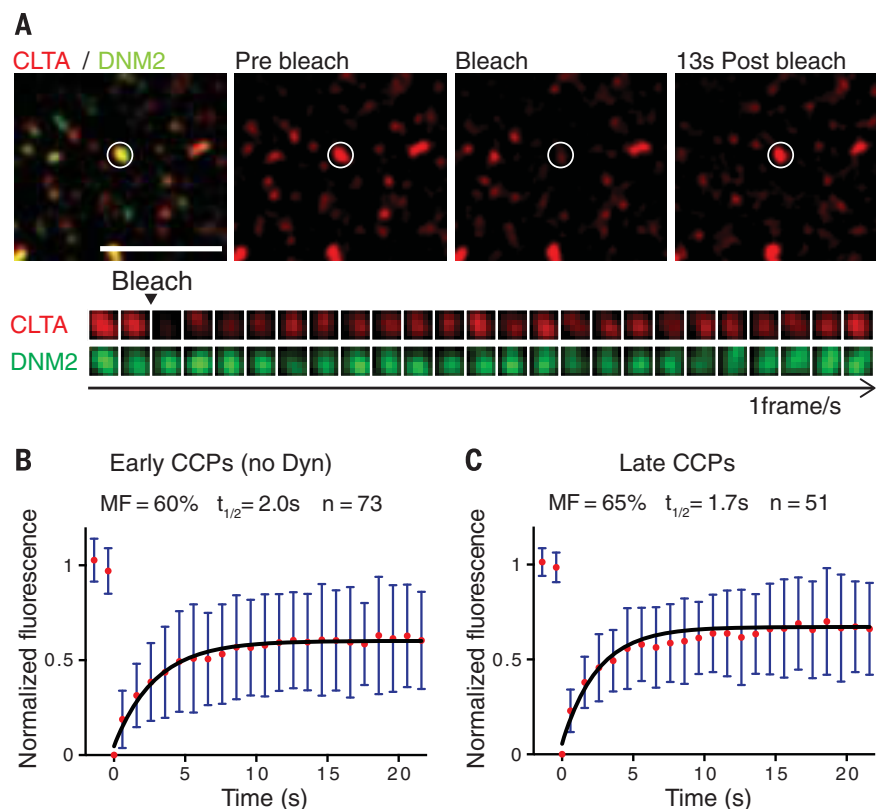
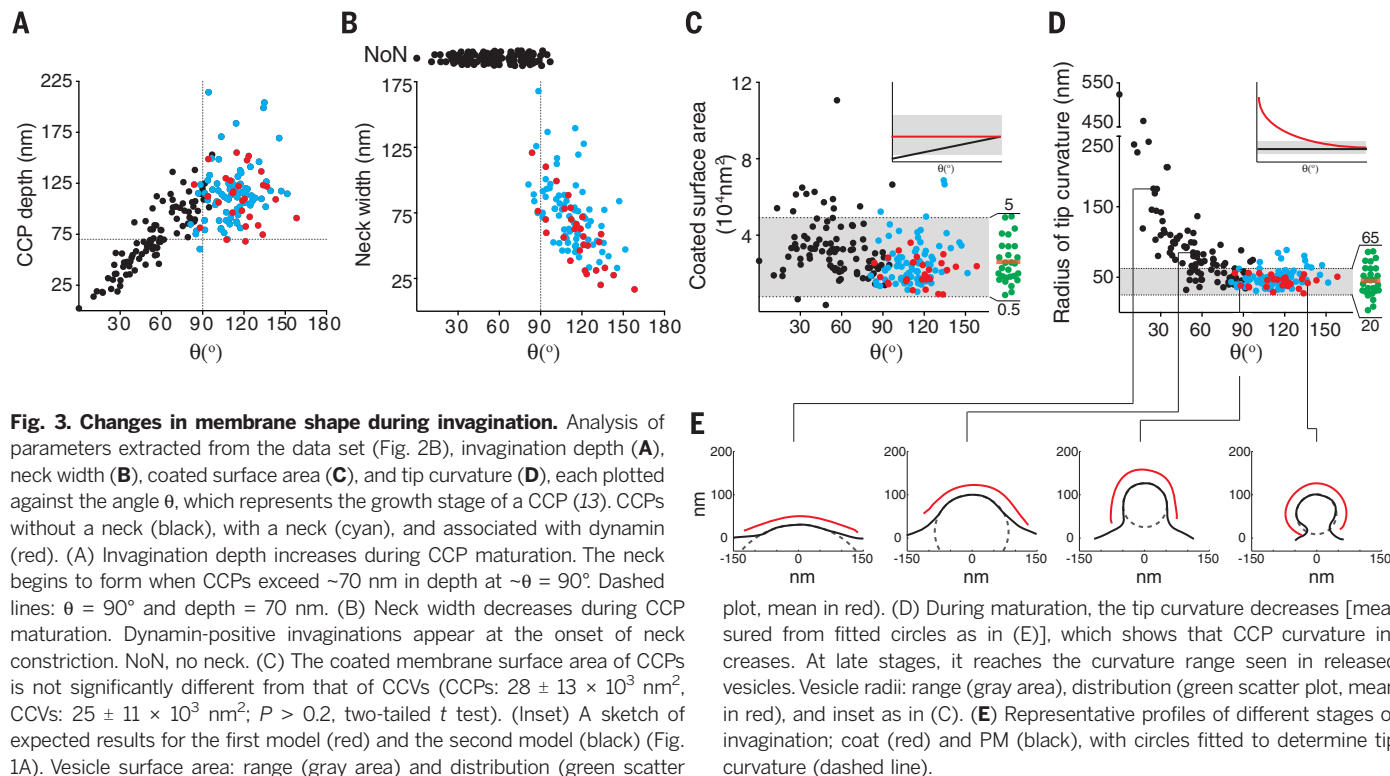
correspond to the early CCPs observed here. Subdomains of the larger clathrin lattices that exist in some cell types may also undergo local rearrangements to produce vesicles (20, 21).



Recruitment of clathrin before membrane bending provides a flat, dynamic array as a platform for cargo recruitment. This implies that the

membrane to be internalized and the size of the future vesicle are not determined by clathrin geometry during assembly into a curved cage but

rather are selected before invagination during cargo recruitment. Rapid clathrin exchange is consistent with a dynamically unstable lattice—dynamic



instability is a common property within networks of low-affinity protein interactions (22). It would allow for stochastic abortion of sites that initiate but fail to cross a growth- or cargo-mediated checkpoint (19, 23–25) before investing energy in membrane bending. During invagination, further exchange would allow clathrin reorganization and bending of the lattice into a defined cage that requires active disassembly.

REFERENCES AND NOTES

1. F. M. Brodsky, *Annu. Rev. Cell Dev. Biol.* **28**, 309–336 (2012).
2. H. T. McMahon, E. Boucrot, *Nat. Rev. Mol. Cell Biol.* **12**, 517–533 (2011).
3. S. M. Ferguson, P. De Camilli, *Nat. Rev. Mol. Cell Biol.* **13**, 75–88 (2012).
4. E. Cocucci, F. Aguet, S. Boulant, T. Kirchhausen, *Cell* **150**, 495–507 (2012).
5. E. Ungewickell, D. Branton, *Nature* **289**, 420–422 (1981).
6. J. Heuser, *J. Cell Biol.* **84**, 560–583 (1980).
7. T. Kirchhausen, *Curr. Opin. Struct. Biol.* **3**, 182–188 (1993).
8. A. Grassart et al., *J. Cell Biol.* **205**, 721–735 (2014).
9. J. B. Doyon et al., *Nat. Cell Biol.* **13**, 331–337 (2011).
10. F. Aguet, C. N. Antonescu, M. Mettlen, S. L. Schmid, G. Danuser, *Dev. Cell* **26**, 279–291 (2013).
11. W. Kukulski et al., *J. Cell Biol.* **192**, 111–119 (2011).
12. W. Kukulski, M. Schorb, M. Kaksonen, J. A. G. Briggs, *Cell* **150**, 508–520 (2012).
13. Materials and methods are available as supplementary materials on Science Online.
14. S. Morlot, A. Roux, *Annu. Rev. Biophys.* **42**, 629–649 (2013).
15. T. Kirchhausen, D. Owen, S. C. Harrison, *Cold Spring Harb. Perspect. Biol.* **6**, a016725 (2014).
16. D. Loecker, M. Wiensisch, O. Kochubey, J. Klingauf, *Traffic* **6**, 918–929 (2005).
17. X. Wu et al., *J. Cell Biol.* **155**, 291–300 (2001).
18. L. von Kleist et al., *Cell* **146**, 471–484 (2011).
19. D. Loecker et al., *PLOS Biol.* **7**, e57 (2009).
20. J. Grove et al., *Mol. Biol. Cell* **25**, 3581–3594 (2014).
21. S. Saffarian, E. Cocucci, T. Kirchhausen, *PLOS Biol.* **7**, e1000191 (2009).
22. E. M. Schmid, H. T. McMahon, *Nature* **448**, 883–888 (2007).
23. M. Mettlen, D. Loecker, D. Yarar, G. Danuser, S. L. Schmid, *J. Cell Biol.* **188**, 919–933 (2010).
24. A. G. Henry et al., *Dev. Cell* **23**, 519–532 (2012).
25. M. Ehrlich et al., *Cell* **118**, 591–605 (2004).

ACKNOWLEDGMENTS

We thank members of the Kaksonen and Briggs laboratories for helpful discussion; B. Podbilewicz, J. Ries, and P. Lénárt for critically reading the manuscript; the EMBL electron and advanced light microscopy facilities; and A. Politi and J. Ellenberg for single-site FRAP software. O.A. was supported by the Marie Curie Actions COFUND (European Commission Cofunding of Regional, National, and International Programme) [grant no. 229597; EMBL Interdisciplinary Postdoc (EIPD)]. Computer codes used are available upon request.

SUPPLEMENTARY MATERIALS

www.sciencemag.org/content/348/6241/1369/suppl/DC1
Materials and Methods
Figs. S1 to S5
Tables S1 to S2
Movies S1 to S7
References (26–31)

19 February 2015; accepted 13 May 2015
10.1126/science.aaa9555

TRANSCRIPTION

Recruitment of RNA polymerase II by the pioneer transcription factor PHA-4

H.-T. Hsu,¹ H.-M. Chen,¹ Z. Yang,² J. Wang,³ N. K. Lee,¹ A. Burger,⁴ K. Zaret,² T. Liu,^{3,5} E. Levine,⁴ S. E. Mango^{1,*}

Pioneer transcription factors initiate cell-fate changes by binding to silent target genes. They are among the first factors to bind key regulatory sites and facilitate chromatin opening. Here, we identify an additional role for pioneer factors. In early *Caenorhabditis elegans* foregut development, the pioneer factor PHA-4/FoxA binds promoters and recruits RNA polymerase II (Pol II), often in a poised configuration in which Pol II accumulates near transcription start sites. At a later developmental stage, PHA-4 promotes chromatin opening. We found many more genes with poised RNA polymerase than had been observed previously in unstaged embryos, revealing that early embryos accumulate poised Pol II and that poising is dynamic. Our results suggest that Pol II recruitment, in addition to chromatin opening, is an important feature of PHA-4 pioneer factor activity.

Embryonic development depends on precise patterns of gene expression that are orchestrated by key transcription factors such as pioneer transcription factors. Pioneer factors function at the earliest stage of transcriptional onset to facilitate chromatin opening at cis-regulatory sites, which enables additional factors to bind DNA (1). The founding pioneer factor is mammalian FoxA1, which associates with liver genes and promotes chromatin accessibility before transcriptional activation. In vitro, FoxA proteins bind nucleosomes and block chromatin compaction by H1 linker histones (1), and in vivo FoxA proteins open chromatin with the histone variant H2A.Z (2). It is unknown whether chromatin opening is the sole mechanism of transcriptional priming induced by pioneer transcription factors.

In *Caenorhabditis elegans*, *pha-4* encodes a selector gene that specifies foregut fate (3). *pha-4* is orthologous to FoxA proteins (4, 5) and interacts with H2A.Z (2), raising the question of whether *pha-4* functions as a pioneer transcription factor in addition to its selector activities. We performed five tests that revealed that *pha-4* had pioneer activity. First, PHA-4 associated with target genes *M05B5.2*, *ceh-22*, and *myo-2* beginning at the 8E stage (“E” for endodermal cells), when PHA-4 was first detected (Fig. 1, A and B, and fig. S1A). We observed binding to promoters that are activated at early, mid-, or late embryogenesis and confirmed that the mid- (*ceh-22*) and late-stage (*myo-2*) genes were not expressed in our 8E sample (gastrulation stage). These data indicate that PHA-4 associates with endogenous foregut promoters hours before transcriptional onset, which is as

expected for a pioneer factor. Second, we determined that PHA-4 bound nucleosomal DNA in vitro equivalently to its orthologs FoxA1 and FoxA2 (Fig. 1C). Third, chromatin sites bound by PHA-4 in vivo [measured with chromatin immunoprecipitation (ChIP)] (6) lacked stable nucleosomes [measured with formaldehyde-assisted isolation of regulatory elements (FAIRE)] (fig. S1C) (7), indicating PHA-4 association with open chromatin. Moreover, regions bound by PHA-4 were enriched for activating histone marks H3K4me2, H3K4me3, and acetylated H3K27 (fig. S1C) (8). Fourth, single-cell analysis with artificial chromosomes (Fig. 1D) revealed that chromatin was open in the foregut, where PHA-4 is expressed, but not in other cell types, which lack PHA-4, nor with a target promoter bearing a mutated PHA-4-binding site (Fig. 1E) (9). Fifth, we tracked PHA-4 association with chromatin during mitosis and observed that a portion of PHA-4 was retained on DNA in dividing foregut cells (fig. S2) (10). Together, the results reveal that PHA-4 fulfilled the criteria of a pioneer transcription factor (Fig. 1 and fig. S1B). It associated with binding sites early in development, bound DNA packaged in nucleosomes in vitro, and decompacted chromatin in vivo.

To examine the role of PHA-4 in transcription, we mapped Pol II occupancy by means of genome-wide ChIP-sequencing (ChIP-seq). Previous studies with *C. elegans* Pol II had focused on relatively late time points, after transcription was established for many genes (6, 11). Our interest was earlier stages, before transcriptional onset. We analyzed early embryos after PHA-4 bound to target genes but before their transcription (~8E stage) and compared those embryos to mid-stage, transcriptionally active embryos (bean stage) (staging is provided in fig. S3). To localize Pol II, we mapped its position relative to the transcription start site (TSS) (12) and calculated three scores: promoter occupancy for Pol II spanning the TSS (Fig. 2A), Pol II within gene bodies (Fig. 2B), and the poising index as the ratio of the promoter to the gene body values (Fig. 2C). The poising index reflects the relative quantity of

¹Department of Molecular and Cellular Biology, Harvard University, Cambridge, MA, USA. ²Department of Cell and Developmental Biology, University of Pennsylvania, Philadelphia, PA, USA. ³Department of Biochemistry, University at Buffalo, Buffalo, NY, USA. ⁴Department of Physics and Center for Systems Biology, Harvard University, Cambridge, MA, USA. ⁵Department of Biostatistics, University at Buffalo, Buffalo, NY 14214, USA.

*Corresponding author. E-mail: smango@mcb.harvard.edu

Pol II close to the site of transcriptional initiation (12). Poising has been detected in diverse organisms including, to a degree, *C. elegans* (12, 13).

We began by surveying the whole genome. In early embryos, most genes showed little Pol II at either promoters or gene bodies (Fig. 2, A and B), suggesting that most of the genome was inactive. However, ~20% of genes had Pol II near the TSS and little Pol II within gene bodies, leading to a high poising index (≥ 2.5) (Fig. 2C). As development progressed, the Pol II signal for both promoters and gene bodies increased, resulting in a broad range of poising values (Fig. 2C and fig. S4C). This result suggested that the mid-stage poising scores reflected a surge in Pol II activity at the level of initiation and elongation, and that poising in *C. elegans* is temporally regulated, similar to other animals (12). Most genes had docked Pol II, in which Pol II bound just upstream of the TSS (14) (Fig. 2D) (11). Pol II “pausing” was also observed 3 to the TSS, like other species (12, 14),

but we observed fewer cases of pausing as compared with docking. We suggest that poising in *C. elegans* is more prevalent than had been previously recognized. Earlier studies observed some poising in starved larvae and in samples bearing mixtures of stages (6, 13, 14). In our samples, poising was associated with both early and mid-stages, with index values typically higher in early embryos because occupancy of Pol II within gene bodies was low. Our analysis gives a picture of Pol II loading and transcriptional onset during embryogenesis.

We next examined Pol II at foregut-associated genes. We observed an enrichment of poised Pol II: 27% of foregut genes were poised early compared with 17% for the whole genome (Fig. 2C). At the bean stage, 36% of PHA-4-bound promoters had a poising index >2.5 , compared with 29% for the whole genome. We confirmed the ChIP-seq result by means of ChIP-quantitative polymerase chain reaction (PCR) for four foregut

genes exhibiting different Pol II poising scores (11). For example, Pol II was poised at the *ceh-22* promoter in early embryos before transcriptional onset, but it subsequently decreased at the TSS and increased in the gene body (Fig. 2E and fig. S4B). Quantitative reverse transcriptase-PCR (RT-PCR) analysis demonstrated that *ceh-22* mRNA was activated in mid-embryos, as expected (Fig. 3, B and C) (11, 15). These data suggest that poised Pol II often reflects preparation for transcriptional activation (12). Consistent with this idea, genes with poised Pol II were associated with Gene Ontology (GO) terms “embryonic development” and “embryonic morphogenesis” (table S1). However, poising likely has additional roles because we also detected embryonic poised Pol II at a subset of genes not expressed in embryos (such as *mex-3*) or associated with GO terms such as “post-embryonic development.”

Pol II poising at developmentally expressed genes has been observed in *Drosophila* embryos

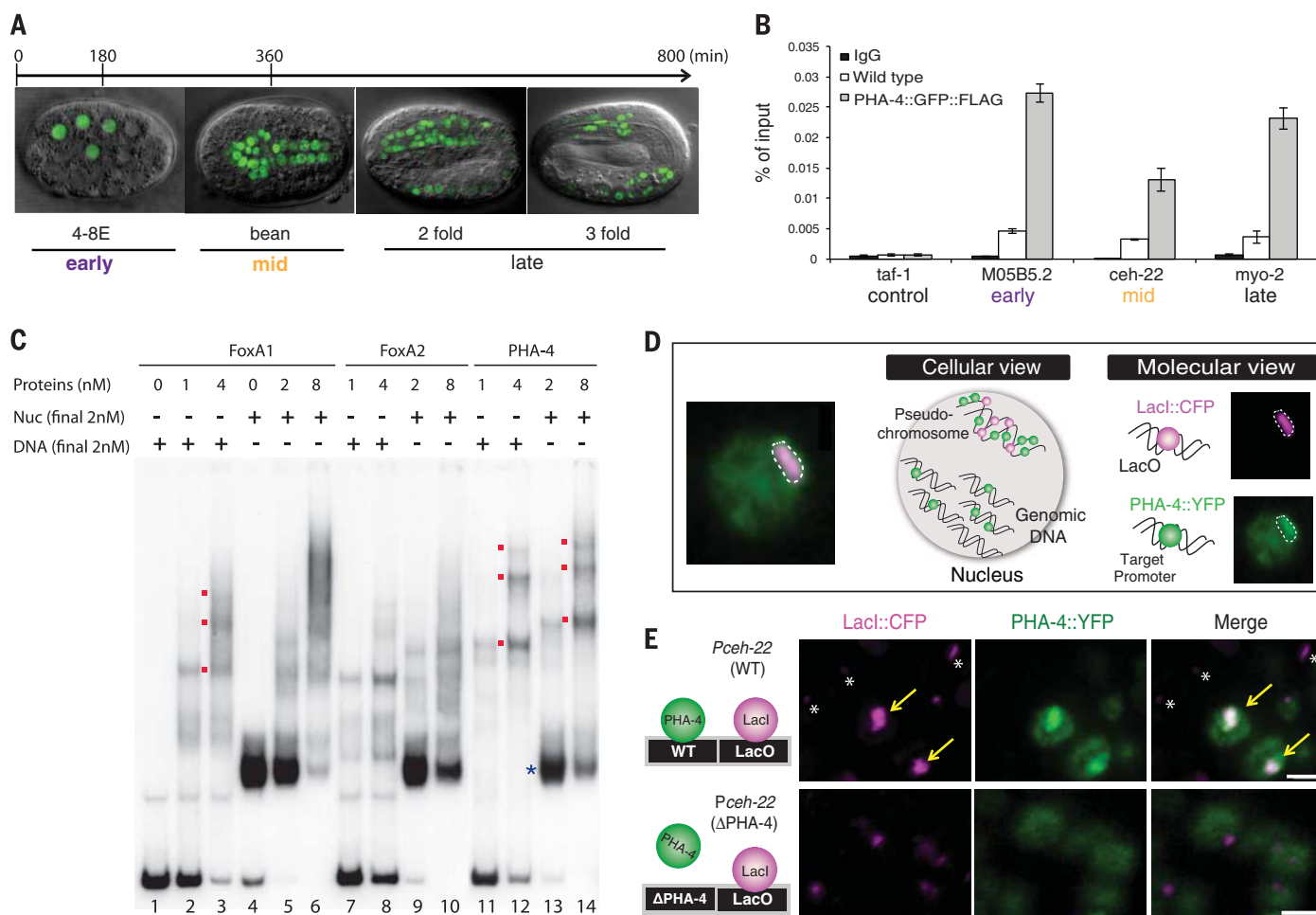


Fig. 1. PHA-4 is a pioneer factor. (A) PHA-4::green fluorescent protein (GFP) (green) during stages of embryogenesis. Early embryos are enriched for 8E stage, and mid-embryos are enriched for bean stage (11). (B) PHA-4::GFP::FLAG (11) binding endogenous targets *M05B5.2* (expressed early), *ceh-22* (mid), and *myo-2* (late), detected with ChIP-quantitative PCR. Wild-type embryos lack FLAG, a negative control. *taf-1* is not a PHA-4 target. $n = 3$ replicates, mean \pm SEM. (C) PHA-4 binds nucleosomes. Shown is recombinant PHA-4 compared with FoxA proteins incubated with the albumin

enhancer containing a FoxA1 binding site as free DNA (DNA) or nucleosomal (Nuc) DNA. Bound PHA-4 generated slow migrating bands (red). (D) Artificial chromosomes with PHA-4::yellow fluorescent protein (YFP) bound target promoters in single cells. (E) PHA-4::YFP (green) bound artificial chromosomes (purple, LacI) bearing the *ceh-22* promoter (arrows). PHA-4::YFP binding was abolished when *ceh-22* carried a mutated PHA-4 binding site (Δ PHA-4; bottom). Asterisks mark artificial chromosomes in nonforegut cells. Scale bar, 2 μ m.

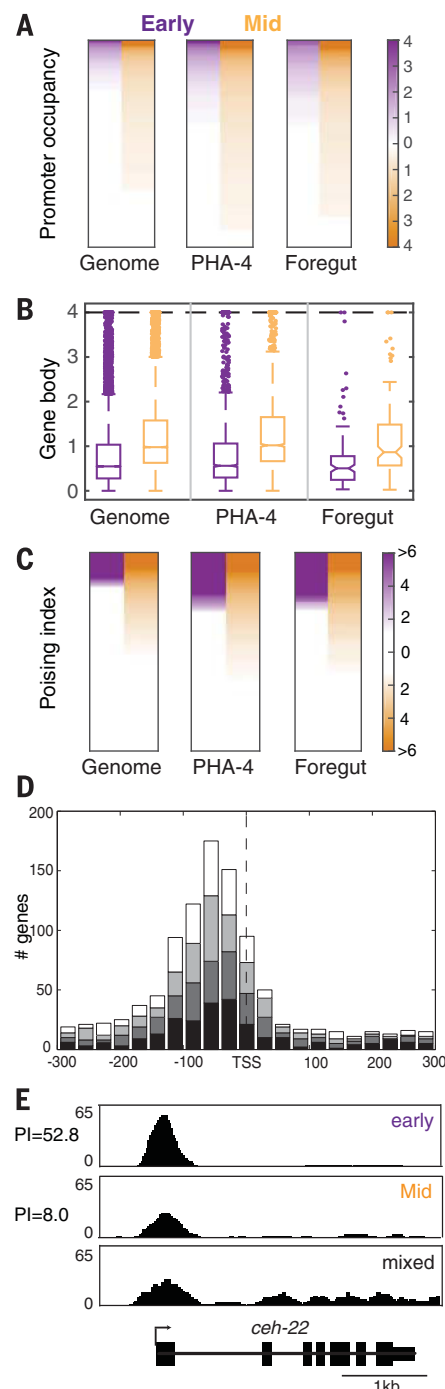


Fig. 2. Early embryos accumulate poised Pol II. (A) Pol II occupancy at promoters (enrichment over input). (B) Normalized gene activity scores for Pol II occupancy within gene bodies. (C) Poising index. For (A) to (C), numbers are provided in table S3; “Early” and “Mid” denote stages. (D) Pol II is enriched upstream of the TSS. Genes with Pol II peaks near defined TSSs (11) were divided into four quartiles according to gene body activity scores (from low, black, to high, white) and graphed for Pol II across the gene. (E) Pol II at the *ceh-22* locus in early, mid-, and late or mixed stage embryos. Mixed population sample is from (6).

(16), but poising in *C. elegans* had been associated predominantly with starvation (6, 13). A likely explanation for the difference between the prior studies and ours is the embryonic stage (11). For example, we found that mixtures of embryos with a range of ages lacked poised Pol II for *ceh-22*, underscoring the importance of staging (fig. S4A).

To test whether *pha-4* affects Pol II occupancy, we performed Pol II ChIP with a *pha-4(ts)* temperature-sensitive strain that combines *pha-4(zu225nonsense)* with *smg-1(cc546ts)* (fig. S6A) (17). *smg-1(cc546)* alone served as a control. Growth of *pha-4(ts)* was complicated because *pha-4* is an essential gene, and therefore we relied on ChIP-quantitative PCR, which requires less material.

At restrictive temperature, *pha-4* mutants failed to accumulate poised Pol II at three tested loci (*ceh-22*, *T06D8.3*, and *K10D3.4*) or elongating Pol II at one (*M05B5.2*) (Fig. 3A and fig. S6B) (11). *mig-38*, which has PHA-4 bound but is expressed broadly, was not affected by *pha-4(ts)* (Fig. 3A). Recent studies found that Pol II poising was not tissue-specific for *Drosophila* muscle (16), but our analysis indicates that PHA-4 helps Pol II associate with its target foregut genes in worms.

Pioneer transcription factors promote chromatin opening at target genes to modulate gene expression. We therefore wondered whether chromatin opening by PHA-4 affected Pol II loading. We adapted FAIRE (7, 11) to track regions of the *C. elegans* genome with absent or unstable nucleosomes. In older, wild-type embryos,

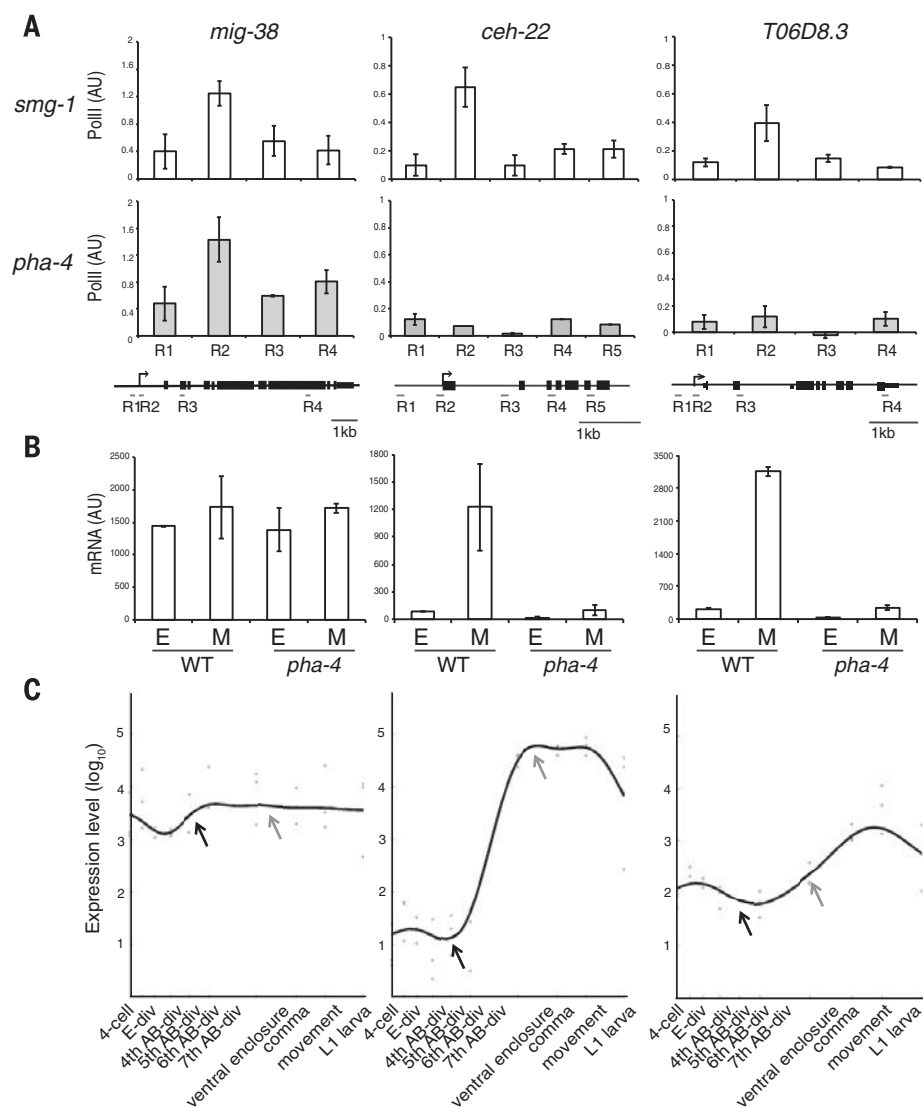


Fig. 3. PHA-4 is required for Pol II occupancy at foregut genes. (A) Pol II occupancy at *mig-38* (poised, ubiquitous) versus *ceh-22* and *T06D8.3* (poised, foregut) in *smg-1* control versus *pha-4(ts)* embryos, normalized to *eft-3* (set at 1) and *srw-99* (set at 0). Error bars indicate $n = 3$ replicates, mean \pm SEM. (B) mRNA abundance (quantitative RT-PCR) for *mig-38*, *ceh-22*, and *T06D8.3* for wild-type or *pha-4(ts)* embryos early (E) or mid (M). $n = 3$ replicates, mean \pm SEM. (C) Gene expression profiles from (20). Early stage (dark gray arrowhead) is at the fifth and sixth AB-div. Mid-stage (light gray arrowhead) is equivalent to ventral enclosure.

we found a strong correlation between PHA-4 binding and open chromatin, characterized by a high FAIRE signal, at both promoters (H2A.Z⁺, H3K4me3⁺, and H3K27ac⁺) and enhancers (H3K4me1/2⁺) (fig. S7). Conversely, Pol II occupancy was only weakly correlated with open chromatin (fig. S7A), which is similar to *Drosophila* (18). To determine the contribution of *pha-4* to chromatin opening, we surveyed three foregut genes by means of FAIRE-quantitative PCR at early and mid-stages after *pha-4* inactivation (Fig. 4A). At the 8E stage, *pha-4(ts)* embryos had a FAIRE signal equivalent to wild-type embryos for *ceh-22* and *K10D3.4*, suggesting that PHA-4 did not contribute to chromatin opening at these early stages. *T06D8.3*, however, showed a ~10% decrease in FAIRE, suggesting nucleosomes depended on *pha-4* for at least some opening. In mid-stage embryos, reduction of *pha-4*

lead to a decrease in open FAIRE regions spanning the PHA-4 binding site and the Pol II binding site for *T06D8.3* and *K10D3.4*. The effect was less dramatic for *ceh-22*, with a small reduction at the PHA-4 binding region. Nevertheless, PHA-4 still promoted *ceh-22* opening. These data suggest that PHA-4 promotes chromatin opening at mid-stages, at least for the surveyed genes, but has less of an effect early.

We extended these results in three ways. First, we determined that *pha-4(ts)* had no impact on three nonforegut genes (*eft-3*, *mig-38*, and *srw-99*) (Fig. 4A). Second, we used artificial chromosomes bearing PHA-4 target promoters and fluorescently tagged PHA-4 to examine chromatin opening in single cells (9). We observed decompaction of artificial chromosomes in the foregut of mid-stage embryos but not early embryos (Fig. 4, B to D) (9). Artificial chromosomes in nonforegut cells failed

to decompact at either stage (Fig. 4, B and C). Third, a comparison of wild-type 4E embryos (with little to no PHA-4) and 8E embryos (with detectable PHA-4) revealed a decrease in FAIRE values at the 8E for both foregut and nonforegut genes (fig. S7). Thus, PHA-4 binding did not induce detectable decompaction at the 8E stage compared with the 4E. The data suggest that PHA-4 induces decompaction predominantly at mid-stages, after Pol II binding.

This study reveals widespread poised Pol II during *C. elegans* development and shows that the pioneer transcription factor PHA-4 contributes to Pol II recruitment at poised and transcribed genes within the foregut. PHA-4 activity is critical during early embryonic stages when we observe Pol II recruitment, suggesting these early events are essential for proper organogenesis (17). *C. elegans* embryos develop in 13 hours, with rapid

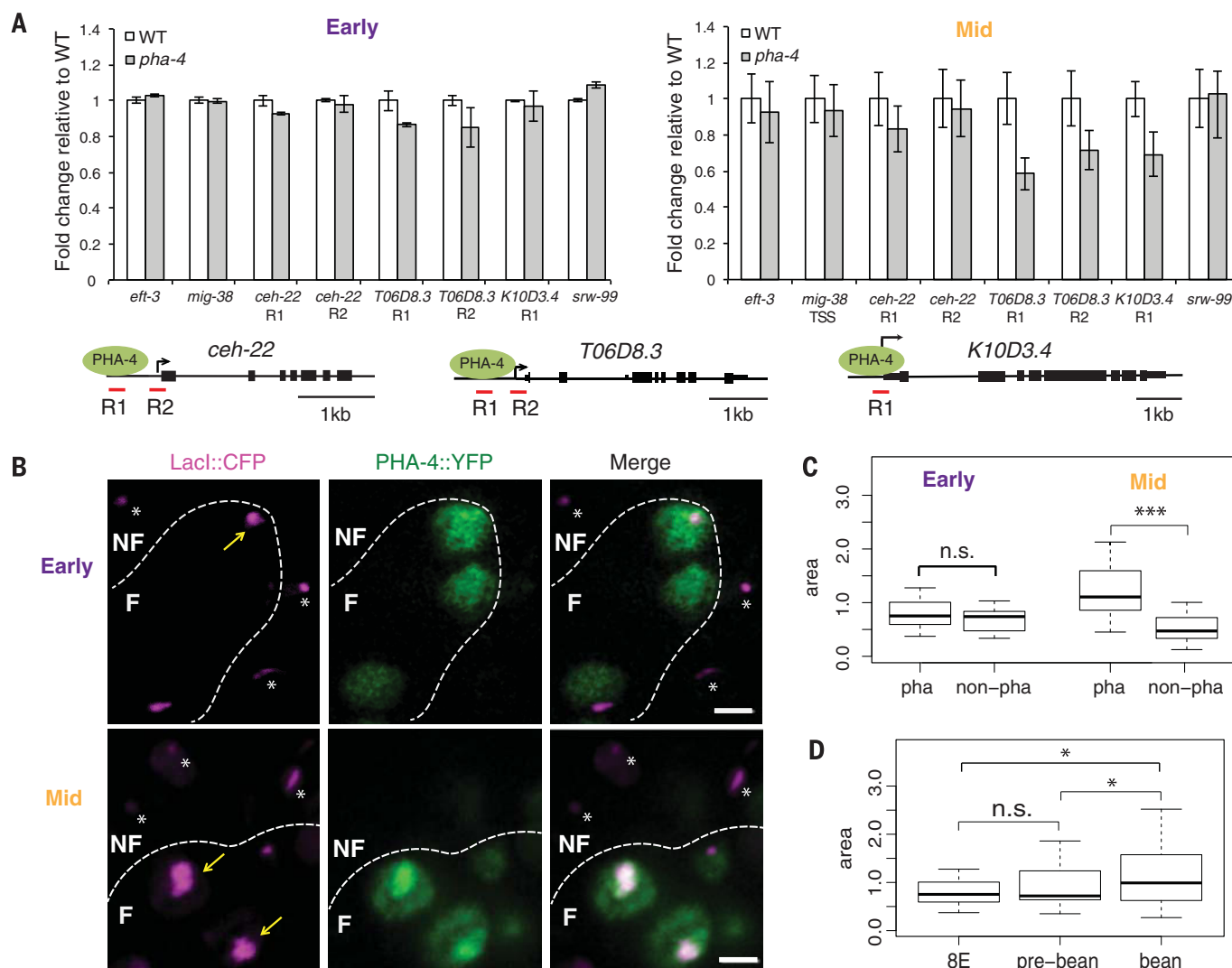


Fig. 4. PHA-4 promotes chromatin openness during mid-stage embryogenesis. (A) Chromatin opening tracked by FAIRE-quantitative PCR. Early (left), FAIRE signals for three poised foregut genes were similar between wild-type (white) and *pha-4(ts)* (gray). Mid- (right), FAIRE signals were reduced at poised foregut genes in *pha-4(ts)* embryos. The gene structures show positions for PHA-4 binding (R1) and TSS (R2) sites. *n* = 3 replicates, mean ± SEM. (B)

Artificial chromosomes (CFP::LacI, purple) bearing the *ceh-22* promoter bound by PHA-4::YFP (green) in early and mid-stage embryos. Dotted lines distinguish foregut (F) from nonforegut (NF). Scale bar, 2 μm. (C) Areas of artificial chromosomes carrying the *ceh-22* promoter in foregut (pha) versus nonforegut (non-pha). (D) Areas of artificial chromosomes carrying the *ceh-22* promoter in the foregut at different stages. **P* = 0.01 to 0.05; ****P* < 0.001.

changes in gene expression. Pol II poisoning may accommodate these dynamics by promoting rapid and/or synchronous transcriptional onset (12, 19). Recruitment of poised Pol II is followed by decompaction of chromatin. One appealing hypothesis is that deposition of Pol II at TSS regions may participate in chromatin opening, along with PHA-4 (18). This scenario predicts that Pol II binds to regions that would otherwise contain stable nucleosomes, a prediction that is borne out by our FAIRE analysis, and that Pol II interferes with the construction of nucleosomes. It will be of interest to see whether other pioneer factors or FoxA proteins also poise Pol II.

REFERENCES AND NOTES

- M. Iwafuchi-Doi, K. S. Zaret, *Genes Dev.* **28**, 2679–2692 (2014).
- D. L. D. L. Updike, S. E. S. E. Mango, *PLOS Genet.* **2**, e161 (2006).
- S. E. Mango, *Annu. Rev. Cell Dev. Biol.* **25**, 597–628 (2009).
- M. A. Horner *et al.*, *Genes Dev.* **12**, 1947–1952 (1998).
- J. M. Kalb *et al.*, *Development* **125**, 2171–2180 (1998).
- M. Zhong *et al.*, *PLOS Genet.* **6**, e1000848 (2010).
- P. G. Giresi, J. Kim, R. M. McDaniell, V. R. Iyer, J. D. Lieb, *Genome Res.* **17**, 877–885 (2007).
- J. W. K. Ho *et al.*, *Nature* **512**, 449–452 (2014).
- T. H. I. Fakhouri, J. Stevenson, A. D. Chisholm, S. E. Mango, *PLOS Genet.* **6**, e1001060 (2010).
- J. M. Caravaca *et al.*, *Genes Dev.* **27**, 251–260 (2013).
- Materials and methods are available as supplementary materials on Science Online.
- K. Adelman, J. T. Lis, *Nat. Rev. Genet.* **13**, 720–731 (2012).
- L. R. Baugh, J. Demodena, P. W. Sternberg, *Science* **324**, 92–94 (2009).
- C. S. C. S. Maxwell *et al.*, *Cell Reports* **6**, 455–466 (2014).
- C. A. Kuchenthal, W. Chen, P. G. Okkema, *Genesis* **31**, 156–166 (2001).
- B. Gaertner *et al.*, *Cell Reports* **2**, 1670–1683 (2012).
- J. C. Kiefer, P. A. Smith, S. E. Mango, *Dev. Biol.* **303**, 611–624 (2007).
- D. A. Gilchrist *et al.*, *Cell* **143**, 540–551 (2010).
- A. N. Boettiger, M. Levine, *Science* **325**, 471–473 (2009).
- M. Levin, T. Hashimshony, F. Wagner, I. Yanai, *Dev. Cell* **22**, 1101–1108 (2012).

ACKNOWLEDGMENTS

We thank J. Whetstone for ChIP advice, A. Schier and S. von Stetina for comments, and G. Marnellos and M. Clamp for informatics. Some strains were obtained from the Caenorhabditis Genetics Center (CGC), funded by NIH P40OD010440. S.E.M. received support from the MacArthur Foundation and grant NIH R37GM056264. E.L. received support from grant NSFMCB-1413134, and K.S.Z. received support from grant NIH R37GM36477. Sequencing data are accessible from the National Center for Biotechnology Information Gene Expression Omnibus: GSM1666978 R1.CE.8E.ChIP GSM1666979, R1.CE.8E.Input GSM1666980, R2.CE.8E.ChIP GSM1666981, R2.CE.8E.Input GSM1666982, R1.CE.BE.ChIP GSM1666983, and R1.CE.BE.Input.

SUPPLEMENTARY MATERIALS

www.sciencemag.org/content/348/6241/1372/suppl/DC1

Materials and Methods

Supplementary Text

Figs. S1 to S7

Tables S1 to S3

References

13 March 2015; accepted 12 May 2015

10.1126/science.aab1223

DRUG DEVELOPMENT

Phthalimide conjugation as a strategy for in vivo target protein degradation

Georg E. Winter,^{1*} Dennis L. Buckley,^{1*} Joshia Paulk,¹ Justin M. Roberts,¹ Amanda Souza,¹ Sirano Dhe-Paganon,² James E. Bradner^{1,3†}

The development of effective pharmacological inhibitors of multidomain scaffold proteins, notably transcription factors, is a particularly challenging problem. In part, this is because many small-molecule antagonists disrupt the activity of only one domain in the target protein. We devised a chemical strategy that promotes ligand-dependent target protein degradation using as an example the transcriptional coactivator BRD4, a protein critical for cancer cell growth and survival. We appended a competitive antagonist of BET bromodomains to a phthalimide moiety to hijack the cereblon E3 ubiquitin ligase complex. The resultant compound, dBET1, induced highly selective cereblon-dependent BET protein degradation in vitro and in vivo and delayed leukemia progression in mice. A second series of probes resulted in selective degradation of the cytosolic protein FKBP12. This chemical strategy for controlling target protein stability may have implications for therapeutically targeting previously intractable proteins.

Phthalimide-based drugs emerged in the 1950s. Among the most notable was thalidomide, developed initially as a sedative but infamously withdrawn from human use owing to catastrophic teratogenicity (1). More recently, the phthalimides have been successfully repurposed for erythema nodosum leprosum, multiple myeloma (MM), and myelodysplasia. The efficacy of thalidomide, lenalidomide, and pomalidomide in MM (Fig. 1A) has prompted investigation into the mechanism of action of phthalimide immunomodulatory drugs (IMiDs). By ligand-affinity chromatography, cereblon (CRBN)—a component of a cullin-RING ubiquitin ligase (CRL) complex—was identified as the target of thalidomide (2). Recently, our group and others reported that phthalimides prompt CRBN-dependent proteasomal degradation of transcription factors (TFs) IKZF1 and IKZF3 (3, 4). Crystallographic studies now establish that IMiDs bind CRBN to form a cryptic interface that promotes recruitment of IKZF1 and IKZF3 (5).

Ligand-induced target protein destabilization has proven to be an efficacious therapeutic strategy, in particular for cancer, as illustrated by arsenic trioxide-mediated degradation of the PML protein in acute promyelocytic leukemia (6) and estrogen receptor degradation by fulvestrant (7). Historically, target-degrading compounds have emerged serendipitously or through target-specific campaigns in medicinal chemistry. Chemical biologists have devised elegant solutions to modulate protein stability using engineered cellular systems, but these approaches have been limited to non-endogenous fusion proteins (8–11). Others have

achieved the degradation of endogenous proteins through the recruitment of E3 ligases, but these approaches have been limited by the requirement of peptidic ligands (12–14), the use of nonspecific inhibitors (15), and by low cellular potency.

RING-domain E3 ubiquitin-protein ligases lack enzymatic activity and function as adaptors to E2 ubiquitin-conjugating enzymes. Inspired by the retrieval of CRBN using a tethered thalidomide (2), we hypothesized that rational design of bifunctional phthalimide-conjugated ligands could confer CRBN-dependent target protein degradation as chemical adaptors. We selected BRD4 as an exemplary target. BRD4 is a transcriptional coactivator that binds to enhancer and promoter regions by recognition of acetylated lysines on histone proteins and TFs (16). Recently, we developed a direct-acting inhibitor of BET bromodomains (JQ1) (17) that displaces BRD4 from chromatin and leads to impaired signal transduction from TFs to RNA polymerase II (18–20). Silencing of BRD4 expression by RNA interference in murine and human models of MM and acute myeloid leukemia (AML) elicited rapid transcriptional down-regulation of the MYC oncogene and a potent antiproliferative response (19, 21). These and other studies in cancer, inflammation (22), and heart disease (23, 24) establish a desirable mechanistic and translational purpose to target BRD4 for selective degradation.

Having shown that the carboxyl group on JQ1 (25) and the aryl ring of thalidomide (5) can tolerate chemical substitution, we designed the bifunctional dBET1 to have preserved BRD4 affinity and an inactive epimeric dBET1(R) as a stereochemical control (Fig. 1, A and B). Selectivity profiling confirmed potent and BET-specific target engagement among 32 bromodomains (BromoScan) (Fig. 1C and tables S1 and S2). A high-resolution crystal structure (1.0 Å) of dBET1 bound to BRD4(1) confirmed the mode of molecular recognition, comparable to JQ1 (Fig. 1D, fig. S1, and

¹Department of Medical Oncology, Dana-Farber Cancer Institute, Boston, MA 02115, USA. ²Department of Cancer Biology, Dana-Farber Cancer Institute, Boston, MA 02115, USA. ³Department of Medicine, Harvard Medical School, Boston, MA 02115, USA.

*These authors contributed equally to this research. †Corresponding author. E-mail: james_bradner@dfci.harvard.edu

changes in gene expression. Pol II poisoning may accommodate these dynamics by promoting rapid and/or synchronous transcriptional onset (12, 19). Recruitment of poised Pol II is followed by decompaction of chromatin. One appealing hypothesis is that deposition of Pol II at TSS regions may participate in chromatin opening, along with PHA-4 (18). This scenario predicts that Pol II binds to regions that would otherwise contain stable nucleosomes, a prediction that is borne out by our FAIRE analysis, and that Pol II interferes with the construction of nucleosomes. It will be of interest to see whether other pioneer factors or FoxA proteins also poise Pol II.

REFERENCES AND NOTES

- M. Iwafuchi-Doi, K. S. Zaret, *Genes Dev.* **28**, 2679–2692 (2014).
- D. L. D. L. Updike, S. E. S. E. Mango, *PLOS Genet.* **2**, e161 (2006).
- S. E. Mango, *Annu. Rev. Cell Dev. Biol.* **25**, 597–628 (2009).
- M. A. Horner *et al.*, *Genes Dev.* **12**, 1947–1952 (1998).
- J. M. Kalb *et al.*, *Development* **125**, 2171–2180 (1998).
- M. Zhong *et al.*, *PLOS Genet.* **6**, e1000848 (2010).
- P. G. Giresi, J. Kim, R. M. McDaniell, V. R. Iyer, J. D. Lieb, *Genome Res.* **17**, 877–885 (2007).
- J. W. K. Ho *et al.*, *Nature* **512**, 449–452 (2014).
- T. H. I. Fakhouri, J. Stevenson, A. D. Chisholm, S. E. Mango, *PLOS Genet.* **6**, e1001060 (2010).
- J. M. Caravaca *et al.*, *Genes Dev.* **27**, 251–260 (2013).
- Materials and methods are available as supplementary materials on Science Online.
- K. Adelman, J. T. Lis, *Nat. Rev. Genet.* **13**, 720–731 (2012).
- L. R. Baugh, J. Demodena, P. W. Sternberg, *Science* **324**, 92–94 (2009).
- C. S. C. S. Maxwell *et al.*, *Cell Reports* **6**, 455–466 (2014).
- C. A. Kuchenthal, W. Chen, P. G. Okkema, *Genesis* **31**, 156–166 (2001).
- B. Gaertner *et al.*, *Cell Reports* **2**, 1670–1683 (2012).
- J. C. Kiefer, P. A. Smith, S. E. Mango, *Dev. Biol.* **303**, 611–624 (2007).
- D. A. Gilchrist *et al.*, *Cell* **143**, 540–551 (2010).
- A. N. Boettiger, M. Levine, *Science* **325**, 471–473 (2009).
- M. Levin, T. Hashimshony, F. Wagner, I. Yanai, *Dev. Cell* **22**, 1101–1108 (2012).

ACKNOWLEDGMENTS

We thank J. Whetstone for ChIP advice, A. Schier and S. von Stetina for comments, and G. Marnellos and M. Clamp for informatics. Some strains were obtained from the Caenorhabditis Genetics Center (CGC), funded by NIH P40OD010440. S.E.M. received support from the MacArthur Foundation and grant NIH R37GM056264. E.L. received support from grant NSFMCB-1413134, and K.S.Z. received support from grant NIH R37GM36477. Sequencing data are accessible from the National Center for Biotechnology Information Gene Expression Omnibus: GSM1666978 R1.CE.8E.ChIP GSM1666979, R1.CE.8E.Input GSM1666980, R2.CE.8E.ChIP GSM1666981, R2.CE.8E.Input GSM1666982, R1.CE.BE.ChIP GSM1666983, and R1.CE.BE.Input.

SUPPLEMENTARY MATERIALS

www.sciencemag.org/content/348/6241/1372/suppl/DC1

Materials and Methods

Supplementary Text

Figs. S1 to S7

Tables S1 to S3

References

13 March 2015; accepted 12 May 2015

10.1126/science.aab1223

DRUG DEVELOPMENT

Phthalimide conjugation as a strategy for in vivo target protein degradation

Georg E. Winter,^{1,*} Dennis L. Buckley,^{1,*} Joshiawa Paulk,¹ Justin M. Roberts,¹ Amanda Souza,¹ Sirano Dhe-Paganon,² James E. Bradner^{1,3,†}

The development of effective pharmacological inhibitors of multidomain scaffold proteins, notably transcription factors, is a particularly challenging problem. In part, this is because many small-molecule antagonists disrupt the activity of only one domain in the target protein. We devised a chemical strategy that promotes ligand-dependent target protein degradation using as an example the transcriptional coactivator BRD4, a protein critical for cancer cell growth and survival. We appended a competitive antagonist of BET bromodomains to a phthalimide moiety to hijack the cereblon E3 ubiquitin ligase complex. The resultant compound, dBET1, induced highly selective cereblon-dependent BET protein degradation in vitro and in vivo and delayed leukemia progression in mice. A second series of probes resulted in selective degradation of the cytosolic protein FKBP12. This chemical strategy for controlling target protein stability may have implications for therapeutically targeting previously intractable proteins.

Phthalimide-based drugs emerged in the 1950s. Among the most notable was thalidomide, developed initially as a sedative but infamously withdrawn from human use owing to catastrophic teratogenicity (1). More recently, the phthalimides have been successfully repurposed for erythema nodosum leprosum, multiple myeloma (MM), and myelodysplasia. The efficacy of thalidomide, lenalidomide, and pomalidomide in MM (Fig. 1A) has prompted investigation into the mechanism of action of phthalimide immunomodulatory drugs (IMiDs). By ligand-affinity chromatography, cereblon (CRBN)—a component of a cullin-RING ubiquitin ligase (CRL) complex—was identified as the target of thalidomide (2). Recently, our group and others reported that phthalimides prompt CRBN-dependent proteasomal degradation of transcription factors (TFs) IKZF1 and IKZF3 (3, 4). Crystallographic studies now establish that IMiDs bind CRBN to form a cryptic interface that promotes recruitment of IKZF1 and IKZF3 (5).

Ligand-induced target protein destabilization has proven to be an efficacious therapeutic strategy, in particular for cancer, as illustrated by arsenic trioxide-mediated degradation of the PML protein in acute promyelocytic leukemia (6) and estrogen receptor degradation by fulvestrant (7). Historically, target-degrading compounds have emerged serendipitously or through target-specific campaigns in medicinal chemistry. Chemical biologists have devised elegant solutions to modulate protein stability using engineered cellular systems, but these approaches have been limited to non-endogenous fusion proteins (8–11). Others have

achieved the degradation of endogenous proteins through the recruitment of E3 ligases, but these approaches have been limited by the requirement of peptidic ligands (12–14), the use of nonspecific inhibitors (15), and by low cellular potency.

RING-domain E3 ubiquitin-protein ligases lack enzymatic activity and function as adaptors to E2 ubiquitin-conjugating enzymes. Inspired by the retrieval of CRBN using a tethered thalidomide (2), we hypothesized that rational design of bi-functional phthalimide-conjugated ligands could confer CRBN-dependent target protein degradation as chemical adaptors. We selected BRD4 as an exemplary target. BRD4 is a transcriptional coactivator that binds to enhancer and promoter regions by recognition of acetylated lysines on histone proteins and TFs (16). Recently, we developed a direct-acting inhibitor of BET bromodomains (JQ1) (17) that displaces BRD4 from chromatin and leads to impaired signal transduction from TFs to RNA polymerase II (18–20). Silencing of BRD4 expression by RNA interference in murine and human models of MM and acute myeloid leukemia (AML) elicited rapid transcriptional down-regulation of the MYC oncogene and a potent antiproliferative response (19, 21). These and other studies in cancer, inflammation (22), and heart disease (23, 24) establish a desirable mechanistic and translational purpose to target BRD4 for selective degradation.

Having shown that the carboxyl group on JQ1 (25) and the aryl ring of thalidomide (5) can tolerate chemical substitution, we designed the bi-functional dBET1 to have preserved BRD4 affinity and an inactive epimeric dBET1(R) as a stereochemical control (Fig. 1, A and B). Selectivity profiling confirmed potent and BET-specific target engagement among 32 bromodomains (BromoScan) (Fig. 1C and tables S1 and S2). A high-resolution crystal structure (1.0 Å) of dBET1 bound to BRD4(1) confirmed the mode of molecular recognition, comparable to JQ1 (Fig. 1D, fig. S1, and

¹Department of Medical Oncology, Dana-Farber Cancer Institute, Boston, MA 02115, USA. ²Department of Cancer Biology, Dana-Farber Cancer Institute, Boston, MA 02115, USA. ³Department of Medicine, Harvard Medical School, Boston, MA 02115, USA.

*These authors contributed equally to this research. †Corresponding author: E-mail: james_bradner@dfci.harvard.edu

table S3). Using the dBET1-BRD4(1) crystal structure and the recently reported structure of CRBN bound to thalidomide (5), we have modeled the feasibility of ternary complex formation in silico. An extended conformation of dBET1 was capable of bridging ordered BRD4(1) and CRBN without destructive steric interactions (Fig. 1E). To experimentally assess the chemical adaptor function of dBET1, we established a homogeneous proximity assay for recombinant human CRBN-DDB1 damage-binding protein 1 (CRBN-DDB1) and BRD4(1) (Fig. 1F). Luminescence arising from proximity of CRBN-DDB1- and BRD4-bound acceptor-donor beads increases with low concentrations of dBET1 and decreases at higher concentrations, consistent with saturation of CRBN and BRD4 binding sites by excess ligand. Competitive incubation with free JQ1 or thalidomide inhibits

ternary complex formation in a stereo-specific manner (Fig. 1G).

To assess the effect of dBET1 in cells, we treated a human AML cell line (MV4;11) for 18 hours with increasing concentrations of dBET1 and assayed endogenous BRD4 levels by immunoblot. Pronounced loss of BRD4 (>85%) was observed with concentrations of dBET1 as low as 100 nM (Fig. 1H). The epimeric control dBET1(R) was inactive (Fig. 1B), which demonstrated that BRD4 degradation requires target protein engagement (fig. S2, A and B). The kinetics of BRD4 degradation were next determined using 100 nM dBET1 in MV4;11 cells. Marked depletion of BRD4 was observed at 1 hour, and complete degradation was observed at 2 hours of treatment (Fig. 1I). A partial recovery in BRD4 abundance at 24 hours establishes the possibility of compound instability, a recognized lia-

bility of phthalimides. To quantify dose-responsive effects on BRD4 protein stability, we developed a cell-count normalized, high-content assay using adherent SUM149 breast cancer cells (Fig. 1J). Depletion of BRD4 was observed for dBET1 [half-maximal effective dose (EC_{50}) = 430 nM] without apparent activity for dBET1(R), confirmed by immunoblot (fig. S2, C and D). Additional cultured adherent and nonadherent human cancer cell lines showed comparable response (SUM159, MOLM13) (fig. S3).

To explore the mechanism of dBET1-induced BRD4 degradation, we studied requirements on proteasome function, BRD4 binding, and CRBN binding using chemical genetic and gene-editing approaches. First, we confirmed that treatment with either JQ1 or thalidomide alone was insufficient to induce BRD4 degradation in MV4;11 cells

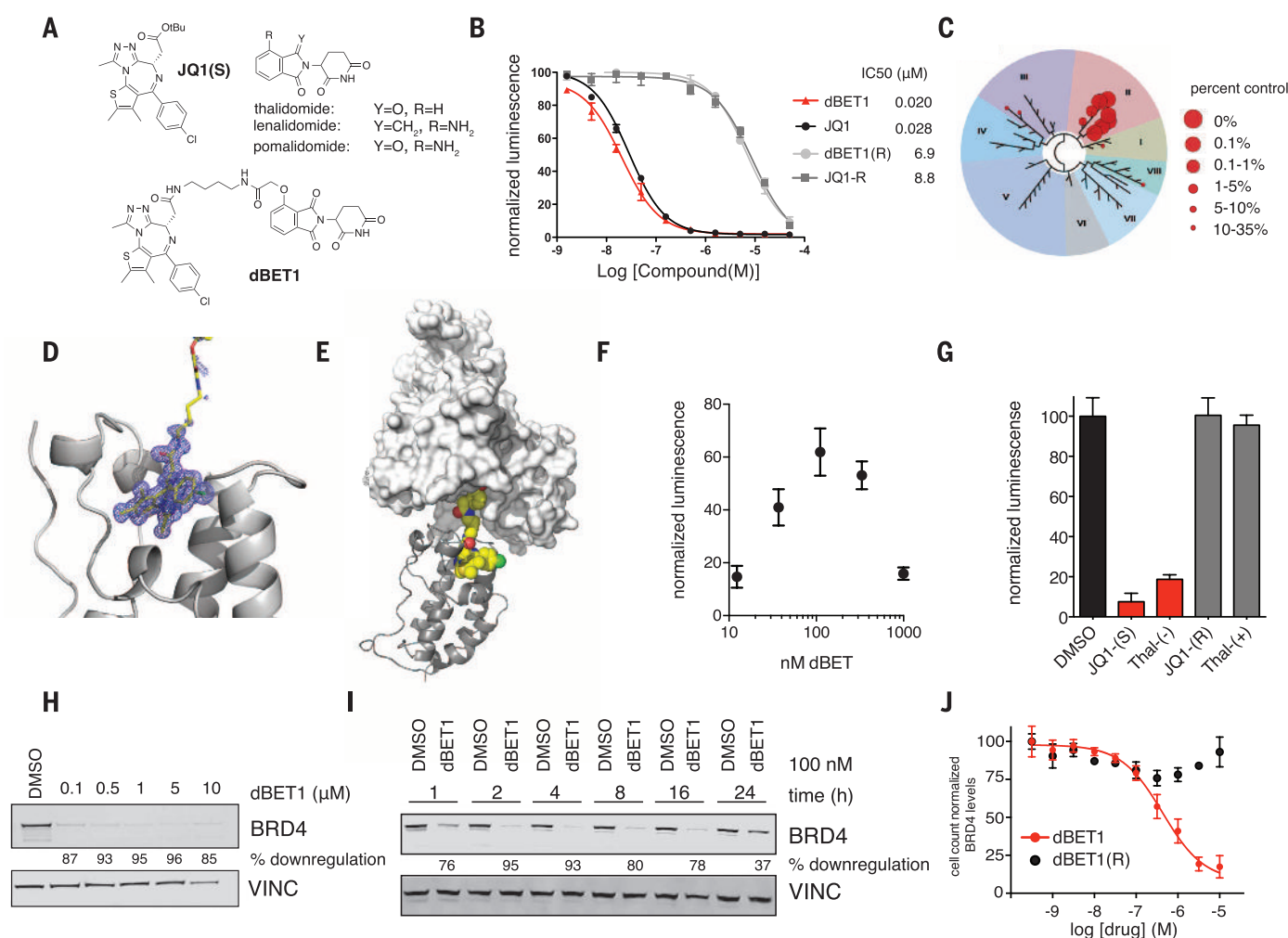


Fig. 1. Design and characterization of dBET1. (A) Chemical structure of JQ1 (S), phthalimides, and dBET1. (B) Vehicle-normalized BRD4 displacement by AlphaScreen (triplicate means \pm SD). (C) Selective displacement of phage-displayed BETs by dBET1 (BromoScan at 1 μ M; $n = 1$). (D) Crystal structure of dBET1 bound to BRD4 bromodomain 1 (E) Docking of (D) into the published DDB1-CRBN structure (F) dBET1-induced ternary complex formation of recombinant BRD4(1) and CRBN-DDB1 by AlphaScreen [quadruplicate means \pm SD; normalized to dimethyl sulfoxide (DMSO)]. (G) Competition of 111 nM dBET1-induced proximity as in (F) in the presence of vehicle (DMSO), JQ1,

thal(-), JQ1(R), and thal(+) all at 1 μ M. Values represent quadruplicate means \pm SD, normalized to DMSO. (H) Immunoblot for BRD4 and vinculin (VINC) after 18 hours of treatment of MV4;11 cells with the indicated concentrations of dBET1. (I) Immunoblot for BRD4 and vinculin after treatment of MV4;11 cells with 100 nM dBET1 for the indicated exposures. (J) Cell count-normalized BRD4 levels as determined by high-content imaging in SUM149 cells treated with the indicated concentrations of dBET1 and dBET1(R) for 18 hours. Values represent triplicate means \pm SD, normalized to DMSO-treated cells and baseline-corrected using immunoblots seen in fig. S2C.

(fig. S4A). Degradation of BRD4 by dBET1 was rescued by the proteasome inhibitor carfilzomib, which established a requirement for proteasome function (Fig. 2A). Pretreatment with excess JQ1 or thalidomide abolished dBET1-induced BRD4 degradation, consistent with a requirement for both BRD4 and CRBN engagement (Fig. 2A). Pretreatment with the NAE1 inhibitor MLN4924 (26) rescued BRD4 stability and established its dependence on CRL activity, as expected for cullin-based ubiquitin ligases that require neddylation for processive E3 ligase activity (4, 27) (fig. S4B). Finally, to definitively confirm the cellular requirement for CRBN, we used a previously published CRBN-deficient human MM cell line (MM1S-CRBN^{-/-}) (4). Whereas treatment of wild-type MM1S^{WT} cells with dBET1 promoted degradation of BRD4, exposure of MM1S-CRBN^{-/-} cells to dBET1 was ineffectual (Fig. 2B). These data provide mechanistic evidence for CRBN-dependent proteasomal degradation of BRD4 by dBET1.

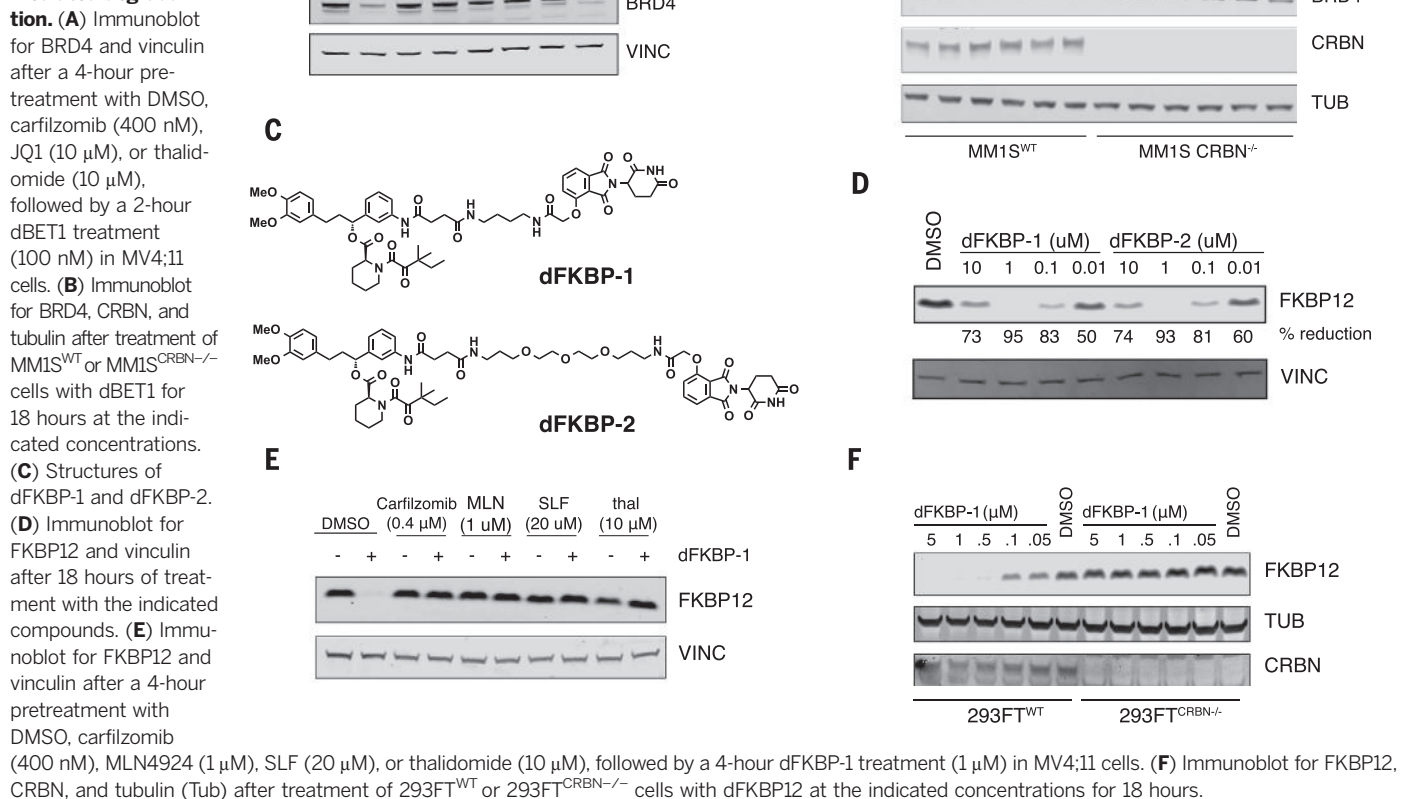
To assess the feasibility of extending this strategy to other protein targets, we designed and synthesized phthalimide-conjugated ligands to the cytosolic signaling protein FKBP12 (FKBP1A). FKBP12 has been extensively studied in the chemical biology literature, which includes studies of engineered target degradation and a growing literature on chemical dimerizers. At a known permissive site on the FKBP12-directed ligand steel factor (SLF), we positioned two chemical spacers

to create the conjugated phthalimides dFKBP-1 and dFKBP-2 (Fig. 2C). Both potently decreased FKBP12 abundance in MV4;11 cells (Fig. 2D). As with dBET1, destabilization of FKBP12 by dFKBP-1 was rescued by pretreatment with carfilzomib, MLN4924, free SLF, or free thalidomide (Fig. 2E). We established CRBN-dependent degradation using previously published isogenic 293FT cell lines that are wild type (293FT-WT) or deficient (293FT-CRBN^{-/-}) (4) for CRBN (Fig. 2F).

An unbiased, proteome-wide approach was selected to assess the cellular consequences of dBET1 treatment on protein abundance, in a quantitative and highly parallel format (28). We compared the immediate impact of dBET1 treatment (250 nM) to JQ1 and vehicle controls in MV4;11 cells. A 2-hour incubation was selected to capture primary, immediate consequences of small-molecule action and to mitigate expected, confounding effects on suppressed transactivation of BRD4 target genes. We prepared three biological sample replicates for each treatment condition using isobaric tagging that allowed the detection of 7429 proteins. After JQ1 treatment, few proteomic changes were observed (Fig. 3A and table S4). Only MYC was significantly depleted more than twofold after 2 hours of JQ1 treatment, which confirmed the reported rapid and selective effect of BET bromodomain inhibition on MYC abundance in AML (Fig. 3, A and C) (21). JQ1 treatment also down-regulated the oncoprotein PIM1 (Fig. 3, A and C).

Treatment with dBET1 elicited a comparable, modest effect on MYC and PIM1 expression. Remarkably, only three additional proteins were identified as significantly ($P < 0.001$) and markedly depleted (to one-fifth) in dBET1-treated cells: BRD2, BRD3, and BRD4 (Fig. 3, B and C). These findings are consistent with the anticipated, BET-specific bromodomain target spectrum of the JQ1 bromodomain-biasing element on dBET1 (17). The remaining BET-family member BRDT is not detectable in MV4;11 cells. To validate these findings, we measured BRD2, BRD3, BRD4, MYC, and PIM1 levels by immunoblot after compound treatment, as above. BET family members were degraded only by dBET1, whereas MYC and PIM1 abundance was decreased by both dBET1 and JQ1 (and to a lesser degree) (Fig. 3D). No effect on Ikaros TF expression was observed in either treatment condition (fig. S5). MYC and PIM1 are often associated with massive adjacent enhancer loci by epigenomic profiling (18, 20), which suggested a transcriptional mechanism of down-regulation. We therefore measured mRNA transcript abundance for each depleted gene product (Fig. 3E). Treatment with either JQ1 or dBET1 down-regulated MYC and PIM1 transcription, suggestive of secondary transcriptional effects. Transcription of BRD4 and BRD3 were unaffected, consistent with posttranscriptional effects. Note that transcription of BRD2 was affected by JQ1 and dBET1, whereas protein stability of the BRD2 gene product

Fig. 2. Chemical and genetic rescue of dBET1- and dFKBP-1-mediated degradation.



was only influenced by dBET1, suggestive of transcriptional and posttranscriptional consequences. These data establish a highly selective effect of dBET1 on target protein stability, proteome-wide.

We next explored the differential antiproliferative consequences of BET degradation with dBET1 to BET bromodomain inhibition with JQ1. Degradation of BRD4 by dBET1 was associated with an enhanced apoptotic response in MV4;11 AML and DHL4 lymphoma cells, as measured by

caspase activation (Caspase-GLO) (Fig. 4A), cleavage of poly(ADP-ribose) polymerase (PARP), cleavage of caspase-3 (immunoblot) (Fig. 4B), and Annexin V staining (flow cytometry) (fig. S6A). Kinetic studies revealed an apoptotic advantage for dBET1 after pulsed treatment followed by washout in MV4;11 cells (Fig. 4, C and D). Indeed, dBET1 induced a potent and superior inhibitory effect on MV4;11 cell proliferation at 24 hours (Fig. 4E).

The rapid biochemical activity and robust apoptotic response of cultured cell lines to dBET1 established the feasibility of assessing effects on primary human AML cells, where ex vivo proliferation is negligible in short-term cultures. Exposure of primary leukemic patient blasts to dBET1 elicited dose-proportionate depletion of BRD4 (Fig. 4F) and improved apoptotic response compared to JQ1 (Annexin V and propidium iodide staining) (Fig. 4G and fig. S6B). Together,

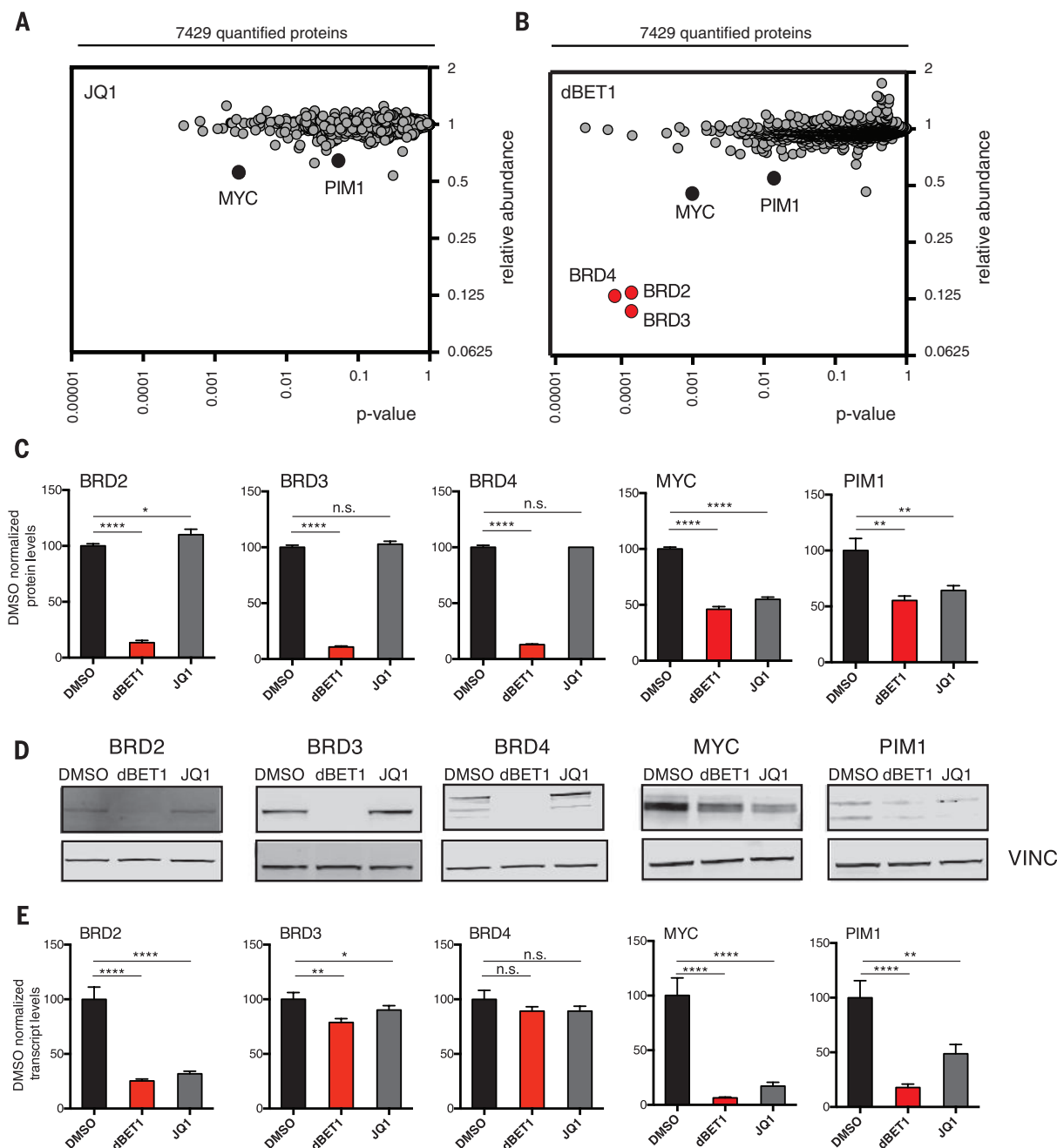


Fig. 3. Selective BET bromodomain degradation established by expression proteomics. MV4;11 cells were treated for 2 hours with DMSO, 250 nM dBET1, or 250 nM JQ1. **(A)** Fold-change in abundance of 7429 proteins comparing JQ1 to vehicle (DMSO) treatment, versus *P* value (*t*-test; triplicate analysis). **(B)** As for (A), but comparing 250 nM dBET1 to vehicle treatment. **(C)** Selected proteins from (A) and (B) normalized to vehicle. Values represent triplicate means \pm SD.

(D) Immunoblot of BRD2, BRD3, BRD4, MYC, PIM1, and vinculin (VINC) after a 2-hour treatment of MV4;11 cells with DMSO, 250 nM dBET1, or 250 nM JQ1. **(E)** Quantitative reverse transcription–polymerase chain reaction analysis of transcript levels of BRD2, BRD3, BRD4, MYC, and PIM1 after a 2-hour treatment of MV4;11 cells with DMSO, 250 nM dBET1, or 250 nM JQ1. Values represent triplicate means \pm SD. **P* = 0.01 to 0.05; ***P* = 0.001 to 0.01; *****P* < 0.0001.

these data exemplify that target degradation can elicit a more pronounced biological consequence than domain-specific target inhibition.

To model the therapeutic opportunity of BRD4 degradation in vivo, we first evaluated the tolerability and antitumor efficacy of dBET1 in a murine hind-limb xenograft model of human MV4;11 leukemia cells (29). As pharmacokinetic studies of dBET1 indicated adequate drug exposure in vivo (fig. S7A), tumor-bearing mice were treated with dBET1 administered by intraperitoneal injection (50 mg/kg body weight daily, ip) or vehicle control. After 14 days of therapy, a first tumor reached institutional limits for tumor size, and the study was terminated for comparative assessment of

efficacy and modulation of BRD4 stability and function. Administration of dBET1 attenuated tumor progression, as determined by serial volumetric measurement (Fig. 4H), and decreased tumor weight was assessed post mortem (fig. S8A). Acute pharmacodynamic degradation of BRD4 was observed by immunoblot 4 hours after a first or second daily treatment with dBET1 (50 mg/kg ip) (Fig. 4I), accompanied by down-regulation of MYC (Fig. 4I). These findings were confirmed by immunohistochemistry at the conclusion of the 14-day efficacy study (Fig. 4J). A statistically significant destabilization of BRD4, down-regulation of MYC, and inhibition of proliferation (Ki67 staining) was observed with dBET1 compared

with vehicle control in excised tumors (Fig. 4J and fig. S8B). Notably, 2 weeks of dBET1 was well tolerated with preservation of animal weight and normal complete blood counts (fig. S7, C and D). To compare the efficacy of BET inhibition to BET degradation, we selected an aggressive disseminated leukemia model (mCherry⁺ MV4;11) and treated animals with established disease using equimolar concentrations of JQ1 and dBET1 for 19 days. Post mortem analysis of leukemic burden in bone marrow by fluorescence-activated cell sorting revealed significantly decreased mCherry⁺ disease with dBET1 administration (Fig. 4K).

In summary, we present a mechanism-based chemical strategy for endogenous target protein

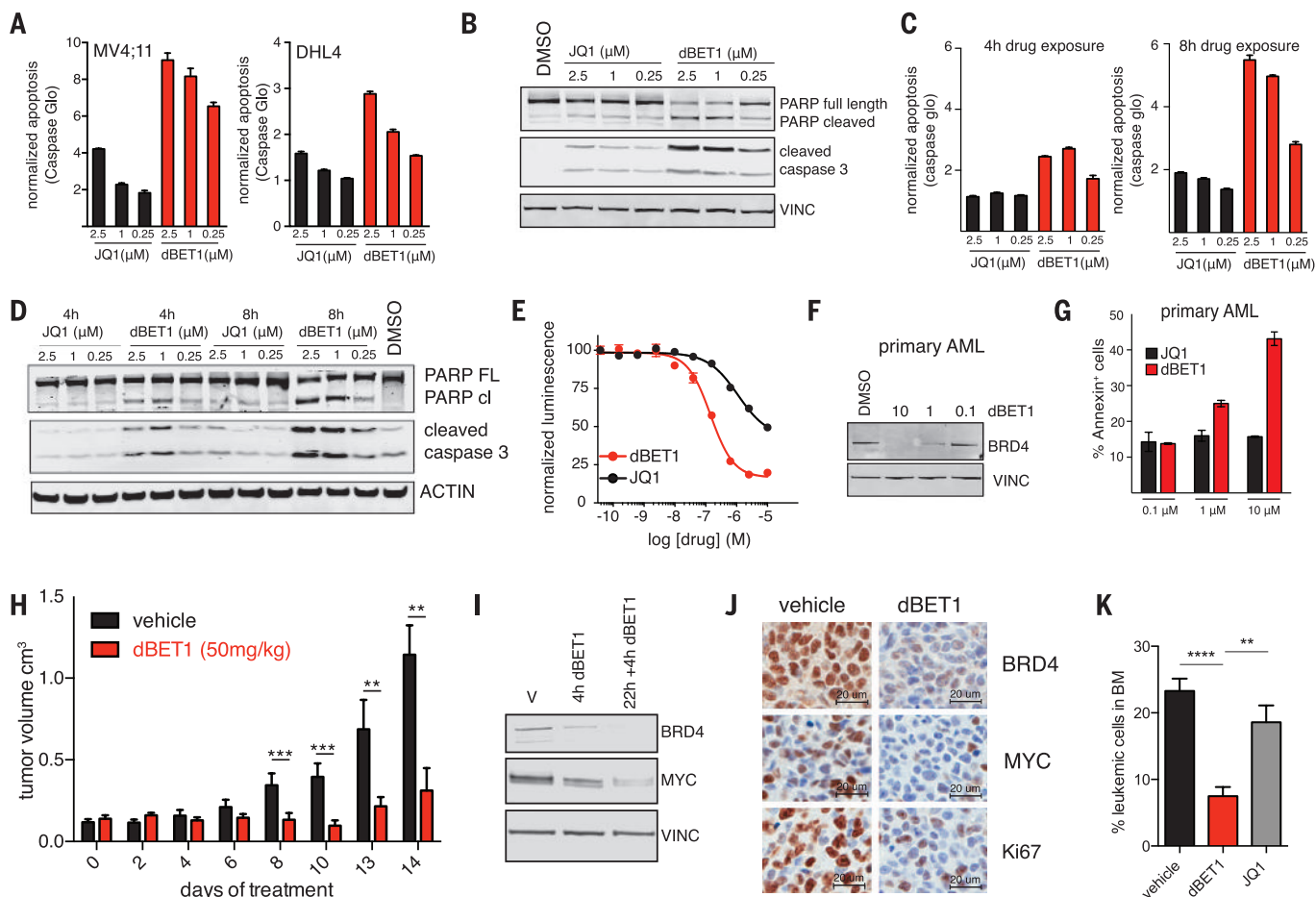


Fig. 4. The kinetic and antileukemic advantage of BET bromodomain degradation. (A) Fold increase of apoptosis, assessed via Caspase-Glo assay relative to DMSO-treated controls, 24 hours of treatment in MV4;11 or DHL4 cells. Values represent quadruplicate means \pm SD. (B) Immunoblot for cleaved caspase 3, PARP cleavage, and vinculin after treatment with dBET1 and JQ1 for 24 hours, as indicated. (C) Fold increase of apoptosis (Caspase-Glo) relative to DMSO-treated controls. MV4;11 cells were treated for 4 or 8 hours with JQ1 or dBET1 at the indicated concentrations. Drug was washed out with phosphate-buffered saline (3 times) before cells were plated in drug-free medium for a final treatment duration of 24 hours. Values represent quadruplicate means \pm SD. (D) Immunoblot for cleaved caspase 3, PARP cleavage, and vinculin after treatment conditions as described in (C). (E) Dose-proportional effect of dBET1 and JQ1 (24 hours) on MV4;11 cellular viability as approximated by adenosine triphosphate-dependent luminescence. Values represent quadruplicate means \pm SD. (F) Immunoblot for BRD4 and vinculin after treatment of

primary patient cells with the indicated concentrations of dBET1 for 24 hours. (G) Annexin V-positive primary patient cells after 24 hours of treatment with either dBET1 or JQ1 at the indicated concentrations. Values represent the average of duplicates and the range as error bars (representative scatter plots in fig. S6). (H) Tumor volume (means \pm SEM) of vehicle-treated mice ($n = 5$) or mice treated with dBET1 (50 mg/kg; $n = 6$) for 14 days. (I) Immunoblot for BRD4, MYC, and vinculin (VINC) by using tumor lysates from mice treated either once for 4 hours or twice for 22 hours and 4 hours, compared with a vehicle-treated control. (J) Immunohistochemistry for BRD4, MYC, and Ki67 of a representative tumor of a dBET1-treated and a control-treated mouse (quantification of three independent areas in fig. S8). (K) Percentage of mCherry⁺ leukemic cells (means \pm SEM) in flushed bone marrow from disseminated MV4;11 xenografts after daily treatment with dBET1 ($n = 8$) and JQ1 ($n = 8$) (both at 63.8 μ mol/kg) or formulation control ($n = 7$) for 19 days. *** $P = 0.0001$ to 0.001 ; other P values as in Fig. 3 legend.

degradation. Phthalimide conjugation to selective small molecules produces CRBN-dependent posttranslational degradation with exquisite target-specific activity. Although this approach is CRBN-dependent, CRBN is ubiquitously expressed in physiologic and pathophysiologic tissues, which supports its broad utility in developmental and disease biology. The increased apoptotic response of primary AML cells to dBET1, even compared with the efficacious tool compound JQ1, highlights the potential superiority of BET degradation over BET bromodomain inhibition and prompts consideration of therapeutic development. Pharmacologic destabilization of BRD4 in vivo also resulted in improved antitumor efficacy in a human leukemia xenograft compared with the effects of JQ1. The extension of this approach to new targets (here, FKBPI2), low molecular mass, high cell permeability, potent cellular activity, and synthetic simplicity addresses limitations associated with prior pioneering systems. We anticipate dFKBPI will also serve as a useful tool for the research community in control of fusion protein stability. A more general implication of this research is the feasibility of approaching intractable protein targets using phthalimide-conjugation of target-binding ligands that may or may not have target-specific inhibitory activity.

REFERENCES AND NOTES

1. J. B. Bartlett, K. Dredge, A. G. Dalgleish, *Nat. Rev. Cancer* **4**, 314–322 (2004).
2. T. Ito et al., *Science* **327**, 1345–1350 (2010).
3. J. Krönke et al., *Science* **343**, 301–305 (2014).
4. G. Lu et al., *Science* **343**, 305–309 (2014).
5. E. S. Fischer et al., *Nature* **512**, 49–53 (2014).
6. V. Lallemand-Breitenbach et al., *J. Exp. Med.* **193**, 1361–1372 (2001).
7. Y.-L. Wu et al., *Mol. Cell* **18**, 413–424 (2005).
8. M. R. Pratt, E. C. Schwartz, T. W. Muir, *Proc. Natl. Acad. Sci. U.S.A.* **104**, 11209–11214 (2007).
9. L. A. Banaszynski, L. C. Chen, L. A. Maynard-Smith, A. G. L. Ooi, T. J. Wandless, *Cell* **126**, 995–1004 (2006).
10. L. A. Banaszynski, M. A. Selmyer, C. H. Contag, T. J. Wandless, S. H. Thorne, *Nat. Med.* **14**, 1123–1127 (2008).
11. T. K. Neklesa et al., *Nat. Chem. Biol.* **7**, 538–543 (2011).
12. K. M. Sakamoto et al., *Proc. Natl. Acad. Sci. U.S.A.* **98**, 8554–8559 (2001).
13. J. S. Schneekloth Jr. et al., *J. Am. Chem. Soc.* **126**, 3748–3754 (2004).
14. J. Hines, J. D. Gough, T. W. Corson, C. M. Crews, *Proc. Natl. Acad. Sci. U.S.A.* **110**, 8942–8947 (2013).
15. Y. Itoh, M. Ishikawa, M. Naito, Y. Hashimoto, *J. Am. Chem. Soc.* **132**, 5820–5826 (2010).
16. P. Filippakopoulos, S. Knapp, *Nat. Rev. Drug Discov.* **13**, 337–356 (2014).
17. P. Filippakopoulos et al., *Nature* **468**, 1067–1073 (2010).
18. B. Chapuy et al., *Cancer Cell* **24**, 777–790 (2013).
19. J. E. Delmore et al., *Cell* **146**, 904–917 (2011).
20. J. Lovén et al., *Cell* **153**, 320–334 (2013).
21. J. Zuber et al., *Nature* **478**, 524–528 (2011).
22. E. Nicodeme et al., *Nature* **468**, 1119–1123 (2010).
23. P. Anand et al., *Cell* **154**, 569–582 (2013).
24. J. D. Brown et al., *Mol. Cell* **56**, 219–231 (2014).
25. L. Anders et al., *Nat. Biotechnol.* **32**, 92–96 (2014).
26. T. A. Soucy et al., *Nature* **458**, 732–736 (2009).
27. R. I. Sufan, M. Ohh, *Neoplasia* **8**, 956–963 (2006).
28. E. L. Huttlin et al., *Cell* **143**, 1174–1189 (2010).
29. J. A. Mertz et al., *Proc. Natl. Acad. Sci. U.S.A.* **108**, 16669–16674 (2011).

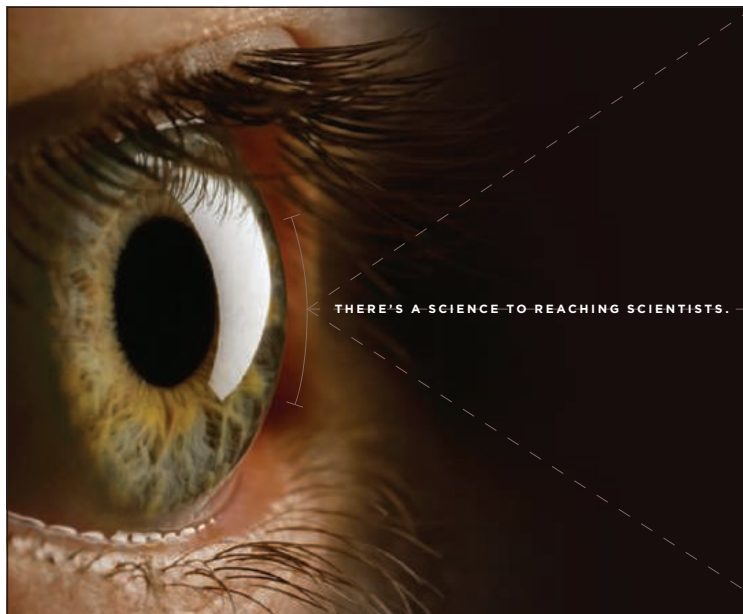
ACKNOWLEDGMENTS

We thank W. Kaelin, S. Orkin, and R. Mazitschek for engaging discussions and W. Kaelin for cellular reagents; S.-H. Seo and S. Deangelo for assistance in the purification of BRD4; C. Ott for help with in vivo model studies; and N. Thoma for CRBN expression reagents. This research was supported by generous philanthropic gifts from Marc Cohen and Alain Cohen, the William Lawrence and Blanche Hughes Foundation, and the NIH (R01-CA176745 and P01-CA066996 to J.E.B.). G.E.W. is supported by an EMBO long-term fellowship. D.L.B. is a Merck Fellow of the Damon Runyon Cancer Research Foundation (DRG-2196-14). Atomic coordinates and structure factors have been deposited in the Protein Data Bank (accession code 4ZC9). Quantitative proteomics studies were performed by R. Kunz of the Thermo Fisher Scientific Center for Multiplexed Proteomics at Harvard Medical School. Dana-Farber Cancer Institute has filed patent applications (62/096,318; 62/128,457; 62/149,170) that include the dBET and dFKBP compositions described in this manuscript. J.E.B. is a Founder of Tensha Therapeutics, a biotechnology company that develops druglike derivatives of JQ1 as investigational cancer therapies.

SUPPLEMENTARY MATERIALS

www.sciencemag.org/content/348/6241/1376/suppl/DC1
Materials and Methods
Figs. S1 to S8
Tables S1 to S3
References (30–36)

17 March 2015; accepted 6 May 2015
Published online 21 May 2015;
10.1126/science.aab1433



Save these Dates!

Postdoc Careers

August 28, 2015

Reserve ads by August 11 to guarantee space

THERE'S A SCIENCE TO REACHING SCIENTISTS.

Faculty Careers

September 18, 2015

Reserve ads by September 1 to guarantee space

For recruitment in science, there's only one **Science**

Two Fantastic Recruiting Opportunities!

POSTDOC CAREERS | August 28, 2015

Be sure to promote your openings to the thousands of scientists who read *Science* to find out about the latest postdoc opportunities.

Reserve space by August 11, 2015.

FACULTY CAREERS | September 18, 2015

Gear up to recruit for the faculty positions at your university with this much anticipated issue that reaches thousands of Ph.D. scientists looking for positions in academia.

Reserve space by September 1, 2015.



Produced by the *Science*/AAAS Custom Publishing Office.

SCIENCECAREERS.ORG

Science Careers
FROM THE JOURNAL SCIENCE  AAAS

To book your ad: advertise@sciencecareers.org

The Americas
202-326-6582

Europe/RoW
+44(0)1223-326500

Japan
+81-3-3219-5777

China/Korea/Singapore/Taiwan
+86-186-0082-9345

Join Keystone Symposia in Asia for our October Conferences on Nutrition and Diabetes

Human Nutrition, Health and Environment

October 14–18, 2015

China World Hotel | Beijing | China

Scientific Organizers: Martin Kussmann, Hannelore Daniel and Jacqueline Pontes Monteiro

Understanding interactions of nutrition and lifestyle with an individual's genetic makeup is vital for maintaining health and delaying disease onset. Toward that end, this meeting aims to: 1) Bring together researchers from traditionally separated disciplines: nutrition, (gen)omics, clinics, physiology, epidemiology, analytics, biomathematics; 2) Advance nutrition research as a quantitative, holistic and molecular science; 3) Review/challenge classical pre-clinical models and clinical study designs, incorporating improved translational in vitro and in vivo models, human intervention study designs, and innovative new tools/technologies for molecular phenotyping; and 4) Connect basic science to patient- and consumer-relevant outputs in terms of personalized dietary/nutritional counseling and monitoring/diagnostics.

Session Topics:

- The Interaction between Human Genome, Diet and Environment
- Translational Models for Human Nutrition and Health
- Human Nutritional and Lifestyle Interventions
- Capturing and Monitoring Human Individuality
- From Nutrigenomics to Systems Nutrition
- Nutrition 2.0 – Translation into Solutions for Human Health
- Global Nutrition and Sustainability

Global Health Travel Award Deadline (for investigators from developing countries): May 12, 2015;

Scholarship & Discounted Abstract Deadline: June 16, 2015; Abstract Deadline: July 14, 2015; Discounted Registration Deadline: August 13, 2015

For additional details, visit www.keystonesymposia.org/15T1.

Diabetes: New Insights into Molecular Mechanisms and Therapeutic Strategies

October 25–29, 2015

Westin Miyako Kyoto | Kyoto | Japan

Scientific Organizers: Takashi Kadowaki, Juleen R. Zierath, Nobuya Inagaki and Barbara B. Kahn

The prevalence of type 2 diabetes is rising to epidemic proportions worldwide. Type 2 diabetes is a complex disease caused by dysfunction of multiple organ systems, and disease susceptibility is profoundly influenced by both genetic and environmental factors. This meeting brings together leading professionals in the academic and pharmaceutical communities with various specialties in diabetes research to share new approaches and research paradigms. The meeting will present the latest discoveries in diabetes research, highlighting essential aspects of diabetes, as well as emerging themes that are likely to provide novel therapeutic approaches.

Session Topics:

- Islet Dysfunction in Diabetes
- Regenerative Medicine in Diabetes
- Gut Biology and Systemic Metabolism
- CNS Control of Metabolism
- Novel Insights into Adipocyte Biology
- Molecular Mechanisms Underlying Insulin Resistance
- Genetics and Epigenetics of Diabetes
- Diabetes and Healthy Lifespan

Scholarship & Discounted Abstract Deadline: June 25, 2015; Abstract Deadline: July 23, 2015; Discounted Registration Deadline: August 25, 2015

For additional details, visit www.keystonesymposia.org/15T2.



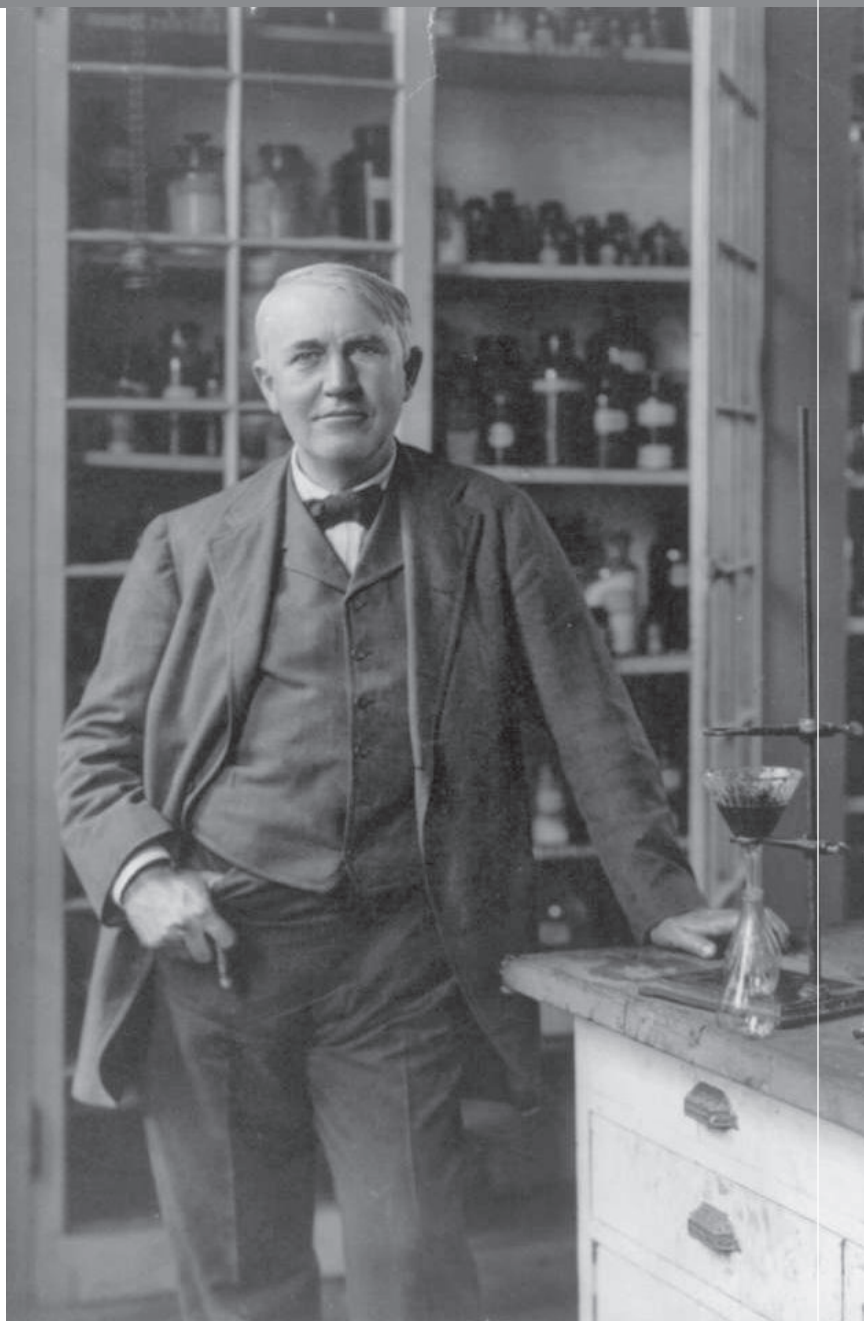
WHAT DO YOU AND THOMAS EDISON HAVE IN COMMON?

AAAS.

By investing in AAAS you join Thomas Edison and the many distinguished individuals whose vision led to the creation of AAAS and our world-renowned journal, *Science*, more than 150 years ago.

Like Edison, you can create a legacy that will last well into the future through planned giving to AAAS. By making AAAS a beneficiary of your will, trust, retirement plan, or life insurance policy, you make a strong investment in our ability to advance science in the service of society for years to come.

To discuss your legacy planning, contact Juli Staiano, Director of Development, at (202) 326-6636, or jstaiano@aaas.org, or visit www.aaas.org/1848 for more information.



"I feel great knowing that I will leave behind a legacy that will be channeled through the AAAS. It also means a lot to me to be able to honor my late parents, too."

—PETER ECKEL
Member, 1848 Society and AAAS Member since 1988



Four-Axis SCARA-Type Robot

Bolster your automated workflows with a self-correcting, learning robot that can employ a new four-axis “selective compliance articulated robot arm,” or SCARA. The Spinnaker Smart Laboratory Robot has built-in vision coupled with Thermo Scientific Momentum 4 software to eliminate the need for users to manually correct for drift that occurs over time by automatically compensating for positional variations. This is particularly important for systems in environmental enclosures, where gaining access to the system can be disruptive. Spinnaker’s robot vision capability and software also guide users through a simple step-wise procedure for configuring automation and teaching the system about its environment. The robot-vision camera doubles as a barcode reader, enabling automatic confirmation of sample identification, simplifying the workflow and contributing to robust sample tracking and system fidelity. The arm’s flexible reach, infinite rotation, and full gravity-neutral joints facilitate positioning when teaching or integrating instruments.

Thermo Fisher Scientific

For info: 800-556-2323

www.thermoscientific.com/spinnaker

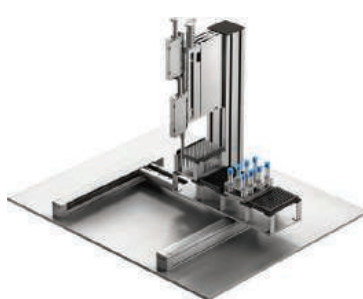
Automated Module

The [MPE]² is a first of its kind automated module that is designed to be used for positive pressure, evaporation, and cap mat sealing. The [MPE]² has a small footprint and can be easily integrated onto any of Hamilton’s liquid handling robotic systems. The [MPE]²’s small size makes it scalable allowing the addition of multiple units on a single liquid handler. The [MPE]² incorporates three functionalities in one. [MPE]² is a positive pressure SPE with a dual circuit even-flow manifold capable of applying up to 100 psi of pressure to the top of an SBS footprint filter plate/column; [MPE]² is an evaporator that can deliver heated air of up to 32°C (90°F) to accelerate evaporation of the liquids contained within the plates/columns; and the [MPE]² is a cap mat sealer that uses air pressure to attach the sealant to the plate.

Hamilton Robotics

For info: 800-648-5950

www.hamiltoncompany.com



Advanced Handling System

The EXCM mini H-gantry is a new high-speed, precise, automated handling system designed for laboratory applications. The planar surface gantry system is fast, accurate, modular, and flexible. It is also plug-and-play for quick and easy start up. Typical applications include transfer of microwell plates, liquid dispensing/pipetting with the addition of a z axis, sample preparation and transport, barcode-based sample identification, sample distribution, and aspirating, incubating, dispensing, and archiving of samples. This system moves samples on a planar x/y axis with an absolute positioning accuracy of ± 0.05 inches and a repetition accuracy of ± 0.01 inches. A new generation of laboratory devices from Festo enables the automated identification and testing of primary samples. With the use of barcode identification, these automated systems prepare the samples for the required tests and distribute samples to the corresponding test stations. Festo systems are available for preanalytical processes, analytical processes, and postanalytical processes.

Festo

For info: 800-993-3786

www.festo.com/us

Nanoliter-Scale Immunoassay

A smaller version of the widely used five-CD Gyrolab xP workstation, Gyrolab xPlore is a more compact, cost-effective, single-CD tool that makes automated nanoliter-scale immunoassays accessible to laboratories of every size. Using proven microfluidic technology, Gyrolab xPlore optimizes immunoassay development, enabling faster assay development, validation, and high throughput analyses in less time than with manual enzyme-linked immunosorbent assay or semi-automated methods. Gyros’ technology delivers high-quality data with broad dynamic ranges and excellent reproducibility while dramatically reducing sample and reagent consumption. Gyrolab systems use precise, automated control of centrifugal and capillary forces to steer liquid flow through nanoliter-scale microfluidic structures contained within Gyrolab CDs, automating the assay workflow. Gyrolab xPlore is a cost-effective tool that will accelerate assay development for discovery and preclinical R&D, help users meet critical data and time requirements for regulated bioanalysis, and improve efficiency in bioprocess development and quality control.

Gyros

For info: +46-(0)-18-56-63-00

www.gyros.com

Capillary Gel Electrophoresis Analyzer

The Qsep100 DNA Analyzer performs rapid, high-sensitivity assays at lower cost per sample compared to similar systems. Capillary gel electrophoresis with laser-induced fluorescence is a powerful analytical tool for DNA analysis and immunoassays, effectively replacing time-consuming and labor-intensive slab-gel electrophoresis technology. Capillary gel electrophoresis technology is recognized as an optimal approach to performing post-polymerase chain reaction separation, detection of DNA

and RNA fragments, and assessing the quality of genomic DNA. The Qsep100 DNA Analyzer uses microcapillary gel electrophoresis combined with fluorescence detection and is capable of performing 200 assays automatically as quickly as 2 minutes per sample. Qsep100 is a fast and highly sensitive analyzer for DNA and RNA assays. The Qsep100 DNA Analyzer quickly resolves DNA fragments in the range of 10 to 20,000 base pairs (bp) with 2 to 4 bp resolution. The compact analyzer is supplied with a 12-well or 96-well sample loader.

Precision Biosystems

For info: 888-490-4443

www.precisionbiosystems.com

Electronically submit your new product description or product literature information! Go to www.sciencemag.org/products/newproducts.dtl for more information.

Newly offered instrumentation, apparatus, and laboratory materials of interest to researchers in all disciplines in academic, industrial, and governmental organizations are featured in this space. Emphasis is given to purpose, chief characteristics, and availability of products and materials. Endorsement by *Science* or AAAS of any products or materials mentioned is not implied. Additional information may be obtained from the manufacturer or supplier.

Will you be meeting a Nobel Prize winner this December?

(If you have a recent PhD you could be.)

Stockholm in the second week of December is a special place. The city is alive with excitement as it welcomes and celebrates the new Nobel Laureates at the annual Nobel Prize ceremony.

If you are a PhD student, you could be here too – meeting a Nobel Laureate and receiving a rather special prize yourself.

The journal *Science* & SciLifeLab have established The *Science* & SciLifeLab Prize for Young Scientists, to recognize and reward excellence in PhD research and support young scientists at the start of their careers. It's about bright minds, bright ideas and bright futures.

Four winners will be selected for this international award. They will have their essays published in the journal *Science* and share a new total of 60,000 USD in prize money. The winners will be awarded in Stockholm, in December, and take part in a unique week of events including meeting leading scientists in their fields.

"The last couple of days have been exhilarating. It has been an experience of a lifetime. Stockholm is a wonderful city and the Award winning ceremony exceeds my wildest dreams."
–Dr. Dan Dominissini, 2014 Prize Winner

Who knows, The *Science* & SciLifeLab Prize for Young Scientists could be a major stepping stone in your career and hopefully one day, during Nobel week, you could be visiting Stockholm in December once again.

The 2015 Prize is now open. The deadline for submissions is August 1, 2015.

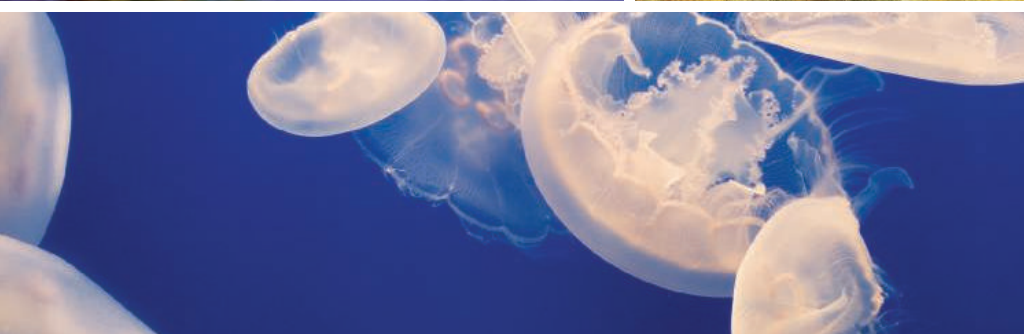
Enter today: www.sciencemag.org/scilifelabprize

The 2015 Prize categories are:

- Cell and Molecular Biology
- Ecology and Environment
- Genomics and Proteomics
- Translational Medicine



This prize is made possible with the kind support of the Knut and Alice Wallenberg Foundation. This Foundation grants funding in two main areas; research projects of high scientific potential and individual support of excellent scientists.



Celebrating 40 Years of Passion in Science

The 2015-16 NEB Catalog & Technical Reference

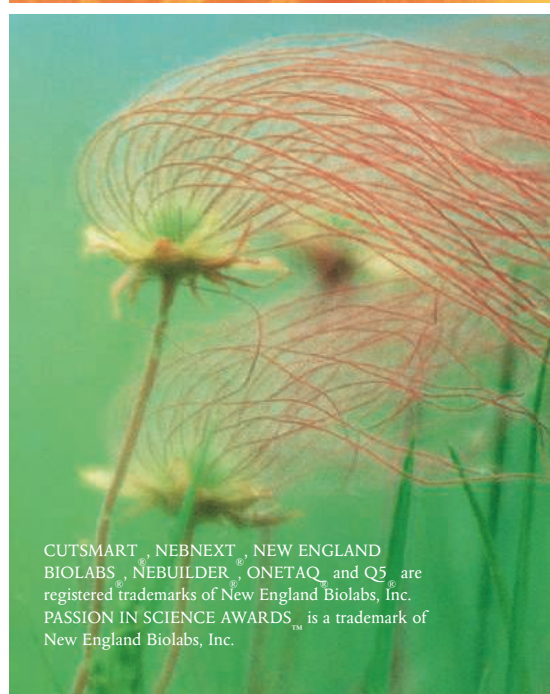
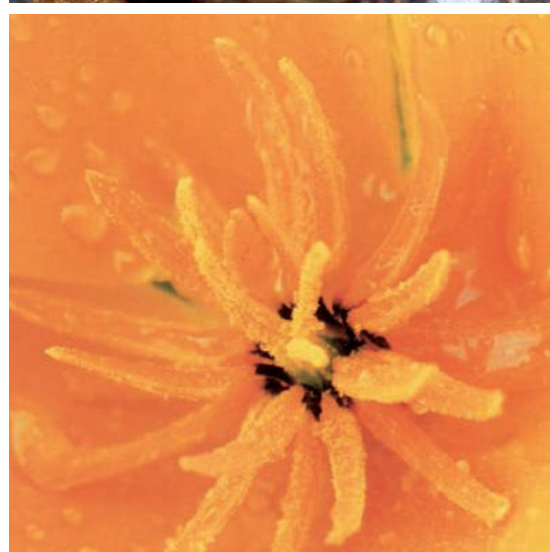
New England Biolabs introduces the latest edition of its award-winning Catalog & Technical Reference, featuring over 50 new products, up-to-date selection charts, protocols and troubleshooting tips. This collectible features your favorite catalog covers from the past 40 years, as well as the inspiring stories of our 2014 Passion in Science Awards™ Winners.

Featured Products:

- > 200 restriction enzymes now 100% active in CutSmart[®] Buffer
- OneTaq[®] and Q5[®] DNA Polymerases – robust amplification of a wide range of templates (routine, AT- and GC-rich)
- NEBuilder[®] HiFi DNA Assembly – virtually error-free assembly of multiple DNA fragments
- NEBNext[®] reagents for NGS library preparation – now includes kits for FFPE DNA, rRNA Depletion and Microbiome DNA

To request a copy, visit

www.neb.com/newcatalog



CUTSMART[®], NEBNext[®], NEW ENGLAND BIOLABS[®], NEBuilder[®], ONETAQ[®], and Q5[®] are registered trademarks of New England Biolabs, Inc. PASSION IN SCIENCE AWARDS[™] is a trademark of New England Biolabs, Inc.



There's only one **Science**

Science Careers Advertising

For full advertising details, go to ScienceCareers.org and click For Employers, or call one of our representatives.

Tracy Holmes

Worldwide Associate Director
Science Careers
Phone: +44 (0) 1223 326525

THE AMERICAS

E-mail: advertise@sciencecareers.org

Fax: +1 (202) 289 6742

Tina Burks

Phone: +1 (202) 326 6577

Nancy Toema

Phone: +1 (202) 326 6578

Online Job Posting Questions

Phone: +1 (202) 312 6375

EUROPE/INDIA/AUSTRALIA/ NEW ZEALAND/REST OF WORLD

E-mail: ads@science-int.co.uk

Fax: +44 (0) 1223 326532

Axel Gesatzki

Phone: +44 (0) 1223 326529

Sarah Lelarge

Phone: +44 (0) 1223 326527

Kelly Grace

Phone: +44 (0) 1223 326528

Online Job Posting Questions

Phone: +44 (0) 1223 326528

JAPAN

Katsuyoshi Fukamizu (Tokyo)

E-mail: kfukamizu@aaas.org
Phone: +81 3 3219 5777

Hiroyuki Mashiki (Kyoto)

E-mail: hmashiki@aaas.org
Phone: +81 75 823 1109

CHINA/KOREA/SINGAPORE/ TAIWAN/THAILAND

Ruolei Wu

Phone: +86 186 0082 9345
E-mail: rwu@aaas.org

All ads submitted for publication must comply with applicable U.S. and non-U.S. laws. *Science* reserves the right to refuse any advertisement at its sole discretion for any reason, including without limitation for offensive language or inappropriate content, and all advertising is subject to publisher approval. *Science* encourages our readers to alert us to any ads that they feel may be discriminatory or offensive.

ScienceCareers

FROM THE JOURNAL SCIENCE 

ScienceCareers.org

EBERHARD KARLS
UNIVERSITÄT
TÜBINGEN



WERNER REICHARDT CENTRE
FOR INTEGRATIVE NEUROSCIENCE

Junior Research Group for Neuroscientists at the Werner Reichardt Centre for Integrative Neuroscience (CIN) in Tübingen

The Werner Reichardt Centre for Integrative Neuroscience (CIN) is an interdisciplinary research institution at the Eberhard Karls University Tübingen, funded by the German Excellence Initiative Program. The CIN strives to deepen our understanding of how the brain generates function and how brain diseases impair functions. It tries to make use of newly acquired insights to help people with brain disorders and to launch new mind- and brain-inspired applications in many areas of engineering and computer science. Its scientific program is guided by the conviction that progress in the understanding of brain function can only be achieved by an integrative approach spanning multiple levels of organization and pooling the knowledge of researchers from many different fields. In order to strengthen specific research areas, the CIN offers a junior group leader (JRG) position for up-and-coming young scientists with a promising track record in any field of basic and applied neuroscience. The CIN strives to increase the number of female scientists. **Therefore qualified female candidates are particularly encouraged to apply.**

The submission deadline for this position is **30 July 2015**.

Framework: The intended duration of the position is for 5 years, with evaluations by external experts at regular intervals. Start-up funds as well as substantial funding for personnel and running costs will be available, but will depend on the applicant's qualifications and prior experience. Appointees will be full members of and active participants in the CIN, which will also provide laboratory and/or office space. The JRG leader will be provided with opportunities to contribute to research-oriented training within the framework of the CIN Graduate Training Centre.

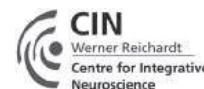
According to German law, severely disabled persons with equal occupational aptitude will be given preferential consideration.

Applicants should submit

- a curriculum vitae,
- up to 5 key publications (as pdf-files),
- a statement of research achievements and future directions (not to exceed 3 pages),
- the names and addresses of at least three referees.

All documents should be submitted electronically and addressed to Prof. Dr. Peter Thier, Chairman of the Werner Reichardt Centre for Integrative Neuroscience (CIN), Tübingen; E-Mail: cin@cin.uni-tuebingen.de

For further information on the CIN go to: www.cin.uni-tuebingen.de



SCHOOL OF MEDICINE
CASE WESTERN RESERVE
UNIVERSITY

Cardiac/Renal Biology

The Department of Physiology and Biophysics at Case Western Reserve University School of Medicine seeks a Cardiac or Renal Physiologist at the rank of Assistant, Associate or Full Professor. Applicants must have a Ph.D., M.D. or equivalent degree and demonstrated academic excellence appropriate for career stage. Individuals seeking appointment at the Assistant Professor level must have at least 3 years of postdoctoral experience, a strong record of scholarly activity and evidence of academic potential are required. Candidates for Associate Professor should have a considerable publication record, evidence of an international reputation and a demonstrated ability to renew funding. For appointment at the Professor level substantial evidence of leadership in the applicant's academic field, outstanding productivity and a sustained funding history are required. Rank will be commensurate with experience.

The successful applicant will have demonstrated academic excellence appropriate for career stage and be expected to develop or continue a robust extramurally-funded research program in the field of cardiac or renal physiology that compliments current programs within the department. Any area of cardiac and renal physiology will be considered, however, we particularly encourage applicants with expertise in the areas of cellular and molecular mechanisms of cardiac muscle contraction, genetics of cardiovascular disease, cardiac electrophysiology and arrhythmias, cardiac regeneration, heart failure, renal pH regulation, molecular mechanisms of renal calcium transport, role of the kidney in blood pressure regulation and molecular and cellular mechanisms of ion transport.

The Department of Physiology and Biophysics includes 18 primary and 32 secondary faculty members. The department has a strong record of cardiac and renal research and faculty members are part of both the Case Western Reserve University Cardiovascular Research Institute and the Kidney Research Center.

Interested candidates should send an electronic application that includes a cover letter, complete curriculum vitae including funding history, a one-page summary of research interests and the names and contact information for four references to: CardioRenalSearch@case.edu.

"In employment, as in education, Case Western Reserve University is committed to Equal Opportunity and Diversity. Women, veterans, members of underrepresented minority groups, and individuals with disabilities are encouraged to apply."

"Case Western Reserve University provides reasonable accommodations to applicants with disabilities. Applicants requiring a reasonable accommodation for any part of the application and hiring process should contact the Office of Inclusion, Diversity and Equal Opportunity at 216-368-8877 to request a reasonable accommodation. Determinations as to granting reasonable accommodations for any applicant will be made on a case-by-case basis."



宁波大学
NINGBO UNIVERSITY



**Ningbo University
invites you
to apply for faculty positions**

About Ningbo University

Founded in 1986 by Sir Yue-Kong Pao and autographed the name by Deng Xiaoping, Ningbo University (NBU) is a young and dynamic university located in the beautiful city of Ningbo by East China Sea, with five campuses covering 160 hectares of land. As a leading comprehensive university in Zhejiang Province, NBU offers programs in economics, law, education, liberal arts, history, science, engineering, agriculture, medicine, and management. The university now receives public funding, as well as continuous support and generous donations from many overseas Chinese and their families including Sir Yue-Kong Pao, Sir Run-Run Shaw, Chao An Chung, Hans Tang, Yue-shu Pao, Cao Guangbiao, Li Dasha, Zhu Xiushan, etc.

Academic Excellence

NBU consists of 22 faculties and offers 75 undergraduate programs, 116 master programs, and 12 Ph.D. programs. It enrolls 31,645 students including 26,527 full-time undergraduates and 5,118 graduate students. Currently NBU has around 1,400 full-time faculty members and 1,000 administrative staff members. Among them there are 5 academicians, 284 full professors, and 721 associate professors.

Research Achievements

With 77 research institutes and 14 key laboratories, NBU is the center of varieties of research and teaching activities. The research and development initiatives of the university, especially in marine science, information science and technology, engineering mechanics, and material science have contributed greatly to the economic development of the region and have been recognized by numerous national awards. The university library has a CNKI Network Administrative Service Center, and a collection of approximately 1,700,000 books and 11500GB digital resources.

International Programs

NBU maintains close links to 47 well-known institutions of higher education in Canada, Germany, France, Great Britain, USA, Sweden, Japan, South Korea and Australia. For example, the Sino-Canada joint-educational program is welcomed by international students with 100% satisfaction.

QUALIFICATIONS

Candidates should at least have (a) a Ph.D. degree in a related discipline, (b) adequate teaching ability and a strong passion for teaching, (c) an outstanding research background and influential publication record in recent three years, and (d) an ability to conduct high-quality research and attract external funding.

REMUNERATION & CONDITIONS OF SERVICE

Salary offered will be commensurate with qualifications and experience. Remuneration package will be highly competitive. For applicants with titles of professor or associate professor, salary and housing compensation can be negotiated on the individual basis. For newly graduate PhD and Postdoctoral, initial appointment will be made on a fixed-term contract, with a housing compensation of 600,000 RMB upon fulfillment of the contract requirements. Re-engagement thereafter is subject to mutual agreement.

APPLICATION

Please submit completed application form, CV and cover letter via email to rsc@nbu.edu.cn. Application forms can be downloaded from <http://www.nbu.edu.cn/shizi>. Recruitment stays open until positions are filled unless otherwise specified. Please visit <http://rsc.nbu.edu.cn> for more details.

INFORMATION ON POSITIONS

SCHOOL OF MARINE SCIENCE

Professor/Associate Professor
Marine Biotechnology/ Marine Sciences/Medicinal Chemistry/ Ocean Engineering/Marine planning and remote sensing /Sea port and environmental ecology/Marine Geographic Information Science

Faculty of Electrical Engineering and Computer Science

Professor/ Associate Professor Wireless Communications / New Generation Communication Networks / Underwater Acoustic Communication / Multimedia Information Processing / Embedded Systems / Integrated Circuit Design / Electronic Design Automation / Database System / Big Data Processing / Software and Theory / Information Security / Mobile Computing / Graphics and Image processing / Power system and Its Automation / Power Electronics / Pattern recognition and Intelligent system / Sensor and Intelligent detection

FACULTY OF SCIENCE

Professor/Associate Professor/Assistant Professor
Condensed Matter
Physics/Microelectronics/Optoelectronics/Solar Cell
Department of Mathematics/Computational Mathematics/Probability and Statistics / Financial Mathematics

FACULTY OF MECHANICAL ENGINEERING AND MECHANICS

Professor/Associate Professor/Assistant Professor
Mechanics/Vehicle
Engineering/ Mechanical
Engineering/Industrial Design

INTERNATIONAL COLLEGE

Professor/Assistant Professor
Accounting

SCHOOL OF MATERIALS SCIENCE AND CHEMICAL ENGINEERING

Assistant/Associate/Full Professors
Polymer Science/Chemical Engineering/Materials Science

SCHOOL OF LAW

Professor/Associate Professor/Assistant Professor
Criminal Law/Criminal Procedure Law/Civil Procedure Law/Civil Law/Electronic Commerce Law

COLLEGE OF TEACHER EDUCATION

Professor/Associate Professor/Assistant Professor
Curriculum and Teaching Methodology/Higher Education/Preschool Education/Educational Economy and Management/Cognitive Psychology/Educational Psychology/Clinical Psychology/School Psychology/Experimental Psychology/Personality Psychology/Social Psychology/Management Psychology/Computer Graphics and Digital Image Processing/Electronic Music, Game Development/3D Animation and Game Development

FACULTY OF MARITIME AND TRANSPORTATION

Professor/Associate Professor/Assistant Professor
Department of Logistics and Transportation/Department of Maritime Technology/Department of Marine Engineering/Department of Naval Architecture and Ocean Engineering

FACULTY OF PHYSICAL EDUCATION

Assistant Professor
Sport Management/Sport Sociology/Human Movement/Sport Training/Sport Physiology

MEDICAL SCHOOL

Professor / Associate Professor
Mechanism And Prevention Of Alzheimer's Disease; Oncology; Genetics; Human Anatomy; Histology And Embryology; Cell Biology; Immunology; Microbiology; Parasitology; Analytical Chemistry; Occupational And Environmental Health; Toxicology

COLLEGE OF ARTS

Professor / Associate Professor / Assistant Professor
Performance Of All Areas, Musicology (Ethnomusicology), Music Composition
Art Design Of All Areas, Digital Arts, Fine Art, Art History, Art/Music Industry, Art/Music Therapy

SCHOOL OF ARCHITECTURE, CIVIL ENGINEERING AND ENVIRONMENT

Professor /Associate Professor /Assistant Professor
Architecture Design/Urban Design/ Urban Planning/Architecture Technology/Human Geography/ Physical Geography/Cartography and Geographic Information System/Environmental Technology/Applied Environmental Microbiology/ Civil Engineering/Engineering Management



The University of Science and Technology of Suzhou is Recruiting High-end Talents in Key Disciplines

Located in the south of Jiangsu Province and the middle of the Yangtze River Delta, Suzhou City sits with the neighbors of Shanghai Metropolitan and Zhejiang Province. Well known for its long history and rich culture, Suzhou was listed as one of the top cities livable in China in 2012.

The University of Science and Technology of Suzhou (USTS) is a comprehensive center of higher education situated in the center of the National High Tech Development Zone just to the west of Suzhou's Old Town. The USTS was established by Chinese central and Jiangsu local government after combining Suzhou Institute of Urban Construction and Environmental Protection (SIUCEP) and Suzhou Railway Teachers College (SRTC) in September 2001, and both of which were formed in early 1980's. It is now administrated primarily by Jiangsu government.

USTS provides well-established 58 programs at the baccalaureate in science, engineering, literature, history, philosophy, law, management, education, arts and economics etc. 15 and 55 of them are first- and second-level master programs. Three disciplines are selected as key disciplines in Jiangsu Province, including the Civil Engineering and Environmental Engineering (subject group), Urban & Rural Planning and Management, and Environment Functional Materials and Technology; It also has 4 key provincial disciplines in Civil Engineering, Urban and Rural Planning, World History, and Landscape Architecture. Additionally, USTS is home to 3 national level specialty disciplines, 6 provincial level specialties and 8 provincial key specialties. The university now has 5 provincial-level key laboratories, 2 provincial-level humanities and social sciences research bases and 9 provincial-level experimental teaching demonstration centers. It also has other excellent public service facilities and resources such as a provincial-level engineering center, a provincial-level technical service platform, a provincial-level colleges and universities social science study base, a university science park, and an enterprise academician workstation.

Our industry-oriented service will focus within Suzhou, covering the whole province and reaching the nation. USTS implements five strategies as "rejuvenating with talents, building with quality, prospering with specialty, promoting with services and harmonizing with culture." Accordingly, it is striving to make itself a base for bringing up high quality applied talents, high-level applied research, top policy-making consulting and high grade culture development serving for the local and industrial development. USTS is endeavoring to develop itself to be a high level local university in the near future with distinctive characteristics in school operation, with a growing national reputation, with significant influence in Jiangsu Province and with a leading position among similar universities in China.

I. Talent Requirements

Positions are available for the following university's leading disciplines in Architecture, Urban and Rural Planning, Landscape Architecture, Environmental Science and Engineering, Municipal Engineering, Civil Engineering, Material Science and Engineering, Public Management, History and other related disciplines and specialties ("talent" is official Chinese parlance for individuals with proven exceptionality in their respective fields). Requirements for these positions are as follows:

1. Minimum of two consecutive years of working experience as an associate professor or equivalent in well-known overseas universities or research institutions following receiving his/her Ph.D. abroad (or four plus years of working experience overseas following receiving his/her Ph.D. in China).
2. Age of under 50 is preferable, but flexible for candidates with outstanding overseas experience.
3. Capable of grasping the trends and directions of development in the his/her field of the discipline, developing a fundamental, strategic and prospective research program, securing funding for undertaking significant science and technology research projects from the national government in accordance with the strategic needs of the country and the international scientific and technological fronts.
4. Having a well-established research record in the field of the discipline, which is internationally-recognized, such as published articles in influential academic journals, mastered key technologies and important patents, etc.
5. Capable of leading a research team to carry out scientific researches comparable international levels of excellence and achieving scientific research progress drawing attention from peers domestic and abroad.
6. Actively cultivating young faculty, promoting international academic exchange, and conducting productive collaborative researches with related organizations in China and abroad.
7. Scrupulously abiding by academic morality, professional ethic moral integrity and rigorous scholarship.

II. Level of Talents

1. Level A: Candidates to be nominated as a member of the Chinese Academic of Sciences.
2. Level B: Distinguished professors selected by "1000 Talent Plan" and "Changjiang Scholars Program", or the national Outstanding Youth Science Foundation.

III. Salaries and Benefits

1. The salary for Level A talents will be negotiated on a case-by-case basis. An annual salary of ¥1,000,000 Yuan (RMB) is offered for Level B Talents.
2. An apartment of 135-240 m² will be provided, the property right of which can be transferred to the talent after the completion of the employment term. An appropriate sum to move will also be provided.
3. A start fund of ¥500,000 Yuan (RMB) to 1,000,000 Yuan (RMB) will be provided for scientific research.
4. Can form a research team with assigned personnel or with autonomously recruited personnel.
5. Office and research space will be provided.
6. Residential matters, visa affairs, settling and children's school admission can be settled properly, job position for spouse can also be arranged, as well as benefits including insurance and medical care will be offered in accordance with relevant regulations of the official policies.
7. The university actively assists top talents when they apply for national and provincial talent projects, and the winners can enjoy simultaneously the fund and correlated benefits offered by both the central and local government.

IV. Contacts

USTS home page: <http://web.usts.edu.cn>

Mailing Address: High Level Talent Office, University of Science and Technology of Suzhou (No. 1 Kerui Road, High-Tech Zone, Suzhou, Jiangsu Province, China, 215009)

Post Code: 215009

Telephone Number: 86-0512-68090233, 86-0512-68092996

Email: grb@mail.usts.edu.cn

Contact Persons: Ms. Zhang, Ms. Cheng

Welcome you to join us for a brighter future!



LABORATORY FOR LASER PLASMAS
SHANGHAI JIAO TONG UNIVERSITY

Multiple Faculty Positions in Lasers, Plasma Physics, and Ultrafast Science

Laboratory for Laser Plasmas, Shanghai Jiao Tong University

The Laboratory for Laser Plasmas at Shanghai Jiao Tong University, founded in 2010, has been becoming a world-renowned research base for laser plasma theory, simulations and experiments, high-intensity laser technology, ultrafast science, and microtarget fabrication, which are applied to fundamental high energy density physics, ultrafast electron microscopy, laser-plasma based particle beams and radiation sources, etc. The Laboratory has established a series of state-of-the-art facilities from high power ultrafast laser systems to high space-time-resolution diagnostic systems.

Aiming at continuous innovation, we are now seeking outstanding scholars in relevant fields to join us. Candidates are expected to hold a Ph.D. degree, preferably with postdoctoral experience, a strong record of academic accomplishments, and with expertise either in high power laser technology, or laser-plasma interaction and applications, or ultrafast science, or high performance computation and visualization of plasma physics. The successful candidates will be expected to develop world-class research programs. The University will provide attractive annual salary, start-up fund, housing allowance together with other benefits from the Laboratory.

All applicants should send a cover letter, a curriculum vitae with a publication list, a research proposal (3-4 pages) and a statement of teaching interest in a single pdf file by August 31, 2015 to Ms. Dan Zhang, Shanghai Jiao Tong University, Shanghai 200240, China, through e-mail to: laser_plasma@sjtu.edu.cn. Please also arrange three reference letters directly to the above e-mail address. Applications after the deadline could be reviewed until the positions are filled.

<http://join.sjtu.edu.cn/>



苏州大学
SOOCHOW UNIVERSITY

**Research Positions open
at Soochow University**

Soochow University, founded in 1900 in Suzhou, is a premier research university in clinical and basic hematology with wide international recognized program in immunology, leukemia and blood and marrow transplantation. With newly established Soochow Institute of Blood and Marrow Transplantation (SIBMT) and substantial funding from Jiangsu government and Soochow University, a major expansion of its research programs is under way.

We are seeking outstanding scientists in the areas of **immunology and malignant hematological disorders, biology of hematopoietic stem cells, blood and marrow transplantation** for Associate Professor and Professor positions. Candidates with strong background in immunology, molecular biology, and animal models are encouraged to apply. Candidates should have a Ph.D. or M.D., splendid track records of scientific achievements, the ability to develop independent research projects and strong interests in translational research. Our institute is dedicated to build a state-of-the-art research platform, offer large collections of clinical samples. Successful candidates will be provided with generous start-up funds and relocation packages and competitive salaries/benefits.

Please send your curriculum vitae, a statement of research interests and accomplishments, future research plans and a list of three references to:

Dr. Depei Wu (wudepei@medmail.com.cn) at the first affiliated hospital of Soochow University, 188# Shizi Street, Suzhou, 215006, China.

USTC —

University of **S**cience and **T**echnology of **C**hina,
offering unlimited space for passionate talents and minds,
rising to be a world leader in science and technology.

Still aspiring to reach new career heights, but frustrated with
current settings (shortages in space, fundings, students...)?



Join us at USTC to realize your new dreams in science.

Find out more at <http://employment.ustc.edu.cn>



Director, Center for Vaccine Research University of Pittsburgh

The University of Pittsburgh is seeking applications for the position of director, Center for Vaccine Research (CVR). This interdepartmental center is dedicated to important research on novel vaccines and highly pathogenic/select agents. The center includes the 15,000-square-foot Vaccine Research Laboratory (VRL) and the Regional Biocontainment Laboratory (RBL), with 10 fully equipped BSL-3 laboratories and four fully equipped ABSL-3 facilities, a necropsy suite, a Clinical Imaging Core (including coupled micro-PET and CT, IVIS Spectrum imaging, and live-cell microscopy), and an Aerobiology Core for computerized quantitative aerosol exposure in animal models.

The CVR faculty includes 12 highly accomplished individuals who are accustomed to working in the center's collaborative environment. Research in the center involves complementary investigations of basic immunology and pathogenesis of infectious diseases and the application of accumulated knowledge to the development of novel human vaccine strategies. The CVR research portfolio totals more than \$30 million in multiyear grants and contracts from NIH, industry, and DoD. Program activity covers diverse viral and bacterial pathogens including studies of equine encephalitic viruses, chikungunya virus, yellow fever virus, Rift Valley fever virus, dengue virus, human and simian immunodeficiency viruses, *Francisella tularensis*, and *Mycobacterium tuberculosis*. The current CVR operating budget is approximately \$10 million. Learn more about the important work taking place at the CVR by visiting: www.cvr.pitt.edu.

Competitive candidates must have a track record of exceptional research in vaccine development or infectious disease pathogenesis and must meet the requirements for the appointment of the academic rank of full professor with tenure. Other key characteristics include a broad vision for new vaccine research, ability to foster collaborations, and significant administrative and leadership experience.

With more than \$400 million of NIH funding, the University of Pittsburgh ranks fifth among more than 3,000 entities that receive NIH support. The University's Schools of the Health Sciences include the Schools of Medicine, Nursing, Dental Medicine, Pharmacy, Health and Rehabilitation Sciences, and the Graduate School of Public Health. The schools serve as the academic partner of UPMC (University of Pittsburgh Medical Center), a global health system with 23 hospitals, more than 60,000 employees, and close to \$11 billion of annual revenue.

The University of Pittsburgh is an Affirmative Action, Equal Opportunity Employer.

Please send curriculum vitae and a letter outlining interest and qualifications to: **Chair, CVR Search Committee, Res Pav 1.9, Hillman Cancer Center, 5117 Centre Avenue, Pittsburgh, PA 15213** or email: DIRofCVR@pitt.edu. To ensure full consideration, materials must be received by **August 15, 2015**.

Empire Scholar Position in the Neurosciences

SUNY Upstate Medical University seeks a neuroscientist at the Associate/Full Professor level to fill a tenured position as part of the New York State Empire Innovator Program, which aims to expand the ranks of world-class faculty in the SUNY system. Research should focus on studying the mechanisms of neurological function, disease, and dysfunction at the cellular, molecular or systems levels. Areas of particular interest that would synergize with existing strengths include, but are not limited to vision, addiction biology, psychiatric genetics, neurological disorders, neurodegenerative diseases, neuro-oncology, and neurodevelopmental disorders. Candidates using stem cell biology, biomarker development, cross-disciplinary translational research, behavioral methods or cutting-edge optical approaches are especially encouraged to apply.

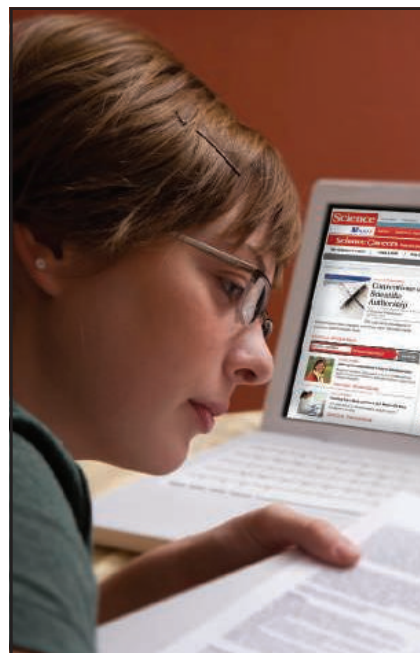
The successful candidate will join a growing team of collaborative and interdisciplinary neuroscientists in Central New York at Upstate Medical University, neighboring Syracuse University, the Syracuse Veterans Hospital, and nearby Cornell and Binghamton Universities. The position is open to individual applicants or to established research teams. Current external research funding is required. Successful candidates will hold joint appointments in a basic science and one of several clinical departments, and will be expected to maintain a vigorous and independently funded research program.

SUNY Upstate offers a highly competitive hard-money state-line salary, a generous start-up package supplemented by contributions from the New York State Empire Innovation fund and access to a unique, integrated clinical-basic science research environment. Neuroscientists at Upstate benefit from a new research building containing 100,000 sq. ft. of laboratory space equipped with state-of-the-art research facilities and research cores that support sophisticated imaging capabilities including deep brain imaging, super-resolution microscopy, and whole genome sequencing and analysis to name a few.

Applicants should submit a cover letter, curriculum vitae and statement of research interests by August 31, 2015 to eisearch@upstate.edu. Applications will be evaluated as they are received and until the position is filled.

UPSTATE
MEDICAL UNIVERSITY

Upstate Medical University is an Equal Opportunity Employer with a strong commitment to diversity and urges members of underrepresented groups to apply.



AAAS is here – helping scientists achieve career success.

Every month, over 400,000 students and scientists visit ScienceCareers.org in search of the information, advice, and opportunities they need to take the next step in their careers.

A complete career resource, free to the public, *Science Careers* offers a suite of tools and services developed specifically for scientists. With hundreds of career development articles, webinars and downloadable booklets filled with practical advice, a community forum providing answers to career questions, and thousands of job listings in academia, government, and industry, *Science Careers* has helped countless individuals prepare themselves for successful careers.

As a AAAS member, your dues help AAAS make this service freely available to the scientific community. If you're not a member, join us. Together we can make a difference.

To learn more, visit
aaas.org/plusyou/sciencecareers



Faculty Position in Atomic, Molecular and Optical (AMO) Physics at Ecole polytechnique fédérale de Lausanne (EPFL)

The EPFL School of Basic Sciences anticipates making a tenure-track faculty appointment in atomic, molecular and optical (AMO) physics at the level of assistant professor. We seek a candidate with the ability to build a strong, independent, experimental research program at the frontiers of AMO physics in a broadly defined sense, ranging from cold-atom physics to solid state quantum systems. The file of the successful candidate will be submitted to the Sandoz Foundation for the funding of the first four years of the chair.

An excellent track record of research in AMO physics is required. The successful applicant is expected to establish and manage an internationally recognized research program in his/her field of activity and be committed to excellence in teaching physics at both the undergraduate and graduate levels.

We offer internationally competitive salaries, benefits, and start-up resources for scientific equipment, as well as annual resources for PhD students, staff and consumables.

Applications including a motivation letter, curriculum vitae, publication list, statement of research plans and teaching interests, as

well as the names and addresses (including email) of at least five references should be submitted in PDF format via the web site :

<https://academicjobsonline.org/ajo/jobs/5618>

by **September 8, 2015**.

For additional information, please contact :

Professor Benoît Deveaud (benoit.deveaud@epfl.ch) or consult the following websites:

www.epfl.ch, sb.epfl.ch and itp.epfl.ch

The EPFL School of Basic Sciences aims for a strong presence of women amongst its faculty, and qualified female candidates are encouraged to apply.

Full Professor (W3) in Macromolecular Matter and Systems

as a joint appointment of the Faculty of Mathematics, Computer Science and Natural Sciences of RWTH Aachen University and the DWI – Leibniz-Institute for Interactive Materials.

We are seeking qualified applicants for a research-focused professorship in the area of Macromolecular and Soft Matter Sciences and as a member of the scientific board of the DWI. The starting date is fall 2015 / spring 2016. Recognized expertise in physics and / or chemistry of macromolecules and soft matter nanoscience is essential. Experience in the management of a larger research group or institute is particularly welcome.

A Ph.D. degree and postdoctoral research and lecturing qualification are requested; an exemplary record of research achievement as an assistant / an associate / a junior professor or university researcher and/or an outstanding career outside academia are highly desirable. Ability in and commitment to teaching within the curriculum of Macromolecular Chemistry are required. German is not necessary to begin but will be expected as a teaching language within the first 5 years.

Please send a cover letter stating research aims, a CV as well as a documentation of your research and teaching activities to the **Dean of the Faculty of Mathematics, Computer Science and Natural Sciences of RWTH Aachen University, Prof. Dr. Stefan Schael, 52056 Aachen, Germany**. The deadline for applications is **August 24, 2015**.

RWTH Aachen University is certified as a family-friendly university and offers a dual career program for partner hiring. RWTH Aachen University and the Leibniz-Gemeinschaft particularly welcome and encourage applications from women, disabled people and ethnic minority groups, recognizing they are underrepresented across RWTH Aachen University. The principles of fair and open competition apply and appointments will be made on merit.



Senior Scientist

NewLink Genetics is a biopharmaceutical company focused on discovering, developing and commercializing novel immuno-oncology products to improve treatment options for patients with cancer. NewLink's portfolio includes biologic and small molecule immunotherapy product candidates intended to treat a wide range of oncology indications.

NewLink's product candidates are designed to harness multiple components of the immune system to combat cancer without significant incremental toxicity, either as a monotherapy or in combination with other treatment regimens.

NewLink is currently searching for a **Senior Scientist** to lead activities to analyze pre-clinical and clinical samples and elucidate the effector pathways of NewLink's scientific portfolio.

For more information on this and other great career opportunities, please visit our Career Page at: www.newlinkgenetics.com/careers

NewLink Genetics is an Equal Opportunity/Affirmative Action Employer. We provide equal employment opportunities to all qualified employees and applicants for employment without regard to race, religion, sex, age, marital status, national origin, sexual orientation, citizenship status, veteran status, disability or any other legally protected status. We prohibit discrimination in decisions concerning recruitment, hiring, compensation, benefits, training, termination, promotions, or any other condition of employment or career development.



VICE PRESIDENT FOR RESEARCH

The University of Cincinnati, a growing and vibrant global research University invites nominations and applications in search of our next Vice President for Research. This individual will play an essential role in the central leadership of the University's research, scholarly and creative programs to facilitate and direct the University's research and discovery initiatives. The University invites letters of nomination, applications (letter of interest, full resume/CV, and contact information of at least five references), or expressions of interest to be submitted to the search firm assisting the University at the email address below. Nominations and applications submitted prior to **August 5, 2015** are preferred; however review of materials will begin immediately and continue until the appointment is made. For a complete position description, please visit http://www.uc.edu/president/priorities/search/search_vp-research.html

Send application materials to:

Porsha L. Williams (pwilliams@parkersearch.com)
770-804-1996 ext: 109

The University of Cincinnati is an Equal Opportunity, Affirmative Action Employer. Ohio law provides that public records, which would include certain search materials such as nominations and applications, be open to the public and the press. Ohio Revised Code Sec. 149.43.

Notice of Nondiscrimination -

<http://www.uc.edu/about/policies/non-discrimination.html>



JAMSTEC

<http://www.jamstec.go.jp/e/>

FY2016 Recruitment of Postdoctoral Fellows

The Japan Agency for Marine-Earth Science and Technology (JAMSTEC) wants to help talented young researchers who have completed promising Ph.D. theses to develop their scientific excellence in the fields of ocean and earth sciences. For this purpose, JAMSTEC has established an international postdoctoral fellowship programme. It is intended that research grants will be provided to successful applicants, which will enable them to work independently on research topics of their choosing: ¥1,000,000 for the first fiscal year and ¥500,000 for each of the second and third years. During the contract period, they will have access to the necessary facilities and equipment at JAMSTEC.

Successful applicants are expected to join our institutes on April 1, 2016 in Yokosuka, Yokohama, Kochi, or Mutsu, Japan.

Required documents must be sent to JAMSTEC by **POST** on or before **July 21, 2015**.

For further information, please visit our website:
<http://www.jamstec.go.jp/e/about/recruit/>



MAX PLANCK GESELLSCHAFT



The Max Planck Society (MPS), the Centro Interdisciplinario de Neurociencia de Valparaíso (CINV), and the Universidad de Valparaíso (UV) intend to establish two independent

MAX PLANCK TANDEM GROUPS IN NEUROSCIENCE RESEARCH

We are seeking candidates for the position of the Principal investigator (PI), with the title of MAX PLANCK TANDEM GROUP LEADER (MPTGL) at the Centro Interdisciplinario de Neurociencia de Valparaíso (CINV) in Valparaíso, Chile. The candidate must be at the beginning of a successful scientific career in the area of **Neurosciences and Computational Neurobiology** with postdoctoral experience, and be highly motivated to develop and carry out a competitive research program on the international level.

Other than the research activities, responsibilities include the supervision of postdocs, students and technicians, and high-level publications. Solid, sustainable ties of collaboration will be developed between the Tandem Groups within their host institution and other universities and research institutes in Chile, and the Max Planck Institutes that are part of the Agreement.

The salary of the position is highly competitive according to local standards. Additional funds will be allocated for staff, supplies and research equipment. The successful candidate will be appointed initially for 5 years with the possibility of two year extension following an outstanding independent external evaluation.

The MPG, CINV and UV seek to increase the number of women in those areas where they are under-represented and therefore explicitly encourage women to apply.

Applications, including a curriculum vitae, list of publications, reprints of three selected papers, a two-page description of scientific achievements, a two-page research plan and three letters of recommendation should be sent electronically as one pdf file to: research.leaders@cinv.cl

Deadline for registration is July 31st 2015. Short-listed candidates will be invited to a selection symposium in Valparaíso, Chile, on November 18th-20th, 2015, at which they will have the opportunity to present their research. For further information and detailed instructions, see <https://cinv.uv.cl/research-leaders>



ASSOCIATE SCIENTIST/ASSISTANT PROFESSOR CHILDREN'S HEALTH RESEARCH CENTER

The Children's Health Research Center (CHRC, Sioux Falls, SD <http://www.sanfordresearch.org/researchcenters/childrenshealth/>), invites applications from researchers for full time faculty at the rank of Associate Scientist within Sanford Research (<http://www.sanfordresearch.org/>) with commensurate rank of Assistant Professor in the Department of Pediatrics of the Sanford School of Medicine at The University of South Dakota. An historic \$400 million gift by philanthropist Denny Sanford has allowed for expansion of Sanford Research and development of the CHRC, an energetic and collegial research community focused on pediatric research.

We seek outstanding scientists with research programs on the underlying mechanisms and/or treatment of congenital defects, developmental disorders, and pediatric diseases. Applicants should hold a PhD, MD or MD/PhD degree and complement the existing strengths and the interdisciplinary and collaborative nature of the CHRC. Candidates will be expected to develop independent research programs with extramural funding. Significant institutional support, including modern laboratory space and state-of-the-art facilities, will be provided at the Sanford Center. In addition, a comprehensive compensation package will be tailored to the individual's qualifications.

Sanford Health is an Equal Opportunity/Affirmative Action Employer. Candidates should submit a single PDF including a detailed *curriculum vitae*, description of research experience and future research plans with specific details on the relevance of their research to pediatric research. Candidates should also submit at least three letters of recommendation. Incomplete candidate packages will not be accepted. All application materials should be sent by email to:

David A. Pearce, Ph.D.

**Director, Children's Health Research Center
Sanford Research**

Professor, Department of Pediatrics

Sanford School of Medicine of The University of South Dakota

2301 E. 60th Street North, Sioux Falls, SD 57104

Telephone: 605-312-6004 FAX: 605-312-6071

Email: researchrecruitment@sanfordhealth.org



Rat der
Eidgenössischen
Technischen
Hochschulen
ETH-Rat

Conseil des
écoles
polytechniques
fédérales
CEPF

Consiglio
dei
politecnici
federali
CPF

Board of the
Swiss Federal
Institutes of
Technology
ETH Board

The Ecole polytechnique fédérale de Lausanne (EPFL) stands for excellent teaching, pioneering fundamental research and the application of the results for the benefit of society. Together with ETH Zurich and the four federal research institutes PSI, WSL, Empa and Eawag, EPFL is part of the ETH Domain, whose strategic management and supervisory body is the ETH Board.

The ETH Board is advertising the position of

President of the Ecole polytechnique fédérale de Lausanne (EPFL)

The incumbent President will be stepping down at the end of 2016. The ETH Board will thus have to propose a successor to the Swiss government, the Federal Council.

Since its integration to the ETH Domain in 1969, EPFL has rapidly become one of the internationally top-ranked universities in the fields of technical and natural sciences as well as life sciences. Currently, more than 13'500 people are studying, working and carrying out research at EPFL. Outstanding research conditions, state-of-the-art infrastructure, an entrepreneurial atmosphere, and an attractive environment provide an ideal setting for creative personalities.

Requirements

The successful candidate must have an excellent international reputation in the exact, natural or engineering sciences. She/he is able to identify and foster outstanding potential and visionary ideas, specify strategic guidelines and address issues in current scientific, technological and societal domains. She/he is committed to excellence in education. Ideally, the successful candidate is an experienced leader in a large organisation, preferably in the field of academics or industry, and has provided evidence of her/his participative management skills and fund-raising abilities. She/he has good networks inside and outside the scientific community and is ready to develop EPFL's future and help shape the entire ETH Domain.

The successful candidate's personality is characterised by a high degree of social competence, assertiveness and the ability to deal with conflict. She/he possesses excellent communication and negotiation skills, which she/he uses both inside and outside the university. She/he is willing to engage with Switzerland's political structures and legislative processes and appreciates its cultural diversity. Finally, the candidate has a very good command of French and English, and preferably knowledge of German.

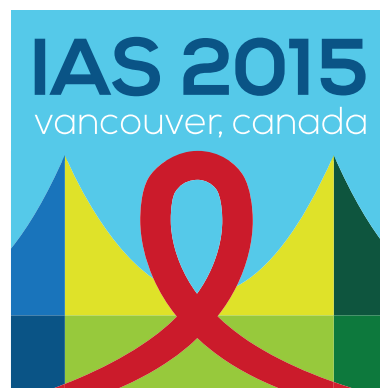
We are looking for a candidate willing to hold office for at least two terms (i.e. eight years) and who could start at the beginning of 2017.

Applications

Applications from women are particularly welcome.

Complete applications (CV and motivation letter) must be sent by July 31, 2015, to the President of the ETH Board, Dr. iur. Fritz Schiesser, ETH-Rat, Haldeliweg 15, CH-8092 Zurich, Switzerland. He will also be available for further information (phone +41 44 632 20 01, schiesser@ethrat.ch). All applications will be treated with strict confidentiality.

MEETINGS



8th IAS Conference on HIV Pathogenesis,
Treatment & Prevention 19-22 July 2015

IAS2015.ORG

Register for IAS 2015!

The IAS 2015 conference programme is shaping up to be one of our strongest ever, and will feature ground-breaking presentations from top investigators covering four conference tracks: Basic Science; Clinical Science; Prevention Science; and Implementation Research. Topics that will be covered include:

- Exploring promising pathways to an HIV vaccine and a cure
- Implementing PrEP and other biomedical interventions
- Optimizing outcomes along the HIV care continuum
- Confronting the dual challenges of HIV co-infections and co-morbidities
- Advancing our understanding of the impact of HIV on key populations

We hope to see you in Vancouver, and to making IAS 2015 our most productive meeting yet!

The 8th biennial IAS Conference on HIV Pathogenesis, Treatment and Prevention (19-22 July, Vancouver, British Columbia) is the largest scientific meeting on HIV. IAS 2015 will bring together a broad cross section of more than 6,000 HIV professionals from around the world, with a focus on moving science into practice. For more information and to register, visit:

www.ias2015.org

POSITIONS OPEN

BIOMEDICAL FACULTY POSITION University of Wisconsin-Madison

The Department of Comparative Biosciences, School of Veterinary Medicine invites applications for Tenure-Track Faculty Position (**ASSISTANT/ASSOCIATE PROFESSOR**). Qualifications include Ph.D. (or DVM/M.D.), postdoctoral experience, ability to develop an extramurally funded research program, and commitment to teaching excellence. Research area is open, but preference will be given to those complementing department strengths including but not limited to: muscle biology, neuroscience, reproductive, developmental or cancer biology, epigenetics, or other biological stress responses (such as inflammation and oxidative stress). Teaching responsibilities based on expertise may include Neuroscience, Physiology, Toxicology, Small Animal Anatomy, or Pharmacology. Send curriculum vitae, brief statements of research interests and teaching philosophies, and three letters of reference in response to PVL 83170 to: **Dr. Jyoti Watters, Search Committee Chair, Department of Comparative Biosciences, University of Wisconsin, 2015 Linden Dr., Madison, WI, 53706** at e-mail: cbs_admin@vetmed.wisc.edu Apply by August 15, 2015. For additional information, see website: <http://www.vetmed.wisc.edu/about-the-school/employment/current-searches/> *Equal Opportunity/Affirmative Action Employer.*

CRANIOMAXILLOFACIAL RESEARCH SCIENTIST, DB-0601-03

The United States Army Institute of Surgical Research (USAISR) has an opening for a Craniomaxillofacial Research Scientist in the Dental and Trauma Research Detachment. The position is to serve as **PRINCIPAL INVESTIGATOR** leading efforts to expand the current craniomaxillofacial bone restoration program for the development of therapeutic products that can be rapidly transitioned to the clinic for treating craniomaxillofacial battle injuries. This position is located in Fort Sam Houston, San Antonio, Texas.

For information about this current vacancy and instructions on how to apply, go to website: <https://www.usajobs.gov/GetJob/PrintPreview/405945000>. The vacancy announcement closes on **14 August 2015**.

For more information please contact **Dr. Kai Leung** at e-mail: kai.p.leung.civ@mail.mil.

USAISR is an Equal Opportunity/Affirmative Action Employer.

GRADUATE STUDENT AND POSTDOCTORAL OPENINGS at The Pennsylvania State University

The Penn State Acoustofluidics Group (website: <http://www.esm.psu.edu/huang/>) is inviting the most motivated, talented postdoc and Ph.D. student candidates to join us. We conduct research at the interface of acoustics, micro/nano technology, and biomedicine. We are interested in candidates with expertise in one of the following fields: Acoustics, Analytical Chemistry, Physics, Biochemistry, Optics, Mechanical Engineering, Biomedical Engineering, Electrical Engineering, Chemical Engineering, Material Science, Chemistry, Biology, or Medicine. Highly-qualified applicants should send to **Prof. Tony Huang** (e-mail: junhuang@psu.edu) the following three documents: (1) curriculum vitae; (2) names and contact information for 3–5 professors who know you; and (3) one short write-up (no more than one page) justifying why you can contribute to our research on acoustofluidics (the fusion of acoustics and fluid mechanics for biomedical applications) and/or microbioacoustics (the fusion of acoustics and micro/nano technology for biomedical applications) and how you will contribute (e.g., what kind of research you would do once you join us).

Post Your Jobs

1 million candidates*
151,000 job applications*

Science Careers

employers.sciencereaders.org



Reach Scientists.
Fill Positions.

* Jan–Dec 2014

Advance
your career
with expert
advice from
**Science
Careers.**



Download Free Career Advice Booklets!
ScienceCareers.org/booklets

Featured Topics:

- Networking
- Industry or Academia
- Job Searching
- Non-Bench Careers
- And More

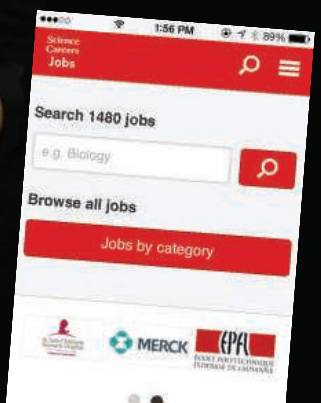


Science Careers

FROM THE JOURNAL SCIENCE

Download the Science Careers jobs app from Science

Jobs are updated 24/7
Search thousands of jobs
on your schedule
Receive push notifications
per your job search criteria



Get a job on the go.

Search worldwide for thousands of scientific jobs in academia, industry, and government. The application process is seamless, linking you directly to job postings from your customized push notifications.



Scan this code to
download app or visit
apps.sciencemag.org
for information.

Science Careers | AAAS
FROM THE JOURNAL SCIENCE

ScienceCareers.org




Assistant Professor in the Energy Cluster

As part of a larger investment to create a new Center for Energy Research, the School of Arts and Sciences at the University of Pennsylvania seeks to add faculty to our newly formed Energy Cluster spanning the natural sciences. Following a first hire in Chemistry, we now invite applications for tenure-track assistant professor whose primary research and teaching affiliation will be in one of the following departments: Biology, Earth and Environmental Science, or Physics & Astronomy. Exceptional senior candidates will be given consideration. The successful candidate will mount an innovative program of fundamental scientific research with impact on our societal energy challenges, and in doing so will forge collaborative links with Penn scientists and engineers involved in energy research.

Applicants must apply online at <http://facultysearches.provost.upenn.edu/postings/590>. Required application materials include: curriculum vitae with a list of publications, and a research and teaching statement that includes the candidate's perspective on how she or he fits into one of the three departments and identifies potential collaborative links with other natural science departments. Applicants should also submit the names and contact information for three individuals who will provide letters of recommendation. Review of applications will begin no later than **September 1st, 2015** and will continue as long as the position remains open. The School of Arts and Sciences is strongly committed to Penn's Action Plan for Faculty Diversity and Excellence and to establishing a more diverse faculty (for more information see: <http://www.upenn.edu/almanac/volumes/v58/n02/diversityplan.html>).

*The University of Pennsylvania is an EOE. Minorities/Women/
Individuals with disabilities/Protected Veterans
are encouraged to apply.*



Special Job Focus:

Immunology

July 10, 2015

Reserve space by June 23*

— THERE'S A SCIENCE TO REACHING SCIENTISTS. —

For recruitment in science, there's only one **Science**

Why choose this immunology section for your advertisement?

- Relevant ads lead off the career section with special Immunology banner
- Bonus distribution to:
 - 8th International AIDS Society (IAS) Conference
19–22 July, Vancouver, British Columbia, Canada
 - Malaria
25–26 July, Girona, Spain.

* Ads accepted until July 6 on a first-come, first-served basis.

SCIENCECAREERS.ORG

To book your ad: advertise@sciencecareers.org

The Americas: 202-326-6582
Japan: +81-3-3219-5777

Europe/RoW: +44-0-1223-326500
China/Korea/Singapore/Taiwan: +86-186-0082-9345



Science Careers
FROM THE JOURNAL SCIENCE | AAAS

Do it for love

At the 65th Lindau Nobel Laureate Meeting, which takes place 28 June to 3 July in Germany, some 650 students and postdocs will mingle with 66 Nobel laureates and attend lectures, panel discussions, and master classes. One of those laureates is Richard J. Roberts, who won the 1993 Nobel Prize in physiology or medicine jointly with Phillip Sharp “for their discoveries of split genes.” In an interview with *Science Careers*, Roberts shared his thoughts on how to build a career in science. This interview was edited for brevity and clarity.

Q: What do you enjoy about science?

A: Science is my hobby as well as my profession. It is enormous fun. Just like every child, when I was young, I was very curious about everything around me. Fortunately, I managed to avoid having that knocked out of me while I was at school, and to this day, I take advantage of my curiosity to explore the life around me. As a result, I think about new things or make discoveries every day.

Q: What traits make a successful scientist?

A: A dogged persistence to solve any problem that comes along. An appreciation that many experiments fail, especially when working in a new field or in areas where we know rather little. I like it when experiments fail repeatedly because it usually means our basic hypothesis—and hence the axioms on which it is based—is wrong and nature is trying to tell us something. A discovery is waiting to be made.

Good scientists are always open to new hypotheses and experimental opportunities. Often, a new technique applied to an old problem will reveal new features that were not predicted—again an opportunity to make a discovery.

Successful scientists will also constantly be on the lookout for good problems to solve. They tend to be skeptical of explanations that seem too simplistic or not well supported by evidence.

Q: How did you move to an independent position?

A: During my postdoc at Harvard in Jack Strominger’s laboratory, I worked fairly independently but with excellent support when I needed it. This made it fairly easy to transition to an official independent position at Cold Spring Harbor Laboratory.



“I think about new things or make discoveries every day.”

Q: What is the right time to transition to independence?

A: As soon as possible. Researchers are easily at their most creative when they are young, because they have no fear. This makes it much easier to challenge dogma and take risks—both essential features of the creative process.

Q: Have you experienced self-doubt?

A: I think most scientists have self-doubt from time to time, but in general, the better ones have very little of it—or at least they don’t share it with others. I have always been fairly confident in my abilities and my

views, although as I get older, I do recognize that my abilities are less than they were when I was younger.

Q: What advice would you offer to those planning a career in scientific research?

A: Find an area that you are completely passionate about and focus on it single-mindedly. That doesn’t mean you can’t change if something more exciting comes along, but you will be happier and more successful if you love what you do. Almost all of biology is at a stage where we know a little, but nothing like as much as we will need to if we want to say we have a good understanding of life. I think bioinformatics is a growth area and absolutely fundamental to future studies of biology. Ultimately, almost everything we need to know about life will come from bioinformatic analysis of DNA sequence. We have to vastly improve our ability to predict function from sequence. ■

Marek Wagner, a postdoc at the University of Bergen in Norway, will be attending the 65th Lindau Nobel Laureate Meeting. For more on life and careers, visit ScienceCareers.org. Send your story to SciCareerEditor@aaas.org.